Engineering Materials and Processes

Jiyang Fan
Paul K. Chu

Silicon Carbide Nanostructures

Fabrication, Structure, and Properties

Springer

Engineering Materials and Processes

Series editor

Brian Derby, Manchester, UK

More information about this series at http://www.springer.com/series/4604

Jiyang Fan · Paul K. Chu

Silicon Carbide Nanostructures

Fabrication, Structure, and Properties

Springer

Jiyang Fan
Department of Physics
Southeast University
Nanjing
China

Paul K. Chu
Department of Physics and Materials Science
City University of Hong Kong
Hong Kong
China

ISSN 1619-0181
ISBN 978-3-319-08725-2 ISBN 978-3-319-08726-9 (eBook)
DOI 10.1007/978-3-319-08726-9

Library of Congress Control Number: 2014944324

Springer Cham Heidelberg New York Dordrecht London

Printed on acid-free paper

Springer is part of Springer Science+Business Media (www.springer.com)

Preface

Although nanostructured silicon carbide is rapidly evolving, the field is still in the infancy stage and full potential of the materials is far from being realized. This book provides the state of the art of the various nanostructures of wide bandgap silicon carbide including nanoparticles, nanowires, nanotubes, porous structures, nanostructured films, and other complex nanostructures. Topics covered in this book include the fabrication methods, polytypes, bulk and surface structures, electronic structures, properties especially electrical and optical ones, as well as potential applications. The target readership is graduate students and researchers in universities, research institutes, and companies working on SiC and related materials in the fields of materials science, physics, chemistry, electronic engineering, biomedical engineering, and biomedicine.

It is impossible to cover all the aspects of the materials in a single book and so our intention is to provide an up-to-date review of the relevant results and present a holistic view of this burgeoning field. As a self-contained monograph, Chap. 1 is the brief introduction and Chap. 2 describes the general properties of bulk silicon carbide in order to provide the necessary background to understand the properties of silicon carbide nanostructures. It covers the bulk structures, surface structures, defects, electronic structures, luminescence properties, infrared and Raman characteristics, as well as common polytypes and pertinent transformation. However, the application of silicon carbide to electronic devices is omitted because there are already several excellent books on this subject. Chapters 3 and 4 address the porous silicon carbide nanostructures and individual silicon carbide nanoparticles with emphasis on the complex relationship between the structure and luminescence properties and mechanisms. Chapters 5 and 6 describe silicon carbide nanowires and nanotubes concentrating on the synthesis, stacking fault defects, unique properties, and applications and Chap. 7 deals with common nanostructured silicon carbide films with focus on ones containing silicon carbide nanocrystals. In Chap. 8, the biological applications of silicon carbide nanostructures are discussed. Topics covered include biomorphic silicon carbide ceramics, biological imaging, and cytotoxicity evaluation.

We express our gratitude to our colleagues, Xinglong Wu, Shining Zhu, Min Xiao, Teng Qiu, Gaoshan Huang, Yimin Yang, and many others, for their cooperation and help. We acknowledge Springer Press, especially senior editor Anthony Doyle, and senior editorial assistants Simon Rees, Claire Protherough, Gabriella Anderson, and Sathya Subramaniam, for their encouragement and patience during the preparation of this book. We also thank our families for their tremendous support without which this book would not have been completed.

Nanjing, May 2014 Jiyang Fan
Hong Kong Paul K. Chu

Contents

1 Introduction 1

2 General Properties of Bulk SiC 7
2.1 SiC Polytypes 7
2.2 Interstellar Origin 9
2.3 Electronic Structures 13
2.4 Defects 17
2.4.1 Intrinsic Point Defects 17
2.4.2 Dislocations and Micropipes 35
2.4.3 Stacking Faults 37
2.4.4 Impurities 48
2.5 Lattice Vibration and Infrared/Raman Spectra 51
2.6 Absorption and Luminescence Properties 69
2.7 Surface Structures 83
2.7.1 Surface Reconstruction 84
2.7.2 SiC–SiO_2 Interface 91
2.7.3 Other Types of Surface Treatment 96
2.8 Polytypic Transformation 97
References 104

3 Porous SiC 115
3.1 Fabrication of Porous SiC by Various Etching Methods 115
3.2 Luminescence from Porous SiC 120
3.3 Sensing with Porous SiC 129
References 129

4 Separate SiC Nanoparticles 131
4.1 Fabrication and Luminescence Properties 131
4.1.1 Chemical Vapor Synthesis 132
4.1.2 Electrochemical/Chemical Etching and Quantum Confinement 136

4.1.3 Solution-Based Chemical Synthesis . . . 157
4.1.4 Laser Ablation Method . . . 159
4.1.5 Other Methods . . . 160
4.1.6 Silicon Carbide Nanospheres . . . 163
4.2 Surface Chemical Functionalization . . . 166
4.3 Theoretical Treatment . . . 169
4.4 Potential Applications . . . 174
4.4.1 Enhancement of Mechanical Properties . . . 174
4.4.2 Superconductivity Enhancement . . . 177
4.4.3 Surface Phonon Polariton and Luminescence Enhancement . . . 178
4.4.4 Electroluminescence and LED . . . 184
4.4.5 Other Applications . . . 186
References . . . 187

5 SiC Nanowires . . . 195
5.1 Synthesis and Optical Properties . . . 195
5.1.1 Vapor–Solid Growth . . . 195
5.1.2 Vapor–Liquid–Solid Growth . . . 202
5.2 Field Electron Emission . . . 216
5.3 Core–Shell Structures . . . 224
5.3.1 SiC/SiO_2 Core/Shell Nanowires . . . 224
5.3.2 Carbon-Coated SiC Nanowires . . . 230
5.3.3 BN-Coated SiC Nanowires . . . 232
5.4 Special Structures . . . 235
5.4.1 Bamboo-Like Structures . . . 235
5.4.2 Beaded Structures . . . 238
5.4.3 Other Periodic Structures . . . 242
5.4.4 Connected Structures . . . 243
5.4.5 Helical Structures . . . 248
5.4.6 Nanobelts . . . 248
5.4.7 Legs on Fibers . . . 251
5.5 Some Characteristics . . . 252
5.6 Theoretical Studies . . . 254
5.7 Applications . . . 258
References . . . 263

6 SiC Nanotubes . . . 271
6.1 Fabrication Using Templates . . . 271
6.1.1 Synthesis Using Carbon Nanotubes/Nanofibers . . . 272
6.1.2 Formation on Core Nanowires . . . 275
6.1.3 Other Templates . . . 277
6.2 Fabrication by Other Methods . . . 279

6.3 Theoretical Studies 280
6.3.1 Structural and Electronic Properties. 280
6.3.2 Adsorption of Small Molecules and Applications 289
6.4 Two-Dimensional SiC Sheets 291
References 292

7 SiC Nanostructured Films 295
7.1 Synthesis by Chemical Vapor Deposition 295
7.2 Fabrication by Ions Implantation 302
7.3 Fabrication by Sputtering 308
References 313

8 Biological Applications 317
8.1 Biomorphic SiC Ceramics 317
8.2 SiC as Implant Coatings 321
8.3 Biological Applications of SiC Nanostructures 322
8.3.1 SiC Nanoparticles 323
8.3.2 SiC Whiskers and Nanoporous Membranes 326
References 329

Chapter 1
Introduction

The constituents of the earth are simple in that there are only about 118 elements that make up all the materials around us. However, our world is also very complex because almost unlimited types of matters (especially crystals and molecules) can be formed by combining these elements in different structural arrangements. In this respect, silicon carbide is unique as it has over two hundred crystalline forms and some polytypes of silicon carbide have been identified from presolar grains in meteorites. Silicon carbide is a wide bandgap semiconductor with excellent electronic characteristics that bode well for application to high-temperature, high-frequency, and high-power electronic devices. Moreover, silicon carbide is a superhard ceramic having a small density as well as superior thermal and mechanical properties. It is environmentally friendly and biocompatible thus having many potential applications in energy area, biomedical engineering, and medicine. Last but not least, both silicon and carbon are abundant on earth and SiC can be produced economically, a big advantage compared to materials composed of noble metals and rare-earth elements.

On the heels on the rapid development of nanoscience and nanotechnology, researchers have been intrigued by the different types of silicon carbide nanostructures and their diverse applications. Many silicon carbide nanostructures ranging from quasi zero-dimensional quantum dots to one-dimensional nanowires and nanotubes as well as quasi two-dimensional nanostructured films have been synthesized and studied. SiC nanostructures possess properties unique to nanomaterials such as the quantum confinement effect, surface effect, and size dependence. In addition, nanostructured SiC has unique electronic structures, outstanding electrical and mechanical properties, superior thermal and chemical stability, and favorable biocompatibility and is suitable for applications to microelectronics, nanoelectronics, photonics, energy storage and conversion, and life science.

J. Fan and P.K. Chu, *Silicon Carbide Nanostructures*,
Engineering Materials and Processes, DOI 10.1007/978-3-319-08726-9_1

Researchers began to notice the diversity and potential applications of SiC nanostructures in the 1990s, about the same time when the fabrication and properties of porous Si and Si nanostructures aroused interest. In the early years, researchers were mainly concerned with porous SiC fabricated by electrochemical etching of bulk single-crystalline SiC. Since the invention of solid-state electronic devices, group IV semiconductors have played a dominant role forming the basis of the microelectronics industry which has introduced to modern living the internet and indispensable electronic gadgets such as personal computers and cell phones. However, in the important application area involving lighting and display, the role of group IV semiconductors is rather limited due to their typical indirect bandgaps. As a result, electron transitions producing luminescence are not efficient compared to direct bandgap semiconductors such as GaAs. Microscopically, in an indirect bandgap semiconductor, light absorption or emission occurs via the transition of an electron between two quantum states with different crystal momentum $\hbar k$, in this process the conservation of energy is readily ensured. However, the small photon momentum cannot ensure conservation of momentum in the transition. Hence, this process typically occurs with absorption or emission of one or a couple of lattice phonons to satisfy conservation of momentum. Such a process involving electrons, photons, and phonons generally has much lower efficiency than the electronic transition in direct bandgap semiconductors in which only electrons and photons, but no phonons, in general, are involved.

Investigation of a porous Si layer containing nanoparticles reveals that the luminescence efficiency of Si nanoparticles can be improved by several orders of magnitude compared to the bulk materials due to spatial confinement of carriers. In addition, luminescence from porous Si shifts from the infrared region of the bulk materials to the visible regime due to the quantum confinement effect, which predicts that the smaller the quantum dot, the wider is the energy gap. Similar to Si, porous SiC shows visible luminescence with enhanced efficiency. These porous materials are generally fabricated by electrochemical etching of bulk SiC crystals in hydrofluoric acids. However, in most cases, luminescence from porous SiC is characteristic of defect-related luminescence and hence, light emission is generally attributed to surface defects although the specific defect types are not identified.

The nanoparticles and nanowires in porous SiC are not separated but rather they are connected to the SiC substrate and in effect a component of the whole porous SiC crystal. Therefore, their properties are between those of the single crystal and individual nanocrystals. Various types of separate SiC nanocrystals have been fabricated and studied. Gas phase reactions and solution-based chemical reactions can produce SiC nanocrystals, and SiC nanocrystals encapsulated in polymers or other solid matrices have also been produced by techniques such as ion implantation followed by annealing. The luminescent properties of these SiC nanocrystals vary and depend on the fabrication approaches and as aforementioned, the light emission is generally ascribed to surface defect states. Colloidal SiC nanocrystals suspended in solvents have been prepared by electrochemical or direct chemical etching of SiC bulk crystals followed by ultrasonic treatment. These SiC colloids show intense and robust visible luminescence with tunable wavelengths obeying

quantum confinement. The light emissions from SiC nanocrystals have quantum yields higher than that of bulk materials by several orders of magnitude. For luminescence originating from quantum confinement, the emission band shifts monotonically to shorter wavelengths as the particle size diminishes. Thus, different emission colours spanning yellow, green, blue, and near UV can be obtained from SiC crystallites with different sizes. Blue light emitting diodes based on SiC nanocrystals have been demonstrated. Furthermore, silicon carbide has high chemical and thermal stability in comparison with other types of nanomaterials. This virtue combined with the ultra stable luminescence enables the use of luminescent SiC nanocrystals in a harsh environment. In conjunction with the excellent biocompatibility, low density and high hardness, SiC nanocrystals are very useful in biology and medicine. Additionally, SiC has long been used as filling materials to enhance the mechanical properties of ceramics and it has been shown that incorporation of SiC nanoparticles into metal nanocomposites can boost the mechanical properties. It has also been found that doping with SiC nanoparticles can substantially enhance the performance of some superconductors.

SiC nanowires have been widely investigated. Several methods have been developed to synthesize the materials and they involve two main growth mechanisms, vapor–solid growth and vapor–liquid–solid growth with the assistance of metal catalysis. In the vapor–solid synthesis, carbon nanotubes can be used as the template. A large portion of the synthesized SiC nanowires has the SiC/amorphous SiO_2 core/shell structure. Carbon-sheathed SiC nanowires have also been observed but are rare. BN-coated SiC nanowires have been prepared. The synthesized SiC nanowires can be as small as several nanometers or as large as several hundreds of nanometers in diameter. Their lengths are generally on the order of micrometers, although SiC nanowires with lengths of a few centimeters have also been reported. Besides nanowires and nanorods, less common quasi one-dimensional SiC nanostructures with different morphologies resembling bamboo, bead, helix, belt, flower, and multi-leg have been produced. The SiC nanowires and similar structures often exhibit visible or near UV luminescence, but the luminescence mechanism is not well understood. SiC nanowires yield stable field electron emission with favorable characteristics such as a low turn-on field. Large-scale and highly ordered SiC nanowire arrays have been prepared and some synthesized SiC nanowires have very sharp ends that are beneficial to field emission. One-dimensional SiC nanostructures may be applied as the building blocks of molecular electronic devices. SiC-based coaxial nanocables such as coaxial SiC/BN nanocables have promising applications in nanoelectronic devices and silicon carbide nanowires that have outstanding mechanical characteristics and electrical conductivity can be utilized to reinforce composite materials or as nanocontacts in a harsh environment.

In comparison with SiC nanowires, SiC nanotubes have been less investigated experimentally. They are generally synthesized using carbon nanotube or semiconductor nanowire templates. The SiC nanotubes are actually not real nanotubes, because the walls of the nanotubes are composed of SiC nanocrystals with different orientations. In other words, they are polycrystalline. The SiC nanotubes

with structures similar to multiwalled carbon nanotubes are rarely observed. In comparison, there have been many theoretical studies on the structure, electronic structure, and molecular adsorption properties of SiC nanotubes based on first-principle calculation or molecular dynamics simulation. This is understandable because the structure of SiC nanotubes is simpler than that of other SiC nanostructures. It consists of fewer atoms than other SiC nanostructure of the same size and smaller computational power is required. The theoretical results are generally consistent with experimental data. Additionally, two-dimensional SiC nanosheets similar to graphene have been investigated theoretically and experimentally.

The research history of SiC films is longer than that of SiC nanoparticles and SiC nanowires. However, in early investigations of SiC films, little attention was paid to the nanoscale microstructures of these films due to limitations in the preparation methods and characterization capability. However, in the last twenty years, researchers have been able to prepare and identify nanostructured SiC films by many methods. Chemical vapor deposition is the most widely used approach to synthesize nanocrystalline SiC films and ion implantation and high-temperature sputtering have also been adopted to fabricate nanostructured SiC films. Many thin SiC films comprise embedded SiC nanocrystals and these nanocrystalline SiC films are potentially useful in electronic devices, solar cells, and sensors. Furthermore, many SiC films yield visible light emission rendering the materials suitable for large-area displays.

As biocompatible materials, SiC nanostructures have potential applications in biological imaging. Silicon carbide is an excellent wear resistant and benign coating on biomedical implants and porous SiC films with ultrasmall pores are semipermeable biomaterials. Biomorphic SiC ceramic materials with a wood-like microstructure have been prepared by infiltrating a wood-derived carbon template with silicon or silicon oxide at high temperature. The biomorphic SiC ceramics coated with bioactive glass shows great promise as dental and orthopedic implants with enhanced mechanical and chemical properties.

Theoretical studies play an important role in understanding the structure and properties of the silicon carbide nanostructures. Common approaches include semiempirical and first-principle calculation as well as molecular dynamics simulation. Many important properties of SiC nanostructures have been predicted. For example, the energy gap of SiC quantum dots depends closely on the dimension and surface composition. Calculation shows that the difference between cohesive energy and energy gap of different polytypes of SiC quantum dots disappears gradually as the size diminishes. As the particle becomes smaller, the surface of the SiC nanocrystals becomes more important and in practice, SiC nanoparticles with a size close to one nanometer resemble giant molecules. As a result, the properties of ultrasmall SiC nanoparticles are distinct from those of bulk materials. For example, they may have a complex luminescence behavior. Theoretical investigations show that the electronic structures and mechanical properties of SiC nanowires depend on the nanowire diameter. SiC nanotubes are generally semiconducting and their bandgap may decrease as the tube diameter decreases. This is contrary to SiC nanocrystals. SiC nanotubes may have an indirect or direct

bandgap depending on the chirality, and some SiC nanotubes may even be metallic when the surface is terminated by hydrogen atoms.

In this book, the various fabrication techniques, properties, and potential applications of SiC nanostructures are described and discussed. Containing the latest information and knowledge in this fledgling field, it serves as a valuable reference for graduate students and researchers who are interested in these fascinating nanostructures.

Chapter 2
General Properties of Bulk SiC

The fabrication and properties of silicon carbide crystals have been extensively studied because as a wide bandgap semiconductor, silicon carbide is ideal for electronic applications requiring high temperature, high frequency, and high power. The electrical and electronic properties as well as device applications of bulk silicon carbide have been reviewed [1–3]. In this chapter, which provides a self-contained framework to facilitate the understanding of the properties of silicon carbide nanostructures, the basic properties of silicon carbide crystals are reviewed.

2.1 SiC Polytypes

Similar to silicon, silicon carbide is a covalently bonded semiconductor. In the crystalline form, each silicon atom is covalently bonded to four neighboring carbon atoms to form a tetrahedron (Fig. 2.1) and vice versa. There are two types of tetrahedrons in the silicon carbide crystal. The first type is obtained by rotating another tetrahedron along its *c*-axis by 180°, and one type of tetrahedron is the mirror image of the other when the *c*-axis is parallel to the mirror. The *c*-axis denotes the direction normal to the Si–C double-atomic layers. In each layer, the silicon (or carbon) atoms have a close-packed hexagonal arrangement. There are three types of sites (named *A*, *B*, *C*) in arranging the Si–C double-atomic layers, and each layer is normal to the *c*-axis (Fig. 2.2).

The three types of double-atomic layers *A*, *B*, and *C* form a periodical series with a specified repeating unit along the *c*-axis forming a specific polytype of the silicon carbide crystal. For example, in 3C-SiC (Fig. 2.3), the stacking sequence of the double-atomic layers is ABCABC… The letter "C" in "3C-SiC" denotes the cubic crystal structure and "3" refers to the number of double-atomic layers in one repeating unit (ABC). 3C-SiC is the only polytype with the cubic crystal structure

J. Fan and P.K. Chu, *Silicon Carbide Nanostructures*,
Engineering Materials and Processes, DOI 10.1007/978-3-319-08726-9_2

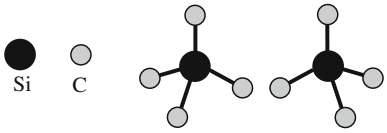

Fig. 2.1 Two types of tetrahedrons forming the building blocks of all SiC crystals with each tetrahedron consisting of one Si atom and four covalently bonded nearest-neighboring C atoms. One type is obtained by rotating another type around its *c*-axis (vertical here) by 180°

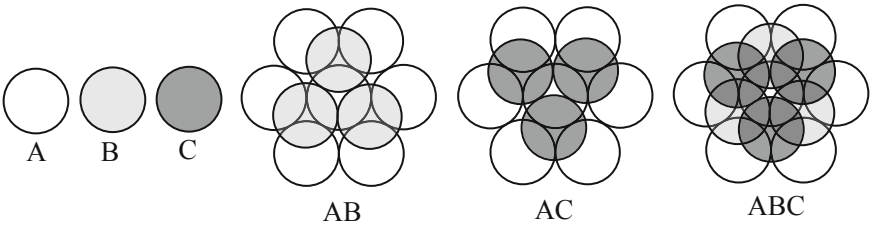

Fig. 2.2 Three types (*A*, *B*, *C*) of Si–C double-atomic layer arrangement along the *c*-axis (stacking direction) through close-packed spheres. The *c*-axis is normal to the paper plane

that is also referred to as β-SiC. The dominant polytypes in silicon carbide are hexagonal. The three most common hexagonal polytypes are 2H, 4H, and 6H and their stacking sequences are ABAB…, ABCBABCB…, and ABCACBAB-CACB…, respectively. Similarly, "H" refers to the hexagonal crystal structure and the number before "H" denotes the number of double-atomic layers in one repeating unit. There are other types of silicon carbide crystals, for instance, 15R-SiC where "R" stands for the rhombohedral crystal structure. It should be noted that one Si (or C) atomic layer in the stacking sequence can have a local cubic (*k*) or hexagonal (*h*) environment with respect to the immediate neighbors, as shown in Fig. 2.3. 3C-SiC has only *k*-type atoms, and 2H-SiC has only *h*-type atoms. The atomic number ratio *k*:*h* is 1:1 in 4H-SiC and 2:1 in 6H-SiC.

As a result of the different stacking sequence of the double-atomic layers, different polytypes of silicon carbide have distinct electronic structures as well as electrical and optical characteristics. For instance, the indirect bandgaps at room temperature of 3C-SiC, 6H-SiC, and 4H-SiC are 2.2 eV, 2.86 (or 3.02) eV, and 3.2–3.3 eV, respectively. The bandgap depends on the temperature and even the measured room-temperature bandgap of a specific polytype may vary in a small range depending on the uncertainty in determining the optical absorption edge and measurement conditions in different laboratories.

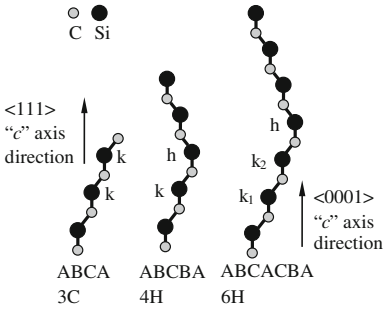

Fig. 2.3 Si–C double-atomic layer arrangement in the three most common polytypes of SiC. The *c*-axis denotes the stacking direction and *k* and *h* denote atoms with the localized cubic and hexagonal crystal symmetry, respectively

2.2 Interstellar Origin

SiC can be produced on earth and also found in outer space. For example, presolar SiC grains have been found in meteorites. Their morphology has been extensively studied by electron microscopy and the elemental and isotopic compositions analysis by mass spectrometry.

Including silicon carbide, five types of presolar matters have been identified in chondrites, namely diamond (about 2.6 nm), graphite (0.8–7 μm), silicon carbide (0.05–20 μm), silicon nitride, and aluminum oxide [4]. The anomalous isotopic compositions of Si, C, O, and N demonstrate that the grains have a presolar origin. Studies on presolar diamond, graphite, and silicon carbide in chondrites show that the abundance is correlated with the chemical and physical properties of the meteorites [5, 6]. Among the various types of presolar grains, silicon carbide grain is the most extensively studied because it contains many elements including minor and trace elements. The strontium isotopic composition determined from individual circumstellar SiC grains extracted from the Murchison meteorite by resonant ionization mass spectrometry confirms the grain origin of *s*-process nucleosynthesis at moderate neutron densities [7].

The polytype distribution of circumstellar SiC has been identified by transmission electron microscopy on presolar silicon carbide in the Murchison carbonaceous meteorite [8]. Only 3C-SiC and 2H-SiC and their intergrowth have been observed (Fig. 2.4). It has been speculated that the structural simplicity results from the low pressure in the circumstellar outflow and corresponding low silicon carbide condensation temperature.

Much effort has been made to explore the origin of the SiC grains. The barium isotopic anomaly observed from SiC meteorite grains is considered to stem from the *s*-process nucleosynthesis in carbon stars that suffer recurrent He shell instability on the asymptotic giant branch (AGB) [9]. Additionally, the Xe, Nd, and Sm anomalies in the same SiC grains show clearly the *s*-signature and the

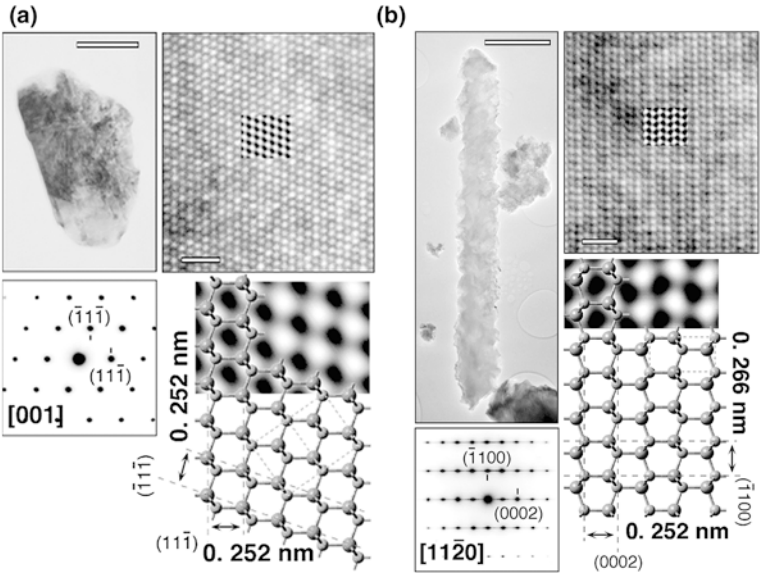

Fig. 2.4 Circumstellar 3C-SiC (**a**) and 2H-SiC (**b**) from Murchison carbonaceous chondrite KJE. Each panel contains the TEM image (*top left*, scale bar: 0.1 μm), selected-area electron diffraction (*SAED*) pattern (*bottom left*), high-resolution TEM (*HRTEM*) image (*top right*, scale bar: 1 nm), and atomic model of the [011] (for 3C-SiC) or [11$\bar{2}$0] (for 2H-SiC) zone axis superimposed on a simulated lattice image (*bottom right*). The tetrahedral stacking direction in the HRTEM image and atomic model is horizontal. Reprinted with permission from [8]. Copyright 2003, AAAS

corresponding interpretation corroborates the carbon-star origin. Another group has studied the isotopic compositions of the carbon, nitrogen, magnesium, silicon, and titanium in the single interstellar silicon carbide grains (with sizes 1–10 μm) extracted from the Murchison carbonaceous chondrite [10]. Scanning electron microscopy (SEM) images of these SiC grains are displayed in Fig. 2.5. All the grains exhibit crystalline features but their morphology varies from euhedral to a fine-grained surface, indicating agglomerates of smaller subgrains. Although many grains possess the hexagonal (Fig. 2.5b) and tetrahedral (Fig. 2.5c) shape, electron diffraction and Raman scattering indicate that the grains are β-SiC. The C and N isotopic compositions along with *s*-process Kr, Xe, Ba, and Nd suggest that the AGB or Wolf-Rayet stars are possible sources of the SiC grains. However, the existing models of nucleosynthesis in these stellar sites cannot account for the details of all the observed isotopic compositions.

The isotopic ratios of 124 presolar SiC grains of types A and B (defined as having $^{12}C/^{13}C < 10$) in an acid-resistant residue of the Murchison carbonaceous meteorite along with that of 28 previously analyzed A + B grains have been studied [11]. The most likely sources of the A + B grains with solar *s*-process abundance are J-type carbon stars although the origin of these stars is still unclear. Born-again AGB stars are possible sources of the A + B grains with enhanced

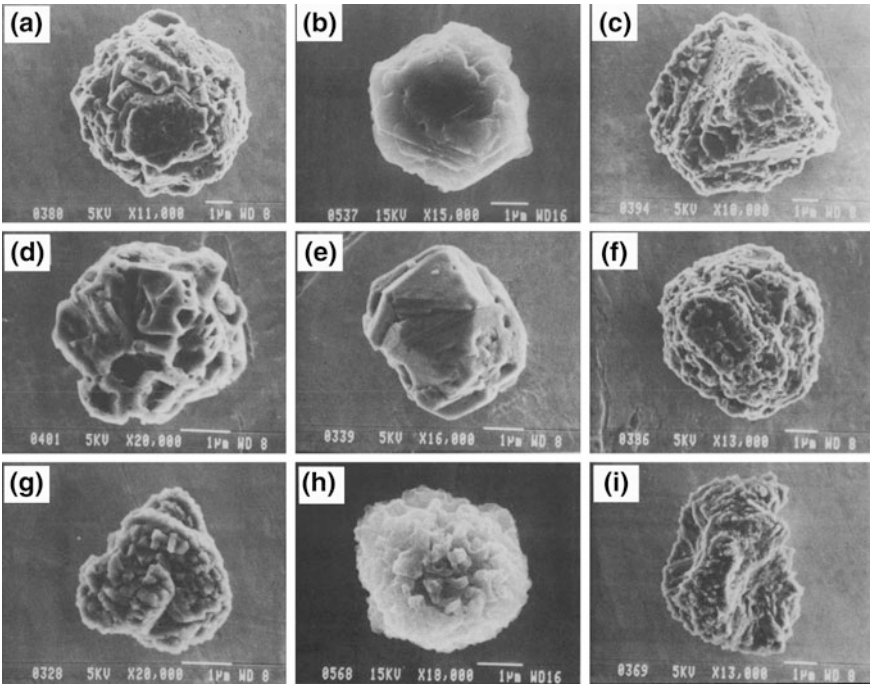

Fig. 2.5 Scanning electron microscopy images of SiC grains extracted from Murchison carbonaceous chondrites KLG (**b** and **h**) and KJH (**a**, **c**, **d**, **e**, **f**, **g**, and **i**). The grains show crystalline features. The morphology varies from euhedral (**a**, **b**, **c**, and **e**) to fine-grained surface indicating agglomerates of smaller subgrains (**g**, **h**, and **i**). Many grains have the hexagonal (**b**) and tetrahedral (**c**) shape. Electron diffraction and Raman scattering studies indicate that the grains are β-SiC. Reprinted with permission from [10]. Copyright 1994, IOP Publishing/on behalf of American Astronomical Society

s-process elemental abundance. In a comparative study, the strontium, zirconium, molybdenum, and barium isotopic compositions predicted for the mass-losing envelopes of AGB stars of solar metallicity and mass 1.5, 3, and 5 $M_{\odot 1}$ are compared with the measurements of single presolar SiC grains from the Murchison meteorite [12]. The predicted isotopic compositions in the envelopes of low-mass AGB stars of solar metallicity agree with the isotopic ratios determined from individual presolar SiC grains, whereas the prediction for intermediate mass stars excludes them as the source of these grains. A multiplicity of low-mass AGB stars with metallicity close to that of the sun with different mass and neutron exposure is required to explain the measured spread in the heavy element isotopic compositions among single presolar SiC grains.

The individual β-SiC nanoparticles with average diameters of 10–20 nm (Fig. 2.6) have been synthesized by laser-induced pyrolysis of gas-phase starting materials [13]. The infrared spectra perfectly match the absorption or emission band profile of the 11 + μm feature observed from carbon-rich AGB stars conducted by the *Infrared Space Observatory*. The 7.5–13.5-μm infrared spectra of

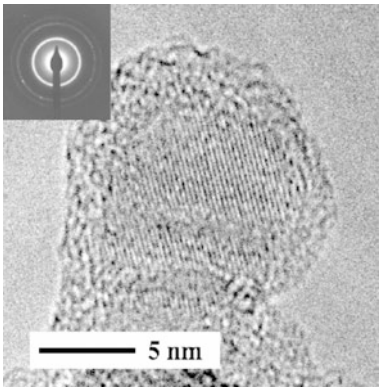

Fig. 2.6 High-resolution TEM image of one particle showing the β-SiC core as determined by the lattice fringe spacing and electron diffraction pattern (*inset*). Reprinted with permission from [13]. Copyright 2003, IOP Publishing/on behalf of American Astronomical Society

32 identified or potential carbon stars have been investigated [14]. Four carbon stars, including AFGL 3068, IRAS 02408 + 5458, AFGL 2477, and AFGL 5625, show the 11-μm SiC feature in absorption. Figure 2.7 shows the self-absorption fits of the infrared absorption spectra of two carbon stars. All of the observed SiC features can be fitted well by α-SiC grains. The observation shows no unambiguous evidence of the presence of β-SiC around these stars. This result seems abnormal since β-SiC is the most commonly observed polytype in meteorites.

Although many studies have suggested that the carbon stars are the sources of SiC grains, other investigations point out that the SiC grains in the meteorites may originate from supernovae. The C, N, Si, Mg–Al, Ca, and Ti isotopic compositions of five single SiC grains 2–9 μm in size extracted from the Murchison carbonaceous meteorite have been determined by ion microprobe [15]. The Ca and Ti anomalies suggest their origin of explosive nucleosynthesis in supernovae and the in situ decay of the radioactive precursors ^{44}Ti and ^{49}V in SiC grains can form in the supernova ejecta. However, no simple formation mechanism can provide a consistent explanation of the isotopic compositions of those grains. Large excess of ^{44}Ca arising from the radioactive decay of short-lived ^{44}Ti, and in ^{46}Ti, ^{49}Ti, and ^{50}Ti has been observed from four graphite grains and five type-X SiC grains extracted from the Murchison meteorite [16]. These grains must have a supernova origin since ^{44}Ti is only produced in supernovae. Furthermore, the Si, C, N, Al, O, and Ti isotopic compositions require a type II supernova source and suggest heterogeneous mixing of different supernova regions including the nickel core. By using secondary ion mass spectrometry, the isotopic compositions of C, N, O, and Si in 849 small (about 1 μm) individual SiC grains extracted from the Murchison meteorite have been determined [17]. The isotopic compositions of the major elements C and Si of most grains are similar to those observed from larger grains, suggesting an AGB star origin of these grains. Highly anomalous isotopic compositions have been found from a nitride grain that comprises Si_3N_4 with little carbon. The isotopic features of C, N, and Si resemble those of the rare type-X SiC grains, suggesting that these two rare constituents of circumstellar matters are formed in type II supernovae. In another study, the type-X SiC particles extracted chemically from meteorites are demonstrated to have chemical and isotopic

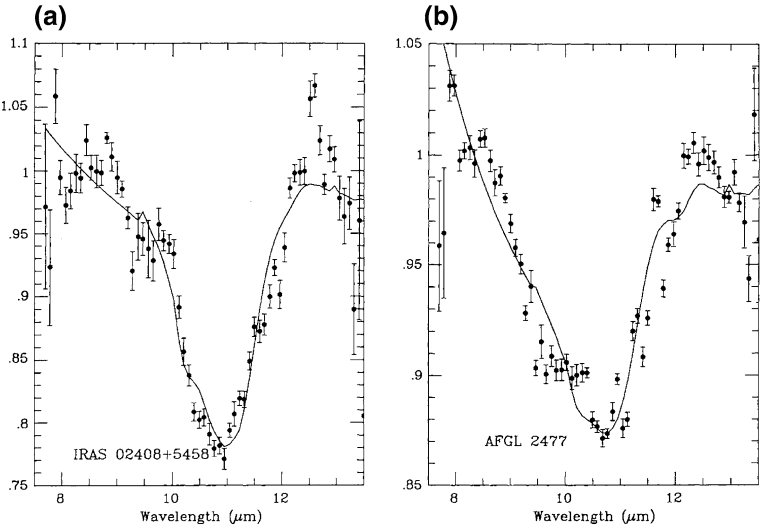

Fig. 2.7 Flux calibrated and normalized infrared spectra of two carbon stars **a** IRAS 02408+5458 and **b** AFGL 2477, showing absorption features with best χ^2-fits using self-absorbed SiC. Reprinted with permission from [14]. Copyright 1997, Oxford University Press/on behalf of Royal Astronomical Society

compositions resembling those from explosive helium burning in ^{14}N-rich matter [18]. It is proposed that these particles are from type Ia supernovae that explode with a cap of helium atop their CO structure. The enhanced abundance of C and Si suggests that silicon carbide is in fact the natural condensate, and it is speculated that the dust grows within the interior of type Ia supernovae during expansion.

2.3 Electronic Structures

SiC is an indirect semiconductor with a wide bandgap. The most common polytypes, 3C, 6H, 4H, and 2H, have room-temperature bandgaps of 2.2 eV, 2.86 (or 3.02) eV, 3.2–3.3 eV, and 3.3 eV (exciton energy gap), respectively. Note that the bandgap subtracted by exciton binding energy is the exciton energy gap. The electronic structure of silicon carbide crystals has been extensively studied by empirical-pseudopotential, tight-binding, and first-principle methods.

The electronic band structures of the four polytypes (3C, 2H, 4H, and 6H) of silicon carbide are calculated using local atomic pseudopotentials for carbon and silicon [19]. The calculated indirect bandgaps of the 3C, 2H, 4H, and 6H polytypes are 2.40, 3.35, 2.80, and 2.45 eV, respectively. The indirect bandgap increases with increasing hexagonality of the polytype, and the trend is qualitatively consistent with experimental results. However, the calculated bandgaps of the 4H and 6H polytypes are significantly smaller than the reported experimental values. This

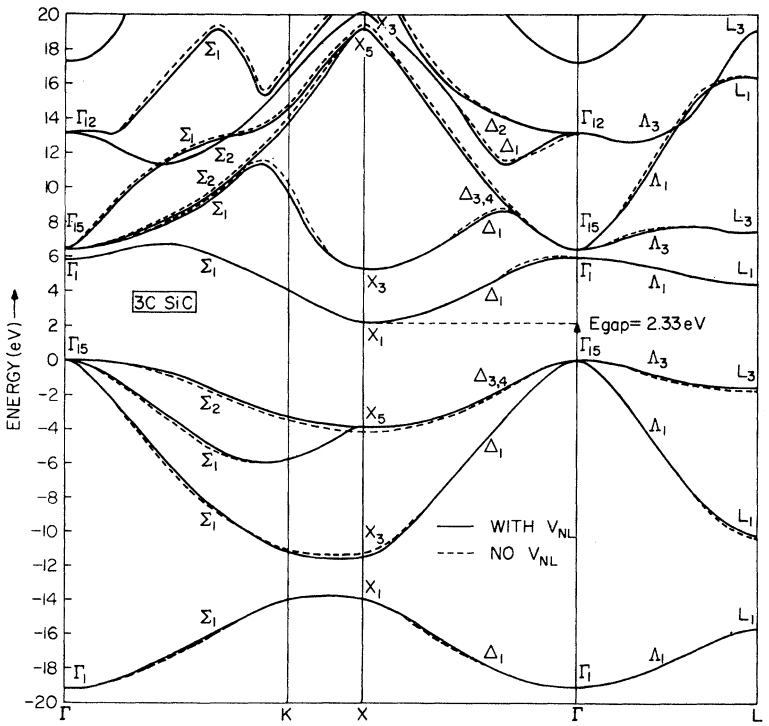

Fig. 2.8 Calculated electronic band structure of 3C-SiC with (*solid line*) and without (*dashed line*) inclusion of a nonlocal angular momentum-dependent potential in the pseudopotential. Reprinted with permission from [20]. Copyright 1972, American Physical Society

is because the energy levels in 4H- and 6H-SiC are calculated without further adjustment of the pseudopotentials, unlike the cases of 3C- and 2H-SiC. The calculated direct bandgaps at Γ differ relatively slightly among the four polytypes, and they are 5.14, 4.46, 4.60, and 4.40 eV for the 3C, 2H, 4H, and 6H polytypes. The energy band structure of 3C-SiC has been calculated by the nonlocal empirical-pseudopotential method [20], which shows that 3C-SiC is an indirect gap semiconductor with the valence-band maximum at Γ_{15v} and conduction-band minimum at X_{1c} (Fig. 2.8). The calculated threshold of the indirect transition is 2.33 eV corresponding to the Γ_{15v}–X_{1c} transition. This agrees well with the experimental value of 2.39 eV [21]. The threshold of the direct transition is 5.90 eV that corresponds to the Γ_{15v}–Γ_{1c} transition.

By interpreting the SiC polytypes as natural superlattices consisting of mutually twisted cubic layers, a method has been developed to calculate the electron band structure of any polytype based on an empirical-pseudopotential description of cubic SiC [22]. The indirect gaps of all SiC polytypes with hexagonality below 50 % are obtained. The calculated bandgaps of hexagonal and rhombohedral polytypes are in excellent agreement with experimental data (Table 2.1). The results also reveal the nearly linear relationship between the indirect gap and the

Table 2.1 Hexagonality and energy gaps (eV) of several SiC polytypes. Reprinted with permission from [22]. Copyright 1994, American Physical Society

Polytype (Ramsdell)	Polytype ABC	Hexagonality (percent)	Theory	Experiment
3C	ABC	0	2.40	2.390
10H	ABCABCBACB	20	2.66	
8H	ABCABACB	25	2.76	2.80
6H	ABCACB	33.3	3.05	3.023
15R	ABCACBCABACABCB	40	3.03	2.986
4H	ABCB	50	3.28	3.263
2H	AB	100	4.04	3.330

hexagonality, in agreement with experiments. 2H-SiC is an exception and its gap can be reproduced only with the proper choice of the interface position.

The electronic structure and wave function of 3C-SiC can be calculated using the first-principle Hartree–Fock–Slater model based on the discrete variational method [23]. The calculated first indirect gap is 2.5 eV that is close to the experimental value of 2.39 eV. The quasiparticle energy of 3C-SiC is evaluated using the first-principle density functional theory (DFT) by adopting the local density approximation (LDA) and nonlocal, norm-conserving pseudopotentials [24]. The localized Gaussian orbital basis sets are utilized. The self-energy operator is evaluated utilizing the *GW* approximation, and it provides energy correction to the LDA calculation. The calculated indirect bandgap is 2.33–2.35 eV that is in good agreement with the experimental value. Another theoretical calculation employing the density functional theory and local density approximation provides the electronic structures of 3C-, 6H-, 4H-, and 2H-SiC (Fig. 2.9) [25]. The calculated indirect bandgaps of 3C-, 6H-, 4H-, and 2H-SiC are 1.27, 1.96, 2.18, and 2.10 eV, respectively. The energy gap increases with increasing hexagonality with the exception of the 2H polytype. The calculation generally underestimates the transition energies in DFT-LDA. This matches the generally accepted notion that the DFT-LDA calculation generally underestimates the fundamental bandgap in semiconductors and insulators by 30–60 %. After introduction of the quasiparticle correction (1.13 eV) to the DFT-LDA band structures, the calculated indirect bandgaps agree with the experimental result. The full-potential linearized augmented-plane-wave method in the density functional theory and local density approximation including spin–orbit interaction has been employed to calculate the bandgaps of 3C-, 2H-, 4H-, and 6H-SiC [26, 27]. The calculated bandgaps are smaller than the measured values by about 1.1 eV. The shape of the bands is consistent with the results obtained from other types of calculation.

The self-consistent ab initio pseudopotential calculation of the electronic properties of 3C, 2H, 4H, and 6H SiC has been performed [28]. The calculated bandgaps are underestimated as well, ranging from 1.04 to 1.28 eV, as a result of the use of the LDA in the calculation. Different polytypes show similar valence-band widths, and

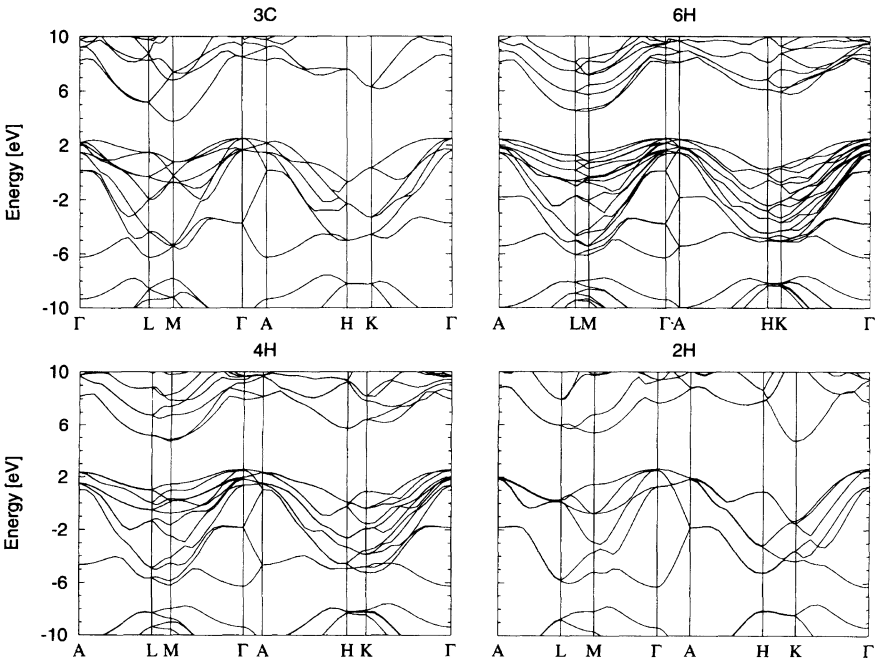

Fig. 2.9 Electronic band structures of 3C-, 6H-, 4H-, and 2H-SiC derived by the first-principle density functional theory using the local density approximation. Reprinted with permission from [25]. Copyright 1994, American Physical Society

they are 15.33, 15.37, 15.41, and 15.49 eV for 3C, 6H, 4H, and 2H polytypes, respectively. The valence-band width increases slightly with hexagonality. In contrast, the bandgap and conduction-band minimum vary significantly as the hexagonality increases. The electronic excitation properties of various SiC polytypes, 6H, 4H, 2H, and 3C, have been studied by combining the first-principle pseudopotential method in the framework of DFT-LDA and proper calculation of the quasiparticle effect [29]. The quasiparticle shifts added to the density functional eigenvalues are evaluated using a model dielectric function and an approximate treatment of the electron self-energy concerning local-field effects and dynamic screening. The calculated indirect bandgaps are in good agreement with the measured values, for instance, 2.59 and 3.25 eV for the 3C and 6H polytypes, respectively.

The dependence of the minimum bandgap and gaps at the relevant k-points on the hexagonality of the SiC polytypes have been summarized [30], as shown in Fig. 2.10. The minimum at K increases from 2H to 3C but shows some nonmonotonic oscillations for the lower-hexagonality polytypes. The dashed line in this figure indicates the well-known linear relationship between the minimum indirect bandgap and hexagonality. This law applies to all hexagonalities. This is the absolute minimum gap except the value very close to 100 % hexagonality. This linear relationship and small deviations very close to 3C can be explained [22].

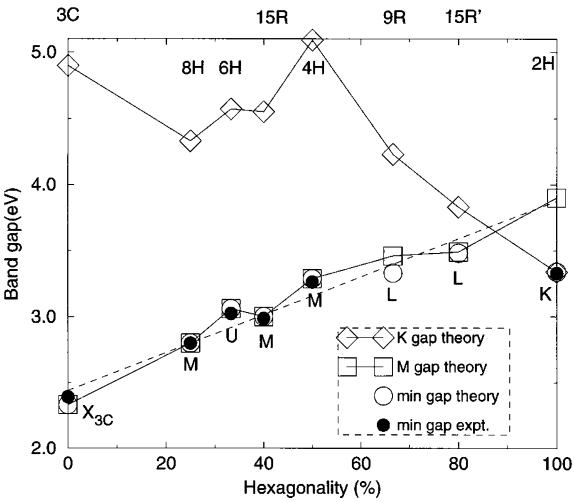

Fig. 2.10 Plot of the minimum and *k*-specific bandgaps of the SiC polytypes as a function of hexagonality. The 1-eV self-energy correction is added to all the LDA calculated gaps. The labels of the minimum gaps indicate their locations in the Brillouin zones and the *M*, *L*, *U*, and *K* signs refer to the hexagonal Brillouin zones. For 15R, the *M* point corresponds to rhombohedral X_R and for 15R′ and 9R, the hexagonal *L* point corresponds to the L_R point. Reprinted with permission from [30]. Copyright 1997, Wiley-VCH Verlag GmbH & Co. KGaA

2.4 Defects

There are many intrinsic defects in as-grown or irradiated silicon carbide crystals, for example, point defects and higher-dimensional defects [31]. Point defects mainly consist of silicon vacancies, carbon vacancies, divacancies, and antisite. The higher-dimensional intrinsic defects comprise dislocations, micropipes, and stacking faults. There are other types of extrinsic defects in silicon carbide crystals associated with impurities. The presence of intrinsic and extrinsic defects in silicon carbide crystals can significantly degrade the performance of SiC-based devices. Moreover, some defects may serve as luminescence centers or nonradiative recombination centers consequently affecting the luminescence properties of silicon carbide. Therefore, identification of these defects, knowledge of the characteristics, and finding approaches to mitigate the effects of these defects are crucial to the application of silicon carbide to electronic devices and light-emitting diodes.

2.4.1 Intrinsic Point Defects

2.4.1.1 Vacancies

Si vacancies in silicon carbide have been extensively studied. Electron spin resonance (ESR) spectroscopy is used to study the electron irradiation-induced defects in

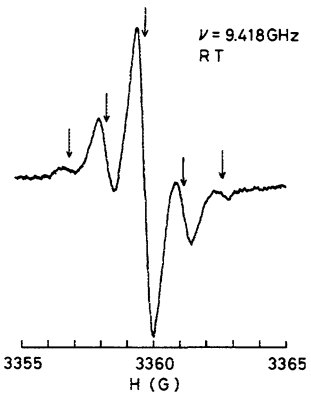

Fig. 2.11 Room-temperature electron spin resonance spectrum of 3C-SiC irradiated by l-MeV electrons with a fluence of 3×10^{18} cm^{-2}. The *arrows* indicate five lines of the *T*1 *center*. Reprinted with permission from [32]. Copyright 1989, AIP Publishing LLC

3C-SiC epitaxial films prepared by chemical vapor deposition [32]. An isotropic ESR center (named *T*1 center) (Fig. 2.11) that consists of five lines equally spaced at about 1.5 G and has a *g* value of about 2.0029 is observed. This center in electron-irradiated 3C-SiC can be annealed in three stages (150, 350, and 750 °C). The *T*1 center is a point defect at the Si site that has 12 second nearest-neighbor Si atoms, and this defect is supposed to be the isolated vacancy at the Si sublattice site. Photoluminescence (PL) reveals a dominant PL line at 1.913 eV, and it disappears after annealing at 100 and 700 °C [33]. The annealing results of the PL line and fractions annealed in each annealing stage agree well with those obtained for the *T*1 ESR center, indicating that the 1.913 eV PL line stems from silicon vacancies in 3C-SiC.

The negatively charged Si vacancy in neutron-irradiated 4H-SiC has been identified by electron paramagnetic resonance and electron nuclear double resonance spectroscopy [34]. The magnetic resonance parameters of the negatively charged Si vacancy are nearly the same for 3C-, 4H-, and 6H-SiC. The ligand hyperfine interactions for the nearest- and next-nearest-neighbor shell of the Si vacancy in 3C-SiC are calculated based on the density functional theory using the local density approximation. The calculated result agrees well with the experimental data, thus supporting the assignment of the defect center and determination of the spin state ($S = 3/2$) also helps to identify the defect.

The irradiation-induced photoluminescence spectrum acquired from the electron-irradiated 4H- and 6H-SiC epitaxial layers and corresponding optically detected magnetic resonance signals from this band have been investigated [35]. The number of no-phonon lines in the deep PL band is equal to the number of inequivalent sites in the respective polytype. These lines are at 1,352 meV (*V*2) and 1,438 meV (*V*1) for 4H-SiC and at 1,366 meV (*V*3), 1,398 meV (*V*2), and 1,433 meV (*V*1) for 6H-SiC (Fig. 2.12). The intensity of the PL lines decreases remarkably after short annealing at 750 °C. Electron spin resonance measurement

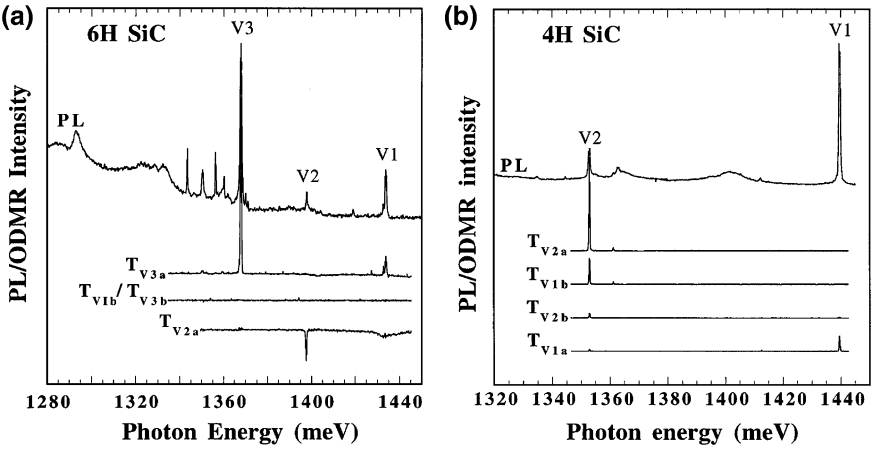

Fig. 2.12 Deep PL band (*top*) and excitation spectrum (*below*) of the various optically detected magnetic resonance signals that are detected from the PL band for the **a** 6H-SiC and **b** 4H-SiC. The samples are 2.5-MeV electron-irradiated epitaxial layers prepared by chemical vapor deposition. Reprinted with permission from [35]. Copyright 2000, American Physical Society

combined with theoretical calculation suggests that the no-phonon lines in the PL originate from internal transitions from an excited state of the neutral Si vacancy at the inequivalent sites in 4H- and 6H-SiC. Moreover, comparison of the characteristics of the triplet states between the polytypes indicates that the *V*2 lines correspond to the hexagonal sites and *V*1 and *V*3 to the cubic sites. The silicon vacancies (V_{Si}) in 3C- and 2H-SiC in all possible charge states are studied using spin-polarized ab initio local spin-density calculation [36]. For the neutral, single, and double negative charge states, the exchange coupling overcomes the Jahn-Teller energies, and the silicon vacancy is found in the high-spin ground state with T_d symmetry. A weak Jahn-Teller effect occurs in the low-spin configuration.

The defects in solids can be ideal centers for generating single-photon emission, which has wide application in quantum communication and quantum computation. This has been demonstrated by the studies of the nitrogen-vacancy defect centers in diamond and nanodiamond [37] showing the virtues of good localization and antiphotobleaching [38, 39]. Silicon carbide as a group IV material also has excellent characteristics [37] that are similar and even superior in some aspects to diamond and thus can be utilized as single-photon sources. The Si vacancy in SiC has been investigated as a promising quantum system for single-defect and single-photon spectroscopy in the infrared region, by electron paramagnetic resonance, optically detected magnetic resonance, and high-resolution PL excitation spectroscopy [40]. The photoluminescence spectra of Si vacancies acquired from 6H- and 4H-SiC are shown in Fig. 2.13. They contain zero-phonon lines accompanied by phonon replicas. The number of zero-phonon lines generally agrees with that of the inequivalent lattice sites in the SiC polytypes. These lines arise at 865 nm (*V*1), 887 nm (*V*2), and 906 nm (*V*3) in 6H-SiC and at 862 nm (*V*1) and 917 nm (*V*2) in

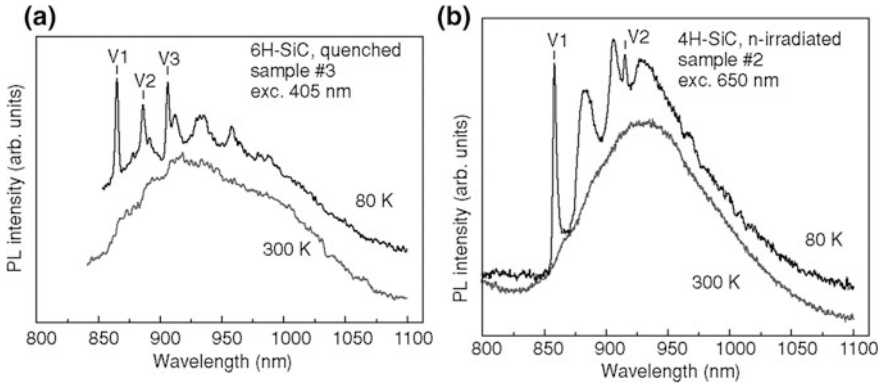

Fig. 2.13 **a** PL spectra acquired from neutron-irradiated 6H-SiC at 80 K and room temperature excited by 405 nm light. **b** PL spectra of neutron-irradiated 4H-SiC at 80 K and room temperature excited by 650-nm light. Reprinted with permission from [40]. Copyright 2011, American Physical Society

4H-SiC. The optically induced inverse population of the ground-state spin sublevels of the silicon vacancies (V_{Si}) is realized in 4H- and 6H-SiC upon irradiation with unpolarized light at low temperature and room temperature [41]. The PL intensity of the zero photon lines changes by a factor of 2–3 at zero magnetic field upon absorption of radio waves with energy equal to the fine structure splitting of spin sublevels of the silicon vacancy ground state. This brings the hope of magnetic resonance detection of a single vacancy. Unlike the intentionally created nitrogen-vacancy defect in diamond, the silicon vacancy is an intrinsic defect and its coherence time is expected to be longer than that of the nitrogen-vacancy defect. The electron spin of the Si vacancy can be controlled by the low-energy radio wave in the range 20–150 MHz, and it is two orders of magnitude smaller than that of the nitrogen-vacancy defect in diamond. Therefore, the Si vacancy in SiC is a very favorable defect in spintronics and quantum information processing.

Except for the silicon vacancy, the carbon vacancy has been investigated. An electron paramagnetic resonance spectrum is obtained from electron-irradiated *p*-type 4H- and 6H-SiC at a temperature above 25 K [42]. This defect center has the C_{3V} symmetry with an electron spin of 1/2, and its configuration is depicted in Fig. 2.14. The detailed hyperfine structure due to its interaction with the four nearest silicon neighbors is obtained by high-frequency electron paramagnetic resonance spectroscopy. In this way, the defect is identified as the positively charged carbon vacancy (V_C^+). Its *g* values and hyperfine tensor are almost the same in both polytypes, and they are independent of the inequivalent lattice sites. The deep levels in *n*-type 4H-SiC epilayers fabricated by chemical vapor deposition are studied by deep-level transient spectroscopy [43]. The Z_1/Z_2 and EH_6/EH_7 centers are dominant in the as-grown samples. Their concentrations increase significantly after electron irradiation at 116 keV, by which only carbon atoms may be displaced. They increase with 0.7 power of the electron fluence of irradiation and their concentrations decrease by

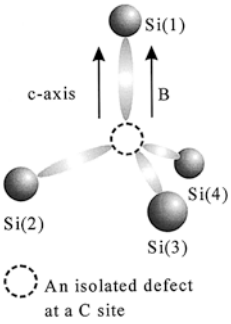

Fig. 2.14 Schematic of an isolated defect (V_C^+) in SiC with the magnetic field parallel to the *c*-axis. The expected symmetries of the hyperfine tensors representing the interaction with the Si (1) and Si (2, 3, 4) are, respectively, C_{3V} and C_{1h}. Reprinted with permission from [42]. Copyright 2001, American Physical Society

annealing at 1,600–1,700 °C. The concentrations of the Z_1/Z_2 and EH_6/EH_7 centers are very close to each other in all kinds of samples (as-grown, as-irradiated, and annealed ones). It has been proposed that both the Z_1/Z_2 and EH_6/EH_7 centers microscopically contain the same defect, possibly the carbon vacancy. However, first-principle calculation carried out on models for the Z_1/Z_2 defects in 4H-SiC shows that a π-bonded dicarbon interstitial complex next to a nitrogen atom, which is ultra thermally stable and has negative-*U* character with donor and acceptor levels close to that of the defect, is the most likely candidate of the Z_1/Z_2 defect [44].

Positron lifetime measurement and Doppler broadening spectroscopy have been employed to study the vacancies in 6H-SiC formed by irradiation of 2.2- and 10-MeV electrons [45]. Both neutral carbon and silicon vacancies are observed from *n*-type SiC, but no vacancies are detected from *p*-type SiC. The defect energy levels in nitrogen-doped 6H-SiC epitaxial layers prepared by chemical vapor deposition and irradiated with 2-MeV electrons and implanted with 300-keV deuterium or hydrogen are investigated by deep-level transient spectroscopy at room temperature [46]. Five levels within the energy gap are observed, and it is proposed that the E_C - 0.51 eV level (E_c referring to the conduction-band minimum energy) originates from a carbon vacancy. The two levels at E_C - 0.34 and E_C - 0.41 eV originate from the occupation of nonequivalent lattice sites. The results for the E_C - 0.62 eV and E_C - 0.64 eV levels support a defect model involving a silicon vacancy on the nonequivalent sites in the 6H lattice.

The neutral and charged Si and C vacancies in 3C- and 4H-SiC are theoretically studied by the density functional theory using the local density approximation as well as local spin-density approximation [47]. A plane-wave-supercell approach is combined with the ultrasoft Vanderbilt pseudopotentials to ensure converged calculation. Generation of the C-site vacancy is generally accompanied by a remarkable Jahn-Teller distortion, whereas only an outward-breathing relaxation occurs at the Si-site vacancy due to strong localization of the neighboring C dangling bonds. As a result, Si vacancies show high-spin configurations and C

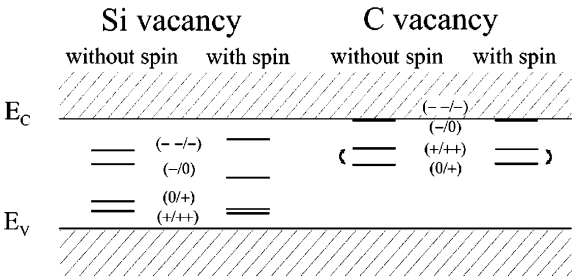

Fig. 2.15 Schematic of the energy levels of the Si and C vacancies at cubic and hexagonal sites in 3C-SiC obtained by local density approximation or local spin-density approximation calculation using the 216-atom supercell. Reprinted with permission from [47]. Copyright 1999, American Physical Society

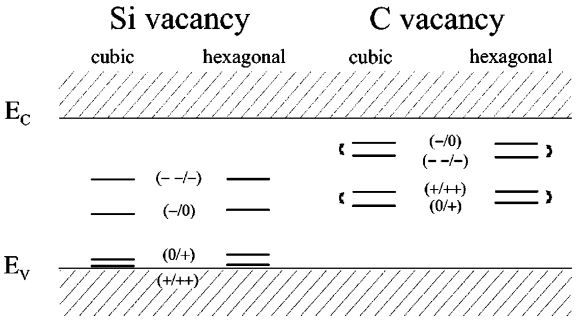

Fig. 2.16 Schematic of the energy levels of the Si and C vacancies in 4H-SiC obtained by local density approximation or local spin-density approximation calculation employing the 128-atom supercell. Reprinted with permission from [47]. Copyright 1999, American Physical Society

vacancies show low-spin configurations with a negative-U behavior. The schematic diagrams of the energy levels of the vacancies are depicted in Figs. 2.15 and 2.16.

Ion implantation of SiC may produce damage in the crystal lattice that is hard to repair. Some of these defects remain even after annealing at a high temperature. One of these persistent defects is observed from 3C-SiC after 120-keV He-ion implantation or 1-MeV electron bombardment. This defect (D_1) exhibits strong low-temperature luminescence, which is independent of the implanted ion, and the luminescence spectrum contains a zero-phonon line (at 6279.8 Å) accompanied by a strong vibronic structure [48]. This luminescence remains after annealing at 1,600 °C. The radiation defects in 6H-SiC produced by ion implantation and electron bombardment have been investigated [49]. The defects also show low-temperature luminescence. This D_1 spectrum persists after annealing at 1,700 °C. Its intensity depends strongly on the defect concentration. The defect is proposed to originate from a divacancy. Unlike the case of 3C-SiC, there are three no-phonon lines in the D_1 band (Fig. 2.17) due to the three nonequivalent sites in

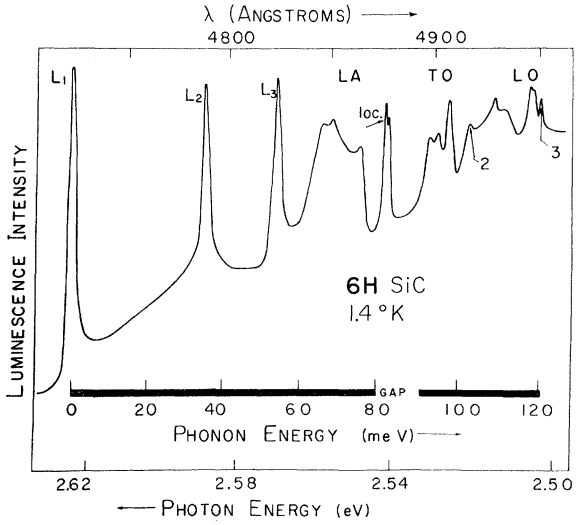

Fig. 2.17 Portion of the 1.4 K D_1 PL spectrum of the 1,300 °C annealed and ion-bombarded 6H-SiC. L_1, L_2, and L_3 are no-phonon lines and most of the phonon replicas belong to the L_1 peak. Reprinted with permission from [49]. Copyright 1972, American Physical Society

6H-SiC. The spectrum shows unusual temperature dependence. The low-temperature (1.4 K) spectrum vanishes as the high temperature (77 K) form emerges, and this abrupt spectral change is ascribed to lattice distortion at low temperature. The D_1 centers with similar properties have also been observed from 4H-SiC [50].

Two negative-U centers have been observed from 4H-SiC by capacitance transient techniques [51]. Each negative-U center generates two levels in the bandgap, one shallower donor level, and one acceptor level, and the electron ionization energy of the acceptor level is larger than that of the donor level. The two-electron emissions from the two acceptor levels result in the previously reported deep-level transient spectroscopy peak related to the Z_1 center. The electron paramagnetic resonance measurement combined with ab initio supercell calculation suggests that the *P*6/*P*7 defect centers in 3-MeV electron-irradiated 4H-SiC originate from the triplet ground states of the neutral divacancy in the axial C_{3v} and monoclinic C_{1h} configurations (Fig. 2.18) [52]. The spin density is located mainly on three nearest C neighbors of the Si vacancy, and it is negligible on the nearest Si neighbors of the C vacancy. The vacancy model for the *P*6/*P*7 centers points out that the interaction between V_{Si} and V_C to form divacancies is significant and so the divacancy is a common defect in SiC. Annealing indicates that the formation of the divacancy is governed mainly by diffusion of V_{Si} and V_C. First-principle calculation indicates that there is a negative-U behavior at $E_V + 0.7$ eV between the charge states ± 1 only for nearest-neighbor divacancies on different lattice sites in 4H-SiC, but not for all the other cases in 4H-SiC or for the cubic divacancy in 3C-SiC [53].

Similar to the case of Si vacancy, the divacancy in SiC can be used as an individually controllable solid state quantum bit. It has been demonstrated that several defect spin states in high-purity semi-insulating 4H-SiC can be optically addressed

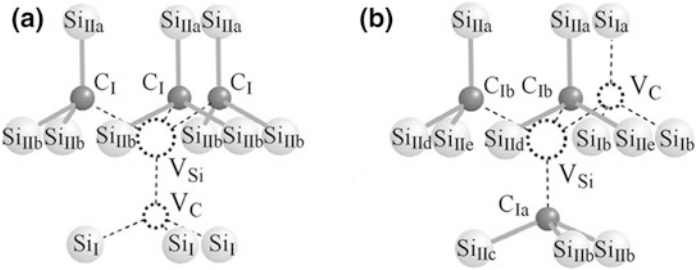

Fig. 2.18 Schematic of the **a** axial (C_{3v}) and **b** monoclinic (C_{1h}) configurations of the divacancy in electron-irradiated 4H-SiC. Reprinted with permission from [52]. Copyright 2006, American Physical Society

and coherently controlled in the time domain at temperature between 20 and 300 K [54]. Using optical and microwave techniques similar to those used in diamond nitrogen-vacancy qubits, researchers have studied the spin-1 ground state of each of the four inequivalent forms of the neutral carbon–silicon divacancy as well as a pair of defect spin states of unidentified origin. These six lines lie in the range of 1.09–1.20 eV at 20 K. These defects are optically active near the telecommunication wavelengths, and they possess desirable spin coherence properties comparable to those of the nitrogen-vacancy center in diamond. These divacancy centers are promising candidates in many photonic, spintronic, and quantum information applications. Further study demonstrates that 4H-, 6H- and 3C-SiC all host coherent and optically addressable defect spin states in the 1.08–1.20-eV range, including states with room-temperature quantum coherence [55]. It suggests that crystal polymorphism in SiC can be a degree of freedom for engineering spin qubits.

It is well known that annealing can change the structure and properties of intrinsic defects especially vacancies. The annealing processes of vacancy-type defects in 3-MeV electron-irradiated and as-grown 6H-SiC are investigated by positron lifetime spectroscopy [56]. A vacancy-type defect giving rise to a positron lifetime of 183 ps is detected from the as-grown *n*-type 6H-SiC. This defect is annihilated after annealing at around 1,400 °C. Electron irradiation produces defects related to carbon vacancies, silicon vacancies, and divacancies. The defects related to carbon vacancies and divacancies are annealed at temperature up to 500 °C, whereas the defects related to silicon vacancies are annealed at around 750 and 1,400 °C. The observed defect is thus suggested to arise from Si vacancies, possibly complexes of silicon vacancies and nitrogen atoms. No vacancy-type defects are detected from *p*-type 6H-SiC even after electron irradiation.

Thermal elimination of the defects in 4H-SiC has been studied [57]. The Z_1/Z_2 and EH_6/EH_7 concentrations are reduced from the initial 10^{12}–10^{13} cm^{-3} to below the detection limit of 1×10^{11} cm^{-3} after thermal oxidation at 1,150–1,300 °C. However, oxidation produces a high concentration ($5–8 \times 10^{12}$ cm^{-3}) of another *HK*0 center ($E_V + 0.78$ eV). Further annealing in argon at 1,550 °C eliminates this *HK*0 center. Therefore, all the major deep defect levels can be eliminated by

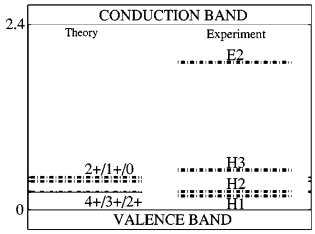

Fig. 2.19 Comparison of the calculated ionization levels of Si antisite in 3C-SiC with the experimental deep-level transient spectroscopy data obtained from Ref. 58. Reprinted with permission from [59]. Copyright 1998, American Physical Society

this two-step thermal treatment and the carrier lifetime in a 98-μm-thick *n*-type 4H-SiC epilayers can be improved from 0.64 to 4.52 μs afterward.

2.4.1.2 Antisites

The antisite defect is generated by occupation of a Si (C) position by a C (Si) atom. Deep-level transient spectroscopy performed on neutron-irradiated 3C-SiC reveals point defect-related centers called *H*1, *H*2, *H*3, and *E*2 [58]. The electronic energy levels of *H* centers are located at 0.18 eV (*H*1), 0.24 eV (*H*2), and 0.514 eV (*H*3) above the valence-band maximum, whereas the level of *E*2 is located at 0.49 eV below the conduction-band minimum. Ninety percent of the produced defects are eliminated by annealing at 350 °C, whereas the concentration of the *E*2 centers increases gradually with annealing of the *H* centers. The theoretical calculation based on the density functional theory with the local density approximation suggests that the *H* centers are ascribed to silicon antisite (Si_C) defects generated by neutron irradiation [59]. In both 3C- and 2H-SiC, the silicon antisite has several ionization levels in the bandgap. These levels in 3C-SiC are calculated by the plane-wave pseudopotential method and the results agree well with the deep-level transient spectroscopy data (Fig. 2.19).

The defect D_I with characteristic photoluminescence (PL) lines that is produced from irradiated SiC has been proposed to arise from the divacancy [48, 49], but the assignment of this defect is debatable and some researchers have suggested its origin to be antisite. A study of the 2-MeV electron-irradiated 4H-SiC (n^+- and p^+-type substrates and epilayers grown by chemical vapor deposition with different levels of *n*- or *p*-type residual doping) reveals a series of emission lines, and this spectrum named E_A consists of several sharp no-phonon lines accompanied by a broad phonon-assisted structure (Fig. 2.20) [60]. Annealing at around 750 °C induces an abrupt change in the spectrum and further annealing at over 750 °C results in the dominance of the strong D_I PL spectrum. Up to 40 no-phonon lines (within 2.8–2.9 eV) are resolved in the E_A spectrum. Photoluminescence excitation spectroscopy shows that the lines come in groups of two to four lines. The characteristics of the line groups suggest that they are attributed to bound-exciton

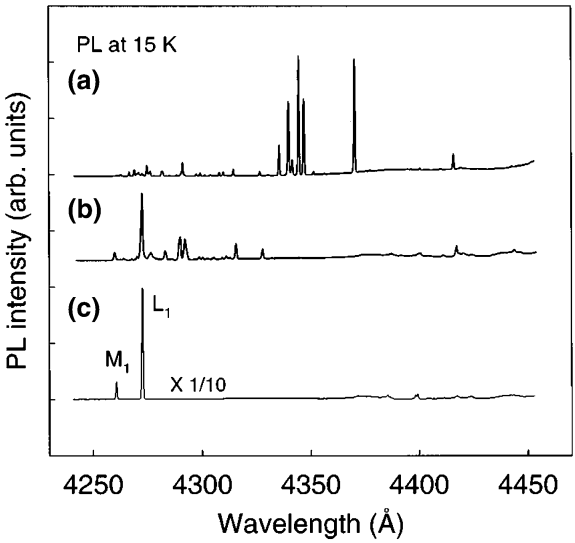

Fig. 2.20 Effects of annealing on the no-phonon lines in the PL spectrum (at 15 K) of 2-MeV electron-irradiated 4H-SiC. **a** No annealing. **b** Annealing at 750 °C. **c** Annealing at 1500 °C. The D_I lines L_1 and M_1 that dominate the spectrum after annealing at 1,500 °C (**c**) are one order of magnitude more intense than the lines of the (**a**) and (**b**) spectra. Reprinted with permission from [60]. Copyright 1999, American Physical Society

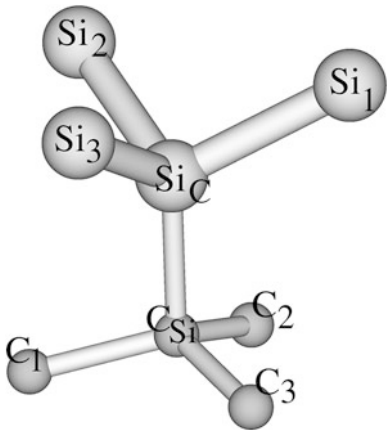

Fig. 2.21 Schematic of the antisite pair at the *k* site in 4H-SiC. For the C_{1h} symmetry in the single positively charged state, the Si(1) and C(1) atoms lie in the mirror plane making the Si(2), Si(3) and C(2), C(3) atoms equivalent. Reprinted with permission from [62]. Copyright 2003, American Physical Society

recombination at isoelectronic defect centers. By using first-principle density functional calculation, the origin of the lines of the E_A spectrum has been investigated [61]. These lines originate from the recombination of a delocalized electron with a localized hole bound to a Si antisite defect (Si_C), which is in proximity with a C antisite (C_{Si}). The most stable antisite pair may generate the most energetic line in the E_A spectrum or the D_I band. The study based on the low-temperature PL and ab initio supercell calculation for 3C- and 4H-SiC shows that the neutral antisite pair (Fig. 2.21) is a good candidate for the D_I defect [62]. The calculated one-electron level of the neutral antisite pair is very close to the measured transition energy of the zero-phonon line, and the calculated local vibration modes can explain the experimental findings. The calculated hyperfine constants of the

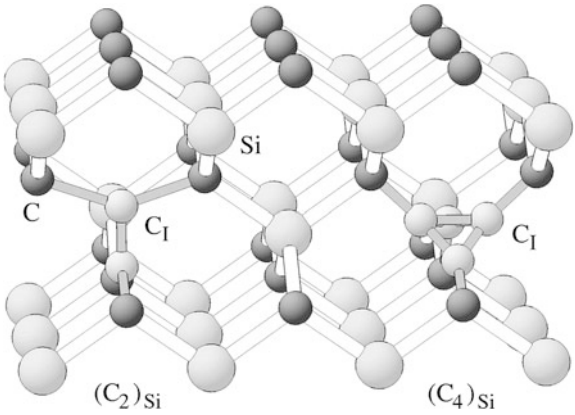

Fig. 2.22 Configuration of the dicarbon antisite $(C_2)_{Si}$ and carbon cluster with four atoms on a silicon site $(C_4)_{Si}$ in 3C-SiC. Reprinted with permission from [66]. Copyright 2004, American Physical Society

antisite pair in its paramagnetic state support this assignment of the D_I center. However, another study based on the local density functional calculation shows that the close-by antisite pair is not stable enough to account for D_I [63]. Instead, D_I is suggested to be related to an isolated Si antisite and the four forms of the close-by antisite pair in 4H-SiC is supposed to give rise to the *a*, *b*, *c*, and *d* members of the E_A PL spectrum.

Another famous persistent intrinsic defect in SiC is D_{II}. This defect center is detected from ion-implanted and annealed (at 1,300 °C) 3C-SiC by low-temperature luminescence spectroscopy [64]. The PL spectrum reveals a number of high-energy localized modes. One mode has an energy of 164.7 meV, which is equivalent to the highest lattice frequency in diamond and far above the 120.5-meV lattice limit of SiC. A carbon di-interstitial is suggested to account for this defect, which arises after annealing at 1,300 °C and persists after annealing at 1,700 °C. The D_{II} center is also observed from the unannealed ion (B, Al, P) implanted 3C-SiC films [65]. The D_{II} zero-phonon line is located at about 2.3 eV. Its intensity increases with annealing temperature, but drops rapidly for annealing temperature above 1,600 °C. The phonon replicas of the D_{II} zero-phonon line are located in the range of 1.98–2.25 eV. The spectral density of the phonon replicas resembles the phonon density of states in diamond, suggesting that the observed spectrum stems from a carbon-associated defect. The structural, electronic, and vibrational properties of the dicarbon antisite complexes have been investigated by the density functional theory to check whether they can account for the D_{II} center [66]. Figure 2.22 shows the configuration of the dicarbon antisite $(C_2)_{Si}$, where two carbon atoms sharing a silicon site are surrounded by a tetrahedron of four carbon atoms. The dicarbon antisite possesses a characteristic vibrational pattern in the frequency range of the D_{II} spectrum but it cannot explain all the experimentally observed phonon replicas. The D_{II}-type centers may be related to larger carbon clusters built on the basis of the dicarbon antisite.

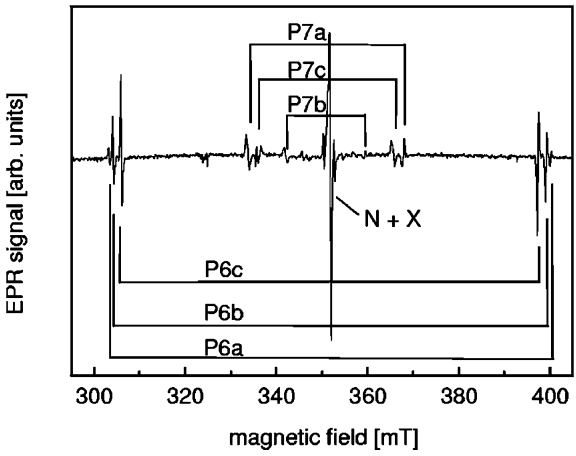

Fig. 2.23 Electron paramagnetic resonance spectrum of neutron-irradiated and 1,000 °C annealed 6H-SiC acquired with the magnetic field parallel to the *c*-axis of the crystal. Six spin-triplet spectra labeled *P6a*, *b*, *c*, and *P7a*, *b*, *c* are observed. Reprinted with permission from [67]. Copyright 2001, American Physical Society

2.4.1.3 Carbon Vacancy–Carbon Antisite Pair

The carbon vacancy–carbon antisite (C_{Si}–V_C) pair is another important point defect in silicon carbide. The *P6*/*P7* spectrum observed from neutron-irradiated and annealed nitrogen-doped 6H-SiC prepared by sublimation is suggested to arise from a photoexcited spin-triplet state of the carbon vacancy–carbon antisite (C_{Si}–V_C) pair [67]. The photoexcited paramagnetic triplet state of this defect in 6H-SiC is observed from all the inequivalent lattice sites and all orientations by electron paramagnetic resonance and magnetic circular dichroism of the absorption. The electron paramagnetic resonance signal comprises six spin-triplet lines (Fig. 2.23). First-principle calculation shows that among several pair defect models, C_{Si}–V_C in the charge state +2 (Fig. 2.24) is the only intrinsic nearest-neighbor pair defect that is diamagnetic in its ground state and has a photoexcited spin-triplet state that can result in the observed electron paramagnetic resonance hyperfine structure and optical transitions. The C_{Si}–V_C pair is observed after irradiation and subsequent annealing above the annealing temperature of the silicon vacancy. Therefore, movement of the carbon atom into the neighboring Si vacancy during annealing may result in the formation of the C_{Si}–V_C defect.

However, the same spectrum generated from electron-irradiated 4H-SiC has been proposed to arise from the triplet ground states of the neutral divacancy [52]. Instead, another experimentally observed defect (*SI*5 center) in 4H-SiC is assigned to the negatively charged carbon vacancy–carbon antisite pair $(C_{Si}V_C)^-$ based on electron paramagnetic resonance and first-principle calculation [68]. The vacancy defects and *SI*5 center are found to play an important role in the semi-insulating property of SiC. Two sets of photoluminescence lines (called A and B) are detected from electron-irradiated and ion-implanted 4H-SiC at 7 K (Fig. 2.25) [69]. The spectral details, temperature dependence, and annealing characteristics suggest that the A and B spectra stem from the neutral on-axis and off-axis carbon antisite–vacancy pairs $(V_CC_{Si})^0$. The relatively impure and highly compensated-doped

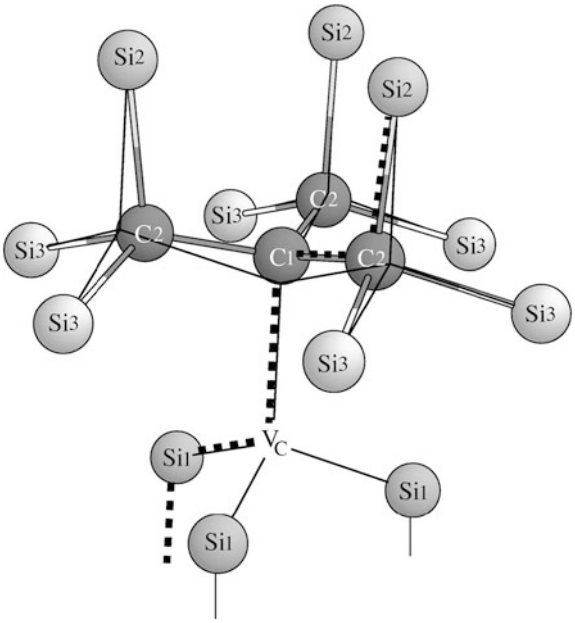

Fig. 2.24 Calculated relaxed structure of $(C_{Si}–V_C)^{2+}$ in 6H-SiC. The thin lines mark the position of the bonds in the ideal lattice. The carbon antisite C1 relaxes by 16 % of the bond length in the ideal crystal away from the vacancy. Reprinted with permission from [67]. Copyright 2001, American Physical Society

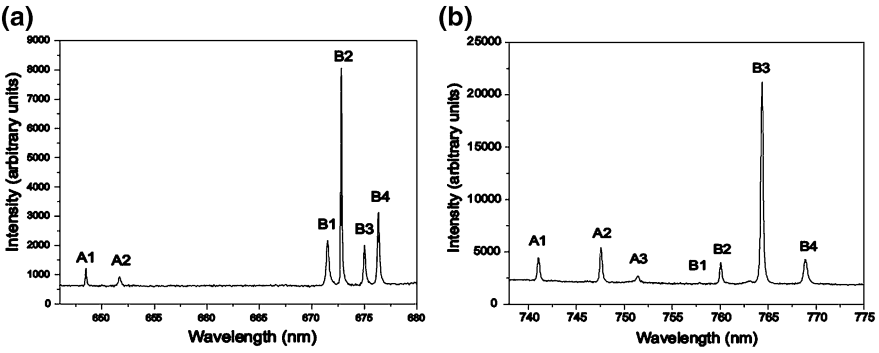

Fig. 2.25 A and B spectra of **a** 4H-SiC and **b** 6H-SiC excited by 488-nm light at 7 K. Reprinted with permission from [69]. Copyright 2009, American Physical Society

samples exhibit very strong A and B PL, whereas the purer largely uncompensated *n* (N)- or *p* (Al)-doped samples exhibit mainly PL of the Si vacancy-related defects and weakly PL of A and B even after annealing at 900 °C.

The carbon antisite–vacancy defect showing A/B PL can serve as a single-photon source [70]. These defects are produced in high-purity, semi-insulating 4H-SiC

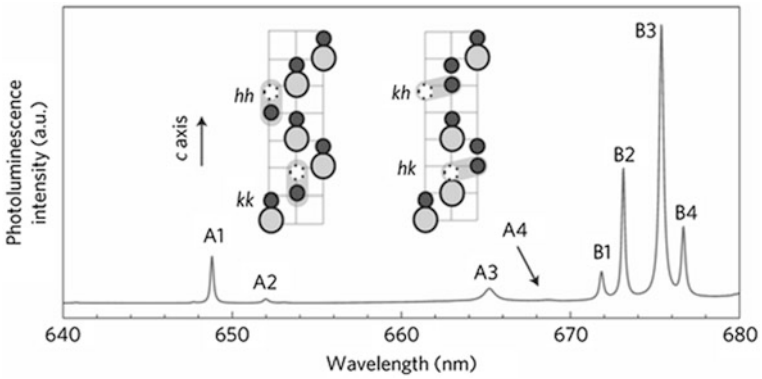

Fig. 2.26 A and B PL lines observed from electron-irradiated 4H-SiC acquired at 80 K. The proposed atomic structure of the defects C_{Si}–V_C yielding the PL is shown in the (1120) plane (small/large circle representing C/Si atom and small open circles denoting vacancies). The carbon antisite–vacancy pair has four possible configurations: *hh*/*kk* axial configurations with C_{3v} symmetry, and *hk*/*kh* basal plane configurations with C_{1h} symmetry. *h*/*k* denotes the hexagonal/cubic site in the SiC lattice. Reprinted with permission from [70]. Copyright 2014, Macmillan Publishers Ltd

wafers by irradiation with 2-MeV electrons followed by annealing. Low electron fluences are adopted to give rise to isolated single defects, and the annealing temperature is tuned to increase/decrease the number of defects. The sample shows obvious A/B PL lines (Fig. 2.26). The lines are at 648.7 nm (A1), 651.8 nm (A2), 665.1 nm (A3), 668.5 nm (A4), 671.7 nm (B1), 673.0 nm (B2), 675.2 nm (B3), and 676.5 nm (B4). These lines arise from the $C_{Si}V_C$ defect. In contrast to the previous assignment [69], the ab initio supercell calculation in combination with group theory indicates that the neutral C_{Si}–V_C pair does not have visible PL and so the positively charged C_{Si}–V_C pair (spin $= 1/2$) with predicted visible PL is proposed as the origin of the A/B PL. PL from single-defect centers is observed by room-temperature confocal microscopy, as shown in Fig. 2.27a. These spectra are in accordance with the A/B lines. Single-photon emission is confirmed using a Hanbury Brown-Twiss interferometer based on the observation that the second-order photon correlation function at zero delay is $g^{(2)}(0) < 0$ (Fig. 2.27b). The typical acquired excited state lifetime is 1.2 ns. Forty-five percent of the defect emitters measured in a sample irradiated and annealed at 300 °C are stable over a long period of time, whereas the other emitters show PL blinking and some eventually photobleach. The samples annealed at higher temperature (500 °C) contain nearly no blinking centers.

2.4.1.4 Studies on Multiple Point Defects

The effects of deviations from stoichiometry on the relative abundances of native defects and electronic properties of 3C-SiC have been investigated by ab initio calculation [71]. The result shows that the dominant defect in a perfectly

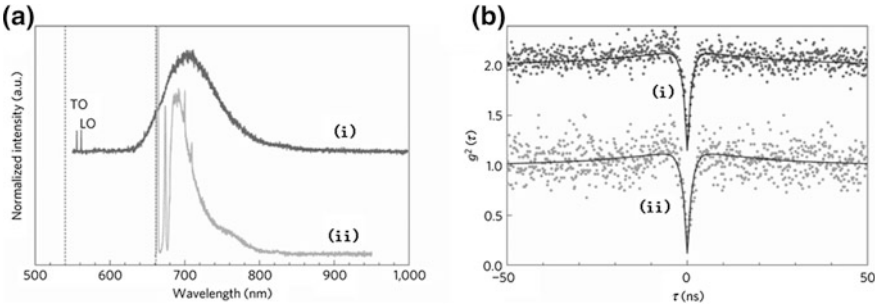

Fig. 2.27 **a** Room-temperature PL spectra of a single-photon source in the irradiated 4H-SiC excited by the 532 nm (i) and 660 nm (ii) lines. The dashed lines denote excitation wavelengths. **b** Corresponding antibunching curves. Reprinted with permission from [70]. Copyright 2014, Macmillan Publishers Ltd

stoichiometric SiC is the electrically inactive Si_C–C_{Si} pair. In Si-rich SiC, the concentrations of the stoichiometry compensating defects depend strongly on the Fermi-level position, and the Si_C antisite and carbon vacancy are separately the dominant defects in *n*- and *p*-type SiC. As a double donor, the carbon vacancy acts as a charge-compensating defect when the Fermi level is lowered and reduces the doping efficiency of acceptors. The electrically inactive C_{Si} antisite dominates in the C-rich SiC regardless of the position of the Fermi level. The slightly C-rich SiC is thus more suitable for *p*-type doping in electronic applications. The electronic and atomic structures of the monovacancies and antisite defects in 4H-SiC in all possible charge states have been investigated using a plane-wave pseudopotential method based on the density functional theory and local spin-density approximation [72]. The calculation indicates no negative-*U* behavior for the carbon vacancies. Hence, the single positive charge state of the carbon vacancy V_C^+ is stable, in agreement with previous experimental result. The silicon antisite Si_C^+ is found to be stable at small values of electron chemical potential. These results agree with previous experiments.

Electrically active defects in 4H-SiC are produced by irradiation of low-energy electrons below the threshold of Si atom displacement [73]. The majority and minority carrier traps induced by radiation are analyzed by capacitance transient techniques. Four electron traps (EH1, Z_1/Z_2, EH3, and EH7) and one hole trap (HS2) are detected (Fig. 2.28) and suggested to be related to the initial displacement of carbon atoms. Their properties are summarized in Table 2.2. The concentrations of these defects increase linearly with irradiation dose, suggesting that no divacancies or di-interstitials are generated. None of the observed defects is found to be an intrinsic defect–impurity complex. The probable candidates for these defects are limited to carbon vacancies, split interstitials, and antisites. No additional defects are detected from samples irradiated by electrons with energies higher than the threshold of Si atom displacement.

The irradiation and annealing effects on defects as well as the defect migration processes in SiC have been extensively studied by theoretical calculation and simulation. Molecular dynamics simulation using a modified Tersoff potential is

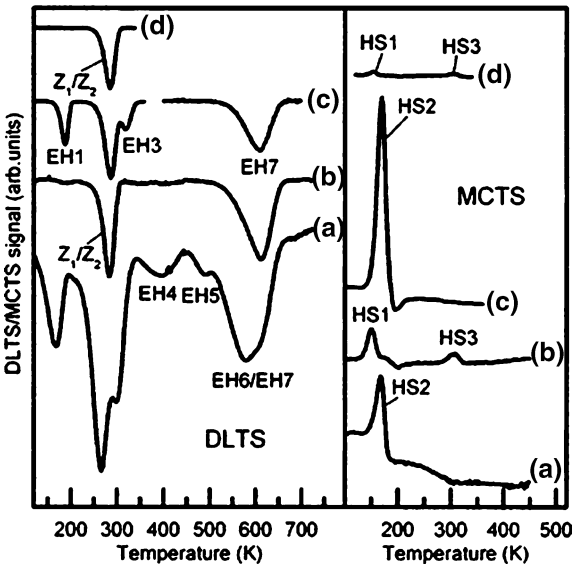

Fig. 2.28 Deep-level transient spectroscopy and minority carrier transient spectroscopy spectra of electron-irradiated 4H-SiC. **a** Irradiation with 9-MeV electrons. **b** Irradiation with 9-MeV electrons and annealing at 950 °C for 1 h. **c** Irradiation with 210-keV electrons. **d** Irradiation with 210-keV electrons and annealing at 950 °C for 1 h. Reprinted with permission from [73]. Copyright 2004, AIP Publishing LLC

Table 2.2 Electrical properties of the defects observed in 4H-SiC irradiated by low-energy electrons. The capture cross section is estimated from the intercept of the Arrhenius plot. Reprinted with permission from [73]. Copyright 2004, AIP Publishing LLC

Position in the bandgap (eV)	Label	Peak temperature, K (for 230-ms rate window)	Capture cross section, cm^2
$E_c - 0.41$	EH1 (SS_1)	188	4×10^{-15}
$E_c - 0.68$	($Z_{1/2}$)	287	2×10^{-14}
$E_c - 0.71$	EH3 (S_2)	320	4×10^{-15}
$E_c - 1.54$	EH7	607	3×10^{-14}
$E_v - 0.39$	HS2	170	2×10^{-14}

used to study the primary damage state and defect production in the displacement cascades in 3C-SiC [74]. Recoils with energies of 0.25–50 keV are simulated at 300 K. It is found that the displacement threshold energy surface is highly anisotropic. The dominant surviving defects are C interstitials and vacancies, whereas only a small fraction of the surviving defects is antisites. The defect clusters are much smaller and rarer compared to those in metals. The simulation also shows that the defect production efficiency decreases with increasing recoil

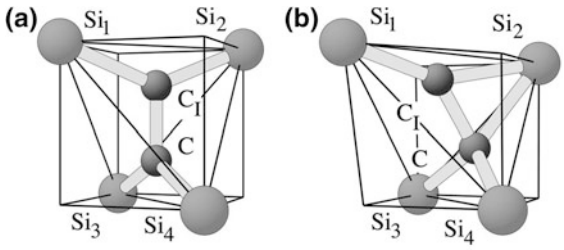

Fig. 2.29 Configuration of the carbon split interstitial $C_{sp\langle 100\rangle}$: **a** $\langle 100\rangle$ orientation with D_{2d}/D_2 symmetry and (**b**) tilted $C_{sp\langle 100\rangle}$. The $C_{spSi\langle 100\rangle}$ configuration corresponds to the untilted $C_{sp\langle 100\rangle}$ with the C–C_I pair replaced by a Si–C_I pair and C neighbors instead of Si neighbors. Reprinted with permission from [77]. Copyright 2003, American Physical Society

energy. The formation energies and properties of the native defects in 3C-SiC are studied by density functional calculation based on the pseudopotential plan-wave method within local density approximation combined with the molecular dynamics simulation using Tersoff potentials [75]. It is found that the most favorable configurations for the C interstitials are $\langle 100\rangle$ and $\langle 110\rangle$ dumbbells with formation energies of 3.16–3.59 eV, and the most favorable Si interstitial is Si tetrahedral surrounded by four C atoms with a formation energy of 6.17 eV. The formation energies of the vacancies and antisite defects obtained by molecular dynamics simulation agree with those obtained by density functional calculation. The long-range migration of point defects in 3C-SiC is subsequently investigated by both molecular dynamics simulation and the nudged elastic band method [76]. The results show that stable C split interstitials can migrate via the first or second nearest-neighbor sites, whereas Si interstitials migrate directly from one tetrahedral position to another neighboring equivalent position by a kick-in/kick-out process. C and Si vacancies jump to one of their equivalent sites through a direct migration mechanism. The calculated migration barriers for C and Si interstitials agree with experiments.

Diffusion of intrinsic defects in 3C-SiC is studied by density functional calculation using the local density approximation or local spin-density approximation [77]. The results show that the vacancies migrate to their own sublattice. The carbon split interstitials (Fig. 2.29) and two silicon interstitials (tetrahedrally carbon-coordinated interstitial in the *p*-type materials and the split interstitial in the compensated and *n*-type materials) are found to be more mobile than the vacancies, thereby playing a prominent role in diffusion. The metastable Si vacancy in *p*-type and compensated SiC is transformed into the more stable vacancy–antisite complex, suppressing its contribution to diffusion processes. The most important migration channels for vacancies and interstitials in 3C-SiC are depicted in Fig. 2.30. The annealing kinetics of mobile intrinsic defects in 3C-SiC is investigated by the same method [78]. The calculated migration and reaction barriers help to determine the annealing mechanisms. The carbon and silicon interstitials have higher mobility than the vacancies, thus driving the annealing mechanisms at lower temperature including vacancy-interstitial recombination and formation of

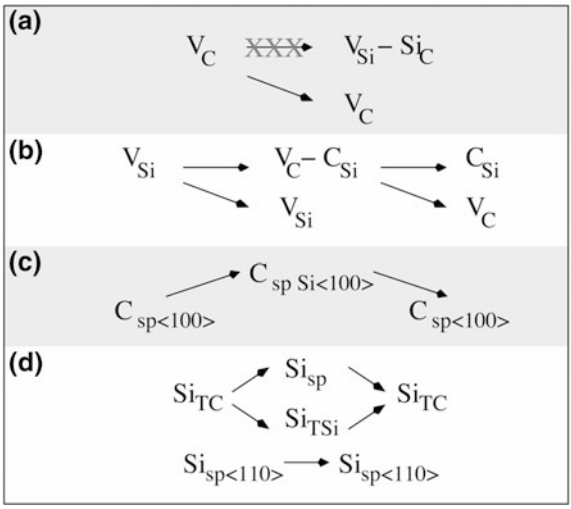

Fig. 2.30 Dominant migration mechanisms of interstitials and vacancies in 3C-SiC: **a** C vacancies (V_C) migrate on the C sublattice only, **b** transformation of the Si vacancy (V_{Si}) into a C vacancy-antisite complex V_C-C_{Si} (*p*-type and compensated) and vacancy migration on the Si sublattice (*n*-type), **c** C-interstitial migration via split-interstitial configurations $C_{sp\langle 100\rangle}$ and $C_{spSi\langle 100\rangle}$, and **d** kick-out mechanism for the C-coordinated Si interstitial (Si_{TC}) via split interstitials ($Si_{sp\langle 100\rangle}$ and $Si_{sp\langle 110\rangle}$) (*p*-type) and direct migration of the Si split-interstitial $Si_{sp\langle 110\rangle}$ (compensated and *n*-type). Reprinted with permission from [77]. Copyright 2003, American Physical Society

interstitial carbon clusters. These clusters emit carbon interstitials at higher temperature. In *p*-type SiC, transformation of the silicon vacancy into the more stable vacancy–antisite complex serves as an annealing mechanism before vacancy migration.

The aggregates of carbon interstitials in 3C- and 4H-SiC have been studied theoretically [79]. Formation of carbon aggregates is found to be energetically favored, and all the carbon clusters are electrically active. The electronic and vibronic properties depend strongly on the polytype of SiC. Additionally, comparison of the calculated local vibration modes of all the defect aggregates to those observed from the *P* and D_{II} PL centers suggests that these centers are related to the $(C_2)_{Si}$ and $[(C_2)_{Si}]_2$ defects, respectively. Migration of vacancies at high temperature is studied by the self-consistent charge density functional-based tight-binding method [80]. The energy barrier for sublattice migration of V_{Si} is shown to be lower than that for V_C, and hence, V_{Si} should anneal out at lower temperature as supported by experiments. The calculation shows that the motion of vacancies can mediate the migration of antisites. Vacancy-assisted diffusion of carbon antisites is much faster than that of silicon antisites, thereby creating carbon antisite clusters. The result shows that the mobility of carbon antisites can trigger the formation of larger antisite complexes.

Fig. 2.31 Interaction between dislocations in parallel glide planes (180×). Reprinted with permission from [81]. Copyright 1960, AIP Publishing LLC

2.4.2 Dislocations and Micropipes

Dislocations and micropipes have long been observed from silicon carbide. The various dislocations and glide elements in 6H-SiC have been investigated by etching in conjunction with optical microscopy and X-ray diffraction microscopy [81]. The conventional etching technique is demonstrated to be suitable for the identification of the intersection of dislocations on the (0001) surfaces. High-density dislocations in the (0001) planes are observed by diffraction microscopy, and dislocations with $[11\bar{2}0]$ vectors are observed in addition to evidence of slip on both the basal planes and "puckered" pyramidal plane. Pileups formed by slip and dislocation walls formed by climb are identified. The dislocations in the parallel glide planes interact with each other (Fig. 2.31), and they line up in a direction perpendicular to the glide planes. Propagation of basal plane dislocations from the off-axis 4H-SiC substrate into the homoepitaxial layer has been investigated by chemical etching, optical microscopy, and transmission electron microscopy [82]. The basal plane dislocations in the substrates are converted into threading edge dislocations in the epilayer at the epilayers/substrate interface. TEM reveals that the converted dislocations are inclined from the *c*-axis toward the down-step direction by about 15°. The in-plane orientation of the inclination is toward the step flow direction within ±10°. The conversion can be interpreted as a result of the image force in the epilayers between flowing growth steps and basal plane dislocations. A theoretical study has been conducted on the 30° and 90° Shockley partial dislocations lying in the {111} and basal planes of cubic and hexagonal silicon carbide [83]. The core structure, energetics, and electronic structure of the dislocations are determined. The thermal activation barriers to glide motion of 30° and 90° Shockley partials are calculated in terms of a process involving the formation and migration of kinks along the dislocation line.

Micropipes that constitute a major defect in mass-produced SiC wafers are hollow tubular defects penetrating the SiC single crystals. Their radius ranges from

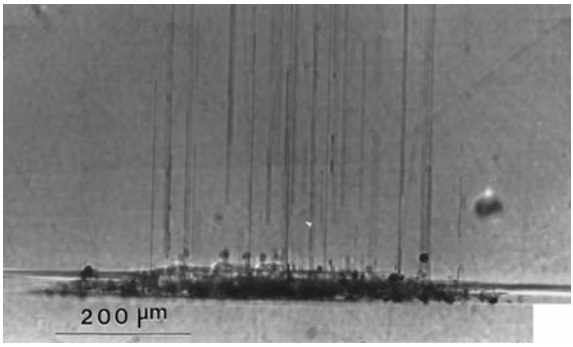

Fig. 2.32 Optical micrograph showing nucleation of micropipes at a group of inclusions during growth in a 4H-SiC wafer. Reprinted with permission from [88]. Copyright 1999, AIP Publishing LLC

a few tens of nanometers to several tens of micrometers and the density at the growth surface ranges from several hundred to less then one micropipe per cm^2 [84]. These micropipe defects can severely hamper the performance of SiC power devices [85]. Micropipe defects in 4H- and 6H-SiC substrates have been found to lead to preavalanche reverse-bias point failure in many epitaxially grown *p-n* junction devices with an area of 1 mm^2 or larger. The SiC power device ratings will be restricted to several amps or less if the defect density is on the order of 100s of micropipes/cm^2.

Many studies indicate that the micropipes in SiC are hollow core dislocations [83]. The dependence of the micropipe radius on the Burgers vector content of the micropipes in different SiC has been analyzed, and the relationship can be explained by Frank's model of a hollow core dislocation when a mixed dislocation is assumed [86]. The origin of micropipes and nanopipes in SiC are hollow superscrew dislocations formed by the attraction of unit screw dislocations to a nanopipe formed at the axis of some triple junctions [87].

A model has been proposed to explain the formation of screw dislocations (including micropipe nucleation) in SiC [88]. Micropipes have been demonstrated to nucleate at the sites of foreign materials inclusions by synchrotron white beam X-ray topography and transmission optical microscopy (Fig. 2.32). Incorporation of the inclusions into the growing crystal can lead to deformation of the protruding ledge that constitutes the overgrowing layer. Deformation is accommodated by the crystal lattice creating pairs of opposite-sign screw dislocations (Fig. 2.33), which then propagate with the growing crystal. Using a series of synchrotron imaging techniques in the reflection geometries, micropipes in 6H-SiC crystals have been mapped [89]. The combined synchrotron white beam X-ray topography techniques and corresponding simulation (Fig. 2.34) demonstrate explicitly that the micropipes are pure superscrew dislocations. The details of the superscrew dislocations, including the spatial distribution of the strain fields, magnitude of the Burgers vectors, dislocation senses, and surface relaxation effects, can also be accurately determined and described by these techniques.

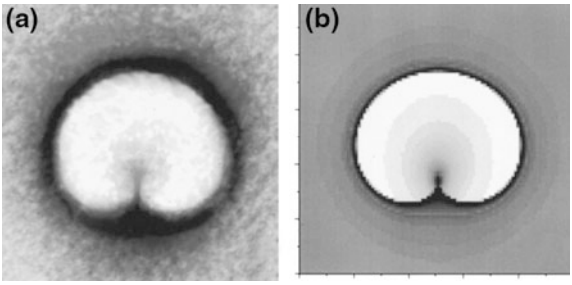

Fig. 2.33 **a** Synchrotron white beam X-ray topography image recorded in the back-reflection geometry from a (0001) Lely platelet showing a pair of opposite-sign screw dislocations. **b** Simulated image of two opposite-sign screw dislocations with 30-μm spacing. The image dimensions are 200 × 200 μm^2. Reprinted with permission from [88]. Copyright 1999, AIP Publishing LLC

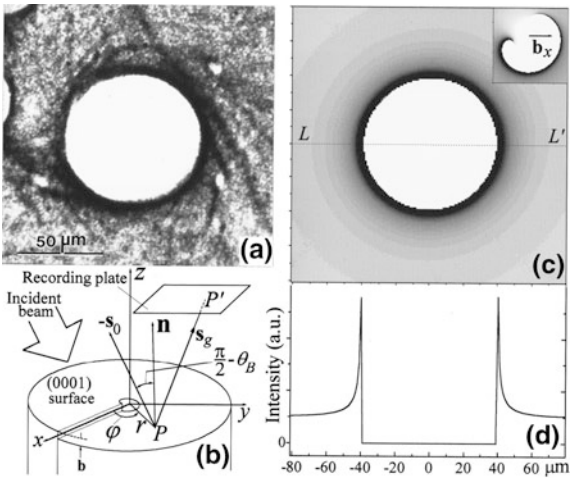

Fig. 2.34 **a** Synchrotron back-reflection topographic image of an 8*c* micropipe under diffraction conditions g = 00024 (and its harmonics), $\theta_B = 81.4°$, and sample-to-film distance equal to 20 cm. **b** Diffraction geometry. **c** Simulation of an 8*c* superscrew dislocation. The inset corresponds to the simulation of a mixed dislocation. **d** Radial diffraction intensity profile of (**c**). Reprinted with permission from [89]. Copyright 1999, AIP Publishing LLC

2.4.3 Stacking Faults

Stacking faults are segments in the SiC crystal where rows of Si–C bilayers deviate from the perfect stacking sequence (along *c*-axis) of the crystal. The defects in single crystalline and polycrystalline SiC are examined by transmission electron microscopy, and the result shows that dislocations are not as common as stacking faults [90]. Dislocations have been observed from nearly all the materials examined (Fig. 2.35). The observed stacking faults are either "stress-induced" extrinsic

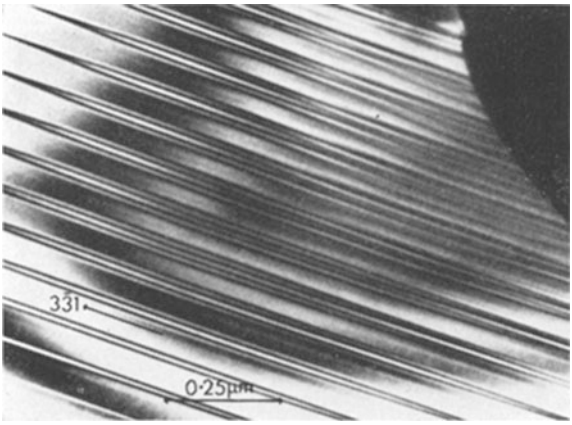

Fig. 2.35 TEM image of the regularly spaced stacking faults in hot-pressed SiC. Reprinted with permission from [90]. Copyright 1972, Springer Science and Business Media

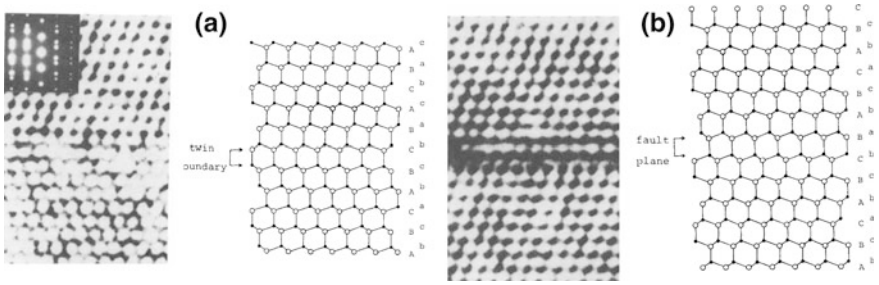

Fig. 2.36 High-resolution TEM images of **a** twin stacking fault and **b** deformation stacking fault found in β-SiC ceramics sintered at 2,000 °C. The right panel shows the structural models based on the stacking sequence. Reprinted with permission from [91]. Copyright 1989, Wiley-VCH Verlag GmbH & Co. KGaA

or "grown-in" intrinsic ones. The stacking fault energy is measured to be 1.9 ergs/cm^2 by the extended node method. The structure of the stacking faults in β-SiC has been investigated by high-resolution transmission electron microscopy (HRTEM) [91]. The HRTEM images of the stacking faults in a specimen sintered at 2,000 °C along with their structure models are shown in Fig. 2.36. There are many twin boundaries with nearly perfect atomic arrangement in each twinned domain. The result shows that the stacking faults initially present in the β-SiC powders are eliminated as grain growth proceeds at elevated temperature.

The effects of stacking faults on the X-ray diffraction profiles of β-SiC powders have been studied by simulation with supercells of up to 100 times the volume of a conventional unit cell [92]. Stacking faults in β-SiC powders give rise to all the features observed from the diffraction pattern, that is, an additional peak at $d = 0.266$ nm, a high background intensity around the peak at $d = 0.252$ nm, and broadening of the β-SiC peaks. The simulation also indicates that the distribution

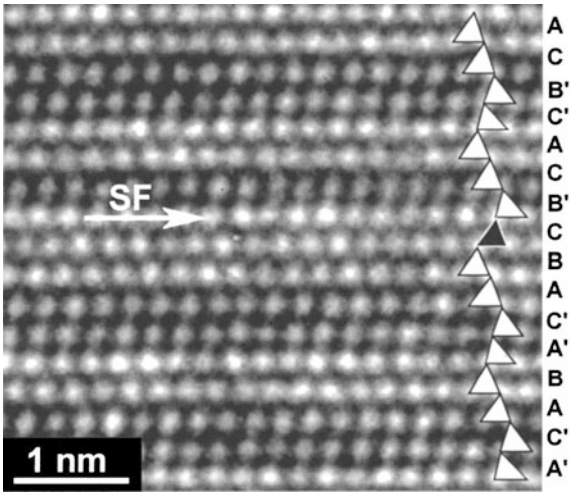

Fig. 2.37 High-resolution TEM image of a stacking fault (marked by *arrow*) in a 4H-SiC diode. Reprinted with permission from [94]. Copyright 2002, AIP Publishing LLC

of the faults is not uniform, although a unique description of the fault population is not available. The deformed 4H- and 6H-SiC single crystals by compression at 1,300 °C have been investigated [93]. All the deformation-induced dislocations are dissociated into two partials bounding a ribbon of intrinsic stacking fault. Using transmission electron microscopy, the stacking fault energy is determined from the separation width of the two partials of dissociated dislocations. It is 14.7 ± 2.5 mJ m^{-2} for 4H-SiC, and 2.9 ± 0.6 mJ m^{-2} for 6H-SiC. The calculated stacking fault energies based on the axial next-nearest-neighbor Ising spin model are within 5 and 40 % of the experimental values for 6H- and 4H-SiC, respectively.

The structure of the stacking faults formed in forward-biased 4H- and 6H-SiC p-n^- diodes is investigated by transmission electron microscopy [94]. The typical fault densities are between 10^3 and 10^4 cm^{-1}, and analysis of the stacking sequences (Fig. 2.37) and partial dislocations bounding the faults indicates that the faults are isolated single-layer Shockley ones bounded by partial dislocations. The stacking faults formed during forward biasing of 4H-SiC p-i-n diodes are identified using light emission imaging and transmission electron microscopy [95]. These faults may have either faulted dislocations or faulted dislocation loops, and the leading partial dislocations of the faulted loops may have either carbon cores or silicon cores, whereas the partials of faulted dislocations are silicon cores. These stacking faults seem to relieve both tension and compression during p-i-n diode operation, indicating the presence of a complex inhomogeneous strain field within the diode. The formation and growth of the stacking faults causing degradation in bipolar p-i-n diodes are studied by electrical, optical, and structural techniques [96], and there are at least three origins for the stacking fault formation, giving rise to faults with different characteristics.

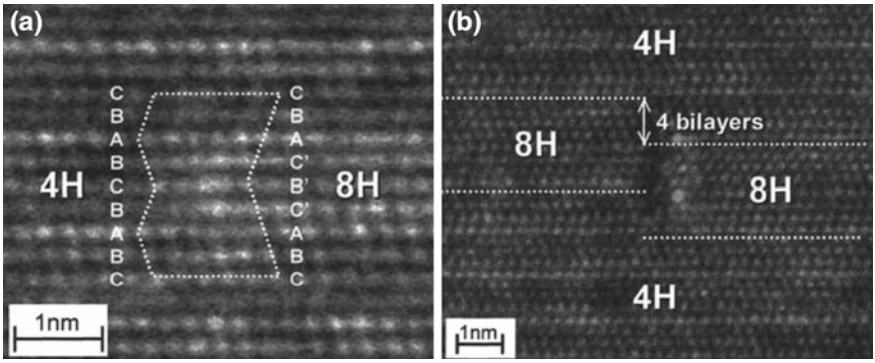

Fig. 2.38 High-resolution TEM images of the stacking faults in the 4H-SiC epilayer. Reprinted with permission from [97]. Copyright 2005, AIP Publishing LLC

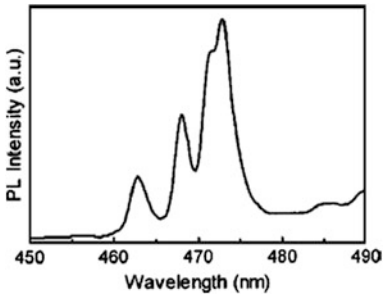

Fig. 2.39 PL spectrum of an in-grown stacking fault in the 4H-SiC epilayer acquired at 9 K excited by the 325-nm line. The four peaks are at 463.1, 468.3, 471.8, and 473.1 nm. Reprinted with permission from [97]. Copyright 2005, AIP Publishing LLC

The structure of in-grown stacking faults in 4H-SiC (0001) epilayers prepared by chemical vapor deposition has been investigated [97]. The in-grown stacking faults nucleate near the substrate/epilayer interface and expand with increasing epilayer thickness in a triangular shape. Transmission electron microscopy confirms that the in-grown stacking fault is the 1*c* of 8H polytype (Fig. 2.38). The low-temperature PL spectrum obtained from the same area (absent in other areas) exhibits four peaks at 463.1, 468.3, 471.8, and 473.1 nm (Fig. 2.39) corresponding to phonon replicas with a bandgap of 2.710 eV, and this confirms the 8H polytype. The epilayers prepared under the conditions of slow growth rate, high temperature, and improved substrate surface have reduced densities of in-grown stacking faults. The density, shape, and structure of the in-grown stacking faults in 4H-SiC (0001) epitaxial layers are investigated by cathodoluminescence, photoluminescence, and transmission electron microscopy [98]. The in-grown stacking faults have the 8H structure (Fig. 2.40) and exhibit a photoluminescence peak at 2.56–2.70 eV. The stacking faults in the Schottky barrier diode lower the barrier height and decrease the breakdown voltage. The stacking faults in 4H-SiC epilayers are studied by

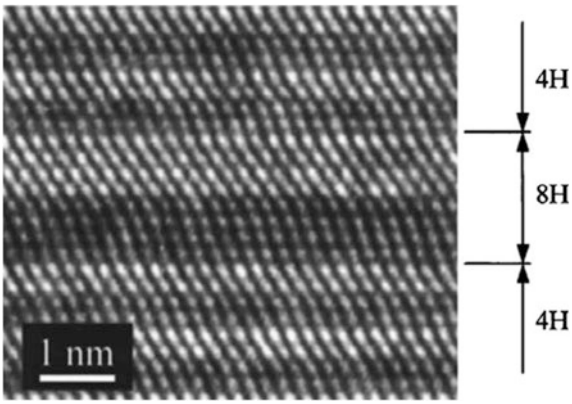

Fig. 2.40 Cross-sectional HRTEM image of an in-grown stacking fault in the 4H-SiC epilayer prepared by chemical vapor deposition. Reprinted with permission from [98]. Copyright 2005, AIP Publishing LLC

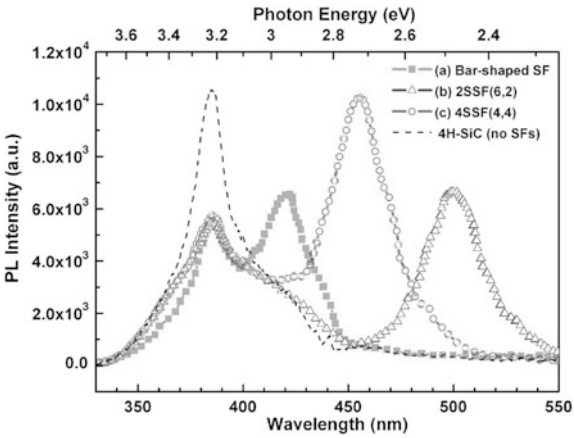

Fig. 2.41 PL spectra obtained from the 4H-SiC epilayer in the areas of: **a** bar-shaped (intrinsic Frank) stacking fault, **b** double Shockley stacking fault (2SSF), and **c** in-grown stacking fault (4SSF). The spectrum acquired from the area without stacking faults (SFs) is shown by the *dashed line*. Reprinted with permission from [99]. Copyright 2008, AIP Publishing LLC

microphotoluminescence spectroscopy and photoluminescence intensity mapping [99]. Three types of stacking faults, namely intrinsic Frank, double Shockley, and in-grown stacking faults, are identified. Each kind of stacking fault shows distinct PL located at 420 nm (intrinsic Frank), 500 nm (double Shockley), and 455 nm (in-grown), respectively (Fig. 2.41). The area without stacking faults shows PL with a peak at 386 nm (close to 4H-SiC bandgap) accompanied by a tail on the low-energy side. The shape and distribution of the stacking faults can be profiled by micro-PL intensity mapping (Fig. 2.42).

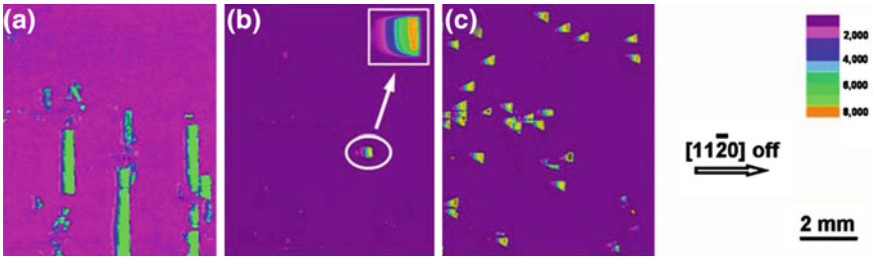

Fig. 2.42 PL intensity mapping of the 4H-SiC epilayer at **a** 420 nm, **b** 500 nm, and **c** 455 nm. Reprinted with permission from [99]. Copyright 2008, AIP Publishing LLC

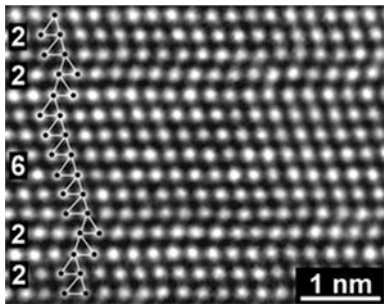

Fig. 2.43 HRTEM image of a stacking fault in the heavily doped *n*-type 4H-SiC crystal. Reprinted with permission from [100]. Copyright 2002, AIP Publishing LLC

The formation and expansion mechanism of stacking faults have been explored. Spontaneous formation of stacking faults is observed from heavily nitrogen-doped ($n > 1\times10^{19}$ cm^{-3}) 4H-polytype SiC crystals by transmission electron microscopy [100]. Faults are present in the as-grown boules and additional faults are generated by annealing in argon at 1,150 °C. All the faults have an identical structure consisting of six layers stacked in a cubic sequence embedded in the 4H-SiC crystal (Fig. 2.43). The stacking faults result from two Shockley partial dislocations gliding on two neighboring basal planes of SiC. The energy of the 4H-SiC with faults may be lower than that of the perfect heavily doped crystal at typical processing temperatures, and this explains the structural transformation. Detailed study shows that the structural transformation is caused by the quantum-well action [101], the electrons in highly *n*-type 4H-SiC enter stacking fault-induced quantum-well states to lower the system energy. The net energy gain derived from the charge neutrality equation shows a dependence on the temperature and nitrogen doping concentration. Doping concentrations in excess of 3×10^{19} cm^{-3} should result in spontaneous formation of double-layer stacking faults at the device-processing temperatures, in agreement with observations. Charge buildup in the stacking faults can produce an electrostatic potential that increases the forward voltage drop in SiC *p-i-n* diodes.

The driving force of stacking fault expansion in 4H-SiC *p-i-n* diodes is investigated by optical emission microscopy and transmission electron microscopy

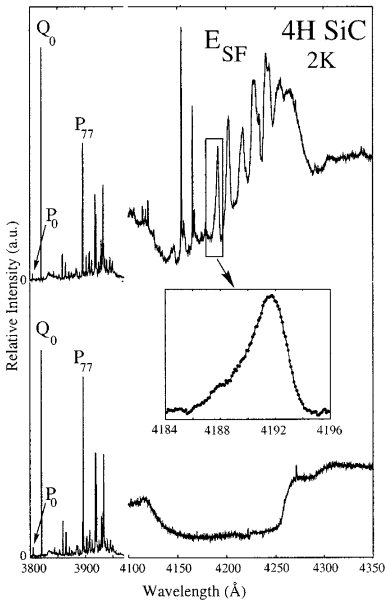

Fig. 2.44 PL spectra of a stressed (*top*) and nonstressed (*bottom*) 4H-SiC diode acquired at 2 K. P_0, Q_0, and P_{77} are the nitrogen-bound exciton lines. A new set of lines labeled E_{SF} appear in the PL spectrum of the stressed diode between 410 and 435 nm. Reprinted with permission from [104]. Copyright 2001, AIP Publishing LLC

[102]. The stacking fault expansion and properties of partial dislocations are inconsistent with stress as the driving force. Instead, the thermodynamic free-energy difference between the perfect and fault structure is suggested as the driving force for stacking fault formation in the diodes. This implies that the hexagonal polytypes of SiC may be metastable at room temperature and may transform to a fault structure if the activation energy of the partial dislocation glide is available. This activation energy can be provided by the electron–hole recombination during operation of the diodes. The nucleation and expansion of stacking faults induced by recombination in 4H- and 6H-SiC epitaxial films have been studied in detail [103]. The activation energy for partial dislocation glide under optical excitation decreases to about 0.25 eV, about 2 eV lower than that for pure thermal activation. The low activation threshold is in good agreement with the observation in forward-operating *p-n*-junction devices, implying that radiation enhanced dislocation glide is a general phenomenon in hexagonal SiC. The elementary process controlling expansion of stacking faults is supposed to be kink pair nucleation aided by the phonon-kick mechanism, based on thermal activation and below-gap excitation spectroscopy of dislocation glide.

Stacking faults can be regarded as a quantum well sandwiched between the normal silicon carbide crystals and the quantum states and energy levels of the stacking faults can be evaluated. The calculated and experimental data provide the basis to understand the formation and properties of stacking faults. A unique luminescence band belonging to the stacking fault is observed from the 4H-SiC bipolar diode after extended forward voltage operation [104]. As shown in Fig. 2.44, a series of lines located between 410 and 435 nm (E_{SF}) is present in the

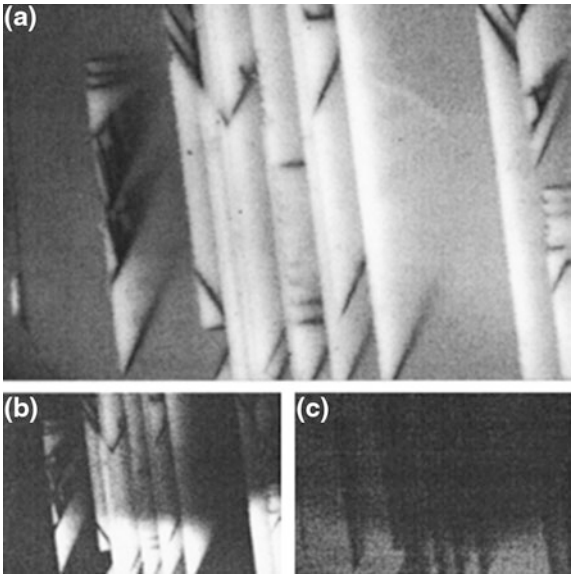

Fig. 2.45 **a** Panchromatic cathodoluminescence image of the stressed 4H-SiC diode showing stacking faults. Cathodoluminescence image of the same diode at **b** 425 nm and **c** 390 nm. Reprinted with permission from [104]. Copyright 2001, AIP Publishing LLC

PL spectrum of the stressed diode but absent in the nonstressed one. The panchromatic cathodoluminescence image (Fig. 2.45a) of the stressed diode contains triangular features that are assigned to the stacking faults. The triangular regions are brighter in the image acquired with a monochromator at 425 nm (Fig. 2.45b), indicating that the E_{SF} emission stems from the entire stacking faults. The band-edge luminescence at 390 nm within the stacking faults is suppressed (Fig. 2.45c), implying competition between two recombination processes. The measured E_{SF} decay time is between 7 and 470 ns and has the same order as that of the intrinsic exciton in 4H-SiC. The E_{SF} emission is attributed to the exciton recombination at the quantum well created by the stacking fault.

The stacking fault-like quantum wells in SiC crystals can be created intentionally. Multiple quantum well structures with 3C-SiC wells between 4H-SiC barriers (consisting of more than 20 heterojunctions) are fabricated by a two-step procedure using solid source molecular beam epitaxy [105]. The structures are produced by selective nucleation of wire-like 3C-SiC nuclei on the terraces of well-prepared hexagonal SiC (0001) substrates followed by a step flow of both the 3C wires and surrounding hexagonal SiC materials (Fig. 2.46). The thickness of the 3C-SiC quantum well is about 2.3 nm (corresponding to three unit cells in $\langle 111 \rangle$ direction), thus giving rise to spatial quantization of electrons. The PL spectrum obtained at 6 K shows dominant L_1 emission line related to the D_1 center (attributed to 4H-SiC) as well as an additional band at around 2.26 eV (Fig. 2.47). These new lines can be explained by a model of a triangular electron quantum well in 3C-SiC.

Low-temperature photoluminescence in 4H/3C/4H-SiC single quantum wells in the 20–50-μm-thick 4H-SiC epitaxial film has been investigated [106]. The

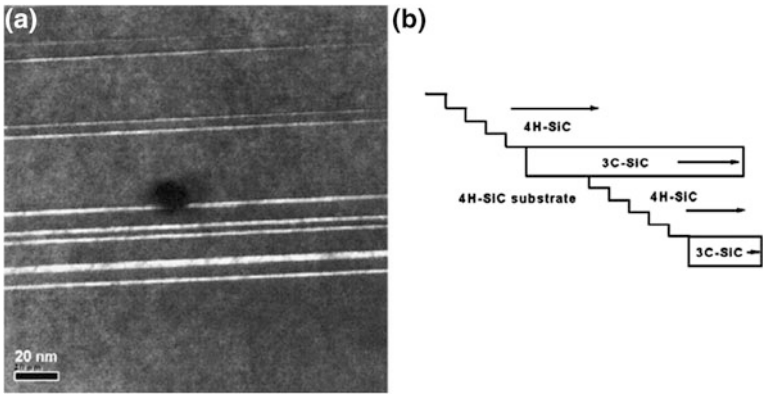

Fig. 2.46 **a** TEM image of the 3C/4H-SiC multiple quantum well structure fabricated on 4H-SiC(0001) by step-controlled epitaxy. **b** Schematic illustration of the formation process of the structure on a tilted substrate. Reprinted with permission from [105]. Copyright 2001, Elsevier

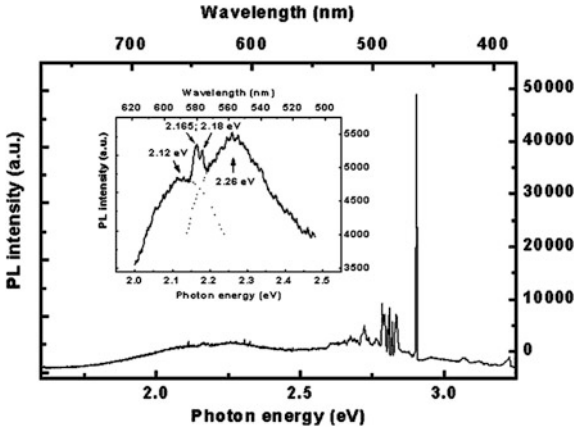

Fig. 2.47 PL spectrum of the 3C/4H-SiC multiple quantum well structure. The *inset* shows the magnified region between 2 and 2.5 eV. Reprinted with permission from [105]. Copyright 2001, Elsevier

quantum well is 3.25 nm thick consisting of thirteen 3C-SiC bilayers as revealed by high-resolution transmission electron microscopy (Fig. 2.48). Figure 2.49 shows a portion of the PL spectrum taken from the same area where the TEM image is taken. In this region, four well resolved peaks between 580 and 600 nm are observed but they are absent in a normal 4H-SiC film. The energy separation between these peaks is approximately equal the energy difference between the four major phonons in 3C-SiC and thus is phonon replicas. An effective exciton energy gap of about 2.177 eV (for the 3C quantum well) is derived, and it is more than 200 meV below the usual exciton bandgap of bulk 3C-SiC as a result of Stark effect due to the built-in electric field in the quantum well in conjunction with the quantum confinement effect. Calculation shows a strong internal electric field on the order of 1 MV/cm to satisfy the observed large red shift of PL, and this field is

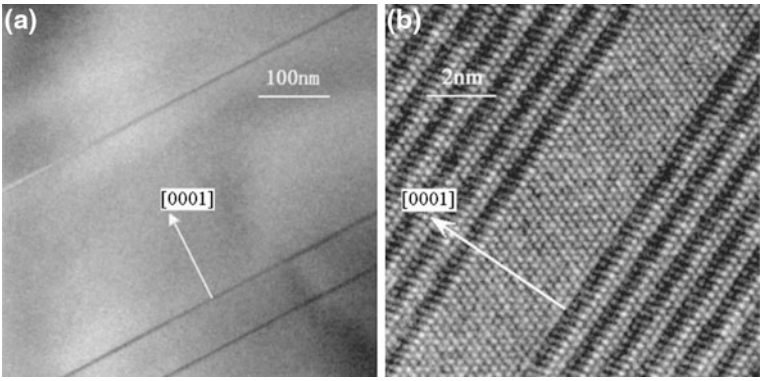

Fig. 2.48 **a** TEM image and **b** high-resolution TEM image of the cross section of an undoped 4H-SiC epitaxial film with 3C inclusions. Reprinted with permission from [106]. Copyright 2003, AIP Publishing LLC

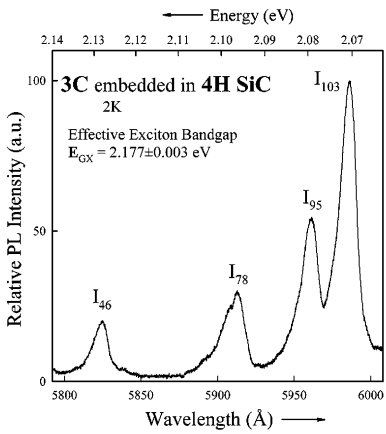

Fig. 2.49 PL spectrum of the 4H-SiC epitaxial film with 3C-SiC inclusions acquired at 2 K. The subscript of the marked lines denotes the momentum-conserving phonon energy in meV. Reprinted with permission from [106]. Copyright 2003, AIP Publishing LLC

proposed to arise from the difference in spontaneous polarization between 3C- and 4H-SiC.

The study using ballistic electron emission microscopy in ultrahigh vacuum indicates that annealing of 4H-SiC wafer in dry oxygen at 1,150 °C for 90 min can produce double stacking faults 3C-SiC inclusions [107]. Distinctive quantum-well structures corresponding to individual inclusions are observed. The two-dimensional quantum-well conduction-band minimum is determined to be approximately 0.53 eV below the conduction-band minimum of bulk 4H-SiC. Macroscopic diode *I–V* and microscopic ballistic electron emission microscopy measurements indicate that there is little variation in the interface state density or fixed charge across the inclusions. The study of the electronic properties of single- and double-layer stacking faults in 4H-SiC clarifies the apparent distinctions of recombination-enhanced defect reactions at these faults [108]. Photoluminescence imaging

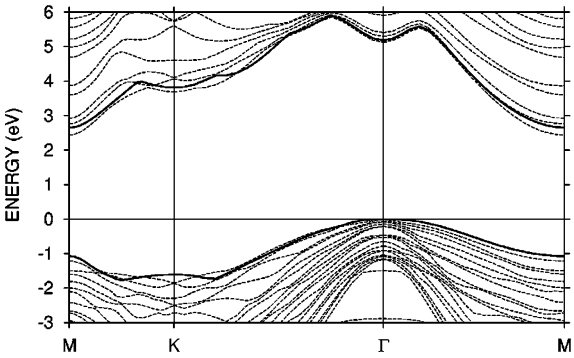

Fig. 2.50 Band edges of 4H-SiC near the fundamental gap projected on the Γ-M-K basal plane calculated by the first-principle method (*solid lines*). The dashed lines show the band-structure results of the model containing the stacking faults. Reprinted with permission from [109]. Copyright 2001, AIP Publishing LLC

spectroscopy and deep-level transient spectroscopy reveal the key constituents of radiative recombination and provide evidence of the nonradiative centers at $E_V + 0.38$ eV responsible for the recombination-enhanced mobility of Si-core partial dislocations. This energy-level model allows the qualitative description of the recombination activity at different types of stacking faults and bounding partial dislocations.

Several groups have theoretically studied stacking faults by first-principle calculation. The first-principle calculation is performed on the stacking faults in 4H-SiC [109]. An interface band in the gap with a maximum depth of 0.2–0.3 eV below the conduction-band minimum at the $\bar{M}$ point is obtained (Fig. 2.50) because the local environment resembles that of the lower gap 6H polytype. The formation energies of the stacking faults in 3C-, 4H-, and 6H-SiC are on the order of a few meV/pair. Hence, the thermodynamic driving force results in growth of the stacking faults in an *n*-type sample. Nonradiative recombination of electrons trapped at the stacking fault with holes provides the necessary energy to overcome the partial dislocation motion barriers required to increase the stacking fault area in a device under forward bias. This explains the observed increase in stacking faults in SiC devices under long-time forward bias operation as well as degradation of the devices by the negative effects of trapping electrons on transport. Trapping of electrons in the stacking fault interface states in 4H-SiC serves as a driving force for growth of stacking faults, because the energy to create the additional stacking fault area is offset by energy gained by capturing electrons in an interface localized state below the conduction band [110]. Screening significantly reduces the potential barrier (for electrons) adjacent to the quantum well.

The structurally different stacking faults that can be introduced by glide along the (0001) basal plane in 3C-, 4H-, and 6H-SiC have been studied based on local density approximation using the density functional theory [111–113]. The band-structure calculation reveals that both types of stacking faults in 4H-SiC and two of

the three different types of stacking faults in 6H-SiC induce quasi-two-dimensional energy states in the bandgap at about 0.2 eV below the conduction-band minimum, thus being electrically active in *n*-type SiC [111]. The third type of stacking faults in 6H-SiC and the only stacking fault in 3C-SiC do not give rise to states clearly separated from the band edges, but instead produce rather strongly localized states with energies very close to the band edges [112]. Figure 2.51 displays the calculated band structure of the perfect 6H-SiC and the 6H-SiC containing stacking faults. There are three types of stacking faults in 6H-SiC that can be introduced by dislocation glide: stacking fault (42), defined as (A|CABAC) inside the faulted cell, stacking fault (3111), defined as (AB|ABAC), and stacking fault (24), defined as (ABC|BAC). Herein, "|" denotes the slip plane. Strong localization of the stacking fault gap state wave function is within roughly 10–15 Å perpendicular to the stacking fault plane. This quantum-well-like feature of certain stacking faults in SiC can be understood in terms of the remarkable conduction-band offsets between cubic and hexagonal polytypes. The stacking fault energies are also calculated using the supercell method and axial next-nearest-neighbor Ising model method. Both calculated results agree well with the measured low stacking fault energies determined experimentally. The 4H-SiC that contains two, three, and four stacking faults in neighboring glide planes has also been investigated [113]. The structural defects can be viewed as thin 3C-like inclusions in the 4H-SiC matrix. The stacking fault energy of two stacking faults in adjacent basal planes is reduced by approximately a factor of 4 relative to that of one isolated stacking fault. This implies that double stacking faults (3C-like inclusions 1.25 nm in thickness) may be quite common in 4H-SiC.

2.4.4 Impurities

Nitrogen donor is an important impurity in silicon carbide, and it has been intensively studied. Boron and nitrogen impurities in 6H-SiC single crystals have been studied by electron spin resonance spectroscopy [114] and both impurities substitute for carbon and occupy the three nonequivalent carbon sites with equal probability. The hyperfine structure is well resolved for both species. The nitrogen hyperfine structure is interpretable in terms of some *s* character for the unpaired electron, whereas the boron hyperfine structure indicates predominantly *p* character. Infrared absorption and Hall effect measurements are utilized to study nitrogen-doped 6H-SiC single crystals [115]. Three sets of infrared absorption lines are observed and attributed to transitions from the $1s(A_1)$ and 1 $s(E)$ ground states to $2p_0$, $2p_\pm$, $3p_0$, and $3p_\pm$, excited states of the nitrogen donors on the *h* lattice site of 6H-SiC and from $1s(A_1)$ to $2p_\pm$ and $3p_\pm$ states of the nitrogen donors on k_1 and k_2 lattice sites. The ground-state binding energies of these donor species are 81.0, 137.6, and 142.4 meV, respectively. The *h* donor center exhibits valley–orbit splitting of 12.6 meV. Figure 2.52 shows the schematic of the energy levels of the nitrogen donors residing at *h*, k_1, and k_2 lattice sites as determined from infrared

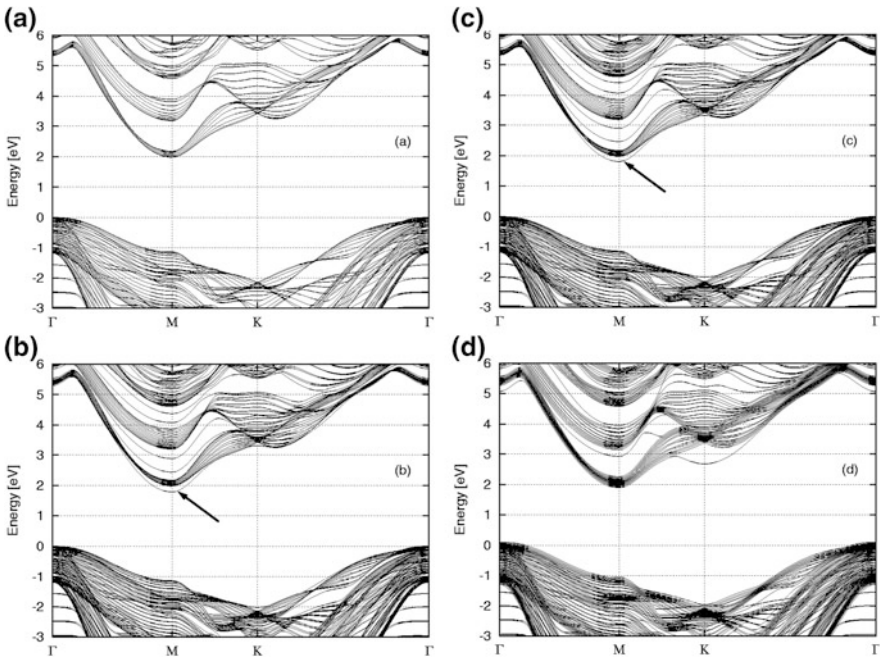

Fig. 2.51 Kohn-Sham band structure of the 96 atom supercells for **a** perfect 6H-SiC, **b** with stacking fault (42), **c** with stacking fault (24), and **d** with stacking fault (3111). The arrows point to the split-off bands below the conduction band caused by the stacking fault. Reprinted with permission from [112]. Copyright 2003, American Physical Society

spectra. The transverse and longitudinal effective electron masses are 0.24 ± 0.01 and 0.34 ± 0.02 m_0, respectively, as obtained by fitting the effective-mass formalism to the observed transition energies. The energy positions of the ground and excited states of the nitrogen donor in the nitrogen-doped 4H-SiC are also investigated [116]. The two electrically active levels (Hall effect) and three series of absorption lines (infrared spectra) are assigned to two nitrogen donor species that substitute on the two inequivalent lattice sites (h, k) in 4H-SiC. The nitrogen donors on hexagonal sites (h) exhibit a valley–orbit splitting of the ground-state level of 7.6 meV. The energies of the excited states of both nitrogen donors are identified by effective-mass approximation assuming the transverse effective mass of 0.18 m_0 and longitudinal effective mass of 0.22 m_0.

Several other types of impurities have also been investigated. Trace impurities of vanadium (V) in the SiC crystals prepared by a modified Lely process are detected based on the strong and polytype-dependent photoluminescence in the 1.3–1.5-μm near-infrared region as well as by infrared absorption [117]. The spectra originate from the intra-3d-shell transitions $^2E(3d^1)$ -> $^2T_2$ $(3d^1)$ of V^{4+}_{Si} $(3d^1)$. Electron spin resonance spectroscopy reveals that V_{Si} in SiC serves as a deep acceptor and possibly also as a deep donor. The vanadium impurity is suggested to be able to reduce the minority carrier lifetime in SiC-based

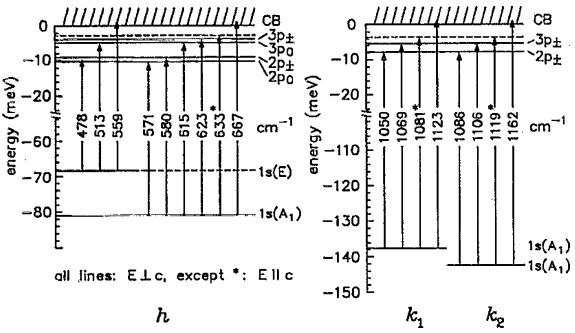

Fig. 2.52 Energy levels of nitrogen donors residing at the h, k_1, and k_2 lattice sites of nitrogen-doped 6H-SiC. Reprinted with permission from [115]. Copyright 1992, AIP Publishing LLC

optoelectronic devices. Intense erbium luminescence around 1.54 μm at 2–300 K is observed from Er^{3+}-implanted 4H-, 6H-, 15R-, and 3C-SiC samples [118]. The ion implant fluence is about 10^{13} erbium ions/cm^2, and the implanted samples are annealed at 1,700 °C. The most striking feature about the spectra is that the relative integrated intensity of the erbium luminescence is nearly constant from 2 to 400 K. This is different from the narrower gap semiconductors in which the 1.54-μm luminescence is observed to drop significantly. No major difference exists in the spectra of the hexagonal and rhombohedral polytypes, but there is a difference for cubic SiC. Hydrogen impurities in 3C-SiC have been studied theoretically based on ab initio density functional supercell calculation, employing the local density approximation [119]. The stable configurations and formation energies of various hydrogen and dihydrogen defects are calculated. The interstitial H is readily incorporated into the p-type 3C-SiC during growth and acts as a shallow donor compensating the acceptors. In n-type 3C-SiC, interstitial H_2 is more stable, but its formation energy is too high to allow for significant incorporation. (V_C + H) behaves as a hole trap and (V_{Si} + H) as an electron trap. The implanted hydrogen is favorably trapped by V_{Si}. The electron trap V_{Si} can be passivated by four hydrogen atoms but V_C remains a hole trap. Low-temperature hydrogen annealing of SiC introduces a sufficient amount of interstitial hydrogen for complete passivation of the p-type materials. In the n-type materials, the dominant defects are (V_{Si} + nH) electron traps that can reduce the free-carrier concentration. High-temperature annealing in hydrogen is effective in introducing hydrogen even to the n-type materials. It is suggested that some of the paramagnetic signals that have been assigned to pure vacancies may arise from (V + nH) complexes.

The microscopic and electronic structures of several important shallow donors and acceptors in 6H-, 4H- and 3C-SiC determined by electron paramagnetic resonance, electron nuclear double resonance, and optical absorption and emission spectroscopy have been well reviewed [120]. The electrical data obtained by deep-level transient spectroscopy on deep defect centers in the 3C-, 4H-, and 6H-SiC are summarized [31]. Emphasis is placed on intrinsic defect centers in the as-grown, ion-implanted, and electron-irradiated materials as well as on defect centers caused by doping of transition metals (vanadium, titanium, chromium, and scandium).

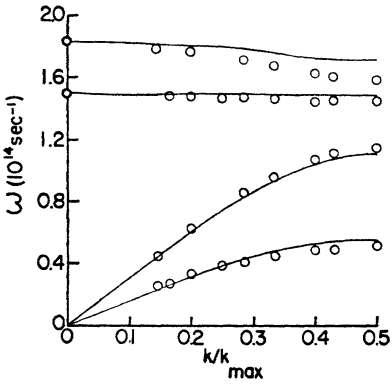

Fig. 2.53 Calculated phonon dispersion curves (*solid lines*) of cubic SiC in the ⟨111⟩ direction. The *circles* denote measured values obtained from Ref. [122] ($k_{max} = 2\pi/a$). Reprinted with permission from [121]. Copyright 1969, American Physical Society

2.5 Lattice Vibration and Infrared/Raman Spectra

The lattice dynamical vibration properties of silicon carbide and associated infrared and Raman scattering characteristics have been extensively studied. The phonon dispersion curves in the various symmetry directions in cubic SiC are derived using a rigid ion model consisting of short-range central and noncentral interactions and long-range Coulombic interactions among ions with the appropriate effective ionic charges [121]. The calculated dispersion curve in the ⟨111⟩ direction (Fig. 2.53) is compared to Raman data acquired from various polytypes of SiC [122, 123], and the agreement between calculation and experiments is very good. The phonon density of states and Debye characteristic temperature of SiC are also derived. The adiabatic bond-charge model is applied to the 3C, 6H, 4H, and 2H polytypes of SiC [124]. The short-range elastic forces are described by two-body and three-body interactions among silicon ions, carbon ions, and bond charges, whereas the long-range Coulomb forces are taken into account by the Ewald technique. The model parameters are fitted to the frequencies obtained from Raman and luminescence measurements. The resulting phonon dispersion curves along the high symmetry lines in the fcc and hexagonal Brillouin zone agree with experimental results. In the 3C case, the calculation yields the same eigenvectors as ab initio calculation. The independent elastic constants of the different polytypes are derived using the resulting sound velocities, and they agree reasonably well with experimental ones. The plane-wave pseudopotential approach of the density functional theory employing the local density approximation is used to study the ground-state properties of the 3C, 2H, and 4H polytypes of SiC [125]. The linear response theory within the density functional theory is employed to determine the dynamic lattice properties of 3C-SiC. The phonon dispersion curves of cubic SiC are intermediate between those of Si and diamond but not average and consistent with measured values (Fig. 2.54). The phonon dispersion curves of 2H- and 4H-SiC are also derived. The calculated ground-state properties of the cubic 3C and hexagonal 2H and 4H

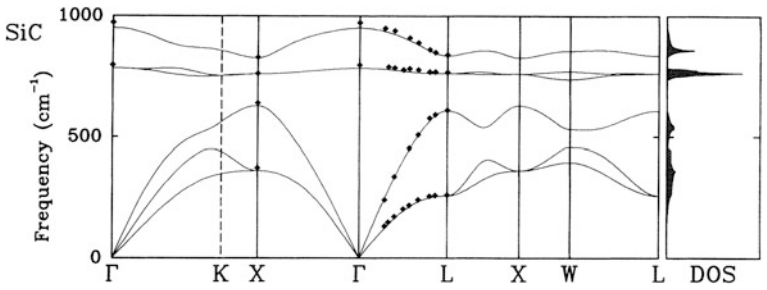

Fig. 2.54 Calculated phonon dispersion curves and density of states (*DOS*) of 3C-SiC. The *diamond signs* denote the experimental first-order Raman scattering data obtained from Ref. [123]. Reprinted with permission from [125]. Copyright 1994, American Physical Society

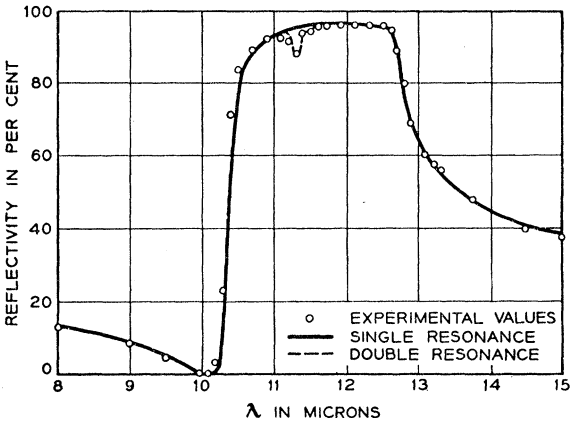

Fig. 2.55 Reflectivity versus wavelength of the extraordinary ray in α-II SiC. The *circles* denote measured values and the *solid line* is the calculated curve. Reprinted with permission from [126]. Copyright 1959, American Physical Society

polytypes of SiC are quite similar, especially concerning ground-state energies and volumes as well as the valence charge densities along the bonding and stacking directions. In contrast to elemental crystals like Si and diamond, SiC has noticeable ionicity, that is, charge asymmetry. The employed calculation procedure has limitations in that it neglects the effects of the vibrational energy and crystal entropy.

Infrared spectroscopy imparts information about the lattice vibration properties of various polytypes of silicon carbide. The infrared transmission and reflectivity of several hexagonal SiC crystals in the 1–25-μm spectral region have been measured [126], and the reflectance spectra of both ordinary and extraordinary rays have been obtained (Figs. 2.55 and 2.56). Resonance occurs at 12.60 and 12.73 μm, respectively, and based on the reflectivity data, the high-frequency dielectric constant is calculated to be 6.7. The reflectance spectra can be fitted within experimental errors by the classical dispersion theory using the properly selected dispersion parameters, and the low frequency dielectric constant is derived to be 10.0 accordingly. The study of the surface effect suggests that

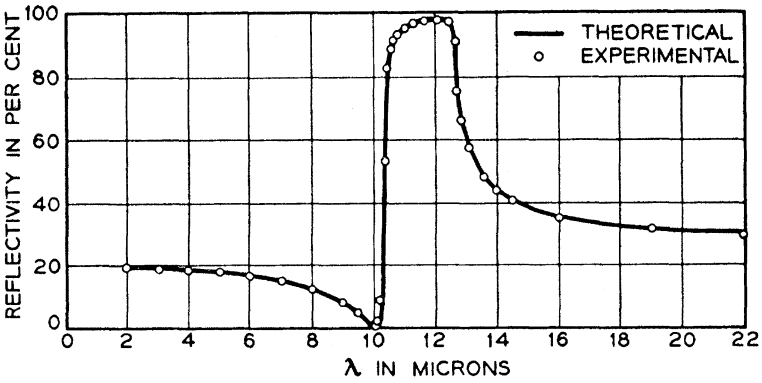

Fig. 2.56 Reflectivity versus wavelength of the ordinary ray in α-II SiC. The *circles* denote measured values and the *solid line* shows the calculated curve. Reprinted with permission from [126]. Copyright 1959, American Physical Society

reflectivity is an intrinsic property of the crystal. The absorption coefficient is derived as a function of wavelength in the range 1–10 μm based on the transmission measurement data. The transmission and reflection of 3C-SiC films are investigated in the 1–15-μm range [127], and the results are analyzed by the classical dispersion theory. The dispersion parameters for the fundamental resonance at 12.60 μm are essentially the same as those of the ordinary ray in the hexagonal α-II SiC. The measured and calculated transmission and reflection spectra are displayed in Fig. 2.57. In the immediate region of resonance, the agreement between theory and experiments is very good for both transmission and reflection. However, at the shorter wavelengths, the theory predicts higher transmission values and smaller reflection values because other absorption mechanisms such as free-carrier absorption are neglected in the theoretical treatment.

Multiple phonon absorption processes also occur in silicon carbide. The featured infrared absorption bands obtained from SiC have been interpreted as arising from multiple phonon absorption [128]. The phonon energies obtained by measuring the indirect interband absorption in SiC are 0.045 eV (TA), 0.067 eV (LA), 0.0955 eV (TO), and 0.1055 eV (LO). The ten infrared absorption peaks in the energy range of 0.130–0.300-eV stem from multiple phonon absorption, and Fig. 2.58 depicts a part of the infrared absorption spectrum. The four predicted summation bands show good agreement with the corresponding peaks of the measured spectrum.

Since the infrared reflection spectrum depends on many sample parameters, the infrared spectra of SiC films can provide useful information about the status of the films. Several unusual features are present in the infrared reflection spectra of CVD SiC films concerning the surface roughness and possible conducting layers at the film–substrate interface [129]. The free-carrier concentration and thickness of the film can be determined from the reflectance extrema. These values show good agreement with the values obtained by other methods, and hence, infrared reflectance measurement can nondestructively assess the fabricated films. Spectral

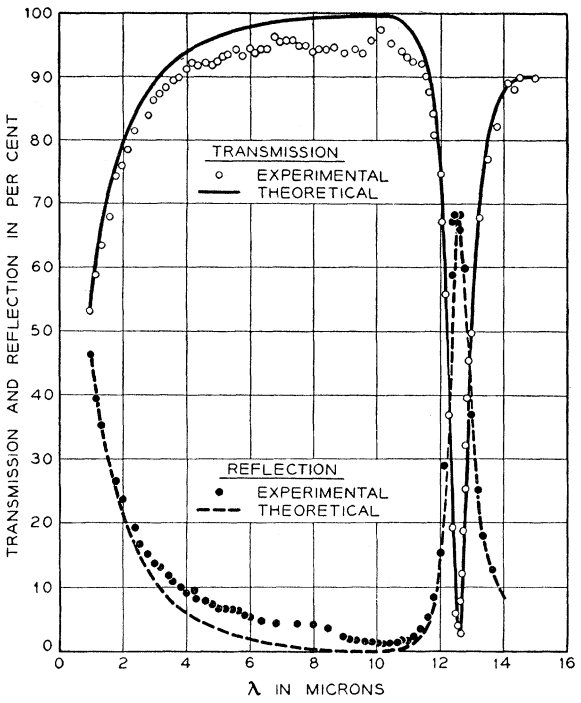

Fig. 2.57 Transmission and reflection of a 0.06-μm-thick β-SiC film. Reprinted with permission from [127]. Copyright 1959, American Physical Society

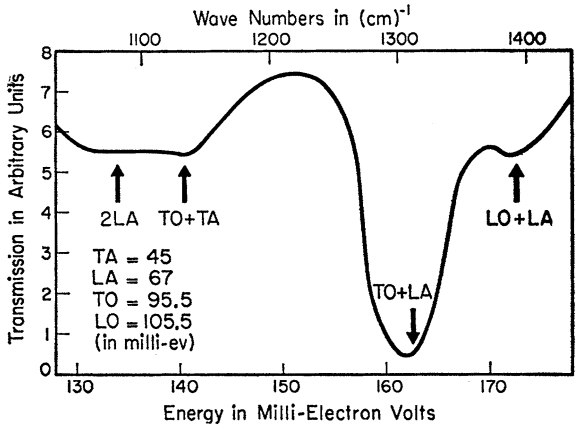

Fig. 2.58 Two-phonon optical acoustical summation bands in the infrared spectrum of SiC. The *arrows* point to the energy values calculated using the four assigned phonon energies. Reprinted with permission from [128]. Copyright 1961, American Physical Society

analysis may also reveal the crystal anisotropy, as demonstrated by the polarized infrared reflectivity spectra of 6H-SiC single crystals at different incident angles [130]. A sharp line in the reststrahl band is observed from the extraordinary ray, and its line shape depends on the incident angle. Numerical calculation based on a Lorentz oscillator model demonstrates that this sharp line arises from the crystal anisotropy of 6H-SiC suggesting that the infrared reflectivity of many anisotropic

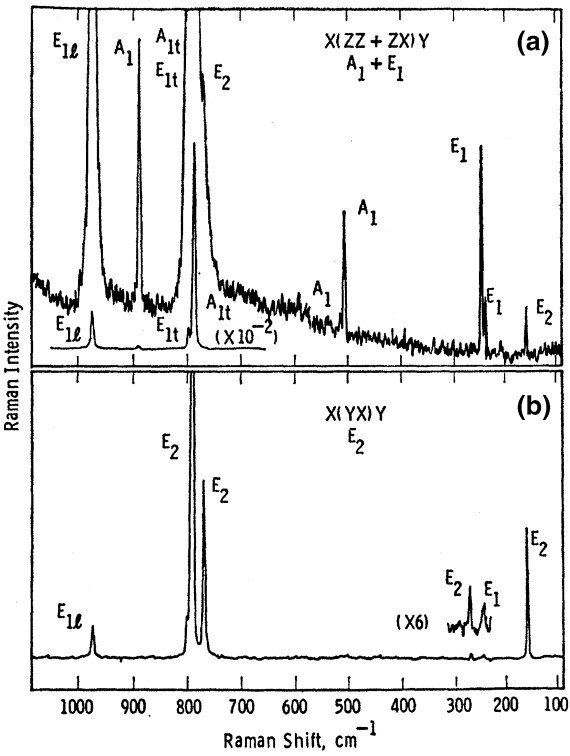

Fig. 2.59 Full one-phonon emission Raman spectrum of 6H-SiC crystal with arrangements permitting **a** A_1 and E_1 modes, and **b** E_2 modes. Reprinted with permission from [122]. Copyright 1968, American Physical Society

solids may depend on the incident angle. Infrared ellipsometry is used to determine the free-electron concentrations in bulk and epitaxial nitrogen-doped 4H- and 6H-SiC [131] as well as epitaxial layer thickness. Data obtained from 6H-SiC can be modeled well if the large effective-mass anisotropy is taken into account, whereas effective-mass anisotropy has no noticeable effects on the 4H-SiC spectra. The two-phonon interaction influences the line shape in the region between 1,300 and 1,700 cm^{-1} and should be considered in calculating the free-carrier concentration.

Raman scattering conveys structural information about the lattice dynamical vibration properties of solids. Examination of Raman scattering in 6H-SiC crystals [122] revealed fifteen phonon-lines (Fig. 2.59). Polarized light is used to identify the mode symmetry, and the modes are classified by large zone analysis yielding dispersion like curves (Fig. 2.60). All observed narrow lines can be explained, and only two of the expected lines are not observed. Analysis of the dependence of phonon energy on propagation direction indicates that certain infrared and Raman active modes have extremely small infrared strength due to the specific polytype structure of 6H-SiC.

The first-order Raman spectra of more polytypes of SiC crystals, including 3C, 4H, 6H, 15R, and 21 R, have been acquired [123], and the phonon dispersion curves are established based on the Raman measurements. Overall, 9 lines are

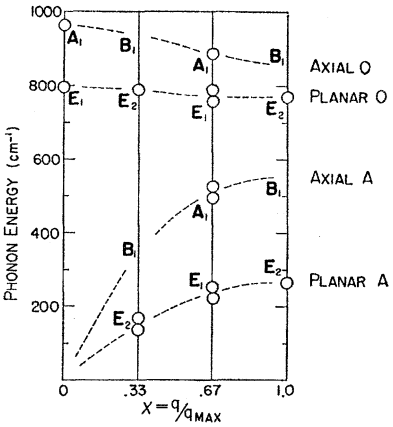

Fig. 2.60 Plot of experimental data of 6H-SiC in the form of dispersion curves in the large zone. The doublet separation is exaggerated. This figure is valid for weak modes for any phonon propagation direction and appropriate for strong modes only when the phonon propagation direction is along the *c*-axis. Reprinted with permission from [122]. Copyright 1968, American Physical Society

observed from 4H-SiC, 16 lines from 15R-SiC, and 14 lines from 21R-SiC. The symmetry of each phonon mode is determined by analyzing the polarization. The modes are classified using a standard large zone and then the positions of the three groups of one-phonon lines and 15 previously observed lines in 6H-SiC are assembled in a single large zone (Fig. 2.61). This assignment results in a set of SiC phonon dispersion curves confirming the existence of a common phonon spectrum for all SiC polytypes in the axial direction. The velocities of the longitudinal and transverse acoustic phonon waves derived from the dispersion curves are in good agreement with experimental results.

A theoretical method based on bond polarizability is adopted to calculate the Raman intensity profiles of the folded modes of silicon carbide [132]. The relative Raman intensity of the folded modes is calculated using bond Raman polarizability together with the eigenvectors of the linear-chain model. In this method, the bonds in a unit cell are classified into groups in which the individual Raman polarizability is equivalent. The Raman polarizability is expressed as the sum of the product of the bond Raman polarizability and relative displacement of the end atoms linked by the bond. The calculated Raman intensity profiles are in qualitative agreement with the experimental Raman spectra of the folded modes arising from TA and TO phonon branches along the *c* direction (Fig. 2.62). The calculated dispersion curves are compared to the measured ones in Fig. 2.63. The calculated frequencies of the TA branch are slightly smaller than the measured values, whereas there are slightly larger deviations from the measured values (as much as 20 cm^{-1}) for the TO branch at around the zone edge. The calculation may fit the experimental data better if the force constants between the second-neighbor planes are taken into account. The results indicate that measurement of the Raman frequencies and intensities is a useful technique for identifying the polytype structure of SiC.

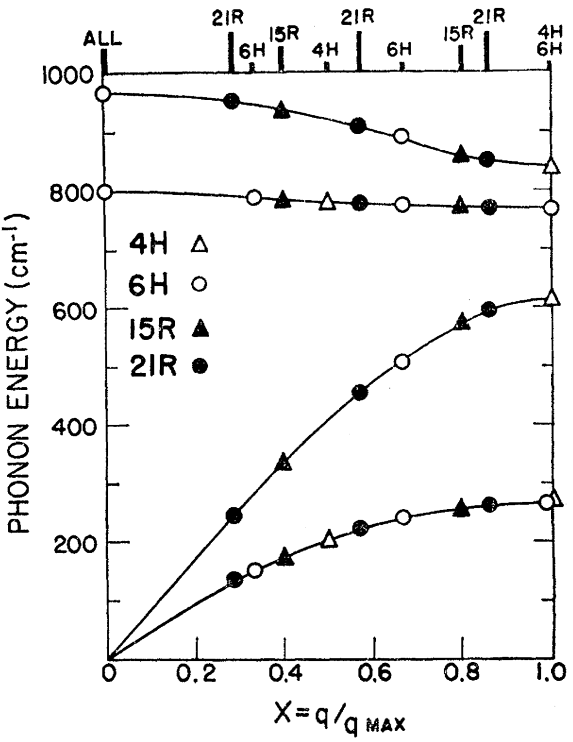

Fig. 2.61 Combined dispersion curves based on measured Raman data obtained from four polytypes of SiC. The Raman accessible values of $x = q/q_{max}$ are marked at the *top* of the figure. Reprinted with permission from [123]. Copyright 1968, American Physical Society

Raman scattering is utilized to evaluate SiC heteroepitaxial thin layers [133]. The heteroepitaxial layer of 3C-SiC can be grown on the (0001) surface of 6H-SiC platelets using conditions similar to those used to fabricate 3C-SiC on Si. The Raman spectra are acquired in the backscattering geometry using the 514.5-nm laser line at room temperature. The incident light is normal to the 3C (111) and 6H (0001) surfaces and polarized in a vertical plane. Figure 2.64 shows the TO and LO regions of the Raman spectra of the 6H-SiC sample before and after growth of the epitaxial layers. The intensity is normalized to the 6H-SiC main peaks at 789 cm^{-1} in the TO region and 967 cm^{-1} in the LO region. In the TO region, the intensity of the peak corresponding to the 3C-SiC TO phonon mode (796 cm^{-1}) increases after epitaxy, whereas in the LO region, the peak corresponding to 3C-SiC LO phonon mode (972 cm^{-1}) and the diminished peak of 6H LO phonon are observed. The layer thickness is about 10–15 μm, and the surface exhibits a single-crystal reflection high-energy electron diffraction pattern. The results indicate that the 3C-SiC (111) layer is heteroepitaxially grown on the 6H-SiC (0001) surface. This is understandable because that the atomic arrangements on the (111) plane of 3C-SiC and the (0001) plane of 6H-SiC are identical and the only structural difference between 3C in the [111] direction and 6H in the [0001] direction is the stacking order. Using a revised lattice dynamics model and the bond polarizability concept, the Raman intensity profiles in SiC polytypes are examined [134]. The

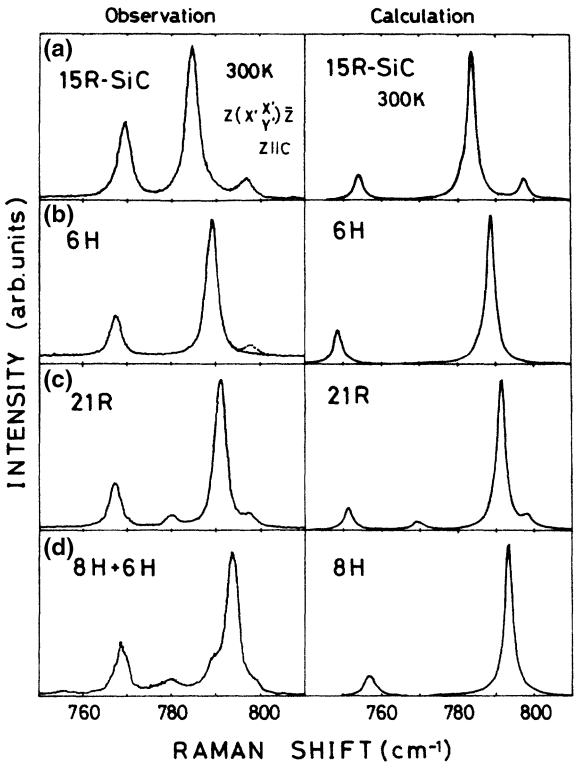

Fig. 2.62 Comparison between the measured and calculated Raman spectra of the folded TO modes of the four polytypes of SiC: **a** 15R, **b** 6H, **c** 21R, and **d** 8H. Reprinted with permission from [132]. Copyright 1986, American Physical Society

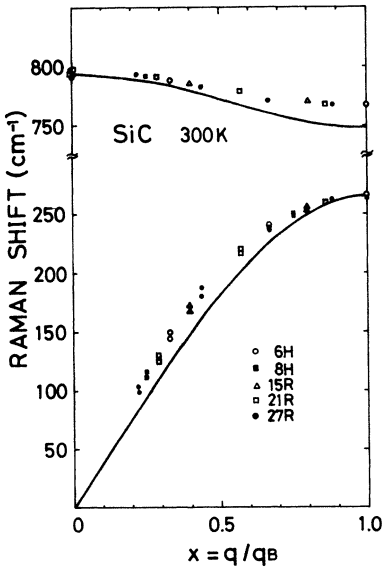

Fig. 2.63 Assembled phonon dispersion curves in the basic zone based on the data acquired from five polytypes of SiC. The *solid lines* are the calculated curves by the linear-chain model. Reprinted with permission from [132]. Copyright 1986, American Physical Society

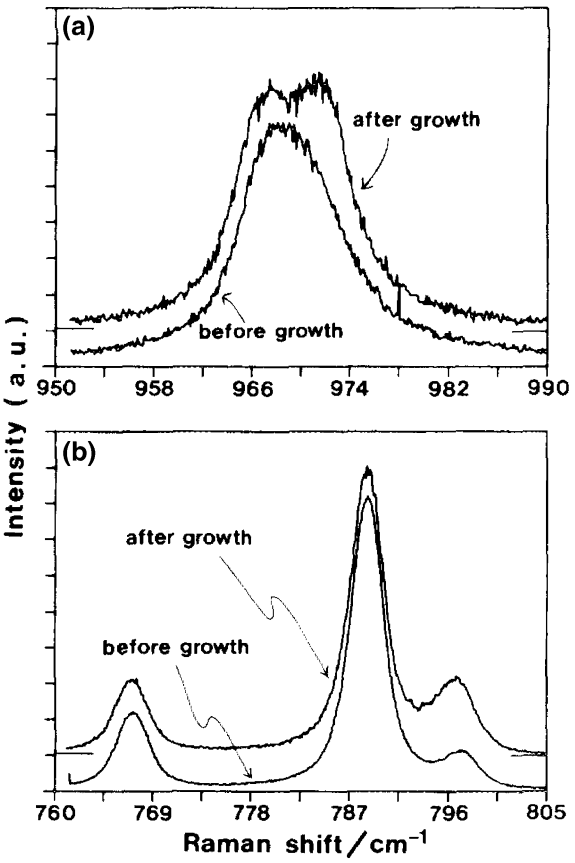

Fig. 2.64 **a** LO and **b** TO regions of the Raman spectra of 6H-SiC before and after growth of the epitaxial layer of cubic SiC on the (0001) surface. The intensities are normalized using the 6H-SiC main peaks at 789 cm^{-1} in the TO region and 967 cm^{-1} in the LO region. Reprinted with permission from [133]. Copyright 1987, AIP Publishing LLC

force constant parameters of a linear-chain model are such determined that the calculated phonon dispersion and Raman intensity profiles fit the experimental results. The employed lattice dynamics model takes into account the third-neighbor plane forces and the differences between the force in the hexagonal and cubic configurations. Quantitative agreement between the calculated and observed Raman profiles is obtained for the folded modes of the TO and TA branches for a number of polytypes. This agreement indicates that the set of force constants can be commonly used for any polytype of SiC and the bond polarizability concept is applicable to folded modes of both acoustic and optical branches.

The first- and second-order Raman spectra of semi-insulating 4H-SiC have been investigated at room temperature by nonresonant excitation [135]. The results are compared to Raman spectra obtained from *n*-type-doped 4H- and 6H-SiC. The second-order Raman spectra (Fig. 2.65) of *n*-type-doped and semi-insulating 4H-SiC are quite similar. The optical branches of the second-order Raman spectra are different between 4H- and 6H-SiC and more complicated than the two-phonon Raman spectra of 3C-SiC. The two-phonon spectra are assigned by comparison

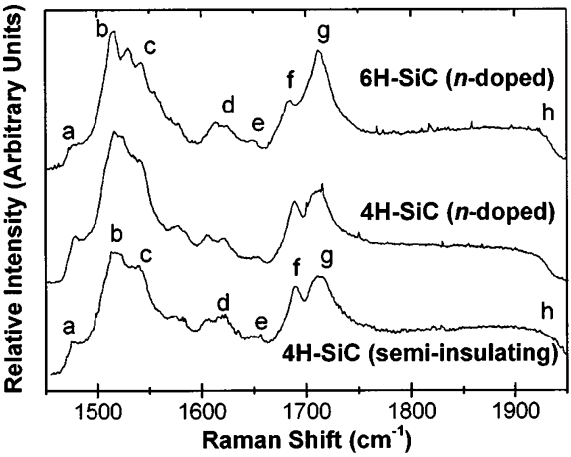

Fig. 2.65 Second-order Raman spectra acquired from semi-insulating 4H-SiC and *n*-type (nitrogen concentration: 2.1×10^{18} cm^{-3}) 4H- and 6H-SiC. Reprinted with permission from [135]. Copyright 1999, American Physical Society

with calculation, and both overtones and combination bands are present in the second-order Raman spectra of 4H- and 6H-SiC.

The lattice compression and pressure can affect the lattice dynamical properties of silicon carbide and also the Raman spectra. The pressure dependences of the optical phonons and transverse effective charge in 3C-SiC have been experimentally investigated [136]. The first-order Raman spectra of 3C-SiC are acquired at different hydrostatic pressure up to 22.5 GPa (Fig. 2.66). The measured LO(Γ, at the Brillouin-zone center) and TO(Γ) phonon energies can be described within experimental errors by the following least-square fits:

$$\begin{aligned}\omega_{\mathrm{TO}} &= (796.5 \pm 0.3) + (3734 \pm 30)\left[-\frac{\Delta a}{a_0}\right], \\ \omega_{\mathrm{LO}} &= (973 \pm 0.3) + (4532 \pm 30)\left[-\frac{\Delta a}{a_0}\right],\end{aligned} \tag{2.1}$$

where ω_{TO} and ω_{LO} are in cm^{-1} and a_0 is the lattice constant at room temperature. The fitted curve is shown in Fig. 2.66. The quadratic fit to the measured phonon energies versus pressure (Fig. 2.66) gives rise a sublinear relationship:

$$\begin{aligned}\omega_{\mathrm{TO}} &= (796.2 \pm 0.3) + (3.88 \pm 0.08)p - (2.2 \pm 0.4) \times 10^{-2}p^2, \\ \omega_{\mathrm{LO}} &= (972.7 \pm 0.3) + (4.75 \pm 0.09)p - (2.5 \pm 0.4) \times 10^{-2}p^2,\end{aligned} \tag{2.2}$$

with ω_{TO} and ω_{LO} given in cm^{-1} and p in GPa. The mode-Grüneisen parameters $\gamma_i = -\partial \ln \omega_i / \partial \ln V$ for the TO(Γ) and LO(Γ) phonons are evaluated from the coefficient of the linear term in $\Delta a/a_0$ of Eq. (2.1). They are $\gamma_{\mathrm{LO}} = 1.55 \pm 0.01$ and $\gamma_{\mathrm{TO}} = 1.56 \pm 0.01$. The LO(Γ)–TO(Γ) splitting increases linearly with lattice compression (Fig. 2.67) and also shows a sublinear dependence on pressure. The corresponding mode-Grüneisen parameter is $\gamma_{\mathrm{LO-TO}} = 1.52 \pm 0.05$. This

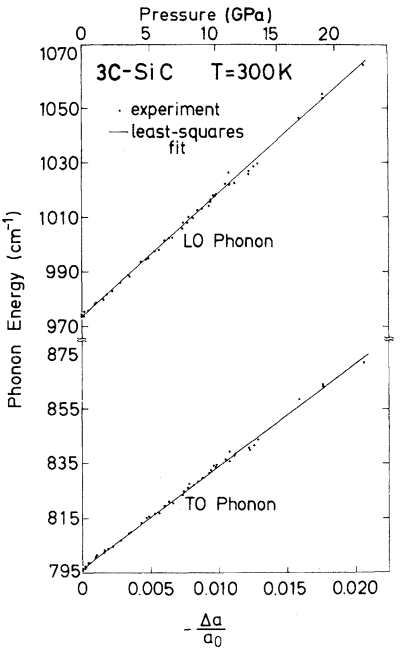

Fig. 2.66 Plot of the measured LO(Γ) and TO(Γ) phonon energies versus relative lattice compression (linear lower scale) and pressure (upper scale) in 3C-SiC crystals. The *solid lines* are least-square fits of the experimental points. Reprinted with permission from [136]. Copyright 1982, American Physical Society

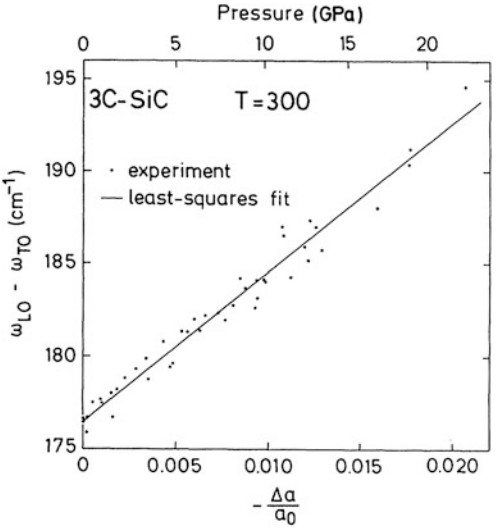

Fig. 2.67 Plot of the LO(Γ)–TO(Γ) splitting versus lattice compression and pressure in 3C-SiC crystals. The *solid lines* through the experimental points is the least-square fit. Reprinted with permission from [136]. Copyright 1982, American Physical Society

increasing splitting implies an increase in the transverse effective charge under pressure. The transverse effective charge is defined as the macroscopic dipole moment per unit displacement of the sublattice (Si or C) when the macroscopic electric field in the crystal is kept zero. The relationship between the transverse effective charge and lattice compression is explained by the microscopic

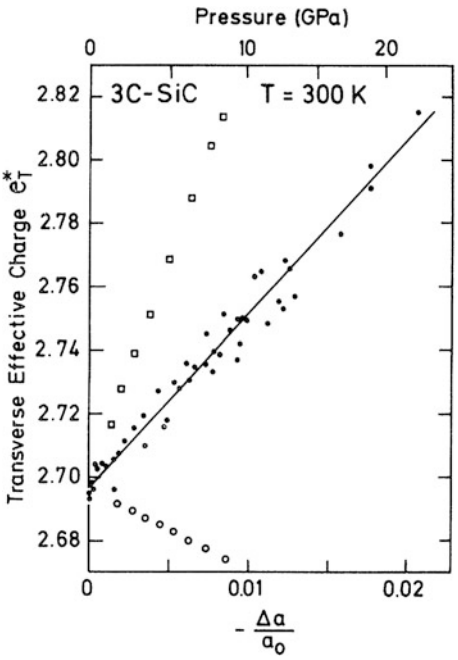

Fig. 2.68 Plot of transverse effective charge versus lattice compression and pressure in 3C-SiC crystals. The data are acquired from the measured pressure dependence of the LO and TO phonons in Figs. 2.66 and 2.67. The solid line is the least-square fit. The squares represent the full pseudopotential calculation result and the open circles are the calculated results based on the bond–orbital model. The calculated transverse effective charges for $\Delta a = 0$ are renormalized to the experimental values in both cases. Reprinted with permission from [136]. Copyright 1982, American Physical Society

pseudopotential calculation but cannot be explained by the semi-empirical models such as the bond orbital model (Fig. 2.68). The line width of the long-wavelength optical phonons of 3C-SiC increases with pressure at above 10 GPa (Fig. 2.69) [137]. This is supposed to arise from the increase in the decay rate as Γ optical phonons decay into two acoustical phonons. Different results are obtained from the low-temperature (6 K) experimental and theoretical study of the pressure dependence of the line widths of the TO and LO phonons in 3C-SiC [138]. While the line width of the TO mode remains unchanged at pressure up to 35 GPa, that of the LO mode exhibits a monotonic increase up to 26 GPa, followed by an abrupt decrease above this pressure. The experimental results agree well with first-principle calculation, and this anomalous behavior is proposed to originate from the aharmonic effect.

The pressure effect in the Raman spectra of 6H-SiC shows features different from 3C-SiC. The TO and LO modes of 6H-SiC are observed at pressure of up to 95 GPa, indicating the structural stability of the 6H polytype [139]. The sample remains optically transparent at 95 GPa, and there is no sign of the expected metallic phase. The LO(Γ) and TO(Γ) Raman frequencies increase with pressure.

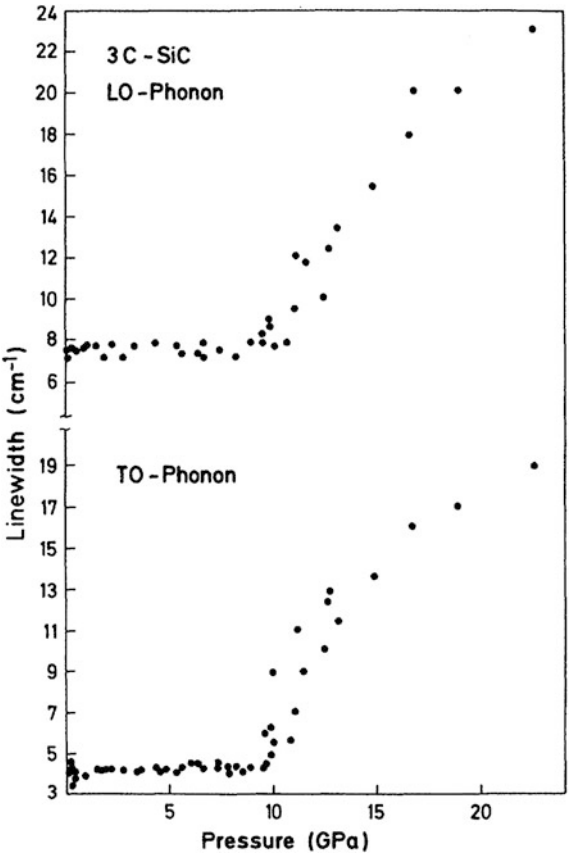

Fig. 2.69 Plot of LO(Γ) and TO(Γ) Raman line widths versus pressure in 3C-SiC crystals. Reprinted with permission from [137]. Copyright 1982, American Physical Society

The LO–TO splitting is 181 cm^{-1} at ambient pressure and increases rapidly below 60 GPa, whereas it tends to saturate at 205 cm^{-1} over 60 GPa (Fig. 2.70). The transverse effective charge increases with pressure at low pressure until reaching a maximum at about 40 GPa and then decreases (Fig. 2.71). This suggests increased covalent binding at high pressure, and this variation agrees with the proposed theory. The mode-Grüneisen parameters γ of the SiC LO and TO modes are derived from experimental data. Comparison of the density variation of γ with diamond and Si leads to the conclusion that γ of the LO mode in 6H-SiC is softer than that of the TO mode, and they both exhibit anomalous decrease.

The temperature effect on the lattice dynamical properties has been investigated. The temperature dependence of the long-wavelength optical phonons of 3C-SiC up to 750 K shows that the TO and LO phonon Raman lines shift to lower frequencies and broaden with temperature (Fig. 2.72) [140]. The shift in the LO line is stronger than that of the TO line, while the LO–TO splitting decreases with temperature. The line width also increases with temperature, and this is explained by assuming that the lifetime of the optical phonon is determined by its decay into

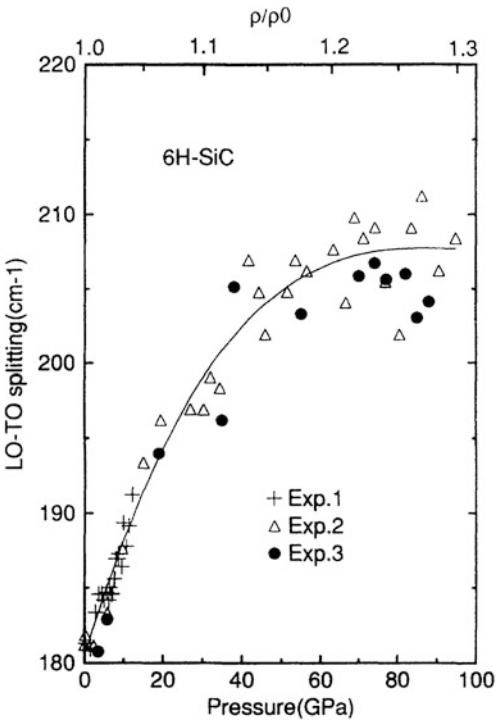

Fig. 2.70 LO–TO splitting in 6H-SiC as a function of pressure obtained by three different experiments. The upper scale is the density variation from the equation of state of 6H-SiC and the *solid curve* represents the quadratic fit of the data. Reprinted with permission from [139]. Copyright 1994, American Physical Society

two LA phonons, similar to the cases of Si and Ge. The transverse effective charge decreases slightly with temperature. The temperature and pressure data elucidate the explicit temperature contribution to the temperature dependence of the transverse effective charge. The results also agree with calculation based on the pseudopotential expression for charges. The temperature dependence of the Raman spectra of 3C-SiC microcrystalline films consisting of randomly oriented crystallites of about 100 nm is quite different from that of 3C-SiC single crystals [141]. The Raman spectra are acquired at elevated temperature up to 1,700 K, and the temperature dependence of the TO and LO phonon frequencies is consistent with that of 3C-SiC single crystals, but the Raman lines are much broader. This can be attributed to the effects of stacking faults by comparing the experimental results with simulated Raman intensity profiles of 3C-SiC comprising randomly distributed stacking faults. The simulated line width and disorder-induced peak shift show good agreement with experiments provided that the average stacking fault distance is assumed to be 6 Å. The Raman lines show irreversible narrowing at temperature above 1,900 K possibly arising from annealing of the stacking faults in 3C-SiC.

The phonon–plasmon coupled mode in SiC and Raman scattering from these coupled modes have been investigated. The plasmon arises when a polar semiconductor is highly doped and plasmon oscillation refers to long-wavelength

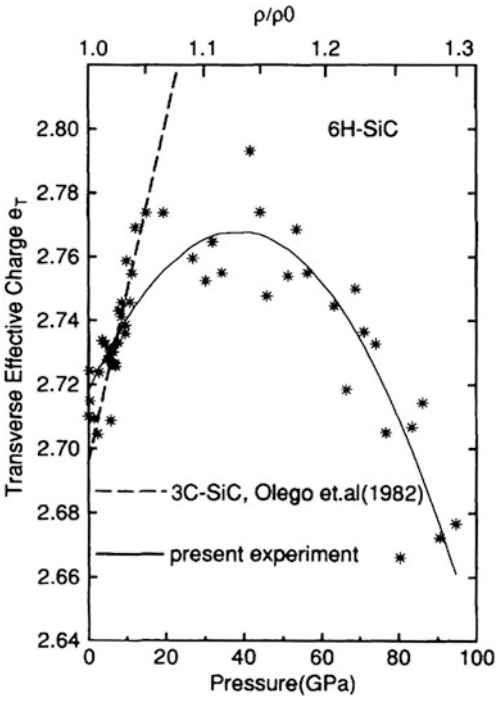

Fig. 2.71 Transverse effective charge as a function of pressure. Reprinted with permission from [139]. Copyright 1994, American Physical Society

electron density oscillation. It is a longitudinal vibrational mode of the electron gas, and the energy quantum is called plasmon. The plasmon oscillation can couple to the electric field of the long-wavelength LO phonon to give rise to the phonon–plasmon coupled mode. The Raman data acquired from nitrogen-doped 6H- and 15R-SiC reveal the valley–orbit transitions for donors on nonequivalent sites in the two types of SiC [142]. The transitions can be grouped into two widely separated energy regions, suggesting that the donor wave functions are sensitive to the impurity potential beyond the central cell. The Raman symmetry of the valley–orbit transitions is found to be E_2 that provides some understanding of the position of the conduction-band minima in the Brillouin zone. The Raman spectrum shows a shifted asymmetric LO phonon line (Fig. 2.73) interpreted as the LO phonon–plasmon coupled mode (L^+). This suggests a metallic system, and the calculated mobility is in agreement with measured values in heavily doped samples. The asymmetry of the mode and absence of the L^- LO phonon–plasmon coupled mode may be caused by the short electron collision lifetime. The efficiency of light scattering from an LO phonon coupled to a single component plasmon in a semiconductor is derived by the semi-classical theory [143]. Two terms contribute to the efficiency. The first one arises from the modulation of polarizability by atomic displacements and the macroscopic longitudinal field obeying the ordinary Raman polarization selection rules. The second term comes from free-electron charge density fluctuation that obeys different selection rules and is proportional to

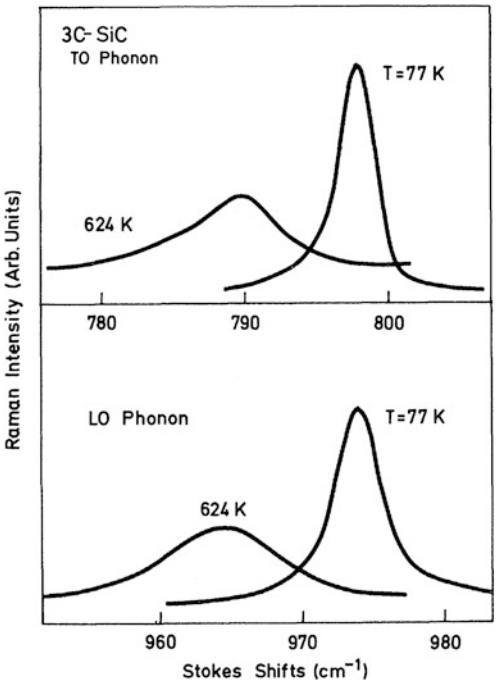

Fig. 2.72 First-order Raman lines of 3C-SiC recorded at two temperatures. Reprinted with permission from [140]. Copyright 1982, American Physical Society

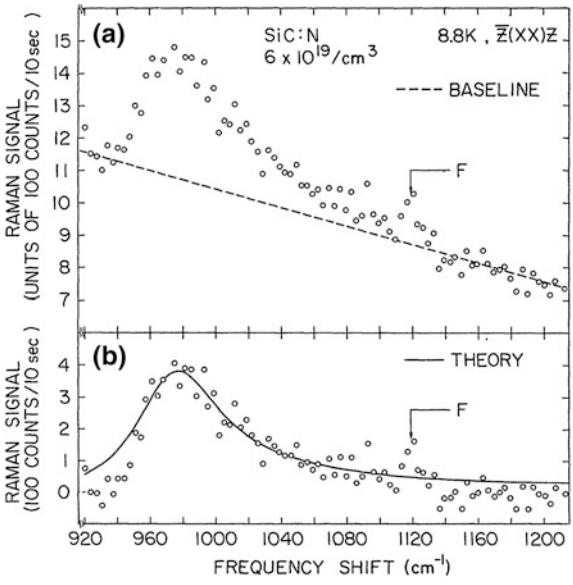

Fig. 2.73 **a** Photon-counting spectrum of the shifted A_1(LO) phonon of nitrogen-doped 6H-SiC measured at 8.8 K. **b** Shifted A_1(LO) phonon with the baseline of part (**a**) (*dashed line*) subtracted and theoretical fit (*solid line*). Reprinted with permission from [142]. Copyright 1972, American Physical Society

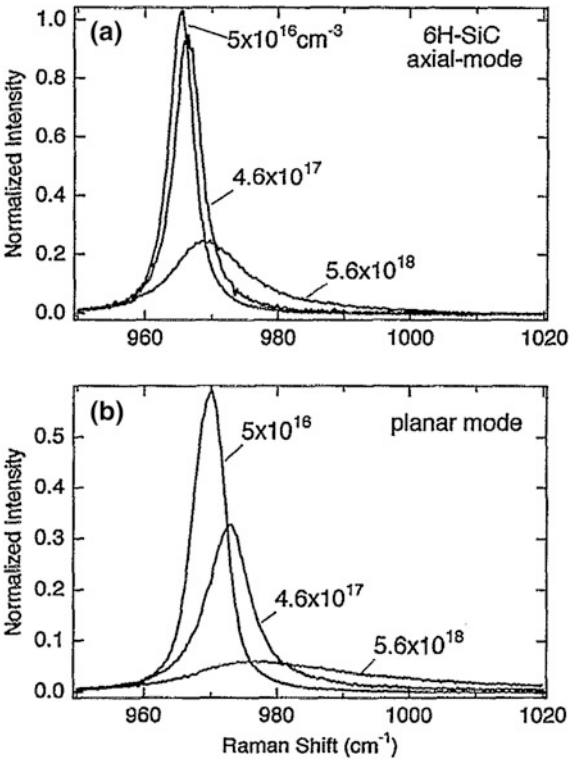

Fig. 2.74 Raman profiles of **a** axial and **b** planar LO phonon–plasmon coupled modes of *n*-type 6H-SiC with different carrier concentrations. Reprinted with permission from [144]. Copyright 1995, AIP Publishing LLC

the square of the wave vector transferred. This theory combined with experimental data provides insight to coupled plasmon–phonon scattering in heavily nitrogen-doped 6H-SiC. The dominant light scattering mechanism is polarizability modulation, whereas the density mechanism is predicted to be 3,500 times weaker. The absolute efficiency of the coupled mode spectrum in doped materials and A_1(LO) phonon in lightly doped crystals has also been derived.

The Raman profiles of the axial and planar LO phonon–plasmon coupled modes in *n*-type 6H- and 4H-SiC bulk crystals with free-carrier concentrations of 10^{16}–10^{18} cm^{-3} have been studied [144]. In the axial mode, the direction of plasmon oscillation and atomic displacement are parallel to the *c*-axis, whereas in the planar mode, they are perpendicular to the *c*-axis. In 6H-SiC, the planar mode exhibits more dramatic variations in the peak intensity, width, as well as shift with carrier concentrations than the axial mode (Fig. 2.74). In contrast, the spectra of 4H-SiC show no noticeable difference in the peak intensity and width between the axial and planar modes, but the planar mode shows a slightly bigger peak shift than the axial mode (Fig. 2.75). The anisotropic plasmon frequencies and carrier damping constants are derived using a fit of the calculated band shape with the experimental Raman band profiles, and the agreement between the experimental and calculated

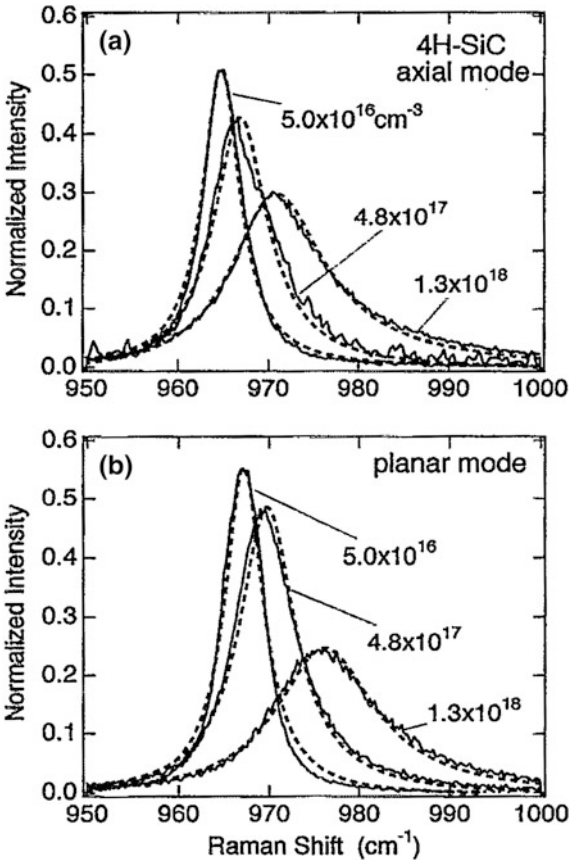

Fig. 2.75 Comparison between measured (*solid line*) and calculated (*dotted line*) Raman spectra of **a** axial and **b** planar LO phonon–plasmon coupled modes in *n*-type 4H-SiC with different concentrations. Reprinted with permission from [144]. Copyright 1995, AIP Publishing LLC

profiles is rather good. Using the plasmon frequencies in combination with the carrier concentrations obtained from Hall measurements, the longitudinal ($m_{\|}$) and transverse ($m_{\perp}$) effective masses of electrons can be derived, namely $m_{\|} = 1.4m_0$ and $m_{\perp} = 0.35m_0$ for 6H-SiC and $m_{\|} = 0.48m_0$ and $m_{\perp} = 0.30m_0$ for 4H-SiC. The carrier mobility obtained from the Raman analysis is also anisotropic.

The relationship between the LO phonon–plasmon coupled mode position and carrier concentration can be used to map the carrier concentration spatially. This is demonstrated by the semi-insulating and *n*-type-nitrogen-doped (concentration between 2.1×10^{18} and 1.2×10^{19} cm^{-3}) 4H-SiC and 6H-SiC [145]. Significant coupling between the A_1 longitudinal optical (LO) phonon and plasmon mode is observed, and there is direct correlation between the position of the coupled mode peak and carrier concentration. Figure 2.76a shows the nitrogen concentration estimated from the coupled LO phonon frequency across the wafer. The spatial dependence is not the same in different SiC wafers, and the concentration profile is generally not symmetrical with respect to wafer rotation. The wafer center has a large carrier concentration, and the far edges have doping levels much smaller than

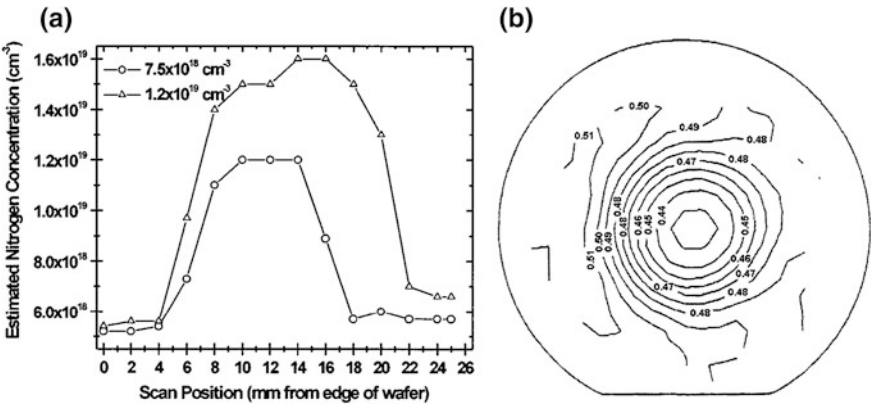

Fig. 2.76 **a** Estimated carrier concentration profile across two heavily doped 4H-SiC wafers determined by Raman spectroscopy with nominal nitrogen concentrations denoted in the legend. **b** Resistivity map for the 4H-SiC wafer nominally doped with 1.2×10^{19} cm^{-3}. Reprinted with permission from [145]. Copyright 1998, AIP Publishing LLC

the nominal value specified for the wafer. Figure 2.76b shows the resistivity map of a doped SiC wafer confirming the spatially nonuniform dopant concentration. The resistivity variation in the most heavily doped wafer is consistent with the observed carrier concentration variation obtained by Raman measurement of the same wafer. The results indicate that Raman scattering can be employed as a noncontact, nondestructive, and in situ probe for the spatial distribution of carriers in SiC wafers.

2.6 Absorption and Luminescence Properties

Light absorption and emission are very important optical processes in solids. On the one hand, they can serve as probes of the electronic structures and defect characteristics of solids. On the other hand, luminescence from solids has applications in many areas including displays, lighting, information communication, etc. As a wide bandgap semiconductor, the luminescence properties of silicon carbide have technological and commercial interests.

As a direct probe method for energy band structures, light absorption by some common polytypes of silicon carbide has been extensively investigated. Choyke and Patrick have acquired UV–Vis absorption spectra from hexagonal SiC at temperature from 77 to 717 K [146]. Figure 2.77 shows the absorption spectrum [$\alpha^{1/2}$ versus E (photon energy)] at 700 K along with the fit. The fit is the sum of the following two terms representing phonon absorption and phonon emission, respectively:

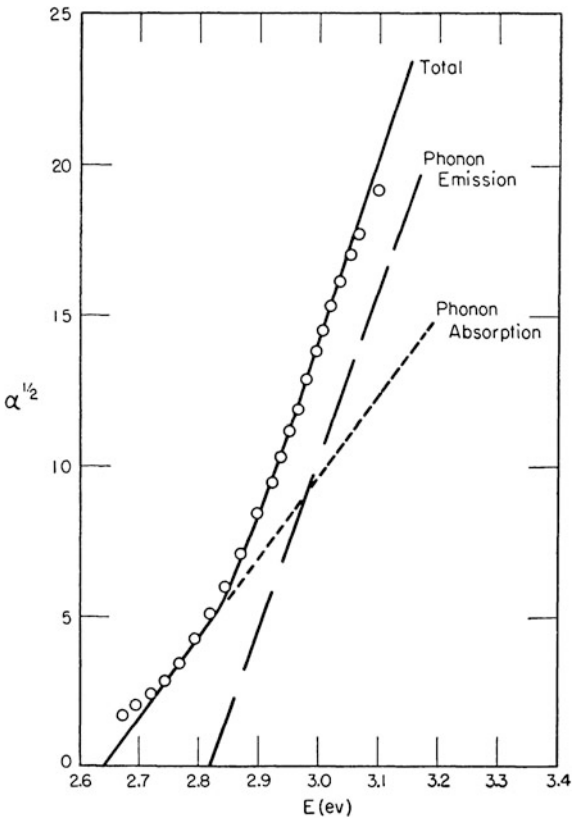

Fig. 2.77 Comparison between observed and calculated absorption by hexagonal silicon carbide at 700 K. Reprinted with permission from [146]. Copyright 1957, American Physical Society

$$\alpha^{\frac{1}{2}}(\text{abs.}) = \left[\frac{A}{e^{\theta/T} - 1}\right]^{\frac{1}{2}} \left[h\nu - (E_g - k\theta)\right], \tag{2.3}$$

$$\alpha^{\frac{1}{2}}(\text{emiss.}) = \left[\frac{A}{1 - e^{-\theta/T}}\right]^{\frac{1}{2}} \left[h\nu - (E_g + k\theta)\right], \tag{2.4}$$

where α is the absorption constant corresponding to absorption or emission of a phonon, h is Planck's constant, ν is the photon frequency, E_g is the energy gap of silicon carbide, k is Boltzmann's constant, and A is a constant depending on the properties of the materials and electron–phonon interaction. To obtain the best fit based on Eqs. (2.3) and (2.4), $k\theta$ (phonon energy) = 0.09 eV and A = 2,500. The good fit indicates that the interband transitions in SiC are indirect. The minimum energy gap at 300 K is 2.86 eV and above this temperature, $dE_g/dT = -3.3 \times 10^{-4}$ eV/degree. Four higher-energy absorption edges are observed by studying absorption of 1.8-μm-thick 6H-SiC prepared by grinding and polishing [147]. Three indirect absorption edges (Fig. 2.78) are observed at 3.0, 3.7, and

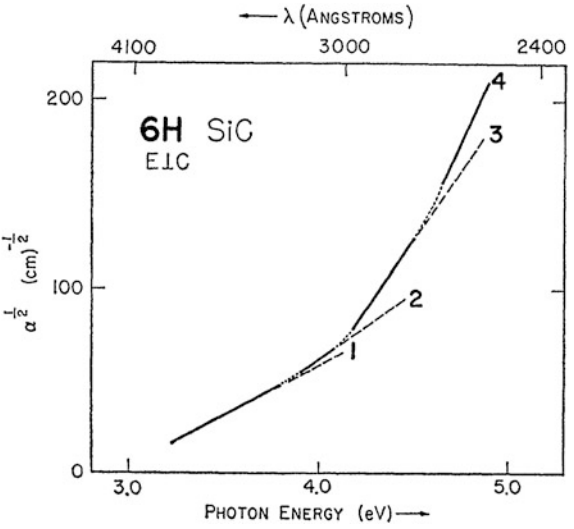

Fig. 2.78 Plot of $\alpha^{1/2}$ versus $h\nu$ for the UV–Vis absorption spectrum of 6H-SiC with data obtained from many samples. The measured values are on the straight-line segments (*solid*) or in the transitional regions (*dotted*). The four straight-line segments are extrapolations (*dashed*). Reprinted with permission from [147]. Copyright 1968, American Physical Society

4.1 eV (from fitted lines 1, 2, and 3), whereas the fourth absorption edge is at 4.6 eV (from line 4) but cannot be definitively identified as direct or indirect. The following simplified equation is used to fit the experimental data:

$$\alpha = \sum_i \alpha_i = \sum_i A_i (h\nu - E_{gi})^2, \tag{2.5}$$

where α is the absorption constant in cm^{-1}, A_i is a constant, and E_{gi} is the energy threshold. A_i and E_{gi} are chosen to yield the best fit, and in this equation, the effects of excitons and phonons are neglected since they are not observed experimentally.

The absorption coefficients of 4H-SiC in the wavelength range between 325 and 390 nm have been determined at room temperature [148]. The absorption coefficient from 335 to 390 nm is measured using a Xe arc lamp as the light source and the light propagates along the *c*-axis, whereas the 325-nm absorption coefficient is determined using a He–Cd laser source. The results are displayed in Fig. 2.79. At high energy, the square root of the absorption coefficient is proportional to the wavelength, as required by the indirect bandgap nature. By using the known relationship between the bandgap and temperature, the absorption coefficients of 4H-SiC at 2 K can be derived. The absorption coefficients of 4H-, 6H- and 3C-SiC between 297 and 390 nm are measured at room temperature using xenon and tungsten lamps together with lasers of several wavelengths [149]. On the basis of the temperature dependence of the bandgaps, the absorption coefficients at 2 K are estimated.

Donor–acceptor pair luminescence plays an important role in silicon carbide. Photoluminescence from the donor–acceptor pairs in cubic SiC excited by a laser at 1.8 K has been studied in detail [150]. The spectrum consists of a series of lines, and some of them are displayed in Fig. 2.80. The lines arise from the nitrogen

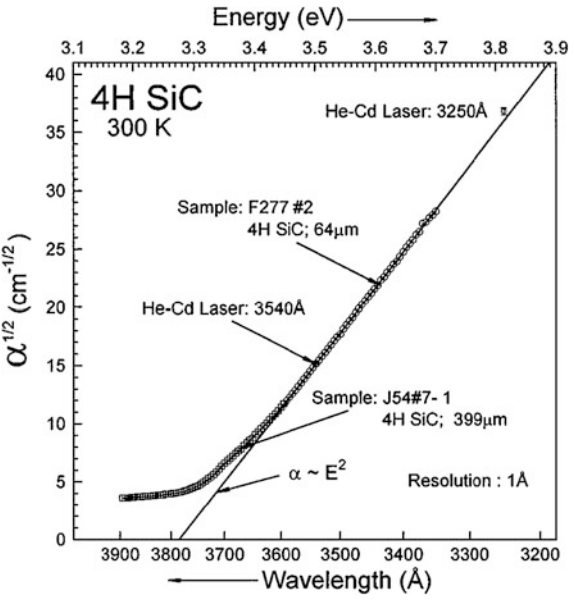

Fig. 2.79 Square root of the absorption coefficient versus wavelength of 4H-SiC. Reprinted with permission from [148]. Copyright 1998, AIP Publishing LLC

(N)-aluminum (Al) pairs (donor N in C sites and acceptor Al in Si sites) based on the crystal growth and freedom from extraneous lines. The following relationship is employed to analyze the origin of the observed luminescence lines [151]:

$$h\upsilon = E_g - (E_D + E_A) - E_C + E_{vdW}, \tag{2.6}$$

where E_g is the bandgap, E_D and E_A are the donor and acceptor ionization energies, E_C is the Coulombic interaction energy between the donor and acceptor ions after electron–hole recombination, and E_{vdW} is the interaction energy between the neutral donor and acceptor atoms before recombination. E_C has discrete values allowed by the lattice structure and so for a given donor, E_g is evaluated for each shell (denoted by an integer m) of equidistant acceptors. The same table of donor–acceptor shell substructure components of GaP is used to determine the shell numbers in cubic SiC, considering the identical (zinc-blende) crystal structures. In the N–Al spectrum of cubic SiC, the lines are well resolved up to the 80th shell and extrapolation yields the photon energy for distant donor–acceptor pairs, $h\upsilon_\infty$, of 2.0934 eV. With the aid of the bandgap of the cubic SiC (2.39 eV), the donor and acceptor ionization energies can be derived, $E_D = 118$ meV for N, and $E_A = (179\text{ meV}) + E_x$, for Al. Here, E_x represents the exciton binding energy. The donor–acceptor spectrum exhibits as an envelope at low resolution (Fig. 2.81), and the low-resolution spectrum shows several phonon replicas from which the phonon energies are derived to be 69, 94, and 118 meV.

Donor- and acceptor-related luminescence from 4H-, 6H-, and 3C-SiC single crystals has been investigated in the temperature range between 2 and 450 K [152].

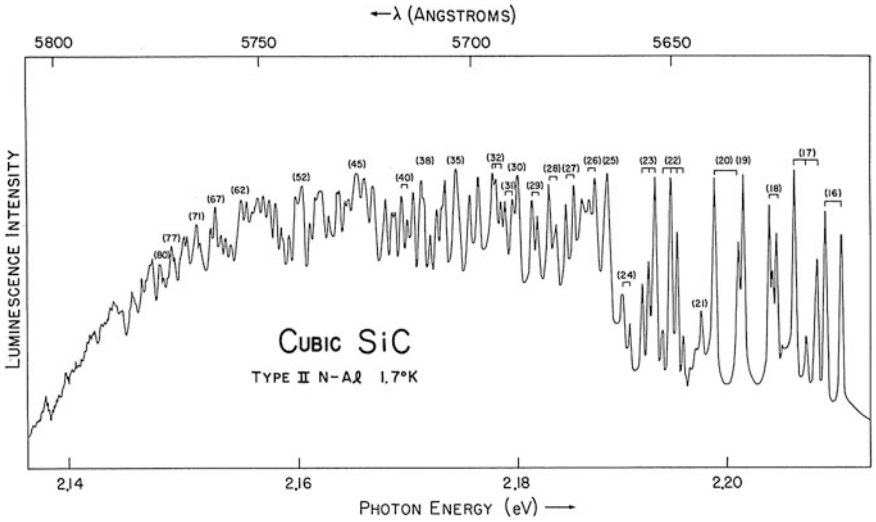

Fig. 2.80 Photoluminescence lines for shell numbers bigger than 15. The shell numbers (m) are displayed in brackets and shell substructure components are identified for small m. Reprinted with permission from [150]. Copyright 1970, American Physical Society

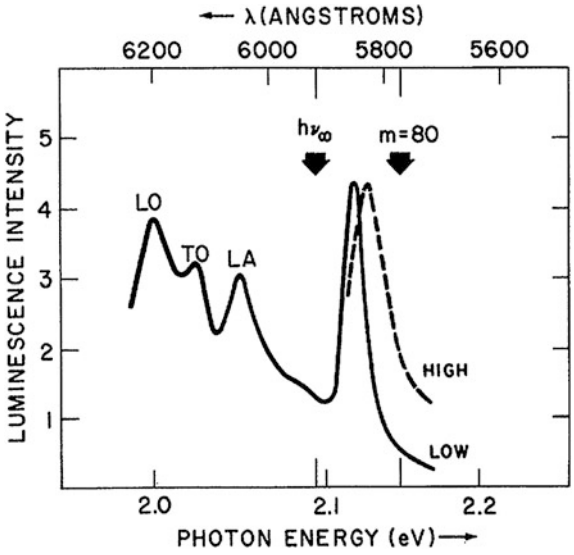

Fig. 2.81 Low-resolution envelope of the donor–acceptor PL spectrum (*strongest peak*) and phonon replicas (LA, TO, and LO). The solid and dashed lines are obtained at small and large excitation intensities, respectively. The position of the $m = 80$ line shown in Fig. 2.80 is marked and the photon energy of the distant pair, $h\nu_{\infty} = 2.0934$ eV, is also marked. Reprinted with permission from [150]. Copyright 1970, American Physical Society

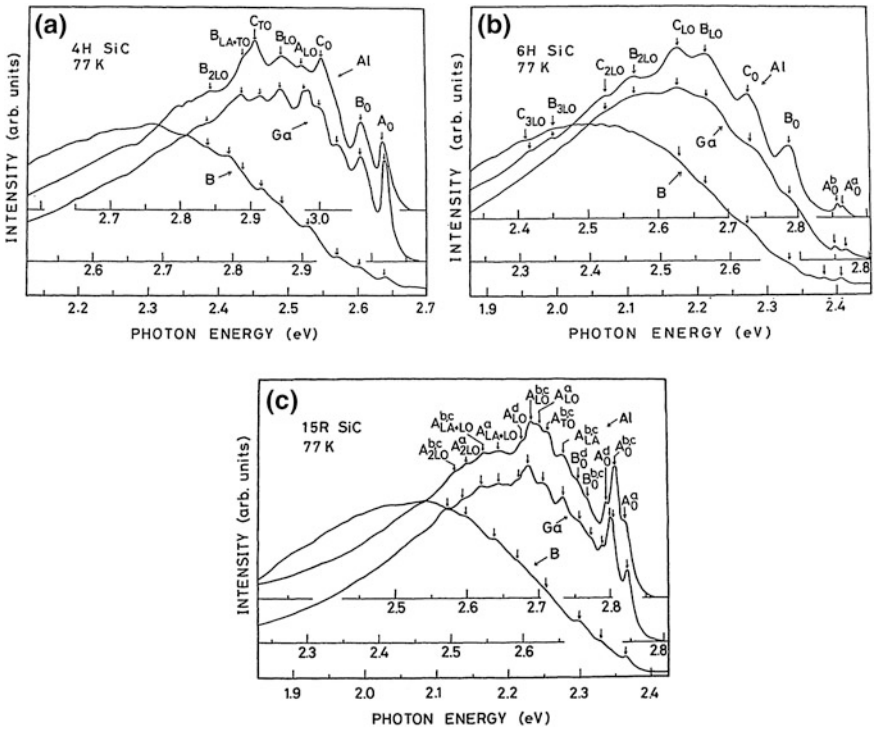

Fig. 2.82 Photoluminescence spectra of Al-doped, Ga-doped, and B-doped **a** 4H, **b** 6H, and **c** 15R SiC single crystals at 77 K. The *subscripts* indicate the types of phonons and *superscripts* indicate the types of sites, which acceptors substitute for. Reprinted with permission from [153]. Copyright 1980, American Physical Society

The SiC crystals containing A1, Ga, or B acceptors are studied, and the luminescence color varies from violet to near-infrared depending on the energy level of the acceptor and polytype. All the luminescence at low temperature is proposed to be due to pair recombination between the unintentionally introduced nitrogen donor and respective acceptor. Each PL spectrum shows a zero-phonon line and several phonon replicas. The higher temperature spectrum consists of another emission band stemming from recombination of free electrons with bound holes at the acceptors. The ionization energies of the acceptors are determined from the luminescence spectra and thermal quenching of the emission intensity. The B acceptor has higher ionization energy than Al and Ga, and so it shows a different luminescence spectrum in comparison and it is intense even at room temperature. The ionization energies of A1, Ga, and B in 4H-SiC are 168 meV + E_x, 249 meV + E_x, and 628 meV + E_x, respectively, where E_x is the exciton binding energy on the order of 10 meV. It has been demonstrated that the site-dependent impurity levels are caused by nonequivalent sites in 4H, 6H, and 15R SiC [153]. Figure 2.82 shows the luminescence spectra of these three polytypes of SiC at 77 K. These spectra show three series of peaks, A_0, B_0, and C_0 along with the respective phonon replicas. *B* and *C* arise from the donor–

Table 2.3 Ionization energies of donors and acceptors in cubic-like sites (E^C) and hexagonal-like sites (E^H), their average ratios, and free-exciton binding energies (E_x) in 3C, 4H, 6H, and 15R SiC. Reprinted with permission from [153]. Copyright 1980, American Physical Society

Ionization energy (meV)						
	Site	N	Al	Ga	B	E_x
3C	*C*	56.5	254	343	735	13.5
6H	*C*	155	249	333	723	78
	H	100	239	317	698	
	E^C/E^H	1.55	1.040	1.050	1.036	
15R	*C*	112	236	320	700	40
			230	311		
			223	305		
	H	64	221	300	666	
			206	282		
	E^C/E^H	1.75	1.076	1.072		
4H	*C*	124				20
			191	267	647	
	H	66				
	E^C/E^H	1.88	1.0	1.0	1.0	

acceptor pair transitions, and *A* is attributed to free-to-acceptor transition. The peak intensity ratios of C_0 to B_0 under high-intensity excitation, where both the *B* and *C* series appearing with full intensity are, respectively, 0.96 for 4H, 1.9 for 6H, and 1.4 for 15 R SiC. These values agree well with the ratios of the number of cubic-to-hexagonal-like sites (1 for 4H, 2 for 6H, and 1.5 for 15R). Hence, the B and C series of emission lines arise from donor–acceptor pair transitions between acceptors and donors in hexagonal-like and cubic-like sites, respectively, as suggested previously [154]. This implies that every impurity atom enters each type of site with the same equal probability. Further analysis based on the configuration coordinate phonon spectra supports the notion that all the impurities in cubic sites occupy deeper levels than those in hexagonal sites (Table 2.3). The ratios of the ionization energies between the cubic and hexagonal sites, which are roughly constant and independent of the polytypes and impurity types, are 1.0–1.08 for acceptors and 1.55–1.88 for donors. The origin of the site effect on the impurity level is explained by assuming a local dielectric constant and local effective mass based on the quantum defect model. The exciton binding energy depends almost linearly on the ionization energy of nitrogen donors in 3C, 4H, 6H, and 15R SiC.

The donor–acceptor pair light emission from silicon carbide can persist at elevated temperature. The highly efficient visible luminescence from N- and B-doped 6H-SiC epilayers is observed at room temperature [155]. Figure 2.83 displays the PL spectra of two samples with B concentrations of 2×10^{17} cm^{-3}

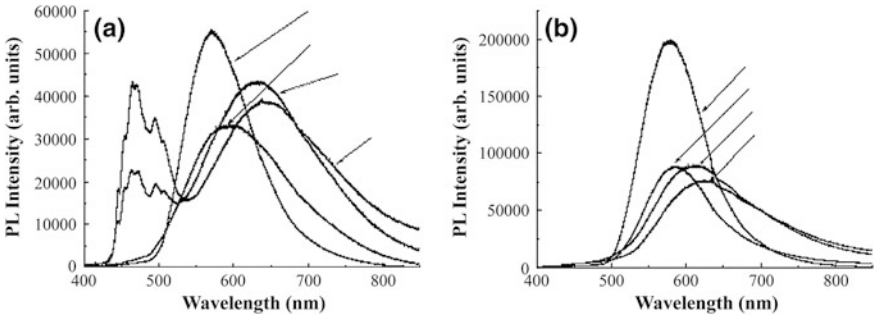

Fig. 2.83 Photoluminescence spectra of N- and B-doped 6H-SiC epilayers excited by 351 nm at different temperatures. The B concentrations are **a** 2×10^{17} cm^{-3} (sample 1) and **b** 2×10^{18} cm^{-3} (sample 2), respectively. Reprinted with permission from [155]. Copyright 2006, AIP Publishing LLC

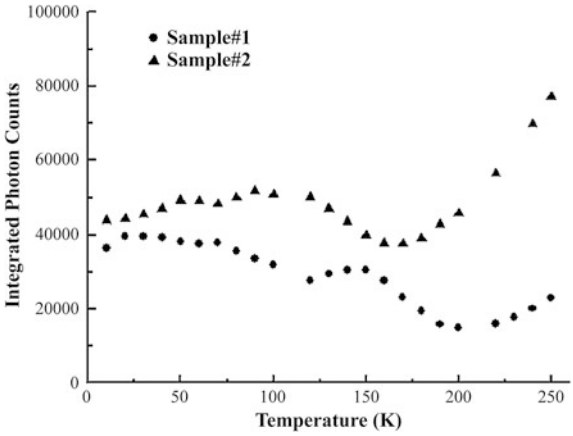

Fig. 2.84 Integrated photon count in the PL spectrum as a function of temperature for low and highly doped 6H-SiC. Reprinted with permission from [155]. Copyright 2006, AIP Publishing LLC

(sample 1) and (b) 2×10^{18} cm^{-3} (sample 2). The N concentration is approximately 4×10^{18} cm^{-3} in both samples. The temperature varies from 10 to 250 K in the PL measurements. The sample with a small B concentration shows both N–B donor–acceptor emission at approximately 630 nm and N–Al (unintentionally introduced) donor–acceptor emission at 460 nm at temperature below 100 K. However, the N–Al emission is quenched above 100 K. The peak wavelength of the N–B emission gradually shifts to 576 nm with increasing temperature. The N–B emission band is broad with a full width at half maximum (FWHM) of 110 nm at 250 K. The sample with a large B concentration shows only the N–B emission even at low temperature. The PL intensity from the highly doped sample at high temperature is significantly larger (Fig. 2.84). A high internal quantum efficiency of 95 % is estimated for the highly B-doped sample at 250 K. The donor–acceptor recombination lifetimes are 2.5 and 5.0 ms for samples 1 and 2, respectively, as determined from the time-resolved photoluminescence measurement, and in good

agreement with the calculated value based on the rate equation. It has also been demonstrated that when the N and B concentrations are in a range of 10^{18} cm^{-3}, 6H-SiC shows the most intense luminescence when the concentration difference between the donors and acceptors is about 4.6×10^{18} cm^{-3} [156]. The PL spectrum has a maximum at about 587 nm with an FWHM of 120 nm. However, the obtained lifetimes are 0.5, 30 ns, 0.5, 1.2, and 1.1 μs for different samples and much smaller than those reported in Ref. [155].

Some specific luminescence lines observed from bulk silicon carbide are ascribed to recombination of excitons bound to impurities or free-to-bound recombination. The exciton–impurity complex is discussed in Ref. [157], and various donors and acceptors in Si have been investigated leading to the observation of luminescence arising from the decay of the exciton bound to impurities [158]. The phonon-assisted indirect transitions involving the exciton–impurity complexes in SiC generally give rise to a series of emission lines, from which the energies of the phonons involved can be derived. Choyke and Patrick have reported photoluminescence from 6H-SiC, showing 50 lines at low temperature [159]. Figure 2.85 depicts the PL spectrum collected at 6 K. It shows three no-phonon lines, P_0, R_0, and S_0 caused by exciton recombination at the three non-equivalent unionized nitrogen donors along with the phonon replicas. For example, P_0 is related to a series of lines. The P series are due to recombination at the P nitrogen center with emission of one of 17 phonons. The displacement of a P line from P_0 corresponds to the energy of a phonon. The 17 measured phonon

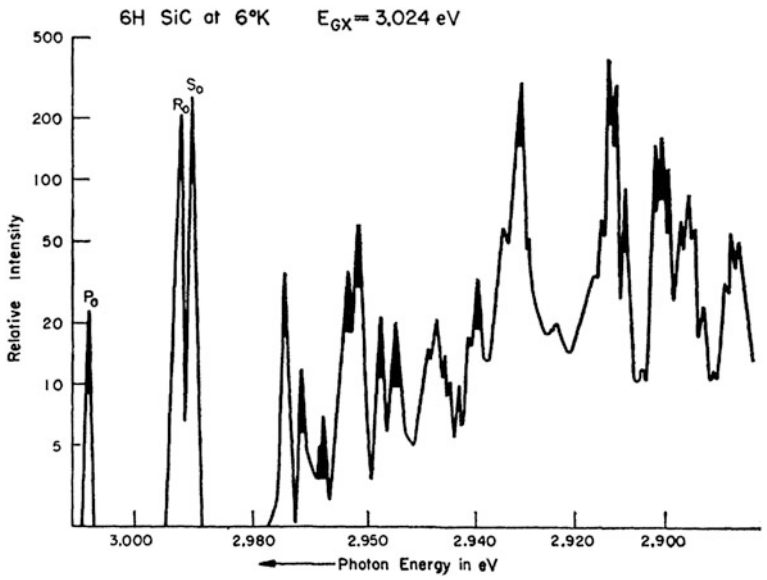

Fig. 2.85 Photoluminescence spectrum obtained from 6H-SiC at 6 K. The black peaks belong to the P series. Reprinted with permission from [159]. Copyright 1962, American Physical Society

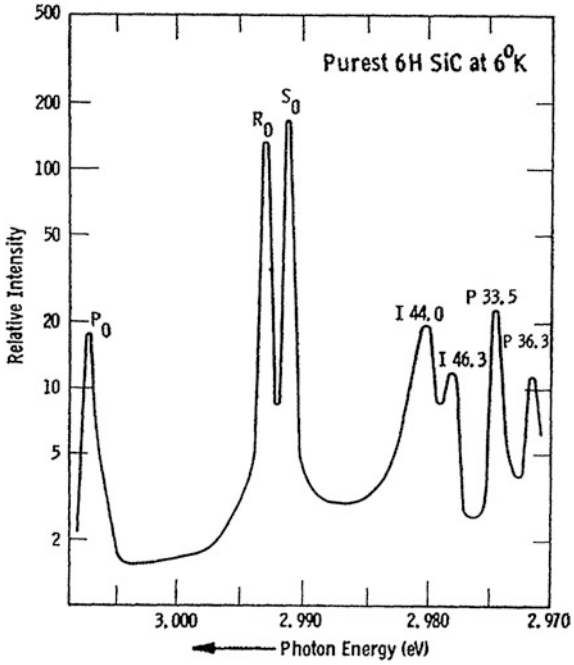

Fig. 2.86 Photoluminescence spectrum of the purest 6H-SiC sample at 6 K. Two additional intrinsic lines (*I* 44.0 and *I* 46.3) due to recombination of free excitons are shown and the numbers are the phonon energies in meV. Reprinted with permission from [159]. Copyright 1962, American Physical Society

energies can be assembled into an appropriate extended Brillouin zone. The spin–orbit splitting of the valence bands is found to be only 4.8 meV, suggesting that the hole is confined to the carbon sublattice. Luminescence due to recombination of free excitons involving phonons has also been observed (Fig. 2.86).

Besides the excitons bound to neutral nitrogen impurity atoms, the exciton bound to the singly ionized nitrogen impurity can yield luminescence in 6H-SiC [160]. Photoluminescence from the ionized nitrogen–exciton complexes in N-doped 6H-SiC is observed at 6 K, and the PL spectrum is shown in Fig. 2.87. The ionization energies of the three nonequivalent nitrogen donors are 0.17, 0.20, and 0.23 eV, respectively. The observed quenching of edge emission in the impure samples is ascribed to exciton hopping. Figure 2.88 displays the energy ranges of the two distinct luminescence spectra arising separately from the exciton–neutral nitrogen complex (four-particle complex) or exciton–ionized nitrogen complex (three-particle complex). The three-particle spectrum extends into the lower-energy region with multi-phonon emission and becomes gradually a continuum. Four-particle emissions have higher photon energies than three-particle emissions because the exciton is more tightly bound to ionized nitrogen atoms than neutral ones. In 15R-SiC, the photoluminescence spectra due to the two kinds of nitrogen–

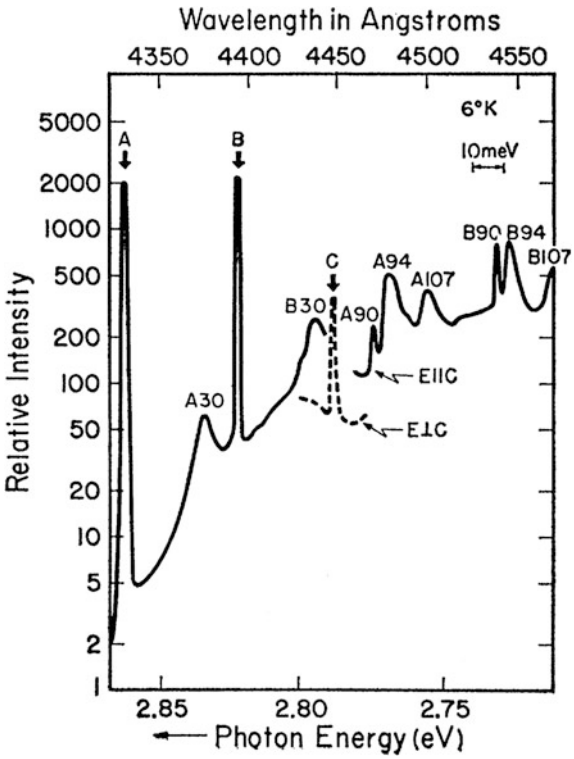

Fig. 2.87 Photoluminescence spectrum of 6H-SiC showing the portion of the ionized nitrogen–exciton complex band, including the no-phonon lines of *A*, *B*, and *C* along with some peaks arising from phonon emission. The peaks are labeled with their series letter and the number indicates the phonon energy in meV. Reprinted with permission from [160]. Copyright 1963, American Physical Society

exciton complexes are very similar to those of 6H-SiC and similar phonon spectra are obtained [161]. The four nitrogen ionization energies are approximately 0.14, 0.16, 0.16, and 0.20 eV, which are smaller than those in 6H-SiC. Only four of the five nonequivalent nitrogen atoms in 15R-SiC are detected from the PL spectra. 15R-SiC also exhibits indirect absorption at the absorption edges. The edges have a similar shape as 6H-SiC due to the similarity in the phonon spectrum. 15R-SiC has an exciton energy gap of 2.986 eV at 6 K, which is smaller than that of 6H-SiC. According to the luminescence from thermally excited states of the exciton–neutral nitrogen complexes, it is proposed that 15R-SiC has a second valence band that splits from the first one by 4.8 meV due to the spin–orbit interaction; the holes are supposed to be largely confined to the carbon sublattice. The result shows evidence of the presence of six conduction-band minima.

Luminescence from the exciton–nitrogen complex and interband absorption in cubic SiC has been investigated [21]. Absorption measurements at 4.2 K demonstrate that 3C-SiC has an indirect absorption edge associated with exciton

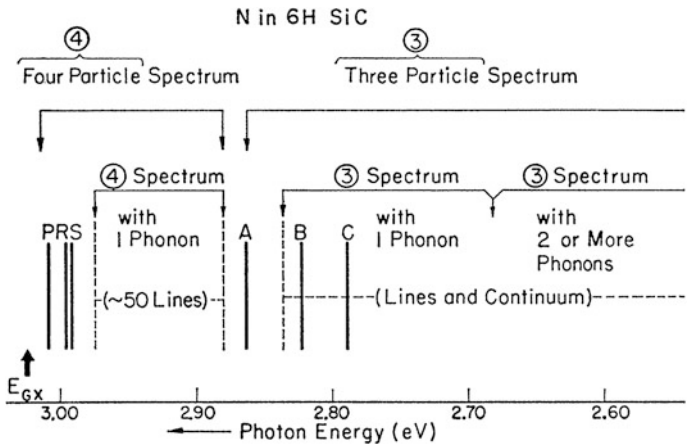

Fig. 2.88 Energies of no-phonon lines *P*, *R*, and *S* of the exciton–neutral nitrogen complex photoluminescence spectrum and *A*, *B*, and *C* of the exciton–ionized nitrogen complex photoluminescence spectrum as well as energy ranges of photons emitted with simultaneous phonon emission. E_{Gx} is the exciton energy gap. Reprinted with permission from [160]. Copyright 1963, American Physical Society

transitions and the exciton energy gap is 2.390 eV. The phonon energies determined from the absorption spectrum are 46, 79, 94, and 103 meV. The exciton–neutral nitrogen complex luminescence spectrum at 6 K provides the accurate phonon energies. The thermally excited states of the complex give rise to additional lines in the luminescence spectrum at higher temperature. Comparison shows that 3C-, 6H-, and 15R-SiC have very close phonon energies, and the values are 46.3 (TA), 79.4 (LA), 94.4 (TO), and 102.8 (LO) meV for 3C-SiC. Choyke and colleagues have found an important empirical correlation between the energy gap and hexagonality (Table 2.4) for seven polytypes of SiC (Fig. 2.89). It is a nearly linear relationship. They have also investigated low-temperature luminescence from the

Table 2.4 E_{Gx} (exciton bandgap) of seven SiC polytypes and corresponding "hexagonal" percentage. Reprinted with permission from [21]. Copyright 1964, American Physical Society

Polytype (Ramsdell notation)	Exciton bandgap E_{Gx}	Jagodzinski notation	Hexagonality *h* (percent)
3C	2.390	k	0
8H	2.80	hkkk	25
21R	2.86	hkkhkkk	29
15R	2.986	hkhkk	40
33R	3.01	hkkhkkhkkhk	36
6H	3.023	hkk	33
4H	3.263	hk	50

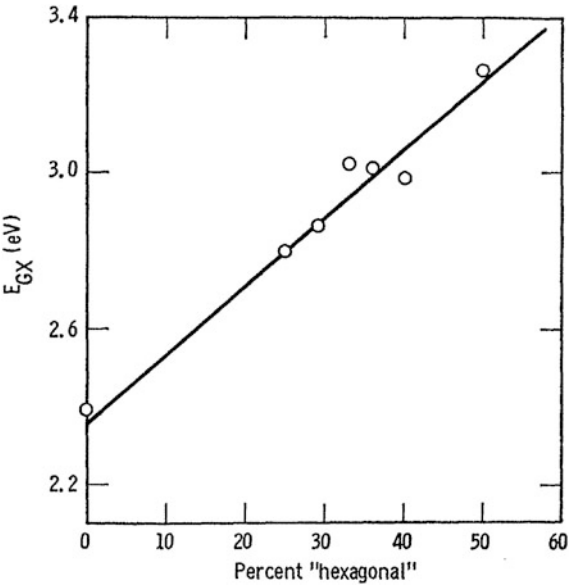

Fig. 2.89 Exciton bandgap E_{Gx} versus hexagonal percentage (hexagonality) of seven SiC polytypes. The values of E_{Gx} are obtained from absorption measurements at 4.2 K or luminescence measurements at 6 K. These values and the hexagonality values are summarized in Table 2.4. Reprinted with permission from [21]. Copyright 1964, American Physical Society

exciton–nitrogen complexes in 4H-SiC [162]. Eighteen phonon energies are derived from the PL spectra. The interpretation of the phonon spectrum suggests positions of low symmetry for the conduction-band minima, requiring a 12-valley model for electrons. It is argued that such a method can be generalized to other SiC polytypes to locate the conduction-band minima. It explains the observed similarity in the phonon spectra of seven SiC polytypes. The relatively large and pure 2H-SiC crystals are fabricated, and their absorption and luminescence properties at 2–8 K are investigated [163]. 2H-SiC shows an indirect energy gap of 3.330 eV that is the largest among all the observed SiC polytypes. The group theory selection rules are utilized to analyze the polarized luminescence in order to determine the active phonons. The spectrum is consistent with the selection rules by assuming that there are conduction-band minima at the *K*-points of the Brillouin zone. SiC resembles diamond more than Si concerning the "trace variable" forces.

Nitrogen-bound exciton luminescence can be used to determine the nitrogen-dopant concentration in silicon carbide, as demonstrated by low-temperature photoluminescence spectroscopy conducted on uncompensated 4H- and 6H-SiC [164]. This is realized by comparing the intensity of the nitrogen-bound exciton lines to that of the free exciton (as an internal reference). A line-fitting method with the proper line shape is employed to separate the contribution of the bound exciton and free-exciton lines in the PL spectrum. The ratio of the bound exciton zero-phonon lines to the free-exciton most intensive phonon replica (around 77 meV) shows good linear dependence on the dopant concentration as determined by capacitance-voltage measurements on both polytypes. When the real line shape, influence of the spectrometer transfer function, and structure of the PL

spectrum in the vicinity of the free-exciton replica are taken into account, the fit allows for the determination of the N-dopant concentration in the ranges between 1×10^{14} and 3×10^{16} cm^{-3} in 4H-SiC and 1×10^{14} and 10^{17} cm^{-3} in 6H-SiC. The free-exciton emission is not observed above these concentrations.

Besides donor–acceptor pair, exciton bound to donor complex, there are other models proposed to explain the low-temperature luminescence lines in silicon carbide. A series of bound exciton lines just below the luminescence of single excitons bound to the shallow nitrogen donors [165] can be attributed to recombination in the multiple bound exciton complexes. This model is supported by the spectral positions, Zeeman effect, and behavior under optical pumping. Two series of near-infrared emission bands are observed from boron-doped 3C-SiC crystals [166]. The dominant series of luminescence bands (at about 1.6 eV) at low temperature is assigned to nitrogen donor–boron acceptor pair recombination. The other series of bands is explained by the free-to-bound transition model concerning the spectral shape of the zero-phonon line and temperature dependence. In this scenario, the electrons in the conduction band recombine with the holes trapped at the boron acceptors to produce luminescence. The ionization energies of the nitrogen donor and boron acceptor are estimated to be 0.05 and 0.73 eV, respectively. The exciton can also be bound to the neutral aluminum acceptor complex in 3C-, 6H-, and 4H-SiC, as confirmed by low-temperature photoluminescence and cathodoluminescence experiments [167]. The correlated lines are observed only from lightly doped *p*-type SiC films, and the intensity increases with aluminum concentration. The multiplicity of the observed lines agrees with the prediction from the symmetry-based models. In another study on low-temperature photoluminescence from the 6H, 4H, and 15R polytypes of SiC [50], a couple of new features different from the well-known emission lines close to the bandgap are observed from the three polytypes and attributed to recombination of the bound excitons at aluminum acceptors. There are two distinct boron-related centers in silicon carbide polytypes, one shallow with ionization energy of 300 meV and the other deep with ionization energy of 650 meV. 4H-SiC homoepitaxial films can be intentionally doped with the shallow boron center by controlling the silicon to carbon source gas ratio during chemical vapor deposition [168]. For samples produced using a small Si/C ratio, the shallow boron centers tend to be incorporated into the silicon sublattice as confirmed by the temperature-dependent Hall effect, admittance spectroscopy, and deep-level transient spectroscopy. A luminescence peak around 383.8 nm is observed from the samples at low temperature, and this peak stems from recombination of an exciton–neutral shallow boron acceptor complex. The first evidence for assignment of this luminescence peak is that its intensity increases with boron concentration, and secondly, the observed momentum-conserving phonon replicas have energies consistent with other previously observed exciton–neutral acceptor complexes in SiC. Lastly, the excited states are observed at elevated temperature and this is similar to the cases of excitons bound to neutral aluminum and gallium acceptors.

Some luminescence lines with previously unknown origins in silicon carbide are ascribed to bound excitons. The D_1 photoluminescence observed from

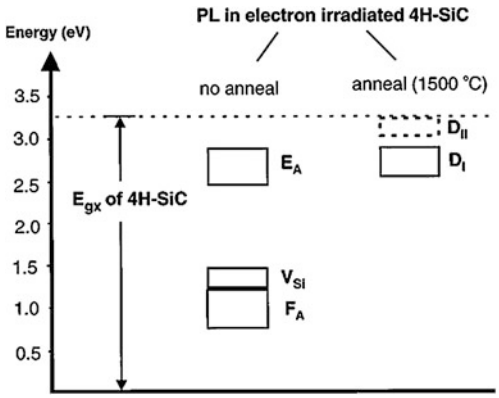

Fig. 2.90 Energy ranges of the main PL spectra of room-temperature electron-irradiated 4H-SiC. The excitonic bandgap energy of 4H-SiC is shown on the left, the case right after electron irradiation in the *middle*, and that after high temperature (about 1,500 °C) annealing on the *right*. Reprinted with permission from [60]. Copyright 1999, American Physical Society

electron-irradiated 4H-SiC has been investigated [169]. At temperature lower than 5 K, the D_1 PL spectrum shows a no-phonon line (L_1, 427.3 nm) and the phonon replicas. The L_1 line decreases rapidly with increasing temperature and meanwhile, two higher-energy no-phonon lines (M_1, 426.1 nm; H_1, 425.7 nm) emerge. At temperature higher than 100 K, the D_1 PL is quenched. The lifetime of the D_1 PL is 450 μs at 1.3 K and 2 μs at 70 K. It is suggested that the D_1 luminescence arises from exciton recombination at an isoelectronic center, with one of the particles of the exciton weakly bound and the other more tightly bound. Another luminescence center has been observed from room-temperature electron-irradiated 4H-SiC, called E_A [60]. The spectrum shows a couple of sharp no-phonon lines together with a broad phonon-assisted structure. Annealing at around 750 °C causes an abrupt change in the PL spectrum, whereas further annealing at temperature above 750 °C results in the dominance of the strong D_1 spectrum (Fig. 2.90). Forty no-phonon lines are observed from the E_A spectrum in the range of 2.8–2.9 eV. Based on photoluminescence excitation spectroscopy, the E_A spectrum is proposed to originate from recombination of the excitons bound to isoelectronic defect centers.

2.7 Surface Structures

Silicon carbide has many polytypes, and each polytype has its own crystal structure and specific surface structure. The surface atoms in silicon carbide alter the bonding structures to terminate partial dangling bonds by forming Si–Si bonds, C–C bonds, double or triple bonds, or bonding with foreign atoms. On the other hand, silicon carbide is a compound semiconductor that is composed of two

elements and both silicon and carbon atoms on the surface can react with various elements such as hydrogen and oxygen to produce different surface chemical structures. Therefore, silicon carbide has rather complex surface structures, which affect its electrical and optical properties. Some surface defects can significantly alter the normal performance of SiC-based electronic devices, and so there has been extensive investigation on the surface structures of silicon carbide. Here, the major phenomena involving the surface of silicon carbide are reviewed briefly.

2.7.1 Surface Reconstruction

In general, on the semiconductor surface, owing to the absence of atoms on the air side of the semiconductor/air interface, the surface atoms experience different forces compared to the interior ones. As a result, the surface structure relaxes and reconstructs to attain the minimum surface energy. Assume that the reconstructed surface has a two-dimensional lattice with unit vectors of $\boldsymbol{b}_1$ and $\boldsymbol{b}_2$, the substrate surface has two-dimensional lattice with unit vectors of $\boldsymbol{a}_1$ and $\boldsymbol{a}_2$, and on a certain substrate crystal surface $X\{hkl\}$, reconstruction is given by ($\boldsymbol{b}_1 \| \boldsymbol{a}_1$, $\boldsymbol{b}_2 \| \boldsymbol{a}_2$), and then we have:

$$b_1 = \mathrm{p}a_1,\ b_2 = \mathrm{q}a_2, \tag{2.7}$$

where p and q are two proportionality factors. In general, the reconstructed surfaces are denoted by the following notations [170]:

$$X\{hkl\}(p \times q),\ X\{hkl\}c(p \times q),\ \text{or}\ X\{hkl\}(p \times q) - R^{\circ}, \tag{2.8}$$

where c represents a possible center, and R° denotes the angles by which the reconstructed surface rotates relative to the substrate surface.

It is very difficult to determine the atomic positions of the reconstructed surface experimentally. Investigators generally utilize scanning tunneling microscopy (STM) and low-energy electron diffraction (LEED) to experimentally study SiC surfaces. First-principle calculation and ab initio molecular dynamics simulation have also been adopted to theoretically study SiC. Based on the experimental and theoretical results, various structural models have been proposed. The (100) surface on cubic SiC is one of the most widely studied surfaces of SiC. This surface has several types of surface reconstruction such as the C-terminated $c(2 \times 2)$ surface, Si-terminated 2×1 surface, and Si-rich 3×2 surface.

The atomic-resolution images obtained by STM reveal that the 3C-SiC(001) surfaces have Si adlayers on the Si-terminated surface [171]. An additional dimer-row model for the surface with extra Si atoms shows structural features consistent with STM and LEED. The unit cell of the Si-saturated (3×2) surface observed by LEED comprises a pair of additional Si dimers on the Si-terminated surface forming a straight line along the direction through the centers of two constituent

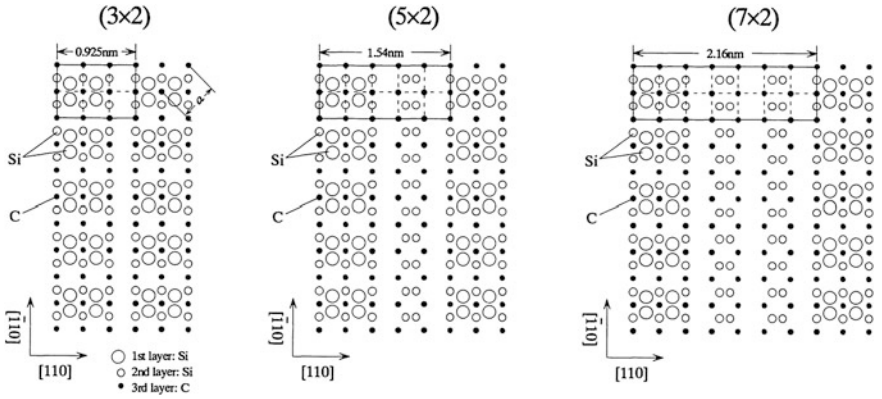

Fig. 2.91 3C-SiC(001)-(3 × 2), (5 × 2), and (7 × 2) structural models. Reprinted with permission from [171]. Copyright 1994, American Physical Society

atoms of a dimmer (Fig. 2.91). There are also reconstruction models for the (5 × 2) and (7 × 2) surfaces in which the unit cell of the uppermost atomic layer also consists of a pair of additional Si dimmers.

Clear atom images of individual Si dimers are observed from the Si-rich 3C-SiC(100)-(3 × 2) surfaces by STM [172]. The samples have a high-quality surface with a low defect density (Fig. 2.92). The STM image shows that the Si–Si dimmers form rows perpendicular to the dimer direction in a (3 × 2) atomic arrangement with clear evidence of asymmetric dimers tilted in the same direction (not alternate tilting). This is a very open atomic surface arrangement. On the top atomic layers, three types of defects are identified, namely missing dimmers (type A), dimer pairs (type B), and dimers having different tilt angles (type C). The proposed structure model is illustrated in Fig. 2.93. This model is based on the clear identification of individual Si atoms from the STM topography (filled and empty electronic states). This model gives a Si-coverage of 1/3, different from conclusions drawn in the aforementioned STM study [171] where there is a coverage of 2/3 with pairs of Si dimers oriented parallel to the rows (Fig. 2.91).

The structural and electronic properties of five different configurations of polar 3C-SiC (001) surfaces are studied by self-consistent ab initio calculation [173]. No dramatic Si dimmers on the Si-terminated (2 × 1) surfaces are found, whereas strong carbon dimmers are found from various C-terminated surfaces serving as the reconstruction building blocks. The 3C-SiC(100)-$c(4 \times 2)$ surface reconstruction is studied by atomic-resolution STM [174]. The STM images agree well with the corresponding STM image calculation (Fig. 2.94). A model of dimer rows is proposed. In this picture, the dimmer row consists of alternatively up and down dimers within the row in an "undulating" type of arrangement so as to reduce the surface stress. The 3C-SiC(100) and Si(100) have different $c(4 \times 2)$ surface reconstruction. The straight, long, and highly stable Si atomic lines self-organized on the 3C-SiC(100) surfaces are observed by STM [175]. The Si atomic lines are composed of

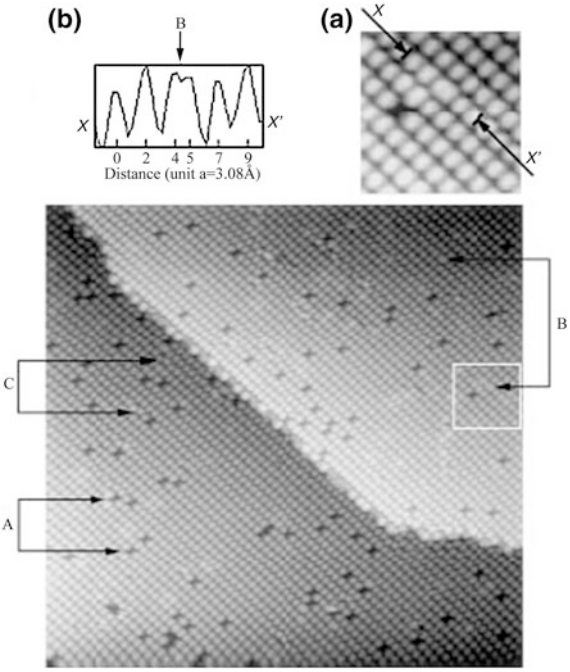

Fig. 2.92 40 × 40 nm STM image (*filled states*) of the 3C-SiC(100)-(3 × 2) surface with *A*, *B*, and *C* denoting three types of defects. **a** Magnified image of the area having type A (*missing dimer*) and *B* (*dimmer pair*) defects. **b** Atomic profile of dimers along the *xx*′-axis displaying the two components of a dimer pair (marked by *B*). Reprinted with permission from [172]. Copyright 1996, American Physical Society

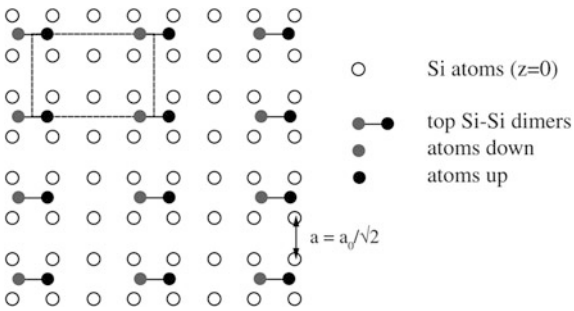

Fig. 2.93 Schematic of the 3 × 2 Si–Si dimers on a nonreconstructed 3C-SiC(100) surface. The surface primitive unit cell parameter is $a = a_0/\sqrt{2}$, and a_0 (4.36 Å) is the 3C-SiC lattice constant. The dashed line refers to the (3 × 2) unit cell. Reprinted with permission from [172]. Copyright 1996, American Physical Society

Si dimers formed by annealing of the primary 3C-SiC(100)-(3 × 2) structure at above 1,000 °C (Fig. 2.95). The number and spacing of the Si atomic lines can be controlled by the annealing time and temperature. The density of the Si atomic lines

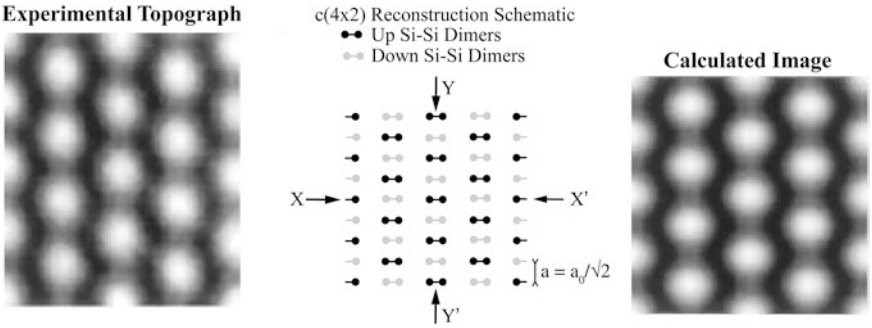

Fig. 2.94 Experimental STM topographical image (filled electronic states) of the Si-terminated 3C-SiC(100)-$c(4 \times 2)$ surface showing the Si dimers (*left panel*) and schematic of this surface showing the alternating up and down dimmers (*middle panel*). The unreconstructed surface primitive lattice parameter is $a = a_0/\sqrt{2}$, where $a_0 = 4.36$ Å is the 3C-SiC lattice constant. The right panel shows the calculated STM image. Reprinted with permission from [174]. Copyright 1997, American Physical Society

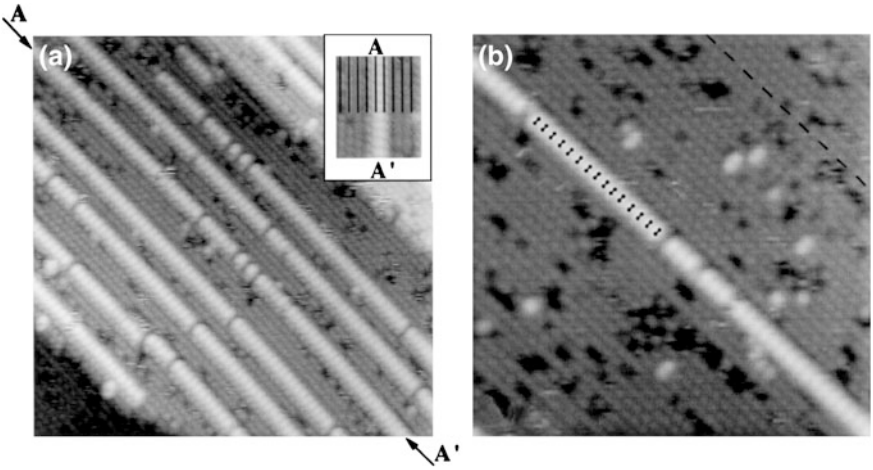

Fig. 2.95 **a** 32 × 32 nm STM topographical image of the 3C-SiC(100)-(3 × 2) surface after annealing at 1,100 °C. There are Si atomic lines along with $c(4 \times 2)$ surface reconstruction between them. **b** 20 × 20 nm STM topographical image of 3C-SiC(100)-(3 × 2) surface after annealing at 1,150 °C. A single Si-dimer line is displayed. The *dark dashed line* in the *top right* corner denotes the $c(4 \times 2)$ dimer-row direction. Reprinted with permission from [175]. Copyright 1997, American Physical Society

decreases with temperature until the isolated Si atomic lines are observed. The phase transition is observed with annealing. The 3C-SiC(100)-(3 × 2) surface transforms to the 3C-SiC(100)-$c(4 \times 2)$ surface on which the Si atomic lines site. These atomic channels form upon the phase transition between the (3 × 2) and $c(4 \times 2)$ reconstruction by selective Si atom organization. Figure 2.96 describes

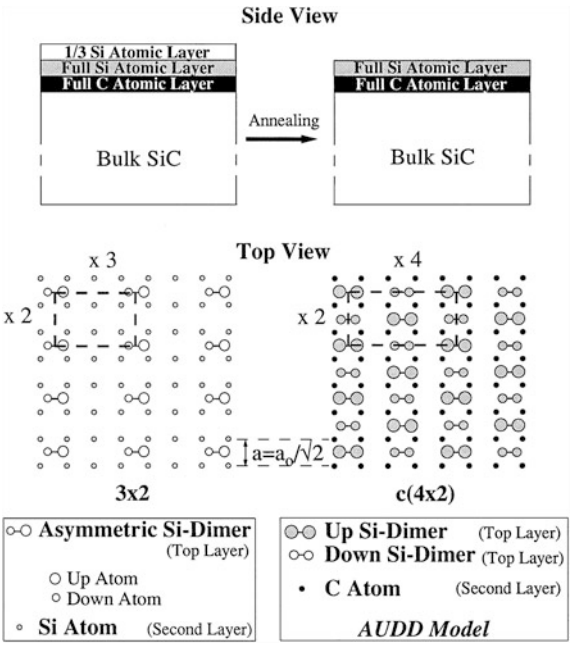

Fig. 2.96 Schematic of the 3C-SiC(100)-(3 × 2) and 3C-SiC(100)-*c*(4 × 2) reconstructed surfaces. Annealing induces phase transition between them. Reprinted with permission from [175]. Copyright 1997, American Physical Society

these two surface reconstructions. The Si atomic lines result in a lateral mismatch between the *c*(4 × 2) Si-dimer rows. Formation of the carbon atomic chains is also observed from the C-terminated 3C-SiC(100) surfaces by atom-resolved STM [176]. These carbon atom lines are thermally stable up to 1,200 °C. They comprise buckled single bond sp^3 C–C dimers with the direction perpendicular to the *sp* C ≡ C triple bond dimers forming a *c*(2 × 2) surface reconstruction. Their density increases with annealing time, and they do not cause or come from surface anti-phase boundaries. The anisotropic tensile or compressive surface stress is proposed as a leading driving force in this carbon *sp* -> sp^3 diamond-like transformation.

The atomic structure of the 3C-SiC(100)-*c*(2 × 2) surface is studied using dynamic calculation of low-energy electron diffraction intensities [177]. The *c*(2 × 2) surface is prepared in an ultrahigh vacuum by removal of surface silicon in high-temperature annealing or deposition of surface carbon by exposing the stoichiometric (2 × 1) surface at 1,125 K to C_2H_4. Both samples contain surfaces terminated with C_2 groups in staggered silicon bridge sites (Fig. 2.97). The difference is that the surface created by silicon sublimation contains weak silicon dimer bonds in the second atomic layer of the *c*(2 × 2) surface, whereas the C_2H_4-generated *c*(2 × 2) surface has no such dimer bonds. Thermal decomposition of C_2H_4 yields hydrogen that saturates silicon dangling bonds in the second atomic layer, thus prohibiting the formation of the Si dimers. Ab initio calculation of the reconstruction of the 3C-SiC(100) surfaces confirms that the lowest energy *c*(2 × 2) reconstructed surface comprises triply bonded carbon dimers in a

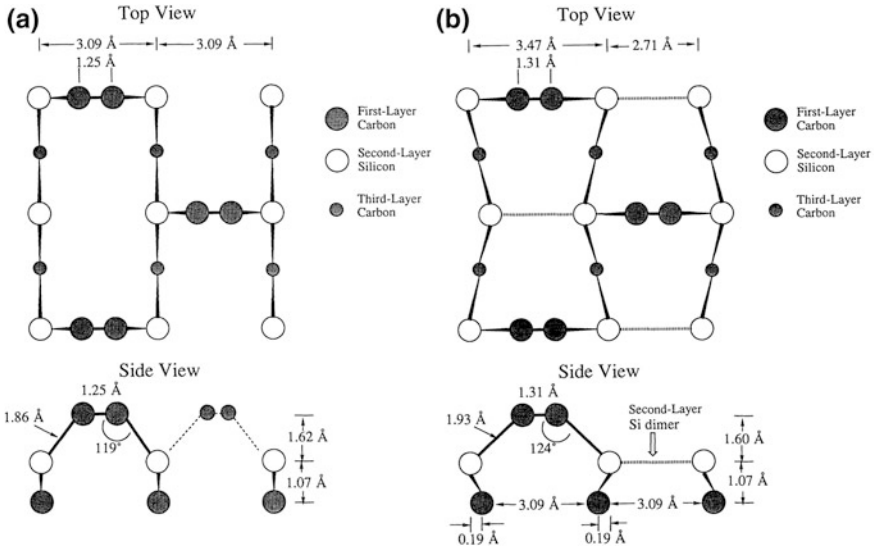

Fig. 2.97 Schematic of the best fit structure of the 3C-SiC(100)-$c(2 \times 2)$ surface produced by **a** C_2H_4 exposure and **b** Si sublimation. Reprinted with permission from [177]. Copyright 1991, American Physical Society

bridging position between neighboring underlying silicon dimers [178]. Additionally, the most stable structure of the (3×2) reconstructed surface with a 1/3 monolayer excess of silicon is an alternate dimer-row structure. In another study, the single-domain 3C-SiC(100)-$c(2 \times 2)$ surface structure is investigated utilizing the polarization dependence of two C-1s and Si-2p absorption as revealed by near edge X-ray absorption fine structure combined with molecular orbital cluster calculation [179]. The surface is terminated with staggered rows of unusual, nearly triply bonded C dimers bridging underlying Si dimers. The electronic structure of the C dimers is determined by resonant valence-band photoemission accompanying C-1s exciton auto-ionization. The ab initio molecular dynamics simulation indicates that under different preparation conditions and thermal treatment, the C-terminated (001) surfaces of 3C-SiC can have different $c(2 \times 2)$ and $p(2 \times 1)$ reconstructions [180]. The atomic structure of the C-terminated 3C-SiC(100)-$c(2 \times 2)$ reconstructed surface is investigated by STM and surface-core-level-resolved photoelectron diffraction [181]. This surface is found to consist of anomalous bridge-bonded C dimers with a C–C bond length of 1.22 Å. The angle-resolved photoemission study identifies two occupied π state bands attributed to the normal and parallel p orbitals of the triple-bonded C dimmers, and this explains the stability of the triple-bonded surface reconstruction.

There are fewer reports on the 3C-SiC(111)-(3×3)-reconstructed surfaces, although this surface structure has been investigated by STM, conventional low-energy electron diffraction (LEED), LEED holography, and density functional theory [182]. STM reveals a single adatom per unit cell. LEED and density

functional theory results reveal a Si tetramer on a twisted Si adlayer with clover-like rings. This twist model with one dangling bond left per unit cell is a novel $(n \times n)$-reconstruction mechanism for group IV (111) surfaces.

Hexagonal SiC may also exhibit the (3×3) reconstruction. The drastic (3×3) reconstructions of 3C-SiC(111), 4H-SiC(0001), and 6H-SiC(0001) surfaces are identified by quantitative LEED and holographic interpretation of diffraction intensities, STM, and Auger electron spectroscopy [183]. This observed (3×3) reconstruction is a new type of semiconductor $(n \times n)$ surface reconstruction, showing the feature of considerable reduction of surface dangling-bonds. A modified version of the (3×3) reconstruction, that is, the 6H-SiC(0001)-(3×3)-Si reconstruction, is observed by STM [184]. The surface has a hexagonal structure with one Si adatom per unit cell. A reconstruction model in which the unit cell comprises 11 Si atoms is proposed. There are three dimers and three rest atoms in the first layer and one adatom in the second layer. In the first layer, the dimers and other atoms form six- and nine-atom rings that surround unoccupied sites of the outermost silicon atoms of the substrate. For the three dangling bonds in a unit cell, one belongs to the adatom and the other two belong to the silicon atoms of the substrate. STM conducted on the 6H-SiC Si-terminated (0001) and C-terminated $(000\bar{1})$ surfaces [185] shows that the (3×3) reconstruction arises after annealing at 850 °C followed by transformation to the $(\sqrt{3} \times \sqrt{3})$ reconstruction after further annealing at 950 °C. The (3×3) surface has a 4/9 monolayer of adatoms, and the $(\sqrt{3} \times \sqrt{3})$ surface has a 1/3 monolayer of adatoms. A new (9×9) reconstruction on the (0001) surface is observed after further annealing the (3×3) surface at 900 °C under a silicon flux. A graphitized surface with a (6×6) reconstruction is observed from the (0001) surface when the temperature is suddenly raised to 1,150 °C without a silicon flux.

Oxidation and HF etching of the 6H-SiC (0001) surface can produce an atomically flat surface on a 100-nm scale with bulk-like periodicity and stoichiometry [186]. The surface dangling-bonds are terminated by hydroxyl groups. Thermal treatment can remove the remaining oxygen from the surface and yield the carbon$\sqrt{3} \times \sqrt{3}$ $R30°$ reconstructed surface where carbon–carbon bonds are present on the surface. The $\sqrt{3} \times \sqrt{3}$ reconstruction of the Si-terminated 6H-SiC(0001) surface is investigated by STM [187]. The STM images are consistent with a structural model composed of 1/3 layer of Si or C adatoms in threefold symmetry sites on top of the outermost Si–C bilayer. Several types of defects are observed from the $\sqrt{3} \times \sqrt{3}$ surfaces. The first-principle total energy calculation determines the chemical identity and adsorption site of the adatoms on the SiC(0001) $\sqrt{3} \times \sqrt{3}$ surface [188]. Over the entire range of thermodynamically allowed chemical potentials, Si adatoms are preferred over C adatoms. The adatoms prefer the T_4 site over the H_3 site for both Si and C. The calculation shows that in the Si-T_4 model, there is a half-filled adatom dangling-bond band at 1.2 eV above the valence-band maximum with a bandwidth of 0.35 eV. The SiC(0001) $\sqrt{3} \times \sqrt{3}$ surface is studied by angle-resolved photoemission spectroscopy [189].

The 6H and 4H polytypes show similar results. A surface state band with semiconducting occupation at around 1.0 eV above the valence-band maximum with a width of about 0.2 eV is observed. The 6H-SiC(0001) $\sqrt{3} \times \sqrt{3}$ $R30°$ and $6\sqrt{3} \times 6\sqrt{3}$ $R30°$ reconstructed surfaces are studied by photoemission spectroscopy [190]. The reconstructed surfaces are fabricated by heating the unreconstructed 1×1 surface to 950 and 1,150 °C, respectively. These surfaces show no oxygen-related signals. The spectral features for the $\sqrt{3}$ reconstruction cannot be explained by a structural model composed of Si or C adatoms on top of a Si–C bilayer. The $6\sqrt{3}$ reconstructed surface contains a larger amount of carbon atoms. The carbon is not graphitic, and graphitization is observed only after the surface is heated to a high temperature. The relaxed and $\sqrt{3} \times \sqrt{3}$ $R30°$ reconstructed 6H-SiC(0001) surfaces are investigated by ab initio calculation in the framework of the density functional theory with the local density approximation [191]. Both the Si- and C-terminated reconstructed surfaces are examined. Eight structural models are optimized for the reconstructed surfaces with Si or C adatoms and Si or C trimers adsorbed in threefold-symmetric T_4 or H_3 positions. For the Si-terminated surface, the optimal surface structure involves Si adatoms in T_4 sites and it is consistent with experimental results. For the C-terminated surface, none of the investigated $\sqrt{3} \times \sqrt{3}$ adatom or trimer configurations is the optimal configuration. STM conducted on the 6H-SiC(0001) $\sqrt{3} \times \sqrt{3}$ surfaces of both *n*- and *p*-type materials with low tunnel currents reveals distinct bands of empty and filled states [192]. The density of states with semiconductor features contains a state about 1 eV above the Fermi level and another state 1 eV below the Fermi level. STM images of the surface taken at positive and negative polarities indicate that these two states are localized in the same spatial position, thus supporting a silicon adatom model that predicts a Mott-Hubbard-type density of states.

2.7.2 SiC–SiO_2 Interface

Silicon carbide has a native oxide on the surface, and this is a big advantage for application in electronic devices. However, in practice, there may be many active defects at the interface between the SiC wafer and surface silicon dioxide layer. The defects significantly degrade the performance of SiC-based electronic devices and much work has been done to investigate SiC/SiO_2 interfaces both experimentally and theoretically. Several types of defects are supposed to be responsible for the degradation of the SiC-based devices, including carbon clusters, silicon suboxides, and Si–C–O clusters. Researchers have also thought of some efficient approaches to mitigate these unfavorable defects.

In hexagonal SiC, the Si-terminated surface has a slower oxidation rate compared to the C-terminated surface and this difference is caused by an unknown interface compound. The angle-resolved XPS study of the oxidized Si-(0001) and

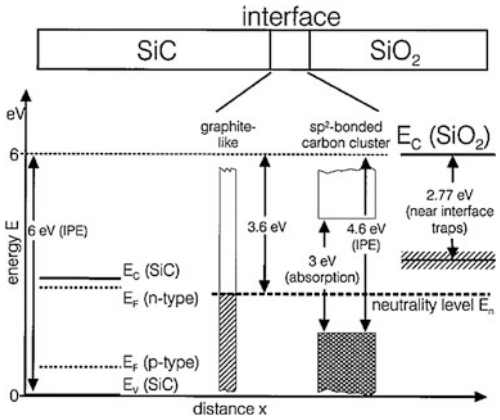

Fig. 2.98 Schematic of the carbon cluster model of the interface states in the SiC/SiO_2 metal-oxide-semiconductor structures. The dominant interface states are the sp^2-bonded carbon clusters with wide energy gaps (3 eV) and graphite-like carbon clusters. The near-interface oxide traps are located at 2.77 eV below the conduction-band minimum of SiO_2. Reprinted with permission from [195]. Copyright 1997, Wiley-VCH Verlag GmbH & Co. KGaA

C-$(000\bar{1})$ surfaces of 6H-SiC reveals the interfacial oxide $Si_4C_{4-x}O_2$ ($x < 2$) [193]. The slow oxidizing Si-(0001) surface has this oxide with a large thickness (1 nm), whereas the C-$(000\bar{1})$ surface has smaller one and it diminishes quickly upon oxidation above 1,000 K. The electronic structure of the SiC/SiO_2 interfaces for different SiC polytypes (3C, 4H, 6H, 15R) is investigated by internal photoemission of electrons [194]. The SiC valence-band maximum is located at 6 eV below the oxide conduction-band edge for all polytypes. The interface states are found in the energy range up to 1.5 eV above the top of the SiC valence band. The electron spectrum is similar to that of sp^2-bonded carbon clusters, demonstrating the existence of elemental carbon at the SiC/SiO_2 interface. Using electrical analysis and internal photoemission spectroscopy, the energy distribution of the electron states at the SiC/SiO_2 interfaces produced by oxidation of various SiC polytypes (3C, 4H, 6H) is determined [195]. Different polytypes show similar distributions of interface traps over the SiC bandgap indicative of a common nature of the interfacial defects. The major defects are proposed to be the carbon clusters at the SiC/SiO_2 interface and near-interfacial defects in SiO_2 (Fig. 2.98). In contrast, no signals from the dopant-related defects and dangling bonds at the SiC surface are observed. A large density of interface states at around 0.1 eV below the conduction band of 4H-SiC at the SiC/SiO_2 interface is revealed in low-temperature electrical measurements and photon-stimulated electron tunneling experiments [196]. These states are ascribed to the defects in the near-interfacial oxide layer, and they can significantly trap the electrons from the SiC. These states may cause degradation of the electron mobility observed from the surface channel of the 4H-SiC/SiO_2 electronic devices.

Electron energy loss spectroscopy (EELS) conducted on the thermally grown SiO_2/6H-SiC (0001) interfaces reveals high carbon concentrations at distinct

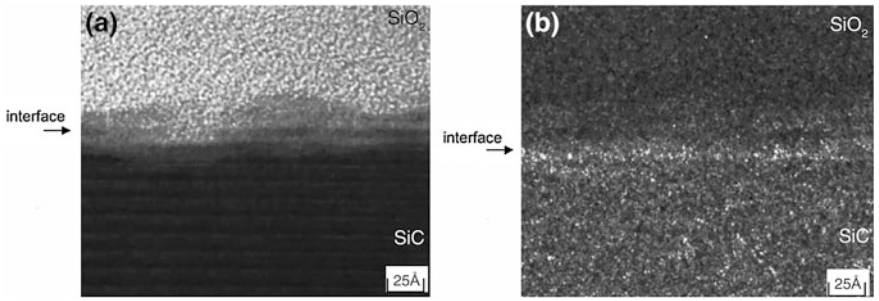

Fig. 2.99 **a** HRTEM image and **b** corresponding electron energy loss spectroscopy map of C at a thermally grown SiO_2/6H-SiC (0001) interface. Reprinted with permission from [197]. Copyright 2000, AIP Publishing LLC

interface regions [197]. These C-rich regions have a thickness of about 1.0–1.5 nm (Fig. 2.99). The oxides are grown on clean *n*-type 6H-SiC at 1,100 °C in a wet oxygen ambient. EELS shows that the CVD-deposited SiO_2/SiC interfaces have no C-rich regions. The interface state density in the metal-oxide-SiC diodes with thermally grown SiO_2 is about 9×10^{11} cm^{-2} eV^{-1} at $E - E_v = 2.0$ eV. This is consistent with the experimental value for the SiC metal-oxide-semiconductor (MOS) diodes without post-oxidation annealing. These C-rich regions may contribute to the low channel mobility in the SiC-based metal-oxide-semiconductor field-effect transistors (MOSFETs). Density functional calculation is employed to study the possible defect structures arising from the interaction between O_2 molecules and an ideal portion of the SiC/SiO_2 interface [198]. The defect structures produced along the calculated oxidation routes remain at the interface in a significant concentration as oxidation ceases. The carbon–carbon bonds can explain most of the observed interfacial states but not the large density near the conduction band of 4H-SiC. These electron traps with very high density near the conduction band of 4H-SiC in the metal-silicon dioxide-SiC structures are called near-interface traps (NIT). By means of capacitance–voltage and thermal dielectric relaxation current analysis, the near-interfacial traps close to the 4H-SiC conduction-band edge in the 4H-SiC-based MOS structures with either thermal or deposited oxide are investigated [199]. The signals corresponding to two groups of trap levels are detected, and the total trapped charge exceeds 1×10^{13} cm^{-2}. The observed density and energy distribution of these traps are nearly identical in all thermal and deposited oxides, suggesting that they are intrinsic defects at the SiO_2/SiC interface. The high-resolution electron microscopy combined with electron energy loss spectroscopy show no sign of graphitic region at the SiO_2/SiC interface or in the bulk SiO_2 at a detection limit of 0.7 nm in samples after re-oxidation. No amorphous carbon is observed near the SiO_2/SiC interface, suggesting that the near-interface traps close to the 4H-SiC conduction band are not related to the carbon structures at the interface. Sometimes, the near-interface traps are assumed to originate from oxides near the interface. The positions of the intrinsic and carbon defects in SiO_2 are investigated by density functional calculation [200].

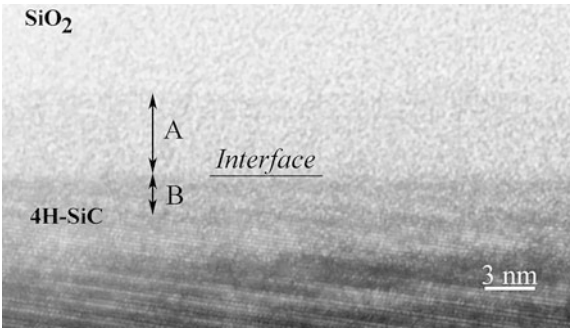

Fig. 2.100 HRTEM image of the SiO_2/4H-SiC interface showing the transition layers *A* (4.8 nm) and *B* (3.3 nm) on either side of the interface. Reprinted with permission from [201]. Copyright 2008, AIP Publishing LLC

The vacancies and oxygen interstitials can be excluded as the origin of the near-interface traps, whereas silicon interstitials and carbon dimers generate gap levels in the energy range inferred from experiments. Using TEM and EELS, the structure and chemistry of the interface of the thermally grown SiO_2/4H-SiC heterostructure are analyzed [201]. Distinct layers several nanometers thick on each side of the interface as well as partial amorphization of the SiC surface are observed (Fig. 2.100). These interfacial layers are ascribed to the formation of a ternary Si–C–O phase during thermal oxidation.

Some efficient methods have been exploited to diminish the surface defects at the SiC/SiO_2 interface so as to improve the performance of the SiC-based MOS devices. Pre-oxidation cleaning of SiC (3C, 4H, 6H polytypes) surfaces by exposing to ultraviolet radiation and oxygen is found to result in significant improvement in the electronic properties of SiC/SiO_2 interfaces [202]. This treatment removes the defect species that are otherwise present at the interface after thermal oxidation of SiC. Carbon clusters are suggested as the diminished defect species responsible for a substantial part of the SiC/SiO_2 interface states. Nitridation is another efficient way to mitigate the defects at the SiC/SiO_2 interface. Analysis of fast and slow traps at the interface of 4H-SiC with oxide grown in O_2, N_2O, and NO indicates that the major positive effect of nitridation is the dramatic reduction of the slow electron trap density [203]. These traps may be the defects in the near-interfacial oxides. This study confirms that nitridation also reduces the fast interface states associated with clustered carbon. Although nitridation has a positive effect in improving the SiC/SiO_2 interface quality, this effect can be saturated. Nitridation with NO significantly reduces the interfacial trap density near the conduction band, but this effect is saturated at 2.5×10^{14} cm^{-2} of nitrogen leaving a trap density that is still higher than that in silicon [204]. Nitrogen passivation results in dissolution of the defects leading to lowered trap energy in the bandgap. This behavior is consistent with a model in which the energy of the trap of carbon clusters or silicon suboxide depends on the defect size. The nitrogen and hydrogen effects on the SiC–SiO_2 interfaces have

been investigated both experimentally and theoretically [205]. The system studied is the Si-terminated SiC faces in metal-oxide-semiconductor structures. H_2 shows no effect on the density of electrically active interface defects, but in contrast, nitridation followed by hydrogenation yields complementary passivation and substantial reduction in the interface defects. First-principle calculation indicates that isolated C dangling bonds can be passivated by H_2, whereas correlated C dangling bonds on neighboring threefold-coordinated C atoms can only be passivated by monatomic H. Different from previous viewpoints regarding the carbon clusters as the SiC–SiO_2 interface defects, carbon is proposed to exist as a bonded Si–C–O interlayer (one to two atomic layers) and the correlated C dangling bonds are supposed to be the major origin of the observed interface defects. The effect of nitridation is proposed to convert the Si–C–O bond into a Si–C–O–N bond along with reduction in threefold C atoms (N replaces threefold C). The hydrogen atoms result in the conversion of Si–C–O–N to Si–C–O–N–H, thus reducing the interfacial states. The residual interface states are ascribed to the Si–Si defects at the interface. Detailed calculation performed on the 4H-SiC/SiO_2 interface by density functional theory [206] reveals that the hole traps near the valence-band edge stem from carbon–carbon bonds, whereas the amphoteric states deep in the bandgap arise from the dangling bonds. The chemical disorder contributes interfacial states with energies close to both band edges. However, the observed electron traps with a large density near the conduction band are proposed to be defects in the oxide near the interface. Silicon interstitials are found to yield a broad distribution of electron traps slightly farther from the conduction-band edge, whereas the carbon dimers substituting for two nearby oxygen atoms in the silica network may give rise to the sharp peak of electron traps with critically high density at about 0.1 eV below the conduction-band edge of 4H-SiC. The analysis also shows that NO or N atoms attack the carbon dimers at the interface, thereby eliminating carbon.

The transconductance of 4H-SiC MOSFETs is typically much lower compared to the 6H-SiC-based devices. Using a modified capacitance–voltage technique, the large area 4H-SiC MOSFETs are studied and the relationship between the SiC/SiO_2 interface trap density and energy in the bandgap is investigated [207]. The interfacial trap density increases toward the conduction-band edge in both polytypes and it is much higher in 4H-SiC compared to 6H-SiC for devices fabricated in the same lot. As a result, the 4H-SiC-based devices will trap more inversion electrons, thus resulting in the lower transconductance with respect to the 6H-SiC-based devices.

There is a question on whether the SiC/SiO_2 interface can be prepared without many interface defects. The highly ordered monolayers of silicon dioxide have been prepared on the hexagonal (0001) 4H and 6H silicon carbide surfaces by hydrogen plasma or etching in hydrogen [208]. Low-energy electron diffraction and Auger electron spectroscopy reveal that the bond angles and distances of the surfaces are in agreement with those of bulk SiO_2. The semiconductor surface is passivated as a result of saturation of all the dangling bonds and it preserves the perfect order also in air. These ideal oxide monolayers may act as a seed for fabricating epitaxial oxides with a small defect density.

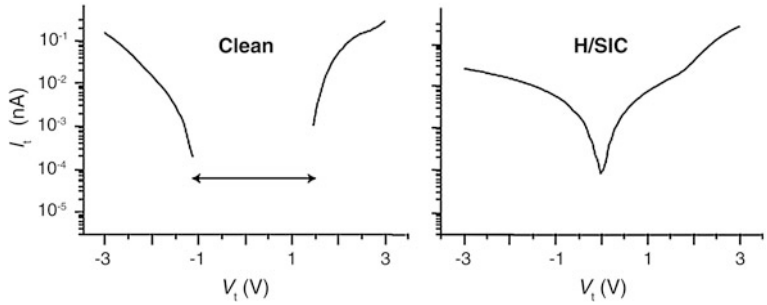

Fig. 2.101 Electronic structure of the clean and H-exposed β-SiC(100) 3 × 2 surface obtained by surface tunneling spectroscopy. The spectra show gap closing of the H-treated β-SiC(100) 3 × 2 surface. Reprinted with permission from [211]. Copyright 2003, Macmillan Publishers Ltd

2.7.3 Other Types of Surface Treatment

Surface functionalization of silicon carbide with species other than oxygen has been pursued. Atomically flat surfaces are fabricated by hydrogen etching of 6H- and 4H-SiC (0001) surfaces at 1,600–1,700 °C [209]. Etching eliminates scratches on the polished substrates and atomic force microscopy images disclose periodic arrays of atomically flat terraces that are a few hundred nanometers wide. The terraces are separated by 1.5-nm-tall steps in the $\langle 1100 \rangle$ directions. Hydrogenated 6H-SiC (0001) and $(000\bar{1})$ surfaces are also obtained by high-temperature hydrogen treatment [210]. The samples exhibit unreconstructed surfaces with a high crystallographic order as revealed by low-energy electron diffraction. Sharp Si–H stretching modes are observed from the SiC (0001) surfaces. The *n*- and *p*-type samples show no surface band bending, indicating that the surfaces are electronically passivated, and densities of charged surface states in the gap are below 7×10^{10} cm^{-2} for *p*-type and 1.7×10^{12} cm^{-2} for *n*-type samples. No surface oxide is detected by X-ray photoelectron spectroscopy after the samples are kept in air for two days. Atomic hydrogen can induce surface metallization on the SiC surface [211]. This is realized on the surface of the single-domain β-SiC(100) thin film prepared on a silicon substrate (Fig. 2.101). Photoelectron and photoabsorption spectroscopies and scanning tunneling techniques show that metallization takes place in the subsurface region of the 3 × 2 reconstruction. Metallization is proposed to arise from the competition between hydrogen termination of surface-dangling bonds and hydrogen-generated steric hindrance below the surface.

Ab initio molecular dynamic simulation shows that water molecules interact differently with Si- and C-terminated 3C-SiC(001) surfaces [212]. The water coverage is selected to be 1/4 to 1 monolayer and water molecules tend to dissociate on the Si-terminated surface leading to the formation of Si–H and Si–OH bonds on the surface. In contrast, the C-terminated surface that does not react with water molecules is hydrophobic.

Organic molecules can be attached to the silicon carbide surface and this type of passivation is often necessary for biological applications of silicon carbide. The alkyl monolayers can be covalently bound to the 3C-SiC surface via a thermal reaction with 1-alkene [213]. The SiC wafer is first treated in a diluted HF solution to remove the native SiO_2 layer and provide a reactive hydroxyl surface. Attachment of ω-functionalized 1-alkene produces a well-defined surface that is covalently bound by the alkyl monolayer. The attached monolayers are covalently attached and the resulting surface is stable under both acidic and alkaline conditions. The alkyl monolayers can also be formed on 3C-SiC by UV irradiation in the presence of alkenes at room temperature [214]. Methyl undec-10-enoate and 2,2,2-trifluoroethyl undec-10-enoate can be bonded to the SiC surfaces, and the ester-terminated surfaces allow for further attachment of amine compounds. Using the density functional simulation, molecular sensitization of the nonpolar SiC(110) surface is studied [215]. Aromatic fragments up to a full porphyrin molecule are considered and the result shows that there is a relatively low affinity between aromatic rings and SiC surface. The only exception is the pyrrole ring that produces an exothermic reaction leading to the stable hybrid interfaces. Functionalization of *n*-type (100) and (111) 3C-SiC surfaces with organosilanes has been reported [216]. The wet chemical technique produces self-assembled monolayers of amino-propyldiethoxymethylsilane and octadecyltrimethoxysilane on the 3C-SiC surfaces. The reaction on the hydroxylated surfaces with organosilanesthe diminishes the surface band bending, suggesting that functionalization results in partial passivation of electrically active surface states.

2.8 Polytypic Transformation

Silicon carbide has many polytypes having different stacking sequences of Si–C double-atomic layers. This property renders silicon carbide a very special semiconductor but what is so special about the material that so many crystal structures exist in nature? Much work has been done with the intention to clarify this mystery. The study also reveals that one polytype of silicon carbide can transform into another polytype under appropriate conditions such as under pressure and there have been many investigations concerning the phase transformation between different polytypes of silicon carbide.

In general, theoretical calculation is utilized to explore the origin of polytypism and structural and electronic differences among different polytypes of silicon carbide. Cheng, Needs, and Heine have presented a model to account for the origin of polytypism in silicon carbide [217]. Ab initio quantum mechanical calculation of the total energies of five simple SiC polytypes with norm-conserving pseudopotentials shows that the system is extremely close to a multiphase degeneracy between all the considered structures. Two mechanisms can split the infinite multiphase degeneracy and give an infinite number of regular SiC structures. The first is a result of the presence of phonons. The second depends on two aspects, an

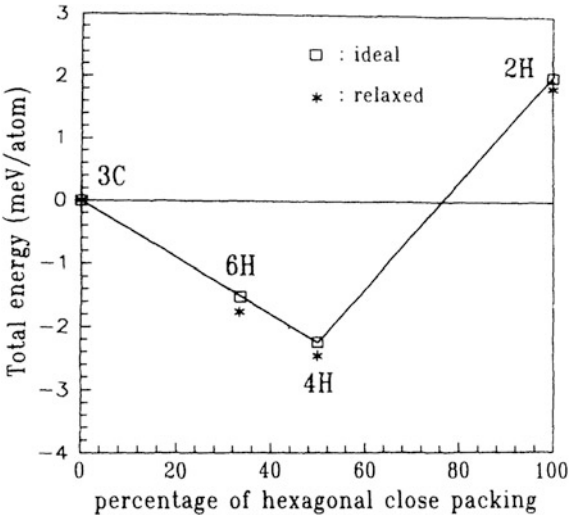

Fig. 2.102 Calculated crystal total energies of the SiC polytypes with respect to that of the 3C structure as a function of the hexagonal close packing percentage. Reprinted with permission from [28]. Copyright 1994, American Physical Society

electronically mediated interaction between planes that need not be long ranged but depends on their separation, thus giving forces on the layers, and the longitudinal relaxation of the interlayer spacings in response to the above forces. There is a paradox regarding the growth of SiC polytypes from the vapor or the melt [218]. Since cubic silicon carbide is not the structure with the lowest energy as shown by calculation, it is perplexing why the cubic structure is preferred. This is explained by calculations as due to the constrained equilibrium when adding one atomic double layer at a time to the growing crystal in the hexagonal direction without allowing rearrangement of the lower layers. The different roles of donor and acceptor impurities have been discussed. The electronic structure calculation indicates that the valence-band offset between different polytypes is small, and therefore, there should be large offsets between the conduction bands due to the different bandgap values. As a result, the acceptors do not favor any particular polytype and donors favor the cubic form since it has the smallest bandgap.

The structural and electronic properties of various polytypes (3C, 2H, 4H, 6H) of SiC have been determined by ab initio pseudopotential calculation [28]. All the polytypes show similar equilibrium lattice constants and bulk moduli. The calculated total energies of the polytypes are very close and the difference is within 4.3 meV/atom (Fig. 2.102). The small difference may account for the polytypism of silicon carbide. 2H-SiC is found to be the most unstable, whereas 4H-SiC has the lowest energy due to the attractive interactions between the alternating cubic and hexagonal stacking layers. The asymmetric charge distribution for a Si–C bond is found to be on the boundary separating the zinc-blende and wurtzite phases and suggested to be related to the polytypism of silicon carbide. The ground-state properties of cubic and hexagonal SiC polytypes are investigated by the softened ab initio pseudopotentials and a total energy minimization procedure [219]. Atomic relaxation within the hexagonal unit cells plays an important role in

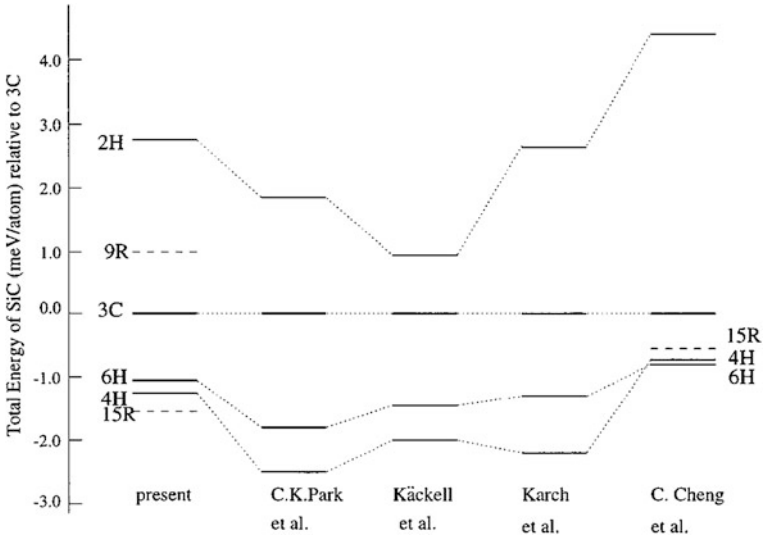

Fig. 2.103 Total energy differences among the various polytypes of SiC calculated by different groups. Reprinted with permission from [220]. Copyright 1998, American Physical Society

yielding the correct structural properties. Calculations using unrelaxed and relaxed geometries give rise to distinct orders of cohesive energies versus percentage of hexagonality in SiC structures. Calculation based on the relaxed structures yields similar results to those in Ref. [28]. The largest difference between the cohesive energies is 3 meV/atom, and the differences in the cohesive energies of different SiC polytypes are smaller than the thermal energies under reasonable crystal growth conditions. Therefore, nonequilibrium effects related to the details of the growth and effects of the vibrating lattice are proposed to be the major forces, driving polytypism during growth of SiC crystals. The zero-temperature total energy differences between more polytypes of SiC (3C, 6H, 4H, 2H, 15R, and 9R) are determined by well-converged all-electron density functional calculation [220]. The order of total energies for different polytypes is consistent with previous calculated results, and the results obtained by different groups are summarized in Fig. 2.103, and these different groups of data show qualitative agreement. The total energies of a variety of silicon carbide polytypes are calculated using the nonorthogonal tight-binding method [221]. The energies of the polytypes computed with up to 62 atoms per unit cell show that the hexagonal wurtzite structure has the highest energy and the 4H structure has the smallest energy while the cubic zinc-blende structure has intermediate energy.

Since the total energy varies only slightly among different polytypes of silicon carbide, as indicated by the aforementioned theoretical calculations, the polytypic transformation between different polytypes takes place relatively readily under various conditions. Synthesis of silicon carbide from silica and carbon as well as silicon and carbon under different conditions is investigated [222]. The primary

synthesized SiC is always β-SiC that can be formed at as low as 525 °C when carbon and silicon are contained in a low melting alloy of aluminum and zinc. β-SiC is stable up to 2,100 °C and starts to morph into α-SiC slowly and monotropically at 2,100 °C until completion at 2,400 °C. The 3C-SiC single crystals in an argon atmosphere transform into 6H-SiC at temperature above 2,150 °C [223]. Raman scattering is performed to determine the spatial distribution and depth profile of the phase-transformed 6H-SiC region in the annealed cubic samples. The phase transformation is explained by the displacement of the atomic double layers. Cubic silicon carbide crystals transform partially into the noncubic stacking sequence at 1,400 °C [224]. The 2H-SiC crystals undergo phase transformation at temperature as low as 400 °C, some form a structure with one-dimensional disorder along the crystal *c*-axis and others become the faulted cubic/6H structure. Dislocations significantly enhance this transformation that takes place through a slip process perpendicular to the *c*-axis. The β to α transformation in conventionally sintered, hot-pressed, and reaction-sintered polycrystalline SiC has been studied. Optical and transmission electron microscopies reveal that the transformation takes place via the rapid growth of composite grains comprising α-SiC plates sandwiched between recrystallized β-SiC envelopes [225]. Growth of these composite grains into the fine-grained β matrix occurs more quickly than thickening of the α plates into the β envelopes. The composite plates are formed by the extreme anisotropy of the interfacial energy between the two polytypes of SiC. That is, the $(111)_\beta \| (0001)_\alpha$ interfaces have energies several orders of magnitude smaller than the random β/α interfaces [226]. The interface between the β and α regions of partially transformed grains always contains thin α lamellae adjacent and parallel to coherent β twins or at stacking faults [227]. These planar defects are nucleation sites for the transformation and growth of the α phase results from the motion of partial dislocations nucleated at the intersection of coherent and incoherent twin boundaries. However, the initial stages of the β to α transformation have a different mechanism, dominated by elimination of high-energy β/α interfaces [228]. The phase transformation from β to α SiC in sintered SiC shows a dependence on the initial β ratio and sintering atmosphere [229]. The transformation rate decreases with increasing initial β ratio in the starting powder and in the presence of nitrogen. No transformation occurs for the initial pure β-SiC powders with 10.34 wt% Y_2O_3 and 2.95 wt% AlN as additives. The materials without phase transformation have a homogeneous microstructure with equiaxed grains. In contrast, the SiC powders with a large initial α/β ratio experience phase transformation containing elongated grains.

The α-to-β transformation in silicon carbide has been observed, although the latter may have a little higher total energy. On account of Si enrichment on the 6H-SiC (0001) surfaces during the formation of the $\sqrt{3} \times \sqrt{3}\ R30°$ reconstructed phase, a cubic stacking sequence appears at the surface [230]. LEED crystallography shows that the ultimate reconstructed surface consists of Si adatoms in T_4 sites and STM discloses mesa-like structures with various atomic periodicities before the formation of the $\sqrt{3} \times \sqrt{3}\ R30°$ phase. This Si-enriched state provides

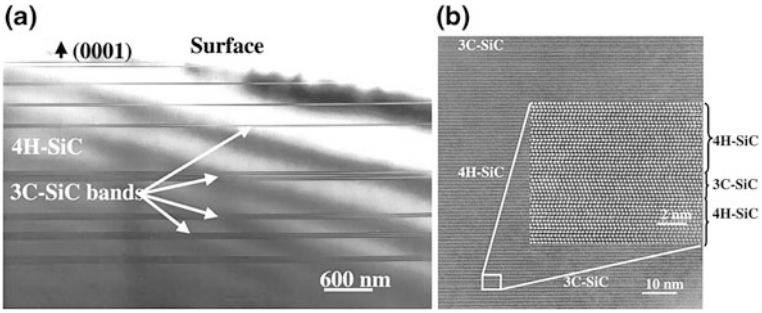

Fig. 2.104 **a** Cross-sectional TEM image of the oxidized 4H-SiC epilayer. The 3C-SiC bands are parallel to the 8°-tilted basal plane. **b** HRTEM image of 4H-SiC and 3C-SiC within a band showing two 3C-SiC sub-bands spaced by 4H-SiC. Higher magnification image in the *inset* indicates that this 3C-SiC sub-band is composed of seven Si–C bilayers. Reprinted with permission from [231]. Copyright 2001, AIP Publishing LLC

atoms for the formation of the modified stacking sequence. Dry thermal oxidation of a highly doped (1.7×10^{19} cm^{-3}) *n*-type 4H-SiC epilayer induces the formation of single and multiple stacking faults, which sometimes give rise to 3C-SiC bands [231]. The single stacking faults and bands of 3C-SiC in a 4H-SiC matrix in the oxidized 4H-SiC epilayer are observed by transmission electron microscopy (Fig. 2.104). These bands are parallel to the 4H-SiC(0001) basal plane but the unoxidized control sample does not show the bands. The cathodoluminescence spectrum (at 300 K) obtained from the oxidized materials shows a new peak at 2.5 eV in addition to the 3.22 eV one belonging to 4H-SiC. This 2.5 eV peak is absent from the sample without oxidation indicating its origin of stacking faults. The motion of Shockley partial dislocations on the parallel (0001) slip planes is supposed to be responsible for the polytypic transformation. The appearance and displacement of the partials are suggested to be caused by stresses induced by the heavy doping in the epilayer or nucleation from defects. However, a study of the 4H-SiC *p-i-n* diodes by emission microscopy and TEM indicates that the properties of the partial dislocations and stacking fault expansion are inconsistent with stress as the driving force [102]. The thermodynamic free-energy difference between the perfect and faulted structures is suggested to be the driving force in the diodes, implying that the hexagonal polytypes of SiC are metastable at room temperature and would transform to a faulted structure when the activation energy of the partial dislocation slip is achieved. The electron–hole recombination during operation of the diodes may offer this activation energy. Calculation predicts that 4H is the most stable polytype at least among 3C, 2H, 4H, 6H, and 15R polytypes, but the energy differences among them are so small that 4H may also convert to other polytypes under certain conditions.

At high pressure, silicon carbide crystals may morph into the rock salt-type structure. The high-pressure properties of SiC are calculated by the ab initio pseudopotential method [232]. Figure 2.105 displays the calculated total energies of the zinc-blende, rock salt, and β-Sn structures of silicon carbide. The zinc-blende

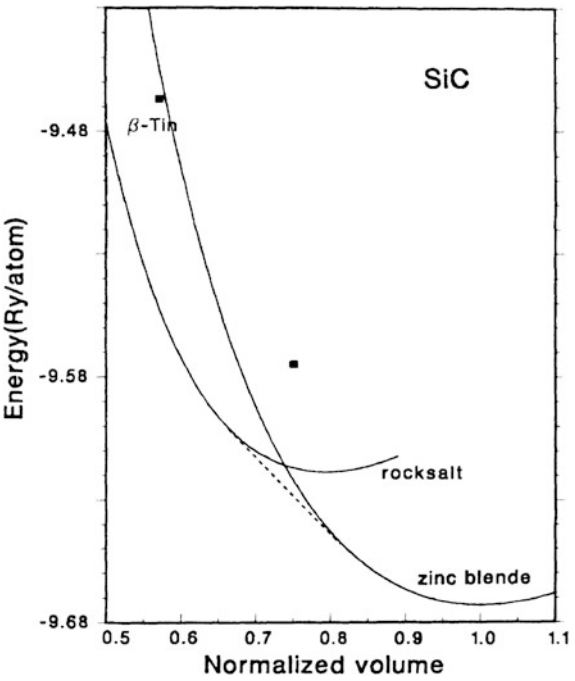

Fig. 2.105 Calculated crystal total energy as a function of volume normalized to the calculated equilibrium volume of 1.0369 nm^3 per atom of the zinc-blende phase of SiC. The dashed line denotes the common tangent of the two curves and solid squares are the energies of the β-Sn phase. Reprinted with permission from [232]. Copyright 1987, American Physical Society

structure is stable up to 660 kbar, above which it transforms into the rock salt phase. The rock salt structure of SiC is more stable than the β-Sn structure. Other possible phases like the B-8 structure are not calculated, and therefore, the calculated threshold transition pressure represents only an upper limit for the transition pressure from zinc-blende to another structure. The calculation also indicates that the indirect bandgap of cubic SiC decreases with increasing pressure. This tendency is similar to that of silicon but not diamond. X-ray diffraction is employed to study the 3C and 6H polytypes of SiC at pressures up to 105 and 95 GPa, respectively [233]. 3C-SiC undergoes phase transition into the rock salt phase at above 100 GPa together with a volume reduction of 20.3 %, whereas 6H-SiC remains stable up to the highest applied pressure but exhibits a premonition of phase transition above 90 GPa. The ab initio density functional theory is also applicable to the determination of the ultrahigh pressure dependence of materials. The pressure-dependent properties of cubic and hexagonal polytypes of SiC are calculated based on the density functional theory using the plane-wave pseudopotential approach [234]. NaCl, NiAs, CsCl, and β-Sn structures of SiC are considered as potential high-pressure phases and the calculation predicts a pressure-induced phase transition from zinc-blende to rock salt at a critical pressure of 0.67 Mbar. However, the calculated transition pressure is lower than the experimental value. The high-pressure transition to the NaCl structure is predicted for 3C-, 2H-, and 4H-SiC.

Isothermal-isobaric molecular dynamics simulation is performed to investigate the pressure-induced structural transformation in SiC [235]. The simulation

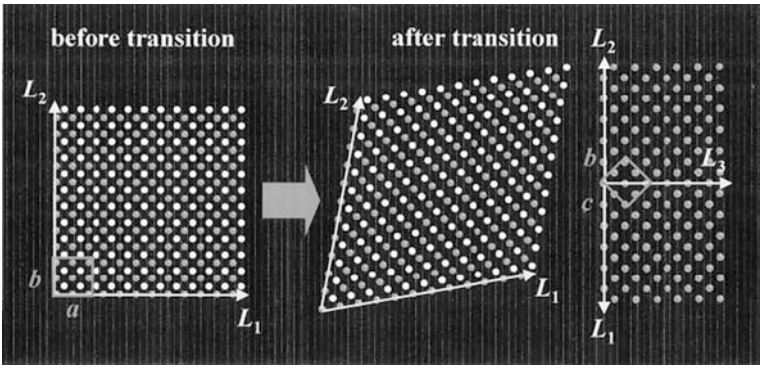

Fig. 2.106 Average atom positions in the molecular dynamics cell prior to and after the zinc-blende to rock salt transition in silicon carbide. The *gray* and *white* balls separately mark the positions of the silicon and carbon atoms. The *square box* shows the unit cell of each structure. Reprinted with permission from [235]. Copyright 2000, American Physical Society

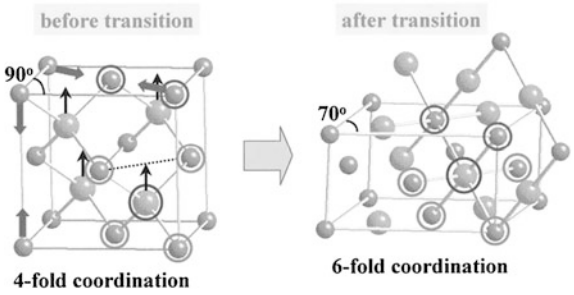

Fig. 2.107 Schematic of mechanism of the SiC phase transformation from the zinc-blende structure to rock salt structure. The *big* and *small* balls show separately the positions of the silicon and carbon atoms. The *arrows* mark the directions along which the atoms move during the phase transformation. Reprinted with permission from [235]. Copyright 2000, American Physical Society

reproduces the reversible transformation between the fourfold coordinated zinc-blende structure and sixfold coordinated rock salt structure. The molecular dynamics cell of the system changes from cubic to monoclinic after the onset of phase transformation from zinc-blende to rock salt (Fig. 2.106). During the cubic-to-monoclinic conversion, the silicon and carbon sublattices shift relatively to each other along the (100) direction in the zinc-blende structure (Fig. 2.107). This direction is the (110) direction in the resultant rock salt structure. The calculated volume changes at the transition and hysteresis agree well with the experimental values. A unified mechanism of high-pressure transformation of the various tetrahedrally bonded polytypes of SiC to the rock salt structure is proposed [236]. It involves several strains and intersublattice motions. Calculation of the energy barriers associated with these transition paths using first-principle pseudopotential method indicates that the 3C transition has a lower enthalpy barrier than the other

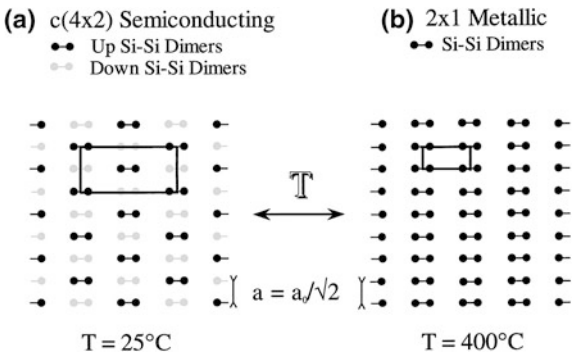

Fig. 2.108 Schematic of the reversible 3C-SiC(100) surface phase transition from a semiconducting $c(4 \times 2)$ reconstruction with alternatively up and down dimmers to a (2×1) metallic reconstruction with all dimers of the same height. The surface unit cells are marked. Reprinted with permission from [238]. Copyright 1997, American Physical Society

polytypes at pressure above the equilibrium transition pressure. Using the proposed effective interatomic interaction potential for SiC, molecular dynamics simulation gives rise to the structural energies in several SiC polytypes [237]. The cubic structure has the lowest energy, followed by the wurtzite and rock salt structures. The pressure for the 3C-to-rock salt transformation from the common tangent is derived to be 90 GPa.

By means of variable temperature scanning tunneling microscopy and angle-resolved photoemission spectroscopy, the transition between two β-SiC(100) surface structures has been observed [238]. There is a reversible temperature-dependent phase transition from a semiconducting $c(4 \times 2)$ surface at 25 °C to a metallic (2×1) structure at 400 °C (Fig. 2.108). This transition stems from the temperature-induced disruption of the $c(4 \times 2)$ structure composed of alternately up and down dimmers into the (2×1) structure with all dimers of the same height. This (2×1) structure gives rise to electronic orbital overlap between the top surface Si atoms leading to surface metallization.

References

1. Harris GL (ed) (1995) Properties of silicon carbide. INSPEC, London
2. Saddow SE, Agarwal A (eds) (2004) Advances in silicon carbide processing and applications. Artech House, Norwood
3. Shur M, Rumyantsev S, Levinshtein M (eds) (2006/2007) SiC materials and devices (vols 1 and 2). World Scientific, Singapore
4. Nicolussi GK, Davis AM, Pellin MJ, Lewis RS, Clayton RN, Amari S (1997) s-Process zirconium in presolar silicon carbide grains. Science 277:1281–1283
5. Huss GR, Lewis RS (1995) Presolar diamond, SiC, and graphite in primitive chondrites: abundances as a function of meteorite class and petrologic type. Geochim Cosmochim Acta 59:115–160

6. Huss GR, Meshik AP, Smith JB, Hohenberg CM (2003) Presolar diamond, silicon carbide, and graphite in carbonaceous chondrites: implications for thermal processing in the solar nebula. Geochim Cosmochim Acta 67:4823–4848
7. Nicolussi GK, Pellin MJ, Lewis RS, Davis AM, Clayton RN, Amari S (1998) Strontium isotopic composition in individual circumstellar silicon carbide grains: a record of *s*-process nucleosynthesis. Phys Rev Lett 81:3583–3586
8. Daulton TL, Bernatowicz TJ, Lewis RS, Messenger S, Stadermann FJ, Amari S (2002) Polytype distribution in circumstellar silicon carbide. Science 296:1852–1855
9. Gallino R, Raiteri CM, Busso M (1993) Carbon stars and isotopic Ba anomalies in meteoritic SiC grains. Astrophys J 410:400–411
10. Hoppe P, Amari S, Zinner E, Ireland T, Lewis RS (1994) Carbon, nitrogen, magnesium, silicon, and titanium isotopic compositions of single interstellar silicon carbide grains from the Murchison carbonaceous chondrite. Astrophys J 430:870–890
11. Amari S, Nittler LR, Zinner E, Lodders K, Lewis RS (2001) Presolar SiC grains of type A and B: their isotopic compositions and stellar origins. Astrophys J 559:463–483
12. Lugaro M, Davis AM, Gallino R, Pellin MJ, Straniero O, Käppeler F (2003) Isotopic compositions of strontium, zirconium, molybdenum, and barium in single presolar SiC grains and asymptotic giant branch stars. Astrophys J 593:486–508
13. Clément D, Mutschke H, Klein R, Henning Th (2003) New laboratory spectra of isolated β-SiC nanoparticles: comparison with spectra taken by the *Infrared Space Observatory*. Astrophys J 594:642–650
14. Speck AK, Barlow MJ, Skinner CJ (1997) The nature of the silicon carbide in carbon star outflows. Mon Not R Astron Soc 288:431–456
15. Amari S, Hoppe P, Zinner E, Lewis RS (1992) Interstellar SiC with unusual isotopic compositions: grains from a supernova. Astrophys J 394:L43–L46
16. Nittler LR, Amari S, Zinner E, Woosley SE, Lewis RS (1996) Extinct ^{44}Ti in presolar graphite and SiC: proof of a supernova origin. Astrophys J 462:L31–L34
17. Hoppe P, Strebel R, Eberhardt P, Amari S, Lewis RS (1996) Small SiC grains and a nitride grain of circumstellar origin from the Murchison meteorite: implications for stellar evolution and nucleosynthesis. Geochim Cosmochim Acta 60:883–907
18. Clayton DD, Arnett D, Kane J, Meyer BS (1997) Type X silicon carbide presolar grains: type Ia supernova condensates. Astrophys J 486:824–834
19. Junginger HG, van Haeringen W (1970) Energy band structures of four polytypes of silicon carbide calculated with the empirical pseudopotential method. Phys Stat Sol 37:709–719
20. Hemstreet LA Jr, Fong CY (1972) Electronic band structure and optical properties of 3C-SiC, BP, and BN. Phys Rev B 6:1464–1480
21. Choyke WJ, Hamilton DR, Patrick L (1964) Optical properties of cubic SiC: luminescence of nitrogen-exciton complexes, and interband absorption. Phys Rev 133:A1163–A1166
22. Backes WH, Bobbert PA, van Haeringen W (1994) Energy-band structure of SiC polytypes by interface matching of electronic wave functions. Phys Rev B 49:7564–7568
23. Lubinsky AR, Ellis DE, Painter GS (1975) Electronic structure and optical properties of 3C-SiC. Phys Rev B 11:1537–1546
24. Rohlfing M, Krüger P, Pollmann J (1993) Quasiparticle band-structure calculations for C, Si, Ge, GaAs, and SiC using Gaussian-orbital basis sets. Phys Rev B 48:17791–17805
25. Käckell P, Wenzien B, Bechstedt F (1994) Electronic properties of cubic and hexagonal SiC polytypes from *ab initio* calculations. Phys Rev B 50:10761–10768
26. Persson C, Lindefelt U (1996) Detailed band structure for 3C-, 2H-, 4H-, 6H-SiC, and Si around the fundamental band gap. Phys Rev B 54:10257–10260
27. Persson C, Lindefelt U (1997) Relativistic band structure calculation of cubic and hexagonal SiC polytypes. J Appl Phys 82:5496–5508
28. Park CH, Cheong B-H, Lee K-H, Chang KJ (1994) Structural and electronic properties of cubic, 2H, 4H, and 6H SiC. Phys Rev B 49:4485–4493
29. Wenzien B, Käckell P, Bechstedt F, Cappellini G (1995) Quasiparticle band structure of silicon carbide polytypes. Phys Rev B 52:10897–10905

30. Lambrecht WRL, Limpijumnong S, Rashkeev SN, Segall B (1997) Electronic band structure of SiC polytypes: a discussion of theory and experiment. Phys Stat Sol (b) 202:5–33
31. Dalibor T, Pensl G, Matsunami H, Kimoto T, Choyke WJ, Schöner A, Nordell N (1997) Deep defect centers in silicon carbide monitored with deep level transient spectroscopy. Phys Stat Sol (a) 162:199–225
32. Itoh H, Hayakawa N, Nashiyama I, Sakuma E (1989) Electron spin resonance in electron-irradiated 3C-SiC. J Appl Phys 66:4529–4531
33. Itoh H, Yoshikawa M, Nashiyama I, Okumura H, Misawa S, Yoshida S (1995) Photoluminescence of radiation induced defects in 3C-SiC epitaxially grown on Si. J Appl Phys 77:837–842
34. Wimbauer T, Meyer BK, Hofstaetter A, Scharmann A, Overhof H (1997) Negatively charged Si vacancy in 4H SiC: a comparison between theory and experiment. Phys Rev B 56:7384–7388
35. Sörman E, Son NT, Chen WM, Kordina O, Hallin C, Janzén E (2000) Silicon vacancy related defect in 4H and 6H SiC. Phys Rev B 61:2613–2620
36. Torpo L, Nieminen RM, Laasonen KE, Pöykkö S (1999) Silicon vacancy in SiC: a high-spin state defect. Appl Phys Lett 74:221–223
37. Fan J, Chu PK (2010) Group IV nanoparticles: synthesis, properties, and biological applications. Small 6:2080–2098
38. Kurtsiefer C, Mayer S, Zarda P, Weinfurter H (2000) Stable solid-state source of single photons. Phys Rev Lett 85:290–293
39. Mizuochi N, Makino T, Kato H, Takeuchi D, Ogura M, Okushi H, Nothaft M, Neumann P, Gali A, Jelezko F, Wrachtrup J, Yamasaki S (2012) Electrically driven single-photon source at room temperature in diamond. Nat Photonics 6:299–303
40. Baranov PG, Bundakova AP, Soltamova AA, Orlinskii SB, Borovykh IV, Zondervan R, Verberk R, Schmidt J (2011) Silicon vacancy in SiC as a promising quantum system for single-defect and single-photon spectroscopy. Phys Rev B 83:125203
41. Soltamov VA, Soltamova AA, Baranov PG, Proskuryakov II (2012) Room temperature coherent spin alignment of silicon vacancies in 4H- and 6H-SiC. Phys Rev Lett 108:226402
42. Son NT, Hai PN, Janzén E (2001) Carbon vacancy-related defect in 4H and 6H SiC. Phys Rev B 63:201201(R)
43. Danno K, Kimoto T (2006) Investigation of deep levels in n-type 4H-SiC epilayers irradiated with low-energy electrons. J Appl Phys 100:113728
44. Eberlein TAG, Jones R, Briddon PR (2003) Z_1/Z_2 defects in 4H-SiC. Phys Rev Lett 90:225502
45. Dannefaer S, Craigen D, Kerr D (1995) Carbon and silicon vacancies in electron-irradiated 6H-SiC. Phys Rev B 51:1928–1930
46. Aboelfotoh MO, Doyle JP (1999) Defect energy levels in electron-irradiated and deuterium-implanted 6H silicon carbide. Phys Rev B 59:10823–10829
47. Zywietz A, Furthmüller J, Bechstedt F (1999) Vacancies in SiC: influence of Jahn-Teller distortions, spin effects, and crystal structure. Phys Rev B 59:15166–15180
48. Choyke J, Patrick L (1971) Photoluminescence of radiation defects in cubic SiC: localized modes and Jahn-Teller effect. Phys Rev B 4:1843–1847
49. Patrick L, Choyke J (1972) Photoluminescence of radiation defects in ion-implanted 6H SiC. Phys Rev B 5:3253–3259
50. Haberstroh Ch, Helbig R, Stein RA (1994) Some new features of the photoluminescence of SiC(6H), SiC(4H), and SiC(15R). J Appl Phys 76:509–513
51. Hemmingsson CG, Son NT, Ellison A, Zhang J, Janzén E (1998) Negative-U centers in 4H silicon carbide. Phys Rev B 58:R10119–R10122
52. Son NT, Carlsson P, ul Hassan J, Janzén E, Umeda T, Isoya J, Gali A, Bockstedte M, Morishita N, Ohshima T, Itoh H (2006) Divacancy in 4H-SiC. Phys Rev Lett 96:055501
53. Torpo L, Staab TEM, Nieminen RM (2002) Divacancy in 3C- and 4H-SiC: an extremely stable defect. Phys Rev B 65:085202

54. Koehl WF, Buckley BB, Heremans FJ, Calusine G, Awschalom DD (2011) Room temperature coherent control of defect spin qubits in silicon carbide. Nature 479:84–88
55. Falk AL, Buckley BB, Calusine G, Koehl WF, Dobrovitski VV, Politi A, Zorman CA, Feng PX-L, Awschalom DD (2013) Polytype control of spin qubits in silicon carbide. Nat Commun 4:1819
56. Kawasuso A, Itoh H, Okada S, Okumura H (1996) Annealing processes of vacancy-type defects in electron-irradiated and as-grown 6H-SiC studied by positron lifetime spectroscopy. J Appl Phys 80:5639–5645
57. Hiyoshi T, Kimoto T (2009) Elimination of the major deep levels in n- and p-Type 4H-SiC by two-step thermal treatment. Appl Phys Exp 2:091101
58. Nagesh V, Farmer JW, Davis RF, Kong HS (1987) Defects in neutron irradiated SiC. Appl Phys Lett 50:1138–1140
59. Torpo L, Pöykkö S, Nieminen RM (1998) Antisites in silicon carbide. Phys Rev B 57:6243–6246
60. Egilsson T, Henry A, Ivanov IG, Lindström JL, Janzén E (1999) Photoluminescence of electron-irradiated 4H-SiC. Phys Rev B 59:8008–8014
61. Eberlein TAG, Fall CJ, Jones R, Briddon PR, Öberg S (2002) Alphabet luminescence lines in 4H-SiC. Phys Rev B 65:184108
62. Gali A, Deák P, Rauls E, Son NT, Ivanov IG, Carlsson FHC, Janzén E, Choyke WJ (2003) Correlation between the antisite pair and the D_{I} center in SiC. Phys Rev B 67:155203
63. Eberlein TAG, Jones R, Öberg S, Briddon PR (2006) Density functional theory calculation of the D_I optical center in SiC. Phys Rev B 74:144106
64. Patrick L, Choyke WJ (1973) Localized vibrational modes of a persistent defect in ion-implanted SiC. J Phys Chem Solids 34:565
65. Freitas JA, Bishop SG, Edmond JA, Ryu J, Davis RF (1987) Photoluminescence spectroscopy of ion-implanted 3C-SiC grown by chemical vapor deposition. J Appl Phys 61:2011–2016
66. Mattausch A, Bockstedte M, Pankratov O (2004) Carbon antisite clusters in SiC: a possible pathway to the D_{II} center. Phys Rev B 69:045322
67. Lingner Th, Greulich-Weber S, Spaeth J-M, Gerstmann U, Rauls E, Hajnal Z, Frauenheim Th, Overhof H (2001) Structure of the silicon vacancy in 6*H*-SiC after annealing identified as the carbon vacancy–carbon antisite pair. Phys Rev B 64:245212
68. Umeda T, Son NT, Isoya J, Janzén E, Ohshima T, Morishita N, Itoh H, Gali A, Bockstedte M (2006) Identification of the carbon antisite-vacancy pair in 4*H*-SiC. Phys Rev Lett 96:145501
69. Steeds JW (2009) Photoluminescence study of the carbon antisite-vacancy pair in 4H- and 6H-SiC. Phys Rev B 80:245202
70. Castelletto S, Johnson BC, Ivády V, Stavrias N, Umeda T, Gali A, Ohshima T (2014) A silicon carbide room-temperature single-photon source. Nat Mater 13:151–156
71. Wang C, Bernholc J, Davis RF (1988) Formation energies, abundances, and the electronic structure of native defects in cubic SiC. Phys Rev B 38:12752–12755
72. Torpo L, Marlo M, Staab TEM, Nieminen RM (2001) Comprehensive *ab initio* study of properties of monovacancies and antisites in 4H-SiC. J Phys: Condens Matter 13:6203–6231
73. Storasta L, Bergman JP, Janzén E, Henry A, Lu J (2004) Deep levels created by low energy electron irradiation in 4H-SiC. J Appl Phys 96:4909–4915
74. Devanathan R, Weber WJ, Gao F (2001) Atomic scale simulation of defect production in irradiated 3C-SiC. J Appl Phys 90:2303–2309
75. Gao F, Bylaska EJ, Weber WJ, Corrales LR (2001) Ab initio and empirical-potential studies of defect properties in 3C-SiC. Phys Rev B 64:245208
76. Gao F, Weber WJ, Posselt M, Belko V (2004) Atomistic study of intrinsic defect migration in 3C-SiC. Phys Rev B 69:245205
77. Bockstedte M, Mattausch A, Pankratov O (2003) *Ab initio* study of the migration of intrinsic defects in 3*C*-SiC. Phys Rev B 68:205201

78. Bockstedte M, Mattausch A, Pankratov O (2004) *Ab initio* study of the annealing of vacancies and interstitials in cubic SiC: vacancy-interstitial recombination and aggregation of carbon interstitials. Phys Rev B 69:235202
79. Gali A, Deák P, Ordejón P, Son NT, Janzén E, Choyke WJ (2003) Aggregation of carbon interstitials in silicon carbide: a theoretical study. Phys Rev B 68:125201
80. Rauls E, Frauenheim Th, Gali A, Deák P (2003) Theoretical study of vacancy diffusion and vacancy-assisted clustering of antisites in SiC. Phys Rev B 68:155208
81. Amelinckx S, Strumane G, Webb WW (1960) Dislocations in silicon carbide. J Appl Phys 31:1359–1370
82. Ha S, Mieszkowski P, Skowronski M, Rowland LB (2002) Dislocation conversion in 4H silicon carbide epitaxy. J Cryst Growth 244:257–266
83. Blumenau AT, Fall CJ, Jones R, Öberg S, Frauenheim T, Briddon PR (2003) Structure and motion of basal dislocations in silicon carbide. Phys Rev B 68:174108
84. Heindl J, Strunk HP, Heydemann VD, Pensl G (1997) Micropipes: hollow tubes in silicon carbide. Phys Stat Sol (a) 162:251–262
85. Neudeck PG, Powell JA (1994) Performance limiting micropipe defects in silicon carbide wafers. IEEE Electron Device Lett 15:63–65
86. Heindl J, Dorsch W, Strunk HP, Müller G, Eckstein R, Hofmann D, Winnacker A (1998) Dislocation content of micropipes in SiC. Phys Rev Lett 80:740–741
87. Pirouz P (1998) On micropipes and nanopipes in SiC and GaN. Philos Mag 78:727–736
88. Dudley M, Huang XR, Huang W, Powell A, Wang S, Neudeck P, Skowronski M (1999) The mechanism of micropipe nucleation at inclusions in silicon carbide. Appl Phys Lett 75:784–786
89. Huang XR, Dudley M, Vetter WM, Huang W, Wang S, Carter CH (1999) Direct evidence of micropipe-related pure superscrew dislocations in SiC. Appl Phys Lett 74:353–355
90. Stevens R (1972) Defects in silicon carbide. J Mater Sci 7:517–521
91. Koumoto K, Takeda S, Pai CH, Sato T, Yanagida H (1989) High-resolution electron microscopy observations of stacking faults in β-SiC. J Am Ceram Soc 72:1985–1987
92. Pujar VV, Cawley JD (1995) Effects of stacking faults on the X-ray diffraction profiles of β-SiC powders. J Am Ceram Soc 78:774–782
93. Hong MH, Samant AV, Pirouz P (2000) Stacking fault energy of 6H-SiC and 4H-SiC single crystals. Philos Mag 80:919–935
94. Liu JQ, Skowronski M, Hallin C, Söderholm R, Lendenmann H (2002) Structure of recombination-induced stacking faults in high-voltage SiC p-n junctions. Appl Phys Lett 80:749–751
95. Twigg ME, Stahlbush RE, Fatemi M, Arthur SD, Fedison JB, Tucker JB, Wang S (2003) Structure of stacking faults formed during the forward bias of 4*H*-SiC *p-i-n* diodes. Appl Phys Lett 82:2410–2412
96. Jacobson H, Bergman JP, Hallin C, Janzén E, Tuomi T, Lendenmann H (2004) Properties and origins of different stacking faults that cause degradation in SiC PiN diodes. J Appl Phys 95:1485–1488
97. Izumi S, Tsuchida H, Kamata I, Tawara T (2005) Structural analysis and reduction of in-grown stacking faults in 4H-SiC epilayers. Appl Phys Lett 86:202108
98. Fujiwara H, Kimoto T, Tojo T, Matsunami H (2005) Characterization of in-grown stacking faults in 4H-SiC (0001) epitaxial layers and its impacts on high-voltage Schottky barrier diodes. Appl Phys Lett 87:051912
99. Feng G, Suda J, Kimoto T (2008) Characterization of stacking faults in 4H-SiC epilayers by room-temperature microphotoluminescence mapping. Appl Phys Lett 92:221906
100. Liu JQ, Chung HJ, Kuhr T, Li Q, Skowronski M (2002) Structural instability of 4H–SiC polytype induced by n-type doping. Appl Phys Lett 80:2111–2113
101. Kuhr TA, Liu JQ, Chung HJ, Skowronski M, Szmulowicz F (2002) Spontaneous formation of stacking faults in highly doped 4H–SiC during annealing. J Appl Phys 92:5863–5871
102. Ha S, Skowronski M, Sumakeris JJ, Paisley MJ, Das MK (2004) Driving force of stacking-fault formation in SiC *p-i-n* diodes. Phys Rev Lett 92:175504

103. Galeckas A, Linnros J, Pirouz P (2006) Recombination-induced stacking faults: evidence for a general mechanism in hexagonal SiC. Phys Rev Lett 96:025502
104. Sridhara SG, Carlsson FHC, Bergman JP, Janzén E (2001) Luminescence from stacking faults in 4H SiC. Appl Phys Lett 79:3944–3946
105. Fissel A, Kaiser U, Schröter B, Richter W, Bechstedt F (2001) MBE growth and properties of SiC multi-quantum well structures. Appl Surf Sci 184:37–42
106. Bai S, Devaty RP, Choyke WJ, Kaiser U, Wagner G, MacMillan MF (2003) Determination of the electric field in 4H/3C/4H-SiC quantum wells due to spontaneous polarization in the 4H SiC matrix. Appl Phys Lett 83:3171–3173
107. Ding Y, Park K-B, Pelz JP, Palle KC, Mikhov MK, Skromme BJ, Meidia H, Mahajan S (2004) Quantum well state of self-forming 3C-SiC inclusions in 4H SiC determined by ballistic electron emission microscopy. Phys Rev B 69:041305(R)
108. Galeckas A, Hallén A, Majdi S, Linnros J, Pirouz P (2006) Combined photoluminescence-imaging and deep-level transient spectroscopy of recombination processes at stacking faults in 4H-SiC. Phys Rev B 74:233203
109. Miao MS, Limpijumnong S, Lambrecht WRL (2001) Stacking fault band structure in 4H-SiC and its impact on electronic devices. Appl Phys Lett 79:4360–4362
110. Lambrecht WRL, Miao MS (2006) Electronic driving force for stacking fault expansion in 4*H*-SiC. Phys Rev B 73:155312
111. Iwata H, Lindefelt U, Öberg S, Briddon PR (2001) Localized electronic states around stacking faults in silicon carbide. Phys Rev B 65:033203
112. Lindefelt U, Iwata H, Öberg S, Briddon PR (2003) Stacking faults in 3C-, 4H-, and 6H-SiC polytypes investigated by an ab initio supercell method. Phys Rev B 67:155204
113. Iwata H, Lindefelt U, Öberg S, Briddon PR (2003) Cubic polytype inclusions in 4H-SiC. J Appl Phys 93:1577–1585
114. Woodbury HH, Ludwig GW (1961) Electron spin resonance studies in SiC. Phys Rev 124:1083–1089
115. Suttrop W, Pensl G, Choyke WJ, Stein R, Leibenzeder S (1992) Hall effect and infrared absorption measurements on nitrogen donors in 6H-silicon carbide. J Appl Phys 72:3708–3713
116. Götz W, Schöner A, Pensl G, Suttrop W, Choyke WJ, Stein R, Leibenzeder S (1993) Nitrogen donors in 4H-silicon carbide. J Appl Phys 73:3332–3338
117. Schneider J, Müller HD, Maier K, Wilkening W, Fuchs F, Dörnen A, Leibenzeder S, Stein R (1990) Infrared spectra and electron spin resonance of vanadium deep level impurities in silicon carbide. Appl Phys Lett 56:1184–1186
118. Choyke WJ, Devaty RP, Clemen LL, Yoganathan M, Pensl G, Hässler Ch (1994) Intense erbium-1.54-μm photoluminescence from 2 to 525 K in ion-implanted 4H, 6H, 15R, and 3C SiC. Appl Phys Lett 65:1668–1670
119. Aradi B, Gali A, Deák P, Lowther JE, Son NT, Janzén E, Choyke WJ (2001) Ab initio density-functional supercell calculations of hydrogen defects in cubic SiC. Phys Rev B 63:245202
120. Greulich-Weber S (1997) EPR and ENDOR investigations of shallow impurities in SiC polytypes. Phys Stat Sol (a) 162:95–151
121. Vetelino JF, Mitra SS (1969) Lattice dynamics of cubic SiC. Phys Rev 178:1349–1352
122. Feldman DW, Parker JH, Choyke WJ, Patrick L (1968) Raman scattering in 6H SiC. Phys Rev 170:698–704
123. Feldman DW, Parker JH, Choyke WJ, Patrick L (1968) Phonon dispersion curves by Raman scattering in SiC, polytypes 3C, 4H, 6H, 15R, and 21R. Phys Rev 173:787–793
124. Hofmann M, Zywietz A, Karch K, Bechstedt F (1994) Lattice dynamics of SiC polytypes within the bond-charge model. Phys Rev B 50:13401–13411
125. Karch K, Pavone P, Windl W, Schütt O, Strauch D (1994) *Ab initio* calculation of structural and lattice-dynamical properties of silicon carbide. Phys Rev B 50:17054–17063
126. Spitzer WG, Kleinman D, Walsh D (1959) Infrared properties of hexagonal silicon carbide. Phys Rev 113:127–132

127. Spitzer WG, Kleinman DA, Frosch CJ (1959) Infrared properties of cubic silicon carbide films. Phys Rev 113:133–136
128. Patrick L, Choyke WJ (1961) Lattice absorption bands in SiC. Phys Rev 123:813–815
129. Holm RT, Klein PH, Nordquist PER (1986) Infrared reflectance evaluation of chemically vapor deposited β-SiC films grown on Si substrates. J Appl Phys 60:1479–1485
130. Engelbrecht F, Helbig R (1993) Effect of crystal anisotropy on the infrared reflectivity of 6H-SiC. Phys Rev B 48:15698–15707
131. Tiwald TE, Woollam JA, Zollner S, Christiansen J, Gregory RB, Wetteroth T, Wilson SR, Powell AR (1999) Carrier concentration and lattice absorption in bulk and epitaxial silicon carbide determined using infrared ellipsometry. Phys Rev B 60:11464–11474
132. Nakashima S, Katahama H, Nakakura Y, Mitsuishi A (1986) Relative Raman intensities of the folded modes in SiC polytypes. Phys Rev B 33:5721–5729
133. Okumura H, Sakuma E, Lee JH, Mukaida H, Misawa S, Endo K, Yoshida S (1987) Raman scattering of SiC: application to the identification of heteroepitaxy of SiC polytypes. J Appl Phys 61:1134–1136
134. Nakashima S, Tahara K (1989) Raman scattering determination of structures for SiC polytypes: quantitative evaluation with a revised model of lattice dynamics. Phys Rev B 40:6339–6344
135. Burton JC, Sun L, Long FH, Feng ZC, Ferguson IT (1999) First- and second-order Raman scattering from semi-insulating 4H-SiC. Phys Rev B 59:7282–7284
136. Olego D, Cardona M, Vogl P (1982) Pressure dependence of the optical phonons and transverse effective charge in 3C-SiC. Phys Rev B 25:3878–3888
137. Olego D, Cardona M (1982) Pressure dependence of Raman phonons of Ge and 3C-SiC. Phys Rev B 25:1151–1160
138. Debernardi A, Ulrich C, Syassen K, Cardona M (1999) Raman linewidths of optical phonons in 3C-SiC under pressure: first-principles calculations and experimental results. Phys Rev B 59:6774–6783
139. Liu J, Vohra YK (1994) Raman modes of 6H polytype of silicon carbide to ultrahigh pressures: a comparison with silicon and diamond. Phys Rev Lett 72:4105–4108
140. Olego D, Cardona M (1982) Temperature dependence of the optical phonons and transverse effective charge in 3C-SiC. Phys Rev B 25:3889–3896
141. Rohmfeld S, Hundhausen M, Ley L (1998) Raman scattering in polycrystalline 3C-SiC: influence of stacking faults. Phys Rev B 58:9858–9862
142. Colwell PJ, Klein MV (1972) Raman scattering from electronic excitations in *n*-type silicon carbide. Phys Rev B 6:498–515
143. Klein MV, Ganguly BN, Colwell PJ (1972) Theoretical and experimental study of Raman scattering from coupled LO-phonon-plasmon modes in silicon carbide. Phys Rev B 6:2380–2388
144. Harima H, Nakashima S, Uemura T (1995) Raman scattering from anisotropic LO-phonon-plasmon-coupled mode in *n*-type 4H- and 6H-SiC. J Appl Phys 78:1996–2005
145. Burton JC, Sun L, Pophristic M, Lukacs SJ, Long FH, Feng ZC, Ferguson IT (1998) Spatial characterization of doped SiC wafers by Raman spectroscopy. J Appl Phys 84:6268–6273
146. Choyke WJ, Patrick L (1957) Absorption of light in alpha SiC near the band edge. Phys Rev 105:1721–1723
147. Choyke WJ, Patrick L (1968) Higher Absorption Edges in 6H-SiC. Phys Rev 172:769–772
148. Sridhara SG, Devaty RP, Choyke WJ (1998) Absorption coefficient of 4H silicon carbide from 3900 to 3250 Å. J Appl Phys 84:2963–2964
149. Sridhara SG, Eperjesi TJ, Devaty RP, Choyke WJ (1999) Penetration depths in the ultraviolet for 4H, 6H and 3C silicon carbide at seven common laser pumping wavelengths. Mater Sci Eng B 61–62:229–233
150. Choyke WJ, Patrick L (1970) Luminescence of donor-acceptor pairs in cubic SiC. Phys Rev B 2:4959–4965
151. Hopfield JJ, Thomas DG, Gershenzon M (1963) Pair spectra in GaP. Phys Rev Lett 10:162–164

152. Suzuki A, Matsunami H, Tanaka T (1977) Photoluminescence due to Al, Ga, and B acceptors in 4H-, 6H-, and 3C-SiC grown from a Si melt. J Electrochem Soc 124:241–246
153. Ikeda M, Matsunami H, Tanaka T (1980) Site effect on the impurity levels in 4H, 6H, and 15R SiC. Phys Rev B 22:2842–2854
154. Hagen SH, Van Kemenade AWC, van der Does de Bye JAW (1973) Donor-acceptor pair spectra in 6H and 4H SiC doped with nitrogen and aluminium. J Lumin 8:18–31
155. Kamiyama S, Maeda T, Nakamura Y, Iwaya M, Amano H, Akasaki I, Kinoshita H, Furusho T, Yoshimoto M, Kimoto T, Suda J, Henry A, Ivanov IG, Bergman JP, Monemar B, Onuma T, Chichibu SF (2006) Extremely high quantum efficiency of donor-acceptor-pair emission in N-and-B-doped 6H-SiC. J Appl Phys 99:093108
156. Ou Y, Jokubavicius V, Kamiyama S, Liu C, Berg RW, Linnarsson M, Yakimova R, Syväjärvi M, Ou H (2011) Donor-acceptor-pair emission characterization in N-B doped fluorescent SiC. Optic Mater Exp 1:1439–1446
157. Lampert MA (1958) Mobile and immobile effective-mass-particle complexes in nonmetallic solids. Phys Rev Lett 1:450–453
158. Haynes JR (1960) Experimental proof of the existence of a new electronic complex in silicon. Phys Rev Lett 4:361–363
159. Choyke WJ, Patrick L (1962) Exciton recombination radiation and phonon spectrum of 6H SiC. Phys Rev 127:1868–1877
160. Hamilton DR, Choyke WJ, Patrick L (1963) Photoluminescence of nitrogen-exciton complexes in 6H SiC. Phys Rev 131:127–133
161. Patrick L, Hamilton DR, Choyke WJ (1963) Optical properties of 15R SiC: luminescence of nitrogen-exciton complexes, and interband absorption. Phys Rev 132:2023–2031
162. Patrick L, Choyke WJ, Hamilton DR (1965) Luminescence of 4H SiC, and location of conduction-band minima in SiC polytypes. Phys Rev 137:A1515–A1520
163. Patrick L, Hamilton DR, Choyke WJ (1966) Growth, luminescence, selection rules, and lattice sums of SiC with wurtzite structure. Phys Rev 143:526–536
164. Ivanov IG, Hallin C, Henry A, Kordina O, Janzén E (1996) Nitrogen doping concentration as determined by photoluminescence in 4H- and 6H-SiC. J Appl Phys 80:3504–3508
165. Dean PJ, Herbert DC, Bimberg D, Choyke WJ (1976) Donor exciton satellites in cubic silicon carbide: multiple bound excitons revisited. Phys Rev Lett 37:1635–1638
166. Kuwabara H, Yamada S (1975) Free-to-bound transition in β-SiC doped with boron. Phys Stat Sol (a) 30:739–746
167. Clemen LL, Devaty RP, MacMillan MF, Yoganathan M, Choyke WJ, Larkin DJ, Powell JA, Edmond JA, Kong HS (1993) Aluminum acceptor four particle bound exciton complex in 4H, 6H, and 3C SiC. Appl Phys Lett 62:2953–2955
168. Sridhara SG, Clemen LL, Devaty RP, Choyke WJ, Larkin DJ, Kong HS, Troffer T, Pensl G (1998) Photoluminescence and transport studies of boron in 4H SiC. J Appl Phys 83:7909–7919
169. Egilsson T, Bergman JP, Ivanov IG, Henry A, Janzén E (1999) Properties of the D_1 bound exciton in 4H-SiC. Phys Rev B 59:1956–1963
170. Lüth H (2010) Solid surfaces, interfaces and thin films, 5th edn. Springer, Berlin
171. Hara S, Misawa S, Yoshida S, Aoyagi Y (1994) Additional dimer-row structure of 3C-SiC(001) surfaces observed by scanning tunneling microscopy. Phys Rev B 50:4548–4553
172. Semond F, Soukiassian P, Mayne A, Dujardin G, Douillard L, Jaussaud C (1996) Atomic structure of the β-SiC(100)-(3 × 2) surface. Phys Rev Lett 77:2013–2016
173. Sabisch M, Krüger P, Mazur A, Rohlfing M, Pollmann J (1996) First-principles calculations of β-SiC(001) surfaces. Phys Rev B 53:13121–13132
174. Soukiassian P, Semond F, Douillard L, Mayne A, Dujardin G, Pizzagalli L, Joachim C (1997) Direct observation of a β-SiC(100)-c(4 × 2) surface reconstruction. Phys Rev Lett 78:907–910
175. Soukiassian P, Semond F, Mayne A, Dujardin G (1997) Highly stable Si atomic line formation on the β-SiC(100) surface. Phys Rev Lett 79:2498–2501

176. Derycke V, Soukiassian P, Mayne A, Dujardin G, Gautier J (1998) Carbon atomic chain formation on the β-SiC(100) surface by controlled sp → sp^3 transformation. Phys Rev Lett 81:5868–5871
177. Powers JM, Wander A, Rous PJ, Van Hove MA, Somorjai GA (1991) Structural analysis of the β-SiC(100)-c(2 × 2) surface reconstruction by automated tensor low-energy electron diffraction. Phys Rev B 44:11159–11166
178. Yan H, Smith AP, Jónsson H (1995) Atomic structure of β-SiC(100) surfaces: an ab initio study. Surf Sci 330:265–275
179. Long JP, Bermudez VM, Ramaker DE (1996) Structural determination of β-SiC(100)-c(2 × 2) from C-1s surface-core-exciton and Si-2p absorption. Phys Rev Lett 76:991–994
180. Catellani A, Galli G, Gygi F (1996) Reconstruction and thermal stability of the cubic SiC (001) surfaces. Phys Rev Lett 77:5090–5093
181. Yeom HW, Shimomura M, Kitamura J, Hara S, Tono K, Matsuda I, Mun BS, Huff WAR, Kono S, Ohta T, Yoshida S, Okushi H, Kajimura K, Fadley CS (1999) Atomic and electronic-band structures of anomalous carbon dimers on 3C-SiC(001)-*c*(2 × 2). Phys Rev Lett 83:1640–1643
182. Starke U, Schardt J, Bernhardt J, Franke M, Reuter K, Wedler H, Heinz K, Furthmüller J, Käckell P, Bechstedt F (1998) Novel reconstruction mechanism for dangling-bond minimization: combined method surface structure determination of SiC(111)-(3 × 3). Phys Rev Lett 80:758–761
183. Schardt J, Bernhardt J, Starke U, Heinz K (2000) Crystallography of the (3 × 3) surface reconstruction of 3C-SiC(111), 4H-SiC(0001), and 6H-SiC(0001) surfaces retrieved by low-energy electron diffraction. Phys Rev B 62:10335–10344
184. Kulakov MA, Henn G, Bullemer B (1996) SiC(0001)3 × 3-Si surface reconstruction—a new insight with a STM. Surf Sci 346:49–54
185. Li L, Tsong IST (1996) Atomic structures of 6H-SiC (0001) and $(000\bar{1})$ surfaces. Surf Sci 351:141–148
186. Starke U, Bram Ch, Steiner P-R, Hartner W, Hammer L, Heinz K, Müller K (1995) The (0001)-surface of 6H-SiC: morphology, composition and structure. Appl Surf Sci 89:175–185
187. Owman F, Mårtensson P (1995) STM study of the SiC(0001) $\sqrt{3} \times \sqrt{3}$ surface. Surf Sci 330:L639–L645
188. Northrup JE, Neugebauer J (1995) Theory of the adatom-induced reconstruction of the SiC(0001) $\sqrt{3} \times \sqrt{3}$ surface. Phys Rev B 52:R17001–R17004
189. Johansson LI, Owman F, Mårtensson P (1996) Surface state on the SiC(0001)-($\sqrt{3} \times \sqrt{3}$) surface. Surf Sci 360:L478–L482
190. Johansson LI, Owman F, Mårtensson P (1996) High-resolution core-level study of 6H-SiC(0001). Phys Rev B 53:13793–13802
191. Sabisch M, Krüger P, Pollmann J (1997) Ab initio calculations of structural and electronic properties of 6H-SiC(0001) surfaces. Phys Rev B 55:10561–10570
192. Ramachandran V, Feenstra RM (1999) Scanning tunneling spectroscopy of Mott-Hubbard states on the 6H-SiC(0001) $\sqrt{3} \times \sqrt{3}$ Surface. Phys Rev Lett 82:1000–1003
193. Hornetz B, Michel H-J, Halbritter J (1994) ARXPS studies of SiO_2–SiC interfaces and oxidation of 6H SiC single crystal Si-(001) and C–$(00\bar{1})$ surfaces. J Mater Res 9:3088–3094
194. Afanas'ev VV, Bassler M, Pensl G, Schulz MJ, von Kamienski ES (1996) Band offsets and electronic structure of SiC/SiO_2 interfaces. J Appl Phys 79:3108–3114
195. Afanas'ev VV, Bassler M, Pensl G, Schulz M (1997) Intrinsic SiC/SiO_2 interface states. Phys Stat Sol (a) 162:321–337
196. Afanas'ev VV, Stesmans A, Bassler M, Pensl G, Schulz MJ (2000) Shallow electron traps at the 4H–SiC/SiO_2 interface. Appl Phys Lett 76:336–337
197. Chang KC, Nuhfer NT, Porter LM, Wahab Q (2000) High-carbon concentrations at the silicon dioxide-silicon carbide interface identified by electron energy loss spectroscopy. Appl Phys Lett 77:2186–2188

198. Knaup JM, Deák P, Frauenheim T, Gali A, Hajnal Z, Choyke WJ (2005) Theoretical study of the mechanism of dry oxidation of 4H-SiC. Phys Rev B 71:235321
199. Pippel E, Woltersdorf J, Ólafsson HÖ, Sveinbjörnsson EÖ (2005) Interfaces between 4H-SiC and SiO_2: microstructure, nanochemistry, and near-interface traps. J Appl Phys 97:034302
200. Knaup JM, Deák P, Frauenheim Th, Gali A, Hajnal Z, Choyke WJ (2005) Defects in SiO_2 as the possible origin of near interface traps in the SiC/SiO_2 system: a systematic theoretical study. Phys Rev B 72:115323
201. Zheleva T, Lelis A, Duscher G, Liu F, Levin I, Das M (2008) Transition layers at the SiO_2/SiC interface. Appl Phys Lett 93:022108
202. Afanas'ev VV, Stesmans A, Bassler M, Pensl G, Schulz MJ, Harris CI (1996) Elimination of SiC/SiO_2 interface states by preoxidation ultraviolet-ozone cleaning. Appl Phys Lett 68:2141–2143
203. Afanas'ev VV, Stesmans A, Ciobanu F, Pensl G, Cheong KY, Dimitrijev S (2003) Mechanisms responsible for improvement of 4H-SiC/SiO_2 interface properties by nitridation. Appl Phys Lett 82:568–570
204. McDonald K, Weller RA, Pantelides ST, Feldman LC, Chung GY, Tin CC, Williams JR (2003) Characterization and modeling of the nitrogen passivation of interface traps in SiO_2/4H-SiC. J Appl Phys 93:2719–2722
205. Wang S, Dhar S, Wang S, Ahyi AC, Franceschetti A, Williams JR, Feldman LC, Pantelides ST (2007) Bonding at the SiC–SiO_2 interface and the effects of nitrogen and hydrogen. Phys Rev Lett 98:026101
206. Deák P, Knaup JM, Hornos T, Thill C, Gali A, Frauenheim T (2007) The mechanism of defect creation and passivation at the SiC/SiO_2 interface. J Phys D: Appl Phys 40:6242–6253
207. Saks NS, Mani SS, Agarwal AK (2000) Interface trap profile near the band edges at the 4H-SiC/SiO_2 interface. Appl Phys Lett 76:2250–2252
208. Bernhardt J, Schardt J, Starke U, Heinz K (1999) Epitaxially ideal oxide-semiconductor interfaces: silicate adlayers on hexagonal (0001) and $(000\bar{1})$ SiC surfaces. Appl Phys Lett 74:1084–1086
209. Ramachandran V, Brady MF, Smith AR, Feenstra RM, Greve DW (1998) Preparation of atomically flat surfaces on silicon carbide using hydrogen etching. J Electron Mater 27:308–312
210. Sieber N, Mantel BF, Seyller Th, Ristein J, Ley L, Heller T, Batchelor DR, Schmeißer D (2001) Electronic and chemical passivation of hexagonal 6H-SiC surfaces by hydrogen termination. Appl Phys Lett 78:1216–1218
211. Derycke V, Soukiassian PG, Amy F, Chabal YJ, D'angelo MD, Enriquez HB, Silly MG (2003) Nanochemistry at the atomic scale revealed in hydrogen-induced semiconductor surface metallization. Nat Mater 2:253–258
212. Cicero G, Catellani A, Galli G (2004) Atomic control of water interaction with biocompatible surfaces: the case of SiC(001). Phys Rev Lett 93:016102
213. Rosso M, Arafat A, Schroën K, Giesbers M, Roper CS, Maboudian R, Zuilhof H (2008) Covalent attachment of organic monolayers to silicon carbide surfaces. Langmuir 24:4007–4012
214. Rosso M, Giesbers M, Arafat A, Schroën K, Zuilhof H (2009) Covalently attached organic monolayers on SiC and Si_xN_4 surfaces: formation using UV light at room temperature. Langmuir 25:2172–2180
215. Catellani A, Calzolari A (2012) Functionalization of SiC(110) surfaces via porphyrin adsorption: ab initio results. J Phys Chem C 116:886–892
216. Schoell SJ, Sachsenhauser M, Oliveros A, Howgate J, Stutzmann M, Brandt MS, Frewin CL, Saddow SE, Sharp ID (2013) Organic functionalization of 3C-SiC surfaces. ACS Appl Mater Interfaces 5:1393–1399

217. Cheng C, Needs RJ, Heine V (1988) Inter-layer interactions and the origin of SiC polytypes. J Phys C: Solid State Phys 21:1049–1063
218. Heine V, Cheng C, Needs RJ (1991) The preference of silicon carbide for growth in the metastable cubic form. J Am Ceram Soc 74:2630–2633
219. Käckell P, Wenzien B, Bechstedt F (1994) Influence of atomic relaxations on the structural properties of SiC polytypes from *ab initio* calculations. Phys Rev B 50:17037–17046
220. Limpijumnong S, Lambrecht WRL (1998) Total energy differences between SiC polytypes revisited. Phys Rev B 57:12017–12022
221. Bernstein N, Gotsis HJ, Papaconstantopoulos DA, Mehl MJ (2005) Tight-binding calculations of the band structure and total energies of the various polytypes of silicon carbide. Phys Rev B 71:075203
222. Baumann HN (1952) The relationship of alpha and beta silicon carbide. J Electrochem Soc 99:109–114
223. Yoo WS, Matsunami H (1991) Solid-state phase transformation in cubic silicon carbide. Jpn J Appl Phys 30:545–553
224. Powell JA, Will HA (1972) Low-temperature solid-state phase transformations in 2H silicon carbide. J Appl Phys 43:1400–1408
225. Heuer AH, Fryburg GA, Ogbuji LU, Mitchell TE (1978) $\beta- > \alpha$ transformation in polycrystalline SiC: I, microstructural aspects. J Am Ceram Soc 61:406–412
226. Mitchell TE, Ogbuji LU, Heuer AH (1978) $\beta- > \alpha$ transformation in polycrystalline SiC: II, interfacial energetics. J Am Ceram Soc 61:412–413
227. Ogbuji LU, Mitchell TE, Heuer AH (1981) The $\beta- > \alpha$ transformation in polycrystalline SiC: III, the thickness of α plates. J Am Ceram Soc 64:91–99
228. Ogbuji LU, Mitchell TE, Heuer AH, Shinozaki S (1981) The $\beta- > \alpha$ transformation in polycrystalline SiC: IV, a comparison of conventionally sintered, hot-pressed, reaction-sintered, and chemically vapor-deposited samples. J Am Ceram Soc 64:100–105
229. Nader M, Aldinger F, Hoffmann MJ (1999) Influence of the α/β-SiC phase transformation on microstructural development and mechanical properties of liquid phase sintered silicon carbide. J Mater Sci 34:1197–1204
230. Starke U, Schardt J, Bernhardt J, Franke M, Heinz K (1999) Stacking transformation from hexagonal to cubic SiC induced by surface reconstruction: a seed for heterostructure growth. Phys Rev Lett 82:2107–2110
231. Okojie RS, Xhang M, Pirouz P, Tumakha S, Jessen G, Brillson LJ (2001) Observation of 4H-SiC to 3C-SiC polytypic transformation during oxidation. Appl Phys Lett 79:3056–3058
232. Chang KJ, Cohen ML (1987) *Ab initio* pseudopotential study of structural and high-pressure properties of SiC. Phys Rev B 35:8196–8201
233. Yoshida M, Onodera A, Ueno M, Takemura K, Shimomura O (1993) Pressure-induced phase transition in SiC. Phys Rev B 48:10587–10590
234. Karch K, Bechstedt F, Pavone P, Strauch D (1996) Pressure-dependent properties of SiC polytypes. Phys Rev B 53:13400–13413
235. Shimojo F, Ebbsjö I, Kalia RK, Nakano A, Rino JP, Vashishta P (2000) Molecular dynamics simulation of structural transformation in silicon carbide under pressure. Phys Rev Lett 84:3338–3341
236. Miao MS, Lambrecht WRL (2003) Unified path for high-pressure transitions of SiC polytypes to the rocksalt structure. Phys Rev B 68:092103
237. Vashishta P, Kalia RK, Nakano A, Rino JP (2007) Interaction potential for silicon carbide: a molecular dynamics study of elastic constants and vibrational density of states for crystalline and amorphous silicon carbide. J Appl Phys 101:103515
238. Aristov VYu, Douillard L, Fauchoux O, Soukiassian P (1997) Temperature-induced semiconducting $c(4 \times 2) \Longleftrightarrow$ metallic (2×1) reversible phase transition on the β-SiC(100) surface. Phys Rev Lett 79:3700–3703

Chapter 3
Porous SiC

There are three motives to investigate surface etching of silicon carbide (SiC). The first is the creation of patterns on SiC for electronic applications, and the second is that porous SiC obtained by etching yields stronger luminescence than the bulk materials. Last but not least, porous SiC has promising applications in sensing.

3.1 Fabrication of Porous SiC by Various Etching Methods

SiC is a polar compound semiconductor, and hence, the opposite faces of {001} wafers have different chemical properties and etched patterns. Theoretical studies show that there are small differences in the X-ray reflection intensity from opposite crystal faces [1]. These differences are determined experimentally to allow for identification of the crystallographic polarity under conditions of careful surface preparation which assures identical diffraction conditions on both sides.

Photoelectrochemical etching of SiC has been extensively investigated. SiC is chemically inert; thus, electrochemical etching is commonly adopted to efficiently etch SiC. By practicing photoelectrochemistry, *n*-type 3C-SiC can be selectively etched while *p*-type 3C-SiC is used as an etch stop [2]. Porous SiC is prepared by anodizing *n*-type 6H-SiC in HF under UV-light illumination [3]. Transmission electron microscopy reveals that the obtained porous SiC network is composed of 10–30-nm pores with interpore spacing ranging from 5 to 150 nm. The selected-area electron diffraction patterns show that the porous layers are single-crystal SiC. The large area etching pattern created on 3C-SiC is displayed in Fig. 3.1 [4]. Photoelectrochemical etching has the advantages of high etching rates and dopant selectivity compared to other etching methods such as reactive ion etching. However, a rough surface morphology results from etching and may be ascribed to the large defect density. The suggested reactions in anodization are:

J. Fan and P.K. Chu, *Silicon Carbide Nanostructures*,
Engineering Materials and Processes, DOI 10.1007/978-3-319-08726-9_3

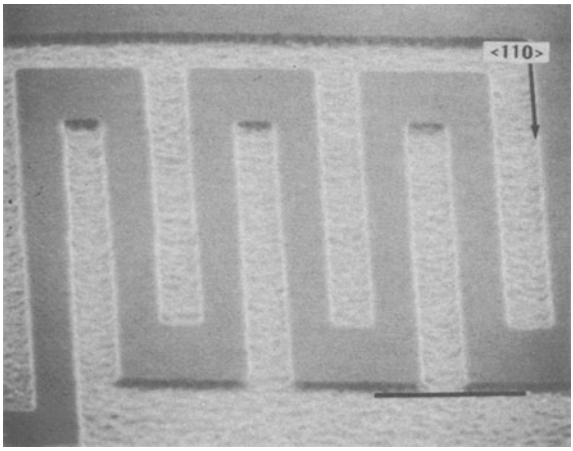

Fig. 3.1 SEM micrograph of serpentine resistor patterns etched into *n*-type 3C-SiC. The *horizontal bar* represents 100 μm. Reprinted with permission from [4]. Copyright 1993, Electrochemical Society

$$SiC + 4H_2O + 8h^+ \rightarrow SiO_2 + CO_2 + 8H^+, \tag{3.1}$$

$$SiC + 2H_2O + 4h^+ \rightarrow SiO + CO + 4H^+. \tag{3.2}$$

The overall reaction is:

$$2SiC + 6H_2O + 12h^+ \rightarrow SiO_2 + CO_2 + SiO + CO + 12H^+. \tag{3.3}$$

Anodic dissolution of 6H-SiC in HF occurs via oxidation of the surface described by the Eqs. 3.1–3.3 followed by removal of the oxide by HF. In a two-step etching method, the 6H-SiC is first anodized to form a deep porous layer which is then removed by thermal oxidation followed by dipping in HF [5]. The *n*-type and *p*-type materials are etched by photoelectrochemical and dark electrochemical techniques, respectively. Etching rates as high as 400 nm/min for *n*-SiC and 2.2 μm/min for *p*-SiC are achieved in anodization which produces nearly mirror surfaces.

Electrochemical anodization has been applied to 3C-SiC [6]. The porous 3C-SiC layer is produced on a 3C-SiC single crystal by anodic dissolution in HF under UV-light illumination. Scanning electron microscopy reveals that the as-prepared 3C-SiC has a porous structure with a minimal size of 20 nm.

A model is presented to explain the formation mechanism of the porous SiC [7]. The porous *n*-type 6H-SiC produced by electrochemical etching with (photo-assisted mode) and without (dark current mode) UV-light illumination is investigated. Photo-assisted etching at a low anode bias produces semi-insulating porous materials with an average fiber thickness below 50 nm. Etching in darkness and at a high bias voltage gives rise to porous SiC with a fiber thickness of 0.5–1 μm and lower resistivity. Self-regulation of fiber size during electrochemical etching arises from Fermi-level pinning to the surface states in thin fibers

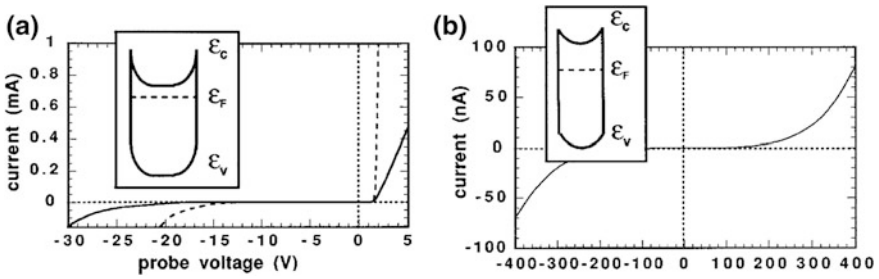

Fig. 3.2 Current–voltage characteristics of a point probe contact on porous 6H-SiC for **a** dark-current-mode fabricated materials (*solid line*) and crystalline SiC (*dashed line*), and **b** photo-assisted-mode fabricated materials. The insets show the proposed zone diagrams. Reprinted with permission from [7]. Copyright 1994, AIP Publishing LLC

(Fig. 3.2). Fermi-level pinning results in the increase in resistivity, thereby blocking fiber dissolution and ensuring the stability of thin fibers in the electrolyte.

Photoelectrochemical etching of highly doped *n*-type 4H-SiC in HF along different crystallographic orientations under low-voltage and/or low-current condition has been studied [8]. Scanning electron microscopy reveals that the pores formed by anodization are anisotropic (Fig. 3.3). The Si terminated crystallographic planes are more resistant to electrolytic attack than the C or mixed C-Si terminated ones. The resultant pore structure is found to be independent of the direction of the applied external electric field.

Special hierarchical structures of SiC can be prepared by electroless chemical etching. The nanoplatelets or ordered nanostructures are created by preferential etching of SiC whiskers in a mixture of hydrofluoric acid and nitric acid (3:1 ratio) at 100 °C [9]. The SEM and TEM images of the pagoda-like SiC nanostructures are shown in Fig. 3.4. A model based on the high-resolution TEM and Raman data (Fig. 3.5) is proposed to explain the etching mechanism. In this model, the

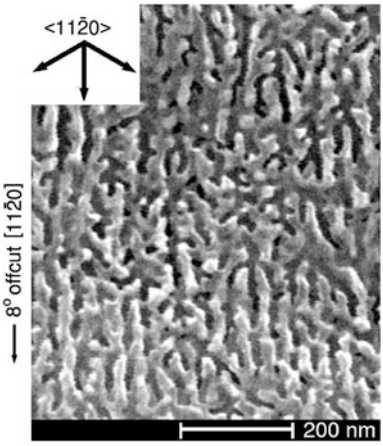

Fig. 3.3 SEM image of an anodized 4H-SiC sample exhibiting the triangular porous morphology. Two micrometers of the materials are removed by reactive ion etching before imaging. Reprinted with permission from [8]. Copyright 2004, AIP Publishing LLC

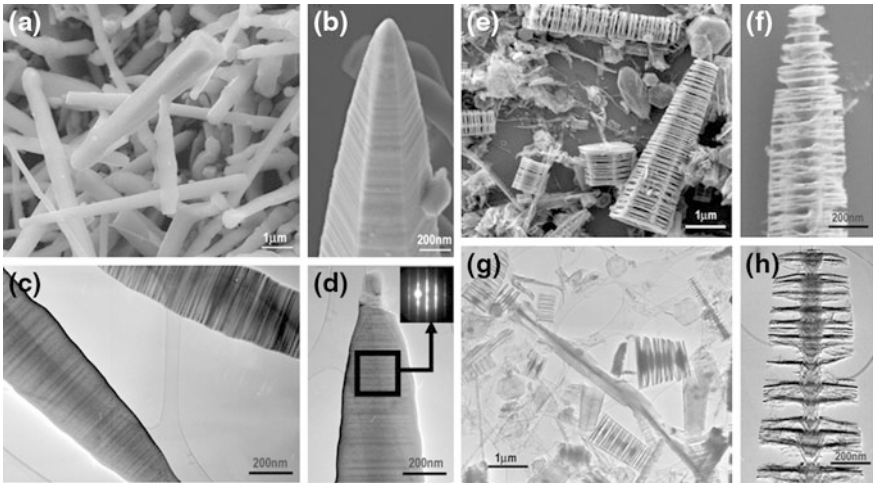

Fig. 3.4 SEM (**a**, **b**) and TEM (**c**, **d**) images of pristine β-SiC whiskers. The inset in *d* is selected-area diffraction pattern of the denoted area. SEM (**e**, **f**) and TEM (**g**, **h**) images of etched SiC whiskers. Reprinted with permission from [9]. Copyright 2006, American Chemical Society

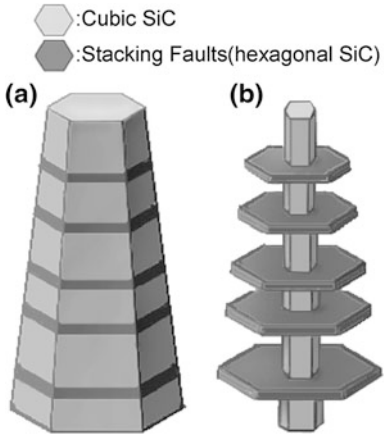

Fig. 3.5 Schematic showing the transformation of a pristine SiC whisker **a** to a nanostructured pagoda-like structure, **b** by selective etching of β-SiC. Reprinted with permission from [9]. Copyright 2006, American Chemical Society

whiskers are composed of β-SiC and periodically distributed stacking faults (α-SiC). Preferential etching of β-SiC with respect to α-SiC produces pagoda-shaped nanostructures. In addition to large area etching, a limited area etching on the SiC is also realized. The *n*-type 4H-SiC is electrochemically etched by HF with a glassy carbon needle electrode (130 μm in diameter) [10] and pores with the same diameter as that of the needles are formed at the SiC/glass carbon contact region. The rate of pore formation increases when sulfuric acid is added to the HF solution.

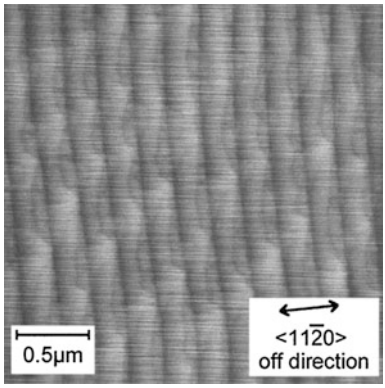

Fig. 3.6 Atomic force microscopy image of the etched 6H-SiC (0001) surface with off direction toward $\langle 11\bar{2}0\rangle$ showing microsteps with triangular depressions. Reprinted with permission from [11]. Copyright 2000, AIP Publishing LLC

Others methods other than conventional chemical or electrochemical etching by hydrofluoric acid have been developed to prepare porous SiC. Step bunching is achieved on the 6H-SiC (0001) vicinal face by etching with HCl [11]. When the substrate is inclined toward $\langle 01\bar{1}0\rangle$ or $\langle 11\bar{2}0\rangle$, continuous parallel and periodic microsteps with six bilayer height are produced perpendicular to the off direction (Fig. 3.6). The combination of Pt assisted chemical etching (in HF and $K_2S_2O_8$ solutions) and reactive ion etching of *n*-type 6H-SiC gives rise to large-scale porous materials [12]. The surface roughness increases dramatically in comparison with individual metal assisted etching or reactive ion etching. Subsequent functionalization of the porous SiC surface with perfluorooctyl trichlorosilane results in a superhydrophobic SiC surface which is stable in both acidic and basic solutions. Mesoporous SiC is fabricated by a modified sol-gel method [13]. Tetraethoxysilane and phenolic resin are used to generate a binary carbonaceous silicon xerogel, and nickel nitrate is used as the pore adjusting reagent. Carbothermal reduction of the binary xerogel at 1,250 °C in argon produces the SiC which has a surface area of 112 $m^2\ g^{-1}$ and mean pore size of 10 nm (Fig. 3.7). The macroporous SiC monoliths with geometric surface areas of 10^5–10^8 m^2 per m^3 are synthesized by

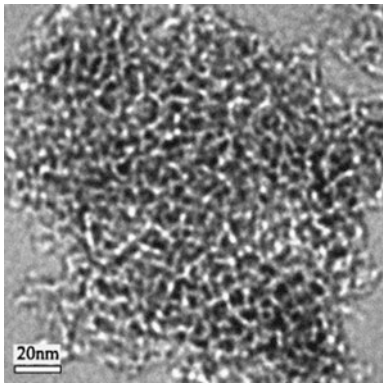

Fig. 3.7 TEM image of porous silicon carbide. Reprinted with permission from [13]. Copyright 2003, Elsevier

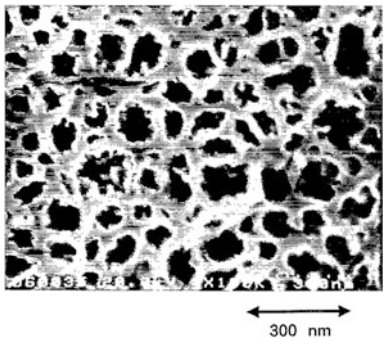

Fig. 3.8 SEM image of the porous 6H-SiC layer fabricated by electrochemical anodization at a current density of 40 mA/cm^2. Reprinted with permission from [17]. Copyright 1994, AIP Publishing LLC

capillary filling of packed beds of polystyrene or silica spheres with low-viscosity preceramic polymers [14]. Subsequent curing, pyrolysis, and removal of spheres result in SiC inverted beaded monoliths that are stable at temperature as high as 1,200 °C.

3.2 Luminescence from Porous SiC

The luminescence properties of porous SiC have attracted much interest since the report of strong luminescence from porous silicon at room temperature [15, 16]. Luminescence is observed from porous SiC fabricated by electrochemical etching of (0001) *n*-type (nitrogen-doped) 6H-SiC wafers [17]. The pore size varies from tens of nanometers to sub-micrometers as shown in Fig. 3.8. The porous layer exhibits intense blue–green luminescence with a maximum at around 460 nm (2.7 eV) at room temperature (Fig. 3.9). The luminescence intensity is about 100

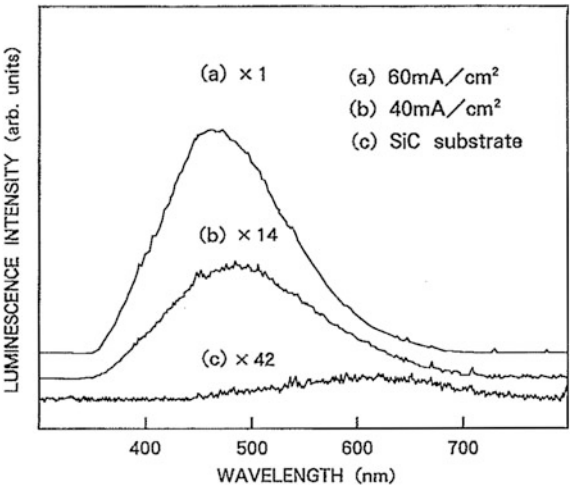

Fig. 3.9 Photoluminescence spectra obtained from porous SiC fabricated at anodization current densities of **a** 60 mA/cm^2, and **b** 40 mA/cm^2. The spectrum of the crystalline 6H-SiC is shown for comparison. Reprinted with permission from [17]. Copyright 1994, AIP Publishing LLC

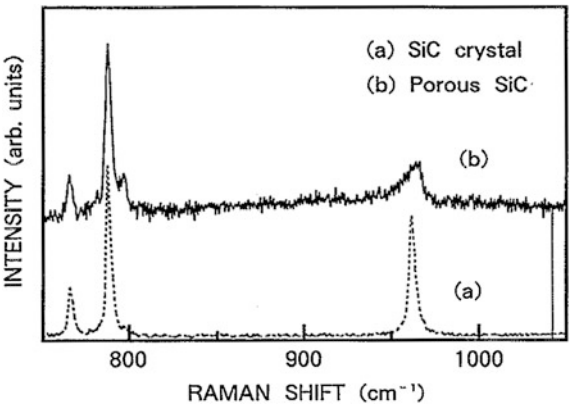

Fig. 3.10 Raman scattering spectra of porous SiC and crystalline SiC. Reprinted with permission from [17]. Copyright 1994, AIP Publishing LLC

times stronger than that arising from donor–acceptor recombination in crystalline 6H-SiC. The peak energy is below the bandgap of crystalline SiC at room temperature, and therefore, this intense blue-green luminescence is suggested to arise from the surface region of porous SiC. Figure 3.10 shows the Raman spectra of the porous and crystalline materials. The porous sample shows a broadened 960 cm^{-1} LO phonon mode, and the holding mode at below 800 cm^{-1} becomes stronger. The similar positions of the TO and LO phonons in both samples indicate that the porous layer retains the crystalline structure of bulk material. The broadening and holding-mode enhancement observed from the porous material may arise from strain defects or phonon confinement. The luminescence decay reveals that the higher porosity (smaller microstructure size) leads to slower decay and a stronger emission. The lifetime varies from 100 picoseconds to nanoseconds, and it is suggested that the carriers in the core crystal are excited and the excited carriers are transferred from the core to surface consequently producing the luminescence.

Porous *p*-type 6H-SiC materials prepared by electrochemical anodization of *p*-type 6H-SiC wafers in HF have a different luminescence behavior [18]. Transmission electron microscopy reveals uniformly dispersed pores in the porous layer with an interpore spacing between 1 and 10 nm (Fig. 3.11). The porous film exhibits as a single crystal. Cathodoluminescence shows a broad band at about 500 nm (2.5 eV) from the sample anodized at 50 mA/cm^2 (Fig. 3.12). A narrow and weaker peak arising at 3.7 eV (above bandgap) is likely related to the interband transition, but it is absent from the luminescence spectrum of the sample anodized at 5 mA/cm^2.

The porous SiC materials obtained by anodization of (mostly *n*-type) 3C-, 6H-, and 4H-SiC crystals show similar luminescence characteristics [19]. The porous material prepared without UV-light illumination has an average fiber size of 0.5–1 μm, whereas that obtained with aid of UV light has a fiber size of smaller than 50 nm. Both materials have the dendritic structure and contain some much smaller fibers. The porous SiC materials prepared from different polytypes yield nearly the same luminescence peak at around 2.5 eV (Fig. 3.13). The close PL

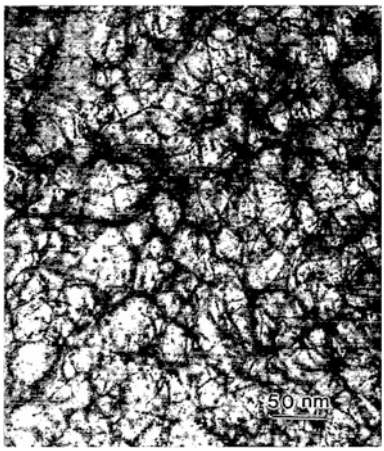

Fig. 3.11 TEM image of porous *p*-type 6H-SiC fabricated by electrochemical anodization at an anodization current density of 50 mA/cm^2. Reprinted with permission from [18]. Copyright 1994, AIP Publishing LLC

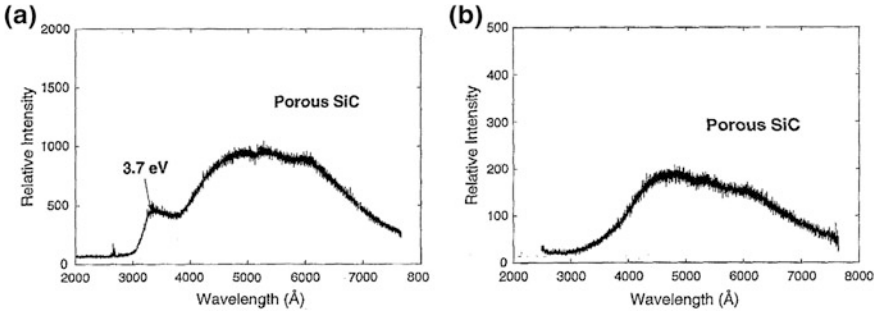

Fig. 3.12 Room-temperature cathodoluminescence spectra of porous *p*-type 6H-SiC anodized at **a** 50 mA/cm^2, and **b** 5 mA/cm^2. Reprinted with permission from [18]. Copyright 1994, AIP Publishing LLC

peak positions observed from the three different polytypes exclude deep defect centers in the bandgap as the origin of the observed PL, because the defects in the bulk materials generally show different emission photon energies due to the large difference in the bandgap energies of 3C, 6H, and 4H polytypes. For instance, the D_1 defect center has an energy comparable to that of the observed PL peak, but the D_1 PL peak position varies by 0.9 eV among these polytypes. Annealing in oxygen at 700 °C quenches the blue–green PL completely (Fig. 3.14), but the emission band is partially recovered by dipping the oxidized crystal in 40 % HF, suggesting that PL is related to defect states in the etched surface. The luminescence peaks at 2.43, 2.22, 2.07, and 1.93 eV are identified in the PL spectra by using selective excitation of the PL by tuning excitation wavelength. The result shows that the change of the fiber size in the porous structure gives rise to no additional PL bands.

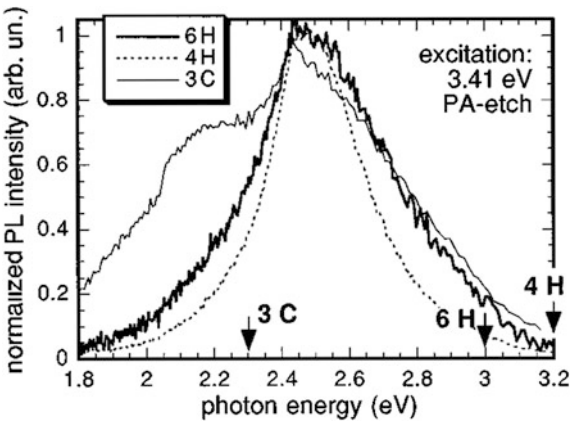

Fig. 3.13 Normalized photoluminescence spectra of the porous silicon carbide prepared by anodization of different polytypes of SiC crystals. The excitation photon energy is above the bandgaps of all the polytypes. Reprinted with permission from [19]. Copyright 1995, AIP Publishing LLC

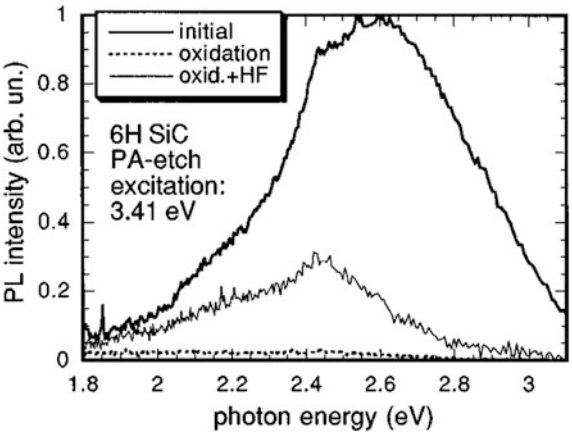

Fig. 3.14 Photoluminescence spectra of the as-prepared, oxidized, and oxidized and HF-dipped porous 6H-SiC. Reprinted with permission from [19]. Copyright 1995, AIP Publishing LLC

Photoluminescence from the porous 6H-SiC prepared by anodization of *n*-type 6H-SiC with a net doping $n_D - n_A$ of 5×10^{18} cm^{-3} is studied [20]. The materials are electrochemically etched in HF (alcohol:50 wt% HF = 1:1) at a current density of 10–500 mA cm^{-2} under UV-light illumination. The size of the crystalline grains in the porous structure is typically 30 nm. The room temperature luminescence spectrum of the porous material is similar to that of the bulk materials (Fig. 3.15) showing a broad band at around 2.65 eV. This luminescence is ascribed to recombination associated with the donor–acceptor pairs, but it is stronger from the porous material by a factor of 100. With regard to porous SiC,

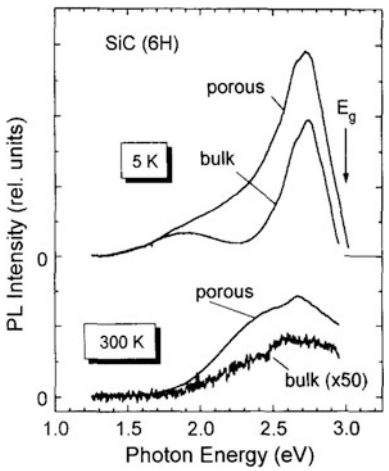

Fig. 3.15 PL spectra obtained from bulk and porous 6H-SiC at 300 and 5 K at an excitation energy of 3.5 eV. Reprinted with permission from [20]. Copyright 1995, Elsevier

the intensity is further increased by a factor of two as the temperature drops from 300 to 5 K. The large increase in PL intensity in porous material is due to the geometrical carrier confinement in the granular and porous material. But no evidence of quantum confinement is observed. Infrared transmission study (Fig. 3.16)

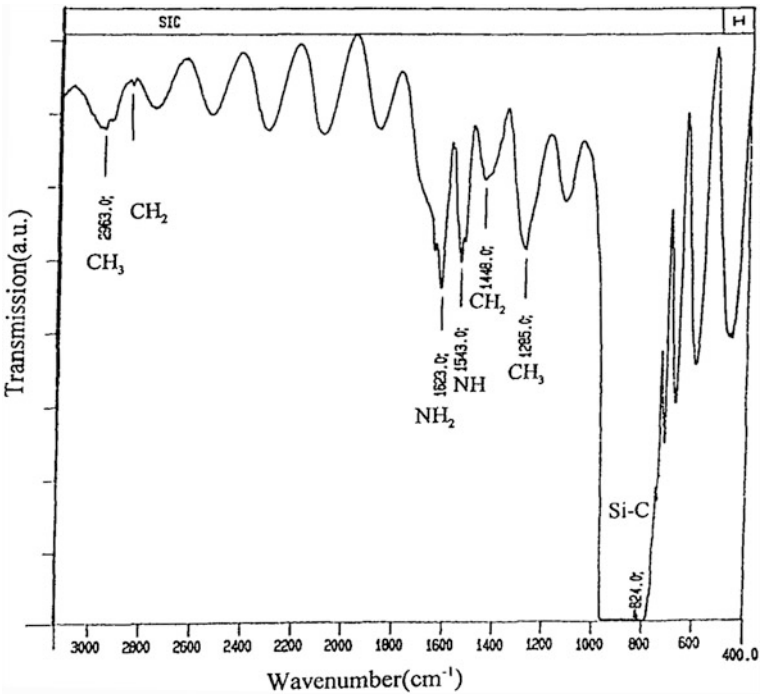

Fig. 3.16 Infrared transmission spectrum of the free-standing porous 6H-SiC layer. Reprinted with permission from [20]. Copyright 1995, Elsevier

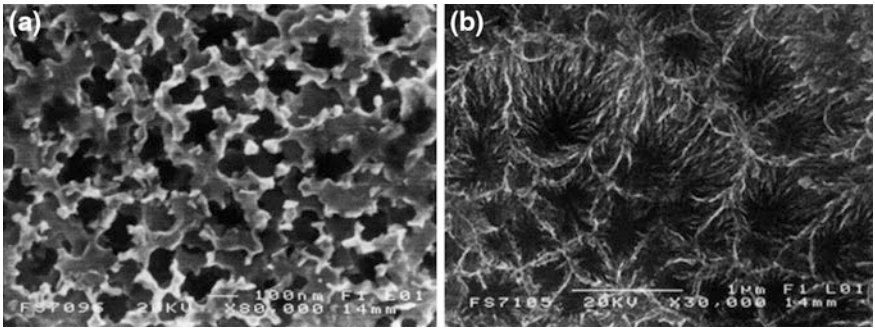

Fig. 3.17 SEM images of **a** porous *n*-type 6H-SiC layer, and **b** super-critically dried porous *p*-type SiC layer. Reprinted with permission from [21]. Copyright 1997, Elsevier

indicates that the porous layer is predominantly terminated by CH_2 and CH_3. The strongest absorption in the 800–1,000 cm^{-1} range is attributed to the Si-C TO and LO phonon vibrations, but the Si-H signal expected at 2,100–2,200 cm^{-1} is not observed. This is because that the Si-H bond is readily oxidized but the C-H bond has stronger resistance to oxidation, thus remaining stable under ambient conditions.

Blue–green photoluminescence is observed from anodized *n*-type and *p*-type 6H-SiC [21]. The starting materials are 6H-SiC single crystals with $n_D - n_A = 2.5 \times 10^{17}$ cm^{-3} (*n*-type, N-doped) and $n_A - n_D = 8.3 \times 10^{17}$ cm^{-3} (*p*-type, Al-doped). The *p*-type samples are etched in darkness in a mixture of HF and ethanol (10–50 wt.% HF:ethanol = 1:1 in volume) at current densities of 20–60 mA cm^{-2}. The *n*-type SiC is etched under UV-light illumination at a constant anodization voltage of 3 V. SEM shows that the pore size and the pore spacing of the anodized *n*-type sample are on the order of 100 nm (Fig. 3.17). The anodized *p*-type sample shows very different dendritic structures with sizes as small as 10 nm. The *n*-type bulk wafer shows an interior defect-related luminescence band at 2.2 eV with a full width at half maximum of 0.5 eV (Fig. 3.18). In contrast, the porous sample shows a broader band at about 2.6 eV, whereas the initial luminescence at 2.2 eV is reduced substantially. The energy of this peak is below the bandgap of bulk 6H-SiC (2.86 eV), and there is no strong dependence on the illumination intensity and HF concentration. The PL spectrum of the porous *p*-type sample shows a strong peak at 2.5 eV similar to the *n*-type sample. The time-dependent PL measurement shows that the blue emission band has decay lifetime in the nanosecond and microsecond regime. It may arise from some surface defect, and no evidence of quantum size effect is observed. In another study of anodized porous *p*-type 6H-SiC, the transmission spectrum shows a very wide transmission edge which may be caused by surface states [22]. The porous sample shows room-temperature PL that is 20 times stronger than that of the bulk material. This PL is temperature independent.

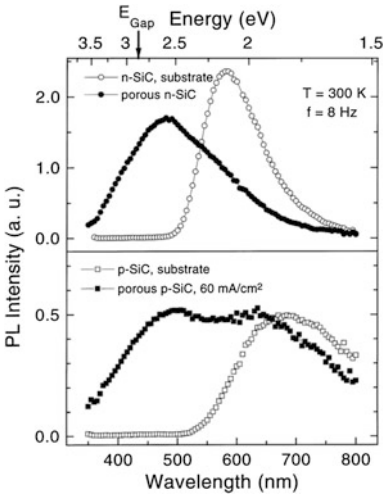

Fig. 3.18 Photoluminescence spectra of porous *n*-type and *p*-type SiC as well as initial bulk wafers. Reprinted with permission from [21]. Copyright 1997, Elsevier

The morphology and luminescence characteristics of porous *n*-type 6H-SiC have been investigated [23]. The Si-terminated *n*-type 6H-SiC (0001) surface is electrochemically etched by diluted HF (5 %) at a current density of 10–80 mA cm^{-2} under UV-light irradiation. Most of the porous samples show irregular triangular etch pits, and the porous nanocrystallites have an average diameter of about 25 nm (Fig. 3.19). In some porous samples, the triangular etch pits are oriented regularly in planes parallel to the surface of the wafer. The cathodoluminescence spectra of the porous layers show peaks in the UV region (Fig. 3.20) with energies above the bandgap of bulk 6H-SiC. The photoluminescence also shifts to blue in the porous SiC, although with a smaller shift. The

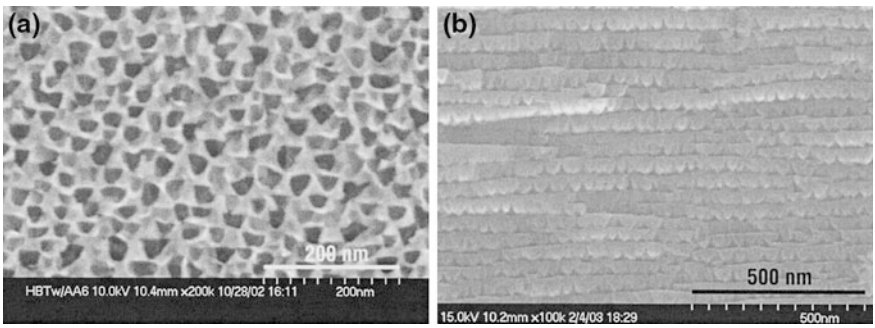

Fig. 3.19 Cross-sectional SEM images of two porous *n*-type 6H-SiC samples prepared by electrochemical etching at 35 mA/cm^2. One **a** has small and triangular nanocrystallites and etching pits, and the other **b** has parallel etching pits. Reprinted with permission from [23]. Copyright 2004, AIP Publishing LLC

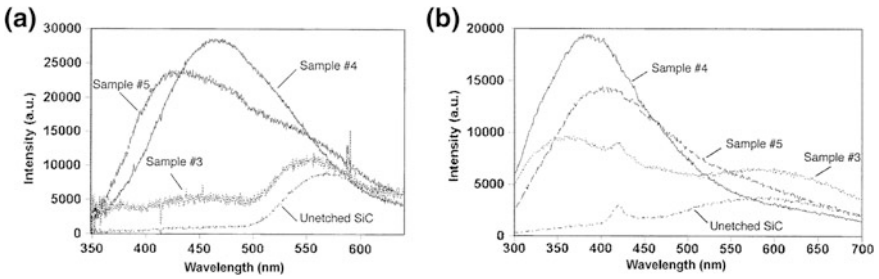

Fig. 3.20 Photoluminescence (**a**, excited at 325 nm), and cathodoluminescence (**b**) spectra of anodized porous 6H-SiC samples and unetched 6H-SiC wafer. Reprinted with permission from [23]. Copyright 2004, AIP Publishing LLC

Raman spectroscopy indicates that the evolution of the blue-shifted cathodoluminescence is strongly correlated with the presence of a broadened low-frequency shoulder on the polar A_1 LO phonon mode of 6H-SiC. The shoulder can be quantitatively described when surface mode scattering is taken into account, implying that surface states induced by etching account for the observed blue-shifted luminescence. An electroless approach is utilized to produce porous SiC [24]. Platinum is deposited on the *n*-type 4H- or 6H-SiC wafer prior to etching to serve a catalyst for the reduction of the oxidant $K_2S_2O_8$. The oxidant in combination with UV-light illumination injects holes into the valence band, and the holes then induce oxidation of the wafer. The resulting silicon dioxide is dissolved in hydrofluoric acid finally producing the porous structure.

The effects of current density on luminescence properties of anodized porous SiC have been investigated [25]. The *n*-type (nitrogen-doped) 6H-SiC crystals are electrochemically etched in an electrolyte under UV-light irradiation. The electrolyte contains HF, ethylene glycol (ethane-1, 2-diol), and hydrogen peroxide (H_2O_2) with a volume ratio of 2:1:1. A pulsed current with a duration of 10 ms and interval of 4 ms is applied during etching and the current densities are 10, 15, and 20 mA cm^{-2}. SEM (Fig. 3.21) shows that the morphology of the porous materials does not depend on the etching current density. The bulk 6H-SiC shows PL at about 410 nm (3.02 eV) at room temperature (Fig. 3.22). In contrast, the PL from the porous samples blue shifts slightly and the shift increases with current density thus showing sign of quantum confinement, but the full width at half maximum of the PL is rather narrow (13–22 nm) compared with that of conventionally observed PL in SiC at room temperature for unknown reason. Raman scattering reveals an intensity enhancement for all the phonon modes with increasing etching current density. The A_1 LO phonon in the porous samples shifts to red compared to the bulk materials (Fig. 3.23), and the red shift is larger for bigger etching current density. This may be related to the tensile stress in the porous samples.

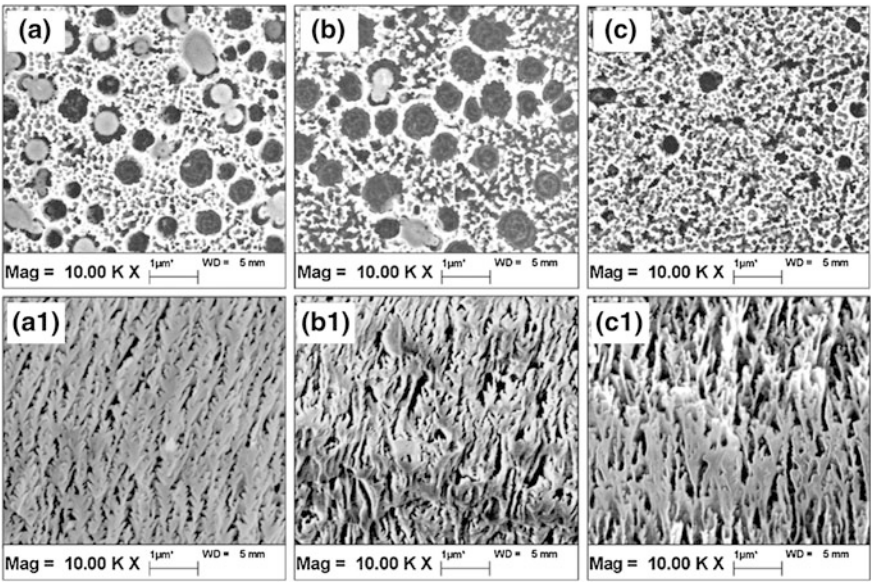

Fig. 3.21 Planar SEM micrographs of porous *n*-type 6H-SiC fabricated by UV-assisted electrochemical etching at current densities of **a** 10, **b** 15, and **c** 20 mA cm^{-2}. The cross-sectional images are shown in (**a1**), (**b1**), and (**c1**), respectively. Reprinted with permission from [25]. Copyright 2013, IOP Publishing

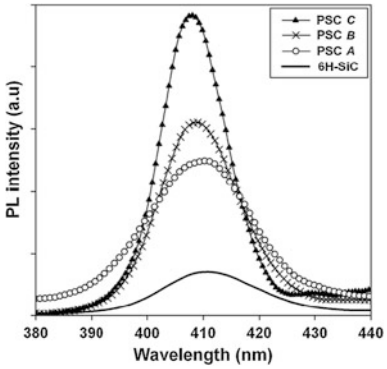

Fig. 3.22 Photoluminescence spectra of the porous 6H-SiC samples prepared at etching current densities of 10 mA cm^{-2} (*PSC A*), 15 mA cm^{-2} (*PSC B*), and 20 mA cm^{-2} (*PSC C*) as well as unetched 6H-SiC. Reprinted with permission from [25]. Copyright 2013, IOP Publishing

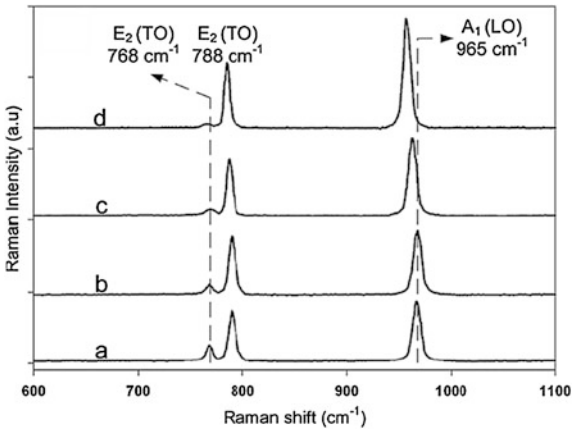

Fig. 3.23 Raman spectra of **a** unetched 6H-SiC and porous 6H-SiC prepared at etching current densities of **b** 10, **c** 15, and **d** 20 mA cm^{-2} in the 600–1,100 cm^{-1} range. Reprinted with permission from [25]. Copyright 2013, IOP Publishing

3.3 Sensing with Porous SiC

Porous SiC, like porous silicon, can be used in sensing applications. Because SiC is chemically inert, sensors composed of porous SiC are well suited for applications in a harsh environment. Preliminary studies indicate that porous SiC fabricated by electrochemical etching can be used to construct humidity sensors [26, 27]. The capacitance and resistance measured are used to derive the humidity in the environment. An NH_3 gas sensor based on porous SiC has also been produced [28], and preliminary data suggest that this sensor can detect changes in the ammonia concentration of about 1–2 ppm.

References

1. Brack K (1965) X-ray method for the determination of the polarity of SiC crystals. J Appl Phys 36:3560–3562
2. Shor JS, Osgood RM, Kurtz AD (1992) Photoelectrochemical conductivity selective etch stops for SiC. Appl Phys Lett 60:1001–1003
3. Shor JS, Grimberg I, Weiss B-Z, Kurtz AD (1993) Direct observation of porous SiC formed by anodization in HF. Appl Phys Lett 62:2836–2838
4. Shor JS, Osgood RM (1993) Broad-area photoelectrochemical etching of *n*-type beta-SiC. J Electrochem Soc 140:L123–L125
5. Shor JS, Kurtz AD (1994) Photoelectrochemical etching of 6H-SiC. J Electrochem Soc 141:778–781
6. Takazawa A, Tamura T, Yamada M (1993) Porous β-SiC fabrication by electrochemical anodization. Jpn J Appl Phys 32:3148–3149

7. Konstantinov AO, Harris CI, Janzén E (1994) Electrical properties and formation mechanism of porous silicon carbide. Appl Phys Lett 65:2699–2701
8. Shishkin Y, Choyke WJ, Devaty RP (2004) Photoelectrochemical etching of *n*-type 4H silicon carbide. J Appl Phys 96:2311–2322
9. Cambaz GZ, Yushin GN, Gogotsi Y, Lutsenko VG (2006) Anisotropic etching of SiC whiskers. Nano Lett 6:548–551
10. Sugita T, Hiramatsu K, Ikeda S, Matsumura M (2013) Fabrication of pores in a silicon carbide wafer by electrochemical etching with a glassy-carbon needle electrode. ACS Appl Mater Interfaces 5:2580–2584
11. Nakamura S, Kimoto T, Matsunami H, Tanaka S, Teraguchi N, Suzuki A (2000) Formation of periodic steps with a unit-cell height on 6H-SiC (0001) surface by HCl etching. Appl Phys Lett 76:3412–3414
12. Liu Y, Lin W, Lin Z, Xiu Y, Wong CP (2012) A combined etching process toward robust superhydrophobic SiC surfaces. Nanotechnology 23:255703
13. Jin G-Q, Guo X-Y (2003) Synthesis and characterization of mesoporous silicon carbide. Micropor Mesopor Mat 60:207–212
14. Sung I-K, Christian I-K, Mitchell M, Kim D-P, Kenis PJA (2005) Tailored macroporous SiCN and SiC structures for high-temperature fuel reforming. Adv Funct Mater 15:1336–1342
15. Lehmann V, Gösele U (1991) Porous silicon formation: a quantum wire effect. Appl Phys Lett 58:856–858
16. Canham LT (1990) Silicon quantum wire array fabrication by electrochemical and chemical dissolution of wafers. Appl Phys Lett 57:1046–1048
17. Matsumoto T, Takahashi J, Tamaki T, Futagi T, Mimura H, Kanemitsu Y (1994) Blue–green luminescence from porous silicon carbide. Appl Phys Lett 64:226–228
18. Shor JS, Bemis L, Kurtz AD, Grimberg I, Weiss BZ, MacMillian MF, Choyke WJ (1994) Characterization of nanocrystallites in porous *p*-type 6H-SiC. J Appl Phys 76:4045–4049
19. Konstantinov AO, Henry A, Harris CI, Janzén E (1995) Photoluminescence studies of porous silicon carbide. Appl Phys Lett 66:2250–2252
20. Petrova-Koch V, Sreseli O, Polisski G, Kovalev D, Muschik T, Koch F (1995) Luminescence enhancement by electrochemical etching of SiC(6H). Thin Solid Films 255:107–110
21. Jessensky O, Müller F, Gösele U (1997) Microstructure and photoluminescence of electrochemically etched porous SiC. Thin Solid Films 297:224–228
22. Kim S, Spanier JE, Herman IP (2000) Optical transmission, photoluminescence, and Raman scattering of porous SiC prepared from *p*-type 6H SiC. Jpn J Appl Phys 39:5875–5878
23. Rittenhouse TL, Bohn PW, Hossain TK, Adesida I, Lindesay J, Marcus A (2004) Surface-state origin for the blueshifted emission in anodically etched porous silicon carbide. J Appl Phys 95:490–496
24. Rittenhouse TL, Bohn PW, Adesida I (2003) Structural and spectroscopic characterization of porous silicon carbide formed by Pt-assisted electroless chemical etching. Solid State Commun 126:245–250
25. Naderi N, Hashim MR, Saron KMA, Rouhi J (2013) Enhanced optical performance of electrochemically etched porous silicon carbide. Semicond Sci Technol 28:025011
26. Connolly EJ, O'Halloran GM, Pham HTM, Sarro PM, French PJ (2002) Comparison of porous silicon, porous polysilicon and porous silicon carbide as materials for humidity sensing applications. Sensor Actuat A 99:25–30
27. Connolly EJ, Pham HTM, Groeneweg J, Sarro PM, French PJ (2004) Relative humidity sensors using porous SiC membranes and Al electrodes. Sensor Actuat B 100:216–220
28. Connolly EJ, Timmer B, Pham HTM, Groeneweg J, Sarro PM, Olthuis W, French PJ (2005) A porous SiC ammonia sensor. Sensor Actuat B 109:44–46

Chapter 4
Separate SiC Nanoparticles

Silicon carbide nanoparticles generally refer to particles about 1–100 nm in size and single crystal in most cases. Silicon carbide nanocrystals smaller than 10 nm are also called SiC quantum dots; in this size regime, on account of the strong spatial confinement of the carriers, SiC nanocrystals exhibit obvious quantum size effects, especially the quantum confinement effect. As a result, the energy gap of the silicon carbide nanocrystals widens and luminescence shifts toward smaller wavelengths (blueshift) gradually as they become smaller. In addition, the quantum yield may be improved by several orders of magnitude relative to that of the bulk materials. Since the dimensions of the nanoparticles are very small, the surface strongly affects their properties. Silicon carbide is a compound semiconductor, and its surface has multiple bonding structures involving Si, C, O, H, and other atoms and so a variety of surface defects can form, consequently resulting in complex luminescence properties. In this chapter, the preparation methods, electronic structures, luminescence properties, and application of silicon carbide nanoparticles are discussed.

4.1 Fabrication and Luminescence Properties

Generally, silicon carbide nanoparticles are synthesized by vapor phase or solution-based chemical reactions. Chemical etching of large silicon carbide single crystals combined with ultrasonic dispersion is another important fabrication method. The luminescence properties of these synthesized SiC nanoparticles have been intensively studied. In general, recombination of conduction band electrons and valence band holes in the interior is an important luminescence mechanism in SiC nanocrystals, whereas recombination of electron–hole pairs with either or both carriers (electrons and holes) located at surface defects is another important luminescence mechanism. The former mechanism shows the size dependence of the luminescence peak wavelength, and the luminescence obeys the quantum

J. Fan and P.K. Chu, *Silicon Carbide Nanostructures*,
Engineering Materials and Processes, DOI 10.1007/978-3-319-08726-9_4

confinement effect. In contrast, defects associated luminescence is expected to show a relatively fixed emission wavelength. These two types of luminescence compete with each other.

4.1.1 Chemical Vapor Synthesis

In 1983, a radiofrequency plasma tube was designed to overcome the problem of overheating in the conventional plasma systems [1]. Using this system, ultrafine and ultrapure silicon carbide powders can be synthesized by radial injection of silane, methane, and hydrogen into the tail flame of the plasma. The composition of the silicon carbide powder varies over a wide range from excess silicon to excess carbon although β-SiC is always the dominant constituent in the product as confirmed by X-ray diffraction. Transmission electron microscopy shows that the synthesized SiC particles are 10–20 nm in size (Fig. 4.1), and XRD reveals a domain size of 7.5 nm and crystal structure of β-SiC. Hypersonic plasma particle deposition has been employed to synthesize silicon carbide coatings on molybdenum substrates [2]. The $SiCl_4$ and CH_4 vapor is injected into the Ar–H_2 plasma as the precursors in deposition. SEM, TEM, and XRD indicate that the silicon carbide coatings are partially consolidated having a layered morphology with all the layers containing nanostructured SiC grains of around 30 nm (Fig. 4.2). Aerosol probe measurement also demonstrates that the small particle residence time (about 50 μs) minimizes particle agglomeration. XRD and FTIR show that the silicon carbide coatings are amorphous (Fig. 4.2) and hydrogenated, and XPS indicates that oxidation of the deposit is limited to the surface (Fig. 4.3).

β-SiC powders containing nanocrystallites smaller than 10 nm are synthesized by thermal decomposition of silicon organic precursors at reduced pressure [3]. The optimal conditions for small grain and particle size, low agglomeration, and high crystallinity are as follows: tetramethylsilane [$Si(CH_3)_4$] precursor, total pressure below 1,000 kPa, precursor partial pressure below 660 Pa, and reaction temperature above 1,400 K. Decomposition of tetramethylsilane at lower

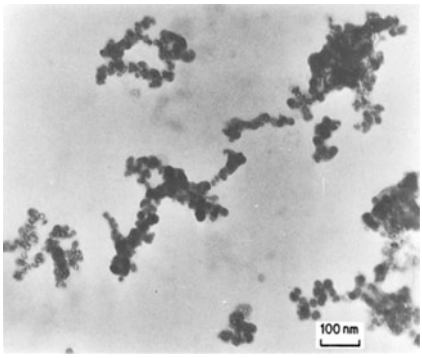

Fig. 4.1 TEM micrograph of the silicon carbide powder. Reprinted with permission from [1]. Copyright 1983, Springer Science and Business Media

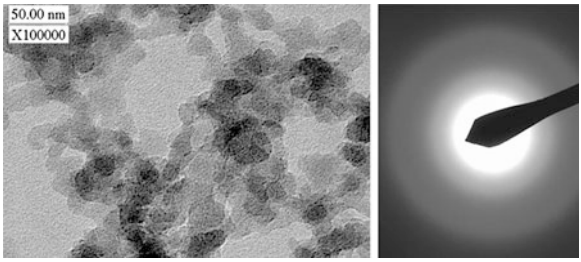

Fig. 4.2 TEM image of the silicon carbide particles collected by hypersonic impacting. Reprinted with permission from [2]. Copyright 1998, Elsevier

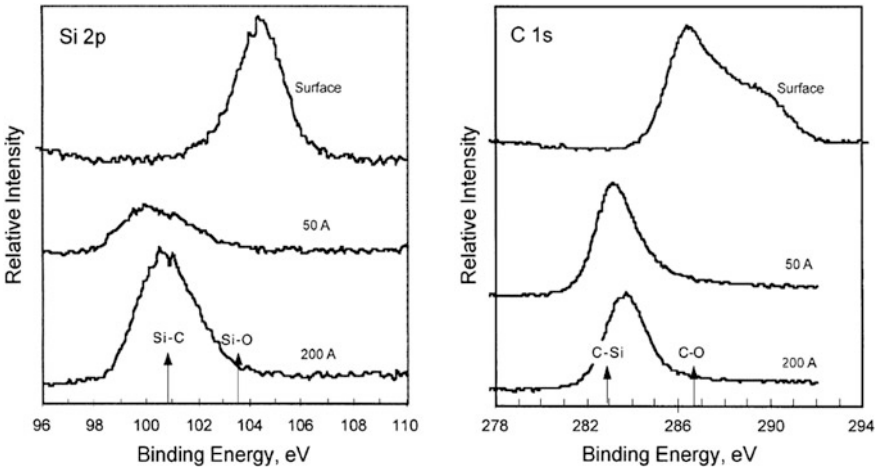

Fig. 4.3 XPS spectra of the Si 2p and C 1s peaks as a function of depth. The proportion of oxygen-bonded silicon and carbon atoms decreases with increasing depth. Reprinted with permission from [2]. Copyright 1998, Elsevier

temperature and lower pressure can also produce SiC nanoparticles [4]. By employing a microwave plasma reactor in the synthesis, the particles are amorphous with size between 4 and 6 nm. The ratio of carbon and silicon can be adjusted by addition of hydrogen.

Laser pyrolysis is a popular method to prepare silicon carbide nanoparticles. Pulsed CO_2 laser-induced decomposition of a gaseous mixture of SiH_4 and C_2H_2 with varying concentrations of the hydrocarbon is used to produce silicon and silicon carbide nanoparticles [5]. Silicon carbide nanoclusters with diameters between 3 and 3.5 nm are deposited on various substrates, but significantly larger nanoparticles are collected from the exhaust line of the reactor. FTIR and XRD reveal that the concentration of SiC in the nanoparticles increases with increasing acetylene flow rates. Besides SiC nanoparticles, there is a substantial portion of free crystalline silicon in the product when a stoichiometric SiH_4/C_2H_2 mixture is used in the synthesis. Pure

SiC nanoparticles can only be synthesized with excess hydrocarbon, and XRD reveals that the SiC nanoparticles comprise crystalline β-SiC.

The properties of the SiC nanocrystallites synthesized by laser pyrolysis have been determined. The nonlinear optical property of the composite materials containing SiC nanocrystallites embedded in photopolymer olygoetheracryalte is investigated [6]. The maximum photoinduced second-harmonic generation for 0.95 SiC hexagonality is 10.1 pm/V in the χ_{222} tensor component. The main contribution is from the guest/host interface. The hexagonal SiC components play a key role in the photoinduced nonlinear optical effect. The electrical and dielectric properties of the SiC nanopowders are modified drastically by annealing at 1,500 °C [7]. The materials exhibit a quasi-insulating characteristic and large effective dielectric constant below this temperature. On the contrary, significant conductivity and a smaller dielectric constant are observed from the materials annealed at a higher temperature. The interface effect is suggested to play a key role in the observed conductivity and dielectric characteristic. The electro-optic phenomenon in electrically poled films based on large-size SiC nanocrystallites as chromophores and polymethyl-methacrylate as host matrix is investigated [8]. For SiC nanocrystallite concentrations between 1 and 3 wt%, the largest effective linear electro-optic coefficient is measured to be 26 pm/V at 0.633 μm. Therefore, polarization at the SiC/polymer boundary plays a key role in the electro-optic phenomenon. Electron paramagnetic resonance is conducted on the core/shell nanocomposites, that is, the SiC nanoparticles encapsulated by conducting polyaniline [9]. Temperature-dependent electron paramagnetic resonance measurement reveals paramagnetic susceptibilities with Curie–Weiss-like features and thermally activated spins in the nanocomposites.

The photoluminescence (PL) properties of SiC nanoparticles are investigated by Raman scattering [10]. The nanoparticles are synthesized by CO_2 laser pyrolysis of a gaseous mixture of silane and acetylene. TEM reveals that SiC particles have a homogeneous composition with a narrow size range of around 10 nm (Fig. 4.4). The high-resolution TEM images reveal that each particle is composed of several crystallites with an average diameter of 2.5 nm, and these crystallites are embedded in an amorphous SiC matrix. Nuclear magnetic resonance indicates the coexistence of amorphous, hexagonal, and cubic SiC structures in the SiC nanoparticles. The Raman spectra obtained from the as-prepared sample SiC229 (Fig. 4.5) and oxidized ones are dominated by broad PL bands. Besides the Si–C and C vibrational signals, the Raman spectrum is dominated by a broadband between 514 and 800 nm attributed to PL. The sample oxidized at the highest temperature exhibits the most intense PL. The infrared transmission spectra (Fig. 4.6) reveal the existence of Si–Si and Si–O bonds on the particle surfaces. Surprisingly, two samples with similar particle sizes show different PL response, and the sample with a larger proportion of the amorphous layer exhibits stronger PL. In addition, after annealing in argon at a temperature low enough to preserve the average particle size but high enough to improve the crystalline structure, drastically diminished PL is observed. These observations suggest that the visible PL originates from the amorphous portion of the SiC nanoparticles and the oxygen-related surface region.

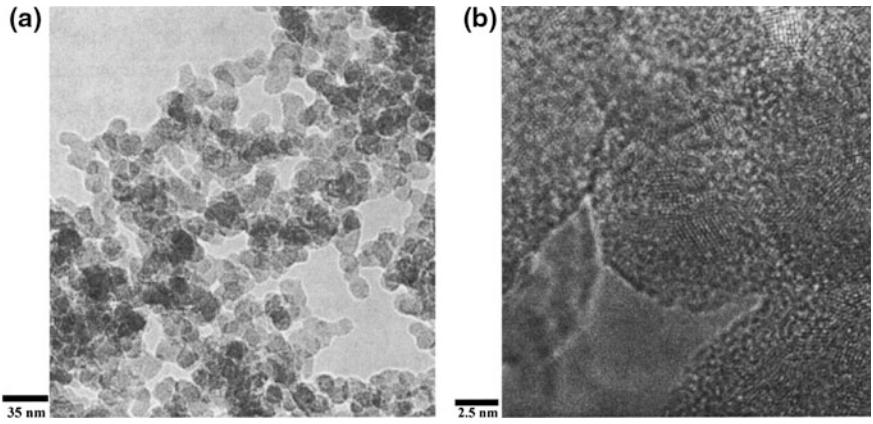

Fig. 4.4 TEM images of the SiC229 sample: *low-resolution image* **a** revealing the particle diameter of about 10 nm and *high-resolution image* **b** showing the amorphous background with a nanocrystallite diameter of about 2–3 nm. Reprinted with permission from [10]. Copyright 2002, American Physical Society

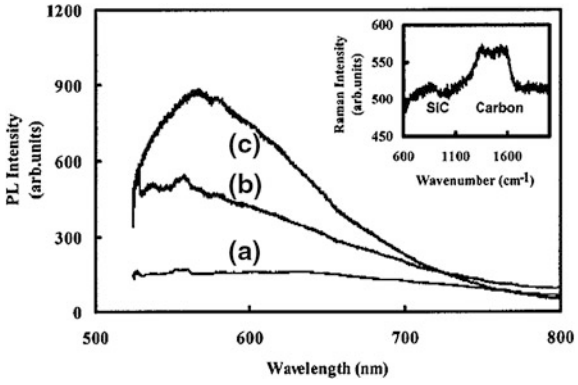

Fig. 4.5 Broad photoluminescence bands in the Raman spectra of SiC229 samples: **a** as-prepared sample and **b**, **c** samples heated in oxygen at 440 °C (**b**) and 970 °C (**c**). The intensity is normalized by weighting factors of 1/3 (**a**), 1 (**b**), and 1/10 (**c**). The *inset* shows the Raman spectrum of the as-prepared SiC229 sample exhibiting vibrational bands of C and SiC. Reprinted with permission from [10] Copyright 2002, American Physical Society

Raman scattering spectra are acquired from laser-synthesized SiC nanoparticles with different size and structure [11] revealing the enhanced vibrational density of states. The numerically simulated spectrum shape shows agreement with the measured spectra for amorphous clusters. The major contribution to the vibrational density of states is the amorphous region in the SiC nanoparticles, and it depends on the nanoparticle size. Photon correlation spectroscopy reveals the dispersion behavior of these SiC nanoparticles suspended in water [12]. The SiC suspension

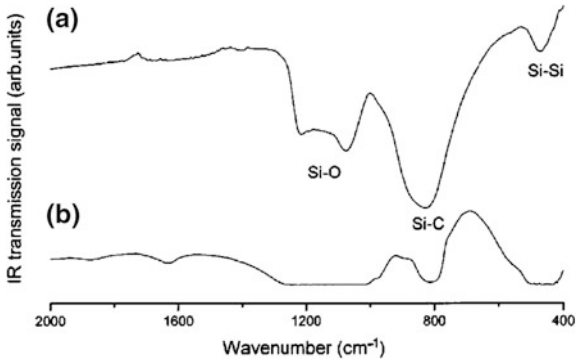

Fig. 4.6 Infrared transmission spectra of the SiC229 sample annealed for 1 h in an oxygen atmosphere at 440 °C (**a**) and 970 °C (**b**). Reprinted with permission from [10] Copyright 2002, American Physical Society

consisting of stoichiometric or silicon-rich nanopowders is readily dispersed in water and stable with time. Ninety-five percentage of the nanoparticles are isolated, indicating the crucial role of the oxidized layer covering the grain of the silicon-rich samples. The carbon-rich powder cannot readily disperse in water because of the inert graphitic carbon layer on the grain surface.

The flame temperature during the synthesis of the SiC nanoparticles by laser pyrolysis using the mixture of SiH_4 and C_2H_2 has a strong influence on the composition of the final product [13]. For the same C/Si atomic ratio in the gas phase, the C/Si ratio in the synthesized powder increases from 0.7 at 875 °C to 1.02 at 1,100 °C, suggesting the effect of C_2H_2 dissociation on particle growth. Enhanced crystallization is observed with increasing reaction temperature by X-ray diffraction, and transmission electron microscopy discloses the presence of 10-nm grains for all laser power (or flame temperature). These grains are mostly amorphous if the synthesis temperature is low, but they contain some crystallites with a mean size of 2 nm, and the quantity increases with temperature as well.

4.1.2 Electrochemical/Chemical Etching and Quantum Confinement

4.1.2.1 3C-SiC Nanocrystals and Quantum Confinement

An experimental protocol to prepare colloidal Si nanoparticles has been developed [14]. The *n*- or *p*-type Si crystals are electrochemically etched in an aqueous mixture of HF and 95 % ethanol (1:1 by volume) to generate porous Si that is then ultrasonically dispersed in water or other solvents to form a suspension with fine Si particles. Transmission electron microscopy reveals that these suspended Si particles are crystalline with sizes ranging from many micrometers to a few nanometers. The Si nanoparticles exhibit luminescence bearing the quantum confinement effect. A similar procedure is employed to fabricate cubic SiC nanocrystals [15]. The polycrystalline 3C-SiC wafer is electrochemically etched in HF and ethanol

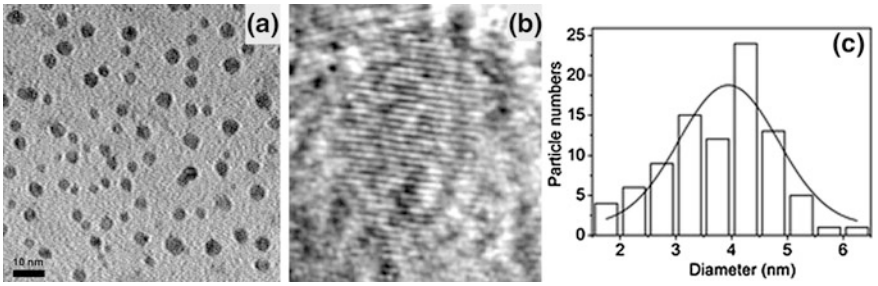

Fig. 4.7 **a** TEM image of the 3C-SiC nanocrystals. **b** HRTEM image of one typical particle. The lattice fringes are assigned to the (111) planes of 3C-SiC. **c** Particle size distribution. The *curve* is the Gaussian fit showing the most probable size of 3.9 nm. Reprinted with permission from [15]. Copyright 2005, American Physical Society

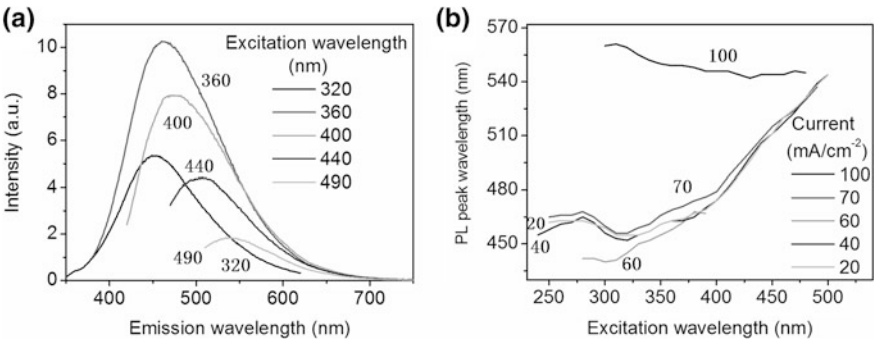

Fig. 4.8 **a** PL spectra of the 3C-SiC nanocrystal aqueous solution obtained at an etching current density of 40 mA/cm^2 excited at different wavelengths. **b** PL maximum wavelength versus excitation wavelength determined from five 3C-SiC nanocrystal aqueous solutions obtained at different etching current densities. Reprinted with permission from [15] Copyright 2005, American Physical Society

(HF:C_2H_5OH = 2:1 by volume) under UV light illumination. The etching current densities are 100, 70, 60, 40, and 20 mA/cm^2. Subsequent sonication in water yields a solution with the suspended SiC nanoparticles which are nearly spherical with diameters varying from 1 to 7 nm (Fig. 4.7). The high-resolution TEM images disclose that these particles are crystalline retaining the crystal structure of bulk 3C-SiC. The colloidal 3C-SiC nanocrystals exhibit strong PL (Fig. 4.8) visible to the naked eyes (Fig. 4.9). The PL spectrum is smooth and shows only one peak implying a single dominant luminescence mechanism. The PL peak shifts to red as the excitation photon energy is reduced. Regardless of the etching conditions, the PL peak obtained from each SiC solution finally reaches a threshold of around 550 nm (2.25 eV) which is close to the indirect bandgap of bulk 3C-SiC at room temperature (2.2 eV) [16], and PL cannot be observed if excited by light with photon energy below the threshold. The PL characteristics suggest the quantum confinement effect and that PL originates from the interband transition in the nanocrystals.

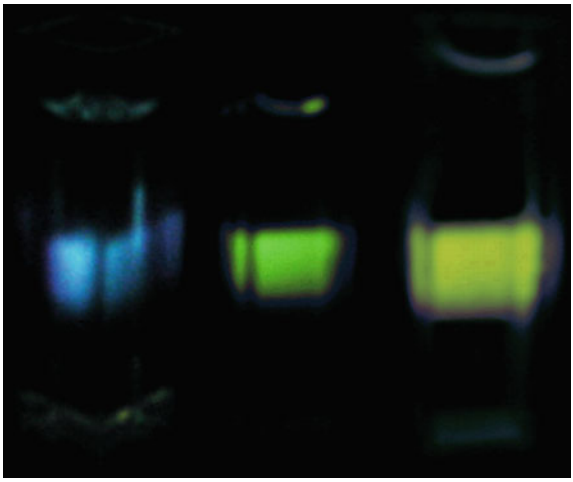

Fig. 4.9 Luminescence image of the 3C-SiC nanocrystal aqueous solution excited by 320, 400, and 450 nm light (from *left* to *right*), respectively. Reprinted with permission from [15] Copyright 2005, American Physical Society

The monotonic PL redshift observed from colloidal 3C-SiC nanocrystals with increasing excitation wavelength can be explained by quantum confinement by taking into account the broad size distribution of the nanocrystals. Figure 4.10 depicts the schematic of the redshift mechanism [17]. According to the quantum confinement effect, the smaller the nanocrystal, the wider is the energy gap and as a result, in a SiC colloid solution, the PL is a superposition of all the emission bands from individual SiC nanocrystals in the solution. When the excitation photon energy decreases gradually (excitation wavelength increases), the threshold size (lower size limit) of excitable nanocrystals (shaded area in Fig. 4.10) increases accordingly, and thus, more small nanocrystals (blank area in Fig. 4.10) cannot be excited, leading to a gradual redshift of the maximum of the superposed PL spectrum. The 3C-SiC nanocrystals suspended in different solvents show similar luminescence behavior (Fig. 4.11) with only a small solvent dependence, further supporting the interband transition mechanism.

Luminescence from Si nanocrystals either in porous Si or as separated Si nanocrystals exhibits the quantum confinement effect [18, 19]. However, no obvious evidence of quantum confinement effect was observed during early studies involving porous SiC and various types of embedded SiC nanocrystals [20]. There are three reasons. First of all, although porous SiC has many nanoparticles and nanowires on the surface, these nanostructures are not separated but rather connected to the SiC substrate to form a single crystal, and hence, electrons and holes undergoing recombination are not confined to the individual nanoparticle/nanowire. Secondly, the nanoparticles and nanowires on the porous SiC surface generally have dimensions of over ten nanometers and in this size regime, the quantum confinement effect becomes rather weak. Thirdly, although some embedded SiC nanoparticles may be as small as several nanometers, surface defects may quench the quantum-confinement luminescence by offering non-radiative recombination pathways or dominate in luminescence similar to the role played by Si=O surface defect in porous Si. In

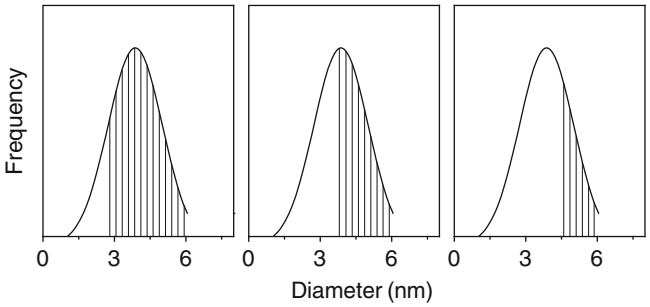

Fig. 4.10 Schematic showing the mechanism of the PL peak redshift with increasing excitation wavelength. The shaded area represents the size range of the excitable particles for a specific excitation wavelength. The excitation wavelength increases from *left* to *right*. Reprinted with permission from [17]. Copyright 2006, AIP Publishing LLC

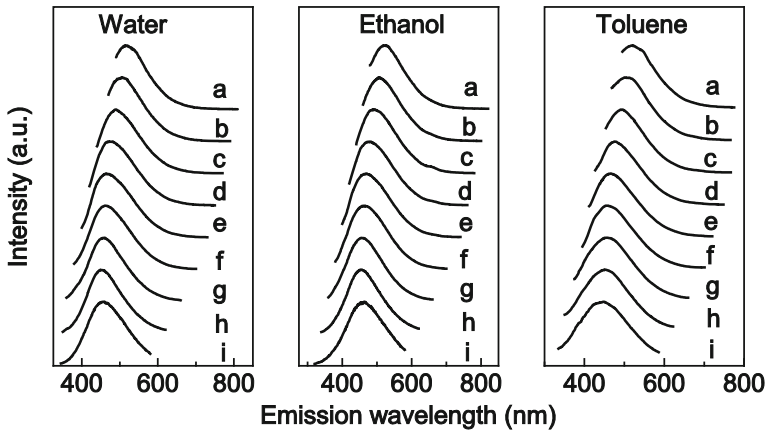

Fig. 4.11 (*a–i*) Normalized PL spectra of 3C-SiC nanocrystals in different solvents excited by 460, 440, 420, 400, 380, 360, 340, 320, and 300 nm light (from *a* to *i*), respectively. Reprinted with permission from [17]. Copyright 2006, AIP Publishing LLC

contrast, the separated ultrasmall colloidal SiC nanocrystals are ideal structures to show the quantum confinement effect. SEM reveals that the main structure (within the SEM resolution limit) on the surface of porous SiC consists of necklace-like wires with typical diameters around tens of nanometers (Fig. 4.12) [21]. Therefore, the ultrasonic treatment plays a key role in producing SiC nanocrystals only a couple of nanometers in size. The porous SiC shown in Fig. 4.12 shows a different reflectance spectrum compared to the pristine SiC (Fig. 4.13). The infrared reflectance spectrum of bulk polycrystalline 3C-SiC contains a reststrahl band in the range of 750–1,000 cm^{-1}, which is the typical spectrum of bulk 3C-SiC. The rise in the reststrahl peak occurs near the bulk transverse optical (TO) phonon frequency at 796 cm^{-1}, and the sharp decrease occurs near the bulk longitudinal optical (LO)

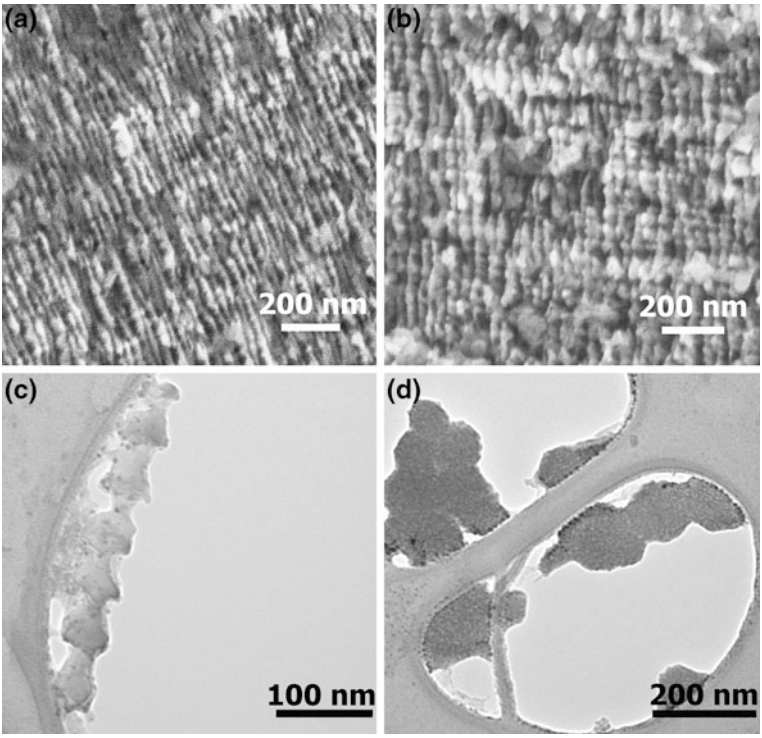

Fig. 4.12 **a**, **b** SEM micrographs of porous polycrystalline 3C-SiC. **c**, **d** TEM images showing several residual 3C-SiC nanowires after ultrasonic treatment, along with 3C-SiC nanocrystals (*small dots*). Reprinted with permission from [21]. Copyright 2009, AIP Publishing LLC

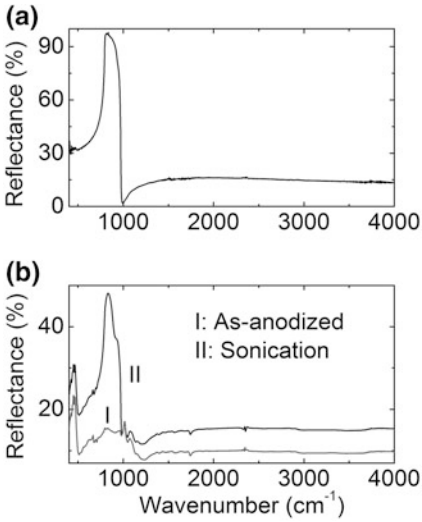

Fig. 4.13 Infrared reflectance spectra of **a** bulk polycrystalline 3C-SiC and **b** as-prepared (*curve I*) and sonicated (*curve II*) porous polycrystalline 3C-SiC. Reprinted with permission from [21]. Copyright 2009, AIP Publishing LLC

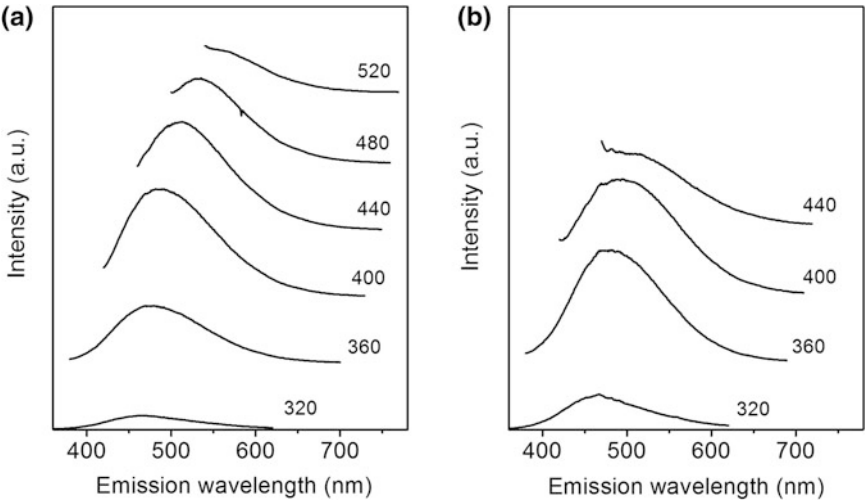

Fig. 4.14 PL spectra of the **a** as-prepared and **b** stored (for over 7 months) 3C-SiC nanocrystal aqueous solution excited at different wavelengths. Reprinted with permission from [22]. Copyright 2006, Elsevier

phonon frequency at 972 cm^{-1}. The as-anodized porous materials show significantly reduced intensity, especially the reststrahl band, and this variation is caused by the rough surface of the porous SiC. After sonication, the original reflectance spectrum is recovered partially due to breaking of the nanowires on the porous surface.

The colloidal 3C-SiC nanocrystals have high stability when they are dispersed in water. After storage in air for over 7 months, some of the larger 3C-SiC crystallites aggregate and precipitate, whereas the smaller ones remain dispersed in water retaining the primary luminescence properties [22]. However, the PL intensity decreases and the PL peak becomes narrower (Fig. 4.14). Smaller and stable SiC nanocrystals continue to be dispersed and show luminescence for more than a couple of years. This virtue renders the benign 3C-SiC nanocrystals superior micro-emitters, especially in biological and medical applications.

The UV–visible light absorption and carrier recombination properties of colloidal 3C-SiC quantum dots have been investigated [23]. The 3C-SiC quantum dots with an average diameter of 4 nm have an indirect energy gap (Fig. 4.15), and the main portion of the absorption spectrum obeys the following equation which describes absorption of indirect bandgap semiconductors:

$$\alpha = A(h\nu - E_g)^2, \tag{4.1}$$

where α is the absorption coefficient, ν is the photon frequency, h is Planck's constant, E_g is the energy gap of the crystallite, and A is a constant. The energy gap obtained by extrapolation of the fitted curve is significantly larger than the bandgap of bulk 3C-SiC, indicating strong quantum confinement. In contrast,

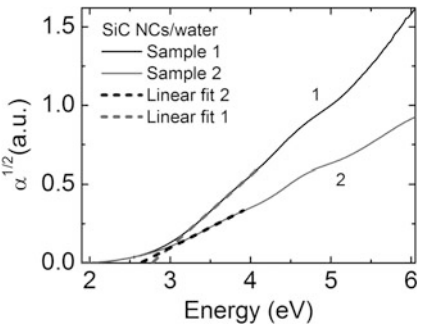

Fig. 4.15 UV–visible absorption spectra of the colloidal 3C-SiC nanocrystals in the aqueous solution obtained from two different samples. The square root of the absorbance is plotted against photon energy. The *broken lines* are the linear fits of the major portion of the spectra, and the extrapolations yield an *x*-intercept of 2.78/2.63 eV for the respective sample. Reprinted with permission from [23]. Copyright 2010, AIP Publishing LLC

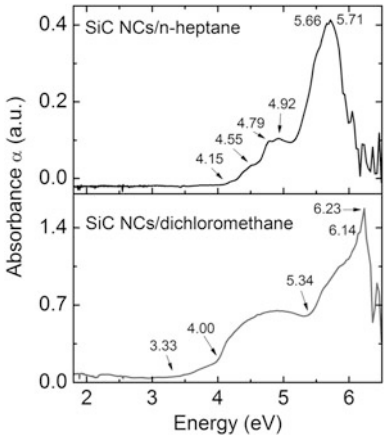

Fig. 4.16 UV–visible absorption spectra of the colloidal 3C-SiC nanocrystals in *n*-heptane and dichloromethane. The feigned peaks beyond 5.71 eV (*upper curve*) and 6.23 eV (*lower curve*) represent experimental errors. Reprinted with permission from [23]. Copyright 2010, AIP Publishing LLC

ultrasmall SiC quantum dots 1 nm in size produce discrete and sharp absorption peaks (Fig. 4.16). Unlike the quasi-continuous distribution of energy levels in bulk silicon carbide, the ultrasmall SiC quantum dots possess discrete energy levels, and this feature lies between those of bulk single crystals and molecules. The discrete peaks also imply that these SiC quantum dots have a narrow size distribution such that the discrete absorption features are not smeared. The time-resolved PL spectra of the colloidal SiC nanocrystals (Fig. 4.17) can be fitted by the following triple-exponential function:

$$I(t) = A_1 e^{-t/\tau_1} + A_2 e^{-t/\tau_2} + A_3 e^{-t/\tau_3}, \tag{4.2}$$

where τ_i and A_i ($i = 1, 2, 3$) represent the lifetime and weight factor of each component. The three components have lifetimes on the order of nanoseconds to

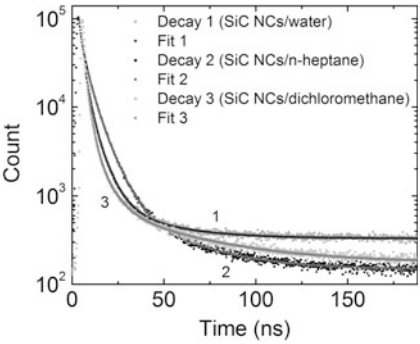

Fig. 4.17 Time-resolved photoluminescence spectra of the 3C-SiC nanocrystals in water, *n*-heptane, and dichloromethane solvents excited by 280 nm light and monitored at 450, 420, and 410 nm, respectively. The *solid lines* are triple-exponential fits with lifetimes and relative amplitudes of [2.6 ns (0.34), 6.7 ns (0.51), 28.9 ns (0.15)], [3.5 ns (0.22), 7.7 ns (0.62), 31.8 ns (0.16)], and [2.2 ns (0.30), 7.3 ns (0.36), 44.7 ns (0.34)], respectively. Reprinted with permission from [23]. Copyright 2010, AIP Publishing LLC

tens of nanoseconds and show dependence on the particle size. The relative amplitude (R_i) of each component can be evaluated by the following equation:

$$R_i = \frac{\int_0^\infty \left(A_i e^{-t/\tau_i}\right) \mathrm{d}t}{\sum_{j=1}^{3} \int_0^\infty \left(A_j e^{-t/\tau_j}\right) \mathrm{d}t} = \frac{A_i \tau_i}{\sum_{j=1}^{3} \left(A_j \tau_j\right)} \quad (i = 1, 2, 3). \tag{4.3}$$

Besides electrochemical etching, direct chemical etching can produce porous SiC and SiC nanocrystals after ultrasonic treatment. The 3C-SiC powder with a micrometer size is etched in a mixture of nitric acid and hydrofluoric acid (65 % HNO_3 :40 % HF = 1:3 in volume) at 100 °C [24]. Nitric acid oxidizes the surface of the SiC crystal into SiO_2, and then, hydrofluoric acid etches the SiO_2, leaving the porous SiC on the surface. Subsequent sonication in ethanol breaks the porous film leading to individual SiC nanocrystals dispersed in ethanol. TEM reveals that the nanocrystals are spherical with an average size of 6.5 nm (Fig. 4.18). The PL peak from the 3C-SiC colloids shifts from 420 to 512 nm as the excitation wavelength increases.

4.1.2.2 Surface Structure of 3C-SiC Nanocrystals

The surface structure of 3C-SiC quantum dots is important because it determines the surface defect states and affects the luminescence properties. 3C-SiC nanocrystals prepared by electrochemical etching and ultrasonic treatment exhibit simple infrared absorption features [25]. Figure 4.19a shows the infrared transmission spectra of 3C-SiC crystallites with different sizes. The strongest absorption at around 738 cm^{-1} is assigned to the TO phonon mode of SiC. The smaller wavenumber with respect to that of bulk SiC (796 cm^{-1}) is due to the phonon confinement effect, and

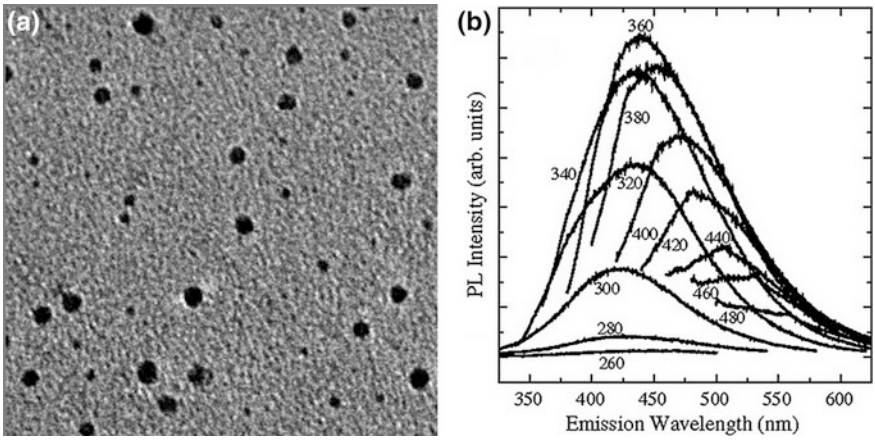

Fig. 4.18 **a** TEM image of the SiC nanoparticles produced by chemical etching followed by sonication. **b** PL spectra of the SiC colloids in ethanol under different excitations. Reprinted with permission from [24]. Copyright 2007, IOP Publishing

the large spectrum width is attributed to the dispersed particle size. The constant and second strongest peak at 482 cm^{-1} is ascribed to the Si–Si bond caused by surface reconstruction of the SiC nanocrystals. The absorption peaks at 1,084 and 1,124 cm^{-1} are assigned to Si–O–Si, C–O–C, or Si–O–C with 1,084 cm^{-1} likely due to Si–O–Si and 1,124 cm^{-1} from C–O–C. The weak absorption peaks at 1,628 and 3,150–3,700 cm^{-1} originate from residual water molecules. The Si–H signal expected at 2,100–2,250 cm^{-1} is not detected. This is different from as-prepared Si nanocrystals whose surface is mainly terminated by hydrogen atoms, but unstable, and oxidization occurs readily after storage in air for a few minutes. This changes the luminescence mechanism from quantum confinement to surface defect (probably Si=O) states related [26]. In contrast, no Si=O defect luminescence (at around 590 nm or 2.1 eV) is observed from the SiC nanocrystals, suggesting that the Si–O–Si bond can form more readily than Si=O on the SiC surface. The polar Si–O–Si surface explains the hydrophilicity of the SiC nanocrystals since the hydrogen bonds can form readily between the bridged oxygen atom and surrounding water molecule. Concerning the 2-day-old SiC nanocrystal solution, the absorption peak at 482 cm^{-1} diminishes, while those at 1,084 and 1,124 cm^{-1} become more intense due to oxidation of Si–Si into Si–O–Si. The 2-month-old sample exhibits spectral features (Fig. 4.19b) similar to those of the fresh sample confirming high surface stability. After ultrasonic treatment, the peak at 482 cm^{-1} is dramatically enhanced, but the 1,084 and 1,124 cm^{-1} peaks diminish. This is caused by breakage of some bridged bonds and recovery of Si–Si bonds. With respect to sample B which contains many micrometer-sized crystallites, the absorption peak of the LO phonon signal at 948 cm^{-1} appears (Fig. 4.19a). This peak shifts to smaller wavenumbers relative to the bulk value (972 cm^{-1}) due to the phonon confinement effect and other surface effects. The peak at 482 cm^{-1} still exists showing Si–Si surface reconstruction. The

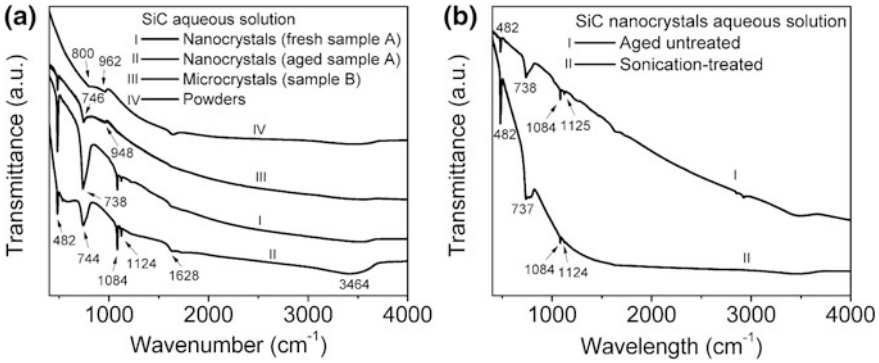

Fig. 4.19 **a** Infrared transmission spectra of the 3C-SiC crystallites embedded in KBr pellets obtained from the SiC aqueous solutions containing quantum dots with an average size of 4 nm (sample *A*), crystallites with sizes ranging from tens of nanometers to many micrometers (sample *B*), and powders large enough to be visible to the naked eyes, respectively. All the spectra are acquired right after evaporation of water from the SiC/KBr pellet. **b** Infrared transmission spectra of sample *A* after storage in air for 2 months with and without sonication before the measurement. Reprinted with permission from [25]. Copyright 2011, Elsevier

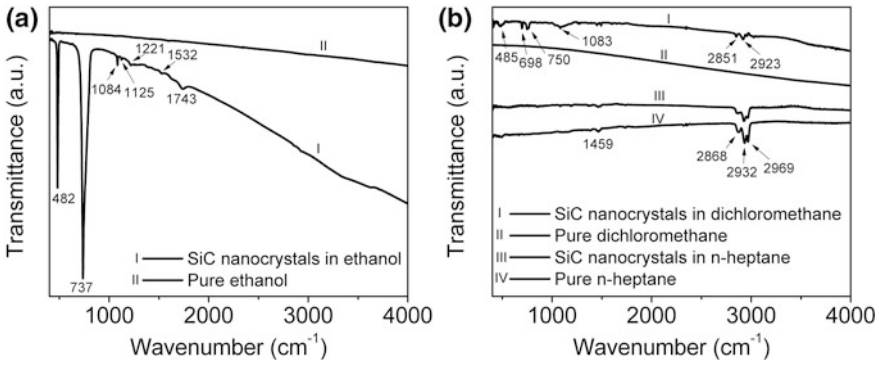

Fig. 4.20 Infrared transmission spectra of the 3C-SiC nanocrystals in KBr pellets obtained from **a** ethanol and **b** dichloromethane or *n*-heptane solutions, respectively. The spectra of the solvents are also shown. All the spectra are obtained right after evaporation of the solvent from the SiC/KBr pellet. Reprinted with permission from [25]. Copyright 2011, Elsevier

absorption peaks at 1,084 and 1,124 cm^{-1} are not observed due to the reduced surface-atom proportion in the micrometer-size crystallites relative to the nanocrystals. The TO and LO phonon modes of the larger pristine SiC powders are observed at 800 and 962 cm^{-1}, respectively, closer to the bulk values. As expected, the surface vibrational modes are absent. The absence of the LO phonon mode in SiC quantum dots indicates that this mode is inactive on this scale possibly caused by the breakdown of the displacement symmetry. The 3C-SiC nanocrystals in ethanol show similar infrared absorption to that of the nanocrystals suspended in water

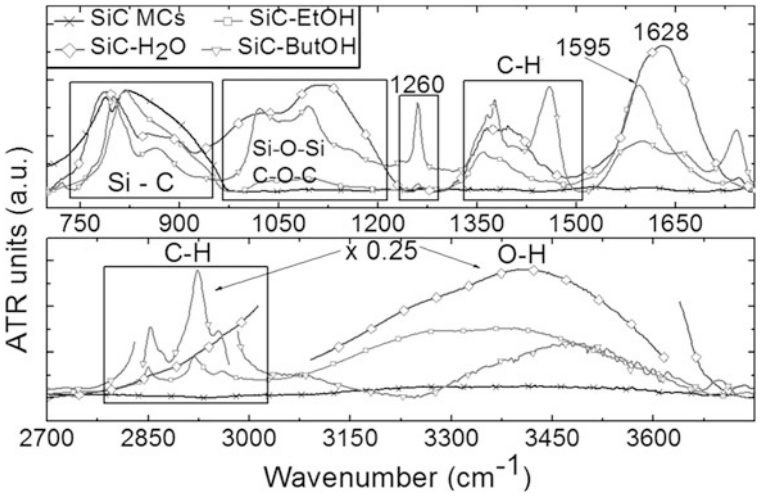

Fig. 4.21 Attenuated internal reflection infrared spectra of the SiC microcrystals (*MCs*) and SiC nanocrystals in ethanol (*EtOH*), water (H_2O), and *n*-butanol (*ButOH*). The spectra are recorded on a multibounce germanium crystal after evaporation of the solvent. Reprinted with permission from [27]. Copyright 2011, AIP Publishing LLC

(Fig. 4.20a), except that the signals of the bridged bonds are weaker. The absorption peak at 1,743 cm^{-1} arises from the C=O-related bonds. The SiC nanocrystals in dichloromethane show very weak infrared absorption (Fig. 4.20b), and it is consistent with the low solubility of SiC particles in this low-polarity solvent. No noticeable signals are detected from SiC nanocrystals suspended in the nonpolar solvent *n*-heptane in which only the smallest SiC particles are dissolved.

The surface structure of 3C-SiC nanocrystals with an average size of 5 nm is investigated by attenuated total internal reflection infrared spectroscopy [27, 28] after evaporation of the solvent. The infrared spectrum (Fig. 4.21) shows only the Si–C signal at 800 cm^{-1}. The absorption peak at 1,595 cm^{-1} from the ethanol and *n*-butanol samples is assigned to surface −OH bending and C=O stretching. The Si–O–Si and C–O–C vibrations are between 1,000 and 1,200 cm^{-1}, and the bands at 1,260 and 1,750 cm^{-1} are symmetric and asymmetric COO– stretching. The band at 1,350 cm^{-1} is attributed to C–H bending, but Si–H vibration is not observed. The Si–O–Si bonds are more stable than Si–H bonds on the surface of the SiC nanocrystal as reported previously [25]. The Raman spectra of the SiC nanocrystals and microcrystals are compared (Fig. 4.22) [27]. The strong TO phonon band at 792 cm^{-1} and LO phonon band at 961 cm^{-1} are observed for the microcrystals. The strong TO phonon vibration appears at nearly the same position from the nanocrystals, but the LO phonon signal is quite weak. This observation is consistent with the infrared absorption result, further indicating that the LO phonon mode is inactive in 3C-SiC nanocrystals [25]. A similar phenomenon has been observed [29], as shown in Fig. 4.23. The Raman spectra of both the pure and the polymer-encapsulated 3C-SiC nanocrystals show strong TO phonon signals at 788.2 and 790.4 cm^{-1}, respectively.

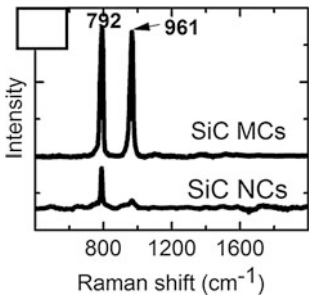

Fig. 4.22 Raman spectra of the SiC microcrystals and nanocrystals. Reprinted with permission from [27]. Copyright 2011, AIP Publishing LLC

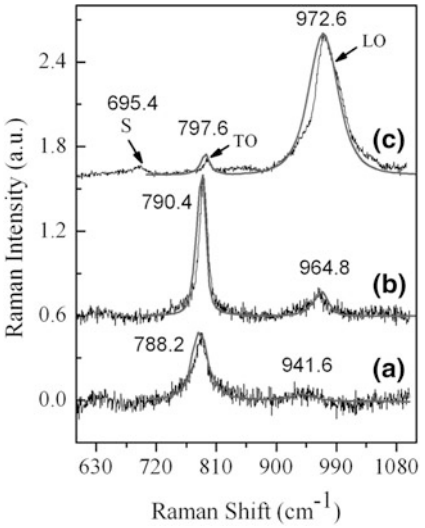

Fig. 4.23 Raman spectra of the **a** assembled 3C-SiC nanocrystals film and **b**, **c** 3C-SiC nanocrystals embedded in the glycerol matrix. **b**, **c** Correspond to regions containing smaller and larger nanocrystals, respectively. Reprinted with permission from [29]. Copyright 2010, Optical Society of America

In contrast, the LO phonon vibration is very weak. However, for larger particles embedded in the polymer matrix, a strong LO phonon mode at 972.6 cm^{-1} is observed, and in this case, the position of the TO and LO phonon vibrations is close to that of the bulk materials, suggesting that these particles are large.

The pH may influence the luminescence properties of silicon carbide colloids [30]. The pH of the aqueous solution of the 3C-SiC nanocrystals is adjusted by adding HCl or NaOH. Besides the blue emission band that obeys quantum confinement, another emission band at 510 nm is supposed to exist for excitation wavelengths larger than 350 nm, and this band appears from particles suspended in an acidic medium but not a basic one (Fig. 4.24). Based on infrared absorption, X-ray photoelectron spectroscopy, and theoretical calculation, the 510-nm emission may arise from structures involving attachment of the H^+ and OH^- to the Si dimers on the surface of the SiC nanocrystal. Surface surfactants are found to influence the luminescence properties of SiC colloids [31], and in some studies, the carboxyl group is proposed to exist on the surfaces of silicon carbide nanocrystals [31, 32]. If this is true, the 510-nm luminescence peak may stem from the carboxyl groups instead.

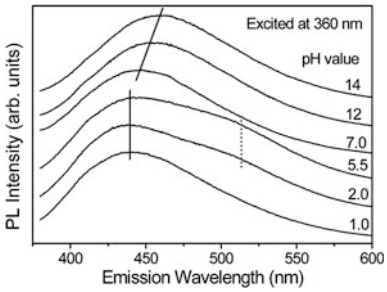

Fig. 4.24 PL spectra of the 3C-SiC nanocrystal aqueous solutions with different pH values as indicated. Reprinted with permission from [30]. Copyright 2009, American Chemical Society

4.1.2.3 Luminescent Films Composed of 3C-SiC Nanocrystals

Colloidal 3C-SiC nanocrystals exhibit stable and strong yellow green to blue luminescence, but it is uncertain whether these luminescence properties can be retained if these nanocrystals are incorporated into solid films. If so, SiC nanocrystals have many useful applications in solid-state lighting and displays. 3C-SiC nanocrystals 1–6 nm in size are embedded in a polystyrene film by casting the toluene solution with dissolved 3C-SiC nanoparticles and polystyrene [33]. The SiC nanoparticle/polystyrene composite film exhibits blue PL under 325-nm excitation (Fig. 4.25). The 3C-SiC nanocrystal/SiO_2 core/shell nanostructures embedded in the Si matrix have been prepared, and they exhibit robust blue luminescence (Fig. 4.26) [34]. The 3C-SiC nanocrystals are introduced into the pores of the naturally oxidized porous Si, followed by annealing in argon to form the 3C-SiC nanocrystal/SiO_2 core/shell nanostructures in Si. Luminescence from the 3C-SiC nanocrystal/SiO_2 nanocomposites is very stable at high temperature.

The 3C-SiC nanocrystals embedded in a glycerol film show stable and tunable PL in the 360–540 nm range (Fig. 4.27) [35]. X-ray photoelectron spectroscopy indicates that the silicon-terminated nanocrystal surface is bonded to the glycerol

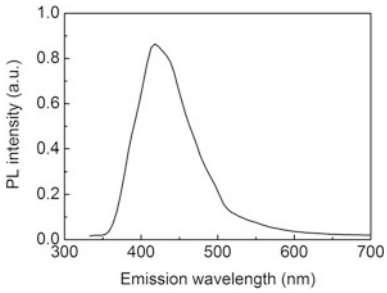

Fig. 4.25 PL spectrum of the 3C-SiC nanocrystallites embedded in a polystyrene film excited by 325 nm light. Reprinted with permission from [33]. Copyright 2005, AIP Publishing LLC

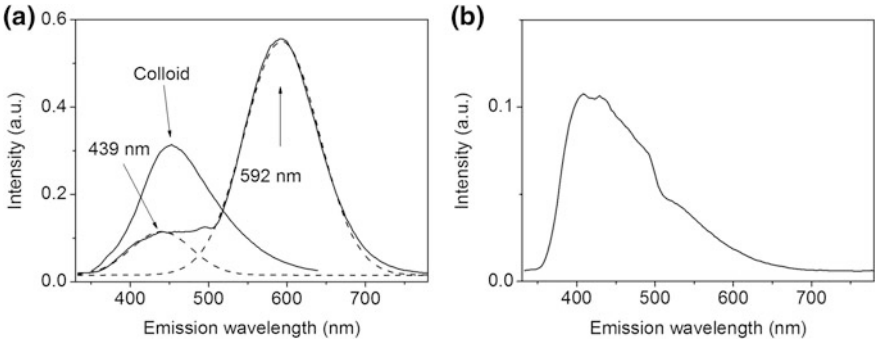

Fig. 4.26 **a** PL spectra of the 3C-SiC nanocrystals embedded in the oxidized porous Si. *Dashed lines* are double-Gaussian fit of the measured spectrum. "Colloid" refers to the original 3C-SiC nanocrystal aqueous solution. **b** PL spectrum of the 3C-SiC nanocrystal/SiO_2 core/shell nanostructures embedded in the Si matrix. Reprinted with permission from [34]. Copyright 2006, Springer Science and Business Media

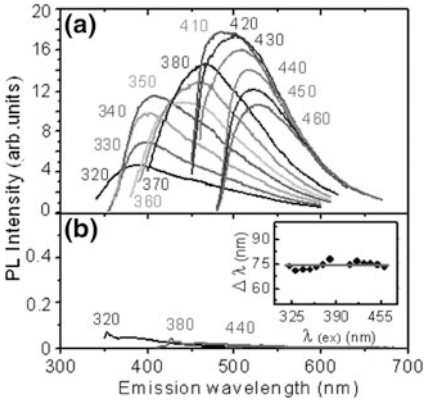

Fig. 4.27 PL spectra of the **a** 3C-SiC nanocrystals/glycerol solid film on a Si wafer under different excitations and **b** pure glycerol excited at three wavelengths. The *inset* shows the difference between emission and excitation wavelengths as a function of excitation wavelength. Reprinted with permission from [35]. Copyright 2010, American Chemical Society

molecules. Calculation based on the density functional theory suggests that the glycerol molecules bonded to the nanocrystals produce dramatic changes in the SiC nanocrystal surface structure leading to a quasi-continuous electronic band associated with the tunable emission wavelengths.

The 3C-SiC nanocrystal–sodium dodecyl sulfonate (SDS) inorganic–organic interlinked solid network shows intense PL [36]. Figure 4.28 shows the high-resolution TEM image of the 3C-SiC nanocrystals embedded in the SDS film. Many 2–4-nm SiC particles are seen, and they have good crystallinity with random crystallographic orientations. PL from this SiC nanocrystal–SDS film shifts from 417 to 491 nm with increasing excitation wavelength (Fig. 4.29) obeying quantum

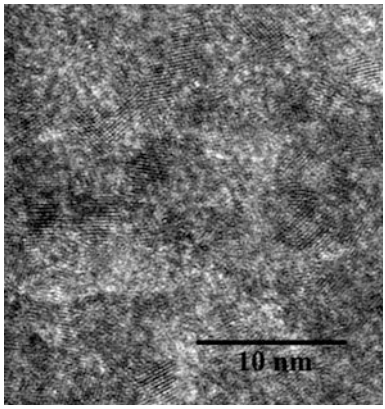

Fig. 4.28 HRTEM image of the 3C-SiC nanocrystal–sodium dodecyl sulfonate composite network film. Reprinted with permission from [36]. Copyright 2012, Royal Society of Chemistry

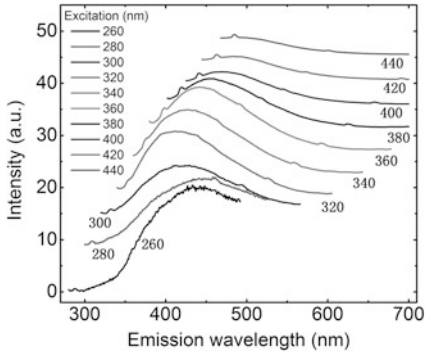

Fig. 4.29 PL spectra of the 3C-SiC nanocrystal–sodium dodecyl sulfonate composite network film under different excitations. Reprinted with permission from [36]. Copyright 2012, Royal Society of Chemistry

confinement. The light emission is very strong and visible to the naked eyes (Fig. 4.30). The time-resolved PL shows a triple-decay curve with an average lifetime of 13.65 ns.

Some other 3C-SiC nanocrystal-incorporated luminescent solid films have been fabricated and investigated, for instance, 3C-SiC nanocrystal/silica nanocomposites [37] and 3C-SiC nanocrystals embedded in the binary poly(allylamine hydrochloride)-sodium poly(styrene sulfonate) polyelectrolytes solid matrix [38]. The photon reabsorption phenomenon occurs between the embedded SiC quantum dots of different sizes. Synthesis of 3C-SiC quantum dots/cetyltrimethylammonium bromide (CTAB) multilayered vesicle core/shell nanostructures has been reported [39]. The Coulombic attraction force between the negatively charged surface of the quantum dot and positively charged ionized CTAB molecules induces the formation of the core/shell nanostructures. The zeta potential distribution of the 3C-SiC nanocrystals suspended in the ethanol solution (pH = 3) is shown in Fig. 4.31. Most particles show a positive zeta potential (net charge) because the negatively charged oxygen atom of the Si–O–Si group on the surface attracts positive ions from the surrounding solvent, thus resulting in an overall positive charge on most particles.

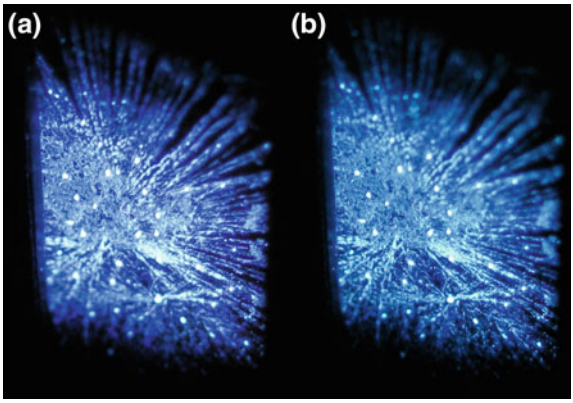

Fig. 4.30 Luminescence photos of the 3C-SiC nanocrystal–sodium dodecyl sulfonate composite network film on a Si wafer excited by **a** 320 nm and **b** 360 nm lines of the Xe lamp. Reprinted with permission from [36]. Copyright 2012, Royal Society of Chemistry

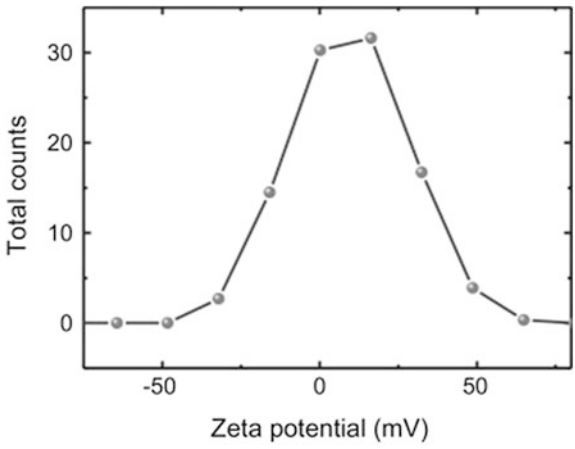

Fig. 4.31 Zeta potential distribution of the 3C-SiC quantum dots suspended in ethanol showing an average value of 9.62 mV. Reprinted with permission from [39]. Copyright 2013, Elsevier

3C-SiC nanocrystals can be directly incorporated into a solid film without using encapsulation materials [40]. Figure 4.32a shows the PL spectra of the 3C-SiC nanocrystals self-assembled film. The spectrum is smooth with a full width at half-maximum (FWHM) of about 110 nm. The PL shifts to red with increasing excitation wavelengths (Fig. 4.32b). These spectral features suggest the quantum confinement luminescence mechanism.

4.1.2.4 More Polytypes of SiC Nanocrystals

There have been many reports on the luminescence properties of cubic silicon carbide nanocrystals. In contrast, relatively little is known about the properties of hexagonal silicon carbide nanocrystals. Unlike cubic silicon carbide, no definite evidence of quantum confinement has been observed from hexagonal silicon carbide.

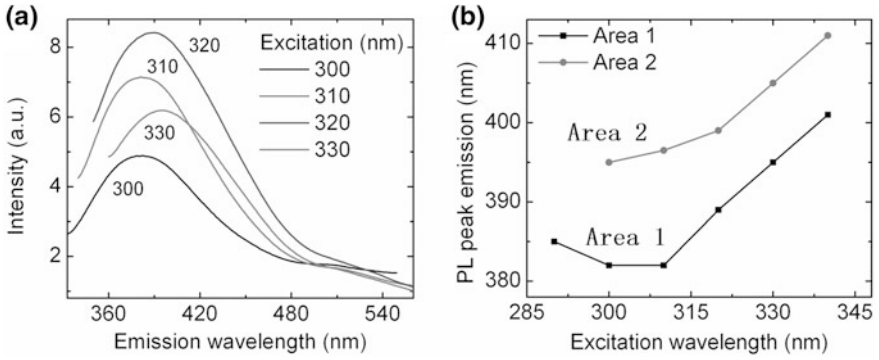

Fig. 4.32 **a** PL spectra of the close-packed 3C-SiC nanocrystal film (area *1*) on a glass slide under different excitations. **b** PL peak wavelength as a function of excitation wavelength (area *1*). The values of another area (area *2*) on the same film are also shown. Reprinted with permission from [40]. Copyright 2011, AIP Publishing LLC

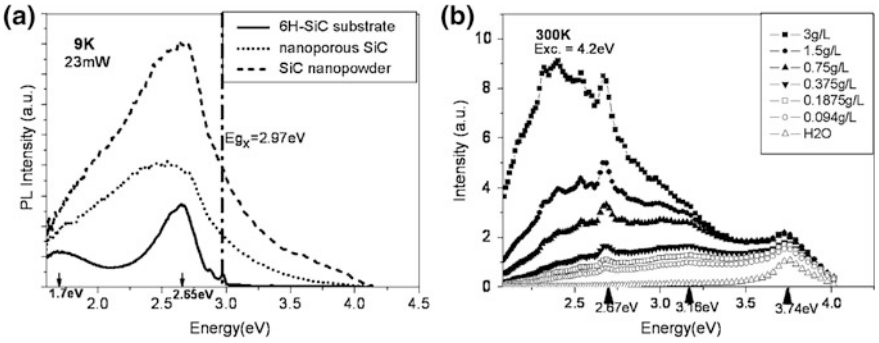

Fig. 4.33 PL spectra **a** of 6H-SiC wafer, porous SiC, and SiC nanopowder. Concentration-dependent normalized (relative to water Raman peak) PL spectra **b** of the nanopowders suspended in water. Reprinted with permission from [41]. Copyright 2007, AIP Publishing LLC

The free porous 6H-SiC layer is prepared by electrochemical etching of *n*-type 6H-SiC. Mechanical grinding of the porous free layer produces the porous SiC nanopowders [41, 42]. The samples exhibit similar PL spectral features with a strong band at around 2.65 eV (Fig. 4.33). The emission is proposed to arise from recombination of the N–Al donor–acceptor electronic states as well as surface states. The diluted nanopowders suspended in water yield a PL peak at around 3.74 eV, which is suggested to arise from the quantum-confined carriers considering its above-bandgap energy. The 6H-SiC nanocrystals dispersed in water and hydrofluoric acid show different PL features [43]. These nanoparticles are fabricated by electrochemical etching of *n*-type bulk 6H-SiC followed by ultrasonic treatment. Transmission electron microscopy reveals that the particles are crystalline with diameters ranging from 1 to 8 nm (Fig. 4.34). The nanoparticles in water show a broad emission band at 2.78 eV (Fig. 4.35) which is below the

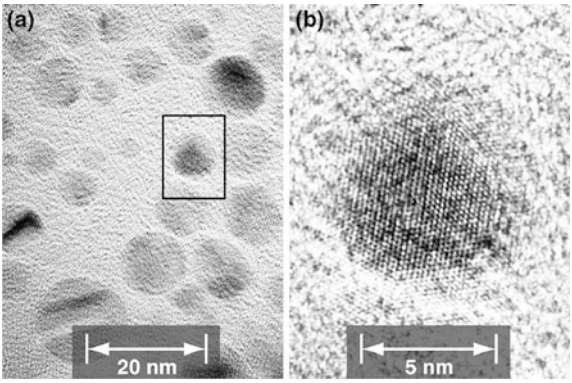

Fig. 4.34 **a** TEM image of 6H-SiC nanoparticles. **b** High-resolution image of a typical nanoparticle showing lattice fringes. Reprinted with permission from [43]. Copyright 2008, AIP Publishing LLC

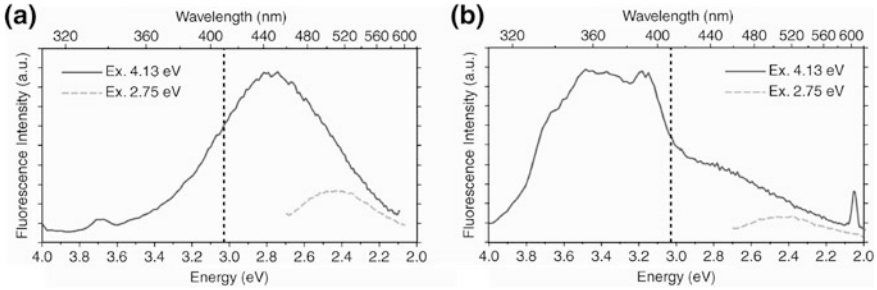

Fig. 4.35 PL spectra of 6H-SiC nanocrystals dispersed in **a** water and **b** HF/ethanol. Reprinted with permission from [43]. Copyright 2008, AIP Publishing LLC

bandgap of bulk 6H-SiC. The PL spectrum of the nanoparticles suspended in HF/ethanol shows an above-bandgap emission band at around 3.5 eV which is suggested to arise from quantum confinement.

The comparative study of PL from SiC quantum dots fabricated by electrochemical etching of bulk 3C-, 6H-, and 4H-SiC single crystals improves our understanding of the properties of SiC quantum dots [44]. These particles are 1–8 nm in size, and Fig. 4.36a–c show the PL spectra under different excitations. Three collections of quantum dots with different bulk SiC origins show similar spectral features. All the PL spectra are smooth and intense. The FWHM values are between 100 and 130 nm. This large linewidth is caused by the broad size distribution of the particles. The PL peak wavelength varies similarly with increasing excitation wavelength for the three samples (Fig. 4.36d). There is a nearly constant emission band at around 452 nm for excitation wavelengths smaller than 320 nm (Zone I), suggesting defect-related luminescence similar to that observed from porous 6H-SiC [45]. The PL peak wavelength shifts to red nearly linearly with increasing excitation

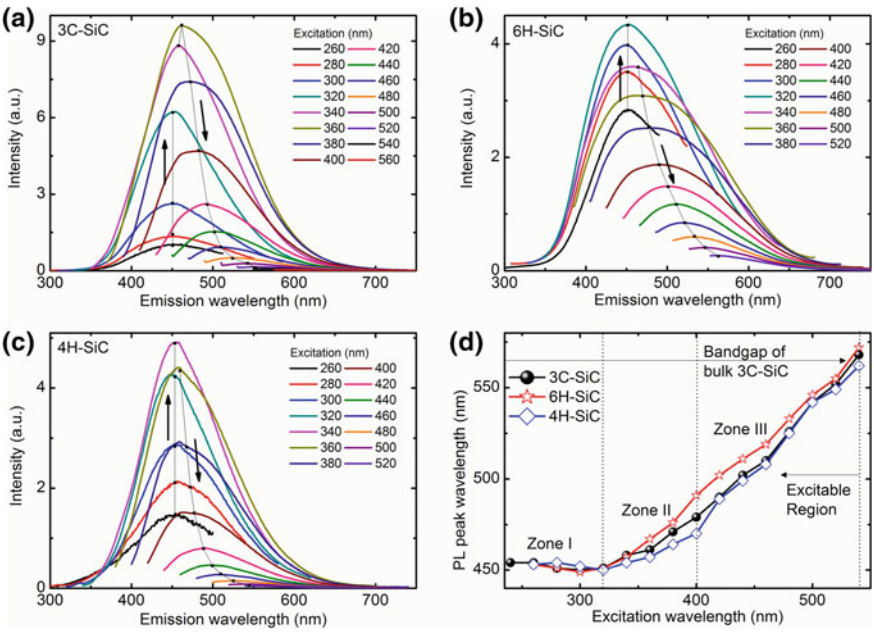

Fig. 4.36 **a–c** PL spectra of three aqueous solutions of SiC quantum dots obtained by electrochemical etching of bulk 3C-, 6H-, and 4H-SiC, respectively. *Black lines* mark the variation trend of the PL peak, and the arrows indicate the direction of increasing excitation wavelength. **d** PL peak wavelength versus excitation wavelength. Reprinted with permission from [44]. Copyright 2012, AIP Publishing LLC

wavelengths over 400 nm before reaching a maximum at around 565 nm (2.2 eV), which is very close to the bandgap of bulk 3C-SiC. These features are characteristic of interband recombination luminescence from 3C-SiC nanocrystals following the quantum confinement effect. The 6H sample shows flatter PL peaks than the 3C and 4H samples probably due to the different size distributions.

The PL excitation (PLE) measurement reveals more similarities among the three collections of SiC quantum dots (Fig. 4.37). The PLE spectra of each sample show three distinct peaks, implying that there are three types of light absorption processes. The PLE spectra monitored at 580 nm for all the samples show an identical peak at about 365 nm (Fig. 4.37d), indicating the same origin. Furthermore, the three PLE bands vanish at about 563 nm, further confirming that the redder part of the PL in each sample corresponds to interband recombination luminescence of the 3C-SiC quantum dots. Hence, the wide excitation band at around 365 nm is associated with light absorption by the cubic SiC quantum dots.

Figure 4.38 shows the time-resolved PL spectra of the three collections of SiC quantum dots. Each spectrum can be fitted by a triple-exponential function. The lifetime and relative amplitude of the three components extracted from the fit are summarized in Table 4.1. Each component in one sample has a counterpart from any

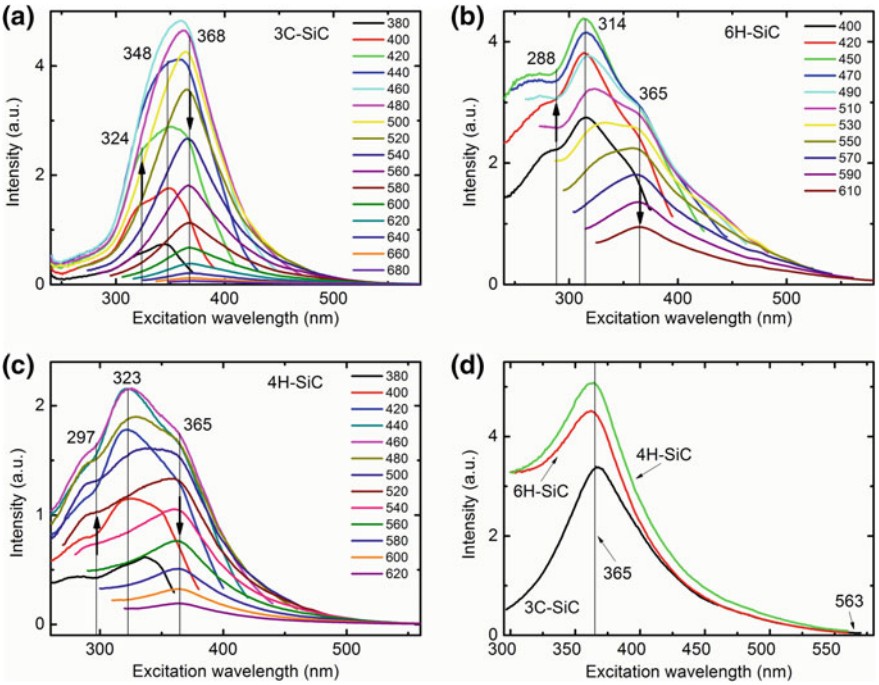

Fig. 4.37 **a–c** PL excitation spectra recorded at different emission wavelengths as indicated. The *black lines* mark the peak positions, and the arrows indicate the direction of increasing emission wavelength. **d** PL excitation spectra for the 580 nm emission. Reprinted with permission from [44]. Copyright 2012, AIP Publishing LLC

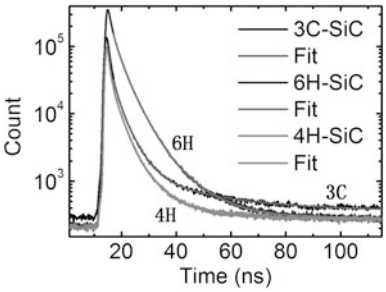

Fig. 4.38 Time-resolved PL spectra excited by 280 nm light and monitored at 420 nm (3C) and 450 nm (6H, 4H). Each spectrum can be fitted by a triple-exponential function. The component lifetime and relative amplitude are summarized in Table 4.1. Reprinted with permission from [44]. Copyright 2012, AIP Publishing LLC

of the other two samples, concluded based on the closeness in the lifetime and relative amplitude. The faster decay component with a lifetime of around 4 ns dominates the blue-band emission of each sample with a relative amplitude of over 60 %, suggesting

Table 4.1 Lifetime (τ) and relative amplitude (R) of the three components in the fitted time-resolved PL spectrum of each aqueous solution of SiC quantum dots obtained by diminishing the size of bulk 3C-, 6H-, and 4H-SiC, respectively. Reprinted with permission from [44]. Copyright 2012, AIP Publishing LLC

Polytype	τ_1 (ns)	R_1 (%)	τ_2 (ns)	R_2 (%)	τ_3 (ns)	R_3 (%)
3C-SiC	1.63	18.7	4.67	60.0	24.8	21.3
6H-SiC	1.66	14.8	4.28	67.1	10.9	18.1
4H-SiC	0.89	14.1	3.38	64.4	10.6	21.5

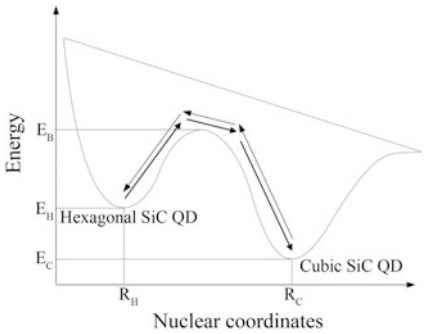

Fig. 4.39 Schematic depicting hexagonal–cubic polytypic transformation of the SiC quantum dot (QD) on a potential energy versus nuclear coordinate *curve*. Reprinted with permission from [44]. Copyright 2012, AIP Publishing LLC

that it is associated with the blue emission band. The slower decay component has a lifetime of over 10 ns and relative amplitude of around 20 %. This may be related to the tunable quantum confinement luminescence from the 3C-SiC quantum dots.

These results indicate that the three collections of SiC quantum dots have the same luminescence mechanisms, one defect-associated blue luminescence, and one tunable quantum-confined luminescence. A polytypic transformation model is proposed to explain this strange behavior (Fig. 4.39). Based on this model, some hexagonal quantum dots can be transformed into cubic ones (and vice versa) by applying ultrasonic waves during preparation, if the energy provided by the ultrasonic wave is large enough to overcome the potential energy barrier of the polytypic transformation. In practice, the bulk 3C-, 6H-, and 4H-SiC have very close cohesive energies [46]. Thus, the differences in the cohesive energy of different polytypes of SiC quantum dots may also be small, making the ultrasonic wave-driven polytypic transformation occur readily. This explains the spectral similarity among the three collections of SiC quantum dots with distinct bulk SiC origins.

The reason for the difficulty in observing the quantum confinement effect from hexagonal silicon carbide in comparison with cubic silicon carbide has been investigated [44]. A semiconductor quantum dot exhibits remarkable quantum confinement only when its size is close to or smaller than its bulk exciton Bohr

diameter [47]. The exciton Bohr radius of silicon carbide can be evaluated using the following equation [48]:

$$R = \frac{4\pi\varepsilon_0\varepsilon_r\hbar^2}{\mu_0 e^2} = \frac{0.053\varepsilon_r}{\mu_0/m_0}\,(\text{nm}), \tag{4.4}$$

where ε_0 and ε_r are the dielectric constant in vacuum and relative permittivity, e is the electron charge, m_0 is the electron mass, $\hbar$ is the reduced Planck's constant, and $\mu_0 = (m_e \times m_h)/(m_e + m_h)$ is the reduced effective mass of the electron–hole pair. The effective masses of electrons and holes of silicon carbide are taken from Ref. [16]. The exciton Bohr radii are evaluated to be 2.0, 0.7, and 1.2 nm for 3C-, 6H-, and 4H-SiC, respectively. The most probable diameter of the SiC quantum dots obtained by electrochemical etching is generally around 3.9 nm which is close to the exciton Bohr diameter of 3C-SiC but larger than those of 4H-SiC and 6H-SiC. This explains the absence of the quantum confinement effect in hexagonal SiC nanocrystals.

4.1.3 Solution-Based Chemical Synthesis

Compared to other group IV nanoparticles such as Si and Ge nanoparticles [49], fewer chemical synthesis methods have been developed to produce SiC nanoparticles. One reason is that silicon carbide crystals have very high melting points resulting from the strong Si–C bonds, and consequently, chemical synthesis of silicon carbide crystals typically needs a very high temperature at ambient pressure.

A one-step reaction involving a single precursor without catalytic assistance can produce SiC with a large surface area under autogenic pressure at an elevated temperature [50]. In this synthesis, dissociation of triethylsilane at 800 °C yields the silicon carbide–carbon nanocomposite and at 1,000 °C produces SiC according to the following reactions:

$$C_6H_{16}Si \xrightarrow{800\,^\circ C} SiC_{(s)} + 2C_{(s)} + nH_{2(g)} + \text{hydrocarbons}_{(g)}, \tag{4.5}$$

$$C_6H_{16}Si \xrightarrow{1{,}000\,^\circ C} SiC_{(s)} + nH_{2(g)} + \text{hydrocarbons}_{(g)}. \tag{4.6}$$

Transmission electron microscopy reveals that the synthesized particles have diameters of 6–12 nm, and high-resolution TEM and the electron diffraction (Fig. 4.40) indicate that they are crystalline 3C-SiC. Nanocasting and carbothermal reduction also produce 8–12 nm-size 3C-SiC nanocrystals with large surface areas [51].

Thermal reduction of phenylsiloxane polymers yields size-controlled, oxide-embedded, and freestanding SiC nanocrystals [52]. Compositional tuning of the polymers is realized by varying the relative amounts of phenyl trichlorosilane ($C_6H_5SiCl_3$) and silicon tetrachloride ($SiCl_4$) during hydrolysis and condensation

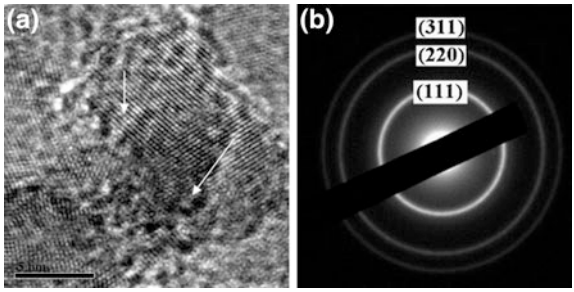

Fig. 4.40 **a** HRTEM image of the SiC sample. **b** Selected-area electron diffraction pattern of the SiC sample. Reprinted with permission from [50]. Copyright 2005, American Chemical Society

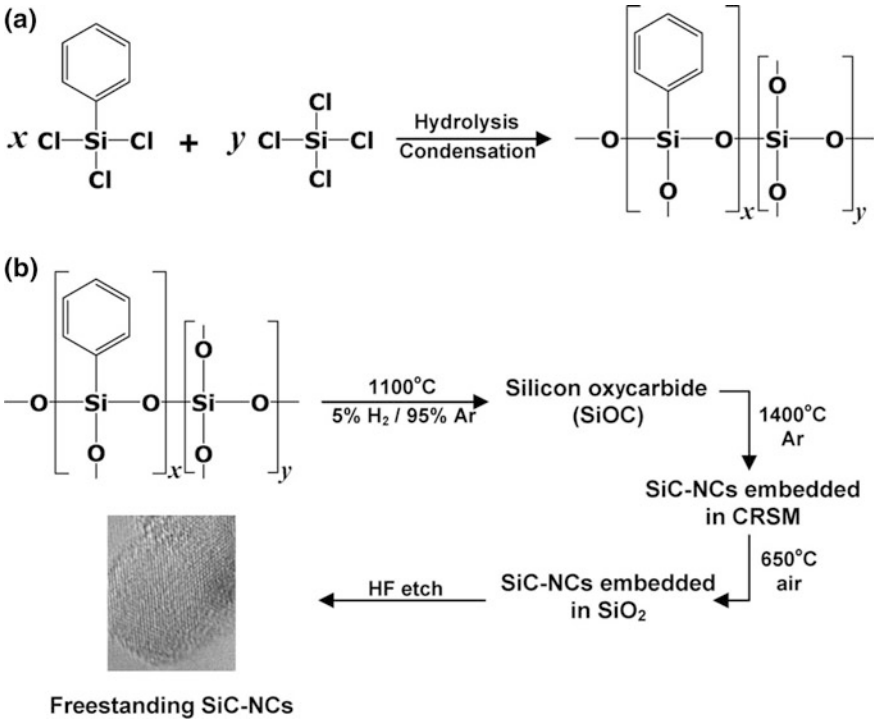

Fig. 4.41 **a** Hydrolysis and cocondensation of various mixtures of $C_6H_5SiCl_3$ and $SiCl_4$ yielding phenylsiloxane polymers $[(C_6H_5SiO_{1.5})_x(SiO_2)_y]_n$. **b** Thermal reduction of $[(C_6H_5SiO_{1.5})_x(SiO_2)_y]_n$ polymers yielding carbon-rich silicon matrix-embedded SiC nanocrystals. Subsequent oxidation of matrix carbon and chemical etching of the SiO_2 matrix yield freestanding size-controlled SiC nanocrystals. Reprinted with permission from [52]. Copyright 2009, American Chemical Society

(Fig. 4.41). Thermal reduction of the condensed copolymers produces the oxide-embedded SiC nanocrystals. X-ray diffraction (Fig. 4.42a) indicates that the average particle size depends on the relative $C_6H_5SiCl_3$ concentration in the initial

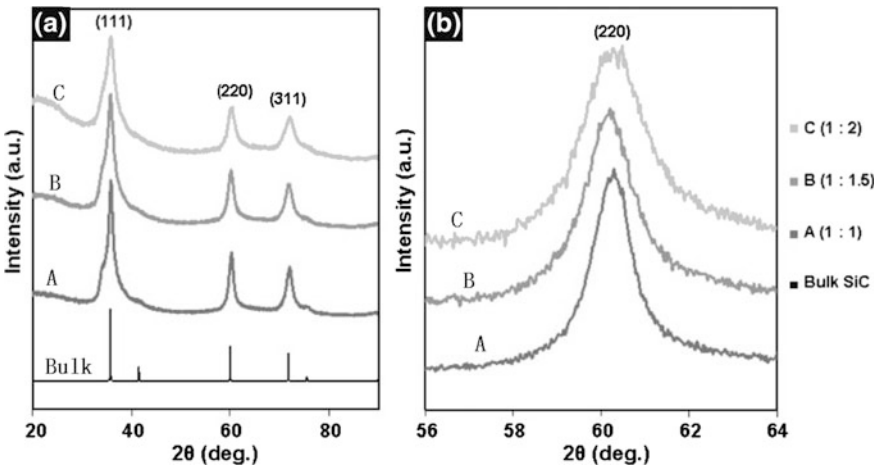

Fig. 4.42 XRD spectra of oxide-embedded SiC nanocrystals indicating size tunability related to phenylsiloxane composition (the $C_6H_5SiO_{1.5}/SiO_2$ ratio). **a** XRD patterns of carbon-rich silica matrix-embedded SiC nanocrystals A3, B3, and C3. They are characteristic of 3C-SiC. **b** Enlarged XRD patterns of the (220) faces of the embedded SiC nanocrystals showing clear crystal size control. Reprinted with permission from [52]. Copyright 2009, American Chemical Society

precursor mixture. In the XRD spectra, the broad reflections at 36°, 60°, and 72° are assigned to the (111), (220), and (311) crystal planes of 3C-SiC, respectively. The peaks broaden as the polymer phenyl concentration is reduced (from samples A3 to C3). The magnified spectra of (220) reflection (Fig. 4.42b) show this trend more clearly. The SiC particle size is calculated to be 9, 7, and 5 nm for samples A3, B3, and C3, respectively, using the XRD peak width based on Scherrer equation. The phenylsiloxane polymer composition controls the particle size. TEM provides similar results. Freestanding SiC nanocrystals are prepared by oxidation of carbon and chemical etching of the SiO_2 matrix. The high-resolution TEM micrographs (Fig. 4.43) disclose good crystallinity and the 3C polytype. The FTIR spectrum obtained from the liberated SiC nanocrystals shows a broad dominant peak at 835 cm^{-1} ascribed to optical phonon vibrations of SiC, a broad vibration peak at 3,400 cm^{-1} arising from O–H stretching, and another peak at about 1,100 cm^{-1} stemming from Si–O bonds. These freestanding SiC particles exhibit no luminescence due to the complex surface chemistry and relatively big crystal size. Thermal processing of the solgel-derived polymers $[(HSiO_{1.5})_{0.95}(R\text{-}SiO_{1.5})_{0.05}]_n$ (R=C_8H_{17}, $C_{10}H_{21}$) can also give rise to SiC nanocrystals [53].

4.1.4 Laser Ablation Method

Laser ablation of silicon wafers immersed in ethanol followed by etching is used to fabricate β-SiC quantum dots [54]. Under laser irradiation, the active carbon atoms

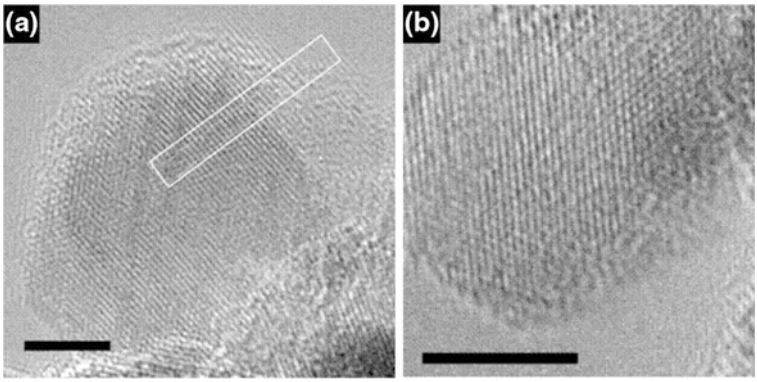

Fig. 4.43 High-resolution TEM images of freestanding SiC nanocrystals from samples **a** A5 and **b** C5, respectively. The scale bars represent 5 nm. Reprinted with permission from [52]. Copyright 2009, American Chemical Society

dissociated from ethanol react with active silicon atoms from the Si wafer producing SiC and Si nanoparticles. Subsequent rinsing in an aqueous HF–H_2O_2 solution dissolves the Si particles leaving only SiC nanoparticles. The use of a mixture of ethanol and toluene (ethanol/toluene = 7:1 by volume) leads to the production of a higher proportion of β-SiC nanoparticles. TEM shows that the sample contains β-SiC nanocrystals a few nanometers in size (Fig. 4.44), and they produce strong and stable violet emission (Fig. 4.45) with the peak wavelength blueshifting significantly relative to the bulk 3C-SiC bandgap, suggesting quantum confinement. The ring-like 3C-SiC nanostructures (Fig. 4.46) have also been observed from the samples prepared using a similar method [55, 56]. About 15 % of the nanoparticles in the pure SiC sample are in the ring structures.

Direct laser ablation of polycrystalline 3C-SiC in water can produce luminescent SiC nanocrystals [57]. Figure 4.46 shows the TEM image of the synthesized SiC nanocrystallites less than 10 nm in size. Most of the nanocrystals are smaller than 5 nm, and they have a zeta potential of −49 mV. Based on the infrared spectroscopy, it is proposed that surface charges related to carboxylate anions account for the long-term stability of the colloidal solutions. These SiC particles show PL at about 2.75 eV which is independent of the laser power.

4.1.5 Other Methods

The particle-size dependence of optical phonon frequencies and dampings of two types of SiC small particles are investigated by Raman scattering and infrared absorption [58]. The particles are fabricated by pyrolysis of polycarbosilane or a reaction between silica and carbon. The spectra can be explained qualitatively by a model of core plasmon and carrier-free layer on the particle surface for particles larger than 30 nm based on Mie's scattering equation or the average dielectric

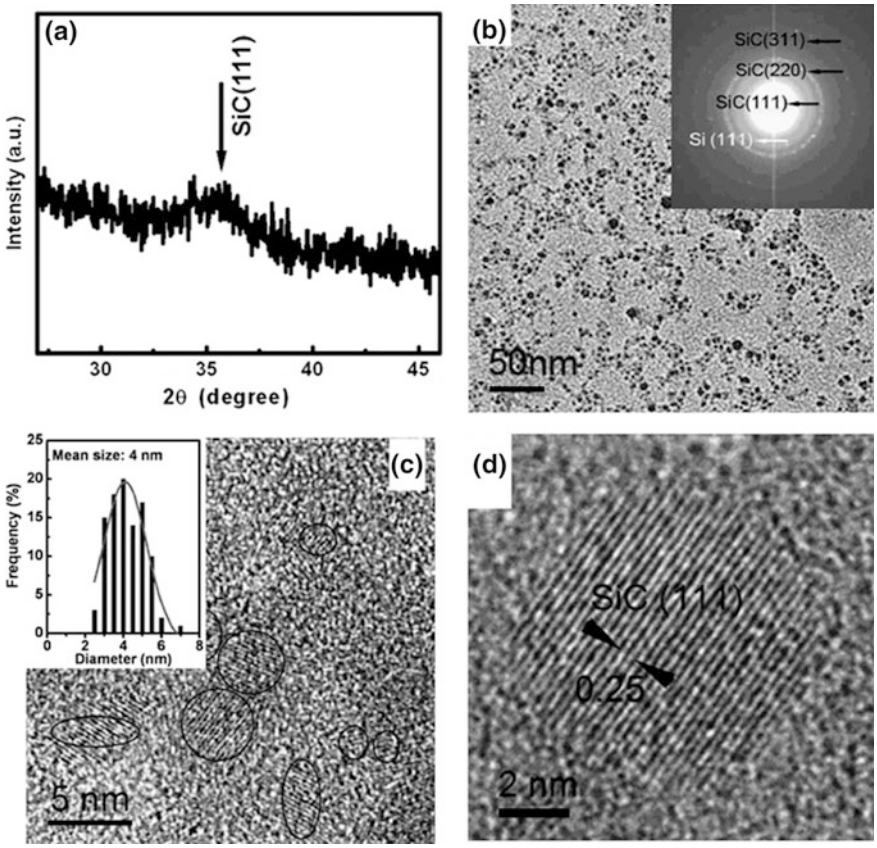

Fig. 4.44 **a** XRD spectrum, **b** TEM image, and **c**, **d** high-resolution TEM images of the as-prepared sample of the laser-ablated Si wafer in a mixed solution (ethanol/toluene = 7:1 by volume). The *inset* in **b** shows the selected-area electron diffraction pattern. The *inset* in **c** shows the size distribution of the nanoparticles. Reprinted with permission from [54]. Copyright 2009, Royal Society of Chemistry

function of Maxwell–Garnet. The particle surface layers have thicknesses between 5 and 40 nm. For particles smaller than 200 nm, the TO phonon frequency (ω_T), LO phonon frequency (ω_L), and corresponding damping depend on the particle size instead of crystallite size. For smaller particles, ω_T and $\omega_L - \omega_T$ become smaller and phonon damping becomes larger. The absorption spectrum of the particles a few nanometers in size exhibits both the crystal-like component and broad symmetric line attributed to the 1-nm-thick amorphous surface layer.

High-energy ball milling of mixed silicon and graphite powders at room temperature produces nanoscale crystalline SiC powders [59]. The SiC structure depends on the milling speed, charge ratio, and milling time. A similar method is used to synthesize β-SiC nanoparticles [60]. The starting graphite and silicon mixture reacts completely to form β-SiC nanoparticles with an average grain size of

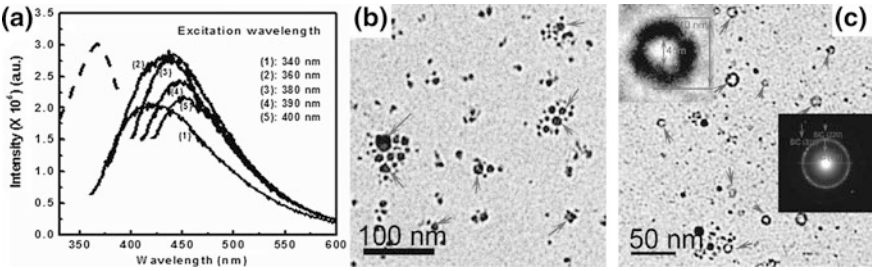

Fig. 4.45 **a** PL spectra of the synthesized β-SiC nanoparticles excited by 340–400 nm light. The *dashed line* is the PL excitation spectrum at 430 nm. Reprinted with permission from [54]. Copyright 2009, Royal Society of Chemistry. **b**, **c** TEM images of SiC nanorings and smaller Si particles. The *left inset* shows the high-resolution image of a nanoring, and *right inset* shows the selected-area electron diffraction pattern of the nanorings corresponding to 3C-SiC. Reprinted with permission from [55]. Copyright 2011, American Chemical Society

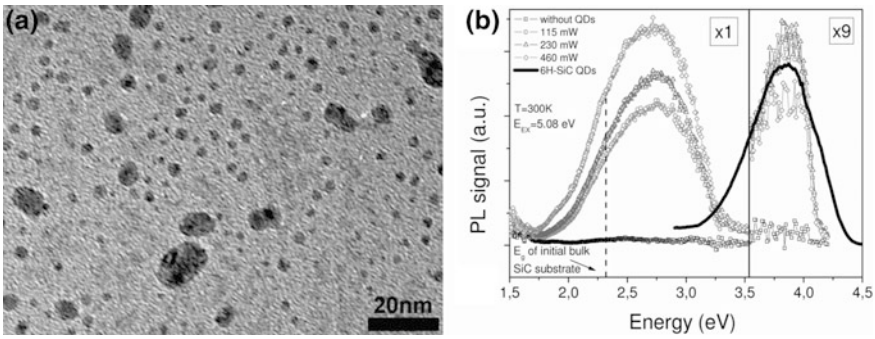

Fig. 4.46 **a** TEM image of the SiC nanocrystals obtained by laser ablation. **b** PL spectra of the SiC nanocrystals in water prepared by using different laser powers. PL spectra of pure water and 6H-SiC nanocrystals reported in Ref. [42] are shown for comparison. The excitation photon energy is 5.08 eV. Reprinted with permission from [57]. Copyright 2011, Wiley-VCH Verlag GmbH & Co. KGaA

8 nm. The grain size decreases gradually with milling time. The nanoparticles exhibit a broad PL band at 387 nm under 325-nm excitation. A carbothermal reduction method has been developed to synthesize SiC nanocrystalline powders using a solution of sugar in silica sol as the starting materials [61]. The sugar is first converted to carbon particles, and the silica and carbon mixture is heated to 1,550–1,800 °C in an argon atmosphere. The particles are smaller than 500 nm with the crystallites smaller than 100 nm. Silicon carbide nanoparticles and nanorods are prepared by the solid-state metathesis reaction of silica, carbon, and magnesium at 600 °C [62]. Electron microscopy indicates that the SiO_2 particles with diameters of 30.6, 66.8, and 213.8 nm yield SiC particles with diameters of 51.3, 92.8, and 278.3 nm, respectively (Fig. 4.47). SiC rods and fibers are fabricated by similar reactions between SiO_2 rods/fibers and C and Mg powders

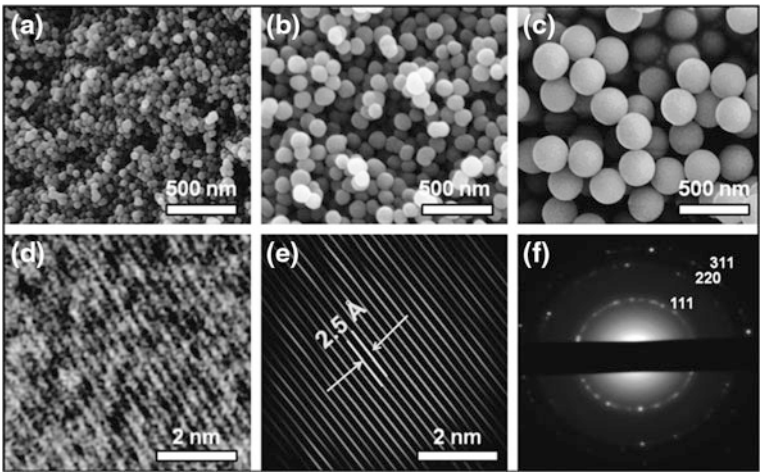

Fig. 4.47 SEM images of SiC nanocrystals with diameters of about **a** 51.3 nm, **b** 92.8 nm, and **c** 278.3 nm and **d** HRTEM image of a SiC nanocrystal; **e** Fourier-transform image of **d** indicating the lattice spacing; and **f** selected-area electron diffraction pattern of the SiC nanocrystals. Reprinted with permission from [62]. Copyright 2013, Royal Society of Chemistry

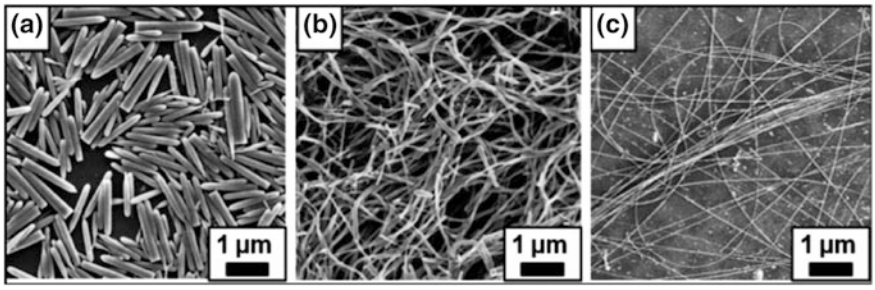

Fig. 4.48 SEM images of SiC **a** rods (length: 1.5 μm, diameter: 0.20 μm), **b** fibers (length > 10 μm, diameter: 0.18 μm), and **c** fibers (length > 25 μm, diameter: 0.050 μm). Reprinted with permission from [62]. Copyright 2013, Royal Society of Chemistry

(Fig. 4.48). Commercial glass wool is also used to synthesize long SiC fibers by this method, and X-ray diffraction confirms that all the products are crystalline β-SiC.

4.1.6 Silicon Carbide Nanospheres

3C-SiC cages, cubes, and nanoparticles are synthesized by vapor–liquid reactions employing methylchlorosilanes and Na as the starting materials [63]. This route is a simplified solvent-free Yajima process, and the precursors are polycarbosilane and NaCl. 3C-SiC with different morphologies is produced with different

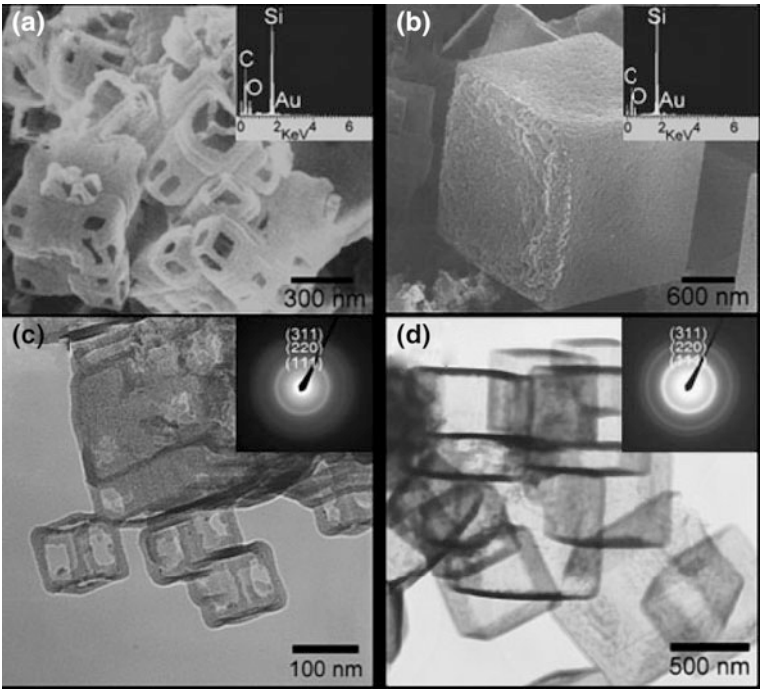

Fig. 4.49 Images of the SiC cubes prepared from $SiMe_2Cl_2$ and Na. SEM images and energy-dispersive X-ray spectroscopy spectra (*insets*) of two types of structures **a** Ia and **b** Ib. Transmission electron microscopy images and electron diffraction patterns (*insets*) of **c** Ia and **d** Ib. Reprinted with permission from [63]. Copyright 2005, Wiley-VCH Verlag GmbH & Co. KGaA

precursors. Figure 4.49 shows the electron microscopy images of two types of SiC structures: Ia and Ib. Ia contains hollow cubic cages with an edge length of 60–400 nm and edge thickness of 40 nm, whereas Ib contains cubes with an edge length of 1–2 μm. Energy-dispersive X-ray spectroscopy reveals the presence of Si, C, and some O in both structures, and TEM indicates that Ia has empty inner space. These hollow cages show a diffused ring electron diffraction pattern indicative of a polycrystalline structure. Ib is composed of hollow polycrystalline 3C-SiC cubes with a wall thickness of 20 nm.

The reaction between $SiCl_4$ (or Si powders), C_6Cl_6, and sodium at 600 °C produces SiC nanospheres [64]. The TEM image and electron diffraction pattern of the product are shown in Fig. 4.50. The SiC hollow nanospheres are 50–100 nm in diameter and 10 nm in shell thickness. The three polycrystalline rings in the electron diffraction pattern correspond to the (111), (220), and (311) planes of 3C-SiC. There are some nanowires and nanoparticles in the product as well, and the SiC hollow nanospheres account for three quarters of the materials. The process forming the SiC hollow nanospheres is shown in the following:

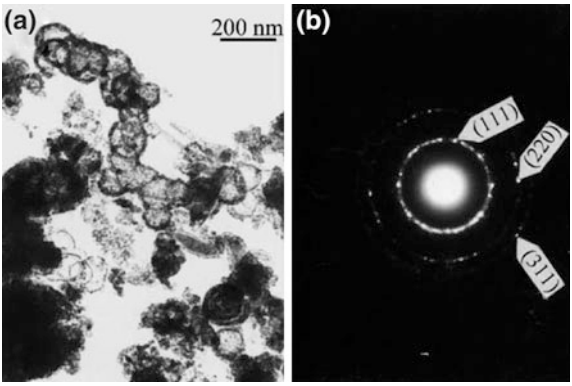

Fig. 4.50 **a** TEM image and **b** electron diffraction pattern of hollow SiC nanospheres. Reprinted with permission from [64]. Copyright 2003, Elsevier

$$\begin{aligned} \mathrm{nC_6Cl_6} + 6\mathrm{nNa} &\rightarrow 6\mathrm{nC(cluster)} + 6\mathrm{nNaCl} \\ &\rightarrow \mathrm{C(sphere\ aggregate)}, \end{aligned} \tag{4.7}$$

$$\mathrm{SiCl_4} + 4\mathrm{Na} \rightarrow \mathrm{Si} + 4\mathrm{NaCl}, \tag{4.8}$$

$$\mathrm{Si} + \mathrm{C} \rightarrow \mathrm{SiC}. \tag{4.9}$$

The three-dimensional hollow SiC sphere assembly is fabricated by embedding polymethylsilane and polysilazane into sacrificial three-dimensional ordered macroporous carbon templates followed by ashing in air after pyrolysis in nitrogen [65]. Figure 4.51 shows the electron microscopy images of the product. The SiC spheres expose partly the empty core through small holes in the shells. The morphology of SiC spheres depends on the sacrificial carbon templates and polymer concentration. The hollow SiC spheres have an outer diameter of 135–896 nm and shell thickness of

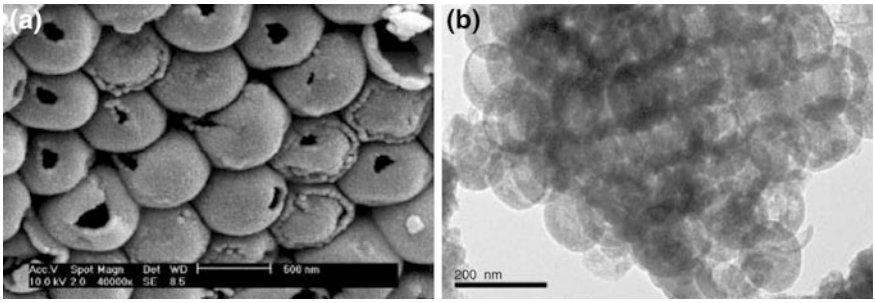

Fig. 4.51 **a** SEM and **b** TEM images of 500 and 135 nm hollow SiC sphere assemblies, respectively. Reprinted with permission from [65]. Copyright 2004, Royal Society of Chemistry

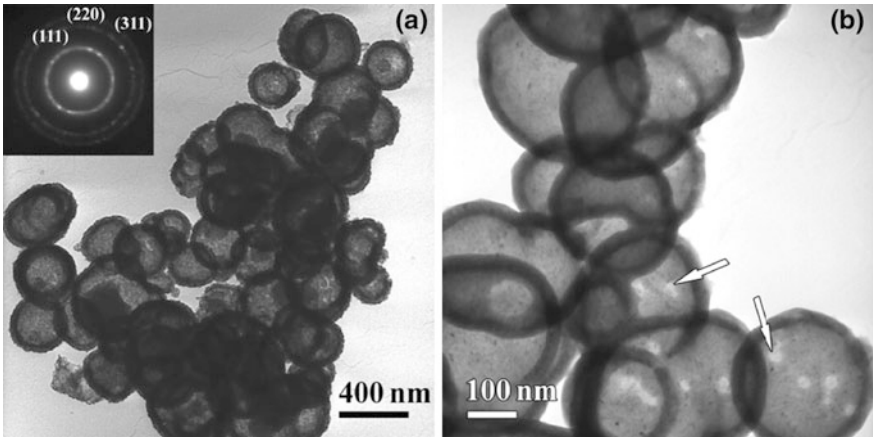

Fig. 4.52 **a** TEM image of hollow SiC spheres after removal of carbon core followed by NaOH treatment. The *inset* is the selected-area electron diffraction pattern of the SiC shell. **b** HRTEM image of hollow SiC spheres. Reprinted with permission from [69]. Copyright 2012, Elsevier

14–79 nm. A vapor–solid reaction between carbon nanoparticles and silicon monoxide vapor that is generated from a mixture of silicon and silica also yields hollow spherical SiC nanocrystals [66]. The size of the hollow spheres depends on that of the pristine carbon nanoparticles. The thickness can be controlled by the siliconization degree and carbon nanoparticle multilayer structures. 3C-SiC hollow nanospheres are prepared with 80 % yield by the reaction between $SiCl_4$, CBr_3H, and Na–K alloy at 130 °C followed by $HClO_4$ treatment at 180 °C [67]. These hollow SiC nanospheres have diameters of 80–120 nm and average shell thickness of 15 nm. Their rough surfaces indicate that they are composed of nanoparticles. The reaction between waste plastics and Si powders at 350–500 °C produces 3C-SiC nanomaterials including nanospheres and coexisting amorphous graphite particles [68]. The molten salt synthesis technique is used to produce SiC shells on carbon black particle templates [69]. Oxidation in air at 600 °C removes the residual carbon cores to obtain the hollow SiC spheres (Fig. 4.52). The SiC shell has an average thickness of 37 nm, and high-resolution TEM (Fig. 4.53) reveals that the SiC shell is composed of 3C-SiC nanocrystals with different orientations.

4.2 Surface Chemical Functionalization

There have been relatively few reports concerning surface modification of silicon carbide nanoparticles. Preparation of aqueous α-SiC suspensions with the acidic form of polyethylene imine has been reported [70]. The SiC powder has an average size of 150 nm. Adsorption of the polyelectrolyte depends on the polyelectrolyte type and charge density on the SiC powder surface in water. The efficiency of the dispersant is determined by the electrostatic interaction between

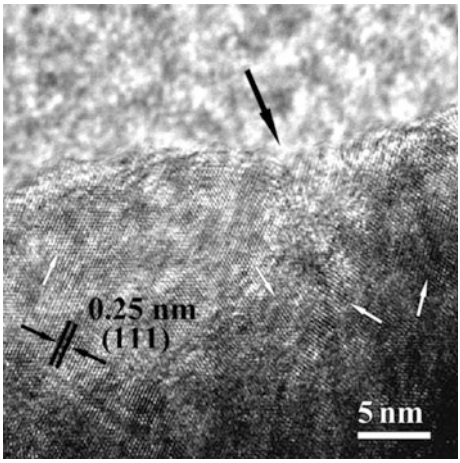

Fig. 4.53 HRTEM image of hollow SiC spheres showing lattice fringes of SiC shell. Reprinted with permission from [69]. Copyright 2012, Elsevier

the positive site of the acidic form of polyethylene imine and oxidized surface of silicon carbide in the acidic media. Good dispersion and stability are achieved by electrostatic and steric stabilization. The stability of the SiC nanoparticle suspension is investigated [71]. The sample consists of 3C-SiC monocrystalline spherical particles with an average diameter of 40 nm and are covered by an amorphous carbon surface layer. Free carbon is eliminated by heating the sample at 650 °C in air leaving an excess of amorphous SiO_2 on the particle surface, and the silica coating is stripped by dipping in HF. Different techniques have been used to characterize the hydrophilic/hydrophobic characteristics of passively oxidized SiC grains [72]. The SiC grains are less soluble in water than silica, and their surface properties do not change with the exposure time to water. The SiC surface appears to be composed of hydrophobic and hydrophilic parts, and the hydrophilic component constitutes 22–42 %. The effects of ionization of polyethylenimine on dispersion of the SiC nanoparticles in water have been investigated by sedimentation and rheological measurements [73]. Polyethylenimine with a lower degree of ionization is beneficial to dispersion of the SiC nanoparticles, whereas that with a higher degree of ionization causes flocculation of the suspension. The dispersion properties of the SiC nanopowder aqueous suspensions are studied in terms of the surface charge, particle size, rheological characteristics, and adsorption [74]. Ammonium polycarboxylate is used as the dispersant to stabilize the suspension. The powder surface charge varies dramatically in presence of the ammonium polycarboxylate dispersant. The dispersant concentration that leads to the maximum degree of dispersion is found to be 2.4 mg/g of SiC (corresponding to the adsorbed amount of 1.10 mg/g) at a pH of 7.5. This is lower than complete monolayer coverage (corresponding to adsorbed amount of 1.75 mg/g) of the particle surface by the dispersant. Surface functionalization with organic

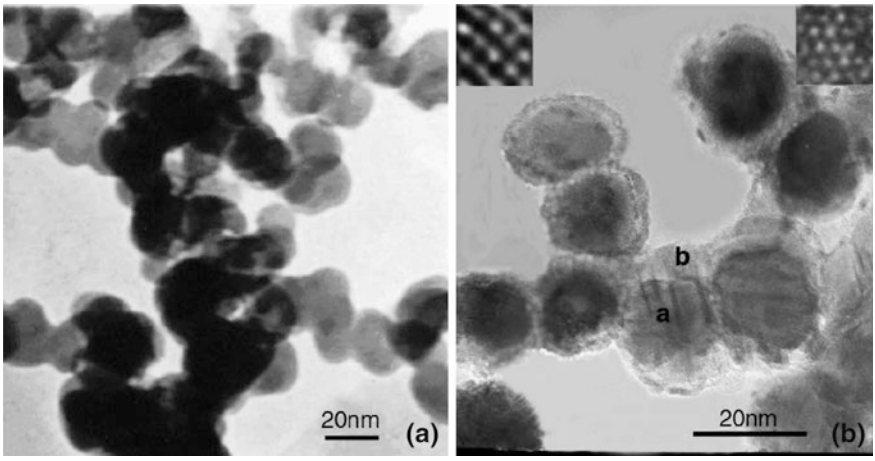

Fig. 4.54 HRTEM images of **a** original SiC nanoparticles and **b** nickel-coated SiC nanoparticles. Reprinted with permission from [77]. Copyright 2006, Elsevier

molecules can improve the dispersion of SiC nanoparticles in non-aqueous media. Grafting of polyacetal onto the SiC nanoparticle surface is investigated [75]. Coating of the SiC nanoparticle surface results in almost complete decomposition of the secondary structure of the agglomerate and formation of primary structures. The sedimentation experiment reveals that the coated SiC nanoparticles are very stable in butanone. Surface modification of SiC nanoparticles by three types of azo radical initiators is investigated [76]. The radicals generated from the azo initiators react with the unsaturated hydrocarbons on the surface of the SiC nanoparticles. As a result, the hydrophobic SiC surface becomes hydrophilic, resulting in improved dispersion stability of the SiC nanoparticles in the aqueous solution. The stability of the SiC nanoparticles in aqueous solutions at various pH values can be controlled by the structure of the azo radical initiators. Owing to the surface carboxyl groups, the stability of the SiC nanoparticles grafted by 2,2′-azobisisobutyronitrile is improved at a pH over 5. The SiC nanoparticles modified with 2,2′-azobis(2-methylpropionamidine)dihydrochloride are stabilized at a pH below 3 due to the formation of amine groups, and SiC nanoparticles modified by 2,2′-azobis[N-(2-carboxyethyl)-2-methylpropionamidine]*n*-hydrate are stabilized at a pH value of 3 or 11 because this azo radical initiator consists of both amine and carboxyl groups.

Surface modification of SiC nanoparticles by electroless nickel plating is investigated [77]. XRD, TEM, and XPS show that a nanoscale agglomerate nickel layer is formed on the surface of the SiC nanoparticles (Fig. 4.54). The real part of the dielectric permittivity and dielectric loss of the nickel-coated SiC nanoparticles are improved significantly compared to the pristine material. The enhanced dielectric properties stem from the increased electrical conductivity rendered by the nickel-coated SiC nanoparticles. The nickel layer as a thin film of contaminant and corresponding skin effect also contribute to the enhancement.

4.3 Theoretical Treatment

In comparison with experimental investigations, there are fewer theoretical studies on the structural and electronic properties of silicon carbide nanoparticles. The major reason lies in the difficulty in fulfilling the requirements for computing the properties of nanocrystals with the size of experimental interest of generally over 1 nm. The large polytype number, diverse surface reconstruction, and complex surface chemical structures of SiC nanocrystals make theoretical assessment even more difficult, because in general, the surface chemistry of SiC nanocrystals cannot be fully determined experimentally. Therefore, it is hard to make a meaningful comparison between the computed and measured results. However, with continuous improvement in the computation power, advance has been made in theoretical investigation of SiC nanocrystals, especially by first-principle method, and the results offer insights into the structural and electronic properties of SiC nanocrystals. One key characteristic of a semiconductor quantum dot is the electronic band structure and associated energy gap. The energy gap is the energy difference between the highest occupied molecular orbital (HOMO) and lowest unoccupied molecular orbital (LUMO) of the quantum dot. It is well known that the density functional theory generally underestimates the energy gaps of semiconductors. However, previous studies of the size dependence of energy gaps of semiconductors such as silicon indicate that the HOMO–LUMO energy gap obtained by the density functional theory and the gap obtained by the more accurate Green's function GW and quantum Monte Carlo calculation show a similar size dependence [78, 79]. Hence, the calculated energy gaps of SiC quantum dots are expected to impart at least qualitatively information about the size and polytype dependence of the energy gap.

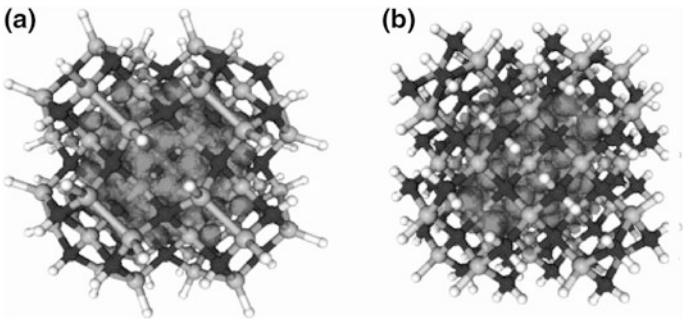

Fig. 4.55 Structure model of two β-SiC quantum dots with the same shape and radius (1.13 nm) but with different surface termination and reconstruction: **a** $C_{62}Si_{80}H_{72}$ with a (2 × 1) Si-terminated surface; **b** $C_{80}Si_{62}H_{120}$ with a (1 × 1) C-terminated surface. *Black* (*gray*) spheres represent C (Si) atoms, and *white* spheres represent H atoms. The *gray* isosurface contains 95 % of the spatial distribution probability of the LUMO state of each quantum dot. Reprinted with permission from [80]. Copyright 2004, American Chemical Society

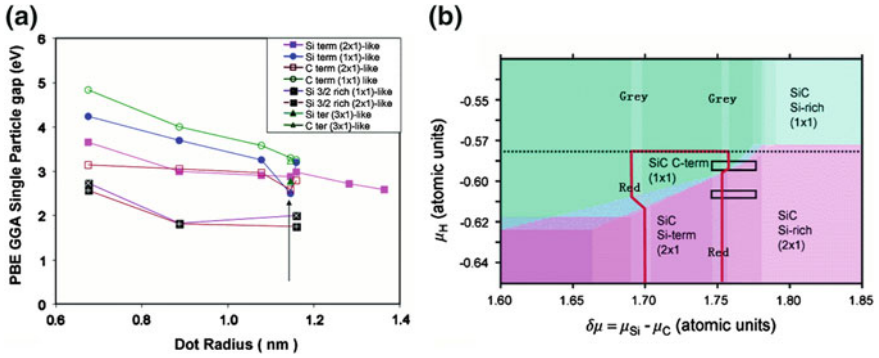

Fig. 4.56 *Left panel* computed single-particle electronic energy gap of β-SiC quantum dots as a function of size for different surface structures. The *arrow* indicates the particle sizes shown in Fig. 4.55. *Right panel* relative stability of SiC dots with different surface structures as a function of the difference between the Si and C chemical potentials ($\delta\mu = \mu_{Si} - \mu_C$) and the hydrogen chemical potential (μ_H). The horizontal *dotted line* indicates the value of μ_H, above which SiC dissociates into silane and methane. The vertical thick *gray lines* denote transition regions where SiC *dots* are not energetically favored compared to pure Si (*left*) or pure C dots (*right*), depending on size and surface structure. SiC quantum dots are stable within the area enclosed in *red*. The *horizontal rectangles* denote examples of values of $\delta\mu$ and μ_H that can be reached experimentally. Reprinted with permission from [80]. Copyright 2004, American Chemical Society

The ab initio computation of SiC quantum dots with diameters of 1–3 nm is performed by means of the density functional theory within the generalized gradient-corrected approximation [80]. For each quantum dot, a cubic β-SiC core structure with six different surface geometries is considered together with three different terminations (C, Si, or Si-rich) and two different surface structures, that is, the ideally terminated or reconstructed (100) facets. Hydrogen termination of the surface is taken into account (Fig. 4.55). The results show that the surface composition and termination play important roles in the optical gaps and thermodynamic stability of these nanoparticles (Fig. 4.56). Irrespective of size, hydrogenated quantum dots with the unreconstructed C-terminated surface and (2×1)-reconstructed Si-terminated surface are the most stable, and they can have a gap difference as large as 1–1.5 eV for the same diameter. In the calculated phase diagram displayed in Fig. 4.56 (right panel), the horizontal dotted line indicates the value of hydrogen chemical potential μ_H, above which bulk β-SiC spontaneously dissociates into CH_4 and SiH_4. The two thick vertical gray bars represent the size and surface-dependent transition region where the value of $\delta\mu$ is so high (low) that pure Si (C) quantum dots are more stable than SiC quantum dots. The region highlighted in red corresponds to the stable region of the SiC dots, where the (1×1) C-terminated and (2×1) Si-terminated structures are the most stable. The computation indicates that the energy gap of β-SiC dots can be engineered as a function of size and surface composition to obtain absorption and emission from UV to green.

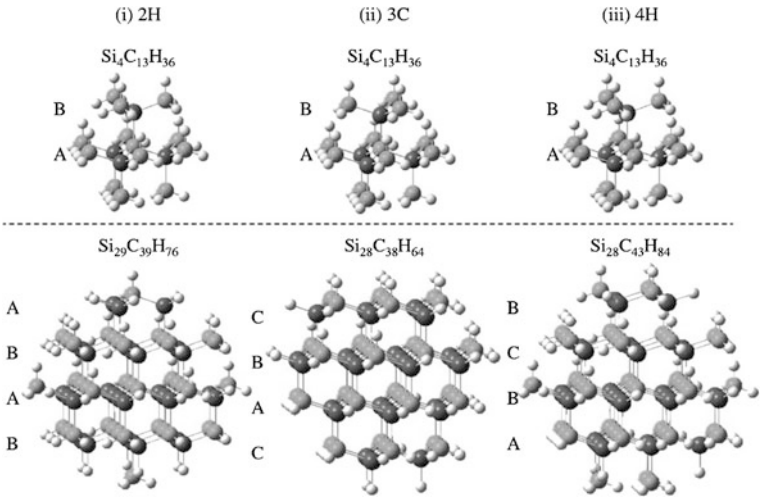

Fig. 4.57 Atomic arrangements of 2H-, 3C-, and 4H-SiC nanoclusters with two sizes. Clusters of 0.70 nm (*upper panel*) exhibit nearly identical structures regardless of the polytype, whereas for 1.11 nm clusters, dramatic structural differences can be observed among different polytypes. Reprinted with permission from [81]. Copyright 2007, AIP Publishing LLC

The dependence of the energy gap and stability on the polytype in silicon carbide nanoclusters is investigated using the density functional theory based on a gradient-corrected approximation [81]. Spherical SiC nanoclusters with diameters up to 2 nm from bulk 2H, 3C, and 4H polytype crystals are considered. Prior to the calculation, the dangling bonds of the surface atoms in the clusters are terminated by hydrogen atoms. Figure 4.57 shows the atomic arrangements in two SiC nanoclusters of different sizes obtained from different polytypes. Clusters 0.70 nm in size have similar structures independent of the parent polytypes. Polytypism of the parent crystals is completely lost in these clusters due to the limited number of bilayers. The 1.11-nm clusters exhibit dramatic structural differences among polytypes. Different from the bulk characteristics, the binding energy difference between different polytypes of clusters with diameters between 0.5 and 2 nm is negligible. This implies that the problem associated with the synthesis of bulk SiC polytypes may disappear for small clusters. For clusters smaller than 1 nm, the variation in the energy gaps with size in three polytypes shows indistinguishable trends (Fig. 4.58). In contrast, the energy gaps of clusters larger than 1 nm exhibit distinct size dependence for different polytypes.

The stability of fullerene-like SiC clusters is investigated by the density functional theory [82]. The carbon fullerene-based SiC clusters stemming from the C_{20} fullerene structure are distorted having open structures. The Si atoms tend to be clustered even if there are only three Si substitutions. Cage-derived Si–C clusters are more energetically favorable than the bowl-derived ones. The HOMO–LUMO gaps of both structures decrease as the number of Si atoms in the cluster increases.

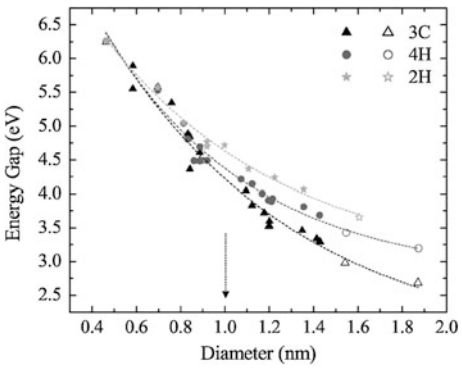

Fig. 4.58 Calculated HOMO–LUMO gap as a function of size for 3C-, 4H-, and 2H-SiC nanoclusters. The *solid* data points are the energy gaps of the relaxed clusters. Open data points correspond to the gaps of larger geometry-unrelaxed clusters. The energy gap difference between relaxed and unrelaxed clusters is expected to be within 0.15 eV. *Dashed lines* serve as visual guide. Reprinted with permission from [81]. Copyright 2007, AIP Publishing LLC

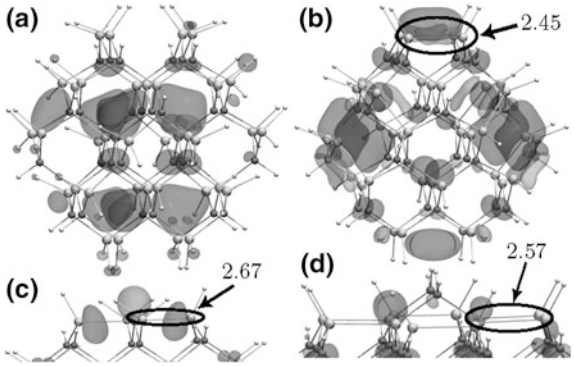

Fig. 4.59 **a** Unreconstructed $d = 1.0$ nm SiC nanocrystal (NC), **b** Si 2 × 1-type reconstruction in $d = 1.0$ nm SiC NC, **c** 3 × 1-type reconstructions in $d = 1.5$ nm SiC NC, and **d** step-like reconstruction in $d = 2.1$ nm SiC NC. The bond lengths of the long Si–Si bonds are denoted in angstrom. *Small* (*big*) *gray* (*white*) and smallest *white* balls represent C (Si) and H atoms, respectively. The lobes are the isosurfaces of the LUMO states. Reprinted with permission from [83]. Copyright 2010, AIP Publishing LLC

The binding energy declines linearly with increasing number of Si atoms, suggesting overall reduced stability. Therefore, it is concluded that there is little chance that SiC fullerene can be formed from carbon-based fullerenes.

The electronic structure and absorption spectra of hydrogenated cubic silicon carbide nanocrystals are investigated by first-principle calculation [83]. The crystal structure is constructed by cutting approximately spherical clusters out of the perfect cubic SiC crystal in such a way that each surface atom has at most two dangling bonds. The diameter of the resulting clusters excluding hydrogen atoms

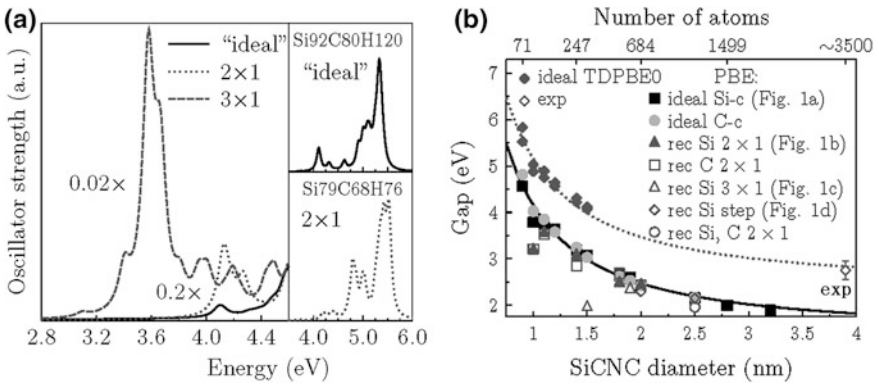

Fig. 4.60 **a** Calculated absorption spectrum of the ensemble of SiC nanocrystals (NCs) with diameters between 1.0 and 1.5 nm. *Solid curve* ideal non-reconstructed NCs; *dotted curve* with 0.2 scaling: 2 × 1-type reconstructed NCs; *dashed curve* with 0.02 scaling: 3 × 1-type reconstructed NCs. *Right part* shows the absorption spectrum of individual NCs: (*top*) an ideal $d = 1.5$ nm and (*bottom*) a 2 × 1 reconstructed $d = 1.4$ nm NC. **b** Calculated energy gaps of SiC NCs with different methods as indicated. The *curves* are the fits. The experimental value is taken from Ref. [84]. "Ideal" ("rec") refers to non-reconstructed (reconstructed). Si-c (C-c) indicates $Si_xC_yH_z$ ($Si_yC_xH_z$) NCs. The sign after "rec" indicates the type of reconstruction; for example, "rec Si 2 × 1" means 2 × 1 reconstructed surface with long Si–Si bonds. Reprinted with permission from [83]. Copyright 2010, AIP Publishing LLC

is between 0.9 and 3.2 nm, and the surface dangling bonds are saturated by hydrogen atoms (Fig. 4.59). The reconstructed surface can substantially change the absorption onset and spectrum shape at higher energy (Fig. 4.60a). The optical gap of small SiC nanocrystals is reduced by surface reconstruction, and different surface reconstructions give rise to different energy gaps for the same particle size (Fig. 4.60b). The calculated absorption energy gap by means of extrapolation agrees well with the measured value [84]. Absorption by 0.9–1.4 nm oxygenated silicon carbide nanoparticles is studied by time-dependent density functional calculation [85], revealing that Si–O and C–O single bonds result in relatively large energy gaps in the ultraviolet region, whereas Si=O and C=O double bonds dramatically reduce the energy gap in the blue and red regions, respectively.

SiC quantum dots terminated by C–H or Si–H bonds are studied by density functional calculation [86]. The size of the SiC quantum dots is chosen to be 0.94–2.49 nm. The calculation shows that the quantum confinement effect is present (absent) in the highest occupied (lowest unoccupied) molecular orbital of the SiC quantum dots regardless of surface termination (Fig. 4.61). The electron affinity of the SiC quantum dot is found to be negative for C–H termination and positive for Si–H termination. The influence of surface passivation (−H, −OH, $-NH_2$) on the electronic structures of the stoichiometric Si_nC_n ($n = 10$–68) quantum dots is investigated by density functional calculation [87]. The HOMO–LUMO gap of SiC nanoparticles depends on the surface chemistry, and the −H passivated dots have the largest energy, followed by the −OH and $-NH_2$ passivated dots.

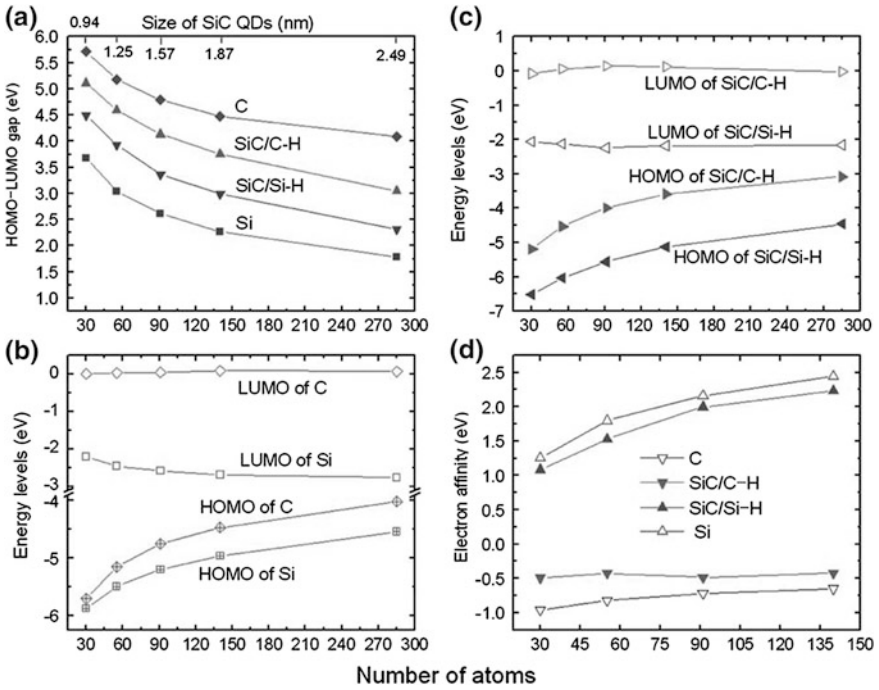

Fig. 4.61 The size dependence of **a** the HOMO–LUMO gaps of C, Si, and SiC quantum dots (QDs), **b** the HOMO and LUMO levels of C and Si QDs, **c** the HOMO and LUMO levels of SiC QDs terminated by C–H or Si–H bonds, and **d** the electron affinities of the C, Si, and SiC QDs. Reprinted with permission from [86]. Copyright 2012, Royal Society of Chemistry

4.4 Potential Applications

Silicon carbide is a unique wide-bandgap semiconductor with excellent properties such as high hardness, low density, high thermal stability, good radiation resistance, and biological compatibility. Moreover, silicon carbide nanocrystals have tunable energy gaps showing adjustable and robust luminescence spanning the visible and near-UV regions. Therefore, SiC nanoparticles have immense application potential.

4.4.1 Enhancement of Mechanical Properties

SiC nanoparticles are widely used to improve the mechanical properties of metals and ceramics due to their superior mechanical characteristics. Nanocomposites consisting of a nanocrystalline Ni matrix with a grain size of 15–20 nm are reinforced with up to 3 wt% sub-micrometer SiC particles [88]. The

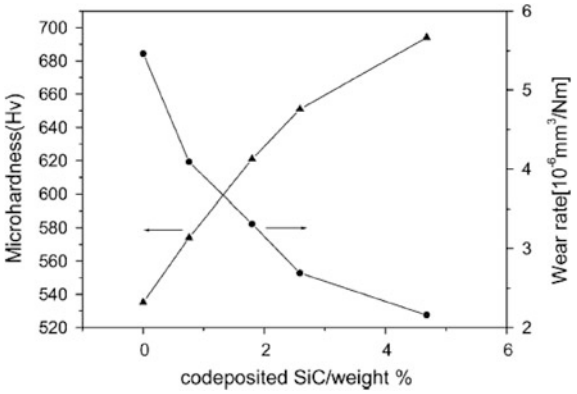

Fig. 4.62 Microhardness and wear rate of the Ni–Co/SiC nanocomposite coatings versus weight percentage of SiC particulates in the nanocomposite coating. Reprinted with permission from [90]. Copyright 2006, Elsevier

microhardness values are about two times larger than those of polycrystalline Ni-SiC composites. Further study is conducted on nanocomposites containing up to 10.5 vol% SiC particulates (average size of 400 nm) [89]. These nanocomposites possess improved mechanical properties including hardness, yield, and tensile stress than conventional Ni-SiC composites with micrometer grain size. The materials have tensile strength up to four times that of conventional polycrystalline Ni and twice that of conventional polycrystalline Ni-SiC with a comparable SiC content. The nanocomposites with a SiC content of less than 2 vol% have higher tensile and yield strength as well as increased tensile ductility than pure nanocrystalline nickel with a comparable grain size. However, an excessively large SiC content reduces the strength and ductility due to possible particle clustering.

SiC nanoparticles affect the mechanical properties of Ni–Co/SiC nanocomposite coatings prepared by electrodeposition [90]. The SiC nanoparticles have a mean diameter of 50 nm, and the microhardness and wear and corrosion resistance of the nanocomposite coatings increase with nano-SiC concentration (Fig. 4.62). The codeposited SiC nanoparticles are uniformly distributed in the Ni–Co matrix and contribute to the enhanced microhardness and wear resistance. For the Ni/SiC nanocomposite coatings containing SiC nanoparticulates with a mean size of 50 nm, the microhardness and wear and corrosion resistance also increase with SiC nanoparticle concentration [91].

The fracture behavior of Al_2O_3 containing 5 vol% 15-nm SiC particles is investigated [92]. The strength increases from 560 MPa for Al_2O_3 to 760 MPa for the composite materials. The average strength of the composites increases to about 1,000 MPa after annealing at 1,300 °C for 2 h. The observed strengthening and toughening are believed to be due to machining-induced compressive surface stress. In another study involving alumina containing 17 vol% silicon carbide, the minimum creep rate of the nanocomposite is three orders of magnitude smaller and the creep life is 10 times longer than those of pure alumina [93]. The bending strength of the Al_2O_3/5 vol% SiC densified by spark plasma sintering at 1,450 °C is as high as 1,000 MPa [94]. The SiC particulates are 70 nm in size, and electron microscopy indicates that the SiC particles are mainly concentrated in the Al_2O_3

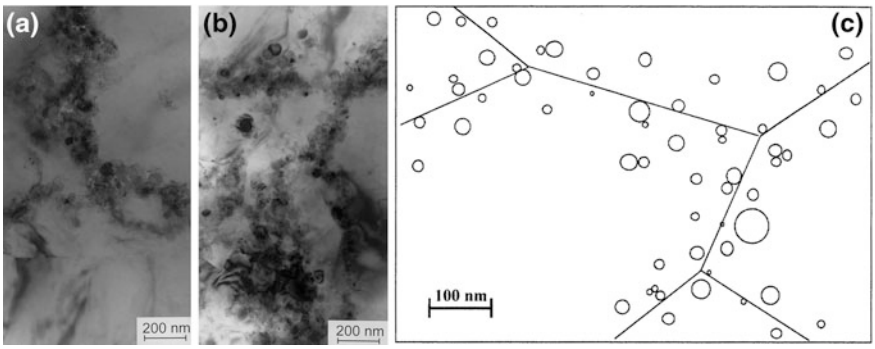

Fig. 4.63 Transmission electron micrographs of Mg/3 vol% SiC nanoparticles: powder only mixed (**a**) and also milled for 8 h before extrusion (**b**). **c** Schematic of the milled composite after extrusion. The SiC nanoparticles decorate the grain boundaries of the metal matrix and form together with the matrix along the grain boundaries a nanostructured linked network. Reprinted with permission from [98]. Copyright 2001, Elsevier

grains. SiC nanoparticles can also enhance the mechanical properties of aluminum. The microstructure and mechanical properties of aluminum-based nanocomposites containing SiC nanoparticles smaller than 30 nm are determined [95]. The yield strength of the A356 alloy is improved by more than 50 % by the addition of 2.0 wt% of SC nanoparticles.

The Si_3N_4 matrix dispersed with less than 10 vol% SiC nanoparticles shows the same order of resistivity and dielectric properties as the pure materials, but improved mechanical properties [96]. The strength of the Si_3N_4/SiC nanocomposites at 1,400 °C is 70–100 % of its room temperature strength [97]. The creep and oxidation resistance are very high and comparable to or better than those of the best Si_3N_4-based materials previously reported.

Mg is reinforced with SiC nanoparticles with an average diameter of 30 nm [98]. In the case of mixed powders (Fig. 4.63), the nanoparticles decorate the elongated coarse-grained Mg grain boundaries after extrusion and for the milled powders, a sub-micrometer grained Mg structure in which the SiC nanoparticles decorate the shear band in the heavily deformed Mg is formed and at least partly dispersed in the sub-micrometer matrix grains after extrusion. The milled composite has the largest flow stress and smallest creep rates in comparison with other composites and pure magnesium. Another study shows that the microhardness of SiC nanoparticle-reinforced magnesium composites is improved with increasing fraction of SiC nanoparticles [99] and the microhardness of AZ91D/5 wt% SiC increases by 75 % compared to AZ91D.

SiC nanoparticles can improve the properties of epoxies [100]. The nanoparticles are superior to micrometer-size particles in enhancing the thermal and mechanical properties of the SiC/epoxy composite. Nanoparticle infusion improves the thermal stability of the composite by enhancing cross-linking in the polymer. The SiC nanoparticles act as fillers in the voids of the composites to

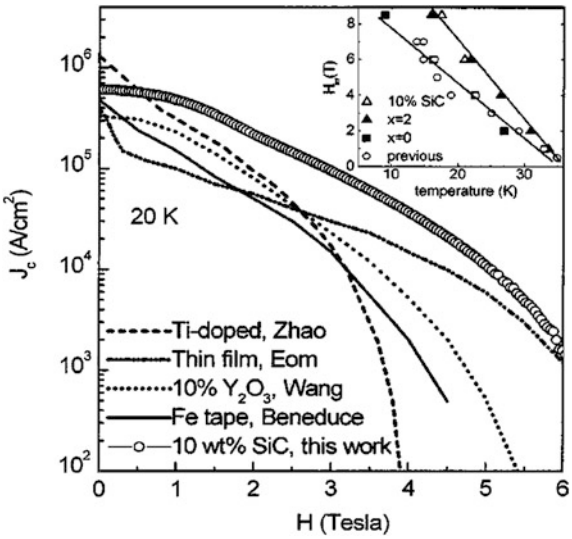

Fig. 4.64 Comparison of magnetic $J_c(H)$ at 20 K for the 10 wt% SiC-doped MgB_2 sample and samples from other works: Ti-doped, Y_2O_3-doped, thin film with strong pinning, and Fe/MgB_2 tape. The *inset* shows the temperature dependence of the irreversibility field for SiC-doped MgB_2 with different SiC content (*triangles* and *squares*) and for previously prepared undoped MgB_2 (*round symbols*) . Reprinted with permission from [102]. Copyright 2002, AIP Publishing LLC

boost the mechanical properties. Carbon nanotube (80 nm) and SiC nanoparticle composites have superior mechanical properties [101]. The three-point bending strength and fracture toughness are improved by about 10 % relative to monolithic SiC ceramics fabricated by a similar process due to strengthening and toughening caused by carbon nanotubes in the matrix.

4.4.2 Superconductivity Enhancement

SiC nanoparticles have been demonstrated to be able to significantly enhance the properties of MgB_2 superconductors. Doping of MgB_2 with (10–100 nm) SiC nanoparticles and the improved flux pinning in $MgB_{2-x}(SiC)_{x/2}$ with $x = 0$, 0.2, and 0.3 and 10 wt% nano-SiC-doped MgB_2 samples are studied [102]. Cosubstitution of B by Si and C counterbalances the single-element doping effect, reducing T_c (critical temperature) by only 1.5 K. Moreover, intragrain pinning centers effective at high fields and high temperature are generated and J_c (critical current density) (Fig. 4.64) and H_{irr} (irreversibility field) are significantly enhanced. The critical current density of the 10 wt% doped sample increases by a factor of 42 at 20 K/5 T compared to the undoped sample, and it reaches 2.4×10^5 A/cm^2 at 20 K/2 T which is comparable to the J_c values of the best Ag/Bi-2223

tapes. The critical current density at 20 K/4 T is twice that of the best MgB_2 thin films and an order of magnitude larger than that of the best Fe/MgB_2 tapes.

The effects of the incorporation of 30-nm SiO_2 and SiC on the microstructure and superconducting properties of in situ-processed MgB_2/Fe tapes are studied [103]. Mg or MgH_2 powders are the Mg source, and the use of MgH_2 instead of Mg powders improves the correlation between the MgB_2 grains and improved J_C. SiC doping effectively enhances J_C with regard to the starting powder mixtures of MgH_2 + B and Mg + B. In contrast, SiO_2 is only effective for the Mg + B powder mixture. The highest J_C value of 6,500 A cm^{-2} at 4.2 K/12 T is observed from the 10 at% SiC-doped tape. The SiC doping improves the irreversibility field from 17 to 23 T and pinning characteristics. However, excessive SiC doping degrades J_C in the low-field region. Further measurements on the 10 at% SiC-doped MgB_2 indicate that the upper critical field H_{c2} is systematically enhanced by SiC doping and by lowering reaction temperature [104]. H_{c2} (10 K) exceeds 33 T, and the extrapolated zero temperature value exceeds 40 T. Only 8–17 % of the MgB_2 cross section carries current as revealed by the Rowell analysis. A higher reaction temperature is found to improve the connectivity but degrade H_{c2} and flux pinning.

The mechanism pertaining to the enhancement of the electromagnetic properties of MgB_2 by doping with SiC nanoparticles is studied [105]. The mechanism is based on the sintering temperature effect on the lattice parameters, carbon content, and electromagnetic properties. The optimal doping effect is attained when carbon substitution and MgB_2 formation take place at the same time at a low temperature. Carbon substitution accounts for the enhancement in both H_{c2} and flux pinning. Carbon substitution for boron results in disorder in lattice sites and increase in the resistivity and consequently enhancement in H_{c2}. Carbon substitution combined with low-temperature processing leads to reduced grain size, fluctuation in T_c, extra defects, and embedded inclusions, which enhance flux pinning.

4.4.3 Surface Phonon Polariton and Luminescence Enhancement

Like surface plasmons in metals, the surface phonons in silicon carbide can couple with incident photons producing surface phonon polaritons. This is an interesting phenomenon and has potential applications. The excitation energies of the optical Fuchs-Kliewer surface phonons and their relationship with the bulk phonon frequencies in 3C, 4H, and 6H polytypes of silicon carbide epilayers are studied by Auger electron spectroscopy, high-resolution electron energy loss, and Raman scattering [106]. After surface treatment in buffered hydrofluoric acid, loss structures belonging to excitation of Fuchs-Kliewer surface phonons are observed, and the energy is at 115.9 ± 1 meV irrespective of the SiC polytype.

The reflectivity and coherent thermal emission properties of a one-dimensional SiC grating are investigated both experimentally and theoretically [107]. The study

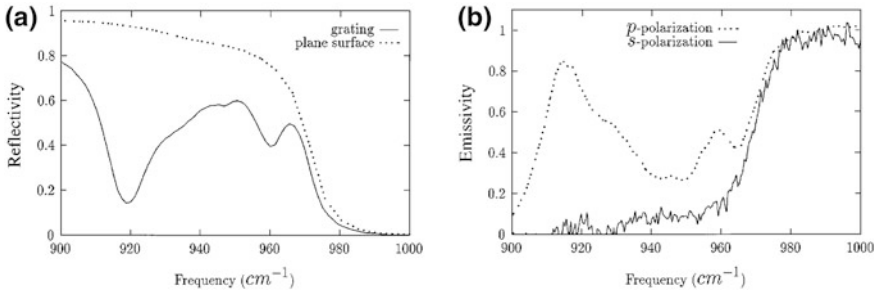

Fig. 4.65 **a** Reflection spectra of the SiC grating and SiC plane surface for *p* polarization at near-normal incidence (incidence angle: 6°). **b** Emission spectra of the SiC grating for both polarizations at near-normal incidence (incidence angle: 6°). Reprinted with permission from [107]. Copyright 1997, American Physical Society

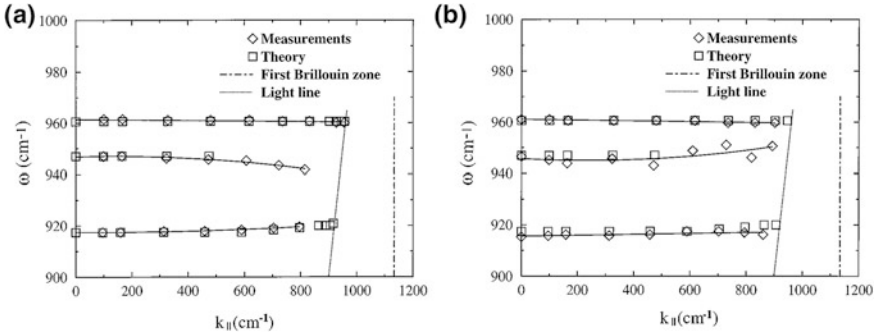

Fig. 4.66 Dispersion relation of the surface phonon polariton on a SiC grating obtained from reflectivity data (**a**) and from emissivity data at 100° (**b**). Reprinted with permission from [107]. Copyright 1997, American Physical Society

is conducted between 10 and 11.5 μm where the real part of the permittivity of SiC is negative. The reflectivity spectra in *p* polarization exhibit obvious dips due to surface phonon polariton excitations as shown in Fig. 4.65a. The reflectivity is different from that of the flat surface. Three dips appear at 917, 947, and 962 cm^{-1}, and these peaks are assigned to surface phonon polaritons. Peaks in the same directions and at the same frequencies are observed from thermal emission (Fig. 4.65b). The peaks at 916, 945, and 961 cm^{-1} for *p* polarization are ascribed to light emission due to thermally excited surface phonon polaritons. Similar effects are not observed for *s* polarization. In both cases, experiments and calculation agree and the dispersion relationship obtained theoretically and experimentally (Fig. 4.66) are consistent. The experimental dispersion relationship is derived from the reflectivity data, whereas the theoretical data are obtained from the simulated reflectivity spectra.

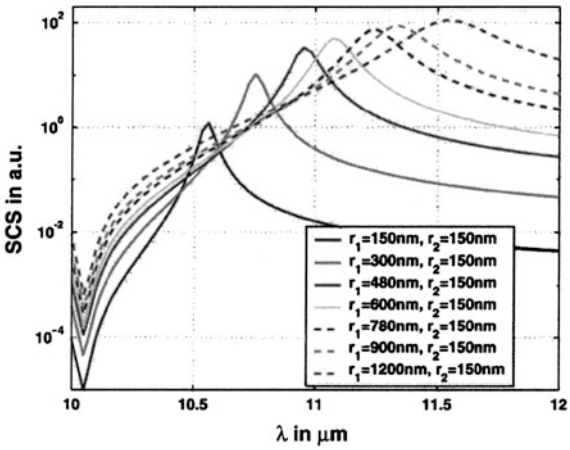

Fig. 4.67 Scattering cross sections of an elliptical 6H-SiC cylinder as a function of the axis ratio (from 1 to 8). Reprinted with permission from [108]. Copyright 2005, Optical Society of America

The boundary element method is adopted to study small-particle phonon–polariton excitation in 6H-SiC [108]. Phonon polaritons are found from the far-infrared spectrum of 10–12 μm. For incident light in near resonance with the phonon polariton, the scattered electromagnetic energy in the far field and near-field amplitude around the structure are all enhanced. Calculation shows that the circular and elliptical cylinders support phonon polaritons at distinguishable wavelengths that are related to the axis ratio of the particle (Fig. 4.67). The scattering-cross-section curve of larger particles broadens and redshifts. The single phonon polariton is split into a band with geometries other than elliptical. Two phonon polaritons are excited for the rectangular cylinders and five phonon polaritons for the triangular cylinders. The phonon polaritons in SiC are shown to be more efficiently excited than plasmon polaritons excited in silver due to the smaller imaginary part of the dielectric constant of SiC.

Critical coupling to surface phonon polaritons in silicon carbide is observed by attenuated total reflection of the mid-infrared radiation through a double scan of the wavelength and incident angle [109]. Critical coupling means complete coupling of laser energy to surface phonon polaritons resulting in disappearing reflectivity and largest enhancement in the surface phonon polariton field over the incident laser field. Critical coupling occurs when the prism coupling loss is equal to loss in silicon carbide and the substrate. In this process, the surface phonon polaritons are launched using evanescent light coupled to the Otto configuration. pL-scale analyte index sensing can be realized on the basis of analysis of surface phonon polaritons in the mid-infrared region excited at the silicon carbide/analyte interface in the Otto configuration [110]. Attenuated total reflectance measurement provides the analyte indices through a double scan of the wavelength and incident angle for analyte volumes as small as 100 pL.

Numerical simulation shows that the incident infrared optical field (10.6 μm) in gold microstructures on the surface of silicon carbide can be enhanced due to excitation of surface phonon polaritons [111]. The enhancement arises from two

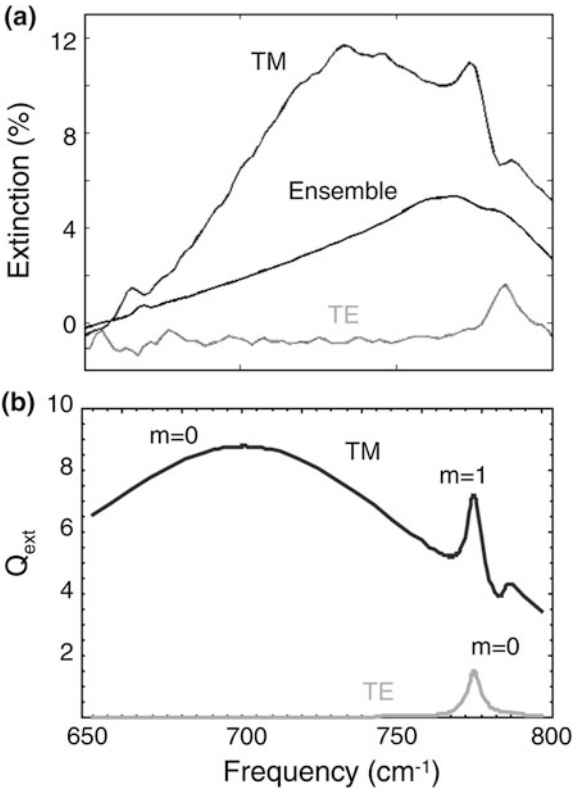

Fig. 4.68 **a** Ensemble, TE (E field perpendicular to long axis), and TM (E field parallel to long axis) polarized extinction spectra of a typical 1-μm-diameter SiC whisker (length: 40–100 μm). **b** Calculated extinction efficiency of an infinitely long 1-μm-diameter SiC cylinder for both TE and TM illumination. The spectrum is dominated by three modes: TM_0, TM_1, and TE_0, where the subscript denotes the *m* number of the mode. Reprinted with permission from [112]. Copyright 2007, American Physical Society

contributions: resonant coupling of the conventional gold antenna and excitation of surface phonon polaritons of SiC. The amplitude of the local field is found to be enhanced by up to 106 times.

Silicon carbide particles exhibit electric and magnetic resonance in the infrared region [112]. Experimental extinction spectra and Mie theory calculation of a single SiC rod reveal three mid-infrared resonant modes. The measured extinction spectrum of a typical SiC rod with a diameter of 1 μm is depicted in Fig. 4.68a. With respect to TM polarization (E field parallel to the whisker's long axis), a sharp peak at 774 cm^{-1} and broader low-frequency peak are observed and for TE polarization (E field perpendicular to long axis), a sharp peak arises at 785 cm^{-1}, whereas there is no featureless extinction at low frequencies. The calculation is performed on the basis of Mie theory for infinitely long cylinders (1 μm in diameter) for normal incidence illumination where the incident, scattered, and interior fields can be considered purely TE or TM. The calculation results (Fig. 4.68b) agree with experimental ones. For TM polarization, the calculated extinction consists of a broad low-frequency peak and a sharp peak at 777 cm^{-1}. The redshift of the low-frequency peak relative to the experimental spectrum may result from off-normal rays by the microscope objective. For TE polarization, a sharp peak also arises at 777 cm^{-1} and it is superimposed on a flat background.

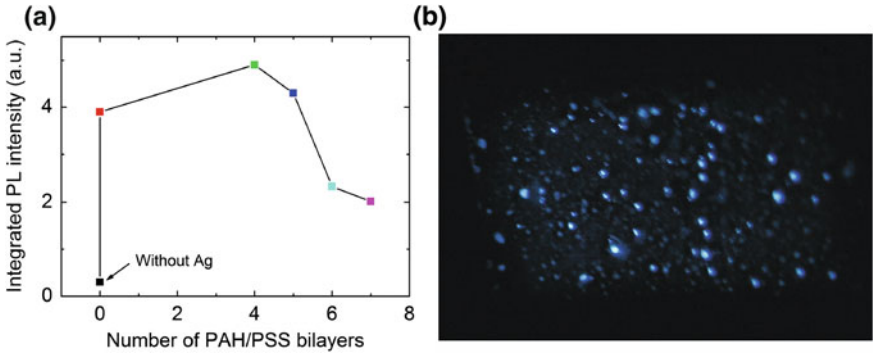

Fig. 4.69 **a** Integrated intensity of the photoluminescence spectrum versus number of bilayers for the SiC nanocrystals/PSS-PAH bilayers/Ag nanoparticles sandwiched structures. **b** Luminescence graph of the sandwiched structure with four PSS-PAH bilayers. Reprinted with permission from [115]. Copyright 2012, Elsevier

The experimentally observed 774 cm^{-1} peak (TM polarization) and 785 cm^{-1} peak (TE polarization) are degenerate, and the actual separation may be caused by experimental complications. The existence of both electric and magnetic resonances may enable design of metamaterials. A theoretical study shows that the silicon carbide spheres embedded in potassium bromide can act as metamaterials [113]. Near-field radiative heat is found to be transferred between these isotropic and dielectric-based metamaterials. The electric and magnetic surface polaritons are excited and mediate the near-field radiative heat transfer. Metamaterials showing negative index in the visible (blue) are realized using cosputtered SiC and Ag nanoparticles on a glass substrate [114]. The real part of the negative index of the metamaterials at 405 nm obtained by the double Michelson interferometry setup show a negative phase delay, and simulation reveals that the metamaterials can yield near-field super-resolution imaging for both TE and TM polarizations.

Surface phonon polaritons can be generated in silicon carbide, whereas luminescence from silicon carbide nanoparticles can be enhanced by surface plasmon polaritons of nearby metals. PL enhancement is observed from the SiC nanocrystals/PSS-PAH bilayers/Ag nanoparticles sandwiched structures [115], where PSS refers to poly(styrene sulfonic acid) sodium salt and PAH refers to poly(allylamine hydrochloride). The PSS-PAH polyelectrolyte bilayers serve as the spacing dielectric. The SiC nanocrystals are about 3.8 nm in size, and the silver crystallites have an irregular shape with an average diameter of 47 nm. The enhancement depends on the bilayer number. The integrated PL intensity can be improved by up to 17 times (Fig. 4.69), and luminescence from the sandwiched structures is bright and visible to the naked eyes. Large fluorescence enhancement is observed from 1 to 6-nm-diameter SiC nanocrystals dispersed in a SDS dielectric film coated with Ag nanoparticles [116]. The enhancement in the integrated fluorescence intensity is 176-fold under 360-nm excitation (Fig. 4.70), and the PL peak intensity receives a 53.3-fold enhancement. Finite element simulation reveals that the absorption enhancement

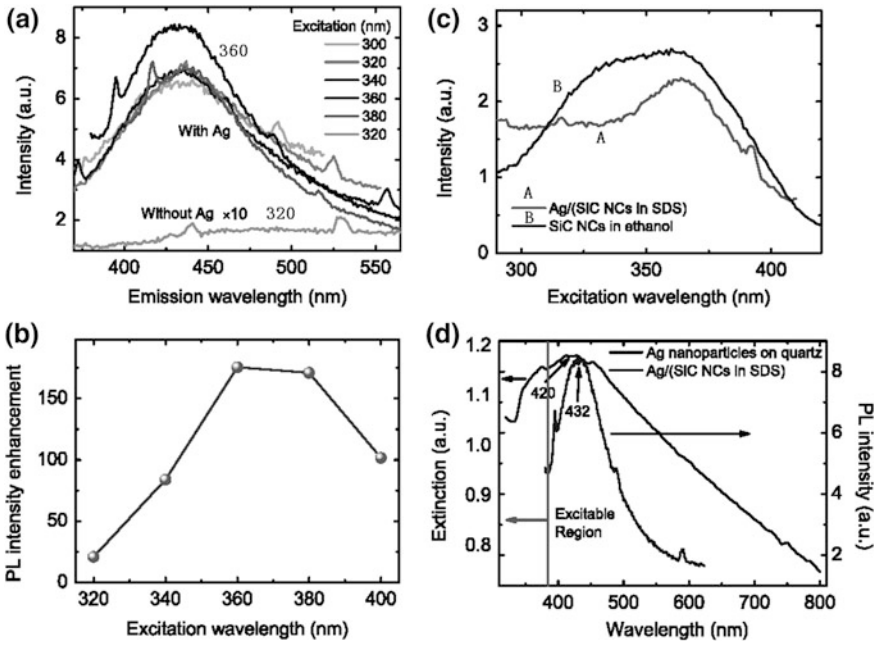

Fig. 4.70 **a** PL spectra of the Ag nanoparticles/(SiC nanocrystals (NCs) in sodium dodecyl sulfonate (SDS) dielectric)/Si wafer under different excitations. The spectrum before Ag deposition is also shown. **b** Ratio of the integrated PL intensity between samples with and without Ag deposition. **c** PL excitation spectra of the Ag/(SiC NCs in SDS dielectric)/Si wafer and the SiC NCs in ethanol for emission wavelengths of 430 and 440 nm, respectively. **d** Comparison of the UV–Vis extinction spectrum (resonance peak: 420 nm) of the Ag nanoparticles on a quartz wafer and the PL spectrum of the Ag/(SiC NCs in SDS dielectric)/Si wafer (peak: 432 nm) excited at 360 nm. Reprinted with permission from [116]. Copyright 2013, IOP Publishing

caused by light concentration at near field of the Ag nanoparticles contributes only slightly to the overall PL enhancement. The Ag nanoparticles exhibit a resonance extinction peak at about 420 nm (Fig. 4.70d), which is very close to the PL peak of the SiC nanoparticles of 432 nm. It is thus concluded that the strong resonant coupling between excited SiC nanocrystals and localized surface plasmons of the Ag nanoparticles plays a dominant role in the big fluorescence enhancement.

Gold colloids encapsulated by silica shells are mixed with SiC nanoparticles to improve PL [117, 118]. The enhancement depends on the silica shell thickness, and an enhancement factor of 12.5 is achieved from gold colloids 20 nm in diameter with a 25-nm shell. The $Au/SiO_2/SiC$ composite exhibits blueshifted (from 582 to 523 nm) PL compared to pure SiC sample. PL enhancement is observed from SiC quantum dots deposited on the nano-Ag/SiN_X substrate [119]. The maximum enhancement factor is 15. The finite-difference time-domain simulation shows that the enhancement arises from the near-field coupling between the SiC nanoparticles and multipolar localized plasmons of the silver nanoparticles. The nonlinear response from the SiC nanoparticles is observed from the same nano-Ag/SiN_X

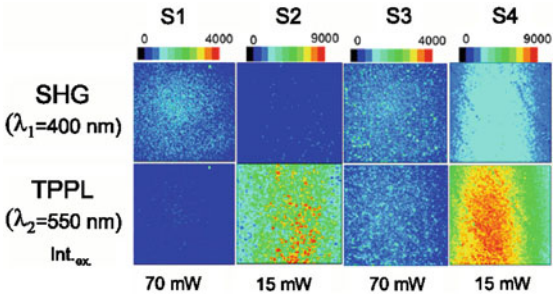

Fig. 4.71 Fluorescence microscopy images of the second-harmonic generation (400 nm, *upper four*) and two-photon-excited photoluminescence (550 nm, *lower four*) excited at 800 nm. The samples are SiN_X (S1), nano-Ag/SiN_X (S2), SiC nanoparticles/SiN_X (S3), and SiC nanoparticles/nano-Ag/SiN_X (S4). The excitation laser power is indicated. Reprinted with permission from [120]. Copyright 2013, IOP Publishing

substrate [120]. The 72-fold enhancement in the second-harmonic generation is observed by localization of the SiC nanoparticles in the strong-field regions and in the case of spectral overlap between the multipolar plasmon modes and excitation and second-harmonic generation lines. The maximum 287-fold enhancement in the two-photon excited luminescence from the SiC nanoparticles is observed from this nano-Ag/SiN_X substrate, and the fluorescence images are shown in Fig. 4.71.

4.4.4 Electroluminescence and LED

Silicon carbide is a favorable semiconductor to fabricate light-emitting diodes (LEDs) because blue to near-UV luminescence can be realized due to the wide bandgap. Some SiC-based LED products are available on the market although the low luminescence efficiency of bulk silicon carbide is the major limitation. The quantum yields of porous silicon carbide and silicon carbide nanocrystals can be several orders of magnitude higher than that of bulk materials. For example, the quantum yield of 3C-SiC quantum dots suspended in water is 17 % [121] which is comparable to that of some direct bandgap semiconductors. Therefore, the SiC nanocrystals are promising materials in blue and near-UV light-emitting diodes.

A blue LED using porous SiC as a luminescent layer has been produced [122]. The ITO/porous SiC junction shows a rectification behavior and blue electroluminescence under forward biasing. The electroluminescence exhibits a very broad spectrum from 350 to 780 nm with a peak at 470 nm (Fig. 4.72), which is similar to the PL spectrum. The blue electroluminescence at low current level is suggested to arise from recombination of the carriers injected from both the SiC substrate and ITO electrode. At a high current level, luminescence is limited by the holes injected from the ITO electrode. However, the quantum efficiency of the porous SiC LED is rather low ($<10^{-5}$), possibly caused by the limited light-emitting area on porous SiC.

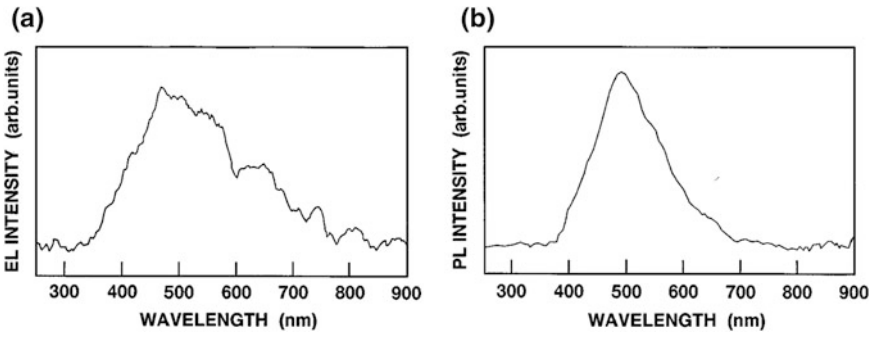

Fig. 4.72 **a** Electroluminescence spectrum from the ITO/porous SiC junction. **b** PL spectrum of a similar porous SiC excited by 325 nm. Reprinted with permission from [122]. Copyright 1994, AIP Publishing LLC

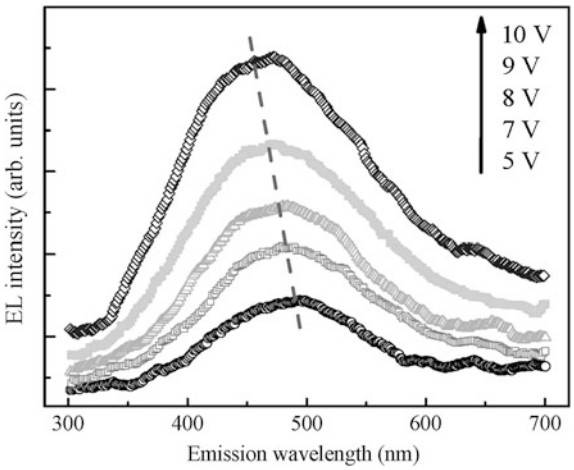

Fig. 4.73 Electroluminescence spectra of the Al/polymer-encapsulated 3C-SiC quantum dot/ITO/glass. The applied voltages are indicated. Reprinted with permission from [123]. Copyright 2012, AIP Publishing LLC

Electroluminescence is observed from an Al/polymer-encapsulated 3C-SiC quantum dot/ITO/glass structure [123]. The primary poly(acrylic acid)-encapsulated 3C-SiC quantum dots smaller than 7 nm in size produce PL with peak wavelengths between 400 and 540 nm. The device shows an electroluminescence spectrum (Fig. 4.73) with the peak wavelength varying between 490 and 460 nm as the applied voltage is increased from 5 to 10 V. The luminescence may stem from carrier recombination in the embedded quantum dots. The device has a low turn-on voltage of 4–5 V. No electroluminescence is observed at voltages lower than 4 V or higher than 11 V, and no quantum efficiency value is obtained.

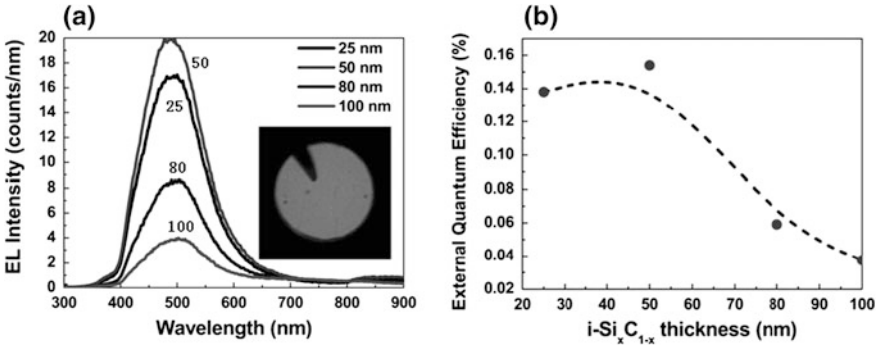

Fig. 4.74 **a** Electroluminescence spectra of Si-rich Si_xC_{1-x} *p–i–n* junction LEDs with different *i*-Si_xC_{1-x} thicknesses. The *inset* is the electroluminescence emission pattern. **b** External quantum efficiency as a function of *i*-Si_xC_{1-x} thickness. Reprinted with permission from [124]. Copyright 2014, IEEE

Si quantum dots and SiC quantum dots codoped Si-rich Si_xC_{1-x} *p–i–n* junction LEDs have been prepared [124]. When the *i*-SiC thickness is varied from 25 nm to 100 nm, the turn-on voltage changes from 6.1 to 10.8 V. The maximum electroluminescence power of the LED with 50-nm-thick *i*-SiC is observed to be 136 nW. The LED shows green electroluminescence at 500 nm (Fig. 4.74a) attributable to the self-trapped excitons at the surface states between the SiC quantum dots and surrounding matrix. The external quantum efficiency of the LED varies with the *i*-SiC thickness reaching 0.158 % for a thickness of 50 nm (Fig. 4.74b). The carrier injection efficiency is enhanced by 46 % by increasing the doping concentration to 10^{16} cm^{-3}, resulting in nearly one order of magnitude improvement in the external quantum efficiency.

4.4.5 Other Applications

SiC nanoparticles are observed to improve the thermal conductivity of liquid suspensions [125]. Spherical/cylindrical SiC particles with average diameters of 26/600 nm are separately dispersed in distilled water and ethylene glycol. The thermal conductivity of the SiC suspensions is significantly enhanced relative to the base liquids. At low concentrations, the thermal conductivity enhancement ratio increases roughly linearly with the volume fraction of the particles. The thermal conductivity of the SiC suspension is proportional to that of the base liquid, and the morphology of the suspended particles affects the thermal conductivity enhancement ratio.

Bi_2Te_3 thermoelectric materials incorporated with *n*-type 100-nm-diameter SiC nanoparticles have been prepared [126] and show improved Seebeck coefficient, decreased electrical conductivity, and reduced thermal conductivity compared to

the Bi_2Te_3 matrix at 323–523 K. The maximum dimensionless figure of merit is improved from 0.99 for Bi_2Te_3 to 1.04 for 0.1 vol% SiC dispersed Bi_2Te_3 at 423 K. The mechanical properties including Vickers hardness, Young's modulus, and fracture toughness are improved after addition of SiC nanoparticles.

SiC nanoparticle doping can change the conductivity of polypyrrole/SiC nanocomposites [127]. The polypyrrole in the polymer nanocomposites possesses improved thermal stability and tolerates a higher decomposition temperature. The electron transport in the polymer nanocomposites follows a quasi-3-d variable range hopping conduction mechanism. The polypyrrole/SiC nanocomposites have higher conductivity than the pure polypyrrole.

Nitrogen-doped SiC nanoparticles with a mean size of 5.96 nm show favorable microwave absorption when they are mixed with paraffin [128]. The complex permittivity of the composites is changed by the SiC particles. The real and imaginary parts of the complex permittivity and dielectric dissipation factor of the composites increase with the volume filling factor of the nitrogen-doped SiC particles. The single-layer composites with 7 wt% doped SiC particles and a thickness of 2.96 mm show a reflection loss smaller than −10 dB (90 % absorption) at 9.8–15.8 GHz and a minimum value of −63.41 dB at 12.17 GHz.

Electrochemical reduction of water to hydrogen in the proximity of the 3C-SiC nanocrystals film supported by glassy carbon substrate is investigated [129]. The 3C-SiC nanocrystals possess superior electrocatalytic activity in the hydrogen evolution reaction due to the large reduction in the activation barrier on the nanocrystal surface enabling efficient dissociation of H_2O molecules. These nanocrystals with surface autocatalytic effects can be used to split water with high efficiency. Theoretical studies indicate that the hydrogen evolution reaction on SiC electrodes happens at preexisting hydrogenated Si–H surface sites by a Heyrovsky–Volmer mechanism [130]. The Heyrovsky reaction takes place where an electron from the substrate reacts with a hydronium adsorbed at a Si–H site, yielding a H_2 molecule and Si dangling bond. The following Volmer reaction regenerates the Si–H and the rise in the conduction band due to quantum confinement accounts for the electrochemical activity of small SiC nanocrystals.

References

1. Hollabaugh CM, Hull DE, Newkirk LR, Petrovic JJ (1983) R.F.-plasma system for the production of ultrafine, ultrapure silicon carbide powder. J Mater Sci 18:3190–3194
2. Rao NP, Tymiak N, Blum J, Neuman A, Lee HJ, Girshick SL, McMurry PH, Heberlein J (1998) Hypersonic plasma particle deposition of nanostructured silicon and silicon carbide. J Aerosol Sci 29:707–720
3. Klein S, Winterer M, Hahn H (1998) Reduced-pressure chemical vapor synthesis of nanocrystalline silicon carbide powders. Chem Vap Deposition 4:143–149
4. Lin H, Gerbec JA, Sushchikh M, McFarland EW (2008) Synthesis of amorphous silicon carbide nanoparticles in a low temperature low pressure plasma reactor. Nanotechnology 19:325601

5. Huisken F, Kohn B, Alexandrescu R, Cojocaru S, Crunteanu A, Ledoux G, Reynaud C (1999) Silicon carbide nanoparticles produced by CO_2 laser pyrolysis of SiH_4/C_2H_2 gas mixtures in a flow reactor. J Nanopart Res 1:293–303
6. Kityk IV, Makowska-Janusik M, Kassiba A, Plucinski KJ (2000) SiC nanocrystals embedded in oligoetheracrylate photopolymer matrices; new promising nonlinear optical materials. Opt Mater 13:449–453
7. Kassiba A, Tabellout M, Charpentier S, Herlin N, Emery JR (2000) Conduction and dielectric behaviour of SiC nano-sized materials. Solid State Commun 115:389–393
8. Bouclé J, Kassiba A, Makowska-Janusik M, Sanetra J, Herlin-Boime N, Bulou A, Kodjikian S (2005) Electro-optic phenomena in guest–host films of PMMA and SiC nanocrystals. Opt Commun 246:415–420
9. Kassiba A, Bednarski W, Pud A, Errien N, Makowska-Janusik M, Laskowski L, Tabellout M, Kodjikian S, Fatyeyeva K, Ogurtsov N, Noskov Y (2007) Hybrid core-shell nanocomposites based on silicon carbide nanoparticles functionalized by conducting polyaniline: electron paramagnetic resonance investigations. J Phys Chem C 111:11544–11551
10. Kassiba A, Makowska-Janusik M, Bouclé J, Bardeau JF, Bulou A, Herlin-Boime N (2002) Photoluminescence features on the Raman spectra of quasistoichiometric SiC nanoparticles: experimental and numerical simulations. Phys. Rev. B 66:155317
11. Makowska-Janusik M, Kassiba A, Bouclé J, Bardeau J-F, Kodjikian S, Désert A (2005) Vibrational density of states in silicon carbide nanoparticles: experiments and numerical simulations. J Phys: Condens Matter 17:5101–5110
12. Bouclé J, Herlin-Boime N, Kassiba A (2005) Influence of silicon and carbon excesses on the aqueous dispersion of SiC nanocrystals for optical application. J Nanopart Res 7:275–285
13. Herlin-Boime N, Vicens J, Dufour C, Ténégal F, Reynaud C, Rizk R (2004) Flame temperature effect on the structure of SiC nanoparticles grown by laser pyrolysis. J Nanopart Res 6:63–70
14. Heinrich JL, Curtis CL, Credo GM, Kavanagh KL, Sailor MJ (1992) Luminescent colloidal silicon suspensions from porous silicon. Science 255:66–68
15. Wu XL, Fan JY, Qiu T, Yang X, Siu GG, Chu PK (2005) Experimental evidence for the quantum confinement effect in 3C-SiC nanocrystallites. Phys Rev Lett 94:026102
16. Madelung, O.: Semiconductors: Data Handbook. Springer, 3rd ed., Berlin (2004)
17. Fan JY, Wu XL, Li HX, Liu HW, Siu GG, Chu PK (2006) Luminescence from colloidal 3C-SiC nanocrystals in different solvents. Appl Phys Lett 88:041909
18. Lehmann V, Gösele U (1991) Porous silicon formation: a quantum wire effect. Appl Phys Lett 58:856–858
19. Canham LT (1990) Silicon quantum wire array fabrication by electrochemical and chemical dissolution of wafers. Appl Phys Lett 57:1046–1048
20. Fan JY, Wu XL, Chu PK (2006) Low-dimensional SiC nanostructures: fabrication, luminescence, and electrical properties. Prog Mater Sci 51:983–1031
21. Fan JY, Li HX, Cui WN (2009) Microstructure and infrared spectral properties of porous polycrystalline and nanocrystalline cubic silicon carbide. Appl Phys Lett 95:021906
22. Fan JY, Wu XL, Zhao PQ, Chu PK (2006) Stability of luminescent 3C-SiC nanocrystallites in aqueous solution. Phys. Lett. A 360:336–338
23. Fan JY, Li HX, Cui WN, Dai DJ, Chu PK (2010) Excitation and recombination photodynamics in colloidal cubic SiC nanocrystals. Appl Phys Lett 97:191911
24. Zhu J, Liu Z, Wu XL, Xu LL, Zhang WC, Chu PK (2007) Luminescent small-diameter 3C-SiC nanocrystals fabricated via a simple chemical etching method. Nanotechnology 18:365603
25. Fan JY, Li HX, Zhang N, Lu RF (2011) Identification of the reconstruction and bonding structure of SiC nanocrystal surface by infrared spectroscopy. Appl Surf Sci 258:627–630
26. Wolkin MV, Jorne J, Fauchet PM, Allan G, Delerue C (1999) Electronic states and luminescence in porous silicon quantum dots: the role of oxygen. Phys Rev Lett 82:197–200

27. Beke D, Szekrényes Z, Balogh I, Veres M, Fazakas É, Varga LK, Kamarás K, Czigány Z, Gali A (2011) Characterization of luminescent silicon carbide nanocrystals prepared by reactive bonding and subsequent wet chemical etching. Appl Phys Lett 99:213108
28. Beke D, Szekrényes Z, Balogh I, Czigány Z, Kamarás K, Gali A (2013) Preparation of small silicon carbide quantum dots by wet chemical etching. J Mater Res 28:44–49
29. Liu LZ, Wang J, Wu XL, Li TH, Chu PK (2010) Longitudinal optical phonon–plasmon coupling in luminescent 3C-SiC nanocrystal films. Opt Lett 35:4024–4026
30. Wu XL, Xiong SJ, Zhu J, Wang J, Shen JC, Chu PK (2009) Identification of surface structures on 3C-SiC nanocrystals with hydrogen and hydroxyl bonding by photoluminescence. Nano Lett 9:4053–4060
31. Zakharko Yu, Botsoa J, Alekseev S, Lysenko V, Bluet J-M, Marty O, Skryshevsky VA, Guillot G (2010) Influence of the interfacial chemical environment on the luminescence of 3C-SiC nanoparticles. J Appl Phys 107:013503
32. Li Y, Chen C, Li J-T, Yang Y, Lin Z-M (2011) Surface charges and optical characteristic of colloidal cubic SiC nanocrystals. Nanoscale Res Lett 6:454
33. Fan JY, Wu XL, Kong F, Qiu T, Huang GS (2005) Luminescent silicon carbide nanocrystallites in 3C-SiC/polystyrene films. Appl Phys Lett 86:171903
34. Fan JY, Wu XL, Li HX, Liu HW, Huang GS, Siu GG, Chu PK (2006) Si-based solid blue emitters from 3C-SiC nanocrystals. Appl Phys A 82:485–487
35. Wang J, Xiong SJ, Wu XL, Li TH, Chu PK (2010) Glycerol-bonded 3C-SiC nanocrystal solid films exhibiting broad and stable violet to blue-green emission. Nano Lett. 10:1466–1471
36. Dai D, Zhang N, Zhang W, Fan J (2012) Highly bright tunable blue-violet photoluminescence in SiC nanocrystal-sodium dodecyl sulfonate crosslinked network. Nanoscale 4:3044–3046
37. Dai D, Fan J, Zhang N (2011) Synthesis and luminescence properties of silica-coated cubic silicon carbide nanocrystal composites. Micro Nano Lett 6:878–880
38. Zhang N, Dai D, Zhang W, Fan J (2012) Photoluminescence and light reabsorption in SiC quantum dots embedded in binary-polyelectrolyte solid matrix. J Appl Phys 112:094315
39. Dai D, Guo X, Fan J (2013) Synthesis and photoluminescence of semiconductor quantum dots/cetyltrimethylammonium bromide vesicle core/shell nanostructures. Appl Surf Sci 276:359–362
40. Fan JY, Li HX, Wang QJ, Dai DJ, Chu PK (2011) UV-blue photoluminescence from close-packed SiC nanocrystal film. Appl Phys Lett 98:081913
41. Botsoa J, Bluet JM, Lysenko V, Marty O, Barbier D, Guillot G (2007) Photoluminescence of 6H-SiC nanostructures fabricated by electrochemical etching. J Appl Phys 102:083526
42. Botsoa J, Bluet JM, Lysenko V, Sfaxi L, Zakharko Y, Marty O, Guillot G (2009) Luminescence mechanisms in 6H-SiC nanocrystals. Phys Rev B 80:155317
43. Rossi AM, Murphy TE, Reipa V (2008) Ultraviolet photoluminescence from 6H silicon carbide nanoparticles. Appl Phys Lett 92:253112
44. Fan J, Li H, Wang J, Xiao M (2012) Fabrication and photoluminescence of SiC quantum dots stemming from 3C, 6H, and 4H polytypes of bulk SiC. Appl Phys Lett 101:131906
45. Matsumoto T, Takahashi J, Tamaki T, Futagi T, Mimura H, Kanemitsu Y (1994) Blue-green luminescence from porous silicon carbide. Appl Phys Lett 64:226–228
46. Käckell P, Wenzien B, Bechstedt F (1994) Influence of atomic relaxations on the structural properties of SiC polytypes from ab initio calculations. Phys Rev B 50:17037–17046
47. Yoffe AD (2001) Semiconductor quantum dots and related systems: electronic, optical, luminescence and related properties of low dimensional systems. Adv Phys 50:1–208
48. Wolfe JP (1982) Thermodynamics of excitons in semiconductors. Phys Today 35:46–54
49. Fan J, Chu PK (2010) Group IV nanoparticles: synthesis, properties, and biological applications. Small 6:2080–2098
50. Pol VG, Pol SV, Gedanken A (2005) Novel synthesis of high surface area silicon carbide by RAPET (reactions under autogenic pressure at elevated temperature) of organosilanes. Chem. Mater. 17:1797–1802

51. Lu A-H, Schmidt W, Kiefer W, Schüth F (2005) High surface area mesoporous SiC synthesized via nanocasting and carbothermal reduction process. J Mater Sci 40:5091–5093
52. Henderson EJ, Veinot JGC (2009) From phenylsiloxane polymer composition to size-controlled silicon carbide nanocrystals. J Am Chem Soc 131:809–815
53. Dasog M, Rachinsky C, Veinot JGC (2011) From Si and C encapsulated SiO_2 to SiC: exploring the influence of sol–gel polymer substitution on thermally induced nanocrystal formation. J Mater Chem 21:12422–12427
54. Yang S, Cai W, Zeng H, Xu X (2009) Ultra-fine β-SiC quantum dots fabricated by laser ablation in reactive liquid at room temperature and their violet emission. J Mater Chem 19:7119–7123
55. Yang S, Cai W, Zhang H, Zeng H, Lei Y (2011) A general strategy for fabricating unique carbide nanostructures with excitation wavelength-dependent light emissions. J Phys Chem C 115:7279–7284
56. Yang S, Kiraly B, Wang WY, Shang S, Cao B, Zeng H, Zhao Y, Li W, Liu Z-K, Cai W, Huang TJ (2012) Fabrication and characterization of beaded SiC quantum rings with anomalous red spectral shift. Adv Mater 24:5598–5603
57. Zakharko Y, Rioux D, Patskovsky S, Lysenko V, Marty O, Bluet JM, Meunier M (2011) Direct synthesis of luminescent SiC quantum dots in water by laser ablation. Phys Status Solidi-R 5:292–294
58. Sasaki Y, Nishina Y, Sato M, Qkamura K (1989) Optical-phonon states of SiC small particles studied by Raman scattering and infrared absorption. Phys Rev B 40:1762–1772
59. Yang Z-G, Shaw LL (1996) Synthesis of nanocrystalline SiC at ambient temperature through high energy reaction milling. Nanostruct Mater 7:873–886
60. Zhang GQ, Wei GD, Zheng KZ, Li L, Xu DP, Wang DY, Xue YF, Su WH (2010) The synthesis of beta-SiC nanoparticles by high-energy mechanical ball milling and their photoluminescence properties. J Nanosci Nanotechnol 10:1951–1955
61. Martin H-P, Ecke R, Müller E (1998) Synthesis of nanocrystalline silicon carbide powder by carbothermal reduction. J Eur Ceram Soc 18:l737–l1742
62. Dasog M, Smith LF, Purkait TK, Veinot JGC (2013) Low temperature synthesis of silicon carbide nanomaterials using a solid-state method. Chem Commun 49:7004–7006
63. Wang CH, Chang YH, Yen MY, Peng CW, Lee CY, Chiu HT (2005) Synthesis of silicon carbide nanostructures via a simplified Yajima process-reaction at the vapor-liquid interface. Adv Mater 17:419–422
64. Shen G, Chen D, Tang K, Qian Y, Zhang S (2003) Silicon carbide hollow nanospheres, nanowires and coaxial nanowires. Chem Phys Lett 375:177–184
65. Wang H, Yu J-S, Li X-D, Kim D-P (2004) Inorganic polymer-derived hollow SiC and filled SiCN sphere assemblies from a 3DOM carbon template. Chem Commun 20:2352–2353
66. Liu Z, Ci L, Jin-Phillipp NY, Rühle M (2007) Vapor-solid reaction for silicon carbide hollow spherical nanocrystals. J Phys Chem C 111:12517–12521
67. Li P, Xu L, Qian Y (2008) Selective synthesis of 3C-SiC hollow nanospheres and nanowires. Cryst Growth Des 8:2431–2436
68. Ju Z, Xu L, Pang Q, Xing Z, Ma X, Qian Y (2009) The synthesis of nanostructured SiC from waste plastics and silicon powder. Nanotechnology 20:355604
69. Ye J, Zhang S, Lee WE (2012) Novel low temperature synthesis and characterisation of hollow silicon carbide spheres. Micropor Mesopor Mat 152:25–30
70. Baklouti S, Pagnoux C, Chartier T, Baumard JF (1997) Processing of aqueous α-Al_2O_3, α-SiO_2 and α-SiC suspensions with polyelectrolytes. J Eur Ceram Soc 17:1387–1392
71. Tartaj P, Reece M, Moya JS (1998) Electrokinetic behavior and stability of silicon carbide nanoparticulate dispersions. J Am Ceram Soc 81:389–394
72. Médout-Marère V, Ghzaoui AEl, Charnay C, Douillard JM, Chauveteau G, Partyka S (2000) Surface heterogeneity of passively oxidized silicon carbide particles: hydrophobic-hydrophilic partition. J Colloid Interf Sci 223:205–214

73. Zhu X, Tang F, Suzuki TS, Sakka Y (2003) Role of the initial degree of ionization of polyethylenimine in the dispersion of silicon carbide nanoparticles. J Am Ceram Soc 86:189–191
74. Singh BP, Jena J, Besra L, Bhattacharjee S (2007) Dispersion of nano-silicon carbide (SiC) powder in aqueous suspensions. J Nanopart Res 9:797–806
75. Che J, Wang X, Xiao Y, Wu X, Zhou L, Yuan W (2007) Effect of inorganic-organic composite coating on the dispersion of silicon carbide nanoparticles in non-aqueous medium. Nanotechnology 18:135706
76. Iijima M, Kamiya H (2008) Surface modification of silicon carbide nanoparticles by azo radical initiators. J Phys Chem C 112:11786–11790
77. Zou G, Cao M, Lin H, Jin H, Kang Y, Chen Y (2006) Nickel layer deposition on SiC nanoparticles by simple electroless plating and its dielectric behaviors. Powder Technol 168:84–88
78. Puzder A, Williamson AJ, Grossman JC, Galli G (2002) Surface chemistry of silicon nanoclusters. Phys Rev Lett 88:097401
79. Zhao X, Wei CM, Yang L, Chou MY (2004) Quantum confinement and electronic properties of silicon nanowires. Phys Rev Lett 92:236805
80. Reboredo FA, Pizzagalli L, Galli G (2004) Computational engineering of the stability and optical gaps of SiC quantum dots. Nano Lett 4:801–804
81. Peng X-H, Nayak SK, Alizadeh A, Varanasi KK, Bhate N, Rowland LB, Kumar SK (2007) First-principles study of the effects of polytype and size on energy gaps in SiC nanoclusters. J Appl Phys 102:024304
82. Huda MN, Ray AK (2008) Evolution of SiC nanocluster from carbon fullerene: a density functional theoretic study. Chem Phys Lett 457:124–129
83. Vörös M, Deák P, Frauenheim T, Gali A (2010) The absorption spectrum of hydrogenated silicon carbide nanocrystals from *ab initio* calculations. Appl Phys Lett 96:051909
84. Fan J, Li H, Jiang J, So LKY, Lam YW, Chu PK (2008) 3C-SiC nanocrystals as fluorescent biological labels. Small 4:1058–1062
85. Vörös M, Deák P, Frauenheim T, Gali A (2010) The absorption of oxygenated silicon carbide nanoparticles. J Chem Phys 133:064705
86. Zhang Z, Dai Y, Yu L, Guo M, Huang B, Whangbo M-H (2012) The surface termination effect on the quantum confinement and electron affinities of 3C-SiC quantum dots: a first-principles study. Nanoscale 4:1592–1597
87. Saha S, Sarkar P (2012) Tuning the HOMO-LUMO gap of SiC quantum dots by surface functionalization. Chem Phys Lett 536:118–122
88. Zimmerman AF, Clark DG, Aust KT, Erb U (2002) Pulse electrodeposition of Ni-SiC nanocomposite. Mater Lett 52:85–90
89. Zimmerman AF, Palumbo G, Aust KT, Erb U (2002) Mechanical properties of nickel silicon carbide nanocomposites. Mat Sci Eng A 328:137–146
90. Shi L, Sun C, Gao P, Zhou F, Liu W (2006) Mechanical properties and wear and corrosion resistance of electrodeposited Ni-Co/SiC nanocomposite coating. Appl Surf Sci 252:3591–3599
91. Vaezi MR, Sadrnezhaad SK, Nikzad L (2008) Electrodeposition of Ni-SiC nano-composite coatings and evaluation of wear and corrosion resistance and electroplating characteristics. Colloid Surf A 315:176–182
92. Zhao J, Stearns LC, Harmer MP, Chan HM, Miller GA (1993) Mechanical behavior of alumina-silicon carbide "nanocomposites". J Am Ceram Soc 76:503–510
93. Ohji T, Nakahira A, Hirano T, Niihara K (1994) Tensile creep behavior of alumina/silicon carbide nanocomposite. J Am Ceram Soc 77:3259–3262
94. Gao L, Wang HZ, Hong JS, Miyamoto H, Miyamoto K, Nishikawa Y, Torre SDDL (1999) Mechanical properties and microstructure of nano-SiC–Al_2O_3 composites densified by spark plasma sintering. J Eur Ceram Soc 19:609–613

95. Yang Y, Lan J, Li X (2004) Study on bulk aluminum matrix nano-composite fabricated by ultrasonic dispersion of nano-sized SiC particles in molten aluminum alloy. Mat Sci Eng A 380:378–383
96. Sawaguchi A, Toda K, Niihara K (1991) Mechanical and electrical properties of silicon nitride-silicon carbide nanocomposite material. J Am Ceram Soc 74:1142–1144
97. Rendtel A, Hübner H, Herrmann M, Schubert C (1998) Silicon nitride/silicon carbide nanocomposite materials: II, hot strength, creep, and oxidation resistance. J Am Ceram Soc 81:1109–1120
98. Ferkel H, Mordike BL (2001) Magnesium strengthened by SiC nanoparticles. Mat Sci Eng A 298:193–199
99. Lan J, Yang Y, Li X (2004) Microstructure and microhardness of SiC nanoparticles reinforced magnesium composites fabricated by ultrasonic method. Mat Sci Eng A 386:284–290
100. Chisholm N, Mahfuz H, Rangari VK, Ashfaq A, Jeelani S (2005) Fabrication and mechanical characterization of carbon/SiC-epoxy nanocomposites. Compos Struct 67:115–124
101. Ma RZ, Wu J, Wei BQ, Liang J, Wu DH (1998) Processing and properties of carbon nanotubes-nano-SiC ceramic. J Mater Sci 33:5243–5246
102. Dou SX, Soltanian S, Horvat J, Wang XL, Zhou SH, Ionescu M, Liu HK, Munroe P, Tomsic M (2002) Enhancement of the critical current density and flux pinning of MgB_2 superconductor by nanoparticle SiC doping. Appl Phys Lett 81:3419–3421
103. Matsumoto A, Kumakura H, Kitaguchi H, Hatakeyama H (2003) Effect of SiO_2 and SiC doping on the powder-in-tube processed MgB_2 tapes. Supercond Sci Technol 16:926–930
104. Matsumoto A, Kumakura H, Kitaguchi H, Senkowicz BJ, Jewell MC, Hellstrom EE, Zhu Y, Voyles PM, Larbalestier DC (2006) Evaluation of connectivity, flux pinning, and upper critical field contributions to the critical current density of bulk pure and SiC-alloyed MgB_2. Appl Phys Lett 89:132508
105. Dou SX, Shcherbakova O, Yeoh WK, Kim JH, Soltanian S, Wang XL, Senatore C, Flukiger R, Dhalle M, Husnjak O, Babic E (2007) Mechanism of enhancement in electromagnetic properties of MgB_2 by nano SiC doping. Phys Rev Lett 98:097002
106. Nienhaus H, Kampen TU, Mönch W (1995) Phonons in 3C-, 4H-, and 6H-SiC. Surf Sci 324:L328–L332
107. Gall JL, Olivier M, Greffet J-J (1997) Experimental and theoretical study of reflection and coherent thermal emission by a SiC grating supporting a surface-phonon polariton. Phys Rev B 55:10105–10114
108. Rockstuhl C, Salt MG, Herzig HP (2005) Analysis of the phonon-polariton response of silicon carbide microparticles and nanoparticles by use of the boundary element method. J Opt Soc Am B 22:481–487
109. Neuner B III, Korobkin D, Fietz C, Carole D, Ferro G, Shvets G (2009) Critically coupled surface phonon-polariton excitation in silicon carbide. Opt Lett 34:2667–2669
110. Neuner B III, Korobkin D, Fietz C, Carole D, Ferro G, Shvets G (2010) Midinfrared index sensing of pL-scale analytes based on surface phonon polaritons in silicon carbide. J Phys Chem C 114:7489–7491
111. Kim HC, Cheng X (2010) Surface phonon polaritons on SiC substrate for surface-enhanced infrared absorption spectroscopy. J Opt Soc Am B 27:2393–2397
112. Schuller JA, Zia R, Taubner T, Brongersma ML (2007) Dielectric metamaterials based on electric and magnetic resonances of silicon carbide particles. Phys Rev Lett 99:107401
113. Francoeur M, Basu S, Petersen SJ (2011) Electric and magnetic surface polariton mediated near-field radiative heat transfer between metamaterials made of silicon carbide particles. Opt Express 19:18774–18788
114. Nehmetallah G, Aylo R, Powers P, Sarangan A, Gao J, Li H, Achari A, Banerjee PP (2012) Co-sputtered SiC + Ag nanomixtures as visible wavelength negative index metamaterials. Opt Express 20:7095–7100

115. Zhang N, Dai DJ, Fan JY (2012) Plasmon-assisted photoluminescence enhancement of SiC nanocrystals by proximal silver nanoparticles. Appl Surf Sci 258:10140–10143
116. Dai D, Dong Z, Fan J (2013) Giant photoluminescence enhancement in SiC nanocrystals by resonant semiconductor exciton-metal surface plasmon coupling. Nanotechnology 24:025201
117. Sui N, Monnier V, Zakharko Y, Chevolot Y, Alekseev S, Bluet J-M, Lysenko V, Souteyrand E (2012) Plasmon-controlled narrower and blue-shifted fluorescence emission in (Au@SiO_2)SiC nanohybrids. J Nanopart Res 14:1004
118. Sui N, Monnier V, Zakharko Y, Chevolot Y, Alekseev S, Bluet J-M, Lysenko V, Souteyrand E (2013) Fluorescent (Au@SiO_2)SiC nanohybrids: influence of gold nanoparticle diameter and SiC nanoparticle surface density. Plasmonics 8:85–92
119. Zakharko Y, Serdiuk T, Nychyporuk T, Géloën A, Lemiti M, Lysenko V (2012) Plasmon-enhanced photoluminescence of SiC quantum dots for cell imaging applications. Plasmonics 7:725–732
120. Zakharko Y, Nychyporuk T, Bonacina L, Lemiti M, Lysenko V (2013) Plasmon-enhanced nonlinear optical properties of SiC nanoparticles. Nanotechnology 24:055703
121. Fan J, Li H, Jiang J, So LKY, Lam YW, Chu PK (2008) 3C-SiC nanocrystals as fluorescent biological labels. Small 4:1058–1062
122. Mimura H, Matsumoto T, Kanemitsu Y (1994) Blue electroluminescence from porous silicon carbide. Appl Phys Lett 65:3350–3352
123. Xiao B, Wu XL, Xu W, Chu PK (2012) Tunable electroluminescence from polymer-passivated 3C-SiC quantum dot thin films. Appl Phys Lett 101:123110
124. Tai H-Y, Cheng C-H, Lin G-R (2014) Blue-green light emission from Si and SiC quantum dots co-doped Si-rich SiC *p-i-n* junction diode. IEEE J Sel Top Quant Electron 20:8200507
125. Xie H, Wang J, Xi T, Liu Y (2002) Thermal conductivity of suspensions containing nanosized SiC particles. Int J Thermophys 23:571–580
126. Zhao L-D, Zhang B-P, Li J-F, Zhou M, Liu W-S, Liu J (2008) Thermoelectric and mechanical properties of nano-SiC-dispersed Bi_2Te_3 fabricated by mechanical alloying and spark plasma sintering. J Alloys Compd 455:259–264
127. Mavinakuli P, Wei S, Wang Q, Karki AB, Dhage S, Wang Z, Young DP, Guo Z (2010) Polypyrrole/silicon carbide nanocomposites with tunable electrical conductivity. J Phys Chem C 114:3874–3882
128. Zhao D-L, Luo F, Zhou W-C (2010) Microwave absorbing property and complex permittivity of nano SiC particles doped with nitrogen. J Alloys Compd 490:190–194
129. He C, Wu X, Shen J, Chu PK (2012) High-efficiency electrochemical hydrogen evolution based on surface autocatalytic effect of ultrathin 3C-SiC nanocrystals. Nano Lett 12:1545–1548
130. Shen X, Pantelides ST (2013) Atomic-scale mechanism of efficient hydrogen evolution at SiC nanocrystal electrodes. J Phys Chem Lett 4:100–104

Chapter 5
SiC Nanowires

There have been a large amount of studies concerning the fabrication and properties of silicon carbide nanowires. In fact, much more knowledge has been learnt about SiC nanowires than other low-dimensional SiC nanostructures. A lot of methods have been developed to synthesize SiC nanowires, and some can yield large-scale and high-quality SiC nanowires and nanowire arrays. Filed electron emission is the most intensively investigated characteristic of SiC nanowires, and there are also some studies involving the luminescence of SiC nanowires. SiC nanorods, nanobelts, and various other forms of one-dimensional nanostructures have also been synthesized and studied.

5.1 Synthesis and Optical Properties

5.1.1 Vapor–Solid Growth

SiC nanowires are synthesized using the vapor–solid reactions during the earliest years of investigations. In 1995, investigators began to use carbon nanotubes as templates for the space-limited synthesis of various carbide nanorods [1]. The SiC nanorods with diameters similar to or much smaller than that of carbon nanotubes are fabricated through reactions between the carbon nanotubes and SiO or Si–I_2. The TEM images show that the SiC nanorods synthesized by the reaction of carbon nanotubes with Si and I_2 at 1,200 °C have lengths on the order of 1 μm and diameters of 2–20 nm, similar to the diameter of the carbon nanotube reactant. X-ray diffraction shows the zinc-blende β-SiC structure of the product. Transmission electron microscopy reveals that the nanorods possess a high density of planar defects. The defects in [111]-oriented rods are rotational twin stacking faults. All the nanorods produced at 1,300–1,400 °C using SiO as the gaseous reactant have rod axis along the [111] direction, but the nanorods prepared at 1,100–1,200 °C using Si

J. Fan and P.K. Chu, *Silicon Carbide Nanostructures*,
Engineering Materials and Processes, DOI 10.1007/978-3-319-08726-9_5

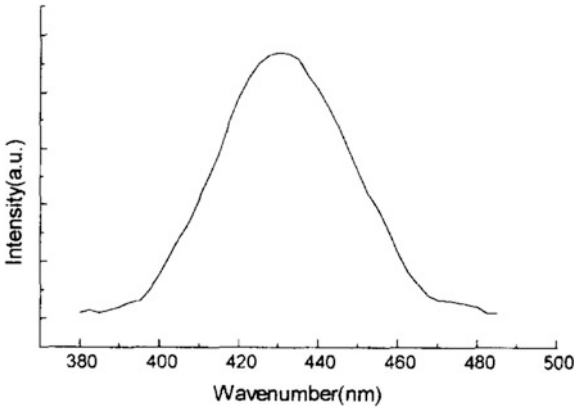

Fig. 5.1 Photoluminescence spectrum of SiC nanorods. Reprinted with permission from [2]. Copyright 1997, Elsevier

and I_2 show varied rod directions, some along the [100] direction although in these rods small defect regions with a [111] direction are also present. This method has been developed into a two-step reaction scheme for the synthesis of SiC nanorods at 1,400 °C [2]. SiO vapor produced via silicon reduction of silica reacts with carbon nanotubes yielding SiC nanorods. Transmission electron microscopy reveals that the nanorods are single-crystalline β-SiC with diameters ranging from 3 to 40 nm. The infrared absorption spectrum comprises a strong Si–C stretching vibration peak at 814 cm^{-1} and another weak Si–O stretching vibration peak at about 1,100 cm^{-1}. This indicates the nanorods mainly consist of SiC but with minor amount of silicon oxide. The Raman spectrum shows a sharp peak at 784 cm^{-1} attributed to TO phonon mode of SiC. The nanorods have photoluminescence peaked at around 430 nm under 260 nm excitation at room temperature (Fig. 5.1). A two-step growth model for the SiC nanorods is proposed as:

$$\mathrm{SiO_2(s)} + \mathrm{Si(s)} \rightarrow 2\mathrm{SiO(v)}, \tag{5.1}$$

$$\mathrm{SiO(v)} + 2\mathrm{C(s)} \rightarrow \mathrm{SiC(s)} + \mathrm{CO(v)}. \tag{5.2}$$

High-resolution TEM observation reveals that the β-SiC nanorods synthesized by the carbon nanotube confined reaction possess many layer faults [3]. In addition, there is a thick amorphous layer on the nanorod surface. The SiC nanorods with uniform diameters can be prepared by suppressing the epitaxial growth on the surface of the initially formed SiC nanorods by effectively carrying away the CO gas by-product from the reaction area [4]. The diameter distribution is consistent with that of the starting carbon nanotubes. The TEM image (Fig. 5.2) of the nanorods produced at 1,400 °C shows that they have uniform diameters ranging from 20 to 25 nm, slightly larger than that of starting carbon nanotubes. The shape of the nanorods can be controlled by thermally adjusting the carbon nanotube shape during the reaction process.

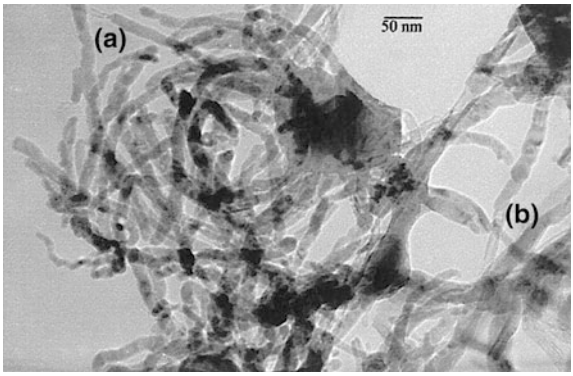

Fig. 5.2 TEM image of SiC nanorods synthesized at 1,400 °C. Reprinted with permission from [4]. Copyright 2000, Elsevier

Raman scattering is conducted on the amorphous silica-sheathed SiC nanorods with diameters of 3–30 nm and lengths of over 1 μm produced by carbon nanotube confinement reaction [5], and most nanorods contain high-density defects including rotational twins and stacking faults. The Raman spectrum (Fig. 5.3a) comprises two strong peaks at 791 and 924 cm^{-1} corresponding to the TO and LO phonon modes of β-SiC, respectively. They shifts to small wave numbers with respect to bulk values (at the Γ point of the Brillouin zone) of β-SiC, which are separately 796 and 972 cm^{-1} for TO and LO phonon modes [6]. Calculation shows that the phonon confinement contributes only a small portion to the large shift of the LO mode frequency and that the Raman spectra can be considered as the Fröhlich enhanced effective density of states of optical phonons (Fig. 5.3b), which becomes crucial because of the broken translation symmetry caused by the interior structure defects in the nanorods. The weak peak at 864 cm^{-1} which has no counterpart in bulk SiC is assigned to the interface-like mode. The calculation and the experiment agree well.

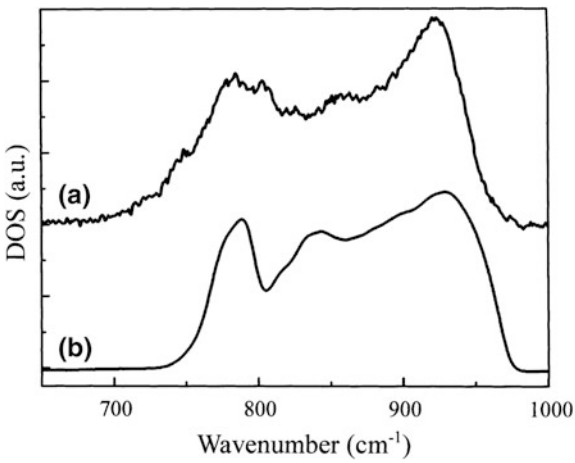

Fig. 5.3 **a** Reduced Stokes Raman spectrum of SiC nanorods. **b** Calculated effective density of optical phonon states for a rectangular SiC nanorod with a cross section of 24 × 24 monolayers by employing a Gaussian broadening factor of 5 cm^{-1}. Reprinted with permission from [5]. Copyright 1999, Elsevier

SiC nanowires can also be synthesized by employing other solid carbon sources other than carbon nanotubes. Carbothermal reduction of SiO_2 (or SiO/Si) powder by carbon black powder produces β-SiC whiskers [7]. The mixed powders are heated at 1,300–1,550 °C in hydrogen atmosphere followed by oxidation at 700 °C in air to eliminate excess carbon. The product contains β-SiC whiskers and spherical particles. The β-SiC whiskers form by the solid–gas (carbon–SiO gas) reaction and have high density of stacking faults, whereas the solid–solid (carbon–Si) reaction yields β-SiC spherical particles with low density of stacking faults. The sizes of the whiskers and particles decrease with decreasing reaction temperature and time. The stacking fault density increases with heating rate due to increased reaction rate.

The solid reaction methods have been developed to synthesize SiC nanowires [8]. These methods involve heating silica gel or fumed silica with activated carbon in a reduction atmosphere. One involves heating silica gel with activated carbon at 1,360 °C in H_2 or NH_3, and the activated carbon is prepared by thermal decomposition of polyethylene glycol at 700 °C in an argon atmosphere. The SEM images (Fig. 5.4) show that the nanowires have diameters of around 350 nm and lengths up to several tens of micrometers. The proposed reactions are as follows:

$$SiO_2 + C \rightarrow SiO + CO, \tag{5.3}$$

$$SiO + 2C \rightarrow SiC + CO. \tag{5.4}$$

The NH_3 and H_2 facilitate the conversion of SiO_2 into SiO which reacts with carbon to yield SiC. The nanowires have wide photoluminescence band centered at about 400 nm (Fig. 5.5). The infrared absorption spectrum contains a strong peak at 810 cm^{-1}, and this value is larger than the TO phonon mode value of bulk β-SiC. The Raman spectrum comprises a broad band at around 780 cm^{-1} corresponding to the TO phonon mode of β-SiC, but it shifts to lower wave numbers by 16 cm^{-1} compared with the bulk value caused by phonon confinement and

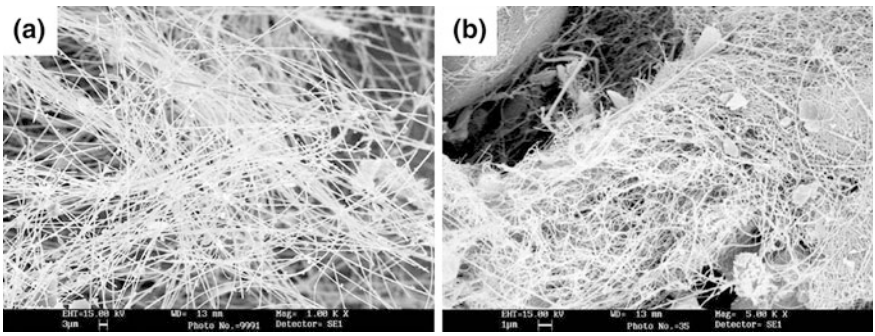

Fig. 5.4 SEM images of β-SiC nanowires synthesized by heating the gel containing activated carbon and silica at 1,360 °C in NH_3 for **a** 4 h and **b** 7 h. The scale bar is 3 μm for (**a**) and 1 μm for (**b**). Reprinted with permission from [8]. Copyright 2002, Royal Society of Chemistry

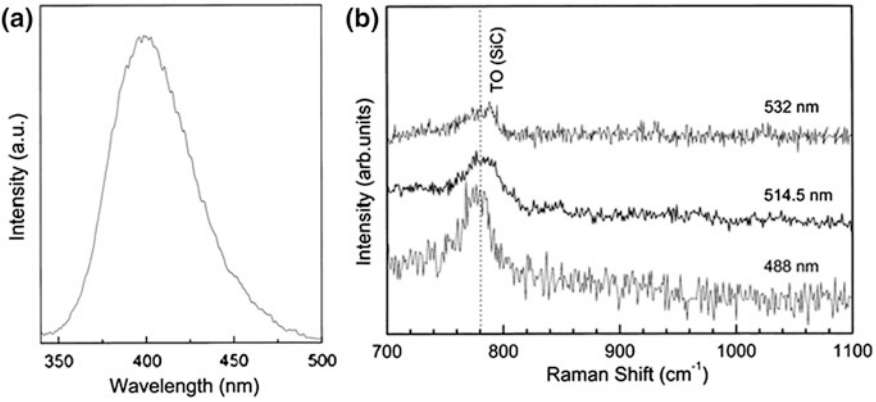

Fig. 5.5 Photoluminescence (**a**) and Raman (**b**) spectra of SiC nanowires synthesized by heating the gel containing activated carbon and silica at 1,360 °C in NH_3 for 7 h. Reprinted with permission from [8]. Copyright 2002, Royal Society of Chemistry

stacking faults. The LO phonon expected to arise at 972 cm^{-1} is absent in the spectrum, and this can be explained by the Raman selection rule for the given experimental geometry of Raman scattering measurement.

Reaction between SiO and amorphous activated carbon at 1,380 °C produces SiC nanorods with diameters of 20–100 nm and lengths of 10–100 μm [9]. Transmission electron microscopy and energy-dispersive spectroscopy reveal that the SiC nanorods grow on either a chain or from facets of SiC nanoparticles. Most of them are straight and orientated along the [111] direction. Branched structures are also present (Fig. 5.6), and on a typical tip of the straight SiC nanorod, there is a thin amorphous layer with thickness of 1–3 nm which consists of Si, C, and a small quantity of O.

Arc-discharge method is used to synthesize β-SiC SiC nanowires with preferential [111] growth direction using SiO_2 powder as filler in a graphite anode [10]. The nanowires have diameters of 3–15 nm and lengths up to several micrometers. The growth of the nanowires is suggested to follow a catalyst-free vapor–solid mechanism. The SiC nanowires have photoluminescence with a single wide emission band centered at 472 nm (Fig. 5.7). The photoluminescence excitation spectrum contains a single peak at 305 nm.

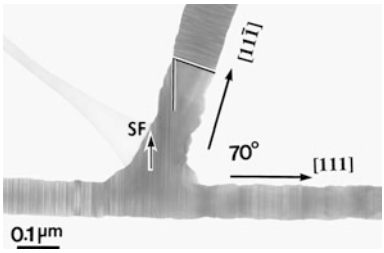

Fig. 5.6 TEM image of a branched SiC nanorod. "SF" denotes stacking fault. Reprinted with permission from [9]. Copyright 2002, Springer Science and Business Media

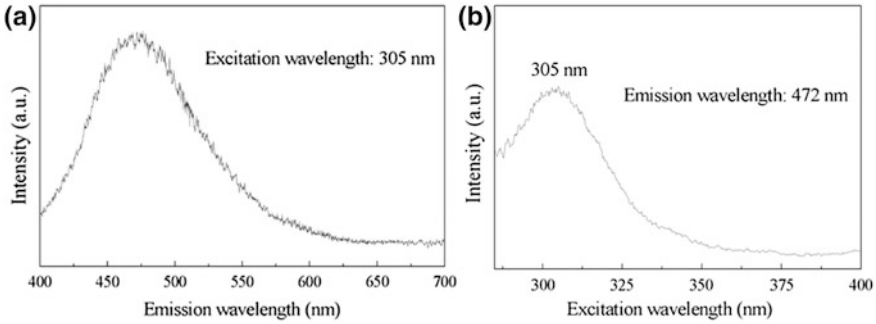

Fig. 5.7 **a** Photoluminescence and **b** photoluminescence excitation spectra of the SiC nanowires. Reprinted with permission from [10]. Copyright 2007, American Chemical Society

Thermal evaporation of ZnS and solid carbon on silicon wafer at 1,100 °C yields aligned SiC nanowire arrays [11]. The nanowires have uniform sizes with a most probable diameter of 8 nm and a smallest diameter of 3 nm, and they usually grow along the [111] direction. They possess a thin oxide shell and contain few stacking faults. The PL spectrum (Fig. 5.8a) consists of a usual 430 nm emission band and another more intense emission band at around 510 nm. The Raman spectrum (Fig. 5.8b) comprises two strong peaks at 787 and 925 cm^{-1}, corresponding to the TO and LO phonon modes of cubic SiC, respectively. They all shift to lower wave numbers relative to bulk material. In particular, the LO phonon line has a large shift of 47 cm^{-1}.

Raman scattering from a single 3C-SiC nanowire has been investigated by surface-enhanced Raman scattering approach [12]. The 3C-SiC nanowires are synthesized by thermal heating of the mixed silicon, silicon oxide, and carbon

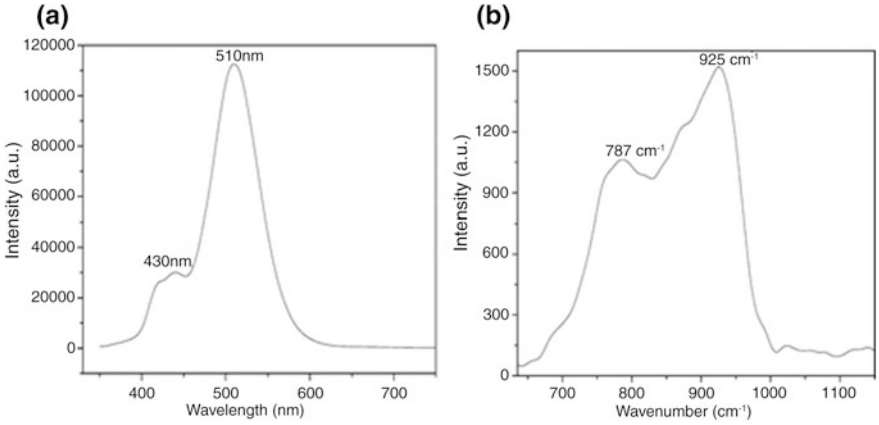

Fig. 5.8 **a** Photoluminescence spectrum (under 325 nm excitation) and **b** Raman spectrum of the oriented SiC nanowires. Reprinted with permission from [11]. Copyright 2007, American Chemical Society

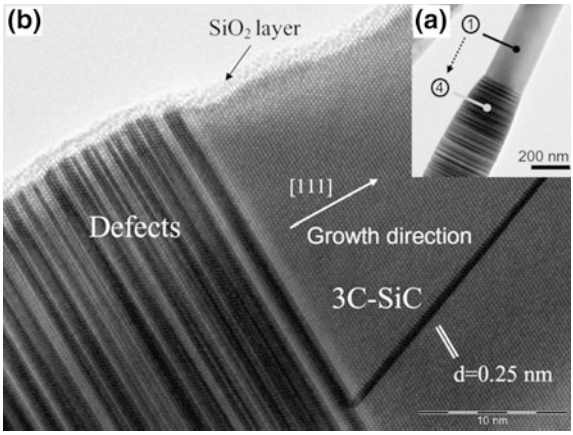

Fig. 5.9 **a** TEM image of a typical SiC nanowire exhibiting an area of random network of stacking faults (*dark part*) and a pure 3C-SiC section (*bright part*). **b** HRTEM image of the interface region between two crystallographic zones. Reprinted with permission from [12]. Copyright 2007, Wiley-VCH Verlag GmbH & Co. KGaA

powders at 1,400 °C under an argon flow. The Raman scattering is enhanced by a structure based on a tungsten tip covered by a thin gold layer, to which the SiC nanowire is attached. Figure 5.9 shows the TEM image of a typical SiC nanowire with diameter of 100 nm. It contains a homogenous region (bright) corresponding to 3C-SiC that grows in the [111] orientation and a second region (dark) exhibiting a random network of stacking faults. The cross-sectional dimension of the 3C-SiC part is uniform, whereas that of the dark zone varies due to the strain relaxation caused by the structural defects. Figure 5.10a shows the enhanced Raman spectrum of an individual SiC nanowire with 40 nm in diameter. The peak centered at 797 cm^{-1} is attributed to a TO mode, and the two shoulders centered at 925 and 955 cm^{-1} are attributed to the LO modes. The peaks at 842 and 896 cm^{-1} are assigned to Fröhlich transitions enhanced by structural defects. The absence of the conventional LO phonon line at around 970 cm^{-1} suggests that this nanowire is not a pure 3C-SiC crystal and contains many stacking faults. The high-resolution TEM image of a nanowire with comparable size is shown in Fig. 5.10b. Note that the whole nanowire is composed of stacking faults and this is different from the case of the nanowires with greater diameters (Fig. 5.9) where the pure 3C crystalline parts are present. The free carrier concentration is calculated to be 10^{18}–10^{19} cm^{-3} by using the Fano interference features of sharp phonon lines.

Highly oriented SiC nanowire arrays are synthesized by chemical vapor reaction of the mixed Si and SiO_2 powders with a piece of carbon cloth with assistance of an ordered nanoporous anodic aluminum oxide template under C_3H_6 gas flow at 1,230 °C [13]. The nanowires are single-crystalline β-SiC with diameters of 30–60 nm and lengths of about 8 μm. They are uniformly oriented along the direction of the pores of the anodic aluminum oxide template (Fig. 5.11a). The nanowires grow along the [111] direction, and they contain a high density of planar defects. The Raman spectrum exhibits two strong and wide peaks at around 794 and 966 cm^{-1} belonging to TO and LO phonon modes of β-SiC. The photoluminescence spectrum (Fig. 5.11b) has a single strong peak centered at around

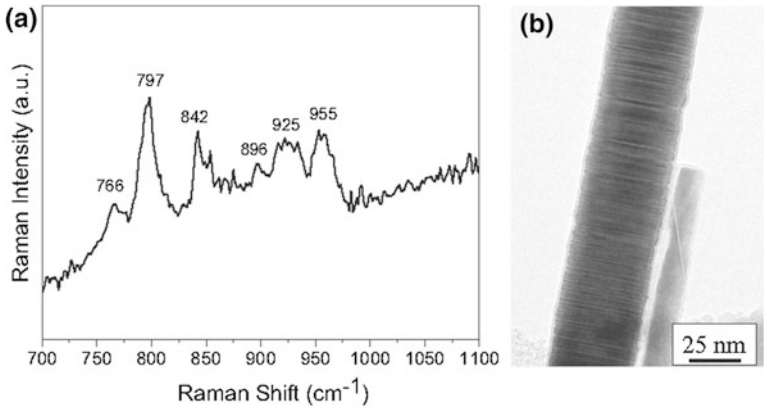

Fig. 5.10 **a** Raman spectrum of a single SiC nanowire with diameter of 40 nm. **b** TEM image of a typical nanowire of the same diameter. The sequence of stacking faults is clearly seen. Reprinted with permission from [12]. Copyright 2007, Wiley-VCH Verlag GmbH & Co. KGaA

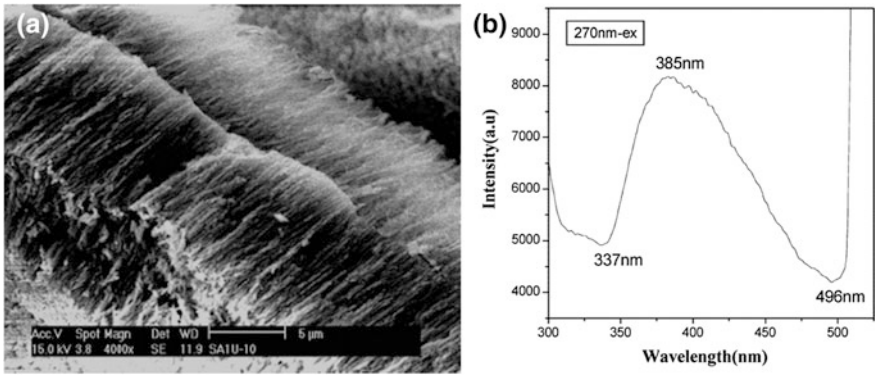

Fig. 5.11 **a** SEM image of oriented SiC nanowire arrays. **b** Photoluminescence spectrum of oriented SiC nanowires under 270 nm excitation. Reprinted with permission from [13]. Copyright 2006, American Chemical Society

385 nm, and this position is far bluer in comparison with most of the reported PL peaks in the SiC nanowires.

5.1.2 Vapor–Liquid–Solid Growth

The vapor–liquid–solid (VLS) growth mechanism is a common nanowire growth mechanism, which dominates the crystal growth process of various types of nanowires. In 1964, Wagner and Ellis presented the concept of VLS growth in studying the crystal growth of Si whiskers [14]. The Si whiskers are grown on a Si wafer (Fig. 5.12a), on which the gold particle is placed prior to the nanowire

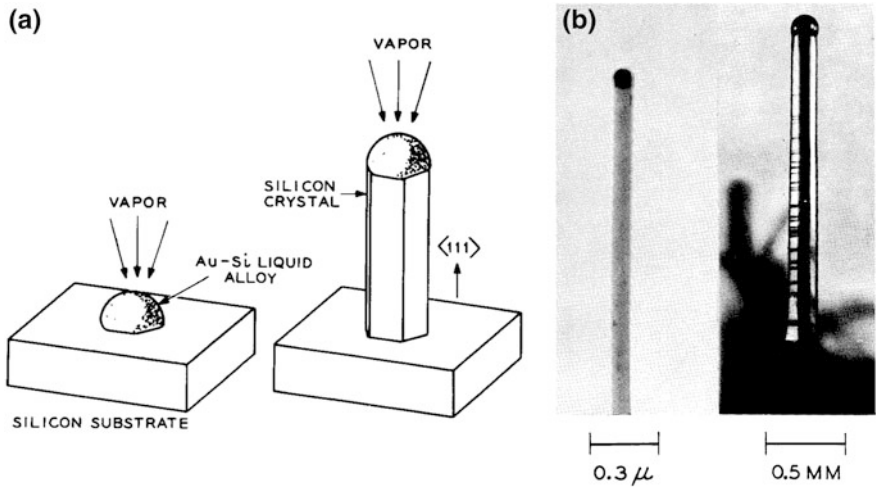

Fig. 5.12 **a** Growth of a Si crystal by vapor–liquid–solid mechanism. *Left* Initial state with liquid droplet on the Si substrate. *Right* Growing crystal with liquid droplet at the tip. **b** TEM images of the Si wires showing solidified Au–Si alloy at the tip, *left* is a 100-nm-diameter whisker and *right* is a twelve-sided 200-μm diameter needle. Reprinted with permission from [14]. Copyright 1964, AIP Publishing LLC

growth. At 950 °C, the gold melts into a droplet of Au–Si alloy. The hydrogen reduction of $SiCl_4$ gives rise to free Si atoms which prefer to dissolve in the alloy droplet to form a supersaturated solution, where the Si whisker starts to grow downward by precipitation of Si atoms. During this process, the Au–Si droplet stays on the tip of the growing Si whisker until Au is consumed or the growth condition is changed. A wide range of cross-sectional dimensions of the Si whiskers can be grown through this VLS method (Fig. 5.12b).

The SiC nanowhiskers are prepared by arc discharge between two graphite electrodes, and the anode is filled with a mixed silicon/graphite powder containing Fe catalyst [15]. Transmission electron microscopy reveals two types of structures in the product, rodlike structures, and nanosized particles (Fig. 5.13). The rods are about 10 nm in diameter and larger than 100 nm in length, and the particles have diameters in the range of 10–20 nm. The rods are only observed when the iron catalyst is used in the arc-discharge reaction. The nanowhiskers have lattice fringes either parallel or perpendicular to the rod axis, as shown in Fig. 5.14. The rods are surrounded by an amorphous layer. The lattice fringe spacings are 0.243 ± 0.010 nm, suggesting that the rods are single-crystalline 3C-SiC with a preferred $\langle 111 \rangle$ growth orientation. In the electron energy loss spectrum of an individual rod, the Si–L, C–K, and Si–K edges are present and there are no signals of Fe, O, and N. A two-stage vapor–liquid–solid growth mechanism is proposed for the whisker growth. At 1,220 °C, a Si/Fe liquid alloy acts as the site at which the whisker begins to grow, and at increased temperatures above 1,410 °C (i.e., the melting point of Si), the whisker can grow without the catalyst through solution

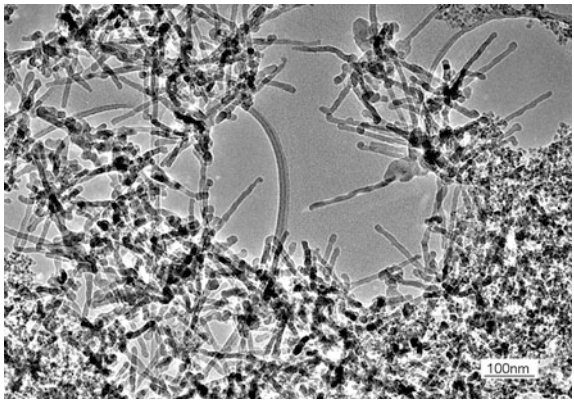

Fig. 5.13 TEM micrograph of SiC whiskers formed by arc-discharge evaporation of a Si/Fe-filled graphite electrode. They are about 10 nm in diameter and more than 100 nm in length. Some small particles can be seen at the *bottom*. Reprinted with permission from [15]. Copyright 2000, Wiley-VCH Verlag GmbH & Co. KGaA

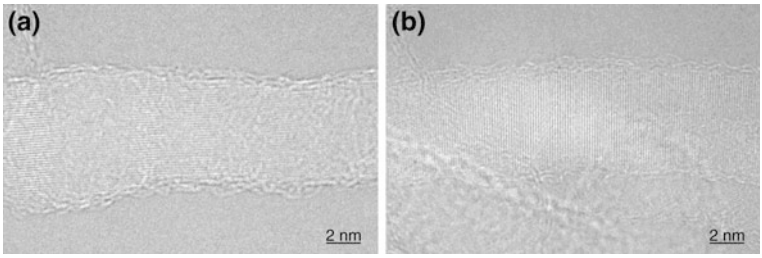

Fig. 5.14 HRTEM images of two SiC nanowhiskers. The lattice fringe of the whisker is oriented parallel (**a**) or perpendicular (**b**) to its axis. The fringe spacing is 0.243 ± 0.010 nm. There is an outer layer of disordered graphite for each whisker. Reprinted with permission from [15]. Copyright 2000, Wiley-VCH Verlag GmbH & Co. KGaA

and precipitation of carbon in the liquid Si tip. For the typical temperature of 2,000 °C at the cathode, the remaining iron catalyst will evaporate, which accounts for the absence of Fe in the final whiskers.

Pyrolysis of polysilazane at 1,700 °C under catalysis of $FeCl_2$ and under nitrogen gas flow yields β-SiC nanorods [16]. The synthesized nanorods have diameters of 80–200 nm and lengths of about 4 μm. They preferentially grow along ⟨111⟩ direction. A solid–liquid–solid mechanism is proposed to explain the growth of the SiC nanorods. Pyrolysis of the polymer generates an amorphous SiCN phase, which then reacts with Fe to a form liquid Si–Fe–C alloy. However, SiC nanorods do not form at this stage because the Si_3N_4 phase forms first, which is more stable at temperatures below 1,500 °C in the presence of N_2. When the temperature is improved to 1,500 °C at which SiC phase is thermodynamically stable, the SiC nanorods begin to grow by dissolving of Si_3N_4 and free carbon in

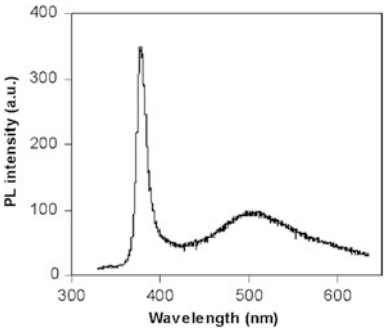

Fig. 5.15 Photoluminescence spectrum of the SiC nanorods under 325 nm excitation. Reprinted with permission from [17]. Copyright 2006, AIP Publishing LLC

Si–Fe–C liquid alloy. These nanorods show PL with two strong bands (Fig. 5.15), one is a strong sharp UV line at 378 nm (3.3 eV) and another is a broad green emission band centered at around 510 nm [17]. Stacking faults could be the origin of the UV emission. The time-resolved PL spectrum of the nanorods can be fit by a double-exponential function giving rise to two time constants of 1.0 and 6.5 ns. The morphology of the SiC nanorods can be controlled by changing the source species pressure during the vapor–liquid–solid growth of the nanowires by pyrolysis of polysilazane [18]. Nanowires with Eiffel tower shape, spindle shape, and modulated diameters and periods have been synthesized using this technique. The precisely controlled growth of SiC nanowires with a conical shape can be realized by tailoring the cooling rate [19]. The SiC nanowires with needlelike, pyramid-like, and ball-like tips are synthesized by adjusting the cooling rate at the respective temperature. The diverse morphologies of the synthesized SiC nanowires result from different degrees of supersaturation and different alloy droplet sizes induced by different cooling rates. The SiC nanorods with periodically tuned cross-sectional dimensions can also be grown by using alternatively interchanged cooling and heating processes (Fig. 5.16). The periodicity of the obtained nanorods shows consistence with the prescribed pyrolysis scheme.

The SiC nanowires can exhibit different morphologies at different growth stages [20]. The nanowires are synthesized by thermal evaporation and reaction of the mixed SiO_2 and C powders under catalysis of iron at 1,500 °C. The nanowires grow by a vapor–liquid–solid process, and they show different types of structures during the successive growth stages (Fig. 5.17). In the first stage, the SiC nanowires exhibit as periodically twinned crystals. In the second stage, they take the form of core–shell structures. The core is crystalline, and its cross-sectional area varies with position along the nanowire growth direction. The shell is amorphous. In the third stage, SiC nanowires still exhibits core–shell structures but the core diameter becomes uniform.

SiC nanowires can be synthesized by reaction of gas and solid source materials at increased temperatures. A reduction–carburization method is employed to

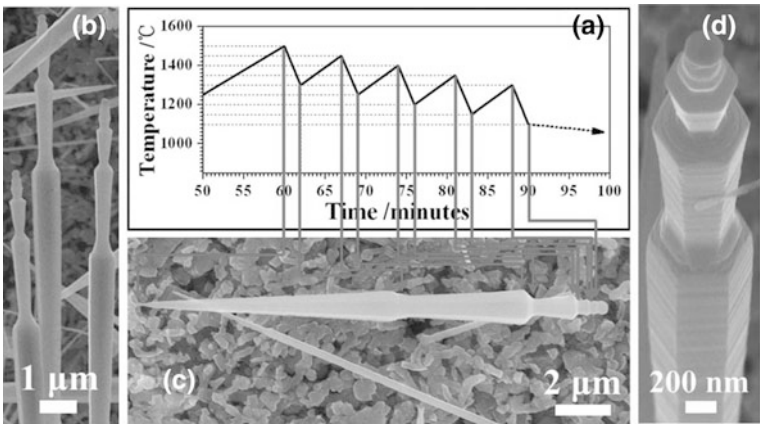

Fig. 5.16 **a** Pyrolysis scheme with an alternatively repeated cooling and heating process (cooling rate: 100 °C min^{-1}, heating rate: 30 °C min^{-1}). **b–d** SiC nanowires with periodic structures. Reprinted with permission from [19]. Copyright 2012, Royal Society of Chemistry

synthesize β-SiC nanowires with Si powder and tetrachloride (CCl_4) as source materials and Na as the reductant at 700 °C [21]. The nanowires have diameters of 15–20 nm and lengths of 5–10 μm, and they grow by the vapor–liquid–solid mechanism. The Raman spectrum (Fig. 5.18a) comprises a strong β-SiC TO phonon mode at 776 cm^{-1} and a very weak LO phonon mode at 954 cm^{-1}. Both Raman lines shift to lower wave numbers by 18–20 cm^{-1} with respect to bulk

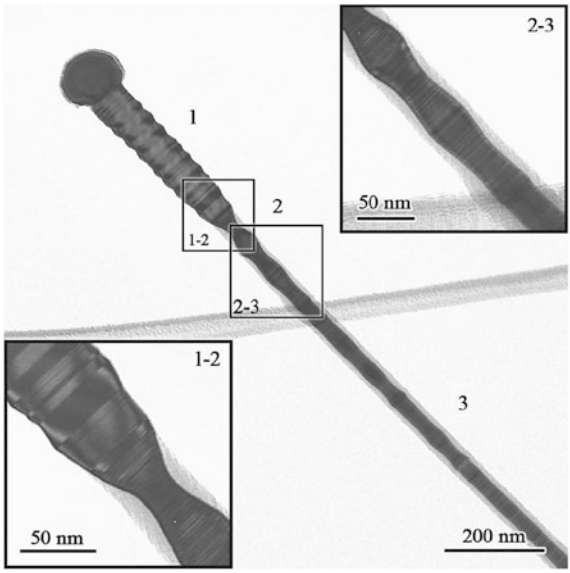

Fig. 5.17 TEM image of a SiC nanowire showing three distinct growth stages. Reprinted with permission from [20]. Copyright 2007, AIP Publishing LLC

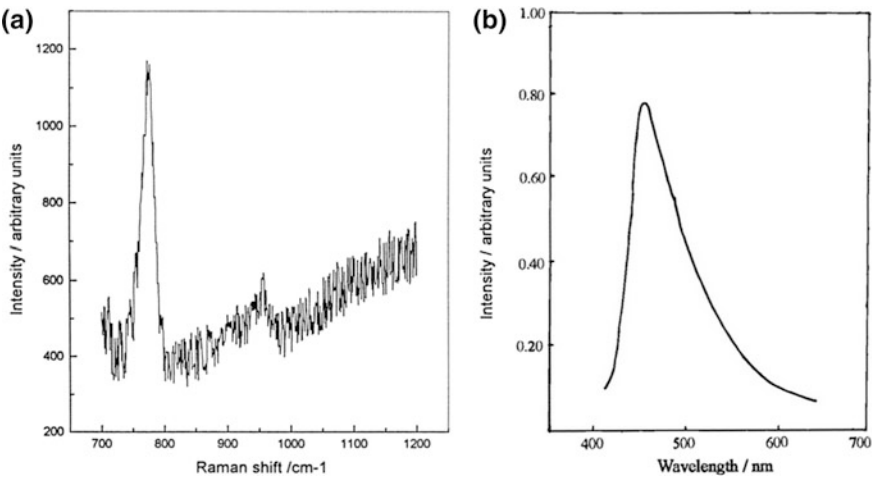

Fig. 5.18 **a** Raman and **b** photoluminescence (excited at 385 nm) spectra of the SiC nanowires. Reprinted with permission from [21]. Copyright 2000, American Chemical Society

values due to the small nanowire diameter and the stacking faults. The PL spectrum (Fig. 5.18b) comprises a single peak at around 448 nm.

The synthesized SiC nanowires usually belong to 3C polytype, but few SiC nanowires show photoluminescence characteristics that can be ascribed to the quantum confinement effect in 3C-SiC. The observed PL spectra in the SiC nanowires generally have significant blue shift relative to the bandgap of bulk 3C-SiC, 2.2 eV at room temperature. At first glance, this behavior seems to be an indication of quantum confinement in that the quantum confinement can result in a larger energy gap in the SiC nanowire than in bulk material. However, most of the synthesized SiC nanowires have diameters over 10 nm, and the quantum confinement effect in this size regime is rather weak, so their energy gaps are expected to be close to the bulk bandgap. Therefore, the usually observed PL in the SiC nanowires with significant blue shift can hard be explained by the quantum confinement effect. Instead, they may originate from some defects including surface defects, interior defects, and defects in the outer silicon oxide shell. Occasionally, the synthesized SiC nanowires have photoluminescence with peaks close to the bulk bandgap, as reported in Ref. [22]. In this study, the 3C-SiC nanowhiskers with [111] axial orientation are synthesized on a Fe-deposited Si substrate in a microwave plasma chemical vapor deposition system in hydrogen and methane atmosphere. The SiC whiskers have diameters between 5 and 38.5 nm with a most probable diameter of 15.4 nm. Figure 5.19 shows the photoluminescence spectra of the nanowhiskers synthesized at different temperatures. The dominant emission band has a peak between 500 and 600 nm, close to the bulk bandgap value of 3C-SiC. There is another weak emission band centered at around 800 nm. The PL intensity increases with the substrate temperature and the Fe film thickness due to the increase in nanowire quantity as demonstrated by the SEM observation.

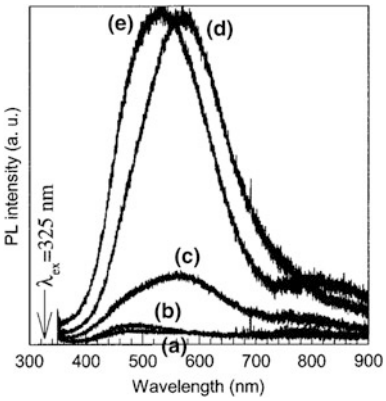

Fig. 5.19 Photoluminescence spectra of several SiC nanowhisker samples synthesized at **a** 800 °C, **b** 850 °C, **c** 900 °C, **d** 950 °C, and **e** 1,000 °C, respectively, with the same thickness of Fe film on the Si substrate. The excitation wavelength is 325 nm. Reprinted with permission from [22]. Copyright 2002, AIP Publishing LLC

Chemical vapor deposition has been utilized to synthesize SiC nanowires that usually grow by the vapor–liquid–solid mechanism. A one-step procedure has been developed to synthesize β-SiC nanorods from the solid carbon and silicon sources on a Si substrate by hot-filament chemical vapor deposition at 1,000 °C with catalysis of impurity metal particles [23]. The atomic hydrogen etches the solid source materials, giving rise to gaseous hydrocarbon radicals (CH_x), hydrosilicon radicals (SiH_x), or organosilicon molecules. These vapor molecules dissociate into Si and C atoms and dissolve in the liquid metal catalyst, leading to growth of SiC nanowires upon supersaturation. The nanorods contain a crystalline β-SiC core and an amorphous silicon oxide shell and grow along the [100] direction (Fig. 5.20). The nanowire diameters are between 10 and 30 nm and the lengths are less than 1 μm. SiC nanowires can also be synthesized at lower temperatures but under higher pressures. β-SiC nanorods are synthesized through a one-step reaction at 400 °C under high pressure [24]. The reaction is carried out in an autoclave using $SiCl_4$ and CCl_4 as reactants and metal Na as coreductant. The nanorods have diameters of 10–40 nm and lengths up to several micrometers. The pressure in the autoclave resulting from vaporization of $SiCl_4$ and CCl_4 reaches about 9 MPa, and as a result, the crystalline SiC can form at relatively low temperature. This reaction is described as:

$$SiCl_4 + CCl_4 + 8Na \rightarrow SiC + 8NaCl. \tag{5.5}$$

The reaction between $SiCl_4$ (or Si powders), C_6Cl_6 (or carbon powder), and sodium can produce various β-SiC nanostructures at different temperatures, including hollow nanospheres and nanowires and coaxial nanowires [25].

Highly aligned SiC nanowires have been synthesized by chemical vapor deposition using methyltrichlorosilane (CH_3SiCl_3) as the source precursor under

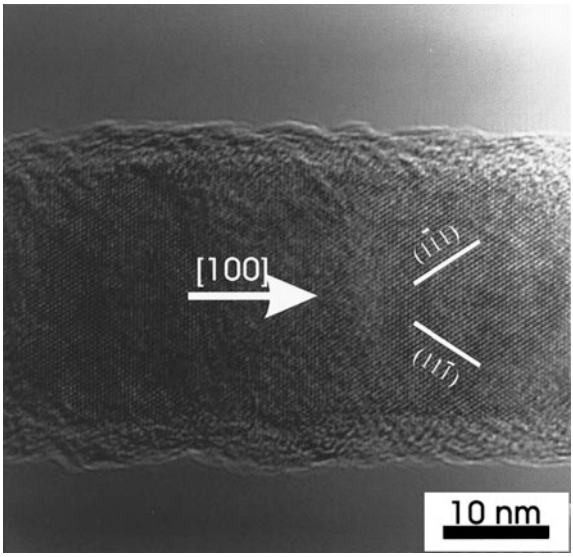

Fig. 5.20 HRTEM image of a β-SiC nanorod. Reprinted with permission from [23]. Copyright 1999, AIP Publishing LLC

hydrogen flow at 950 °C [26]. Ni-deposited Si wafer is taken as the substrate. The nanowires have diameters smaller than 50 nm and lengths up to several micrometers (Fig. 5.21). X-ray diffraction and transmission electron microscopy reveal that the nanowires are single-crystalline 3C-SiC, with a preferential growth direction of ⟨111⟩. They exhibit photoluminescence with a wide emission band centered at around 420 nm under 325 nm excitation.

SiC powder or bulk material can also be used to synthesize SiC nanowires by employing metal-catalyzed vapor–liquid–solid process. Laser ablation of a SiC target at 900 °C yields SiC nanowires with an average diameter of 80 nm and lengths of tens of micrometers [27]. High-resolution TEM observation reveals that the nanowires contain a high density of stacking faults and are wrapped by a

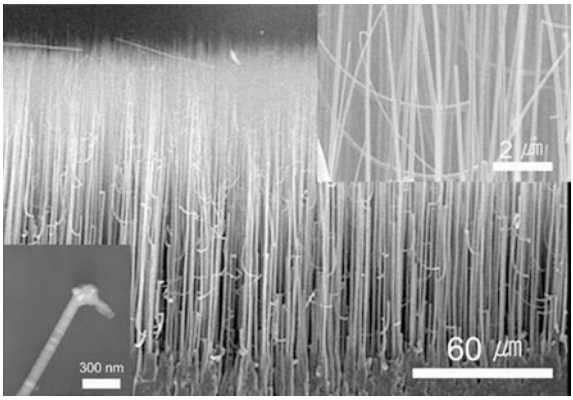

Fig. 5.21 SEM image of vertically aligned SiC nanowires grown on a Si substrate at 1,100 °C under hydrogen flow. The *lower inset* is the TEM image of a SiC nanowire. Reprinted with permission from [26]. Copyright 2004, Elsevier

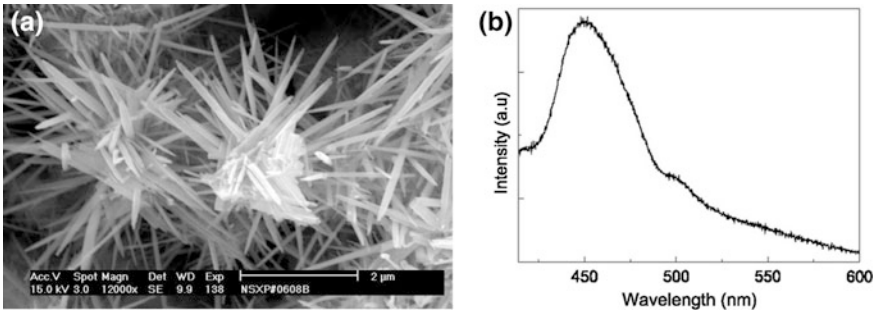

Fig. 5.22 **a** SEM micrograph of bunches of SiC nanowires. **b** PL spectrum of the SiC nanowires under 400 nm excitation at room temperature. Reprinted with permission from [29]. Copyright 2003, Elsevier

silicon oxide layer with thickness of 17 nm. The grown mechanism is a typical vapor–liquid–solid mechanism, in which nanosized iron particles act as catalyst at the tip of each SiC nanowire. The Raman scattering shows that the TO and LO phonon modes of the SiC nanowires shift to lower wave numbers by 12 and 34 cm^{-1} relative to bulk values. The peak shift, band broadening, and asymmetry of the Raman band are explained by the size confinement effect in both radial and growth directions. The needle-shaped 3C-SiC nanowires are synthesized by thermal evaporation of SiC powder with iron as a catalyst in flowing argon atmosphere at 1,700 °C [28, 29]. These bunched SiC nanowires have diameters of 20–50 nm and lengths of 1–2 μm (Fig. 5.22) [29]. They show photoluminescence with a broad band and a dominant peak centered at 450 nm under 400 nm excitation. The full width at half maximum of the dominant peak is 60 nm. There is another weak emission peak at around 500 nm.

The SiC nanowires can be grown by a catalyst-assisted sublimation method [30]. It involves microwave heating-assisted physical vapor transport from a source 4H-SiC wafer to a nearby substrate 4H-SiC wafer in nitrogen atmosphere at 1,650–1,750 °C. The 4H-SiC substrate is coated with a 5 nm thickness metal (Fe, Ni, Pd, Pt) catalyst film prior to the growth, and the nanowires are grown by the vapor–liquid–solid mechanism. They are 15–300 nm in diameter and 10–30 μm in length (Fig. 5.23a–c). Electron backscatter diffraction (EBSD) and selected area electron diffraction confirm the 3C-SiC structure of the nanowires. The nanowire caps are identified by EBSD as Fe_2Si, Ni_3Si, Pd_2Si, and PtSi phases for the nanowires grown with Fe, Ni, Pd, and Pt catalysts, respectively. The nanowires grow along the ⟨112⟩ orientation, different from commonly observed ⟨111⟩ direction. The micro-Raman spectrum (Fig. 5.23d) from single nanowire indicates regions with varying compressive strain in the nanowires and shows modes not arising from the Brillouin zone center, possibly related to defects.

Combustion synthesis of a mixture containing Si-containing compounds (Si elemental, FeSi, $CaSi_2$) and halocarbons [poly(tetrafluoroethylene), $C_{12}F_{10}$,C_2Cl_6, C_6Cl_6] in a calorimetric bomb produces cubic-phase silicon carbide nanofibers

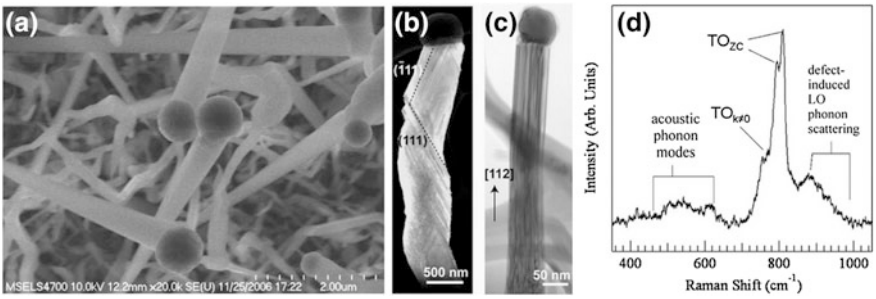

Fig. 5.23 **a** *Cone-shaped* 3C-SiC nanowires with metal–Si compound tips. **b**, **c** Diffraction contrast TEM images of two types of 3C-SiC nanowires with metal–Si compound tips. **b** Twin-like defects are observed on different sets of {111} planes. The twin structure is confirmed by selected area electron diffraction pattern. **c** Planar defects parallel to {111} planes along the wire axis. **d** Micro-Raman spectrum from an isolated SiC nanowire. TO_{ZC} refers to transverse optical phonon at the Brillouin zone center. $TO_{k\neq 0}$ refers to transverse optical phonon from nonzone center ($k \neq 0$) points, whose scattering is forbidden in a perfect single crystal but becomes active in the presence of defects which destroy translation symmetry. Reprinted with permission from [30]. Copyright 2007, American Chemical Society

[31]. The combustion process produces a huge amount of heat resulting in high temperatures, and under this condition, the reactants decomposed to form gaseous radical species for the synthesis. The synthesized SiC nanofibers are 20–100 nm in diameter. Raman scattering shows that the product is composed of mostly cubic polytype of SiC. The combustion product contains also some uniform carbon nanoparticles with diameters of 20–30 nm. Cathodoluminescence in these nanowires at temperatures 77–300 K has been investigated [32]. As shown in Fig. 5.24a, the bulk 3C-SiC has a strong emission band at 2.38 eV (at 77 K), which may be the exciton recombination band. There is another weaker shoulder at around 1.9 eV. The 2.38 eV band vanishes in the spectrum of the nanowires, and the luminescence is dominated by the single strong band centered at 1.9 eV. This emission band diminishes with increasing temperature (Fig. 5.24b). The inset shows the triple-Gaussian decomposition of the spectrum measured at 290 K. The three components are located at around 1.98, 2.30, and 2.77 eV, respectively. The 1.9 eV emission is proposed to arise from some defect in the nanowires since the photon energy is smaller than the bandgap of bulk 3C-SiC.

With the extensive studies of SiC nanowires, more and more fabrication methods have been developed. To date, large scale of SiC nanowires can be readily synthesized by many methods. For example, large areas of centimeter-long SiC nanowires are synthesized by pyrolysis of a polymer precursor (polysilacarbosilane) with ferrocene as the catalyst by chemical vapor deposition at 1,300 °C [33]. These nanowires have diameters of 100–200 nm and lengths of several centimeters (Fig. 5.25), and they are single-crystal β-SiC growing along the ⟨111⟩ direction by vapor–liquid–solid mechanism. X-ray diffraction pattern of the nanowires consists of several strong and sharp peaks, indicating the good

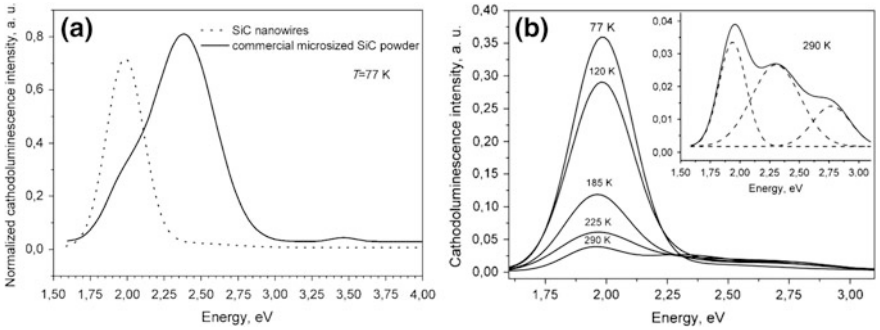

Fig. 5.24 **a** Normalized cathodoluminescence spectra of bulk 3C-SiC and SiC nanowires. **b** Cathodoluminescence spectra of SiC nanowires at different temperatures. The *inset* shows the triple-Gaussian fit of the spectrum measured at 290 K. Reprinted with permission from [32]. Copyright 2009, Wiley-VCH Verlag GmbH & Co. KGaA

crystallinity of the nanowires, whose positions (35.7°, 41.5°, 60.1°, 71.8°, and 75.5°) and intensities agree well with those of β-SiC (111), (200), (220), (311), and (222) planes, respectively. This confirms that β-SiC is the main crystalline phase of the nanowires. The Raman spectrum comprises two sharp peaks at 791.7 and 966.9 cm^{-1} corresponding to the TO and LO phonon modes at the Γ points in β-SiC, but with 4.3 and 5.1 cm^{-1} shifts to low wave numbers, respectively.

The SiOC nanocomposites are adopted to synthesize large-scale SiC nanowires [34]. The mixture of silica sol and sucrose powder is consecutively heated at 90 °C in air and 850 °C in argon atmosphere to give rise to a black powder of SiOC nanocomposites. These nanocomposites are heated up to 1,500 °C in argon atmosphere to produce a white cotton-like product (Fig. 5.26) that is 12 cm in diameter and 1–2 cm in thickness. Scanning electron microscopy reveals that the cotton-like sample contains a large amount of smooth and straight nanowires with

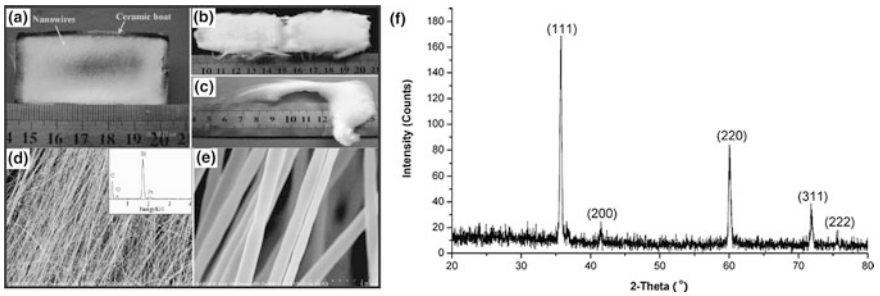

Fig. 5.25 **a** SiC nanowires with lengths of about 1 cm grown vertically on the ceramic wall. **b** Cotton-like products covering the outside back of the ceramic boat. **c** A bundle of fibers with lengths up to several centimeters. The ruler unit is centimeter. **d**, **e** SEM images of the SiC nanowires. The *inset* of **d** shows the energy-dispersive X-ray spectrum. **f** X-ray diffraction pattern of the SiC nanowires. The peak positions and intensities agree well with those of β-SiC. Reprinted with permission from [33]. Copyright 2009, American Chemical Society

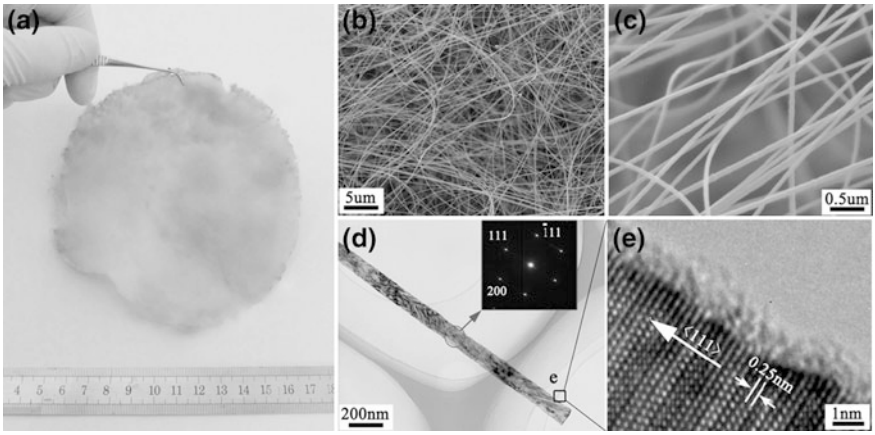

Fig. 5.26 **a** Cotton-like bundles of SiC nanowires. **b** and **c** SEM images of the nanowires. **d** TEM image of one nanowire and corresponding electron diffraction pattern. **e** HRTEM image of a nanowire. Reprinted with permission from [34]. Copyright 2010, IOP Publishing

uniform diameters of about 100 nm. High-resolution TEM observation reveals that the nanowires are β-SiC single crystals which preferentially grow along the [111] direction.

Large-scale centimeter-long single-crystal β-SiC nanowires are prepared using CH_4 as the carbon source and SiO or the mixture of Si and SiO_2 as the silicon source by catalyst-free chemical vapor deposition under superatmospheric pressure at 1,350–1,600 °C [35]. The nanowires have an average diameter of 40 nm (Fig. 5.27). They have single-crystal β-SiC cores and amorphous SiO_2 shell of 1–30 nm in thickness and grow along the [111] direction. The nanowires grow by a vapor–solid mechanism. Their light emission comprises a dominant peak at around 460 nm and two weaker peaks at 442 and 418 nm at room temperature.

Most of the SiC nanowires synthesized with various methods have cubic zinc-blende crystal structures. There have been very few reports on the synthesis of hexagonal polytypes of SiC nanowires. 2H-SiC nanowhiskers are synthesized by the reaction of SiO with methane at 1,300 °C [36]. The whiskers have diameters below 200 nm and lengths over 2 μm (Fig. 5.28a, b). Electron diffraction and high-resolution TEM observation indicate that the nanowhisker is 2H polytype except for a 3C-SiC tip. These nanowhiskers grow along the [0001] orientation, and they contain many stacking faults and microtwins. Their Raman spectrum consists of a strong peak at 796.6 cm^{-1} and a weak peak at 763 cm^{-1} (Fig. 5.28c). Since generally there is only one TO phonon peak at 791 cm^{-1} for 3C-SiC, whereas there are two TO phonon peaks at 764 and 799 cm^{-1} for 2H-SiC, the observed Raman signals are assigned to 2H-SiC. No catalyst is present on the tip of the nanowhisker, and an oxide-assisted growth mechanism is thus proposed, with the reaction:

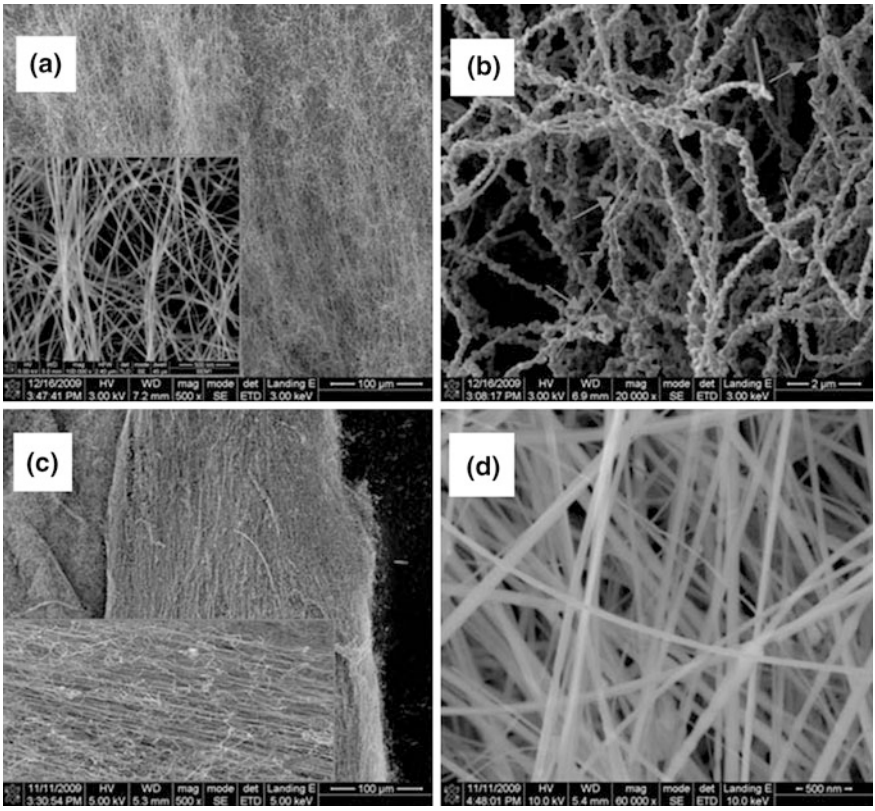

Fig. 5.27 **a** and **b** SEM images of SiC nanowires. **c** and **d** SEM images of the SiC nanowires collected from another area in the ceramic boat. Reprinted with permission from [35]. Copyright 2011, Royal Society of Chemistry

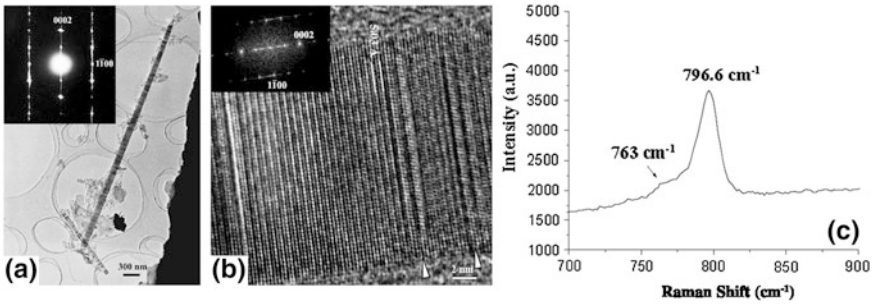

Fig. 5.28 **a** TEM image of a typical SiC nanowhisker. The *inset* shows the electron diffraction pattern indicating the 2H-SiC polytype. **b** HRTEM image of a 2H-SiC nanowhisker (*inset* is the electron diffraction pattern). **c** Raman spectrum of the SiC nanowhiskers. Reprinted with permission from [36]. Copyright 2003, Elsevier

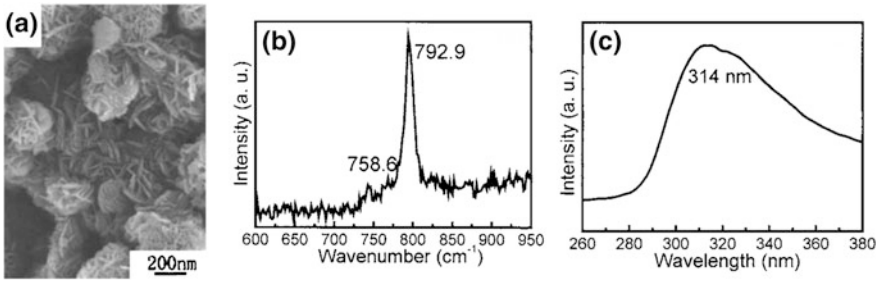

Fig. 5.29 SEM image (**a**), Raman spectrum (**b**), and photoluminescence spectrum (**c**, under 325 nm excitation) of the 2H-SiC nanoflakes. Reprinted with permission from [37]. Copyright 2006, AIP Publishing LLC

$$\mathrm{SiO(g) + CH_4(g) \rightarrow SiC(s) + SiO_2(s) + 2H_2(g).} \tag{5.6}$$

There is a report on the synthesis of 2H-SiC nanoflakes [37]. These nanoflakes are synthesized through a one-step solvothermal route involving reaction of $SiCl_4$ and CaC_2 in an autoclave at 180 °C. The reaction is suggested to be:

$$\mathrm{2CaC_2 + SiCl_4 \rightarrow SiC + 2CaCl_2 + 3C.} \tag{5.7}$$

The X-ray diffraction as well as infrared and Raman spectral analysis confirms that the nanoflakes have a crystalline structure of 2H-SiC. They are 200–500 nm in diameter and 15 nm in thickness (Fig. 5.29) and grow along the [001] direction. The Raman spectrum consists of a strong peak at 792.9 cm^{-1} and a weak shoulder at 758.6 cm^{-1}, characteristic of the 2H-SiC. Their infrared spectrum comprises a strong and wide peak centered at 820 cm^{-1} that is assigned to the optical phonon mode of SiC. The nanoflakes exhibit rare photoluminescence centered at 314 nm possibly arising from the defects in the surface silicon oxide layer.

The catalyst-assisted pyrolysis of polyaluminasilazane (or polysilazane) precursor at 1,350–1,450 °C produces pure or Al-doped 6H-SiC nanowires [38–40]. The catalysts are Fe, $FeCl_2$, or $Fe(NO_3)_3$ powder. Using this vapor–liquid–solid growth approach, the highly oriented SiC nanowire arrays are grown on the 6H-SiC single-crystal substrate [39]. The nanowires grow along the $[\bar{1}102]$ or equivalent direction on 6H-SiC (0001) substrates and along the $[10\bar{1}0]$ or equivalent direction on 6H-SiC $(10\bar{1}0)$ and $(11\bar{2}0)$ substrates (Fig. 5.30). This method can yield highly aligned SiC nanowire arrays. This pyrolysis method also yields 6H-SiC nanowires with triangular prism shape [40], and the nanowires have an average edge width of 700 nm and lengths up to tens of micrometers (Fig. 5.31). The wires are single crystalline with 1 at.% Al dopant and grow along the [102] direction.

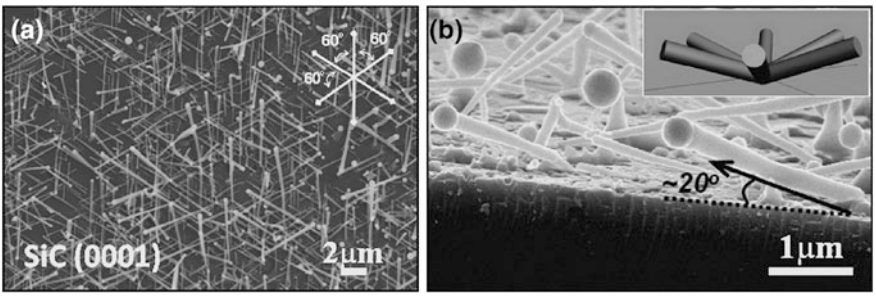

Fig. 5.30 **a** Top-view SEM image of SiC nanowires grown on a 6H-SiC (0001) substrate showing the preferred orientation with six growth directions. **b** Side-view SEM image suggesting the oblique growth of the nanowires on the substrate with an angle of 20° as illustrated by the model in the *inset*. Reprinted with permission from [39]. Copyright 2010, American Chemical Society

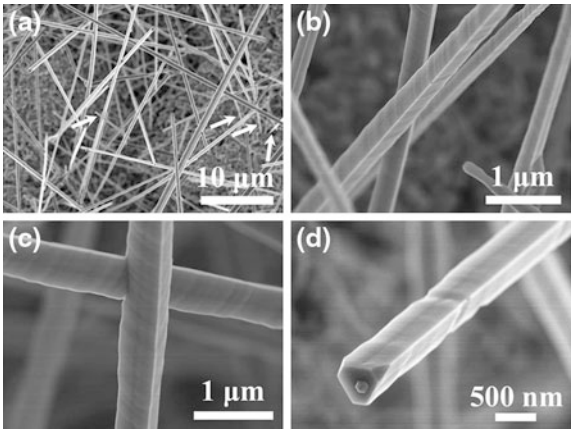

Fig. 5.31 **a** SEM image of the 6H-SiC nanowires with prism-like shape. **b–d** Magnification images of the nanowires. Reprinted with permission from [40]. Copyright 2012, Royal Society of Chemistry

5.2 Field Electron Emission

The field electron emission properties of silicon carbide nanowires have been extensively studied. In 1928, Fowler and Nordheim calculated the electron emission of cold metal in intensive electric fields using the potential barrier tunneling theory based on quantum mechanics [41]. They derived an equation that has been widely used in the study of field electron emissions of SiC nanowires:

$$J \propto A \frac{\mu^{1/2}}{(\chi + \mu)\chi^{1/2}} E^2 e^{-B\frac{\chi^{3/2}}{E}}, \tag{5.8}$$

in which J is the electron current density at the emitter, E is the local electric field at the emitter which could be different from the applied field due to the field

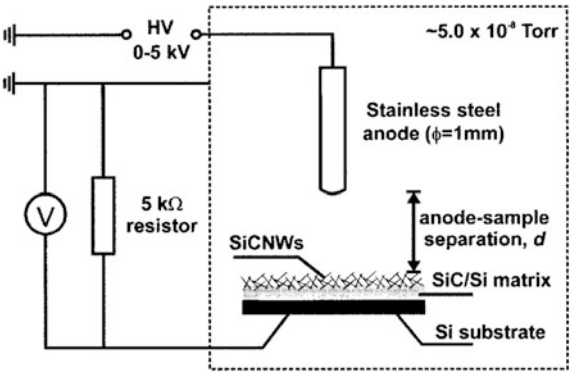

Fig. 5.32 Schematic diagram showing the vacuum chamber setup for measurement of field electron emission of the SiC nanowires. Reprinted with permission from [42]. Copyright 1999, AIP Publishing LLC

enhancement effect of the emitter, A and B are constants, χ is the thermionic work function, and μ is the usual parameter of the electron distribution in the Fermi–Dirac statistics equivalent to the thermodynamic partial potential of an electron. χ and μ are dependent on the material and geometric characteristics of the emitter. When researchers study the field electron emission properties of the SiC nanowires, they generally use a relationship derived from Eq. (5.8):

$$\ln\frac{J}{E^2} = C - D\frac{1}{E}, \tag{5.9}$$

where C and D are two parameters. Therefore, the ln (J/E^2) versus $1/E$ curve is subjected to exhibit as a straight line if the considered electron emission is governed by the quantum tunneling model.

The field emission properties of the SiC nanowires grown on a Si substrate have been investigated [42]. The nanowires are synthesized by hot-filament-assisted chemical vapor deposition with solid silicon and carbon sources. Scanning electron microscopy reveals that the SiC nanowires are randomly aligned and have diameter of around 20 nm. The electron field emission of the SiC nanowires is measured in a vacuum chamber with pressure of 5×10^{-8} Torr (Fig. 5.32). Figure 5.33a shows the emission current–voltage (I–V) curve of the SiC nanowire film at an anode-sample separation of 20–120 μm. These I–V curves can be roughly fit by an exponential function. The estimated turn-on field for current density of 0.01 mA/cm^2 is 20 V/μm and comparable to that of many other field emitters such as diamond films and carbon nanotubes. The lowest emission current density for actual application of flat-panel displays is about 10 mA/cm^2. The threshold field to give rise to this current density is 30 V/μm for the SiC nanowire film. Figure 5.33b displays the Fowler–Nordheim plot of ln(J/E^2) versus $1/E$ for the SiC nanowire film at different anode-sample separations. These roughly-straight lines indicate that the observed currents do originate from the quantum

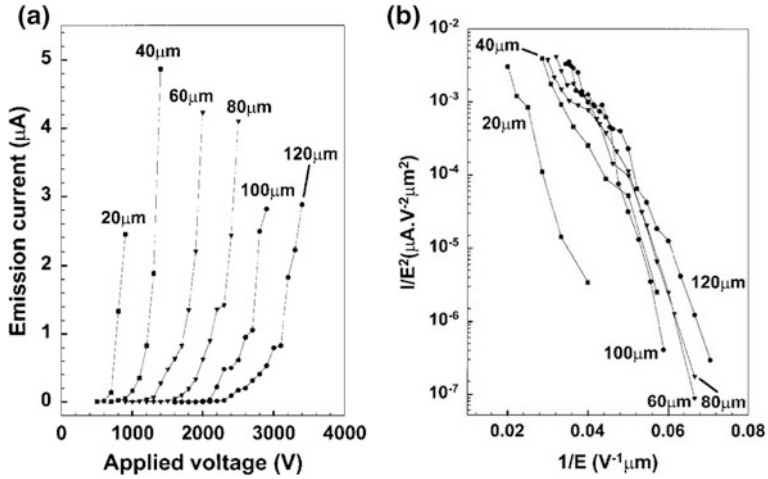

Fig. 5.33 **a** Emission current versus applied voltage for the SiC nanowire film at different anode-sample separations. **b** Fowler–Nordheim plots of the SiC nanowire film at different anode-sample separations. Reprinted with permission from [42]. Copyright 1999, AIP Publishing LLC

process of electron barrier tunneling. The turn-on field is reduced to 13–17 V/μm in the β-SiC nanowires with diameters of 5–20 nm and lengths of 1 μm [43] and to 9 V/μm in those with diameters of 20–70 nm and lengths of 1 μm [44].

Highly aligned SiC nanowire array possesses superior field emission performance [45]. The nanowire array is fabricated by the reaction of SiO with free-standing highly aligned carbon nanotube templates at 1,400 °C. The SEM images (Fig. 5.34) show that the nanowires have similar diameters (10–40 nm), spacing (about 100 nm), and length (up to 2 mm) to those of the aligned carbon nanotubes. The top end of the nanowire array is covered with a layer of the iron/silica

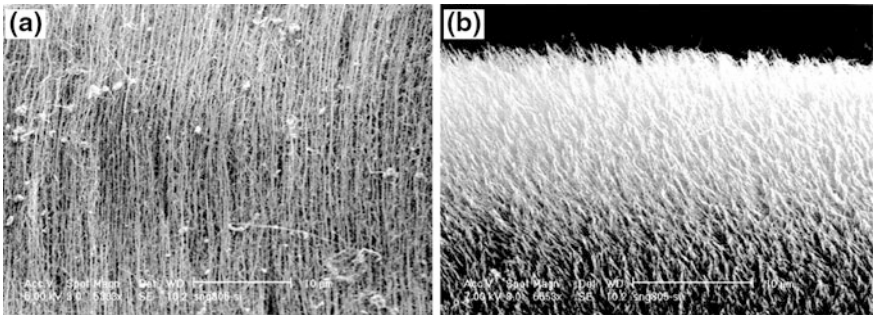

Fig. 5.34 **a** SEM image of oriented SiC nanowire array. The wires are highly aligned and have uniform diameter and interspacing. There are some Si-containing particles on the array surface formed during reaction. **b** Bottom structure of the SiC nanowire array showing high-density, highly oriented, and well-spaced nanowire tips. Reprinted with permission from [45]. Copyright 2000, Wiley-VCH Verlag GmbH & Co. KGaA

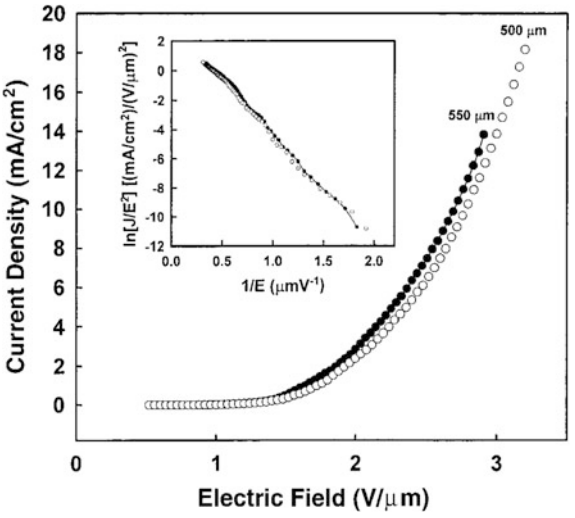

Fig. 5.35 Plot of emission current density versus applied electric field for oriented SiC nanowire film with an emitting area of 3.65 mm^2. The average turn-on field and threshold field are 0.9 and 2.7 V/mm, respectively. The *inset* is the Fowler–Nordheim plot whose linearity indicates the field emission nature. Reprinted with permission from [45]. Copyright 2000, Wiley-VCH Verlag GmbH & Co. KGaA

nanoparticles resulting from those particles present on the top end of the initial nanotube array. The bottom end of the SiC nanowire array (Fig. 5.34b) is composed of highly oriented and well-separated SiC nanowire tips with a very high density of 10^9-10^{10} cm^{-2}. The electron diffraction pattern reveals that the nanowires are β-SiC crystals growing along the ⟨111⟩ direction. Figure 5.35 shows the field emission current density versus applied electric field curve of the nanowire array. The turn-on field corresponding to an emission current density 10 μA/cm^2 is 0.7–1.5 V/μm, and the threshold field corresponding to an emission current density 10 mA/cm^2 is 2.5–3.5 V/μm, which are among the lowest (turn-on or threshold) electric fields for all reported field-emitting materials indicating the promise of the oriented SiC nanowires for practical applications in vacuum microelectronic devices. The nearly linear relationship between $\ln(J/E^2)$ and $1/E$ (inset of Fig. 5.35) clearly demonstrates the field electron emission origin of the measured currents. The field electron emission is very stable, the current fluctuation is only ±3 % during 24 h of continuous operation at 5 mA/cm^2, and there is no significant change in the morphology of the nanowire array during its 24 h continuous emission.

Bunches of needle-shaped silicon carbide nanowires exhibit good field electron emission performance [28]. The needle-shaped nanowires are synthesized by thermal evaporation of SiC powders with ion catalysis, and they have diameters of 20–50 nm and lengths of 1–2 μm (Fig. 5.36a). The needle shape of the nanowires renders them ideal field electron emitters. The turn-on field and threshold field which give rise to an emission current density of 10 μA/cm^2 and 10 mA/cm^2 are 5 and 8.5 V/μm, respectively (Fig. 5.36b). The stable emission current density of 30.8 mA/cm^2 is acquired at electric field of 9.6 V/μm, and the maximum emission current density is 83 mA/cm^2. The good linearity of the curve in the Fowler–Nordheim plot (Fig. 5.36c) demonstrates the field emission nature of the nanowires. The current fluctuation is within ±4 % during 100 h continuous emission at

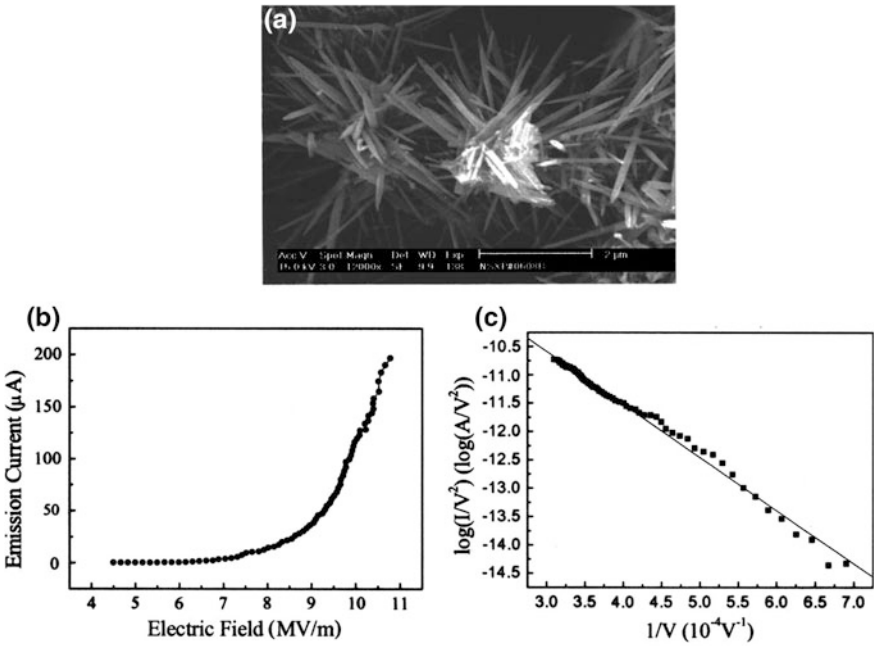

Fig. 5.36 **a** SEM image of bunches of needle-shaped SiC nanowires produced by heating SiC particles in flowing argon atmosphere at 1,700 °C. **b** Field electron emission current versus applied electric field for the nanowires. **c** Corresponding Fowler–Nordheim plot. Reprinted with permission from [28]. Copyright 2002, AIP Publishing LLC

a current of 75 μA that corresponds to a current density of 31 mA/cm^2. The morphology of the sample has no obvious change after the operation.

The SiC–Si composite nanotips show good field emission properties [46]. The Si nanotips are prepared monolithically from Si wafers by electron cyclotron resonance plasma etching technique at 200 °C, and they have diameter of only 1 nm, and the nanotip density ranges from 10^9 to 3×10^{11} cm^{-2}. High-resolution TEM (Fig. 5.37a) and Auger electron spectroscopy analysis demonstrates that the nanotips are composed of monolithic silicon and nanometer-sized SiC cap at the top. The nanotips have a very low turn-on field of 0.35 V/μm which gives rise to a 10 μA/cm^2 emission current density and have a high field emission current density 3.0 mA/cm^2 at an applied field as low as 1.0 V/μm (Fig. 5.37b).

The study shows that the SiC nanowires with sharp ends have better field emission performance in comparison with usual SiC nanowires [47]. The aligned β-SiC nanowires are synthesized in large scale using magnesium-catalyzed co-reduction of $SiCl_4$ and 2-ethoxyethanol in an autoclave at 600 °C. The β-SiC rodlike or needlelike nanostructures can be separately produced by employing different ratio of reactants. The infrared spectrum of the nanowires shows a strong absorption peak at around 814 cm^{-1} attributed to the optical phonon vibration of β-SiC. The Raman spectrum comprises two sharp peaks at 795 and 973 cm^{-1},

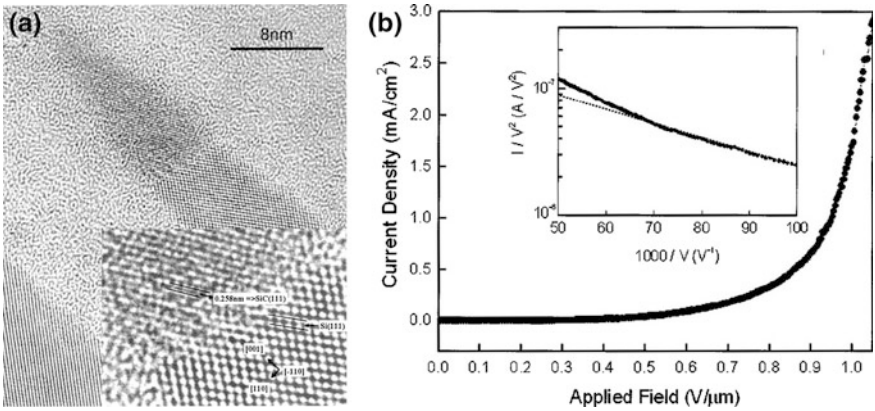

Fig. 5.37 **a** Cross-sectional TEM micrograph of a SiC-capped Si nanotip fabricated by dry etching of *p*-type Si (100) substrate. The *inset* shows magnified lattice image at the interface between Si and SiC. **b** Field emission data of the SiC-capped Si nanotips. The *inset* shows the Fowler–Nordheim plot, and the dashed line represents a linear relationship for an ideal field emitter. Reprinted with permission from [46]. Copyright 2003, AIP Publishing LLC

which are very close to the TO and LO phonon (at the Γ point) wave numbers of bulk β-SiC, respectively. The SiC nanowires synthesized using 1 mL of $SiCl_4$ and 0.21 mL of 2-ethoxyethanol are needlelike with sharp tips (Fig. 5.38a) and thus are favorable for field emission applications. Figure 5.38b shows the emission current density versus applied electric field curve for the needlelike nanowires, and from it, the turn-on field is derived as 1.6 V/μm. In comparison, the turn-on fields for two nanorod samples acquired by taking different reactant ratios are 8.4 and 12 V/μm, respectively. It is clear that the SiC nanowires with sharp tips have better field emission performance.

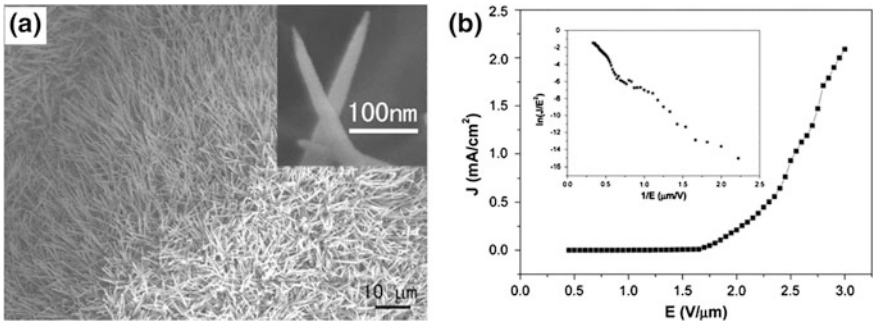

Fig. 5.38 **a** SEM image and **b** field emission current density versus electric field curve of the SiC nanowires synthesized by magnesium-catalyzed co-reduction of a mixture of 1.4 mL $SiCl_4$ and 0.3 mL 2-ethoxyethanol in an autoclave at 600 °C. The *inset* in *right panel* shows the Fowler–Nordheim plot. Reprinted with permission from [47]. Copyright 2006, American Chemical Society

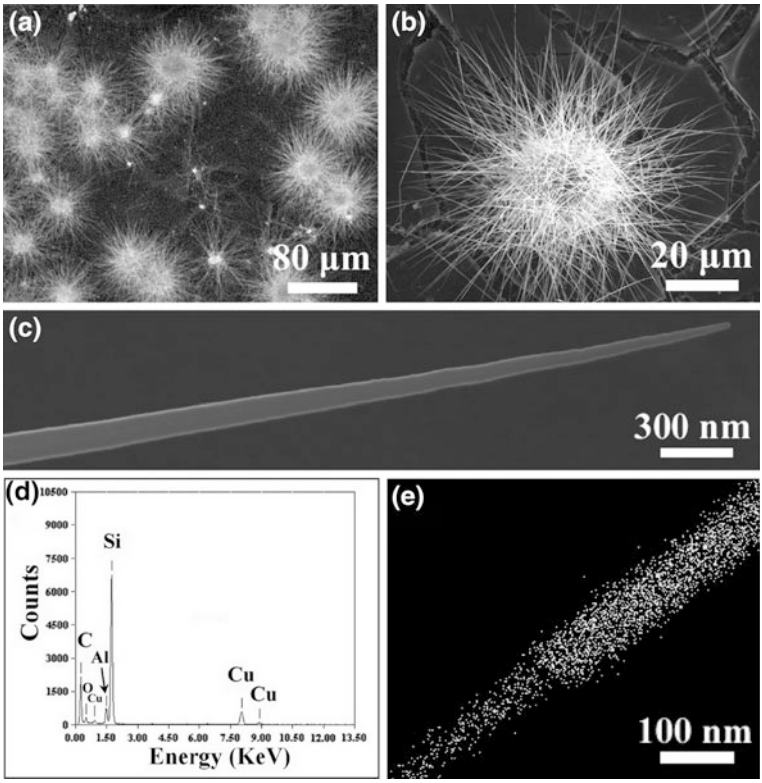

Fig. 5.39 **a** and **b** TEM images of tapered SiC nanowires. **c** Magnification image of a typical tapered SiC nanowire. **d** Energy-dispersive X-ray spectrum of the nanowires. **e** Al-element mapping within one nanowire. Reprinted with permission from [48]. Copyright 2010, American Chemical Society

The SiC nanowires with sharp ends can be produced by pyrolysis of polymer precursors. The 3C-SiC nanowire clusters are synthesized via pyrolysis of polysilazane with catalysis of $Al(NO_3)_3$ at 1,550 °C in an argon atmosphere [48]. The nanowires have a tapered and bamboo-like structure with tiny tips that are several to tens of nanometers in diameter (Figs. 5.39a–c). X-ray diffraction and Al-element imaging (Figs. 5.39d, e) confirm the Al doping in the nanowires. The nanowires possess an extremely low field emission turn-on field of 0.55–1.54 V/μm ascribed to the special tapered and bamboo-like structure of the nanowires and to Al doping. A prototype of the diode-type low-voltage field emission display device employing β-SiC nanowire cathode (Fig. 5.40) has been demonstrated [49]. The nanowires have diameters of 10–50 nm and lengths of several tens of micrometers. This field emission display device (flat vacuum lamps) has low threshold electric field (2 V/μm), high emission current density, and long-term stable performance.

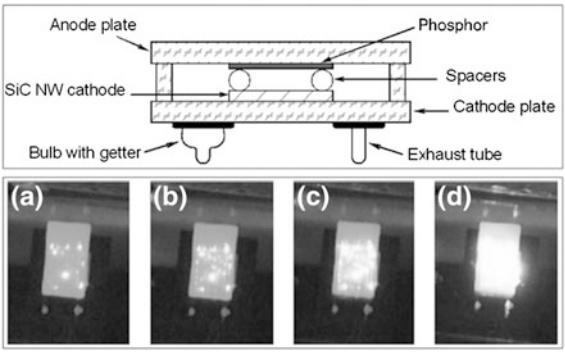

Fig. 5.40 Scheme of field electron emission display device employing 5×5 mm^2 SiC nanowire-based cathode. Field emission (phosphor screen) images are recorded at increasing electric field of **a** 2.3 V/μm, **b** 2.7 V/μm, **c** 3.0 V/μm, and **d** 3.3 V/μm. Reprinted with permission from [49]. Copyright 2008, IOP Publishing

Porous SiC can also show strong field electron emissions. The performance of the field emission of porous SiC can be significantly improved when regular porous structures are designed [50]. The porous structure is conventionally fabricated by electrochemical etching of bulk 6H-SiC. The morphology of the porous SiC depends on the electrochemical conditions used in the synthesis. The porous nanostructures with different morphologies have different field emission characteristics because different porous structures have different local field enhancements. The mesa, pillar, and fin arrays of porous SiC can be separately produced by reactive ion etching, photolithography, or focused ion beam treatment of the original porous structures. The pillar array (Fig. 5.41) has the best field emission performance with a turn-on field (for an emission current of 10 μA) as low as 4.4 V/μm, and the stable emission current density can reach as high as 6 A/cm^2.

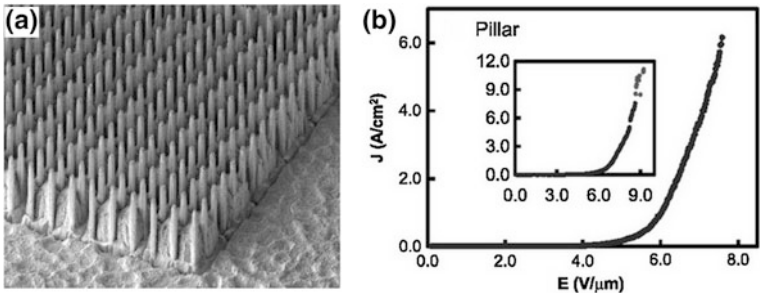

Fig. 5.41 **a** SEM image of porous SiC pillar arrays fabricated by focused ion beam. The image width is 145 μm. **b** Field emission current intensity versus electric field for the pillar arrays. The turn-on field for a current of 10 μA is 4.4 V/μm. The *inset* is the *J–E* curve extended to the failure point of the pillar array showing the emission instability at the material limit. Reprinted with permission from [50]. Copyright 2013, IOP Publishing

5.3 Core–Shell Structures

5.3.1 SiC/SiO_2 Core/Shell Nanowires

Most of the synthesized core-shell-structured SiC nanowires possess amorphous silicon dioxide shells. Carbothermal reduction of sol-gel-derived silica xerogels containing carbon nanoparticles can yield pure or core-shell-structured β-SiC nanorods [51, 52]. The β-SiC nanorods encapsulated by amorphous SiO_2 are achieved by consecutive reduction at 1,650 and 1,800 °C. These nanorods are up to 20 μm long, the nanorod core has a diameter ranging from 10 to 30 nm (Fig. 5.42a), and the amorphous SiO_2 shell has a thickness of 10–35 nm. The β-SiC nanorods without amorphous layer are obtained by carbothermal reduction at 1,650 °C, and they have the same diameter to that of the SiC/SiO_2 nanorod core. The high-resolution TEM image (Fig. 5.42b) reveals that the nanorod core is crystalline β-SiC growing along the ⟨111⟩ direction, and the outer shell is amorphous. Electron diffraction (inset of Fig. 5.42), energy-dispersive X-ray spectroscopy, and XRD confirm that the core is β-SiC and the amorphous shell is SiO_2, which is formed by the reaction of SiO vapor and O_2. Using a similar method, the β-SiC nanowires can be synthesized via vapor–liquid–solid growth taking activated carbon and Fe nanoparticle-embedded sol-gel-derived silica as starting materials at 1,400 °C [53]. The nanowires are composed of 10–30 nm β-SiC cores and amorphous SiO_2 shells. The XRD spectrum (Fig. 5.43a) shows three sharp lines that are assigned to the (111), (220), and (311) lattice planes of β-SiC. The weak peak at $2\theta = 33.5°$ which is close to β-SiC (111) peak is commonly assigned to stacking faults in the nanowires. The background halo pattern is characteristic of that of amorphous materials. The SiC nanowires show photoluminescence

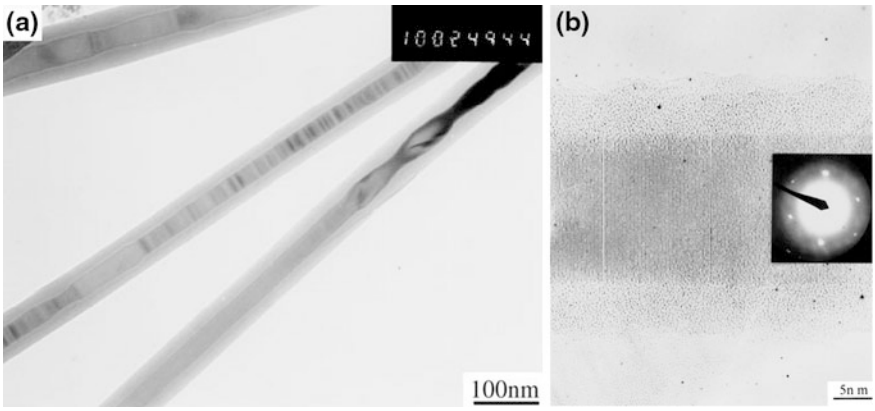

Fig. 5.42 **a** TEM image of the SiC nanorods produced by consecutive carbothermal reductions at 1,650 and 1,800 °C. **b** HRTEM image of a typical nanorod. The lattice fringes correspond to (111) planes of β-SiC. The *inset* is the selected area electron diffraction pattern. Reprinted with permission from [51]. Copyright 1998, Cambridge University Press

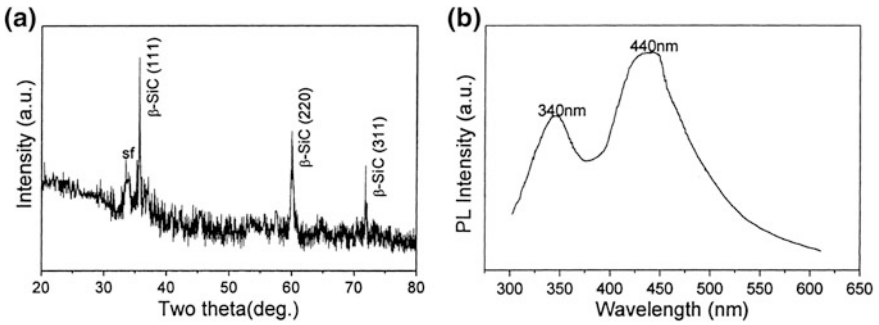

Fig. 5.43 **a** XRD spectrum and **b** PL spectrum under 260 nm excitation of the β-SiC nanowires. Reprinted with permission from [53]. Copyright 2000, Elsevier

(Fig. 5.43b) with two distinct bands centered at around 340 and 440 nm, respectively. The ultraviolet band results from the defect in amorphous SiO_2 shell, and the blue band is associated with the SiC core of the SiC/SiO_2 core/shell nanowires.

The side-by-side biaxially structured SiC–SiO_x ($x = 1$–2) nanowires have been synthesized [54]. The mixture of amorphous SiO and carbon/graphite is heated at 1,500 °C to generate the nanowires. Figure 5.44 (left panel) shows the TEM image of the nanowires situated on a carbon film. The nanowires are uniform with diameters of 50–80 nm and lengths as large as 100 μm. Three types of nanowires are present: pure SiO_x nanowires, coaxially SiO_x sheathed β-SiC nanowires (50 %), and biaxial β-SiC-SiO_x nanowires (30 %). The coaxial β-SiC-SiO_x nanowires grow along the β-SiC ⟨111⟩ direction with a high density of twins and stacking faults whose interfaces are perpendicular to the growth direction. The cross-sectional TEM images (Fig. 5.44, left panel) reveal the geometrical shapes of the coaxial and biaxial nanowires. High-resolution TEM images (Fig. 5.44, right panel) reveal that the biaxial SiC–SiO_x nanowire is composed of two side-by-side silica and β-SiC sub-nanowires. There is also a thin layer of silica on the surface of the β-SiC sub-nanowire, and it possesses a high density of stacking faults and a few twins. The presence of the planar defects leads to the [311] growth direction for the biaxial nanowires, whereas the biaxial nearly defect-free nanowires possess the [211] growth direction. The Young's modulus of the biaxial nanowires is between 50 and 70 GPa.

Two-dimensional nanoscale SiC networks can be prepared by heating SiC–Fe–Co mixture at 1,500 °C in CO atmosphere [55]. High-resolution TEM measurement reveals that most nanowires have a crystalline β-SiC core with lengths up to 100 μm and an amorphous SiO_x ($x = 1 - 2$) shell. The binary Fe–Co catalyst accounts for the SiC network growth. An arc-discharge approach has been developed to synthesize the SiC nanorods sheathed in amorphous SiO_2 by taking the SiC rod containing iron impurity as the anode [56]. The crystalline β-SiC cores have a uniform diameter of 5–20 nm and a length ranging from hundreds of nanometers to several micrometers, and the amorphous silica shells have thicknesses of tens of nanometers. Nanofiber templates are used to synthesize

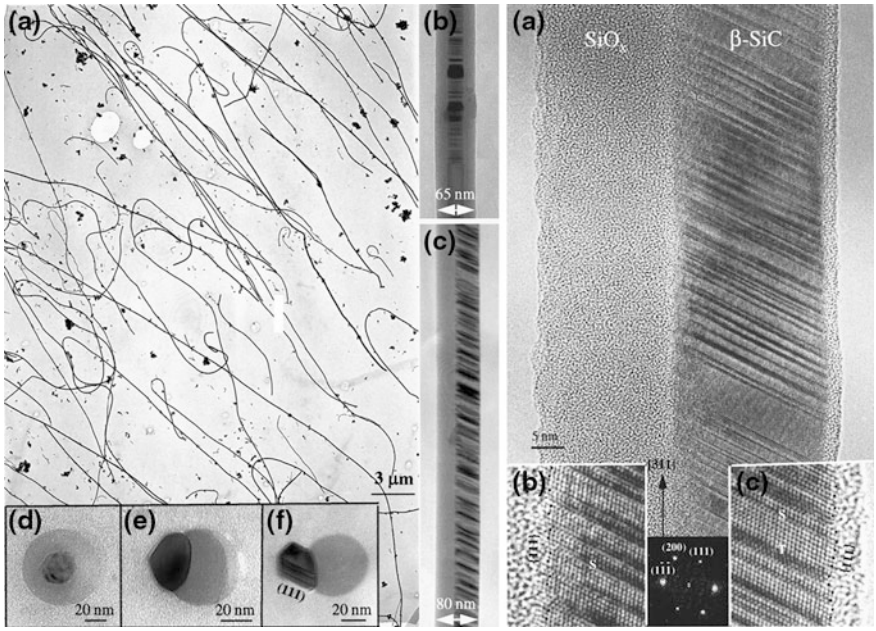

Fig. 5.44 *Left panel* **a** TEM image of the nanowires showing their very large lengths and uniform diameters. **b**, **c** Side view of coaxially and biaxial structure SiC–SiO_x nanowires. **d**–**f** Cross-sectional TEM images of coaxially and biaxial structure SiC–SiO_x nanowires. *Right panel* **a** HRTEM image of a biaxial structure β-SiC-SiO_x nanowire. The bottom Fourier transform image from a defect-free area reveals the [311] growth direction. Magnification images of SiC–SiO_x interface regions on the *left* (**b**) and *right* (**c**) sides of the SiC sub-nanowire showing the {111} facets at the interface. "S" and "T" stand for stacking fault and twin, respectively. Reprinted with permission from [54]. Copyright 2000, AIP Publishing LLC

high-quality SiC nanowires without assistance of any catalyst. The β-SiC nanowires have been synthesized by heating the template of electrospun polyacrylonitrile (PAN) nanofibers and a mixture of silica and graphite powders (to give rise to SiO and CO vapors) at 1,600 °C [57]. The as-prepared nanowires have SiC/graphite core/shell structures, and chemical etching in aqua regia removes the graphite shell. The resultant nanowires (Fig. 5.45) with diameters of 20–40 nm show an amorphous SiO_2 sheath (5 nm in thickness) as determined by electron energy loss spectroscopy, and this shell is formed during etching since the nanowires without etching contain no SiO_2. The SiC/SiO_2 nanowires are uniform in the axial direction, and they have very few stacking faults as confirmed by the sharp and distinct lines in the XRD spectrum.

The SiC–SiO_2 core–shell nanowires have been prepared by heating WO_3/C powder-covered Si substrate with NiO catalysis at 1,000–1,100 °C [58]. Transmission electron microscopy reveals that the SiC cores have diameters of 15–25 nm, and the SiO_2 shells have an average thickness of 20 nm. The thickness of the SiO_2 shell can be reduced by hydrofluoric acid etching (Fig. 5.46a), and the

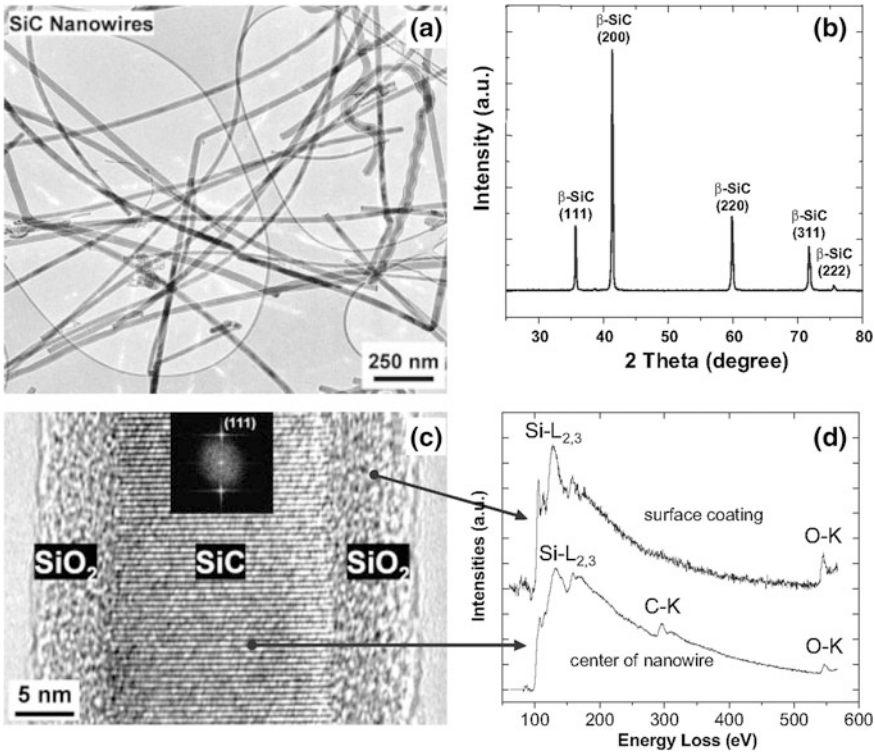

Fig. 5.45 **a** TEM image of SiC nanowires after surface etching with an average diameter of 30 nm. **b** XRD pattern of the nanowires. **c** HRTEM image showing the crystalline SiC core sheathed by an amorphous shell. The fast Fourier transform image in the *inset* indicates the growth direction of β-SiC (111). **d** Electron energy loss spectroscopy conducted on specified points revealing the silica structure of the shell. Reprinted with permission from [57]. Copyright 2005, Wiley-VCH Verlag GmbH & Co. KGaA

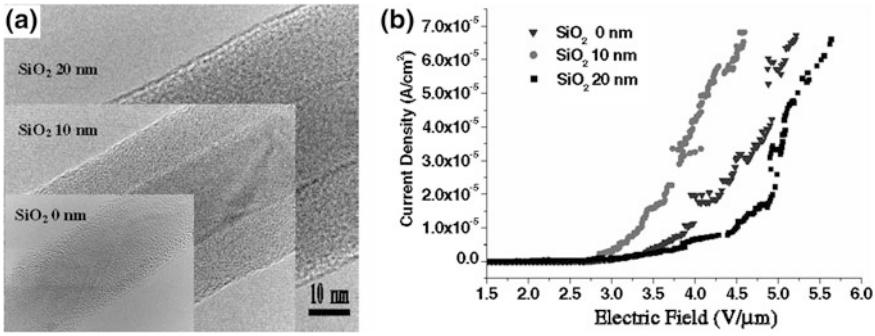

Fig. 5.46 **a** TEM image of β-SiC–SiO_2 core-shell nanowires for various SiO_2 layer thicknesses controlled by HF etching. **b** Field emission current density versus applied electric field curves for the nanowires. Reprinted with permission from [58]. Copyright 2005, IOP Publishing

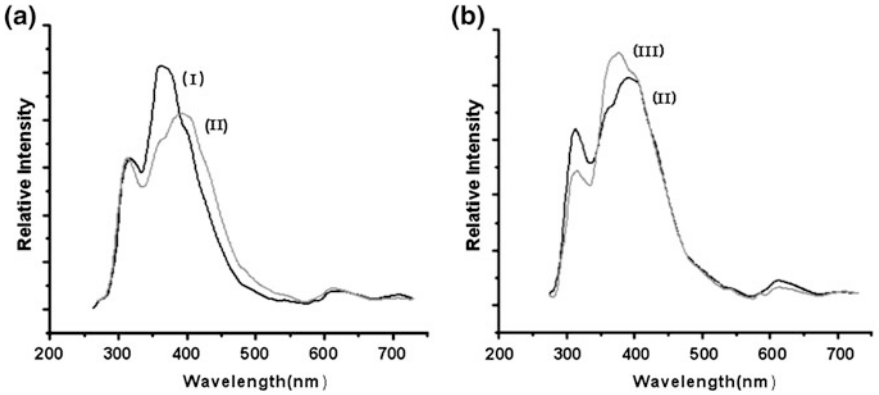

Fig. 5.47 **a** PL spectra of the SiC/SiO_x core/shell nanowires with an average core diameter of 10 nm (I) and 20 nm (II), respectively. **b** PL spectra of the SiC/SiO_x core/shell nanowires with an average core diameter of 20 nm before (II) and after (III) annealing at 950 °C in vacuum. Reprinted with permission from [59]. Copyright 2005, IOP Publishing

nanowires with complete removal of the SiO_2 shell possess a 5-nm-thickness carbon shell. The SiC–SiO_2 nanowires have field electron emission with performance depending on the shell thickness, and the nanowires sheathed by 10-nm-thickness SiO_2 layer has the best field emission characters including the lowest turn-on field (Fig. 5.46b).

High-purity SiC/SiO_x core/shell nanowires can be produced by arc discharge in deionized water between two graphite electrodes with the anode filled with a mixture of graphite, Si and Fe powders as reactants [59]. The obtained SiC/SiO_x nanowires consist of a uniform cubic β-SiC core and an amorphous silicon oxide shell. They have a very small average core diameter of 5 nm, and their length ranges from several hundred nanometers to several micrometers. The nanowires show photoluminescence with double emission bands (Fig. 5.47). The two bands are located at around 317 and 368 nm, respectively, for a sample with an average core diameter of 10 nm. This first band keeps nearly constant, whereas the second shifts to 393 nm in a sample with an average core diameter of 20 nm. After anneal in vacuum at 950 °C, the 317 nm emission band diminishes, whereas the other emission band becomes stronger.

The influence of the amorphous SiO_2 shell on the cathodoluminescence of the 3C-SiC/SiO_2 core/shell nanowires have been investigated [60]. The nanowires are prepared by reaction between carbon monoxide and native oxide on (001) Si substrates at 1,050–1,100 °C catalyzed by nickel nitrate. The main luminescence peak lies at around 2.41 eV. The emission intensity decreases by HF etching showing the enhancement effect of the SiO_2 shell on the luminescence, possibly arising from carrier diffusion from the SiO_2 shell to the SiC core. The cathodoluminescence in two samples of 3C-SiC/SiO_2 nanowires with different shell thicknesses has been comparatively investigated [61]. Two samples (Fig. 5.48a) have similar nanowire core diameter distribution between 15 and 30 nm but have

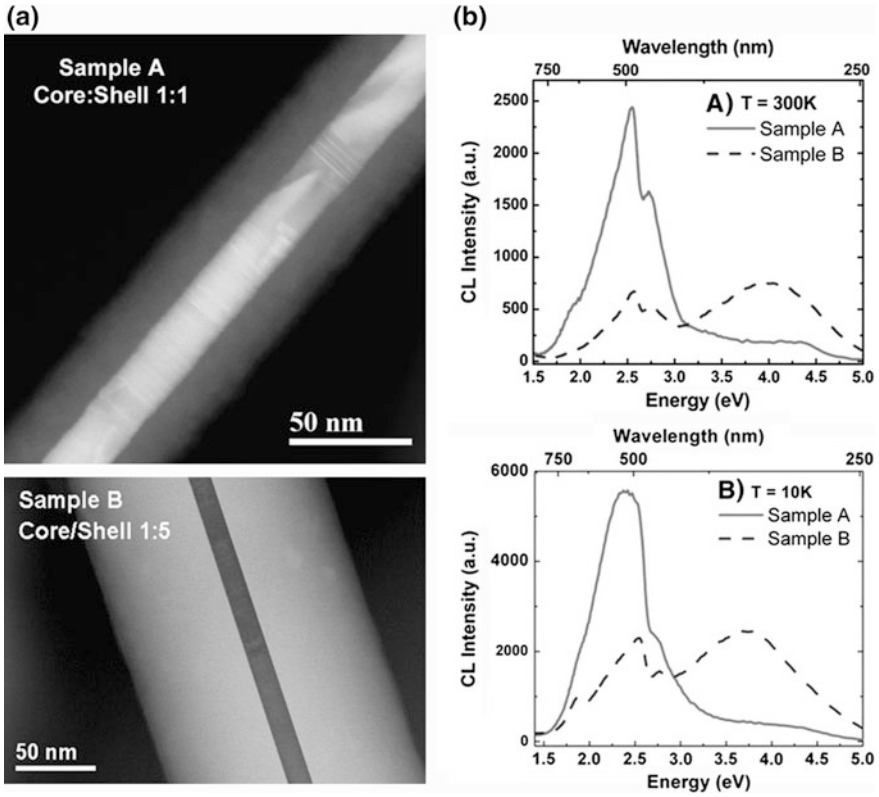

Fig. 5.48 **a** TEM images of two typical SiC/SiO_2 core/shell nanowires from two samples. **b** Cathodoluminescence spectra at room and low temperatures for two samples. Reprinted with permission from [61]. Copyright 2012, Elsevier

distinct core-to-shell ratios of 1:1 and 1:5, respectively. The cathodoluminescence measured at 10 and 300 K (Fig. 5.48b) shows two emission peaks for both samples, at around 2.5 and 4.0 eV. The emission band at around 4.0 eV is stronger in the sample with a thicker silica shell, whereas the emission band at 2.5 eV is stronger in the sample with a thinner shell. This observation suggests that the 4.0 eV emission arises from the silica shell and the 2.5 eV emission stems from the core SiC (possibly from surface defect).

Centimeter-long β-SiC/SiO_2 core/shell nanowires have been synthesized by a catalyst-free chemical vapor deposition at 1,250–1,300 °C in argon atmosphere [62]. The reactants are divided into two groups (Si and SiO_2 powder and WO_3 and graphite powder) and are placed at two sites in the furnace, whereas the product is collected on the graphite paper placed at a third site. The nanowires have diameters of 50–100 nm and lengths up to 10 mm (Fig. 5.49). They have photoluminescence with two distinct peaks centered at 289 and 394 nm which may arise from the surface silica shell.

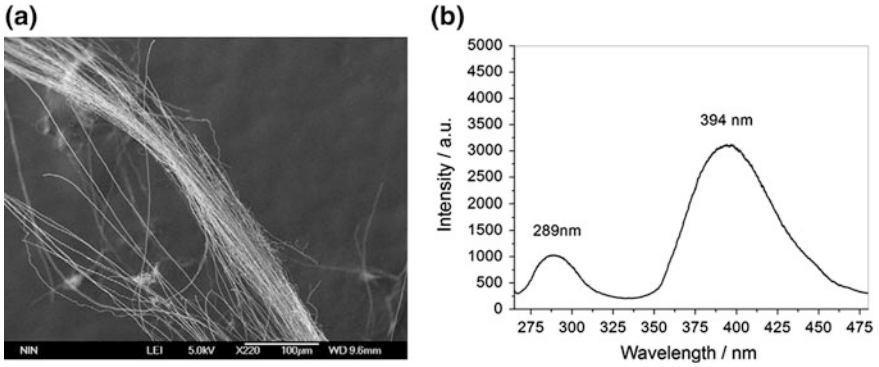

Fig. 5.49 **a** SEM image of ultralong SiC nanowires. **b** PL spectrum of the SiC nanowires under 260 nm excitation at room temperature. Reprinted with permission from [62]. Copyright 2011, Elsevier

5.3.2 Carbon-Coated SiC Nanowires

Although most of the reported SiC nanowires possess a silica shell, researchers have observed that some SiC nanowires obtained under specific conditions possess carbon shells or silica–carbon mixed shells. A thermal evaporation method has been developed to synthesize the SiC–SiO_2–carbon nanotube coaxial nanocables [63]. The nanocables are synthesized by heating a mixture of SiO and Fe powders under flowing CH_4 gas at 1,550 °C. These coaxial nanocables consist of a single-crystalline β-SiC core, amorphous SiO_2 intermediate layer, and a graphitic carbon outer sheath (Fig. 5.50a). The nanocables are 20–50 nm in diameter, and the

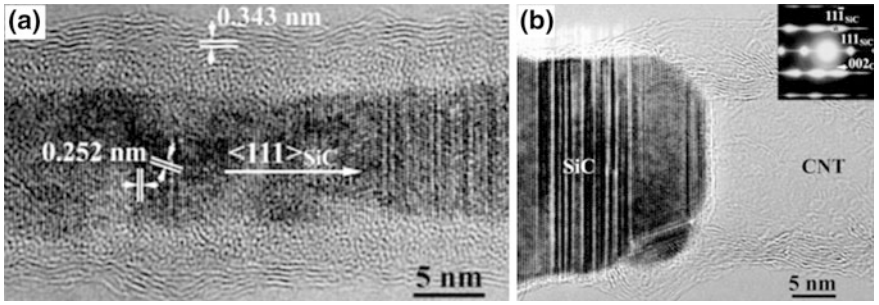

Fig. 5.50 **a** HRTEM image of coaxial nanocable showing single-crystalline β-SiC core, amorphous SiO_2 intermediate layer, and outer graphitic C sheath. **b** HRTEM image of SiC nanorod–carbon nanotube heterojunction. The *inset* shows the selected area electron diffraction pattern. Reprinted with permission from [63]. Copyright 2004, Wiley-VCH Verlag GmbH & Co. KGaA

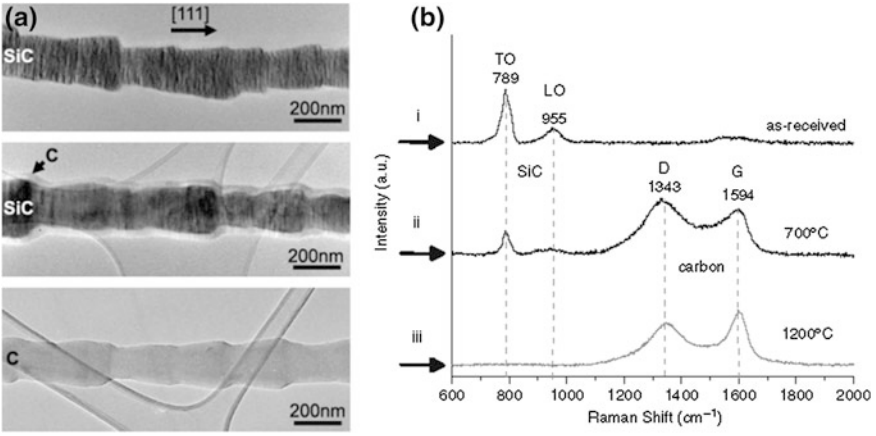

Fig. 5.51 **a** TEM images and **b** Raman spectra of SiC nanowhiskers measured at different stages of transformation to carbon: (*i*) initial: as-prepared SiC nanowhisker, (*ii*) intermediate: carbon coating on SiC nanowhisker, and (*iii*) final: complete transformation into amorphous carbon. The nanowhiskers are treated in Cl_2 at 700 °C (*ii*) and 1200 °C (*iii*). Reprinted with permission from [65]. Copyright 2006, Wiley-VCH Verlag GmbH & Co. KGaA

nanocable cores are 10–30 nm in diameter. The nanochains of SiC-carbon nanotube heterojunctions (Fig. 5.50b) are acquired by annealing the as-prepared nanocables at 1,600 °C in vacuum. The study shows that a SiC nanowire can be transformed into a carbon nanotube or a SiC–C core–shell nanowire owing to Joule heating by applying a current on the order of 10 mA [64].

SiC nanowhiskers can also be transformed into different carbon nanostructures through high-temperature extraction of Si atoms by treatment in Cl_2 or HCl or by vacuum decomposition [65]. High-resolution TEM and Raman analysis shows that chlorination of SiC nanowhiskers results in the amorphous carbon-sheathed SiC whiskers and finally amorphous nanoporous carbon (Fig. 5.51). High-temperature treatment of SiC in HCl yields fullerene-like structures, whereas high-temperature vacuum decomposition yields graphite. SiC–C coaxial nanocables can be synthesized via a solvothermal process using $SiCl_4$, C_6Cl_6, and Na as starting materials at 250 °C under a pressure of 2.2 MPa [66]. The diameter of the nanocables is around 50 nm, and the length is up to one micrometer. The nanocables contain a β-SiC shell coated by an amorphous carbon shell. The field electron emission has been observed from the carbon-coated β-SiC nanowires grown on the Si substrate [67], and the nanowires have diameters between 20 and 50 nm and carbon shell thicknesses of 2–3 nm. The turn-on field corresponding to an emission current density of 10 μA/cm^2 is about 4.2 V/μm.

5.3.3 BN-Coated SiC Nanowires

$SiC/SiO_2/(BN + C)$ core/shell/shell nanocables with diameters of a few tens of nanometers and lengths up to 50 μm are synthesized by means of reactive laser ablation [68]. Transmission electron microscopy and analysis of elemental profile across a nanocable help determine the nanocable structures. The result shows that the nanocable consists of a β-phase silicon carbide core, an amorphous silicon oxide intermediate layer, and graphitic outer shells made of boron nitride and carbon layers separated in the radial direction (Fig. 5.52). In the laser ablation, a mixed and compressed powder of BN, C, SiO, and Li_3N is taken as the starting material. The growth of nanocables comprises two steps. First, the $SiC–SiO_2$ nanowire is formed through a reaction C (solid or vapor) + SiO (gas) → SiC (solid) + SiO_2 (solid). The second step involves coating of the BCN sheath and phase separation of BN and C into nanodomains. The graphitic shell can only form in the presence of Li_3N in the starting material; otherwise, only the $SiC–SiO_2$ wires without any graphitic sheath are formed because C reacts readily with SiO to form SiC/SiO_2. The existence of lithium can advance the formation of graphite-like BN.

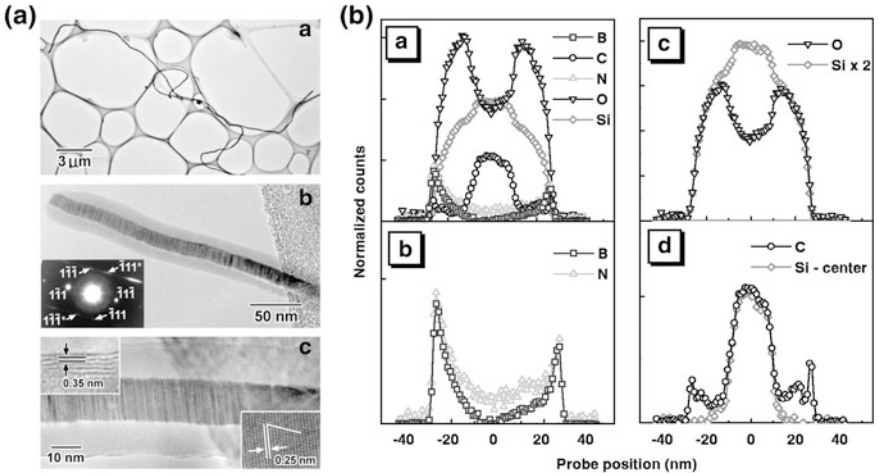

Fig. 5.52 *Left panel* **a** TEM image of nanocables. **b** Magnified image showing a crystalline core and an amorphous layer. Selected area electron diffraction pattern (*inset*) indicates that the core is β-SiC with the ⟨110⟩ axis parallel to the electron beam. The asterisks represent twinning planes. **c** High-resolution image of the nanocable. *Top inset* shows lattice fringes of the outer C-BN layer and *bottom inset* shows lattice fringes of the β-SiC core. *Right panel* Elemental profiles across a nanocable. **a** Profiles of all elements in the nanocable. **b** B and N profiles showing the tubular feature of the outer sheath and unity atomic ratio. **c** Si and O profiles, in which the Si concentration is doubled; the Si:O ratio in the intermediate layer is shown to be 1:2. **D** C profile and reduced profile of Si in the center core, acquired by subtracting the contribution of Si comprised in the SiO_2 layer from the total Si concentration. The Si:C ratio in the wire core is unity. Reprinted with permission from [68]. Copyright 1998, AAAS

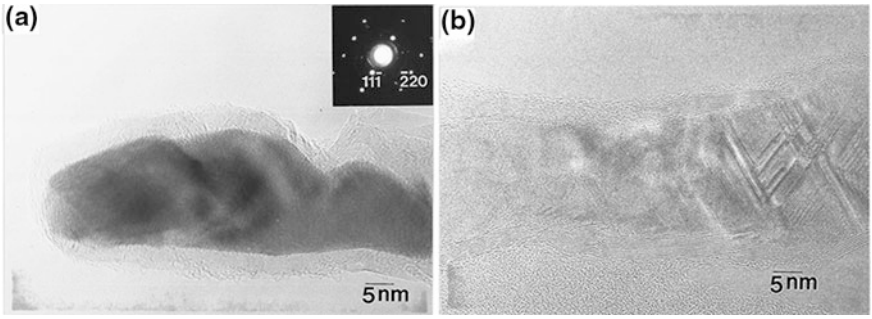

Fig. 5.53 High-resolution TEM images of SiC-filled BN nanotubes. **a** Tip of filled BN nanotube. The inset shows the selected area electron diffraction pattern which corresponds to β-SiC, and the electron beam is along the ⟨112⟩ axis. **b** SiC-filled BN nanotube with high density of planar defects. Reprinted with permission from [69]. Copyright 1999, AIP Publishing LLC

The carbon nanotube template method has been employed to synthesize the silicon carbide nanowires sheathed with boron nitride nanotubes [69]. A mixture of silica and silicon powders reacts with nearby B_2O_3 powder covered with carbon nanotubes at 1,753 K in a flowing nitrogen atmosphere to give rise to the SiC/BN nanowires. Through the carbon nanotube-substitution reaction, carbon nanotubes react with boron oxide vapor in the presence of nitrogen gas to yield BN nanotubes. The reaction of SiO vapor within carbon nanotubes with the inner carbon layers or volatile carbon monooxide in the interior gives rise to SiC nanowires. The obtained sheathed nanowires are as long as the starting carbon nanotubes. High-resolution TEM images (Fig. 5.53) reveal the β-SiC core structure and the good crystallinity of the outer BN shell.

Uniform BN-coated SiC nanowires are synthesized by vapor–liquid–solid growth [70, 71]. Nanoscale Ni-C alloy covering graphite sheet acts as the catalyst, and the mixture of boron and silica is heated at 1,500 °C to simultaneously generate B_2O_2 and SiO gas-phase precursors. The vapor is transported to an area where the highly oriented pyrolitic graphite covered with nickel catalyst grains is placed. Silicon carbide and boron nitride are formed on the surface of highly oriented pyrolitic graphite in the presence of nitrogen at 1,400 °C. The reactions can be described by the following equations [71]:

$$2B(s) + 2SiO_2(s) \rightarrow B_2O_2(g) + 2SiO(g), \tag{5.10}$$

$$SiO(g) + 2C(s) \rightarrow 2SiC(s) + CO(g), \tag{5.11}$$

$$B_2O_2(g) + 2C(s) + N_2(g) \rightarrow 2BN(s) + 2CO(g). \tag{5.12}$$

The nanowire core with diameter ranging from several nanometers to 80 nm is β-SiC growing along the [111] direction, and it contains a great amount of stacking faults and microtwins, as shown in Fig. 5.54a. The nanowire surface is sheathed

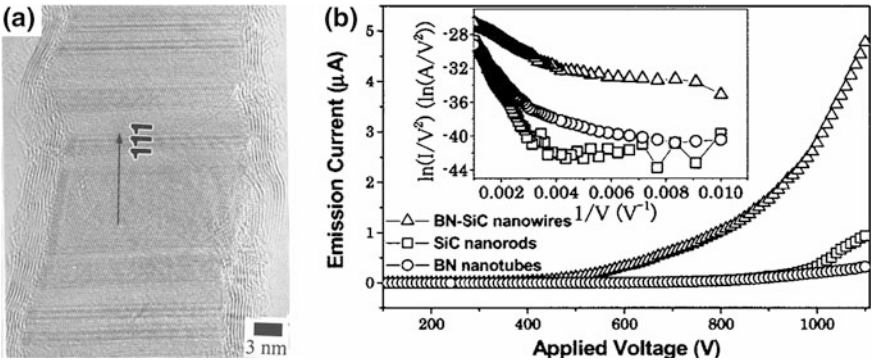

Fig. 5.54 **a** HRTEM image of the BN-coated SiC nanowire. The β-SiC core grows along the [111] direction and has high-density planar defects. Reprinted with permission from [70]. Copyright 2002, AIP Publishing LLC.**b** Field electron emission current versus applied electric voltage for single-crystal SiC nanowires, BN nanotubes, and BN-coated SiC nanowires, respectively. The *inset* shows the Fowler–Nordheim plot. Reprinted with permission from [72]. Copyright 2003, AIP Publishing LLC

with well-crystallized BN with thickness of 2–4 nm. The bicrystalline SiC nanowires with BN coating are also present, and they have a [311] growth axis. The effects of BN coating on antioxidation ability and field emission properties of the SiC nanowires have been studied [72]. Upon oxidation, the SiC nanowires without BN coating crack into nanoparticles or almost fully convert into SiO_2 nanowires at temperatures above 800 K, depending on crystallization degree of the SiC nanowires. After BN coating, the antioxidation ability of the SiC nanowires is improved due to excellent chemical stability of BN at high temperatures. The BN-coated SiC nanowires maintain high resistance to oxidation even at temperatures higher than 1,273 K. The field electron emission performance of the SiC nanowires is also improved after BN sheath. The turn-on field, which is the field to give rise to a current density 10 μA/cm^2, is reduced from above 10 V/μm for the SiC nanowires without coating to below 6 V/μm for the BN-coated SiC nanowires (Fig. 5.54b). The Fowler–Nordheim plots for the three investigated samples show an approximately linear relationship between $\ln(I/V^2)$ and 1/V for applied voltage over 300 V, suggesting that a quantum mechanical tunneling process is responsible for the observed electron emissions.

BN nanotube-coated β-SiC nanowires, with 10–15 nm spacing between the SiC core and the BN nanotube sheath, are synthesized using chemical vapor deposition [73]. Specified post-treatment results in consecutive formations of BN–SiO_2–SiC nanocables, BN nanotube-encapsulated SiC nanowires with reduced diameters, and SiC or C-SiC nanocables encapsulated by C–BN composite nanotubes. A mixture of Si and In_2O_3 powders is heated in a small BN crucible in flowing CH_4 gas at 1,600 °C to yield the composite nanowires. The decomposition of In_2O_3 during heating gives rise to oxygen gas source. The electric current versus voltage measurement shows that the BN nanotube sheath provides excellent electrical insulation for the

encapsulated semiconducting nanowires. β-SiC nanowires can be grown by thermal treatment of Si particles disposed in a graphite crucible in nitrogen atmosphere at 1,200 °C [74], and using a similar method, treatment of a mixture of the boron nitride and Si powders under argon atmosphere produces hexagonal BN-coated β-SiC nanowires. A technique has been developed to synthesize very long SiC-based coaxial nanocables [75] with varied chemical composition of the nanocable outer layers, from silica to carbon and to boron nitride, depending on the composition of the reactant. The SiC nanowires with silica or carbon sheath are prepared by thermal reaction of polypropylene (in an alumina boat) and an equimolar mixture of Si(s) and SiO_2(s) (in another alumina boat) in flowing argon at 1,400 °C. The Si solid can be substituted by an equimolar mixture of Si(s) and B_2O_3(s) to synthesize SiC/BN nanocables. The nanocables consist of a SiC core 30 nm in diameter with lengths up to several hundred nanometers. The thickness of the coating is between 2 and 10 nm. The vapor–solid growth mechanism accounts for the growth of the SiC-based nanocables of various chemical compositions. SiC–SiO_2–BN nanocables are synthesized using SiC–SiO_2 nanocables and ammonia borane as starting materials [76]. The nanocables consist of single-crystalline cubic SiC cores, intermediate amorphous SiO_2 layers, and single-crystalline hexagonal BN sheaths. The nanocables are around 100 nm in diameter and up to 1 mm in length. The intermediate amorphous SiO_2 layers and the outer hexagonal BN sheaths are about 10 and 5 nm thick, respectively. An increase in the amount of ammonia borane results in the transformation of SiC–SiO_2 nanocables into BN nanotubes.

5.4 Special Structures

Besides pure SiC nanowires and core-shell-structured SiC nanowires, various more complex one-dimensional SiC nanostructures have been synthesized and investigated, such as the bamboo- or bead-like SiC nanowires, helical SiC nanowires, and interconnected SiC nanowire networks. The silicon carbide has rather fruitful one-dimensional nanostructures.

5.4.1 Bamboo-Like Structures

Bamboo-like SiC nanofibers have been synthesized by carbothermal reduction of carbonaceous silicon xerogel containing lanthanum nitrate [77]. The xerogel is heated to 1,300 °C in flowing argon gas to synthesize the product, which is then heated in air at 700 °C to eliminate residual carbon and treated by nitric acid and hydrofluoric acid to remove unreacted silica and other impurities. The product contains bamboo-like β-SiC nanofibers with diameters of 40−100 nm and lengths of tens of micrometers to hundreds of micrometers. The nanofibers contain planar stacking faults with the plane direction perpendicular to the fiber axis. A modified

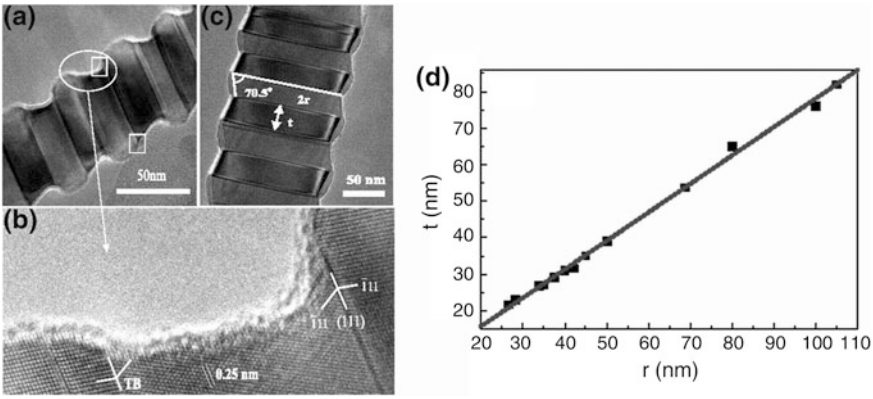

Fig. 5.55 **a** TEM image of a bamboo-like SiC nanowire. **b** HRTEM image of one part of the nanowire. **c** and **d** depict the linear relationship between the twin segment thickness (*t*) and the nanowire radius (*r*). Reprinted with permission from [78]. Copyright 2008, IOP Publishing

method produces the periodically twinned SiC nanowires by carbothermal reduction of a carbonaceous silica xerogel prepared from tetraethoxysilane and biphenyl with iron nitrate as an additive [78]. The twinned β-SiC nanowires have a hexagonal cross section, a diameter of 50–300 nm, and a length of tens of micrometers to hundreds of micrometers. They have periodically twinned segments with a uniform thickness along the entire nanowire axis (Fig. 5.55). The formation of the periodic twin structure ensures the minimum surface energy and strain energy for the synthesized nanowires. The thickness of the twinned segment shows a linear dependence on its diameter.

Single-crystalline bamboo-like β-SiC nanowires with hexagonal cross sections are produced by thermal evaporation of mixed SiO + C + GaN powders at 1,350 °C in an argon atmosphere [79]. The nanowires grow along the ⟨111⟩ direction by a vapor–liquid–solid mechanism. The nanowire comprises a hexagonal stem decorated by larger diameter knots along the whole nanowire axis (Fig. 5.56a–f). The electron diffraction patterns from the stem and knot areas have the same orientation indicating that the whole bamboo-like β-SiC nanowire is a single crystal growing along the ⟨111⟩ direction. The electron diffraction pattern of the stem consists of only bright spots, whereas the pattern of the knot comprises both bright spots and streaks, indicating that the defects exist only in the knot areas. High-resolution TEM images of both stem and knot parts of the β-SiC nanowire reveal the lattice spacing of 0.25 nm corresponding to the {111} planes of β-SiC. The stem shows a uniform structure, whereas the knot possesses stacking faults. Figure 5.56g shows the plot of emission current density versus applied electric field at an anode-sample distance of 100 μm. The turn-on field which corresponds to the generation of a current density 10 $\mu A/cm^2$ is 10.1 V/μm. The Fowler–Nordheim plot shows a linear curve for applied voltages over 1/0.0025 V.

Twinned zigzag 3C-SiC nanoneedles are synthesized by the reaction between silicon vapor and solid multiwalled carbon nanotubes at 1,500 °C [80]. The Si

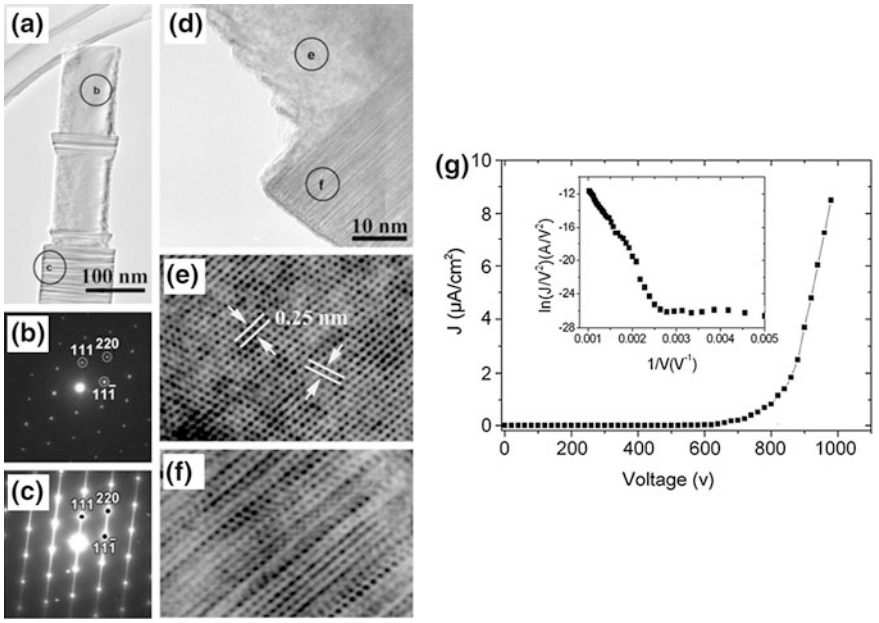

Fig. 5.56 **a** TEM image of a single bamboo-like β-SiC nanowire. Selected area electron diffraction patterns taken from the stem (**b**) and knot (**c**) regions of the bamboo-like β-SiC nanowire. **d** TEM image of the stem/knot interface. HRTEM images of the stem (**e**) and knot (**f**). **g** Field emission current density versus applied voltage curve for the bamboo-like β-SiC nanowires. The *inset* shows the Fowler–Nordheim plot. Reprinted with permission from [79]. Copyright 2006, IOP Publishing

atom in the vapor phase reacts with carbon to form SiC nuclei in the active part of carbon nanotubes, which then grow along the [111] direction to form SiC nanoneedles. The SiC nanoneedle has a zigzag morphology (Fig. 5.57), and it is composed of (111) $[11\bar{2}]$ periodic twined segments. The zigzag morphology is observed from the $[01\bar{1}]$ zone axis. The formation of the twin structures gives rise to SiC nanoneedles with lower cohesive energies than SiC nanoneedles without twin structures, whereas the formation of the periodic $(11\bar{1})$ facets on the nanoneedle surface may ensure the lowest surface energy.

Single-crystalline bamboo-like β-SiC nanowires are synthesized by catalyst-free vapor deposition using silicon and graphite carbon as starting materials [81]. The morphology of the SiC nanowires varies from cylinder, hexagonal prism, to bamboo shapes as the reaction temperature increases from 1,470, 1,550, to 1,630 °C. Figure 5.58 shows the electron microscopy images of the bamboo-like SiC nanowires. The nanowire comprises many decorated knots and truncated hexagonal pyramids. It possesses high-density stacking faults, especially at the tip. The electron diffraction pattern contains spots belonging to β-SiC {220} planes and streaks attributed to the stacking faults. The nanowires grow by a vapor–solid mechanism.

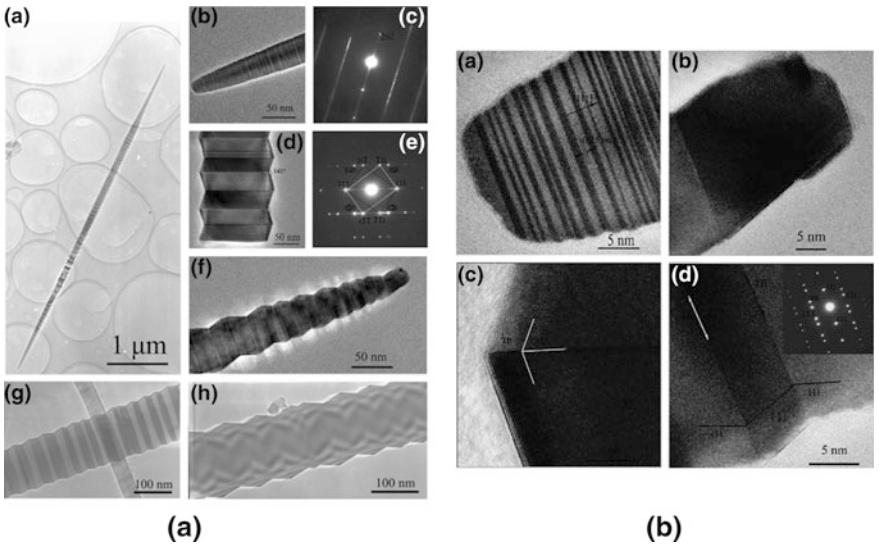

Fig. 5.57 *Left panel* **a** TEM image of the SiC nanoneedle with upper flat surface and lower zigzag surface. **b** Magnification image of flat surface. **c** Electron diffraction pattern of the flat part showing streaks of $(\bar{2}02)$ planes. **d** Magnification image of zigzag surface. **e** Electron diffraction pattern of the zigzag part showing well-defined (111) twinning relationship. **f** Magnification image of zigzag surface. **g** and **h** TEM images of another nanoneedle. *Right panel* HRTEM image of a SiC nanoneedle: **a** flat part, **b** tip of the zigzag part, **c** and **d** neighboring twin segments of the zigzag part from the $[11\bar{1}]$ direction. Reprinted with permission from [80]. Copyright 2007, American Chemical Society

5.4.2 Beaded Structures

The necklace-like β-SiC nanowires have been synthesized by catalyst-free chemical vapor deposition using SiO_2 and graphite powder as starting materials [82]. The SiC nanowires have diameters of 50–100 nm and lengths up to several tens of micrometers (Fig. 5.59). The bead diameter of the necklace-like nanowires ranges from 0.5 to 1.0 μm. The nanowires may grow by a vapor–solid mechanism since there is no metallic droplet in the product.

Silicon carbide-beaded nanochains are prepared from carbothermal reduction of carbonaceous silica xerogel using cetyltrimethylammonium bromide and lanthanum nitrate as additives [83]. The nanochain consists of a stem with diameter of about 50 nm and uniform beads with diameters of 100–200 nm (Fig. 5.60). The proportion of the nanochains in the sample is larger than 60 %. X-ray diffraction spectrum (Fig. 5.60e) reveals that the sample is pure cubic SiC and the peak on the left shoulder of the (111) peak is ascribed to the stacking faults in the nanowires. Most of the nanochains have nearly uniform periodicities, but others have varying periodicities. The dimensions of the beads and stems are approximately homogeneous in one nanochain, but they vary among different nanochains. Many

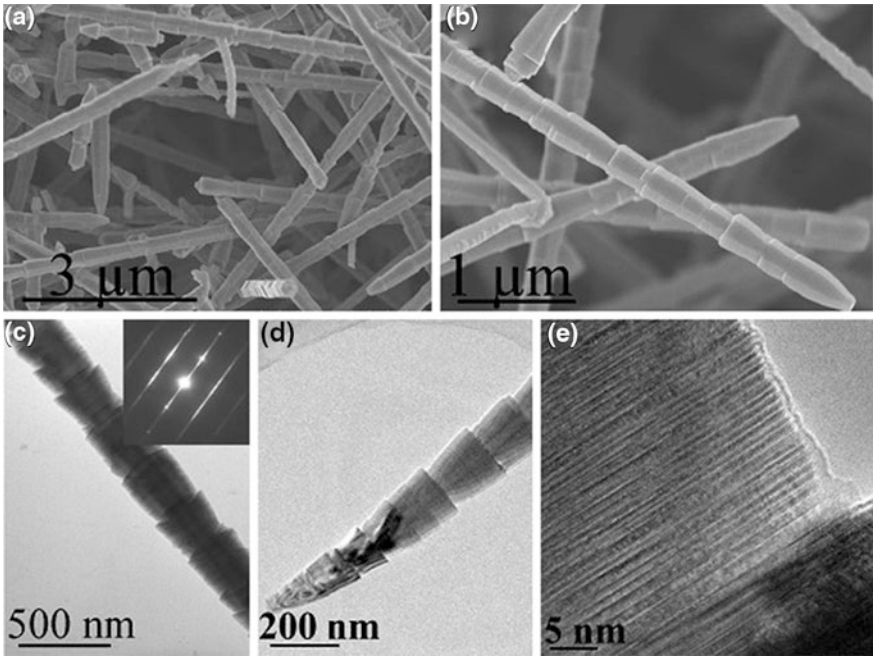

Fig. 5.58 **a** and **b** SEM images of bamboo-like SiC nanowires. **c** TEM image of a SiC nanowire and corresponding electron diffraction pattern (*inset*). **d** TEM image of a nanowire with consecutive truncated cones at the tip. **e** HRTEM image of the junction area. Reprinted with permission from [81]. Copyright 2008, IOP Publishing

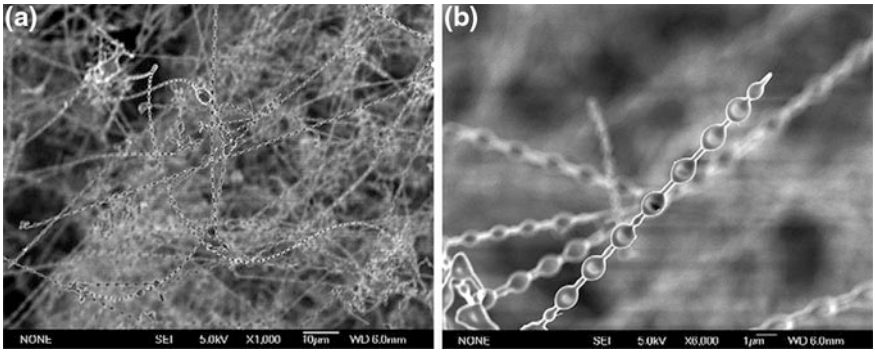

Fig. 5.59 **a** and **b** SEM images of necklace-like SiC nanowires. Reprinted with permission from [82]. Copyright 2006, Elsevier

nanochains have amorphous thin shells. The nanochains preferentially grow along the [111] orientation. The beads of the nanowire comprise a higher concentration of stacking faults as compared with the stem area of the nanowire.

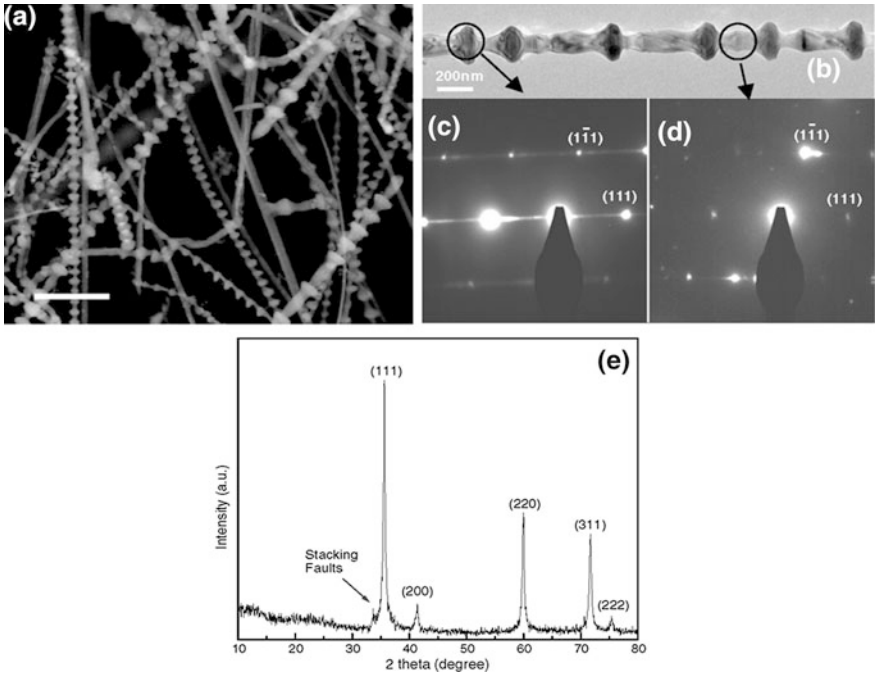

Fig. 5.60 **a** SEM and **b** TEM images of beaded SiC nanochains. The electron diffraction patterns (**c**, **d**) indicate the [111] growth direction, and the streaks are assigned to the stacking faults. **e** XRD pattern of the nanochains. Reprinted with permission from [83]. Copyright 2006, IOP Publishing

The SiC/SiO_2 chainlike nanostructures have been synthesized by catalyst-free chemical vapor reaction using a mixture of $Si–SiO_2$ powder and CH_4 as source materials at 1,200 °C [84]. The main body of the chainlike nanostructure is a single-crystalline β-SiC nanowire with diameter of 20–30 nm and length up to several tens of micrometers (Fig. 5.61a). The β-SiC nanowire preferentially grows along the [111] direction, and it contains a high density of stacking faults and twin defects. The core nanowire is wrapped by a series of 80–100 nm diameter amorphous SiO_2 spheres. The SiC/SiO_2 nanochains show photoluminescence at room temperature, with a narrow band centered at 410 nm and a wide band centered at 490 nm (Fig. 5.61b).

Homogenous $β\text{-}SiC/SiO_2$ chainlike nanowires can be synthesized by chemical vapor reaction using $Si–SiO_2$ powder and C_3H_6 gas as source materials with assistance of anodic aluminum oxide templates [85]. The SEM image (Fig. 5.62) shows that the synthesized nanostructures have uniform structures. Each nanowire comprises many spheres with sizes of 25–30 nm that are connected together by a long core wire with diameter of 15–20 nm. No catalyst particles are found to attach to the resultant nanochains, so they may grow via a vapor–solid mechanism. High-resolution TEM images reveal that the SiC nanochains contain a high density

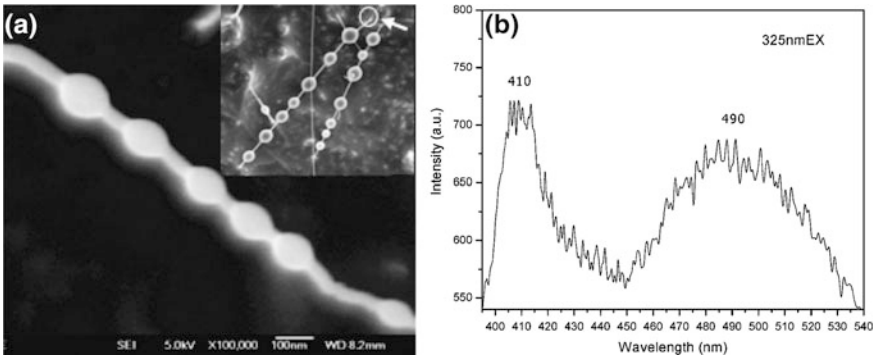

Fig. 5.61 **a** SEM image of the chainlike β-SiC nanowire. The scale bar is 100 nm. The *inset* shows the SEM image of two nanowires on the graphite substrate. **b** Photoluminescence spectrum of the chainlike β-SiC nanowires under 325-nm excitation. Reprinted with permission from [84]. Copyright 2009, American Chemical Society

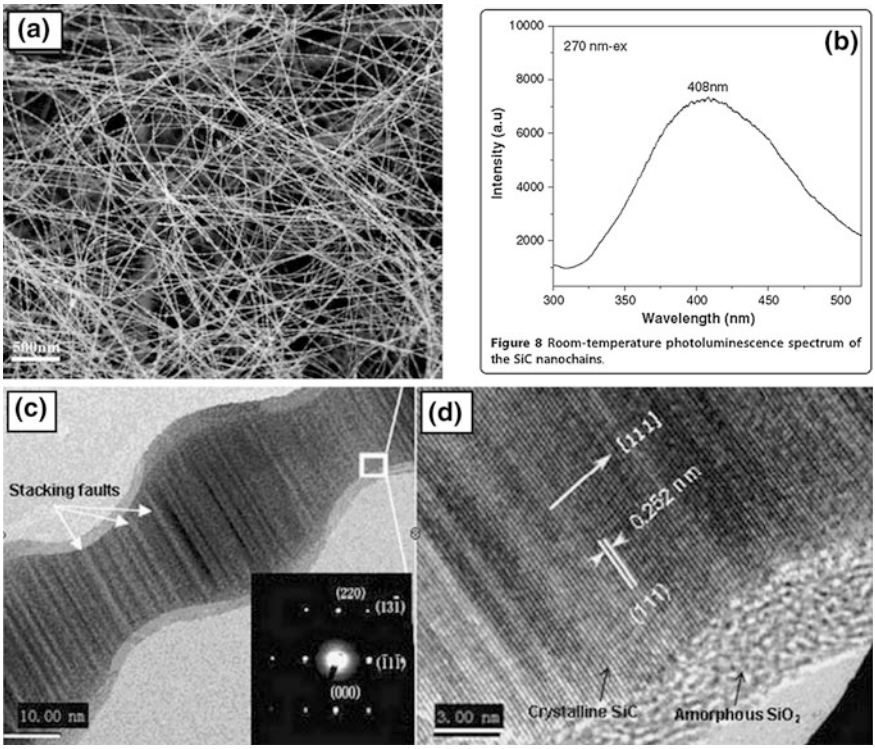

Fig. 5.62 **a** SEM image of the β-SiC/SiO_2 chainlike nanowires. **c**, **d** TEM image of a SiC nanochain. The *inset* is the electron diffraction pattern. *Lower right* HRTEM image of the SiC nanochain. **b** PL spectrum of the SiC nanochains under 270 nm excitation. Reprinted with permission from [85]. Copyright 2011, Springer Science and Business Media

of stacking faults, and the nanochain surface is wrapped by a thin amorphous silica layer with the thickness of 2–5 nm. The TEM observation also indicates that the SiC core grows along the [111] direction. The nanochains show photoluminescence with a single emission band centered at around 408 nm under 270 nm excitation.

5.4.3 Other Periodic Structures

Hierarchical single-crystalline β-SiC nanoarchitectures are synthesized using a catalyst-assisted chemical vapor deposition method [86]. The nanostructures are prepared by heating the mixed SiO, Ga_2O_3, and graphite powder at 1,350 °C in argon atmosphere. Electron microscopy and X-ray diffraction reveal that the nanostructures are single-crystalline β-SiC, and each of them is composed of a core stem growing along the ⟨111⟩ orientation and a series of platelets growing perpendicular to the stem (Fig. 5.63). The core stems have diameters of 10–20 nm, and the branched nanoplatelets have thicknesses of 5–10 nm. The electron diffraction pattern contains both bright spots and streaks, and the streaks are assigned to the stacking faults in the nanostructures. The energy-dispersive X-ray spectroscopy reveals strong signals of Si and C from both the stems and the platelets

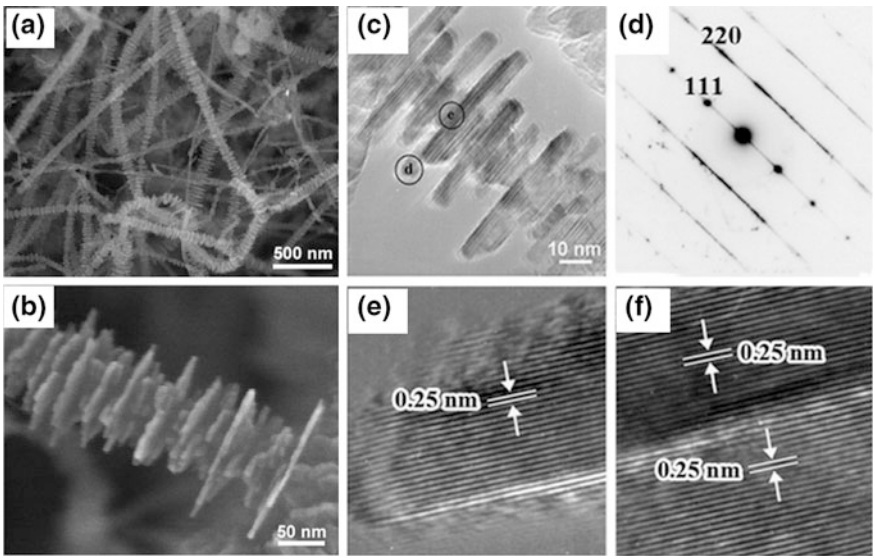

Fig. 5.63 **a**, **b** SEM images of one-dimensional hierarchical β-SiC nanostructures. Each hierarchical structure contains numerous thin nanoplatelets parallel to each other and perpendicular to the core stem. **c** TEM and **e**, **f** HRTEM images and **d** electron diffraction pattern of the nanostructures. Reprinted with permission from [86]. Copyright 2007, Royal Society of Chemistry

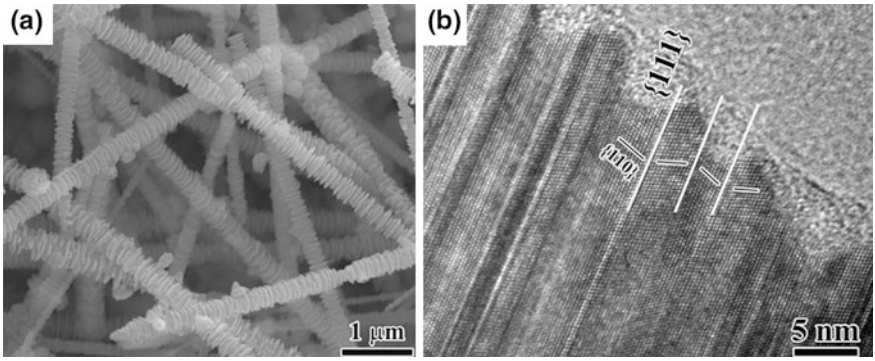

Fig. 5.64 **a** SEM image of periodically twinned SiC nanowires. **b** HRTEM image showing the twinned structure. Reprinted with permission from [88]. Copyright 2010, Elsevier

and confirms their SiC structure. The hierarchical structures grow by a two-step process. They show field electron emission with a turn-on field of 12 V/μm.

β-SiC nanowires with branched fins are prepared by chemical vapor deposition using Si and SiO_2 powders and CH_4 as starting materials [87], and the fin diameter is 100–120 nm, and the core stem diameter is 60–70 nm. Compressibility of periodically twinned β-SiC nanowires is studied using in situ high-pressure X-ray diffraction [88]. The twinned nanowires are synthesized by carbothermal reduction of a carbonaceous silicon xerogel using tetraethoxysilane and biphenyl as source materials, and they are 50–300 nm in diameter and tens to hundreds of micrometers in length (Fig. 5.64). They have periodically twinned segments, hexagonal cross sections, and zigzag outer surfaces. They grow along the ⟨111⟩ direction. The cubic crystal structure is maintained under pressure up to 37.7 GPa. The bulk modulus of the nanowires is 316 GPa, 20–40 % greater than that of SiC with other morphologies, showing that twinning improves the mechanical properties of the SiC nanostructures. Hierarchical and twinned SiC nanowires are synthesized by carbothermal reduction of the xerogel via a vapor–liquid–solid process [89]. The dominant polytype of the nanowires is 3C, but some take the 2H polytype. As a doping material, the SiC nanowires can be doped into the matrix of the nanocrystalline magnesium, where they show good interlocking with the Mg matrix due to their special hierarchical structure. There are well-bonded interfaces between the doped SiC nanowires and the Mg matrix.

5.4.4 Connected Structures

There are many reports on synthesis of the SiC nanowires with interconnected structures. The isolated and branched β-SiC whiskers are synthesized from SiO_2 and carbon black powders via carbothermal reduction at 1,420 °C [90]. The reactant mixtures that contain synthesized whiskers are subjected to additional

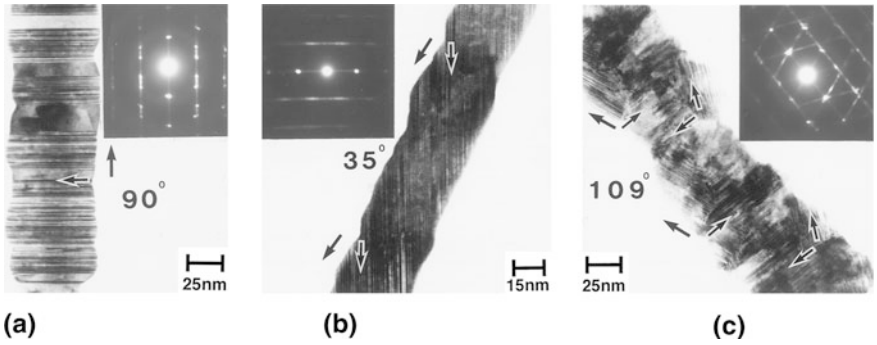

Fig. 5.65 TEM micrographs of three types of β-SiC whiskers: **a** type A, **b** type B, and **c** type C. They are aligned with the electron beam parallel to the ⟨110⟩ zone axis. The *insets* are the corresponding electron diffraction patterns. Reprinted with permission from [90]. Copyright 2000, Wiley-VCH Verlag GmbH & Co. KGaA

heating at 700 °C in air to eliminate excess carbon via oxidation. The nanowires are formed by the gas–solid reaction between SiO and carbon black. Growth planes and growth directions of the whisker depend on the surrounding growth conditions including growth rate, content of stacking faults, and supply of carbon and SiO source. The whiskers are classified into three types (Fig. 5.65) in terms of morphology, growth direction, and stacking fault planes. Type A whisker has relatively flat surface, and the stacking fault planes are perpendicular to the growth direction. Type B whisker has rough surface, and the stacking fault planes are inclined at an angle of 35 ° to the growth direction. Type C has rough sawtooth surface, and the stacking faults exist concurrently in three different {111} planes. The high-resolution TEM images of the whiskers (Fig. 5.66) show that type A whisker contains many stacking faults perpendicular to the growth direction including many twin faults. The surface energy of the {111} planes in β-SiC is much smaller than that of other crystal planes; hence, β-SiC whisker grows easily

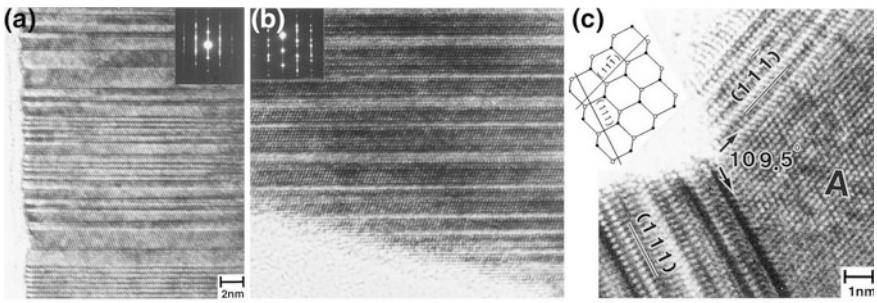

Fig. 5.66 HRTEM images of three types of β-SiC whiskers: **a** type A, **b** type B, and **c** type C. The *insets* show electron diffraction patterns or lattice configuration schematic. Reprinted with permission from [90]. Copyright 2000, Wiley-VCH Verlag GmbH & Co. KGaA

in the ⟨111⟩ direction, and thus, stacking faults can readily be inserted in the {111} planes. The 3C-SiC with a stacking fault has a lower energy than that without stacking faults, and this explains the frequent occurrence of stacking faults in the SiC whiskers. In type B whiskers, the stacking faults that are inclined to the growth direction are present only in a branched whisker with a small thickness, and these whiskers mainly consist of twin faults. The electron diffraction patterns in type C whiskers contain three different directions of streaks that are perpendicular to respective set of stacking fault layers. The defected and branched whiskers have separation angles 125°, 70°, and 109°, respectively. These whiskers separately consist of mixtures of type A and type B, type A, or parallel growth by two pairs of type A and type B whiskers. The difference in growth speed between different types of whiskers results in the whisker deflection.

The β-SiC nanowire networks are synthesized by chemical vapor reaction using a mixture of milled Si and SiC powder and C_3H_6 as starting materials [91], and the synthesized single-crystal β-SiC nanowires with diameter of 20–70 nm grow along the [111] direction. The SiC/SiO_2 core/shell nanowire networks are synthesized by high-temperature evaporation reaction using mixed Si, SiO_2, and graphite powders as source materials at 1,500 °C in argon atmosphere [92]. The SEM observation (Fig. 5.67a) indicates that the product is an interconnected network of wires with diameters of about 180 nm. The TEM examination (Figs. 5.67b, c) reveals that the connected wires are composed of core nanowires about 20 nm in diameter and outer sheaths of amorphous silica.

Biaxial β-SiC nanowires are fabricated by high-temperature chemical vapor reaction using multiwalled carbon nanotubes and Si powder as starting materials at 1,473–1,573 K in vacuum [93]. Transmission electron microscopy reveals Y-shaped structure of the SiC bi-nanowires (Fig. 5.68). The individual nanowires grow along the ⟨111⟩ direction by a vapor–liquid–solid mechanism before they merge and cogrow to form a bi-nanowire. The bi-nanowire grows along the ⟨110⟩, ⟨113⟩, or ⟨112⟩ orientation.

Three-dimensional flowerlike SiC nanostructures are synthesized by thermal reaction of gallium nitride powder, silicon wafer, and methane gas at 1,100 °C [94]. Scanning electron microscopy reveals flowerlike structures with diameter of 1–2 μm and length of 3–5 μm that grow on and are normal to the Si wafer (Fig. 5.69a). A typical flower consists of a stem of interwoven nanowires, a head comprising a bundle of nanowires with diameters of 100–200 nm, and a single catalyst particle attached to the top end of the flower. The existence of the catalyst on the top of the product suggests a vapor–liquid–solid growth mechanism. Note that the thermal decomposition of gallium nitride gives rise to gallium which serves as the catalyst. The cross-sectional view through the layer (Fig. 5.69b) reveals that each flower has a hollow stem with diameter of 400–800 nm which is predominantly normal to the Si substrate. Each flower has a catalyst particle on its tip.

SiC tetrapods have also been synthesized. The adamantane embedded in a methyltrimethoxysilane is spin coated onto a SiO_2 on Si wafer, and the coated

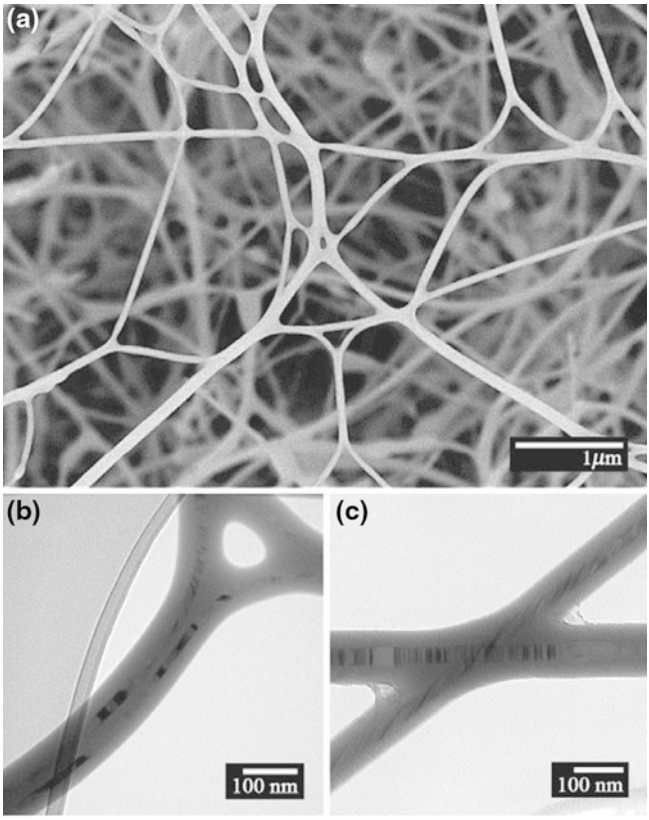

Fig. 5.67 **a** SEM and **b**, **c** TEM images of SiC nanowire networks. Reprinted with permission from [92]. Copyright 2007, IOP Publishing

wafer is treated in microwaves at 850 °C in methane and hydrogen plasma to produce the SiC tetrapods [95]. Figure 5.70a shows the SEM image of the tetrapods. The tetrapod legs are 40 ± 10 nm in diameter and 90 ± 20 nm in length, and the legs have a hexagonal cross section. The TEM observation (Fig. 5.70b) reveals that the legs of the tetrapods are 4H-SiC crystals. Figure 5.70c shows the photoluminescence spectra of individual tetrapods at room temperature. The sharp luminescence line varies among different tetrapods in the 550–800 nm range, and it has a very small full width half maximum of about 5 nm. This variation may be due to the difference in the tetrapod structure. The luminescence lifetime of the tetrapods varies between 1.4 and 6.3 ns. Only the broad luminescence band (without sharp lines) is observed in the measured regions with high density of tetrapods.

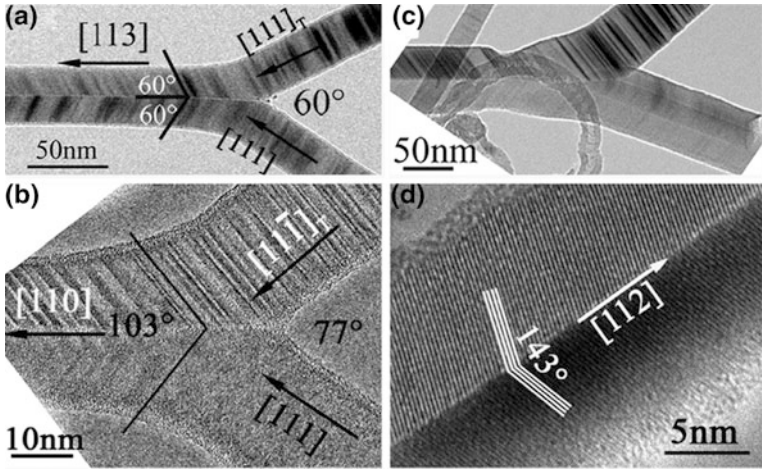

Fig. 5.68 TEM images of SiC bi-nanowires that grow along **a** [113] axis, **b** [110] axis, and **d** [112] axis as well as **c** a SiC bi-nanowire growing from three nanowires. Reprinted with permission from [93]. Copyright 2010, IOP Publishing

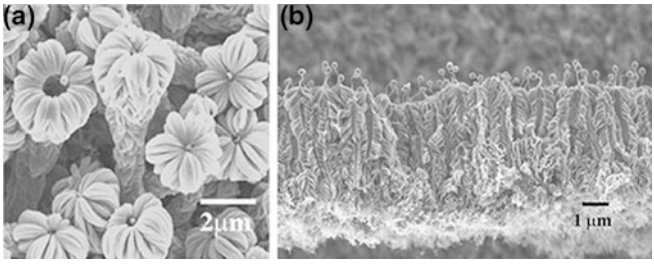

Fig. 5.69 **a** SEM image of SiC nanowire flowers grown on the Si substrate. **b** Cross-sectional view showing highly aligned and closely packed nanowires. Reprinted with permission from [94]. Copyright 2004, IOP Publishing

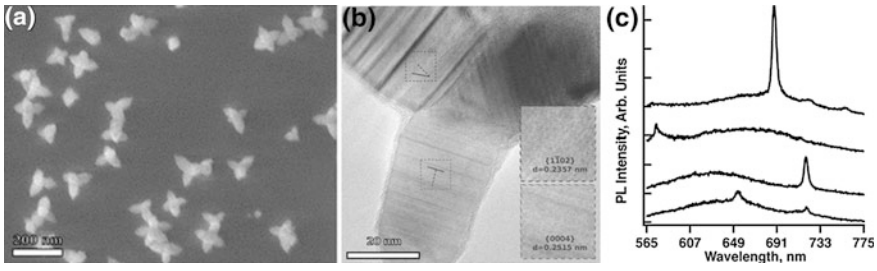

Fig. 5.70 **a** SEM image of the SiC tetrapods grown on the substrate. **b** HRTEM image of a tetrapod showing the lattice spacings for two legs with different orientations. The *insets* indicate the lattice spacings of 4H-SiC. **c** PL spectra of several single tetrapods excited at 532 nm. Reprinted with permission from [95]. Copyright 2013, American Chemical Society

5.4.5 Helical Structures

Helical crystalline β-SiC nanowires sheathed with amorphous silica (SiC/SiO_2) are synthesized by chemical vapor deposition at 1,100 °C [96]. The nanowires are formed on a Si substrate through the reaction $2SiO + C \rightarrow SiC + SiO_2$, decomposition of CH_4 with Fe catalysis provides the carbon source, and the Si substrate surface offers the SiO source. The SiC core has a diameter of 10–40 nm and a helical periodicity of 40–80 nm; it is encapsulated by a uniform layer of amorphous silica with thickness of 30–60 nm (Fig. 5.71). The growth of the helical nanowires may be driven by screw dislocations.

Amorphous SiC nanosprings and biphase (crystalline core/amorphous shell) helical nanowires are synthesized by chemical vapor deposition [97]. Both structures grow by vapor–liquid–solid mechanism, as demonstrated by the NiSi catalyst cap on the nanowire tip (Fig. 5.72a). The formation of the amorphous SiC nanosprings (Fig. 5.72b) is explained by the contact angle anisotropy model primarily proposed to explain the formation of amorphous boron carbide nanosprings. The formation of the biphase helical nanowires is explained by a modified contact angle anisotropy model, and there exists temperature gradient in the catalyst in this model.

5.4.6 Nanobelts

Nanobelt is a thin, narrow, and long belt-like nanostructure. In comparison with SiC nanowires, there have been very few reports on the SiC nanobelts. A lithium-assisted synthetic route have been developed for the growth of 3C-SiC nanobelts at a mild temperature [98]. The nanobelts are prepared by the reaction of CH_3CH_2OH, $SiCl_4$, and Li in an autoclave at 600 °C, and they are characterized by

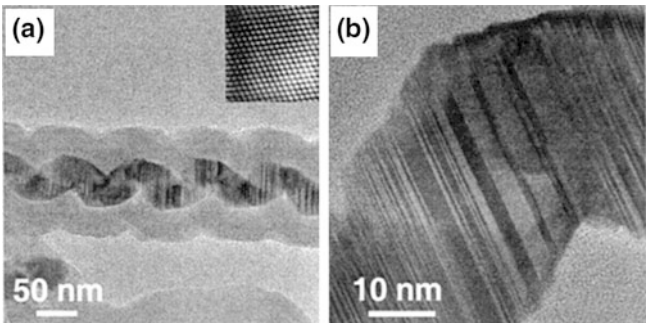

Fig. 5.71 **a** TEM image of a helical SiC nanowire. The *inset* shows the fast Fourier transform filtered lattice image of one part of the helical SiC nanowire in the *right panel* showing that the SiC core is highly crystalline. **b** HRTEM image of a portion of a helical SiC nanowire. Reprinted with permission from [96]. Copyright 2002, American Chemical Society

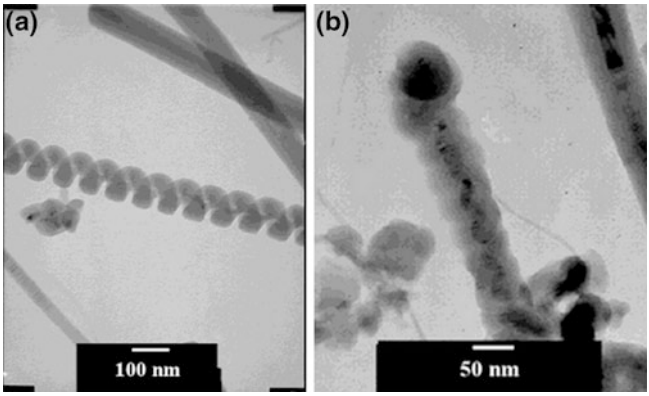

Fig. 5.72 **a** TEM image of amorphous SiC nanospring. **b** TEM image of biphase helical SiC nanowire with NiSi catalyst on its tip. Reprinted with permission from [97]. Copyright 2003, American Chemical Society

various methods (Fig. 5.73). The X-ray diffraction pattern shows strong and sharp lines that belong to 3C-SiC, indicating good crystallization of the nanobelts; the sharp line on the shoulder of the ⟨111⟩ peak arises from the stacking faults in the nanobelts. Electron microscopy confirms the 3C-SiC structure of the nanobelts and shows that the nanobelts are 50–200 nm wide, 20–60 nm thick, and up to tens of micrometers long. The Raman spectrum of the nanobelts comprises two strong peaks at 788.5 and 960.5 cm^{-1}, characteristic of the TO and LO phonons of 3C-

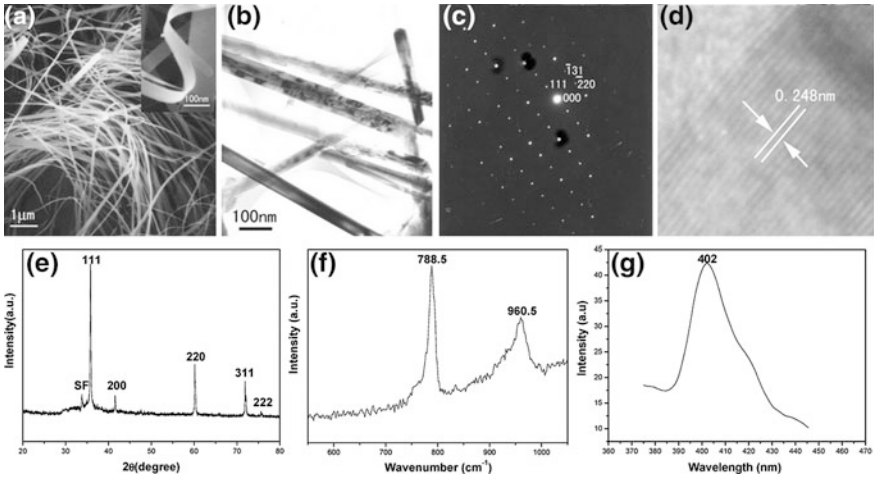

Fig. 5.73 **a** SEM and **b** TEM images of 3C-SiC nanobelts. **c** Electron diffraction pattern and **d** HRTEM image of a 3C-SiC nanobelt. **e** X-ray diffraction pattern, **f** Raman spectrum, and **g** PL spectrum (excited at 229 nm at room temperature) of the 3C-SiC nanobelts. Reprinted with permission from [98]. Copyright 2004, American Chemical Society

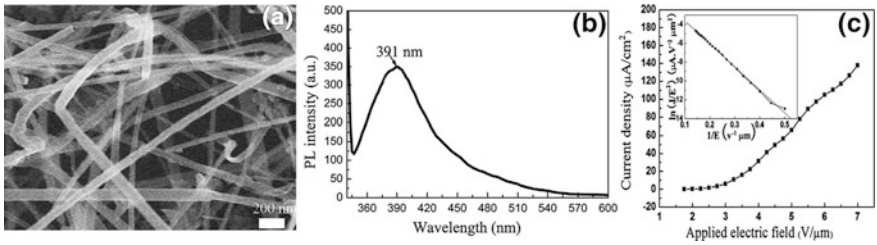

Fig. 5.74 **a** SEM image, **b** PL spectrum (under 325 nm excitation), and **c** field emission current density versus applied electric field curve for 3C-SiC nanobelts. Reprinted with permission from [99]. Copyright 2008, Elsevier

SiC. These two peaks shift to lower wave numbers by 7–12 cm^{-1} relative to that of bulk 3C-SiC caused by phonon confinement and stacking faults. The nanobelts show photoluminescence with one dominant emission band centered at around 402 nm under 229 nm excitation, and there is an additional weak band at around 415 nm. Although there is metal lithium in the starting materials, but the SEM and TEM analyses indicate that the nanobelt growth is not governed by the vapor–liquid–solid mechanism and instead, the lithium acts as a reactant and its reaction with ethanol generates CLi_x gas, which reacts with $SiCl_4$ to give rise to the SiC nanobelts.

Microwave-assisted reaction can produce SiC nanobelts. The 3C-SiC nanobelts with length of many micrometers and an average thickness of 4.4 nm are synthesized by microwave-assisted carbothermal reaction between Si, SiO_2, and charcoal powders [99]. The SEM image (Fig. 5.74) shows that the nanobelts are 20–200 nm wide and up to many micrometers long. The photoluminescence of the nanobelts shows a relatively narrow band centered at around 391 nm under 325 nm excitation. The nanobelts show field electron emission with a low turn-on field of 3.2 V/μm.

The SiC nanoribbons have been synthesized by direct thermal reaction of silicon and carbon black powders at 1,250–1,500 °C in argon atmosphere [100]. The nanoribbons are tens to hundreds of micrometers long, a few micrometers wide, and tens of nanometers thick (Fig. 5.75). The TEM, energy-dispersive X-ray

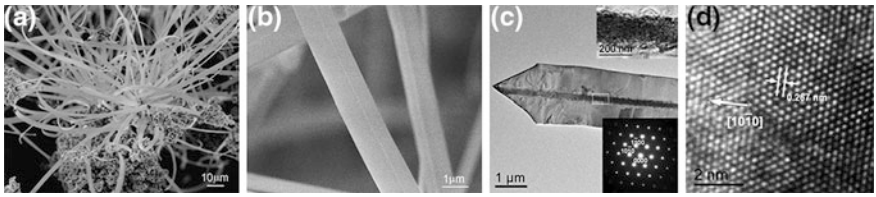

Fig. 5.75 **a**, **b** SEM and **c**, **d** TEM images of the SiC nanobelts. The electron diffraction pattern is also shown. Reprinted with permission from [100]. Copyright 2010, Springer Science and Business Media

spectroscopy, X-ray diffraction, Raman scattering, and X-ray photoelectron spectroscopy reveal that the nanoribbons are wurtzite 2H-SiC and they grow by a vapor–solid mechanism with the growth direction of [10$\bar{1}$0] (Fig. 5.75).

5.4.7 Legs on Fibers

Silicon carbide nanowires can be grown on some nanofiber templates giving rise to hierarchical nanostructures. The needle-shaped 3C-SiC nanowire arrays are grown from the polyacrylonitrile carbon fiber substrate using thermal evaporation of silicon on the carbon fibers in argon atmosphere at 1,600 °C [101]. The polyacrylonitrile carbon fiber is composed of crystallized graphite and amorphous carbon. The SEM observation reveals that many bundles of needle-shaped nanowires are grown on the outer surface of each carbon fiber (Fig. 5.76) and they have an average diameter of 100 nm and lengths of 5–10 μm. X-ray diffraction reveals that the nanoneedles are 3C-SiC. The growth of these SiC nanoneedles could be governed by the vapor–solid mechanism because no metal catalyst is present in the reactants and in the products. The SiC nanoneedles show photoluminescence centered at around 468 nm under 380 nm excitation at room temperature.

Tapered SiC nanowires are grown on the surface of flexible carbon fabric by chemical vapor deposition [102]. The thermal reaction of Si powder with iron nitrate-coated carbon fabric at 1,500 °C in flowing argon gas yields the SiC nanowires which are single-crystalline β-SiC growing along the [111] direction. The nanowire has zigzag facets on the outer surface caused by the quasi-periodic arrangement of twinning structures along the wire axis (Fig. 5.77). This twining structure ensures a lowest surface energy during nanowire growth. The structural characterizations and thermodynamics analysis demonstrate that the tapered SiC nanowires grow by Fe-assisted vapor–liquid–solid process. The nanowires show field electron emission with a very low turn-on field of 1.2 V μm^{-1}.

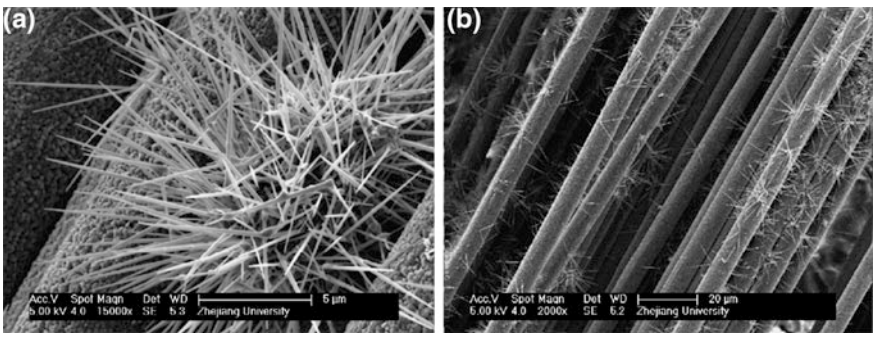

Fig. 5.76 SEM images of needle-shaped SiC nanowires grown on polyacrylonitrile carbon fibers. **a** is higher magnification and **b** is lower magnification images. Reprinted with permission from [101]. Copyright 2008, Elsevier

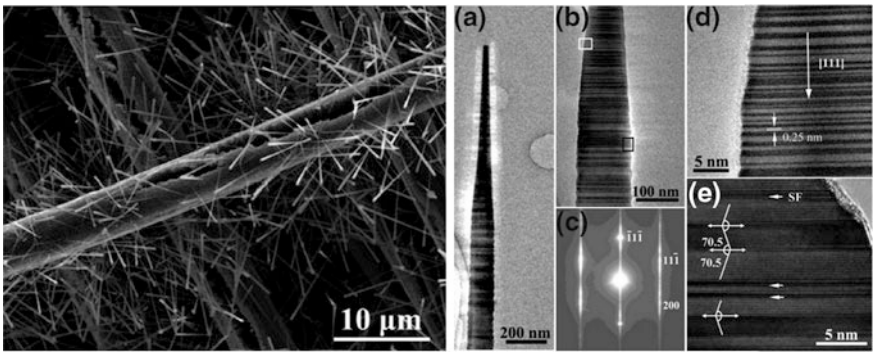

Fig. 5.77 *Left panel* SEM image of tapered SiC nanowires on the carbon fabric. *Right panel* **a** and **b** TEM images of a typical SiC nanowire showing tapered and zigzag facet morphologies. **c** Electron diffraction pattern of tapered SiC nanowires taken along [011] zone axis of cubic SiC. The streaks arise from stacking faults. **d** and **e** HRTEM images of the marked regions in (**b**). Reprinted with permission from [102]. Copyright 2012, American Chemical Society

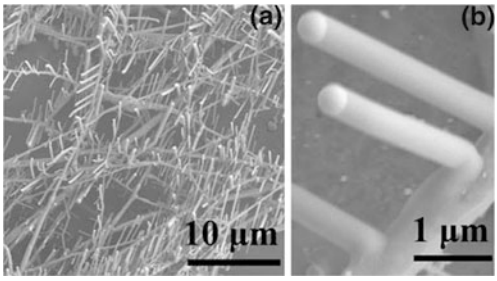

Fig. 5.78 SEM images of the SiC nanorods grown on the silica fibers. Reprinted with permission from [103]. Copyright 2009, Springer Science and Business Media

The β-SiC nanorods grown on electrospun nanofibers are synthesized by carbothermal reduction of Tb-doped SiO_2 nanofibers with graphite at 1,250 °C [103, 104]. The nanorods are 100–300 nm in diameter and 2–3 μm in length (Fig. 5.78), and they grow by the vapor–liquid–solid mechanism with Tb serving as the catalyst. Transmission electron microscopy reveals that the SiC nanorods grow preferentially along the ⟨111⟩ direction. The nanorods exhibit field electron emission with a low turn-on field of 8 V/μm [104].

5.5 Some Characteristics

Besides the commonly concerned field electron emission and luminescence properties, some other properties of the SiC nanowires have also been investigated. The electrical transport as well as optical properties of single-crystalline 3C-SiC

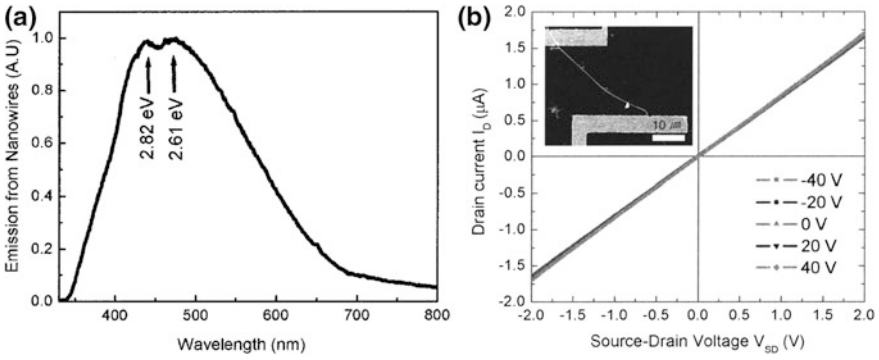

Fig. 5.79 **a** PL spectrum of the SiC nanowires. **b** *I–V* curve for the SiC nanowire connected by Ti/Au electrodes after annealing at 700 °C for different back gating from −40 to 40 V. The *inset* shows the SEM image of the two-terminal SiC nanowire device. Reprinted with permission from [105]. Copyright 2004, AIP Publishing LLC

nanowires have been investigated [105]. The nanowires are fabricated by chemical vapor deposition using Si/SiO_2 wafer and methyltrichlorosilane (CH_3SiCl_3) as source materials under Ni catalysis in flowing hydrogen at 950 °C. These nanowires have diameters smaller than 100 nm and lengths of several micrometers. Transmission electron microscopy reveals that the nanowires grow along the ⟨111⟩ direction. They exhibit blue photoluminescence centered at around 450 nm (Fig. 5.79a) at room temperature. The *I–V* measurement of the nanowires (Fig. 5.79b) indicates that they have low resistivity of 2.2×10^{-2} Ω cm for 0 V gate voltage at room temperature. The estimated electron mobility of the nanowires is 15 $cm^2/(V\ s)$.

Like bulk SiC, the SiC nanowires have good mechanical and thermal properties. The unusually large strain plasticity of ceramic SiC nanowires at near room temperature has been observed in situ by transmission electron microscopy [106]. The continuous plasticity of the SiC nanowires is accompanied by a process of increased dislocation density at an early stage, followed by an obvious lattice distortion, and finally reaches complete amorphization at the most strained region of the nanowire. Superplasticity of single-crystal β-SiC [111] nanowires for over 200 % elongation is observed by in situ axial-tensile scanning electron microscopy [107]. The axial localized plasticity and superplasticity only result from the 3C segments in the SiC nanowires, through dislocation generation, propagation, and amorphization in contrast to the highly defected structural segments that show elastic deformation only due to the lack of slip systems. The measurement of the high mechanical Q factor for singly clamped SiC nanowires by field emission in ultrahigh vacuum [108, 109] reveals a room temperature Q factor of 159,000 after high-temperature in situ cleaning. The SiC nanowires with diameters of 100 nm exhibit strength of about 24 GPa [110] and thus can be used to reinforce the performance of the bulk ceramic composites. The measured thermal conductivities of the single and double β-SiC nanowires are 82 and 73 W/mK, respectively [111],

and these values are smaller than that of bulk material. The dielectric properties of the SiC nanowires depend strongly on their chemical compositions, especially on the carbon content [112]. The complex permittivity calculated from the measured reflectivity decreases with increasing frequency, and the nanowires with higher carbon content show higher complex permittivity.

5.6 Theoretical Studies

The mechanical and electronic properties of the silicon carbide nanowires have been widely investigated theoretically using molecular dynamics simulations and first-principle calculations. The external loading effect on the elastic properties of the 3C-SiC nanowires with different diameters and structural changes is studied using molecular dynamics simulations [113]. The elastic modulus and limit of structural integrity are highly independent of the wire diameter under uniaxial compressive and tensile loading (Fig. 5.80). In contrast, the elastic response and structural deformation mechanism near the elastic limit depend strongly on the nanowire diameter under nonaxial torsional and bending strains. The critical angle of torsion is approximately inversely proportional to the wire radius, and the torsional rigidity increases with the wire radius following a power law. The bending loading shows similar effects. The nonlinear effects play an important role in defining the external bending and torsional strain effect of the nanowires with diameters smaller than 1 nm. Some mechanical properties of the ⟨111⟩-oriented SiC nanowires are comparable or even better than that of carbon nanotubes of similar diameter.

The size dependence of surface stress, surface stiffness, and Young's modulus of a prism cross-sectional nanowire is theoretically investigated [114]. The calculation shows that the edge phase induces the size dependence of the nominal specific surface energy, surface stress, and surface stiffness, whereas the surface phase and the edge phase cause the size dependence of the nominal Young's modulus (Fig. 5.81). The edge and surface effects become more important as the

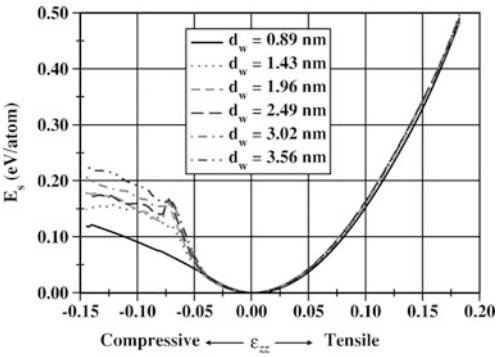

Fig. 5.80 Normalized (per atom) elastic energy as a function of uniaxial compressive strain and tensile strain for six SiC nanowires with different diameters. Reprinted with permission from [113]. Copyright 2006, American Physical Society

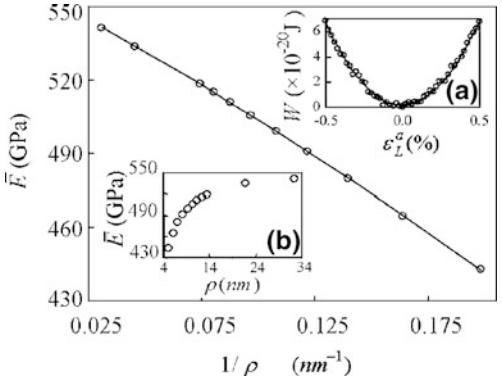

Fig. 5.81 Nominal Young's modulus as a function of the inverse of the cross-sectional perimeter for a [111] β-SiC nanowire. The *solid line* is the model fit. The *inset a* shows the work W done on a nanowire (6 layers) versus the applied strain. The *inset b* shows the nominal Young's modulus of the nanowires versus the cross-sectional perimeter. Reprinted with permission from [114]. Copyright 2008, AIP Publishing LLC

cross-sectional area of a nanowire becomes smaller. The Molecular dynamics simulation conducted on hexagonal prism [111] β-SiC nanowires confirms the soundness of the theoretical approach. The mechanical properties of the [111]-oriented β-SiC nanowires under tension, compression, torsion, and combined loading are investigated using molecular dynamics simulations employing the Tersoff bond-order potential [115]. The collapse of the SiC nanowires is dependent on the size and the temperature under axial tensile-strain. Under axial compressive-strain, the collapse of the SiC nanowires by yielding or column buckling mode is dependent on the length and diameter of the nanowires. Under torsion strain, the SiC nanowires collapse through a crystal to amorphous phase transformation in several atomic layers. The molecular dynamic simulation reveals the influence of microstructure on the brittleness and plasticity of [111]-oriented SiC nanowires [116]. The result shows that the plastic deformation is mainly induced by the antiparallel sliding of 3C grains along an intergranular amorphous film parallel to the (111) plane and inclined at an angle of 19.47° relative to the nanowire axis.

The geometrical and electronic structures of 3C-SiC nanowires growing along the ⟨100⟩ axis are investigated using density functional calculations [117]. The hydrogen-passivated SiC nanowires show the quantum confinement effect in both C- and Si-rich wires, exhibiting as bandgap broadening with decreasing diameter. For the pure SiC nanowires, the dangling bonds strongly reconstruct and the nanowire exhibits metallic property due to the formation of surface states, and the conduction is nearly totally sustained by the outer layer of the nanowire. Figure 5.82 shows the calculated distribution of the density of states and the electronic band structure of the C-coated SiC nanowire.

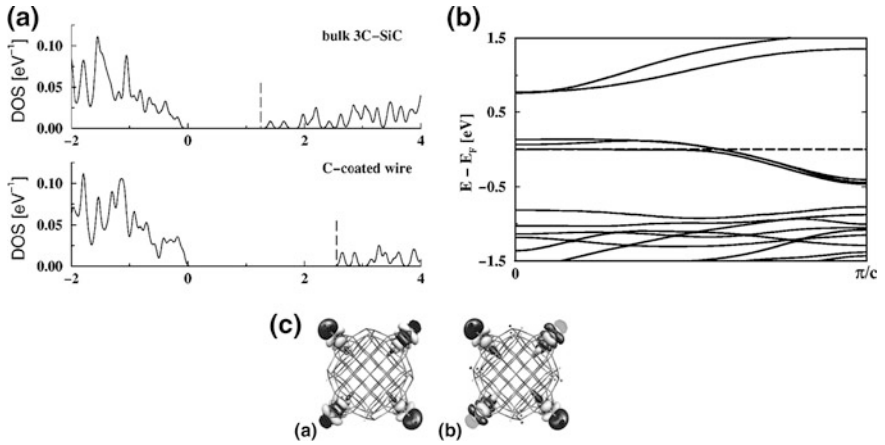

Fig. 5.82 **a** Electronic density of states of bulk 3C-SiC and carbon-coated SiC nanowire. The density of states is normalized to the number of states to allow for a comparison between systems calculated with different simulation cells and aligned to the valence band maximum. The underestimation of the bandgap is not compensated for. **b** Electronic band structure of the C-coated SiC nanowire showing four reconstruction-induced surface states (degenerate two by two) that cross the Fermi level. **c** Wave function iso-surfaces of two of the four surface states of the C-coated SiC nanowire. Reprinted with permission from [117]. Copyright 2005, American Physical Society

The first-principle calculation shows that the bandgap of β-SiC nanowire increases as the diameter decreases as a result of the quantum confinement effect and increases (decreases) slightly with increasing tensile (compressive) stress up to about 12 GPa (Fig. 5.83) [118]. The calculated Young's modulus and tensile strength of the SiC nanowire are about 620 and 52 GPa, respectively, in agreement with the experimental data.

The density functional calculation indicates that the pure SiC nanowires with wurtzite structure that grow along the [0001] direction are semiconductors [119]; however, their bandgap energy decreases with decreasing diameter due to the

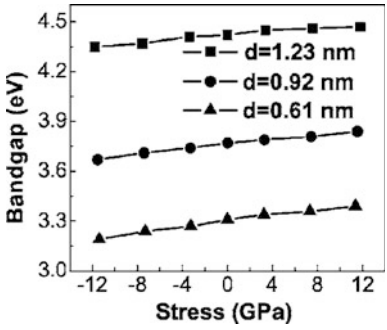

Fig. 5.83 Bandgap as a function of uniaxial stress for [111] β-SiC nanowires with different diameters. Reprinted with permission from [118]. Copyright 2006, AIP Publishing LLC

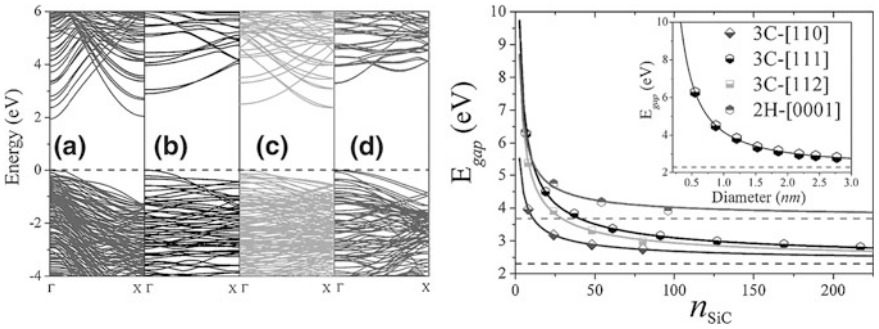

Fig. 5.84 *Left panel* Electronic band structures of the SiC nanowires corresponding to **a** 3C [110], **b** 3C [111], **c** 3C [112], and **d** 2H [0001]. *Right panel* Bandgap of SiC nanowires as a function of nanowire size (the number of SiC units per cell). The *solid lines* are the fitted results. The *inset* shows the bandgap of [111]-oriented 3C-SiC nanowire as a function of diameter. Reprinted with permission from [121]. Copyright 2009, American Chemical Society

presence of surface states. The hydrogen surface termination induces broadened bandgap that follows the quantum confinement effect. The energetics and electronic structures of 2H-SiC nanowires and nanotubes with radius ranging from 0.45 to 2.9 nm are investigated using density functional calculations [120]. The formation energy of the nanowire decreases with increasing wire radius, and the formation energy of the nanotube decreases with increasing wall thickness. The SiC nanotube with faceted single-crystalline wall is energetically more favorable than the cylindrical nanotube. The pure faceted SiC nanowire and nanotube possess indirect bandgaps related to surface states, with gap values smaller than that of bulk SiC. The hydrogen-passivated SiC nanowire and nanotube have direct bandgaps with values greater than those of bulk SiC. The density functional calculation performed on the hydrogenated 3C- and 2H-SiC nanowires shows that the [111]-orientated 3C-SiC nanowire is energetically more stable than other types of nanowires with similar size [121]. This result agrees with the experimental observation that most of the synthesized SiC nanowires are the 3C-SiC nanowires that grow along the [111] orientation. The calculation shows that all the nanowires have direct bandgaps except those grow along the [112] direction (Fig. 5.84, left panel). The direct bandgap character is maintained for 3C-SiC nanowires with diameters up to 2.8 nm. The bandgap of the nanowire increases with decreasing wire size (Fig. 5.84, right panel). The density functional calculation shows that both saturated and unsaturated twinned 3C-SiC nanowires that grow along the [111] direction exhibit semiconducting characteristics [122]. The saturated nanowires have direct bandgaps that increase with decreasing diameter. The 2H stacking inside the 3C stacking shows no influence on the electronic properties of the nanowires.

5.7 Applications

There has been increasing interest on the application of the silicon carbide nanowires. A two-step method has been developed to synthesize the heterojunction of the ZnO nanorods on the SiC nanowires [123]. The SiC nanowires are prepared by heating the Si wafer and the WO_3/C mixed powders under catalysis of NiO in nitrogen atmosphere at 1,050 °C. The diethylzinc is subsequently used as metal-organic source to grow ZnO nanorods on the as-synthesized SiC nanowires at 450 °C. High-resolution TEM images (Fig. 5.85) show that the heterojunction has an atomically abrupt interface and there is no interfacial layer between the ZnO nanorod and the SiC nanowire. The [0001] direction of the ZnO nanowire is perpendicular to the [111] direction of the SiC nanowire at the heterojunction.

The photocatalytic property of the SiC nanowires has been investigated by measuring the photodegradation rate of acetaldehyde catalyzed by SiC [124]. The β-SiC nanowires coated with amorphous SiO_2 are synthesized by the thermal evaporation method. These nanowires exhibit excellent photocatalytic property, as demonstrated by the efficient decomposition of the acetaldehyde under UV light irradiation (Fig. 5.86). The photocatalytic reaction is measured by monitoring the amount of CO_2 gas produced in this process. The SiO_2-coated SiC nanowires show better catalysis effect than the oxide-free SiC nanowires obtained by HF etching.

Silicon carbide nanowires can be used to construct field-effect transistors. A prototype of the field-effect transistor based on the β-SiC nanowires has been demonstrated [125]. These nanowires are synthesized by thermal reaction between

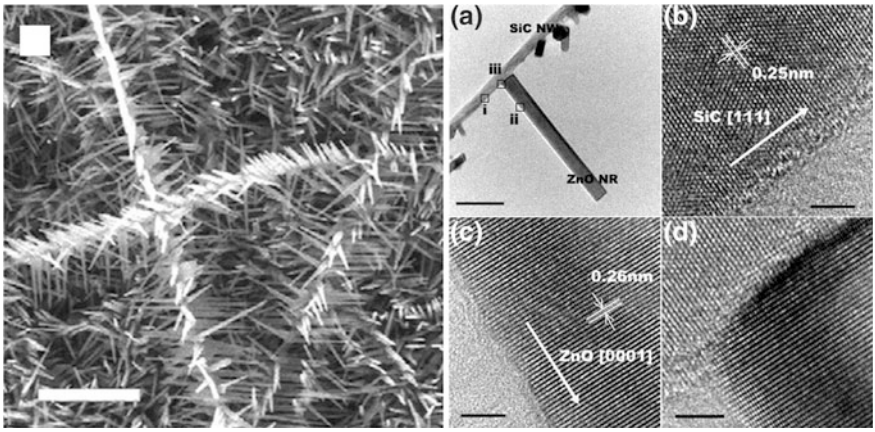

Fig. 5.85 *Left panel* ZnO nanorods grown on β-SiC nanowire. *Right panel* (**a**) TEM image of the ZnO nanorod/SiC nanowire heterojunction. **b–d** High-resolution micrographs of the marked regions in **a**, corresponding to the SiC nanowire (*i*), ZnO nanorod (*ii*), and nanojunction (*iii*), respectively. The scale bar is 100 nm in (**a**) and 2.5 nm in (**b–d**). Reprinted with permission from [123]. Copyright 2005, IOP Publishing

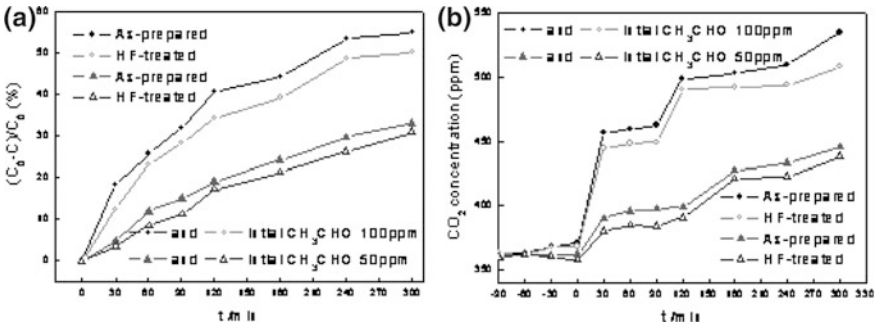

Fig. 5.86 **a** Photodegradation rate of acetaldehyde gas as a function of irradiation time of UV light, and the degradation is catalyzed by the SiC nanowires. C_0 is initial concentration of gaseous acetaldehyde (CH_3CHO), and C is the CH_3CHO concentration at time t. **b** CO_2 concentration (generated by decomposition of acetaldehyde) as a function of irradiation (starting from the zero instant) time. Reprinted with permission from [124]. Copyright 2006, AIP Publishing LLC

the activated carbon fiber and the SiO powder without using catalyst at 1,450 °C. They have diameters 10–25 nm and lengths up to 10 μm. The measured carrier mobility of the *n*-type SiC field-effect transistor is 6.4 and 15.9 $cm^2/(V\ s)$ for applied drain-source voltage of 0.01 and 0.05 V at room temperature (Fig. 5.87), respectively. The SiC field-effect transistor has higher drain current and higher carrier mobility at increased temperature than at room temperature. The electrical properties of 3C-SiC nanowires contacted with two types of ohmic contacts (Ti/Au

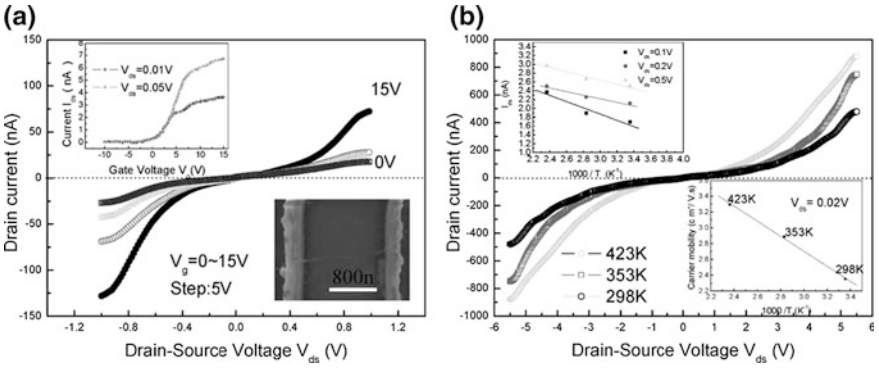

Fig. 5.87 Characteristics of the *n*-type SiC nanowire-based field-effect transistor. **a** Drain current versus voltage recorded at different gate voltages at room temperature. *Lower inset* shows the SiC nanowire bridging two electrodes. *Upper inset* shows drain current versus gate voltage measured at drain voltage 0.01 and 0.05 V, respectively. **b** Drain current as a function of drain-source voltage at different temperatures at gate voltage 5 V. *Lower inset* is the Arrhenius plot of mobility at various temperatures. *Upper inset* shows the temperature dependence of drain current of the SiC nanowire-based field-effect transistor with Au contact electrodes at gate voltage 5 V. Reprinted with permission from [125]. Copyright 2006, IEEE

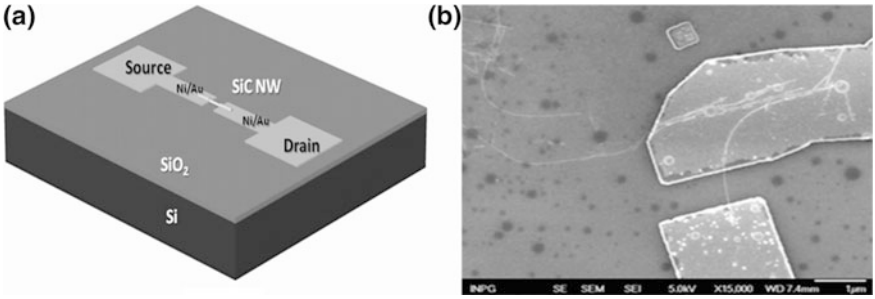

Fig. 5.88 **a** Schematic of SiC nanowire-based field-effect transistor. **b** SEM image of the fabricated device showing a SiC nanowire between two metallic contacts. Reprinted with permission from [127]. Copyright 2011, IEEE

and Ni/Au) are studied [126]. The Ni/Au ohmic contact on SiC nanowires exhibits a lower contact resistance of 5.9×10^{-6} Ω cm^2 in comparison with that of the Ti/Au contact (2.6×10^{-4} Ω cm^2). The SiC nanowire field-effect transistor with Ni/Au ohmic contact has much lower contact resistance and better performance relative to the transistor with Ti/Au contact. The back-gated field-effect transistors based on the 3C-SiC nanowires (Fig. 5.88) have been fabricated [127]. The device shows either ohmic contact or rectifying contact. The ohmic contact transistor has a very weak gating effect, and the device switching off is unachievable because of the high electron concentration along the nanowire. The Schottky contact barrier at source/drain regions is more favorable for improvement of the transistor performance by suppressing the off current. The Schottky contact barrier at high positive gate voltages (over 20 V) is more transparent leading to I_{ON}/I_{OFF} ratio of 103 in contrast to the weak gating effect of the ohmic contact 3C-SiC nanowire transistor. On account of the practical application of the SiC nanowires in electronic devices, the doping level of the SiC nanowires must be controllable. The nitrogen doping of the 3C-SiC nanowires has been demonstrated through a reaction of catalyst-assisted pyrolysis of polymeric precursors with $Co(NO_3)_2$ as catalysts [128]. A relatively low partial pressure is crucial for the doping of nitrogen to the SiC nanowires. The concentration of the doped nitrogen decreases with increasing pyrolysis temperature during growth of the SiC nanowires, and this character can be used for controlled doping of nitrogen in the SiC nanowires.

The self-cleaning glass can be fabricated by coating superhydrophobic SiC nanowires in tetraethyl orthosilicate (TEOS) solution [129]. The coated glass by 10-cycles coating of the SiC nanowires with a high roughness Ra of 1928.9 nm shows high water contact angle up to 160° (Fig. 5.89) and low sliding angle down to 5°. The coated sample shows high chemical stability even after immersion in water for 14 days.

Polyurethane-based nanocomposite film is fabricated by incorporating carbon-coated SiC nanowires into the polymer matrix [130]. Measurement of the electric-field-induced strain indicates that incorporation of 0.5 wt% nanowires in the

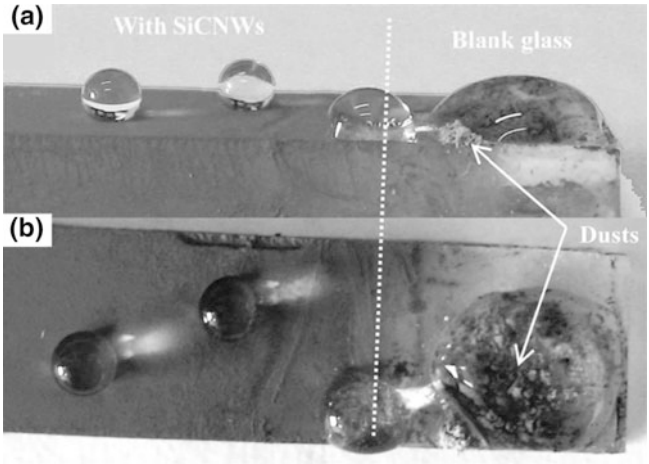

Fig. 5.89 **a** Cross-sectional view and **b** top-view photos of self-cleaning test with dust on SiC nanowires-coated glass and control blank glass. Reprinted with permission from [129]. Copyright 2009, American Chemical Society

polymer increases the strain level by a factor of 1.7 at field strength 6.5 V/μm. The improvement of the electromechanical response is related to a stronger space charge effect in the nanocomposite than in the pure polymer. The electrostatically actuated contact-mode nanoelectromechanical switches based on very thin SiC nanowires have been demonstrated [131]. The SiC nanowires are lithographically patterned from SiC layer with thickness of 50 nm that is heteroepitaxially grown on a Si substrate (Fig. 5.90). Several types of in-plane electrostatic SiC nanowire switches are realized, and the nanowires have diameters as small as 20 nm, and the lateral switching gaps are as narrow as 10 nm. These contact-mode nanomechanical switches show very low turn-on voltages down to 1 V and very short switching times in the submicrosecond range.

The SiC–SiO_2 core–shell nanowire film has good antifriction performance [132], and the maximum static frictional force between the nanowire film and a macroscopic solid surface is 5–12 times that between two macroscopic solids. The wear-resistant nanoscale silicon carbide tips have been prepared by annealing the surface of the nanoscale Si tip exposed to carbon ions [133]. The SiC-covered Si tip maintains its nanoscale sharpness and exhibits wear resistance that is orders of magnitude larger than that of conventional Si tips and at least 100-fold higher than that of SiO-doped diamond-like carbon tips. The sharpness, high wear resistance, and high thermal stability of these tips render them favorable for scanning probe applications.

The electromagnetic wave absorption properties of the 2-mm-thick SiC nanowire–epoxy composite have been investigated in the range of 2–40 GHz [134].

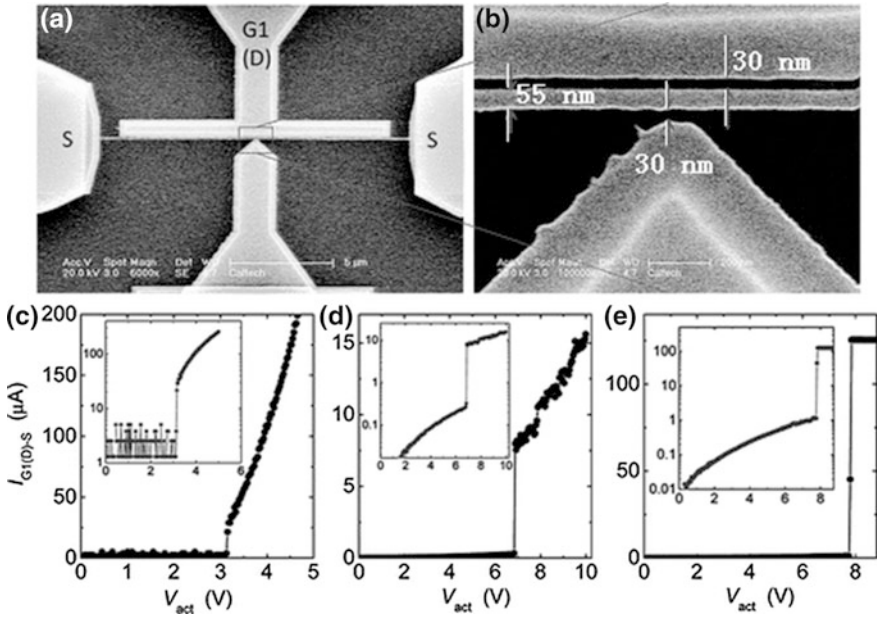

Fig. 5.90 Low-voltage nanoelectromechanical switches based on metallized SiC nanowires. **a** A 15-μm-long and 55-nm-wide SiC nanowire metallized with 30-nm Al on *top*. **b** Magnification micrograph showing the 55-nm-wide nanowire and the 30-nm-wide gap. **c** and **d** Nanoelectromechanical switching events from two 20-μm-long devices, with V_{on} of 3.1 and 7.0 V, respectively. **e** Switching event from a 15-μm-long device, with V_{on} of 7.8 V. The *insets* in (**c**–**e**) are the data shown with measured current in the logarithmic scale. Reprinted with permission from [131]. Copyright 2010, American Chemical Society

The single-crystalline β-SiC nanowires grow along the [111] direction, and they have diameters of 30–70 nm and lengths of 4–10 μm. The 35 wt% SiC nanowire composites show remarkable electromagnetic wave absorptions of −31.7 and −9.8 dB at 8.3 and 27 GHz (Fig. 5.91), respectively. The composite containing 25 wt% SiC nanowire exhibits the minimum reflection loss of −32.4 dB at 31.1 GHz. The electromagnetic wave absorption may arise from the electric conductance loss caused by network-like SiC nanowires in the resin matrix and from the relaxation polarization loss at the interface of the SiC nanowires and the epoxy resin. The microwave absorption property of the β-SiC nanowires synthesized by the reaction of multiwalled carbon nanotubes and Si powder in the presence of molten salts at 1,250 °C has been investigated [135]. These nanowires grow along the [111] direction, and they have diameters of 20–80 nm and lengths up to several tens of micrometers. A minimum reflection loss of 217.4 dB at 11.2 GHz is acquired for the silicone matrix incorporated by 30 wt% SiC nanowires.

The SiC nanowires can serve as the host for accommodating metal catalysts. The Pd nanoparticles attached on the surfaces of the selectively etched periodically

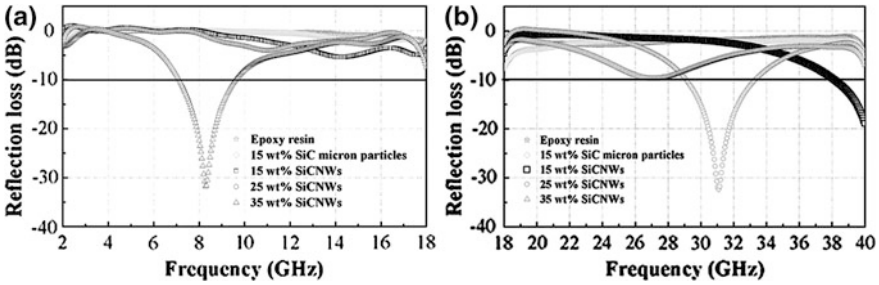

Fig. 5.91 Frequency dependences of reflection loss for epoxy resin, composite with 15 wt% SiC micrometer-sized particles, and composites with 15, 25, and 35 wt% SiC nanowires at 2–18 GHz (**a**) and 18–40 GHz (**b**), respectively. Reprinted with permission from [134]. Copyright 2010, American Chemical Society

twinned SiC nanowires [136] show prohibited migration and coalescence, and as a result, such attached Pd nanoparticles show improved stability during their catalysis for combustion of methane.

References

1. Dai H, Wong EW, Lu YZ, Fan S, Lieber CM (1995) Synthesis and characterization of carbide nanorods. Nature 375:769–772
2. Han W, Fan S, Li Q, Liang W, Gu B, Yu D (1997) Continuous synthesis and characterization of silicon carbide nanorods. Chem Phys Lett 265:374–378
3. Zhu J, Fan S (1999) Nanostructure of GaN and SiC nanowires based on carbon nanotubes. J Mater Res 14:1175–1177
4. Tang CC, Fan SS, Dang HY, Zhao JH, Zhang C, Li P, Gu Q (2000) Growth of SiC nanorods prepared by carbon nanotubes-confined reaction. J Cryst Growth 210:595–599
5. Zhang S-L, Zhu B-F, Huang F, Yan Y, Shang E-Y, Fan S, Han W (1999) Effect of defects on optical phonon Raman spectra in SiC nanorods. Solid State Commun 111:647–651
6. Feldman DW, Parker JH, Choyke WJ, Patrick L (1968) Phonon dispersion curves by Raman scattering in SiC, polytypes 3C, 4H, 6H, 15R, and 21R. Phys Rev 173:787–793
7. Seo WS, Koumoto K (1996) Stacking faults in β-SiC formed during carbothermal reduction of SiO2. J Am Ceram Soc 79:1777–1782
8. Gundiah G, Madhav GV, Govindaraj A, Seikh MM, Rao CNR (2002) Synthesis and characterization of silicon carbide, silicon oxynitride and silicon nitride nanowires. J Mater Chem 12:1606–1611
9. Gao YH, Bando Y, Kurashima K, Sato T (2002) SiC nanorods prepared from SiO and activated carbon. J Mater Sci 37:2023–2029
10. Chiu S-C, Huang C-W, Li Y-Y (2007) Synthesis of high-purity silicon carbide nanowires by a catalyst-free arc-discharge method. J Phys Chem C 111:10294–10297
11. Niu JJ, Wang JN (2007) A simple route to synthesize scales of aligned single-crystalline SiC nanowires arrays with very small diameter and optical properties. J Phys Chem B 111:4368–4373
12. Bechelany M, Brioude A, Cornu D, Ferro G, Miele P (2007) A Raman spectroscopy study of individual SiC nanowires. Adv Funct Mater 17:939–943

13. Li Z, Zhang J, Meng A, Guo J (2006) Large-area highly-oriented SiC nanowire arrays: synthesis, Raman, and photoluminescence properties. J Phys Chem B 110:22382–22386
14. Wagner RS, Ellis WC (1964) Vapor-liquid-solid mechanism of single crystal growth. Appl Phys Lett 4:89–90
15. Seeger T, Kohler-Redlich P, Rühle M (2000) Synthesis of nanometer-sized SiC whiskers in the arc-discharge. Adv Mater 12:279–282
16. Yang W, Miao H, Xie Z, Zhang L, An L (2004) Synthesis of silicon carbide nanorods by catalyst-assisted pyrolysis of polymeric precursor. Chem Phys Lett 383:441–444
17. Zhang L, Yang W, Jin H, Zheng Z, Xie Z, Miao H, An L (2006) Ultraviolet photoluminescence from 3C-SiC nanorods. Appl Phys Lett 89:143101
18. Wang H, Xie Z, Yang W, Fang J, An L (2008) Morphology control in the vapor-liquid-solid growth of SiC nanowires. Cryst Growth Des 8:3893–3896
19. Feng W, Ma J, Yang W (2012) Precise control on the growth of SiC nanowires. CrystEngComm 14:1210–1212
20. Shim HW, Huang H (2007) Three-stage transition during silicon carbide nanowire growth. Appl Phys Lett 90:083106
21. Hu JQ, Lu QY, Tang KB, Deng B, Jiang RR, Qian YT, Yu WC, Zhou GE, Liu XM, Wu JX (2000) Synthesis and characterization of SiC nanowires through a reduction-carburization route. J Phys Chem B 104:5251–5254
22. Zhang Y, Nishitani-Gamo M, Xiao C, Ando T (2002) Synthesis of 3C-SiC nanowhiskers and emission of visible photoluminescence. J Appl Phys 91:6066–6070
23. Zhou XT, Wang N, Lai HL, Peng HY, Bello I, Wong NB, Lee CS, Lee ST (1999) β-SiC nanorods synthesized by hot filament chemical vapor deposition. Appl Phys Lett 74:3942–3944
24. Lu Q, Hu J, Tang K, Qian Y (1999) Growth of SiC nanorods at low temperature. Appl Phys Lett 75:507–509
25. Shen G, Chen D, Tang K, Qian Y, Zhang S (2003) Silicon carbide hollow nanospheres, nanowires and coaxial nanowires. Chem Phys Lett 375:177–184
26. Choi H-J, Seong H-K, Lee J-C, Sung Y-M (2004) Growth and modulation of silicon carbide nanowires. J Cryst Growth 269:472–478
27. Shi W, Zheng Y, Peng H, Wang N, Lee CS, Lee S-T (2000) Laser ablation synthesis and optical characterization of silicon carbide nanowires. J Am Ceram Soc 83:3228–3230
28. Wu ZS, Deng SZ, Xu NS, Chen J, Zhou J, Chen J (2002) Needle-shaped silicon carbide nanowires: Synthesis and field electron emission properties. Appl Phys Lett 80:3829–3831
29. Feng DH, Jia TQ, Li XX, Xu ZZ, Chen J, Deng SZ, Wu ZS, Xu NS (2003) Catalytic synthesis and photoluminescence of needle-shaped 3C-SiC nanowires. Solid State Commun 128:295–297
30. Sundaresan SG, Davydov AV, Vaudin MD, Levin I, Maslar JE, Tian Y-L, Rao MV (2007) Growth of silicon carbide nanowires by a microwave heating-assisted physical vapor transport process using group VIII metal catalysts. Chem Mater 19:5531–5537
31. Huczko A, Bystrzejewski M, Lange H, Fabianowska A, Cudziło S, Panas A, Szala M (2005) Combustion synthesis as a novel method for production of 1-D SiC nanostructures. J Phys Chem B 109:16244–16251
32. Huczko A, Dabrowska A, Savchyn V, Popov AI, Karbovnyk I (2009) Silicon carbide nanowires: synthesis and cathodoluminescence. Phys Status Solidi B 246:2806–2808
33. Li G-Y, Li X-D, Chen Z-D, Wang J, Wang H, Che R-C (2009) Large areas of centimeters-long SiC nanowires synthesized by pyrolysis of a polymer precursor by a CVD route. J Phys Chem C 113:17655–17660
34. Zhang X, Huang X, Wen G, Geng X, Zhu J, Zhang T, Bai H (2010) Novel SiOC nanocomposites for high-yield preparation of ultra-large-scale SiC nanowires. Nanotechnology 21:385601
35. Lin L (2011) Synthesis and optical property of large-scale centimetres-long silicon carbide nanowires by catalyst-free CVD route under superatmospheric pressure conditions. Nanoscale 3:1582–1591

36. Yao Y, Lee ST, Li FH (2003) Direct synthesis of 2H-SiC nanowhiskers. Chem Phys Lett 381:628–633
37. Zou G, Dong C, Xiong K, Li H, Jiang C, Qian Y (2006) Low-temperature solvothermal route to 2H-SiC nanoflakes. Appl Phys Lett 88:071913
38. Gao F, Yang W, Wang H, Fan Y, Xie Z, An L (2008) Controlled Al-doped single-crystalline 6H-SiC nanowires. Cryst Growth Des 8:1461–1464
39. Wang H, Lin L, Yang W, Xie Z, An L (2010) Preferred orientation of SiC nanowires induced by substrates. J Phys Chem C 114:2591–2594
40. Gao F, Feng W, Wei G, Zheng J, Wang M, Yang W (2012) Triangular prism-shaped p-type 6H-SiC nanowires. CrystEngComm 14:488–491
41. Fowler RH, Nordheim L (1928) Electron emission in intense electric fields. Proc R Soc London, Ser A 119:173–181
42. Wong KW, Zhou XT, Au FCK, Lai HL, Lee CS, Lee ST (1999) Field-emission characteristics of SiC nanowires prepared by chemical-vapor deposition. Appl Phys Lett 75:2918–2920
43. Zhou XT, Lai HL, Peng HY, Au FCK, Liao LS, Wang N, Bello I, Lee CS, Lee ST (2000) Thin β-SiC nanorods and their field emission properties. Chem Phys Lett 318:58–62
44. Lai HL, Wong NB, Zhou XT, Peng HY, Au FCK, Wang N, Bello I, Lee CS, Lee ST, Duan XF (2000) Straight β-SiC nanorods synthesized by using C-Si-SiO_2. Appl Phys Lett 76:294–296
45. Pan Z, Lai H-L, Au FCK, Duan X, Zhou W, Shi W, Wang N, Lee C-S, Wong N-B, Lee S-T, Xie S (2000) Oriented silicon carbide nanowires: synthesis and field emission properties. Adv Mater 12:1186–1190
46. Lo HC, Das D, Hwang JS, Chen KH, Hsu CH, Chen CF, Chen LC (2003) SiC-capped nanotip arrays for field emission with ultralow turn-on field. Appl Phy Lett 83:1420–1422
47. Xi G, Liu Y, Liu X, Wang X, Qian Y (2006) Mg-catalyzed autoclave synthesis of aligned silicon carbide nanostructures. J Phys Chem B 110:14172–14178
48. Zhang X, Chen Y, Xie Z, Yang W (2010) Shape and doping enhanced field emission properties of quasialigned 3C-SiC nanowires. J Phys Chem C 114:8251–8255
49. Kim D-W, Choi Y-J, Choi KJ, Park J-G, Park J-H, Pimenov SM, Frolov VD, Abanshin NP, Gorfinkel BI, Rossukanyi NM, Rukovishnikov AI (2008) Stable field emission performance of SiC-nanowire-based cathodes. Nanotechnology 19:225706
50. Kang M-G, Lezec HJ, Sharifi F (2013) Stable field emission from nanoporous silicon carbide. Nanotechnology 24:065201
51. Meng GW, Zhang LD, Mo CM, Zhang SY, Qin Y, Feng SP, Li HJ (1998) Preparation of β-SiC nanorods with and without amorphous SiO_2 wrapping layers. J Mater Res 13:2533–2538
52. Meng GW, Cui Z, Zhang LD, Phillipp F (2000) Growth and characterization of nanostructured β-SiC via carbothermal reduction of SiO_2 xerogels containing carbon nanoparticles. J Cryst Growth 209:801–806
53. Liang CH, Meng GW, Zhang LD, Wu YC, Cui Z (2000) Large-scale synthesis of β-SiC nanowires by using mesoporous silica embedded with Fe nanoparticles. Chem Phys Lett 329:323–328
54. Wang ZL, Dai ZR, Gao RP, Bai ZG, Gole JL (2000) Side-by-side silicon carbide-silica biaxial nanowires: Synthesis, structure, and mechanical properties. Appl Phys Lett 77:3349–3351
55. Zhu YQ, Hu WB, Hsu WK, Terrones M, Grobert N, Hare JP, Kroto HW, Walton DRM, Terrones H (1999) SiC-SiO_x heterojunctions in nanowires. J Mater Chem 9:3173–3178
56. Li YB, Xie SS, Zou XP, Tang DS, Liu ZQ, Zhou WY, Wang G (2001) Large-scale synthesis of β-SiC nanorods in the arc-discharge. J Cryst Growth 223:125–128
57. Ye H, Titchenal N, Gogotsi Y, Ko F (2005) SiC nanowires synthesized from electrospun nanofiber templates. Adv Mater 17:1531–1535
58. Ryu Y, Tak Y, Yong K (2005) Direct growth of core-shell SiC-SiO_2 nanowires and field emission characteristics. Nanotechnology 16:S370–S374

59. Liu X-M, Yao K-F (2005) Large-scale synthesis and photoluminescence properties of SiC/SiO_x nanocables. Nanotechnology 16:2932–2935
60. Fabbri F, Rossi F, Attolini G, Salviati G, Iannotta S, Aversa L, Verucchi R, Nardi M, Fukata N, Dierre B, Sekiguchi T (2010) Enhancement of the core near-band-edge emission induced by an amorphous shell in coaxial one-dimensional nanostructure: the case of SiC/SiO_2 core/shell self-organized nanowires. Nanotechnology 21:345702
61. Fabbri F, Rossi F, Attolini G, Salviati G, Dierre B, Sekiguchi T, Fukata N (2012) Luminescence properties of SiC/SiO_2 core-shell nanowires with different radial structure. Mater Lett 71:137–140
62. Wei J, Li K, Chen J, Yuan H (2011) Synthesis of centimeter-scale ultra-long SiC nanowires by simple catalyst-free chemical vapor deposition. J Cryst Growth 335:160–164
63. Li Y, Bando Y, Golberg D (2004) SiC-SiO_2-C coaxial nanocables and chains of carbon nanotube-SiC heterojunctions. Adv Mater 16:93–96
64. Kohno H, Mori Y, Ichikawa S, Ohno Y, Yonenaga I, Takeda S (2009) Transformation of a SiC nanowire into a carbon nanotube. Nanoscale 1:344–346
65. Cambaz ZG, Yushin GN, Gogotsi Y, Vyshnyakova KL, Pereselentseva LN (2006) Formation of carbide-derived carbon on β-silicon carbide whiskers. J Am Ceram Soc 89:509–514
66. Wang X-Y, Zhai H-Z, Cao C-B, Cai H-N, Wang Y, Chan HLW (2009) One-step synthesis of orientation accumulation SiC-C coaxial nanocables at low temperature. J Mater Chem 19:2958–2962
67. Ryu YH, Park BT, Song YH, Yong K (2004) Carbon-coated SiC nanowires: direct synthesis from Si and field emission characteristics. J Cryst Growth 271:99–104
68. Zhang Y, Suenaga K, Colliex C, Iijima S (1998) Coaxial nanocable: silicon carbide and silicon oxide sheathed with boron nitride and carbon. Science 281:973–975
69. Han W, Redlich P, Ernst F, Rühle M (1999) Synthesizing boron nitride nanotubes filled with SiC nanowires by using carbon nanotubes as templates. Appl Phys Lett 75:1875–1877
70. Tang CC, Bando Y, Sato T, Kurashima K, Ding XX, Gan ZW, Qi SR (2002) SiC and its bicrystalline nanowires with uniform BN coatings. Appl Phys Lett 80:4641–4643
71. Tang C, Bando Y, Sato T, Kurashima K (2002) Uniform boron nitride coatings on silicon carbide nanowires. Adv Mater 14:1046–1049
72. Tang C, Bando Y (2003) Effect of BN coatings on oxidation resistance and field emission of SiC nanowires. Appl Phys Lett 83:659–661
73. Li Y, Dorozhkin PS, Bando Y, Golberg D (2005) Controllable modification of SiC nanowires encapsulated in BN nanotubes. Adv Mater 17:545–549
74. Saulig-Wenger K, Cornu D, Chassagneux F, Ferro G, Epicier T, Miele P (2002) Direct synthesis of β-SiC and h-BN coated β-SiC nanowires. Solid State Commun 124:157–161
75. Bechelany M, Brioude A, Stadelmann P, Ferro G, Cornu D, Miele P (2007) Very long SiC-based coaxial nanocables with tunable chemical composition. Adv Funct Mater 17:3251–3257
76. Zhong B, Song L, Huang X, Zhang X, Wen G, Zhou Y (2011) Novel coaxial SiC-SiO_2-BN nanocable: large-scale synthesis, formation mechanism and photoluminescence property. J Mater Chem 21:14432–14440
77. Hao Y-J, Jin G-Q, Han X-D, Guo X-Y (2006) Synthesis and characterization of bamboo-like SiC nanofibers. Mater Lett 60:1334–1337
78. Wang D-H, Xu D, Wang Q, Hao Y-J, Jin G-Q, Guo X-Y, Tu KN (2008) Periodically twinned SiC nanowires. Nanotechnology 19:215602
79. Shen G, Bando Y, Ye C, Liu B, Golberg D (2006) Synthesis, characterization and field-emission properties of bamboo-like β-SiC nanowires. Nanotechnology 17:3468–3472
80. Wu R, Pan Y, Yang G, Gao M, Wu L, Chen J, Zhai R, Lin J (2007) Twinned SiC zigzag nanoneedles. J Phys Chem C 111:6233–6237
81. Wu R, Li B, Gao M, Chen J, Zhu Q, Pan Y (2008) Tuning the morphologies of SiC nanowires via the control of growth temperature, and their photoluminescence properties. Nanotechnology 19:335602

82. Wei J, Li K-Z, Li H-J, Fu Q-G, Zhang L (2006) Growth and morphology of one-dimensional SiC nanostructures without catalyst assistant. Mater Chem Phys 95:140–144
83. Hao Y-J, Wagner JB, Su DS, Jin G-Q, Guo X-Y (2006) Beaded silicon carbide nanochains via carbothermal reduction of carbonaceous silica xerogel. Nanotechnology 17:2870–2874
84. Li Z, Gao W, Meng A, Geng Z, Gao L (2009) Large-scale synthesis and Raman and photoluminescence properties of single crystalline β-SiC nanowires periodically wrapped by amorphous SiO2 nanospheres 2. J Phys Chem C 113:91–96
85. Meng A, Zhang M, Gao W, Sun S, Li Z (2011) Large-scale synthesis of β-SiC nanochains and their Raman/photoluminescence properties. Nanoscale Res Lett 6:34
86. Shen G, Bando Y, Golberg D (2007) Self-assembled hierarchical single-crystalline β-SiC nanoarchitectures. Cryst Growth Des 7:35–38
87. Guo JZ, Zuo Y, Li ZJ, Gao WD, Zhang JL (2007) Preparation of SiC nanowires with fins by chemical vapor deposition. Physica E 39:262–266
88. Lin ZJ, Wang L, Zhang J, Guo X-Y, Yang W, Mao H-K, Zhao Y (2010) Nanoscale twinning-induced elastic strengthening in silicon carbide nanowires. Scripta Mater 63:981–984
89. Pozuelo M, Kao WH, Yang J-M (2013) High-resolution TEM characterization of SiC nanowires as reinforcements in a nanocrystalline Mg-matrix. Mater Charact 77:81–88
90. Seo W-S, Koumoto K, Aria S (2000) Morphology and stacking faults of β-silicon carbide whisker synthesized by carbothermal reduction. J Am Ceram Soc 83:2584–2592
91. Li HJ, Li ZJ, Meng AL, Li KZ, Zhang XN, Xu YP (2003) SiC nanowire networks. J Alloy Compd 352:279–282
92. Shim HW, Huang H (2007) Nanowebs and nanocables of silicon carbide. Nanotechnology 18:335607
93. Wu C, Liao X, Chen J (2010) The formation of symmetric SiC bi-nanowires with a Y-shaped junction. Nanotechnology 21:405303
94. Ho GW, Wong ASW, Kang D-J, Welland ME (2004) Three-dimensional crystalline SiC nanowire flowers. Nanotechnology 15:996–999
95. Magyar AP, Aharonovich I, Baram M, Hu EL (2013) Photoluminescent SiC tetrapods. Nano Lett 13:1210–1215
96. Zhang H-F, Wang C-M, Wang L-S (2002) Helical crystalline SiC/SiO_2 core-shell nanowires. Nano Lett 2:941–944
97. Zhang D, Alkhateeb A, Han H, Mahmood H, McIlroy DN, Norton MG (2003) Silicon carbide nanosprings. Nano Lett 3:983–987
98. Xi G, Peng Y, Wan S, Li T, Yu W, Qian Y (2004) Lithium-assisted synthesis and characterization of crystalline 3C-SiC nanobelts. J Phys Chem B 108:20102–20104
99. Wei G, Qin W, Kim R, Sun J, Zhu P, Wang G, Wang L, Zhang D, Zheng K (2008) Quantum confinement effect and field emission characteristics of ultrathin 3C-SiC nanobelts. Chem Phys Lett 461:242–245
100. Zhang H, Ding W, He K, Li M (2010) Synthesis and characterization of crystalline silicon carbide nanoribbons. Nanoscale Res Lett 5:1264–1271
101. Chen J, Wu R, Yang G, Pan Y, Lin J, Wu L, Zhai R (2008) Synthesis and photoluminescence of needle-shaped 3C-SiC nanowires on the substrate of PAN carbon fiber. J Alloy Compd 456:320–323
102. Wu R, Zhou K, Wei J, Huang Y, Su F, Chen J, Wang L (2012) Growth of tapered SiC nanowires on flexible carbon fabric: toward field emission applications. J Phys Chem C 116:12940–12945
103. Zhou J-Y, Chen Z-Y, Zhou M, Gao X-P, Xie E-Q (2009) SiC nanorods grown on electrospun nanofibers using Tb as catalyst: fabrication, characterization, and photoluminescence properties. Nanoscale Res Lett 4:814–819
104. Zhou J-Y, Chen Z-Y, Xu X-B, Zhou M, Ma Z-W, Zhao J-G, Li R-S, Xie E-Q (2010) Terbium-catalyzed selective area growth of SiC nanorods: synthesis, optimal growth, and field emission properties. J Am Ceram Soc 93:488–493

105. Seong H-K, Choi H-J, Lee S-K, Lee J-I, Choi D-J (2004) Optical and electrical transport properties in silicon carbide nanowires. Appl Phys Lett 85:1256–1258
106. Han XD, Zhang YF, Zheng K, Zhang XN, Zhang Z, Hao YJ, Guo XY, Yuan J, Wang ZL (2007) Low-temperature in situ large strain plasticity of ceramic SiC nanowires and its atomic-scale mechanism. Nano Lett 7:452–457
107. Zhang Y, Han X, Zheng K, Zhang Z, Zhang X, Fu J, Ji Y, Hao Y, Guo X, Wang Z (2007) Direct observation of super-plasticity of beta-SiC nanowires at low temperature. Adv Funct Mater 17:3435–3440
108. Perisanu S, Vincent P, Ayari A, Choueib M, Purcell ST, Bechelany M, Cornu D (2007) High Q factor for mechanical resonances of batch-fabricated SiC nanowires. Appl Phys Lett 90:043113
109. Perisanu S, Gouttenoire V, Vincent P, Ayari A, Choueib M, Bechelany M, Cornu D, Purcell ST (2008) Mechanical properties of SiC nanowires determined by scanning electron and field emission microscopies. Phys Rev B 77:165434
110. Yang W, Araki H, Tang C, Thaveethavorn S, Kohyama A, Suzuki H, Noda T (2005) Single-crystal SiC nanowires with a thin carbon coating for stronger and tougher ceramic composites. Adv Mater 17:1519–1523
111. Lee KM, Choi TY, Lee SK, Poulikakos D (2010) Focused ion beam-assisted manipulation of single and double β-SiC nanowires and their thermal conductivity measurements by the four-point-probe 3-ω method. Nanotechnology 21:125301
112. Jänis A, Yao Y, Klement U (2011) Dielectric properties of SiC nanowires with different chemical compositions. IEEE T Nanotechnol 10:751–756
113. Makeev MA, Srivastava D, Menon M (2006) Silicon carbide nanowires under external loads: an atomistic simulation study. Phys Rev B 74:165303
114. Zhang T-Y, Luo M, Chan WK (2008) Size-dependent surface stress, surface stiffness, and Young's modulus of hexagonal prism [111] β-SiC nanowires. J Appl Phys 103:104308
115. Wang Z, Zu X, Gao F, Weber WJ (2008) Atomistic simulations of the mechanical properties of silicon carbide nanowires. Phys Rev B 77:224113
116. Wang J, Lu C, Wang Q, Xiao P, Ke F, Bai Y, Shen Y, Liao X, Gao H (2012) Influence of microstructures on mechanical behaviours of SiC nanowires: a molecular dynamics study. Nanotechnology 23:025703
117. Rurali R (2005) Electronic and structural properties of silicon carbide nanowires. Phys Rev B 71:205405
118. Yan B, Zhou G, Duan W, Wu J, Gu B-L (2006) Uniaxial-stress effects on electronic properties of silicon carbide nanowires. Appl Phys Lett 89:023104
119. Durandurdu M (2006) Electronic and mechanical properties of wurtzite type SiC nanowires. Phys Stat Sol (b) 243:R37–R39
120. Wang Z, Zhao M, He T, Zhang X, Xi Z, Yan S, Liu X, Xia Y (2009) First-principles study of faceted single-crystalline silicon carbide nanowires and nanotubes. J Phys Chem C 113:856–861
121. Wang Z, Zhao M, He T, Zhang H, Zhang X, Xi Z, Yan S, Liu X, Xia Y (2009) Orientation-dependent stability and quantum-confinement effects of silicon carbide nanowires. J Phys Chem C 113:12731–12735
122. Wang Z, Wang S, Zhang C, Li J (2011) First principles study of the electronic properties of twinned SiC nanowires. J Nanopart Res 13:185–191
123. Tak YJ, Ryu YH, Yong K (2005) Atomically abrupt heteronanojunction of ZnO nanorods on SiC nanowires prepared by a two-step process. Nanotechnology 16:1712–1716
124. Zhou W, Yan L, Wang Y, Zhang Y (2006) SiC nanowires: a photocatalytic nanomaterial. Appl Phys Lett 89:013105
125. Zhou WM, Fang F, Hou ZY, Yan LJ, Zhang YF (2006) Field-effect transistor based on β-SiC nanowire. IEEE Electr Device L 27:463–465
126. Jang C-O, Kim T-H, Lee S-Y, Kim D-J, Lee S-K (2008) Low-resistance ohmic contacts to SiC nanowires and their applications to field-effect transistors. Nanotechnology 19:345203

127. Rogdakis K, Bano E, Montes L, Bechelany M, Cornu D, Zekentes K (2011) Rectifying source and drain contacts for effective carrier transport modulation of extremely doped SiC nanowire FETs. IEEE T Nanotechnol 10:980–984
128. He Z, Wang L, Gao F, Wei G, Zheng J, Cheng X, Tang B, Yang W (2013) Synthesis of n-type SiC nanowires with tailored doping levels. CrystEngComm 15:2354–2358
129. Niu JJ, Wang JN (2009) A novel self-cleaning coating with silicon carbide nanowires. J Phys Chem B 113:2909–2912
130. Guiffard B, Guyomar D, Seveyrat L, Chowanek Y, Bechelany M, Cornu D, Miele P (2009) Enhanced electroactive properties of polyurethane films loaded with carbon-coated SiC nanowires. J Phys D: Appl Phys 42:055503
131. Feng XL, Matheny MH, Zorman CA, Mehregany M, Roukes ML (2010) Low voltage nanoelectromechanical switches based on silicon carbide nanowires. Nano Lett 10:2891–2896
132. Shim HW, Kuppers JD, Huang H (2009) Strong friction of silicon carbide nanowire films. Nanotechnology 20:025704
133. Lantz MA, Gotsmann B, Jaroenapibal P, Jacobs TDB, O'Connor SD, Sridharan K, Carpick RW (2012) Wear-resistant nanoscale silicon carbide tips for scanning probe applications. Adv Funct Mater 22:1639–1645
134. Chiu S-C, Yu H-C, Li Y-Y (2010) High electromagnetic wave absorption performance of silicon carbide nanowires in the Gigahertz range. J Phys Chem C 114:1947–1952
135. Wu R, Zhou K, Yang Z, Qian X, Wei J, Liu L, Huang Y, Kong L, Wang L (2013) Molten-salt-mediated synthesis of SiC nanowires for microwave absorption applications. CrystEngComm 15:570–576
136. Guo X-N, Shang R-J, Wang D-H, Jin G-Q, Guo X-Y, Tu KN (2010) Avoiding loss of catalytic activity of Pd nanoparticles partially embedded in nanoditches in SiC nanowires. Nanoscale Res Lett 5:332–337

Chapter 6
SiC Nanotubes

In most cases, the silicon carbide nanotubes have been fabricated with assistance of some templates. Unlike carbon nanotubes, the silicon carbide nanotubes contain two types of elements, silicon, and carbon; therefore, the structure of the SiC nanotube is basically different from that of the carbon nanotube. In fact, most of the currently reported SiC nanotubes are not standard sp^2-bonded graphite-like nanotubes and instead, the walls of these nanotubes have sp^3-bonded bulk-SiC-like crystal structures. Some are only the rolled-up nanostructures of bulk SiC, and others are composed of polycrystalline SiC particles. Several factors account for the difficulty in synthesizing actual SiC nanotubes. First, the Si atoms on the surface of the SiC nanotubes are readily oxidized even at room temperature and this will destroy the nanotube structure. Secondly, the theoretical study shows that the SiC nanowires may be more stable than the SiC nanotubes of the same diameter in the common experimentally approachable (a few nanometers or larger) size regime. Thirdly, unlike graphene which can be directly prepared by exfoliation of graphite, there is no graphite-like sp^2-structured SiC crystal in nature from which the actual SiC nanotubes can be extracted. Therefore, the research field of SiC nanotubes is somewhat strange in that the experimentalists generally synthesize bulk-like sp^3-structured SiC nanotubes, whereas the theorists generally investigate the structures and properties of actual sp^2-structured SiC nanotubes.

6.1 Fabrication Using Templates

In general, silicon carbide nanotubes are fabricated by using some templates, especially carbon nanotubes, where the silicon source material reacts with the carbon nanotube to yield SiC nanotube that maintains the morphology of the mother nanotube. Silicon carbide nanotube can also be synthesized as the shell of some core material, and subsequent removal of the core nanowire by acid etching gives rise to relatively pure SiC nanotube.

J. Fan and P.K. Chu, *Silicon Carbide Nanostructures*,
Engineering Materials and Processes, DOI 10.1007/978-3-319-08726-9_6

6.1.1 Synthesis Using Carbon Nanotubes/Nanofibers

Shape memory synthesis is one of the earliest methods used to synthesize SiC nanotubes [1]. The SiO vapor generated by heating a Si/SiO_2 mixture at 1,200–1,350 °C serves as the silicon source material, the subsequent gas–solid reaction between SiO and a shaped carbon template at lower temperature 1,000–1,250 °C yields β-SiC material that has the same shape as the initial carbon material. The gas–solid reaction between SiO vapor and carbon nanotubes produces SiC nanotubes with internal diameter of 30–100 nm, whereas the reaction between SiO and carbon nanofibers produces SiC nanotubes with internal diameter of 10–80 nm (Fig. 6.1). X-ray diffraction confirms that the product is pure β-SiC with relatively good crystallization. The lattice fringes are parallel to the axis of the tube (Fig. 6.1) and have an interlayer distance of 0.36 nm, which is consistent with the spacing of two C planes in β-SiC (0.359 nm). The SiC nanotubes can act as favorable catalyst support in the reaction of low-temperature selective oxidation of H_2S into sulfur [2]. The SiC nanotubes improve both desulfurization activity of the catalyst and the solid sulfur storage capacity.

Silicon carbide nanowires and nanotubes have been prepared by thermal reaction between SiO and multiwalled carbon nanotubes [3]. Both β-SiC nanowires and biaxial $SiC–SiO_x$ nanowires (Fig. 6.2a) are observed, but the most interesting structure found is the multiwalled SiC nanotubes (Fig. 6.2b), which have interlayer spacing of 3.5–4.5 Å. They are produced by the reaction of Si (via

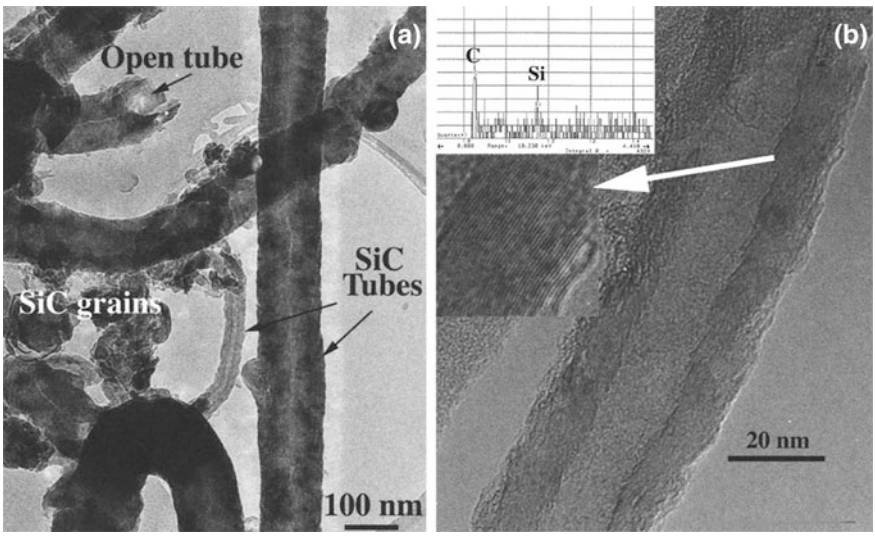

Fig. 6.1 **a** TEM and **b** high-resolution TEM images of the SiC nanotubes obtained by shape memory synthesis from carbon nanofibers. Reprinted with permission from [1]. Copyright 2001, Elsevier

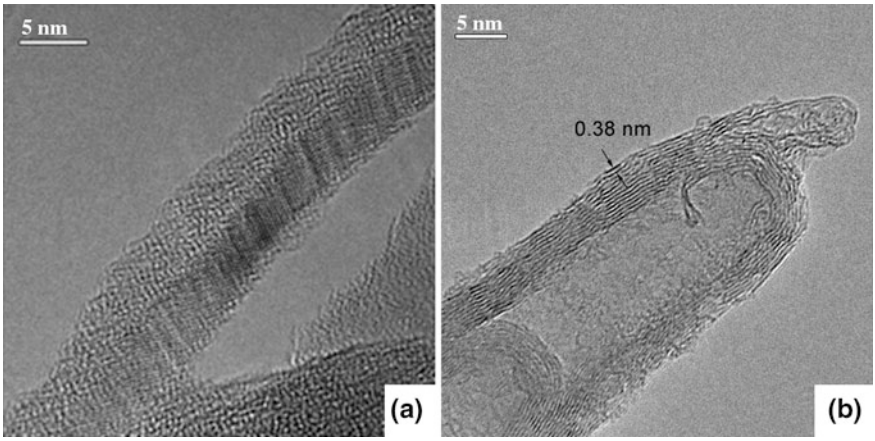

Fig. 6.2 **a** HRTEM image of the biaxial SiC–amorphous SiO_x nanowire obtained by reaction between Si and carbon nanotubes. **b** HRTEM image of a SiC nanotube with 3.8 Å interlayer spacing. Reprinted with permission from [3]. Copyright 2002, American Chemical Society

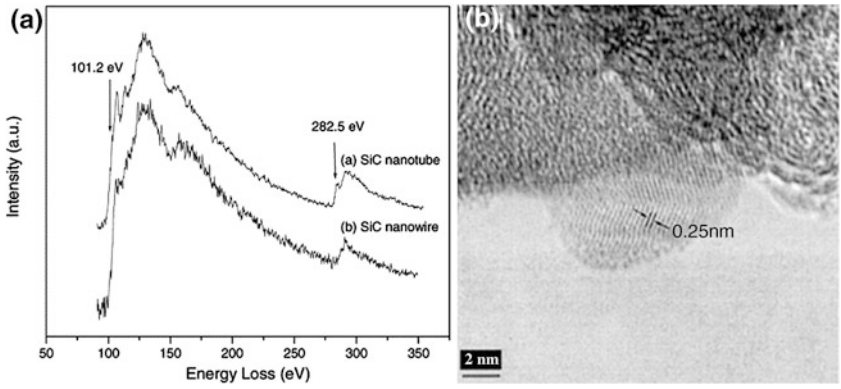

Fig. 6.3 **a** Electron energy loss spectra of a single SiC nanotube and a single SiC nanowire obtained from the same sample. **b** HRTEM image of the SiC nanotube after electron beam annealing for 5 min. Reprinted with permission from [3]. Copyright 2002, American Chemical Society

disproportionation of SiO) and the templates of the multiwalled carbon nanotube at 935 °C. The elemental mapping confirms that there are silicon and carbon elements in the outer layer of the nanotube. The electron energy loss spectroscopy measurement of a single multiwalled SiC nanotube indicates that the Si $L_{3,2}$-edge shifts to a higher energy at 101.2 eV from 99.3 eV of pure Si and the C *K*-edge shifts to a lower energy at 282.5 eV from 284 eV of pure carbon, showing strong chemical bonding between Si and C. The electron energy loss spectra of the SiC nanotubes and the β-SiC nanowires (Fig. 6.3a) are quite similar except for the pre-

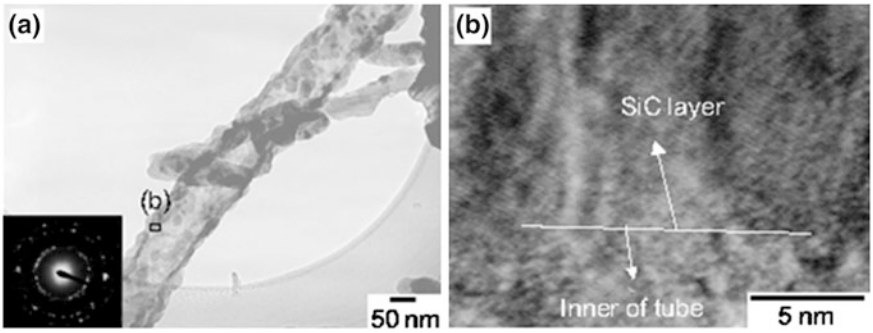

Fig. 6.4 **a** TEM and **b** HRTEM images of single-phase silicon carbide nanotube. Reprinted with permission from [4]. Copyright 2005, Wiley-VCH Verlag GmbH & Co. KGaA

edge peaks, further confirming the β-SiC structure of the nanotubes. The multi-walled SiC nanotubes will gradually transform to β-SiC crystals after continuous electron beam annealing under TEM (Fig. 6.3b), and the ultimately formed crystalline structure possesses a lattice spacing of 2.5 Å, corresponding to that of the {111} planes of β-SiC. This further confirms that the as-synthesized nanotube is indeed a SiC nanotube.

Single-phase SiC nanotubes have been synthesized by reaction of carbon nanotubes with Si powder at 1,200 °C [4]. Transmission electron microscopy reveals the existence of both single-phase SiC nanotubes and C−SiC coaxial nanotubes, the latter are carbon nanotubes sheathed by SiC layer. The single-phase SiC nanotubes are polycrystalline and comprise grains with size of around 20 nm. The ratio of number of single-phase SiC nanotubes (Fig. 6.4) to C−SiC nanotubes increases after heating the sample at 600 °C in air resulting from removal of the remaining carbon.

The SiC nanotubes have been synthesized by high-temperature reaction between multiwalled carbon nanotubes and Si powder in flowing ammonia at 1,350 °C [5]. The SEM and TEM observations (Fig. 6.5a) reveal that the SiC nanotubes are carbon-filled and open-ended, and they have lengths between 0.7–1 μm and diameters between 45–70 nm. Raman spectrum (Fig. 6.5b) of the nanotubes comprises a strong peak at 900 cm^{-1}, which is assigned to the LO mode of SiC but with a significant red shift relative to bulk value due to phonon confinement effect. This Raman peak is asymmetric with a broad tail toward low frequencies, which may be caused by mixing of hexagonal and cubic polytypes in the nanotubes. The electron diffraction analysis shows that cubic polytype SiC dominates over other hexagonal polytypes SiC in the sample. The infrared absorption spectrum (Fig. 6.5c) comprises a sharp band at around 790 cm^{-1} (TO phonon) with a shoulder at 950 cm^{-1} (LO phonon), and both shifts to lower frequencies relative to bulk values due to spatial confinement.

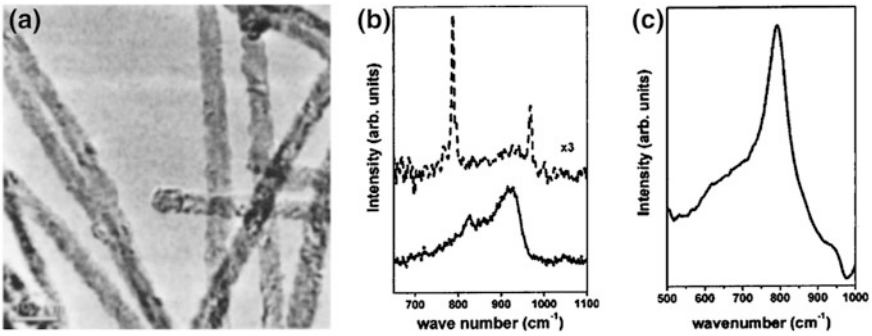

Fig. 6.5 *Left panel* TEM image of the SiC nanotubes. *Middle panel* Raman spectra of the as-produced SiC nanotubes (*lower*), and reference sample (*upper*). *Right panel* infrared absorption spectrum of the SiC nanotubes. Reprinted with permission from [5]. Copyright 2005, AIP Publishing LLC

6.1.2 Formation on Core Nanowires

The SiC/ZnS nanocables and SiC nanotubes and other structures have been synthesized using ZnS nanowires, nanoribbons, and sheets as templates by two-stage thermal reactions [6]. During this synthesis, a mixture of SiO and ZnS powders are first heated at 1,150 °C in flowing argon and then heated at 1,400 °C in flowing CH_4 gas. The obtained SiC/ZnS nanocables comprise ZnS cores with diameter of 50–130 nm and polycrystalline SiC shells with thickness of 15–50 nm. The removal of the ZnS cores from the nanocables by HCl etching gives rise to open-ended, straight, and uniform SiC nanotubes (Fig. 6.6a–f). The high-resolution TEM observation of a SiC tube wall reveals the presence of numerous nanocrystals with sizes of 4–10 nm exhibiting (111) lattice fringes of β-SiC. The electron diffraction pattern shows continuous polycrystalline rings corresponding to (111), (220), and (311) planes of β-SiC, confirming that the SiC nanotube is a polycrystal rather than a single crystal. The energy-dispersive X-ray spectrum reveals the chemical composition of SiC in the nanotube wall. The SiC nanotubes show room temperature photoluminescence with a strong symmetric emission band centered at 517 nm. Large and irregular thin SiC tubes or bags are prepared by HCl etching of the as-prepared ZnS sheets encapsulated by SiC layers (Fig. 6.6g–i). The electron diffraction confirms that these structures are also polycrystalline β-SiC.

Various hollow SiC nanostructures can be synthesized by employing ZnO nanostructure templates [7]. The SiC shell layers are deposited on one-, two-, and three-dimensional complex-shaped ZnO nanostructures via chemical vapor deposition using SiH_4 and CH_4 gases as starting materials at temperature 250–300 °C. Fruitful SiC-shelled nanostructures are obtained after removal of the ZnO templates by HCl etching (Fig. 6.7). The synthesized SiC nanoshells are amorphous due to the low reaction temperature employed, as demonstrated by the halo-like electron diffraction pattern (inset of Fig. 6.7).

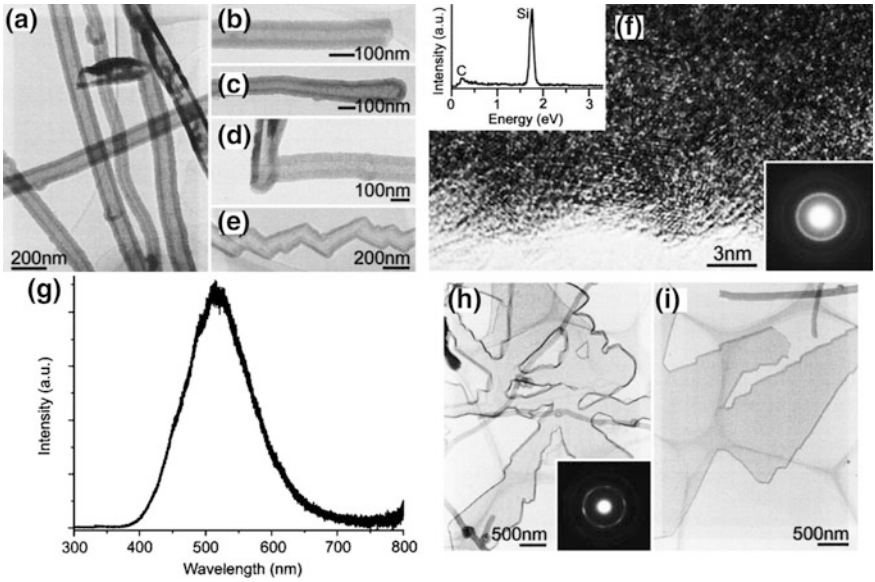

Fig. 6.6 **a–e** TEM images of the SiC nanotubes. **f** HRTEM image of a SiC nanotube wall. *Left inset* is the energy-dispersive X-ray spectrum. *Right inset* is the electron diffraction pattern showing (111), (220), and (311) plane reflections of β-SiC. **g** Room-temperature PL spectrum of the SiC nanotubes. (**h**, **i**) TEM images of large SiC thin tubes or bags with irregular shapes. Reprinted with permission from [6]. Copyright 2004, AIP Publishing LLC

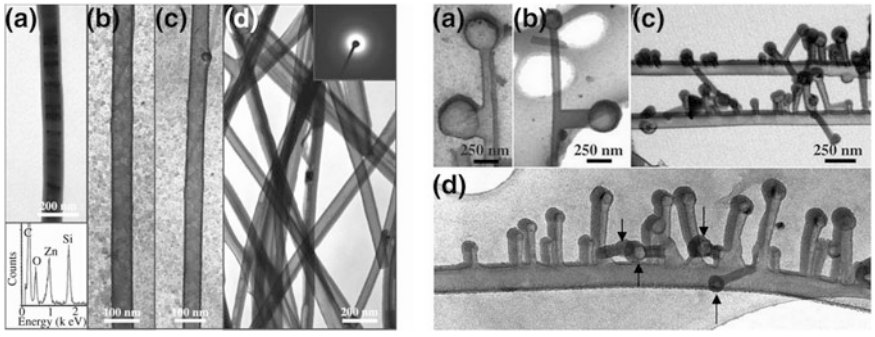

Fig. 6.7 *Left panel* **a** TEM image of ZnO–SiC core–shell nanobelt. The *inset* is the energy-dispersive X-ray spectrum showing elements of C, Si, O, and Zn. **b–d** TEM images of the SiC nanotubes after removal of ZnO cores. The *inset* is an electron diffraction pattern. *Right panel* TEM images of the SiC hollow nanojunctions. Reprinted with permission from [7]. Copyright 2006, Wiley-VCH Verlag GmbH & Co. KGaA

Silicon carbide nanotubes have been fabricated by magnetron sputtering at room temperature using SiC target as source material and electrospun polyvinylpyrolidone nanofibers as templates [8]. The polyvinylpyrolidone core is eliminated by

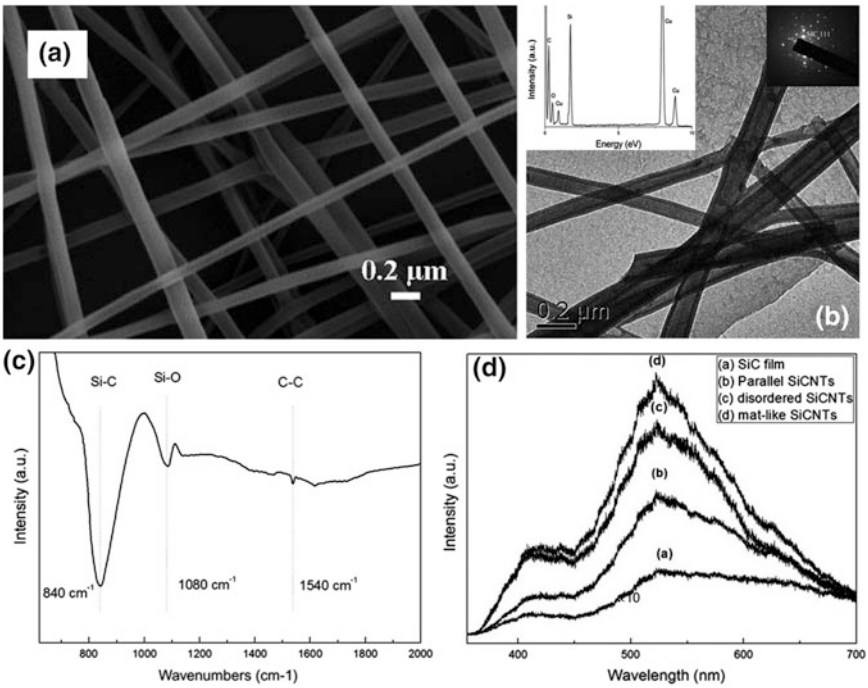

Fig. 6.8 **a** SEM and **b** TEM images of the SiC nanotubes. *Left inset* is the energy-dispersive X-ray spectrum showing C, Si, and O elements. *Right inset* is the electron diffraction pattern, in accordance with β-SiC (111) lattice planes. **c** Infrared transmission and **d** PL spectrum of the SiC nanotubes. Reprinted with permission from [8]. Copyright 2009, Elsevier

anneal at 500 °C and further anneal at 1,250 °C yields well-crystallized SiC nanotubes. SEM and TEM measurements (Fig. 6.8a, b) reveal that the nanotubes have an average diameter of 150 nm and a wall thickness of about 40 nm. The energy-dispersive X-ray spectroscopy shows that the nanotubes comprise Si, C, and O elements. The infrared absorption (Fig. 6.8c, d), X-ray diffraction, and electron diffraction measurements indicate that the annealed nanotubes are polycrystalline SiC crystals coated with SiO_2 and free carbon. The nanotubes have photoluminescence with two peaks centered at 420 and 523 nm, respectively. The SiC nanotubes can also be synthesized using Ge or Si nanowires as templates [9, 10].

6.1.3 Other Templates

The alumina template has been used to synthesize well-aligned tubular SiC arrays by thermal decomposition of polymethylsilane at 1,250 °C in argon atmosphere [11]. The template is removed by HF etching. The wall morphology (Fig. 6.9) can

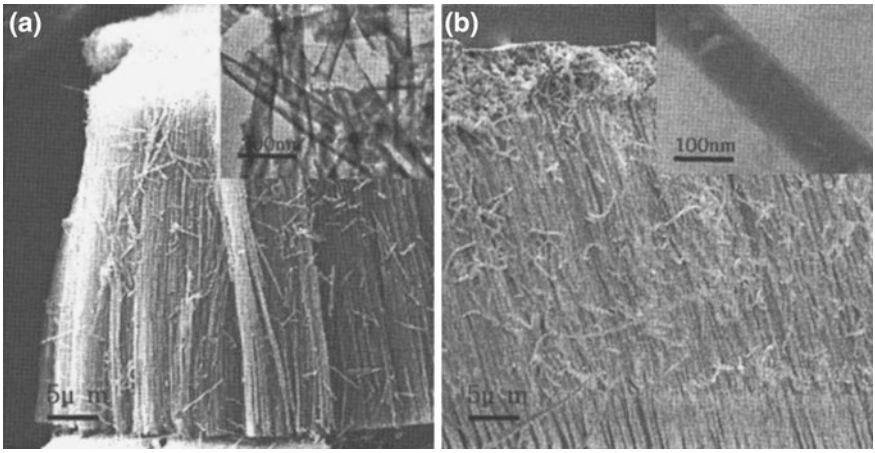

Fig. 6.9 SEM images of 100-nm diameter tubular SiC **a** nanotubes and **b** nanorods obtained from polymethylsilane. The *insets* show TEM images. Reprinted with permission from [11]. Copyright 2005, AIP Publishing LLC

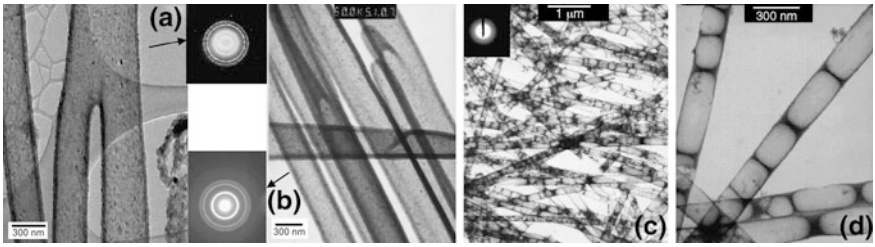

Fig. 6.10 TEM images and selected area electron diffraction patterns for the **a**, **b** CVD-derived SiC nanotubes after anneal in argon at 1,600 °C and **c**, **d** bamboo-like SiC nanofibers obtained from pyrolysis of polymers. Reprinted with permission from [12]. Copyright 2005, Elsevier

be tuned by changing the number of infiltration steps, the initial infiltration yields tubular SiC arrays with wall thickness of 35 nm and diameter of 200 nm, whereas the repeated infiltration yields SiC nanorods.

Tubular and bamboo-like SiC nanostructures can be synthesized by CVD or pyrolysis inside porous alumina (thickness: 60 μm, pore size: 250 nm) using carbosilane as precursors in flowing nitrogen gas at 1,000 °C [12]. The alumina template is removed by HF etching. A post-anneal at 1,600 °C in argon alters the morphology of the product. The as-prepared SiC nanotubes by CVD are amorphous and transform into polycrystalline β-SiC nanotubes after annealing at 1,600 °C (Fig. 6.10a, b). The SiC nanotubes have outer diameter of 200–300 nm and wall thickness of 20–40 nm and length up to the thickness of the original

alumina template. Pyrolysis of the polymer gives rise to amorphous bamboo-like SiC nanofibers (Fig. 6.10c, d), and they convert into a collection of single-crystal SiC nanofibers and other small particles after anneal at 1,600 °C.

Mesoporous silica has been employed to synthesize the high surface area SiC materials including whiskers and nanotubes [13]. The SiC materials are prepared by carbothermal reduction of mesoporous silica/sucrose composites. The SiC whiskers growing in the [111] direction are achieved at reaction temperature of 1,250 or 1,300 °C and reduction duration up to 14 h. The whiskers have diameters of 50–90 nm and lengths larger than 20 μm. The reaction with a prolonged period of 20 h at 1,250 or 1,300 °C yields SiC nanotubes with diameters of 60–100 nm and lengths larger than 10 μm. The C/β-SiC/Si hybrid microtubes have been fabricated by releasing prestressed C/Si bilayer structures followed by post-annealing [14]. The β-SiC nanoparticles with size of 3–5 nm form at the C/Si interface via solid phase reaction. The Raman spectrum of the hybrid microtubes comprises two peaks at 776–783 and 921–941 cm^{-1}, corresponding to the TO and LO phonon modes of β-SiC nanoparticles.

6.2 Fabrication by Other Methods

The SiC nanotubes with very small diameters have been synthesized under supercritically hydrothermal conditions without use of metal catalyst [15]. The nanotubes are prepared by hydrothermal reaction of 50-nm diameter SiC powder and 30-nm diameter SiO_2 powder in distilled water under stirring in a sealed reaction kettle at temperature of 470 °C and pressure of 8.0 MPa. The product comprises crystalline β-SiC nanotubes and some carbon grains. The nanotubes (Fig. 6.11a, b) are multiwalled, with a very thin hollow core, and their outer diameters are smaller than 10 nm and their lengths are many micrometers. The lattice fringes have a spacing of 0.25 nm, in consistent with the spacing of β-SiC (111) planes. The nanotubes have a thin amorphous silica sheath. X-ray diffraction and the electron diffraction confirm the single crystalline β-SiC phase of the nanotubes. A small amount of SiC nanotubes with lattice spacing ranging from 0.26 to 0.30 nm are also present, suggesting that these nanotubes are carbon-deficient SiC nanotubes. The Raman spectrum of the nanotubes (Fig. 6.11c) comprises two peaks at 775.7 and 997.7 cm^{-1}, which are assigned to the TO and LO phonon modes of β-SiC nanostructures; however, the LO mode shows a significant blue shift rather than generally observed red shift relative to bulk value. The signals at 1,329.8 and 1,568.8 cm^{-1} are graphite E_{2g} and A_{1g} modes, indicating that the graphitic carbon coexists in the SiC nanotube sample. The infrared spectrum of the sample (Fig. 6.11d) comprises a strong absorption band at 791 cm^{-1} corresponding to the TO phonon mode of β-SiC, and the absorption bands at 472 and 1,107 cm^{-1} are attributed to silica, including silica shells of SiC nanotubes and unreacted SiO_2 in the sample.

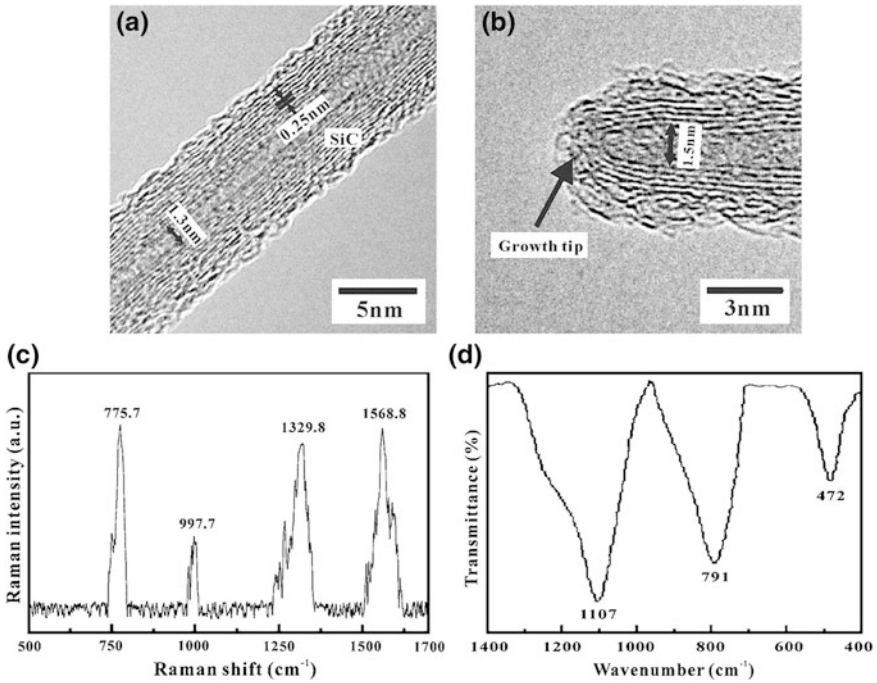

Fig. 6.11 HRTEM images of SiC nanotubes showing multiwalled crystalline SiC layer. **a** Tubular body with interlayer spacing of 0.25 nm corresponding to β-SiC {111} planes. **b** Nanotube tip with semicircular structure and diameter of 1.5 nm in the inner pore. **c** Raman spectrum of the SiC nanotubes. The peaks at 775.7 and 997.7 cm^{-1} belong to TO and LO phonon modes of β-SiC and peaks at 1,329.8 and 1,568.8 cm^{-1} correspond to graphite E_{2g} and A_{1g} modes. **d** Infrared spectrum of the SiC nanotubes. Reprinted with permission from [15]. Copyright 2006, AIP Publishing LLC

The tubular single-crystal β-SiC nanostructures have been prepared by simple thermal evaporation of C_{60} on a Si substrate without using template and catalyst [16]. The tubular SiC nanostructures have diameters 40–100 nm and lengths up to several micrometers. TEM analysis shows that the tubular nanostructure is β-SiC single crystal growing along [111] direction (Fig. 6.12). The tubular β-SiC shows good field electron emission character with a turn-on field smaller than 5 V/μm.

6.3 Theoretical Studies

6.3.1 Structural and Electronic Properties

The density functional calculation predicts the existence of the graphitic and tubular form of silicon carbide [17]. Figure 6.13a, b show atomic geometries and

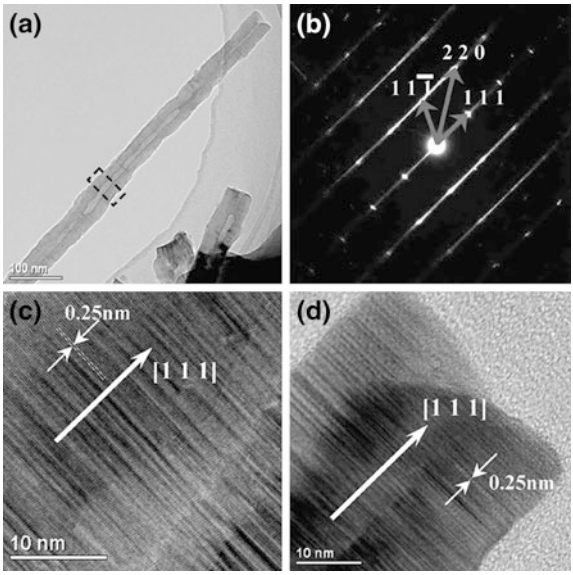

Fig. 6.12 **a** TEM image of tubular SiC nanostructure. **b** Corresponding selected area electron diffraction pattern. HRTEM images taken from **c** the marked area in **a** and from **d** the *top* of an open end. Reprinted with permission from [16]. Copyright 2009, Royal Society of Chemistry

corresponding electronic band structures of SiC nanotubes with helicities of (5, 5) and (9, 0). The band structure possesses an indirect gap for the (5, 5) nanotube and a direct gap for the (9, 0) nanotube. The optical transition between the highest occupied band and lowest unoccupied band is allowed in the (9, 0) nanotubes and thus there should be strong light absorption and emission. The direct bandgap of (n, 0) nanotubes ($n = 6$–8) decreases with decreasing number n. The elastic energy of the SiC nanotube increases with decreasing diameter (Fig. 6.13c) and is smaller than that of the carbon nanotube of the same diameter.

In comparison with carbon nanotubes, silicon carbide nanotubes may have more types because there are two types of elements in the SiC nanotubes. The structure and stability of various SiC nanotube structures have been investigated using the generalized tight-binding molecular dynamics scheme and ab initio method [18]. The system size is limited to a maximum of 72 atoms due to the computational demand of the ab initio method. Hydrogen atoms are attached to the edge atoms to passivate all dangling bonds. The calculation demonstrates two highly stable distinct geometries for each chirality (zigzag or armchair) of SiC nanotube, as shown in Fig. 6.14. Both nanotubes are constructed by rolling up the corresponding graphene-like two-dimensional sheet. Both sheets contain a Si to C ratio of 1:1. Type 1 hexagonal network consists of alternating Si and C atoms, and each Si atoms have only C atoms as nearest neighbors and vice versa. Type 2 structure is obtained when each Si atom have two C atoms and one Si atom as nearest neighbors and vice versa. The total energy calculation using ab initio method demonstrates that type 1 structure is more stable than type 2 structures by 0.43 eV per SiC atom pair. In type 1 SiC nanotubes, the armchair (6, 6) nanotube is slightly more stable than the zigzag (12, 0) nanotube by 0.05 eV per SiC atom

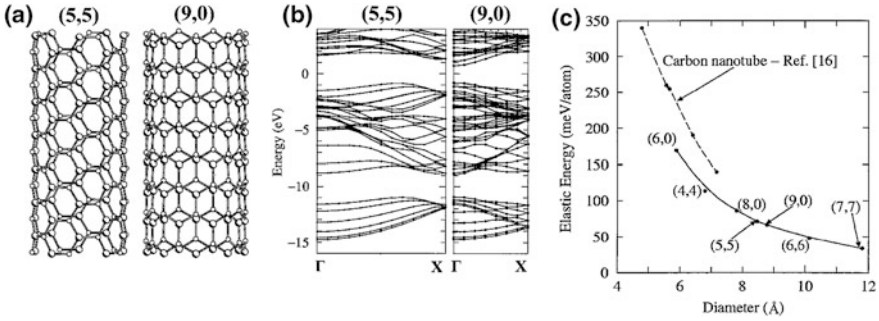

Fig. 6.13 **a** Atomic geometries and **b** corresponding electronic band structures of armchair-type (5, 5) and zigzag-type (9, 0) nanotubes. The hatched and open circles denote Si and C atoms, respectively. **c** Strain energy of SiC nanotubes versus diameter. The helical indices of SiC nanotubes are denoted. The *solid* and *dotted lines* are guides to the eye. Reprinted with permission from [17]. Copyright 2002, AIP Publishing LLC

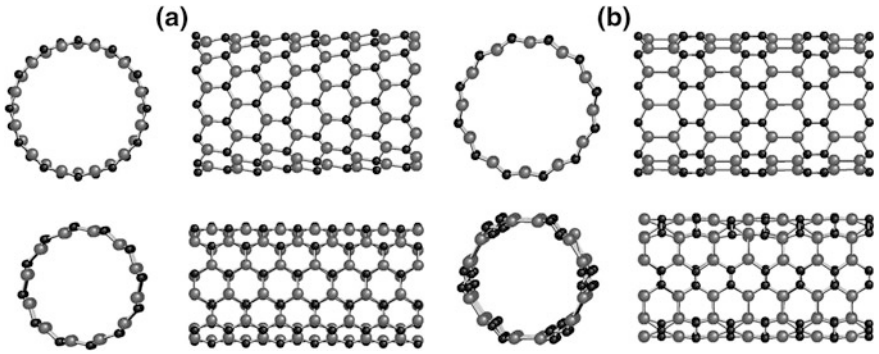

Fig. 6.14 **a** Type 1 and **b** type 2 single-walled SiC nanotubes of zigzag (*top*) and armchair (*bottom*) chirality obtained by rolling up corresponding graphene-like sheet and performing generalized tight-binding molecular dynamics relaxation. *Gray* (*black*) balls denote Si (C) atoms. Si and C atoms lie in different rolled planes. Reprinted with permission from [18]. Copyright 2004, American Physical Society

pair. On the contrary, in type 2 SiC nanotubes, the zigzag (12, 0) nanotube is more stable than the armchair (6, 6) nanotube by 0.45 eV per SiC atom pair. However, the energy differences between all structures considered are expected to diminish with increasing diameter of the nanotubes. The Si–C bond length is 1.87 Å, irrespective of the nanotube type, and this value is slightly smaller than that of 3C-SiC structure, 1.89 Å. The calculation of the density of states (Fig. 6.15a) shows that these two types of SiC nanotube have quite different bandgap values. Type 1 SiC nanotubes have large bandgaps, 3.23 and 3.53 eV for zigzag and armchair chiralities, respectively. These values are similar to the bandgap values of bulk SiC (3–3.3 eV). In contrast, the bandgap values for type 2 nanotubes are much smaller, 0.7 and 0.5 eV for zigzag and armchair chiralities, respectively.

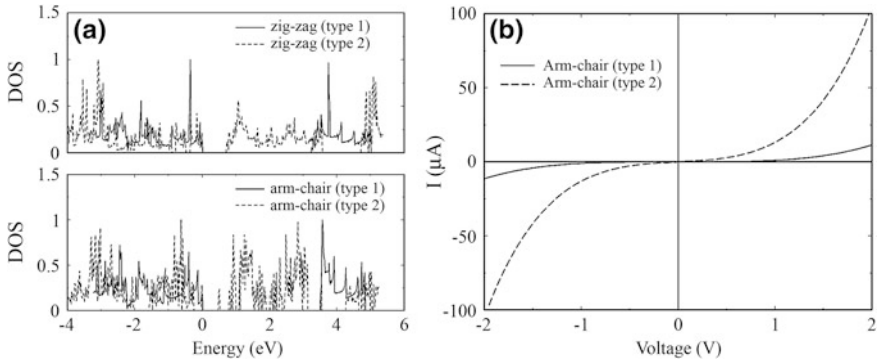

Fig. 6.15 **a** Density of states (DOS) for the zigzag and armchair SiC nanotubes showing reduction in the gap for type 2 nanotube. **b** Current versus voltage curves for two types of armchair SiC nanotubes showing a significant enhancement in current for type 2 nanotube. Reprinted with permission from [18]. Copyright 2004, American Physical Society

These values are very close to those of carbon nanotubes. This bandgap difference in two types of SiC nanotubes results in their different behaviors in the *I–V* characteristics (Fig. 6.15b), and the current value is much higher for type 2 SiC nanotubes at the same voltage.

The geometrics, strain energy, and electronic structures of SiC nanotubes with different diameters and chiralities have been investigated using density functional calculations [19]. In the considered nanotubes, the Si and C atoms are alternatively distributed in the crystal without any adjacent Si or C atoms. The average Si–C bond length in equilibrium configuration is about 1.80 Å. The strain energy in (5, 5) SiC nanotubes (relative to 3C-SiC) is as high as 0.686 eV/atom. The strain energy decreases with increasing nanotube diameter (Fig. 6.16a). All the considered SiC nanotubes are semiconductors and the bandgap increases with increasing diameter (Fig. 6.16b). The armchair and chiral SiC nanotubes have an indirect bandgap, similar to 3C-SiC, whereas the zigzag SiC nanotubes have a direct bandgap at the Γ point (Fig. 6.17). The highest occupied valance band and the lowest unoccupied conduction band states highly localize to C and Si atoms, respectively. When an H atom is chemically adsorbed above a C atom at the exterior of the tube, the hybridization of the C atom will change from sp^2 to sp^3, breaking the nearby *p–p* bonds and generating a local state close to the lowest unoccupied conduction band. This local state is half-occupied and therefore serves as a donor state, and thus, this hydrogen-decorated SiC nanotube shows character of *n*-type semiconductor. By contrast, an H atom chemically adsorbed on a Si atom results in a local state with energy close to the highest occupied valence band. This half-occupied state acts as an acceptor state and this hydrogen-decorated SiC nanotube shows character of *p*-type semiconductor. Further calculation [20] shows that hydrogenation of all the Si atoms renders the (8, 0) and (6, 6) SiC nanotubes metallic with very high density of states at the Fermi level. Hydrogenation of all the C atoms results in increase of the bandgap of the (8, 0) SiC nanotube to 2.6 eV

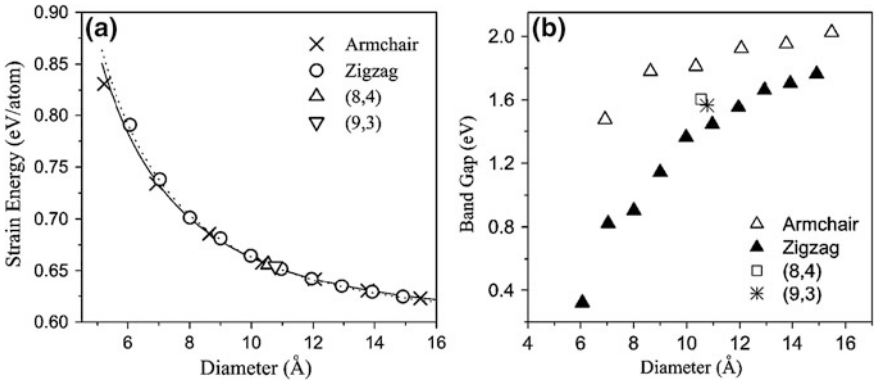

Fig. 6.16 **a** Strain energy in SiC nanotubes relative to 3C-SiC as a function of diameter. The *solid* and *dotted lines* are the fit. **b** Bandgap of armchair, zigzag, and chiral SiC nanotubes as a function of diameter. Reprinted with permission from [19]. Copyright 2005, American Physical Society

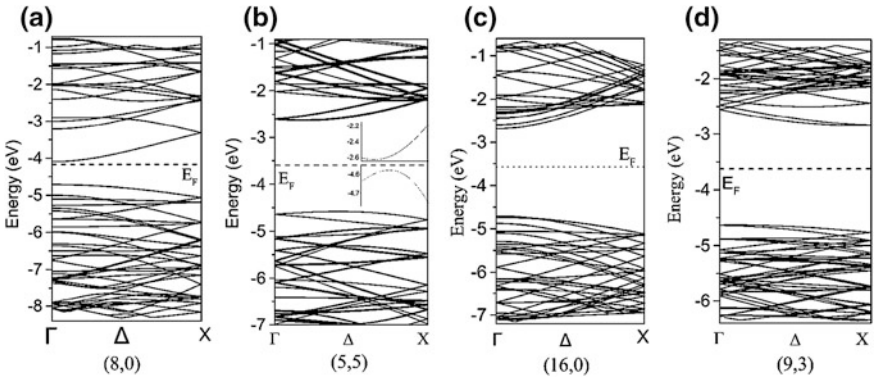

Fig. 6.17 Band structures along the nanotube axis of **a** zigzag (8, 0), **b** armchair (5, 5), **c** zigzag (16, 0), and **d** chiral (9, 3) SiC nanotubes. The Fermi levels E_F of these nanotubes are denoted by *dashed lines*. Reprinted with permission from [19]. Copyright 2005, American Physical Society

and decrease of the bandgap of the (6, 6) SiC nanotube to 1.47 eV. Hydrogenation of all the Si and C atoms results in a highly increased bandgap in the SiC nanotubes. Besides hydrogen atoms, other chemical groups adsorbed on the SiC nanotubes may also strongly alter their electronic structures [21]. The calculation shows that the XH_3 radical ($X = \{C, Si\}$) can be chemically adsorbed on Si sites or C sites on the tube wall, with the adsorption energies ranging from -2.01 to -2.90 eV for a (5, 5) SiC nanotube. The electronic structure of XH_3-decorated SiC nanotube exhibits characteristics of *n*-type and *p*-type semiconductors for XH_3 adsorbed on a C atom and a Si atom, respectively.

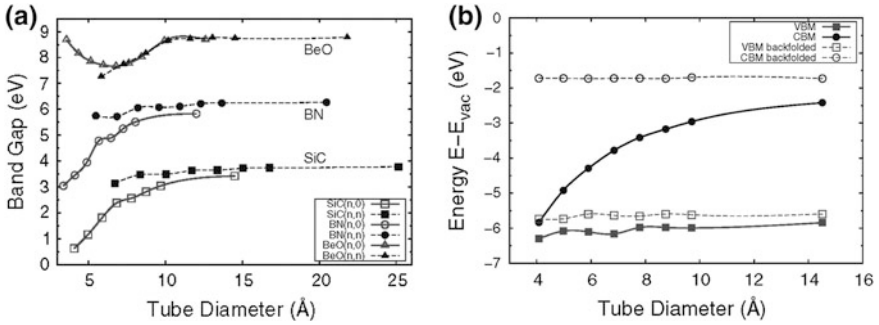

Fig. 6.18 **a** Fundamental gap of graphitic SiC, BN, and BeO (n, 0) zigzag and (n, n) armchair nanotubes as a function of tube diameter. **b** Valence band maximum (VBM) and conduction band minimum (CBM) energies in zigzag SiC nanotubes as a function of tube diameter. Full symbols result from nanotube calculations and open symbols follow from backfolding the bands of the graphitic SiC sheet. The *solid* and *dashed lines* are guides to the eye. Reprinted with permission from [22]. Copyright 2007, American Physical Society

The structural, elastic, and electronic properties of single-walled graphitic SiC, BN, and BeO nanotubes in zigzag and armchair configurations have been investigated using density functional theory employing self-interaction-corrected pseudopotentials [22]. The structural and elastic properties of all zigzag and armchair nanotubes considered are largely independent of nanotube helicity. In contrast, the electronic structures of SiC and BN nanotubes are sensitively dependent on nanotube helicity (Fig. 6.18a). The bandgap in zigzag and armchair BeO nanotubes varies peculiarly for small diameters, no bandgap breakdown occurs and the bandgap has a minimum for zigzag BeO nanotubes. These phenomena are caused by the qualitative difference in the nature of the lower conduction band states in SiC and BN nanotubes (Fig. 6.18b) as compared to BeO nanotubes and by the increasing ionicity from SiC, BN, to BeO.

The geometric and electronic structures of three types of armchair SiC nanotubes have been investigated using hybrid density functional theory and the finite cluster approximation [23]. Figure 6.19a–c display the atomic arrangements of the three types of nanotubes. The dangling bonds are terminated by hydrogen atoms. The cohesive energy saturates at 4.63 eV for type 1 nanotube and at around 4.44 eV for type 2 and 3 nanotubes. The bandgaps of type 1 nanotubes are bigger than the bulk 3C-SiC bandgap and range from 2.78 to 2.91 eV (Fig. 6.19d). In contrast, type 2 and type 3 nanotubes have much lower bandgaps. The bandgap of the newly proposed type 3 SiC nanotube decreases monotonically with increasing tube diameter, from 1.22 to 0.79 eV. This behavior is different from that of type 1 and type 2 nanotubes. All three types of tubes are nonmagnetic. The properties of single-walled hydrogen-terminated zigzag SiC nanotube have been investigated similarly [24]. Figure 6.20a–c display the atomic arrangements of the three types of nanotubes. Type 1 structure is more stable than type 2 structure. The cohesive

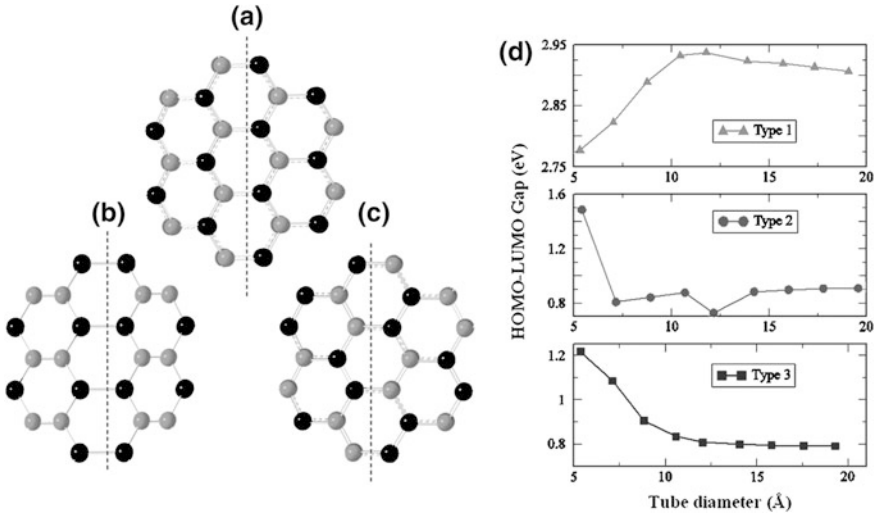

Fig. 6.19 Atomic arrangements of **a** type 1, **b** type 2, and **c** type 3 armchair SiC nanotubes. The carbon (*silicon*) atoms are *gray* (*black*). The *dashed lines* represent the orientation of tube axis. **d** Highest occupied molecular orbital-lowest unoccupied molecular orbital gap versus tube diameter for three types of nanotubes. Reprinted with permission from [23]. Copyright 2008, American Physical Society

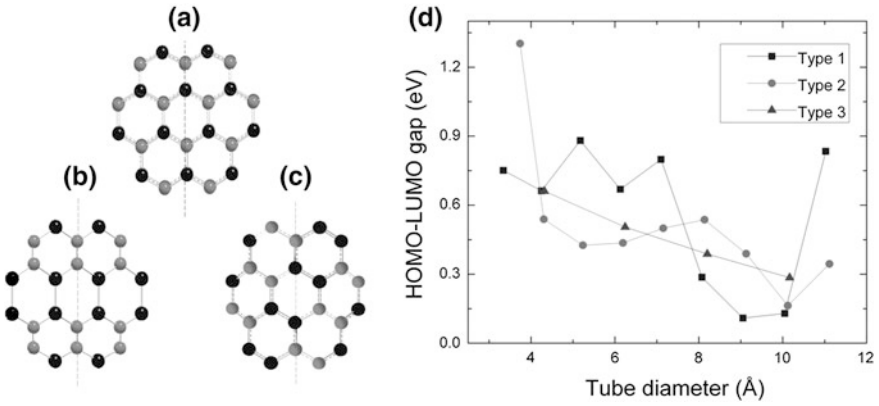

Fig. 6.20 Atomic arrangements of **a** type 1, **b** type 2, and **c** type 3 zigzag SiC nanotubes. The carbon (*silicon*) atoms are *gray* (*black*). The *dashed lines* represent the orientation of tube axis. **d** Highest occupied molecular orbital-lowest unoccupied molecular orbital gap versus tube diameter for three types of nanotubes. Reprinted with permission from [24]. Copyright 2007, IOP Publishing

energy per atom of type 3 nanotubes lies between those of type 1 and type 2. The bandgap of type 3 nanotubes decreases monotonically with increasing diameter, whereas those of type 1 and type 2 nanotubes oscillate with increasing diameter

(Fig. 6.20d). The structural and electronic properties of chiral SiC nanotubes have also been investigated using hybrid density functional theory [25]. All the SiC nanotubes considered are semiconductors with bandgaps ranging from 0.20 to 2.9 eV. Like other types of SiC nanotubes, the structural stability of the chiral nanotubes increases with diameter, and it is independent of the chiral angle.

Impurities present in a semiconductor can strongly affect its electronic structures and properties. The nitrogen and boron atoms are common contaminations in bulk SiC. Nitrogen preferentially substitutes the carbon site resulting in *n*-type conductivity in bulk SiC, whereas boron substitutes carbon (silicon) site leading to a deep (shallow) acceptor in bulk SiC. The effects of the boron and nitrogen impurities on the electronic structures of the armchair and zigzag SiC nanotubes have been investigated by ab initio supercell calculations [26]. The calculation shows that the nitrogen can only act as an *n*-type dopant in the small bandgap (<2.3 eV) SiC nanotubes, whereas it is rather a compensating center for both holes and electrons in wider bandgap SiC nanotubes. When nitrogen acts as an *n*-type dopant, the corresponding ionization energy is about 0.3 eV, about 0.15–0.2 eV deeper than in bulk SiC polytypes. Similar to the case of bulk SiC, in SiC nanotubes, boron that substitutes for silicon (B_{Si}) acts as a relatively shallow acceptor and B_C acts as a relatively deep acceptor, and the energy levels are similar to that in bulk SiC. The properties of the boron substitutional defect show no significant difference between armchair and zigzag SiC nanotubes. Hydrogen can be readily incorporated into SiC nanotubes as an impurity during their growth. The effect of one or two hydrogen impurity atoms in armchair and zigzag SiC nanotubes on their properties have been investigated using ab initio supercell calculations beyond the standard density functional theory [27]. Hydrogen atoms can be adsorbed onto the SiC nanotubes when they are present in the proximity of the nanotube. The calculation shows that a single hydrogen atom can act either as a donor or as an acceptor, depending on its adsorption site. The hydrogen atoms adsorbed on both sites are approximately equally stable and thus these defects compensate each other in SiC nanotubes. Like hydrogen, the oxygen plays an important role in SiC nanotubes. The effects of oxygen on the properties of the SiC nanotubes must be seriously considered. The density functional calculation shows that the formation energies of interstitial oxygen and O_C defects are negative [28]; thus, in many actual growth processes for the SiC nanotubes, the oxygen atoms may readily be incorporated into the nanotubes, especially at elevated temperatures. The calculation shows that pure single-walled SiC nanotubes tend to be oxidized in the presence of ambient oxygen. At low temperatures, the basic structure of the SiC nanotubes is not destroyed by oxidation, but interstitial oxygen defects form. At elevated temperatures, the electrically active O_C defect may form too. Although electrically inactive, the interstitial oxygen atoms diffuse fast in the SiC nanotubes even at room temperature. Spin-polarized density functional theory has been employed to investigate the structural and electronic properties of vacancies and antisites in zigzag, armchair, and chiral SiC nanotubes [29]. Antisites have lower formation energies relative to vacancies, resulting in an empty energy level near the conduction band minimum for both Si_C and C_{Si}. A carbon

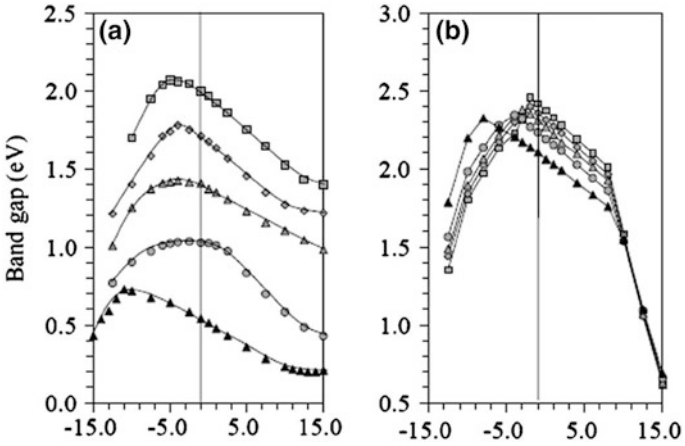

Fig. 6.21 Bandgap of zigzag **a** and armchair **b** SiC nanotubes as a function of uniaxial strain (% in unit, >0 for tension and <0 for compression). Reprinted with permission from [31]. Copyright 2008, AIP Publishing LLC

vacancy generates a pair of bonding and antibonding energy levels within the bandgap. A silicon vacancy has the largest formation energy and generates one spin-up occupied level within the valence band and three nearly degenerate (one spin-up and two spin-down) spin-polarized levels within the bandgap.

The stability of single-walled SiC nanotubes relative to SiC nanowires and against heating has been investigated using classical molecular dynamics simulations [30]. The simulation indicates that the SiC nanotubes are more stable than the SiC nanowires for diameters below about 1.6 nm, and the SiC nanowires are more stable than the nanotubes for greater diameters. This partially explains the difficulty in synthesizing actual SiC nanotubes. The SiC nanotubes with free ends will reconstruct to form a closed cap containing nonhexagonal defects at 1,100 K, which acts as the nucleation site for heterogeneous melting as the temperature increases to 1,620 K. The SiC nanotubes without free ends begin to melt at about 1,820 K by homogeneous nucleation within the wall starting from thermally activated defects. The first-principle calculation reveals that uniaxial strain applied on the single-walled SiC nanotubes alters their electronic band structures [31]. The electronic structure can be changed by mechanical strain in a wide energy range. The bandgap of the nanotube decreases with increasing uniaxial tensile strain, whereas it increases first and decreases then with increasing uniaxial compressive strain (Fig. 6.21).

The electronic band structure and optical dielectric function of single-walled zigzag, armchair, and chiral SiC nanotubes as well as single honeycomb SiC sheets have been investigated within density functional theory with local density approximation [32]. Figure 6.22a, b show the calculated band structure and density of states for the graphitic hexagonal SiC sheet. It is clearly a semiconductor with a direct bandgap of 2.58 eV. The valence band maximum and the conduction band

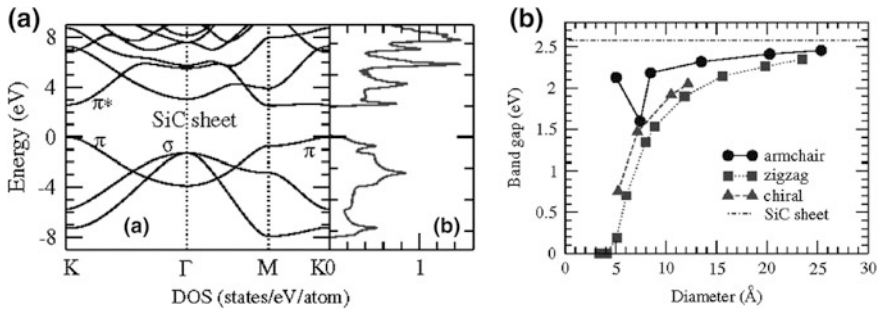

Fig. 6.22 **a** Band structure and **b** density of states (DOS) of the SiC sheet. The zero energy is at the top of the valence band. **c** Calculated bandgap of the SiC nanotubes versus diameter. The bandgap of the SiC sheet is also shown as the *dashed-dotted line*. Reprinted with permission from [32]. Copyright 2007, American Physical Society

minimum both occur at the point *K* in the Brillouin zone. All the SiC nanotubes are found to be semiconductors except for the ultrasmall (3, 0) and (4, 0) zigzag tubes which are metallic. The zigzag SiC nanotubes have a direct bandgap. The bandgap value of the small SiC nanotubes increases with increasing diameter and it gradually approaches the bandgap value of the SiC sheet for diameters over 2 nm (Fig. 6.22c). The static dielectric constants for all the SiC nanotubes are almost independent of diameter and chirality.

The structural properties and energetics of nanotip and nanocone materials based on SiC nanotubes have been investigated using density functional calculations [33]. The calculation shows that edges made of multiple atoms are more stable than those made of a single atom. Tips with edges containing pentagon–heptagon defects are energetically more favorable than edges containing four-member rings and are thus suitable as tip materials for atomic force microscopy and scanning tunneling microscopy applications.

6.3.2 Adsorption of Small Molecules and Applications

The theoretical study shows that silicon carbide nanotubes are very promising materials for hydrogen storages [34]. The density functional calculation reveals an increase of 20 % in the binding energy of H_2 in SiC nanotubes compared with carbon nanotubes (Fig. 6.23), which may result from the alternative charges that exist in the SiC nanotube wall. The classical Monte Carlo simulation of nanotube bundles reveals an even larger increase in the storage capacity in SiC nanotubes, especially at low temperatures and at high pressures. Therefore, the SiC nanotubes seem to be more favorable than carbon nanotubes in hydrogen storage.

The first-principle calculation indicates that CO and HCN molecules can be absorbed to Si atoms on the wall of SiC nanotubes with binding energies as high as

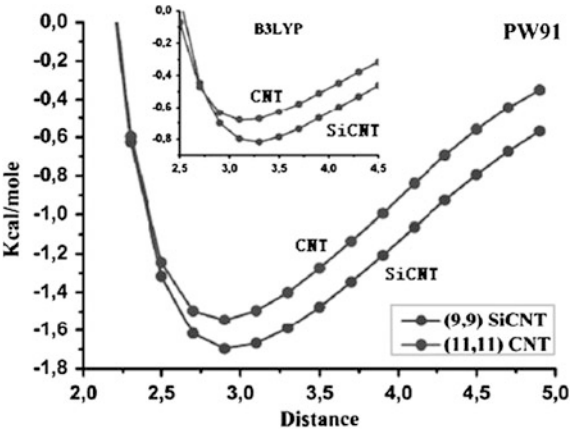

Fig. 6.23 Potential energy curves of an H_2 molecule that perpendicularly approaches the middle part of a hexagon of the (9, 9) SiC nanotube's and (11, 11) carbon nanotube's outer walls. Reprinted with permission from [34]. Copyright 2006, American Chemical Society

0.70 eV and can attract finite charge from SiC nanotubes [35]. Similar to oxygen molecules, the CO and HCN molecules adsorbed on SiC nanotubes may induce significant change in the conductivity of the nanotubes; hence, the SiC nanotubes are potential gas sensors for CO and HCN detection. The first-principle calculation reveals that NO and NNO molecules can be chemisorbed on SiC nanotubes with an appreciable binding energy [36]. The SiC nanotube–NO complex has large adsorption energy of −0.7 eV. This complex has magnetism and even ferromagnetism in the case of more than one adsorbed NO molecules. This property may be used for sensing the amount of adsorbed NO molecules. In contrast, the SiC nanotube–NNO complex is nonmagnetic. The interaction between formaldehyde (HCOH) and infinitely long zigzag single-walled SiC nanotubes has been investigated using density functional theory [37]. In comparison with the weak adsorption on carbon nanotubes, HCOH molecule is chemisorbed to the Si–C bond of SiC nanotubes with appreciable adsorption energy. The Si–C pair is also very sensitive to the adsorption of the second HCOH molecule. The bandgap of the SiC nanotube decreases gradually with increasing adsorbed HCOH molecules, resulting in an increase of conductivity of the nanotube. Density functional calculation shows that the SiC nanotube can effectively break the N–H bond of ammonia and the O–H bond of H–OX (X=H, CH_3, and C_2H_5) [38]. This process contains two steps: first, the NH_3 (or H–OX) molecule is adsorbed on the Si atom of the SiC nanotube, and then, the adsorbed molecule is cleaved to an atomic H and a NH_2 (or OX) group. The adsorption of a series of transition metal atoms on single-walled SiC nanotubes has been investigated using density functional calculations [39]. Many transition metal atoms are found to be chemically adsorbed on the outer surface of the single-walled SiC nanotubes, with binding energies ranging from 1.17 eV (for Cu) to 3.18 eV (for Pt). The adsorbed metal atoms change the electronic structures of the single-walled SiC nanotubes, and this change is nearly independent of the adsorption site. One exception is Ti, the (8, 0) single-walled SiC nanotube exhibits characteristic of metal as Ti is adsorbed onto H site and characteristic of semiconductor as Ti is adsorbed onto C site.

6.4 Two-Dimensional SiC Sheets

Electronic structures of SiC nanoribbons have been investigated by spin-polarized first-principle calculations [40]. The calculation shows that the two-dimensional SiC sheet has a direct energy gap of 2.55 eV at the K point in the hexagonal Brillouin zone (Fig. 6.24a, b). This value is smaller than the gap obtained by self-interaction-corrected density functional calculation, suggesting that the calculation method employed in this study can give rise to qualitatively correct but quantitatively inaccurate results. All dangling σ bonds at the ribbon edges are saturated by hydrogen atoms for the calculation of the armchair and zigzag SiC nanoribbons (Fig. 6.24c, d). The armchair SiC nanoribbons with different widths have similar band structures and they are nonmagnetic semiconductors with a direct bandgap at the Γ point (Fig. 6.24e). The energy gap versus ribbon width curve exhibits a three-family behavior (Fig. 6.24f), similar to the case of armchair graphene nanoribbons. However, the energy gap increases with ribbon width for SiC nanoribbons, in comparison with the decrease for graphene nanoribbons. The zigzag nanoribbons are magnetic metals and the spin polarization stems from the unpaired electrons localized on the ribbon edges. The zigzag nanoribbons narrower than 4 nm have half-metallic characters (Fig. 6.24g). The theoretical calculation based on the tight-binding model reveals that in the SiC nanoribbons, the charge redistribution at the ribbon edge is responsible for the bandgap oscillation with

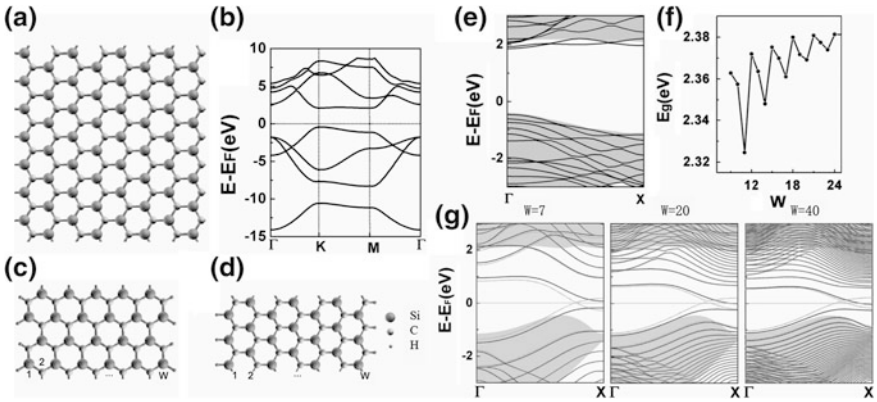

Fig. 6.24 **a** Geometry and **b** electronic band structure of the two-dimensional SiC sheet. Geometric structures of **c** armchair and **d** zigzag SiC nanoribbons with a width W. The nanoribbon width W is defined as the number of dimer lines (*lines* along the ribbon direction) for an armchair nanoribbon and the number of zigzag chains for a zigzag nanoribbon. **e** Band structure of armchair SiC nanoribbon with $W = 11$. Shaded areas show the projected band structure of a two-dimensional graphitic SiC sheet. **f** Bandgap of armchair SiC nanoribbons as a function of ribbon width W. **g** Spin-polarized band structures of zigzag SiC nanoribbons with $W = 7$, 20, and 40. *Thin lines* are spin-up bands and *thick lines* are spin-down bands. *Shaded areas* show the projected band structure of a two-dimensional graphitic SiC sheet. Reprinted with permission from [40]. Copyright 2008, AIP Publishing LLC

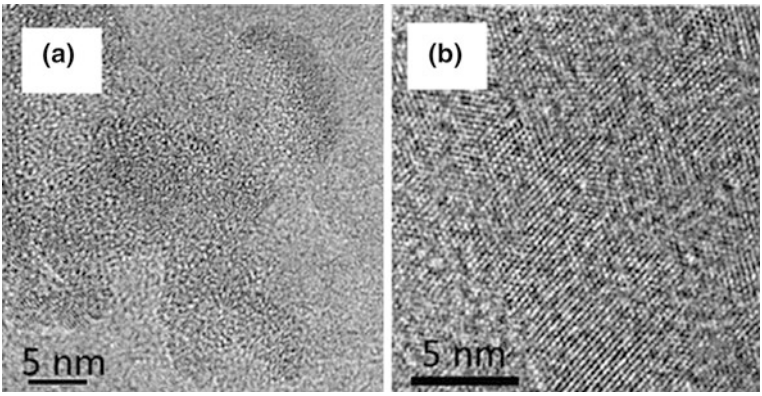

Fig. 6.25 **a** HRTEM image of two-dimensional SiC nanoflake supported by an ultrathin graphene layer. **b** HRTEM image of large SiC nanosheets. The lattice fringe spacing is 0.28 nm. Reprinted with permission from [43]. Copyright 2012, American Chemical Society

ribbon width [41]. Another first-principle calculation reveals that the two-dimensional graphitic SiC sheet will acquire net magnetic moment when a Si-vacancy defect is present or the As, P, B, or N substitutional atom is present [42]. In contrast, the single C-vacancy, Si and C divacancy, and antisite defects do not induce magnetic moment in the SiC sheet.

Some signs of existence of two-dimensional SiC nanoflakes with thickness down to 0.5–1.5 nm have been presented by exfoliation of bulk SiC in polar solutions [43]. The nanosheets are prepared by sonication of the SiC powder in nmethyl-pyrrolidone or isopropyl alcohol. Figure 6.25 shows the high-resolution TEM image of the nanosheet on graphene. The lattice fringe spacing is around 0.28 nm. The fast Fourier transformation pattern reveals a sixfold symmetry of this sheet. The measurement of more nanoflakes reveals sixfold-symmetry lattice fringes with spacings ranging from 0.24 to 0.28 nm. These values are bigger than the lattice parameter of graphene, 0.21 nm. The energy-dispersive X-ray spectroscopy shows that the nanosheet is mainly composed of silicon and carbon elements. The combined transmission electron microscopy, X-ray diffraction, and X-ray photoelectron spectroscopy measurements indicate that the as-prepared ultrathin layers consist of graphitic SiC, graphene, and embedded ultrathin wurtzite SiC.

References

1. Pham-Huu C, Keller N, Ehret G, Ledoux MJ (2001) The first preparation of silicon carbide nanotubes by shape memory synthesis and their catalytic potential. J Catal 200:400–410
2. Nhut J-M, Vieira R, Pesant L, Tessonnier J-P, Keller N, Ehret G, Pham-Huu C, Ledoux MJ (2002) Synthesis and catalytic uses of carbon and silicon carbide nanostructures. Catal Today 76:11–32

3. Sun X-H, Li C-P, Wong W-K, Wong N-B, Lee C-S, Lee S-T, Teo B-K (2002) Formation of silicon carbide nanotubes and nanowires via reaction of silicon (from disproportionation of silicon monoxide) with carbon nanotubes. J Am Chem Soc 124:14464–14471
4. Taguchi T, Igawa N, Yamamoto H, Jitsukawa S (2005) Synthesis of silicon carbide nanotubes. J Am Ceram Soc 88:459–461
5. Borowiak-Palen E, Ruemmeli MH, Gemming T, Knupfer M, Biedermann K, Leonhardt A, Pichler T, Kalenczuk RJ (2005) Bulk synthesis of carbon-filled silicon carbide nanotubes with a narrow diameter distribution. J Appl Phys 97:056102
6. Hu JQ, Bando Y, Zhan JH, Golberg D (2004) Fabrication of ZnS/SiC nanocables, SiC-shelled ZnS nanoribbons (and sheets), and SiC nanotubes (and tubes). Appl Phys Lett 85:2932–2934
7. Zhou J, Liu J, Yang R, Lao C, Gao P, Tummala R, Xu NS, Wang ZL (2006) SiC-shell nanostructures fabricated by replicating ZnO nano-objects: a technique for producing hollow nanostructures of desired shape. Small 2:1344–1347
8. Zhou J, Zhou M, Chen Z, Zhang Z, Chen C, Li R, Gao X, Xie E (2009) SiC nanotubes arrays fabricated by sputtering using electrospun PVP nanofiber as templates. Surf Coat Tech 203:3219–3223
9. Dřínek V, Šubrt J, Klementová M, Rieder M, Fajgar R (2009) From shelled Ge nanowires to SiC nanotubes. Nanotechnology 20:035606
10. Latu-Romain L, Ollivier M, Mantoux A, Auvert G, Chaix-Pluchery O, Sarigiannidou E, Bano E, Pelissier B, Roukoss C, Roussel H, Dhalluin F, Salem B, Jegenyes N, Ferro G, Chaussende D, Baron T (2011) From Si nanowire to SiC nanotube. J Nanopart Res 13:5425–5433
11. Wang H, Li X-D, Kim T-S, Kim D-P (2005) Inorganic polymer-derived tubular SiC arrays from sacrificial alumina templates. Appl Phys Lett 86:173104
12. Cheng Q-M, Interrante LV, Lienhard M, Shen Q, Wu Z (2005) Methylene-bridged carbosilanes and polycarbosilanes as precursors to silicon carbide—from ceramic composites to SiC nanomaterials. J Eur Ceram Soc 25:233–241
13. Yang Z, Xia Y, Mokaya R (2004) High surface area silicon carbide whiskers and nanotubes nanocast using mesoporous silica. Chem Mater 16:3877–3884
14. Huang GS, Mei YF, Cavallo F, Baunack S, Coric E, Gemming T, Bertram F, Christen J, Fu RKY, Chu PK, Schmidt OG (2009) Fabrication and optical properties of C/β-SiC/Si hybrid rolled-up microtubes. J Appl Phys 105:016103
15. Pei LZ, Tang YH, Chen YW, Guo C, Li XX, Yuan Y, Zhang Y (2006) Preparation of silicon carbide nanotubes by hydrothermal method. J Appl Phys 99:114306
16. Cui H, Sun Y, Yang GZ, Chen J, Jiang D, Wang CX (2009) Template- and catalyst-free synthesis, growth mechanism and excellent field emission properties of large scale single-crystalline tubular β-SiC. Chem Commun 6243–6245
17. Miyamoto Y, Yu BD (2002) Computational designing of graphitic silicon carbide and its tubular forms. Appl Phys Lett 80:586–588
18. Menon M, Richter E, Mavrandonakis A, Froudakis G, Andriotis AN (2004) Structure and stability of SiC nanotubes. Phys Rev B 69:115322
19. Zhao M, Xia Y, Li F, Zhang RQ, Lee S-T (2005) Strain energy and electronic structures of silicon carbide nanotubes: density functional calculations. Phys Rev B 71:085312
20. Zhao M, Xia Y, Zhang RQ, Lee S-T (2005) Manipulating the electronic structures of silicon carbide nanotubes by selected hydrogenation. J Chem Phys 122:214707
21. Li F, Xi Y-Y, Zhao M-W, Liu X-D, Huang B-D, Yang Z-H, Ji Y-J, Song C (2005) Density-functional theory calculations of XH_3-decorated SiC nanotubes (X={C, Si}): structures, energetics, and electronic structures. J Appl Phys 97:104311
22. Baumeier B, Krüger P, Pollmann J (2007) Structural, elastic, and electronic properties of SiC, BN, and BeO nanotubes. Phys Rev B 76:085407
23. Alam KM, Ray AK (2008) Hybrid density functional study of armchair SiC nanotubes. Phys Rev B 77:035436
24. Alam KM, Ray AK (2007) A hybrid density functional study of zigzag SiC nanotubes. Nanotechnology 18:495706

25. Alfieri G, Kimoto T (2009) The structural and electronic properties of chiral SiC nanotubes: a hybrid density functional study. Nanotechnology 20:285703
26. Gali A (2006) Ab initio study of nitrogen and boron substitutional impurities in single-wall SiC nanotubes. Phys Rev B 73:245415
27. Gali A (2007) Ab initio theoretical study of hydrogen and its interaction with boron acceptors and nitrogen donors in single-wall silicon carbide nanotubes. Phys Rev B 75:085416
28. Szabó Á, Gali A (2009) Effect of oxygen on single-wall silicon carbide nanotubes studied by first-principles calculations. Phys Rev B 80:075425
29. Baierle RJ, Piquini P, Neves LP, Miwa RH (2006) Ab initio study of native defects in SiC nanotubes. Phys Rev B 74:155425
30. Zhang Y, Huang H (2008) Stability of single-wall silicon carbide nanotubes - molecular dynamics simulations. Comp Mater Sci 43:664–669
31. Wang Z, Zu X, Xiao H, Gao F, Weber WJ (2008) Tuning the band structures of single walled silicon carbide nanotubes with uniaxial strain: a first principles study. Appl Phys Lett 92:183116
32. Wu IJ, Guo GY (2007) Optical properties of SiC nanotubes: an *ab initio* study. Phys. Rev. B 76:035343
33. Mavrandonakis A, Froudakis GE, Andriotis A, Menon M (2006) Silicon carbide nanotube tips: promising materials for atomic force microscopy and/or scanning tunneling microscopy. Appl Phys Lett 89:123126
34. Mpourmpakis G, Froudakis GE, Lithoxoos GP, Samios J (2006) SiC nanotubes: a novel material for hydrogen storage. Nano Lett 6:1581–1583
35. Wu RQ, Yang M, Lu YH, Feng YP, Huang ZG, Wu QY (2008) Silicon carbide nanotubes as potential gas sensors for CO and HCN detection. J Phys Chem C 112:15985–15988
36. Gao G, Kang HS (2008) First principles study of NO and NNO chemisorption on silicon carbide nanotubes and other nanotubes. J Chem Theory Comput 4:1690–1697
37. Wang X, Liew KM (2011) Silicon carbide nanotubes serving as a highly sensitive gas chemical sensor for formaldehyde. J Phys Chem C 115:10388–10393
38. Zhao J-X, Xiao B, Ding Y-H (2009) Theoretical prediction of the N-H and O-H bonds cleavage catalyzed by the single-walled silicon carbide nanotube. J Phys Chem C 113:16736–16740
39. Zhao J-X, Ding Y-H (2008) Silicon carbide nanotubes functionalized by transition metal atoms: a density-functional study. J Phys Chem C 112:2558–2564
40. Sun L, Li Y, Li Z, Li Q, Zhou Z, Chen Z, Yang J, Hou JG (2008) Electronic structures of SiC nanoribbons. J Chem Phys 129:174114
41. Zhao K, Zhao M, Wang Z, Fan Y (2010) Tight-binding model for the electronic structures of SiC and BN nanoribbons. Physica E 43:440–445
42. Bekaroglu E, Topsakal M, Cahangirov S, Ciraci S (2010) First-principles study of defects and adatoms in silicon carbide honeycomb structures. Phys Rev B 81:075433
43. Lin SS (2012) Light-emitting two-dimensional ultrathin silicon carbide. J Phys Chem C 116:3951–3955

Chapter 7
SiC Nanostructured Films

Silicon carbide films have been intensively investigated concerning their fabrications and properties. In general, the thickness of the fabricated silicon carbide films can range from many micrometers to many nanometers. In this chapter, however, we shall focus on the nanostructured SiC films including the films with thickness on the nanoscale and the films comprising SiC nanocrystals. We shall summarize the fabrication, structures, and properties of these nanostructured SiC films.

7.1 Synthesis by Chemical Vapor Deposition

Chemical vapor deposition is an important method for the preparation of the silicon carbide films. Internal stress in 3C-SiC epilayers grown on Si substrates by chemical vapor deposition using SiH_4–C_3H_8–H_2 as starting materials at 1,350 °C have been investigated by Raman scattering [1]. Raman scattering from the 3C-SiC epitaxial layers grown on Si(001) and Si(111) substrates shows that the LO phonon frequencies shift to the lower frequency side compared with stress-free 3C-SiC films. The frequency shift gives an estimate of the tensile stress of the 3C-SiC epilayer on Si(001) to be 5.4×10^9 dyn/cm^2. The stress difference between the 3C-SiC films on Si(001) and on Si(111) is smaller than that expected from the elastic deformation theory. A set of formulas have been derived [2, 3] to describe the Raman shifts of diamond and zinc-blende semiconductors under axial stress. The Raman shifts under hydrostatic pressure and uniaxial and biaxial stresses only act as special cases of the general formulas. Raman scattering measurements from a series of chemical vapor-deposited 3C-SiC films on (100) Si with thickness between 60 nm and 17 μm (Fig. 7.1) show that the Raman spectra in samples with SiC thickness greater than 4 μm exhibit a sharp and strong feature that obeys the selection rule for the 3C-SiC LO(Γ) phonon line. The stresses in 3C-SiC extracted

J. Fan and P.K. Chu, *Silicon Carbide Nanostructures*,
Engineering Materials and Processes, DOI 10.1007/978-3-319-08726-9_7

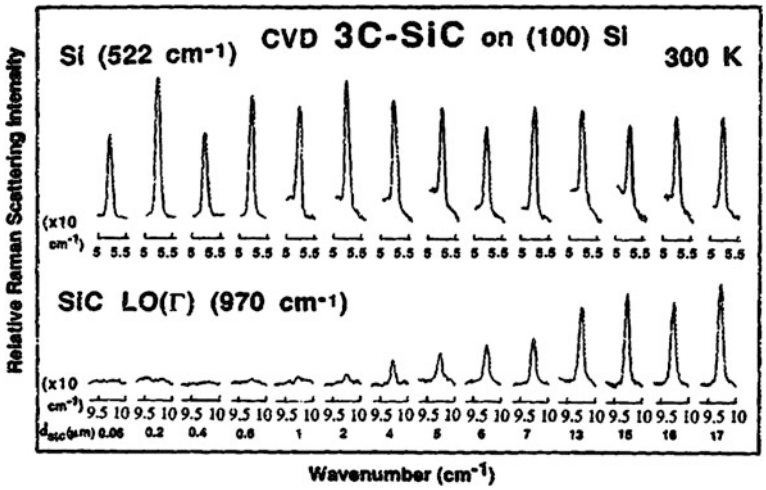

Fig. 7.1 Raman spectra of 14 chemical vapor-deposited 3C-SiC/Si samples with the SiC film thickness varying from 60 nm to 17 μm. Reprinted with permission from [3]. Copyright 1988, AIP Publishing LLC

from these data are between 0.3 and 1.1 GPa. 3C-SiC and Si have a large lattice mismatch of 20 %, but the difference in Raman shift between 3C-SiC/Si and free 3C-SiC films is smaller than 2 cm^{-1}, corresponding to strains of 0.1–0.2 %. The Raman signals from the SiC film and the Si substrate exhibit identical polarization behavior confirming their same crystalline orientations. The 3C-SiC LO(Γ) phonon signal shows an enhancement by a factor of 2 or 3 after removal of the Si substrate owing to multiple reflections in free 3C-SiC films.

Photoluminescence at 4.2 K in as-grown and ion-implanted 3C-SiC films grown by chemical vapor deposition on Si(100) substrates have been investigated [4]. The *D*1- and *D*2-defect PL bands previously observed in ion-implanted Lely-grown SiC are observed in the as-grown un-implanted films (Fig. 7.2), and they possess higher defect concentration than the vapor transport Lely-grown 3C-SiC crystals. The ion implantation in the SiC films causes significant enhancement in the intensities of the *D*1- and *D*2-defect bands. Their intensities in both as-grown and ion-implanted films increase after annealing at temperature up to 1,600 °C and above this temperature, the intensity of the *D*2 zero-phonon line decreases sharply, suggesting possible lattice recovery which quenches this defect emission band. The intensity of the *D*1 emission band remains nearly constant after annealing at temperature above 1,600 °C and up to 1,800 °C. Similar to the Lely-grown SiC, the spectral details of these defects-related PL bands and their annealing behaviors in the SiC films are independent of the implanted-ion species.

The photoluminescence at 2 K in 26 3C-SiC films with thickness of 60 nm to 25 μm grown on (100) Si by chemical vapor deposition have been investigated [5]. The bound-exciton PL spectrum (Fig. 7.3a) for the 3C-SiC-free film comprises the nitrogen-bound-exciton zero-phonon line N_0 along with its (one, two, and three)

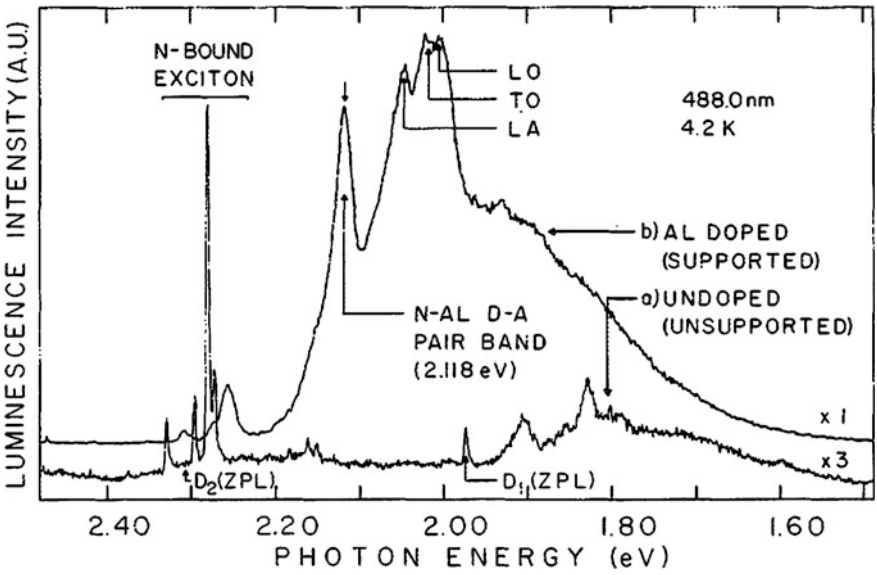

Fig. 7.2 PL spectra obtained from as-grown CVD 3C-SiC films. Spectrum **a** is from an undoped film that has been removed from its Si substrate. Spectrum **b** is from an Al-doped film on its Si substrate. Reprinted with permission from [4]. Copyright 1987, AIP Publishing LLC

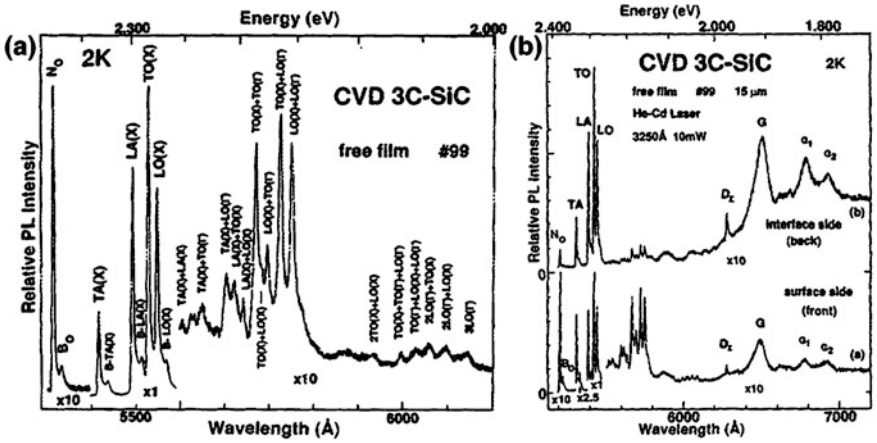

Fig. 7.3 **a** PL spectrum at 2 K showing the nitrogen-bound-exciton lines in a high-quality CVD free 3C-SiC film. **b** PL spectra at 2 K from both sides of a 15 μm CVD 3C-SiC film. Reprinted with permission from [5]. Copyright 1968, AIP Publishing LLC

phonon replicas. It also contains a *B*-series bound-exciton line (B_0) and its phonon replicas that are related to some unidentified impurity. The B_0 line shifts to lower energy side by 7 meV relative to the nitrogen-bound-exciton zero-phonon line.

The bound-exciton lines have a full width at half maximum (FWHM) smaller than 2 meV. The PL spectra (Fig. 7.3b) obtained from the front and back sides of a 3C-SiC film with thickness of 15 μm show much stronger bound-exciton lines in the near surface region than the near interface region. The D_I line is related to vacancies. The G band (near 1.90–1.92 eV) and its phonon replicas G_1 and G_2 bands as well as a background (below 1.95 eV) are all stronger in the interface layer than in the surface layer. This G band is associated with dislocations and extended defects. The very thin SiC films exhibit another defect-related W band near 2.15 eV.

Hydrogenated nanocrystalline silicon carbide films deposited on Si or corning glass substrates have been prepared by chemical vapor deposition using a mixture of methane, silane, and hydrogen as source gases [6]. Their infrared absorption spectrum shows a 3C-SiC TO phonon absorption band at around 794 cm^{-1}. The Raman spectrum (Fig. 7.4a) consists of three main peaks at 785.3, 986.4, and 1,606.5 cm^{-1} and a weak shoulder peak at 1,390.2 cm^{-1}. The first two bands are assigned to TO and LO phonon modes of SiC, and the peaks at 1,606.5 and 1,390.2 cm^{-1} are attributed to disordered graphite. The sample has strong room temperature photoluminescence centered at around 2.64 eV under 351 nm excitation, but the PL shifts to 2.2 eV under 325 nm excitation [7]. Figure 7.4b shows the PL and absorption spectra of two samples [8] prepared under different source gas ratios, and the flow ratio of $H_2/SiH_4/CH_4$ is 100:10:3 for sample D and 100:5:1 for sample E. Their time-resolved PL spectra (Fig. 7.4c) can be fit by double-exponential function with two decay time constants of 166 and 772 ps for sample D and 246 and 974 ps for sample E, respectively. These values are at least two orders of magnitude smaller than that of the bound-exciton transitions in bulk 3C-

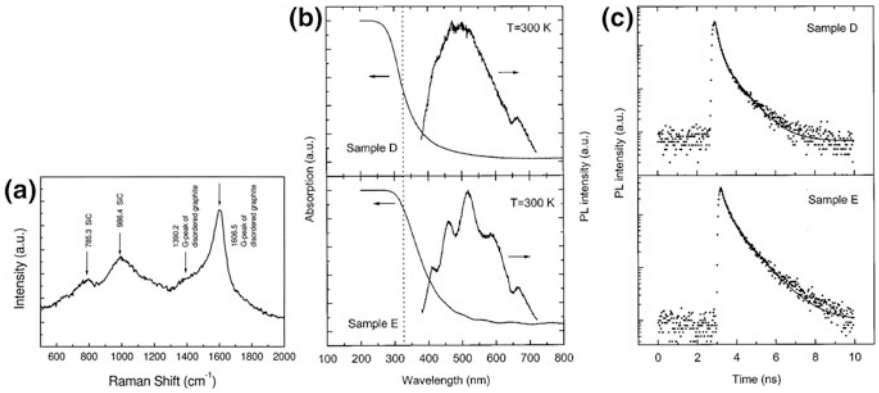

Fig. 7.4 **a** Raman spectrum of the chemical vapor-deposited SiC nanocrystalline film. Reprinted with permission from [6]. Copyright 2000, Elsevier. **b** Room temperature optical absorption and PL spectra (excited at 351 nm) and **c** time-resolved PL spectra (excited at 400 nm) of two chemical vapor-deposited SiC films. The *solid lines* show the double-exponential fit to the experimental data. Reprinted with permission from [8]. Copyright 2000, AIP Publishing LLC

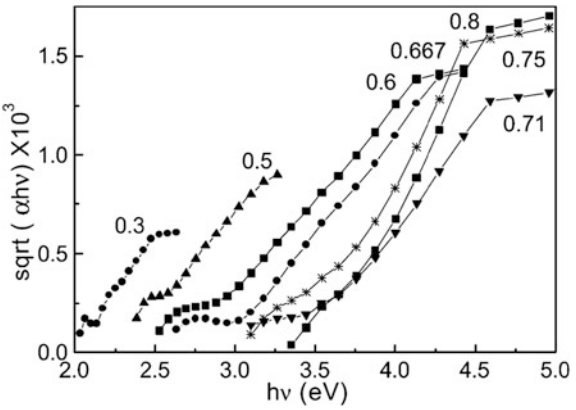

Fig. 7.5 Absorption (*square root* of absorbance) as a function of photon energy in a-SiC:H films that were prepared with different acetylene fractions. Reprinted with permission from [9]. Copyright 2001, Elsevier

SiC at low temperature. The double-exponential decay law suggests that multiple states are involved in the radiative recombination.

Hydrogenated amorphous silicon carbon films (a-SiC:H) prepared from a gas mixture of silane and acetylene by catalytic chemical vapor deposition [9] have optical bandgaps that increase with increasing acetylene to silane ratio (Fig. 7.5). The bandgap reaches 3.6 eV for a ratio over 0.8. The deposition rate decreases drastically with increasing acetylene fraction. These silicon carbide films have visible photoluminescence at room temperature. Nanocrystalline SiC films deposited by plasma-enhanced chemical vapor deposition at different gas flow ratios and at different deposition temperatures from 80 to 575 °C have been investigated [10]. Diethylsilane ($C_4H_{12}Si$) is the source gas, and different concentrations of hydrogen, argon, or helium are used as the dilution gases. The infrared spectral analysis indicates that the SiC nanocrystals embedded in the amorphous film begin to form at 300 °C. The crystallization degree increases with increasing temperature, and the crystalline fraction reaches 65 % at 575 °C. The hydrogen dilution gas results in the highest crystalline fraction. The high-resolution TEM measurement reveals the existence of the SiC nanocrystallites in the amorphous matrix with their sizes ranging from 2 to 10 nm (Fig. 7.6). The refractive index of the film increases roughly linearly with temperature. The optical bandgap of the film can be derived from the absorption spectrum using the following relation:

$$\alpha h\nu = B(h\nu - E_g)^2, \tag{7.1}$$

where α is the absorption coefficient, B is a constant, $h\nu$ is the photon energy, and E_g is the bandgap. Another characteristic value E_{04} is defined as the energy at which α equals 10^4 cm^{-1}. As shown in Fig. 7.6, both E_g and E_{04} increase monotonically with increasing deposition temperature. The bandgap value varies from 2.6 to 4.47 eV as the temperature increases from 80 to 575 °C, showing a large blueshift relative to the bulk value. The micro-Raman measurement reveals an average crystallite size of 4 nm. The TEM observation shows that the crystallite sizes are 2–10 nm and that only the concentration of the nanocrystallites in the

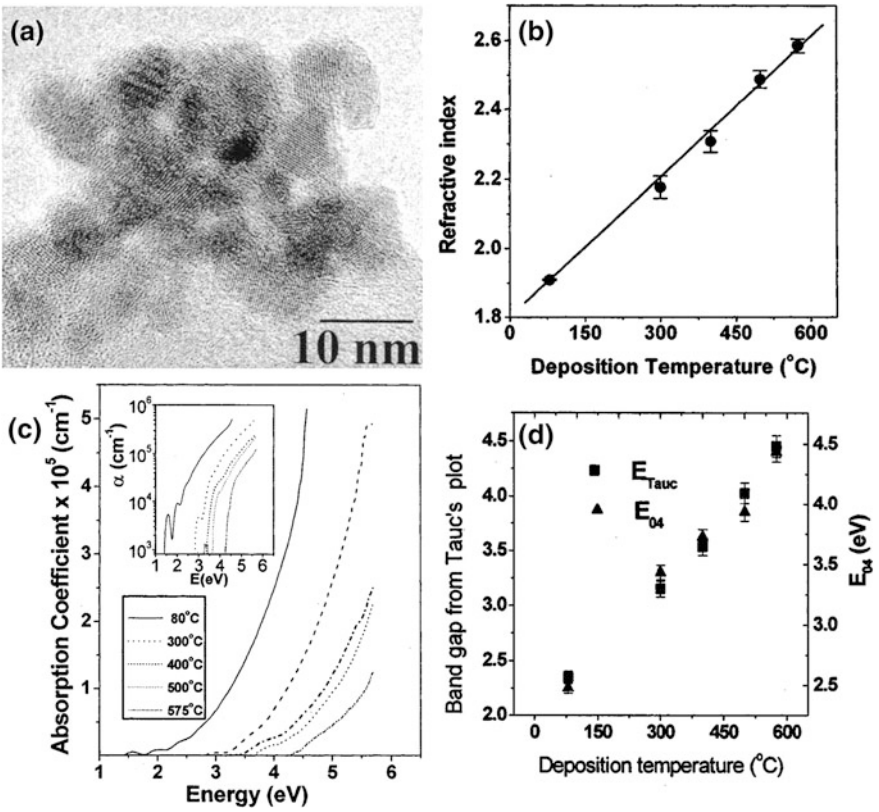

Fig. 7.6 **a** HRTEM image of the SiC film deposited with hydrogen dilution at 575 °C. **b** Refractive index versus deposition temperature. **c** Optical absorption spectra for the films deposited at different temperatures. The *inset* shows the same spectra in logarithmic scale. **d** Bandgap E_g and E_{04} as a function of deposition temperature. Reprinted with permission from [10]. Copyright 2003, AIP Publishing LLC

amorphous matrix increases with deposition temperature, whereas their sizes do not increase significantly with deposition temperature. Considering that the bandgap value is determined by both the amorphous SiC and the SiC nanocrystallites, hence the origin of large bandgap values is ascribed to the presence of nanocrystallites in the films.

Nanocrystalline silicon carbide films deposited on molybdenum substrates by thermal plasma chemical vapor deposition at substrate temperature of 750–1,250 °C [11] are mainly composed of β-SiC nanocrystallites. Characterization of the films by use of nanoindentation shows that their average grain size, crystalline fraction in the film, and film hardness all increase with increasing substrate temperature (Fig. 7.7). The average grain sizes are between 10 and 20 nm, the crystalline fraction is 80–85 %, and the film hardness is about 50 GPa in the film obtained with substrate temperature above 1,200 °C.

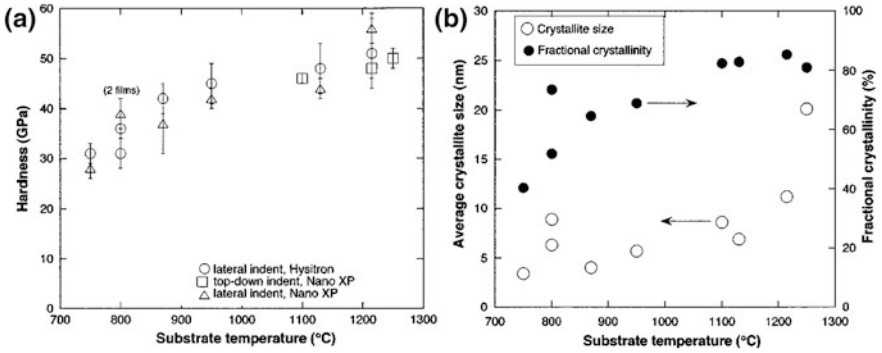

Fig. 7.7 **a** Film hardness as a function of substrate temperature during deposition of SiC film measured by nanoindenter. **b** Average crystallite size and crystalline fraction as a function of substrate temperature. Reprinted with permission from [11]. Copyright 2005, AIP Publishing LLC

Undoped and *n*- and *p*-type hydrogenated nanocrystalline 3C-SiC films have been deposited on glass and silicon substrates at substrate temperature of 300 °C by hot-wire chemical vapor deposition [12]. Monomethylsilane and hydrogen are the source gases for deposition of undoped films. Phosphine and hexamethyldisilazane are phosphorous and nitrogen sources for *n*-type doping, and dimethylaluminumhydride is aluminum source for *p*-type doping. Figure 7.8 shows the cross-sectional TEM images of the undoped films deposited at different H_2/monomethylsilane ratios, and the corresponding ring electron diffraction pattern corresponds to the crystalline phases of 3C-SiC. The XRD analysis indicates that the average grain size in the film increases from 6.4 to 16.6 nm with increasing deposition temperature. The grain size affects the dark conductivity and the dielectric functions of the films. The former increases from 5.8×10^{-11} to 6.2×10^{-6} S/cm as the grain size increases from 6.4 to 16.6 nm. The dark conductivities are 5.32 and 7.67×10^{-4} S/cm for the *n*- and *p*-type films, respectively. The absorption data reveal that *p*-type doping significantly affects absorption coefficients above the bandgap of the doped film, whereas the absorption coefficients below the bandgap of the *n*-type film are affected by free carrier absorption and localized states within the bandgap.

Silicon carbide films with different carbon concentrations have been synthesized by inductively coupled plasma chemical vapor deposition using a $SiH_4/CH_4/H_2$ gas mixture at a substrate temperature of 500 °C [13]. The film obtained with carbon concentration of 49 at% is composed of nanocrystalline cubic silicon carbide without any phase of silicon, graphite, or diamond crystallites (Fig. 7.9). The average size of SiC crystallites is about 6 nm. Polycrystalline silicon and amorphous silicon carbide coexist in the films obtained with lower carbon concentrations, and amorphous carbon and silicon carbide coexist in the films obtained with higher carbon concentrations.

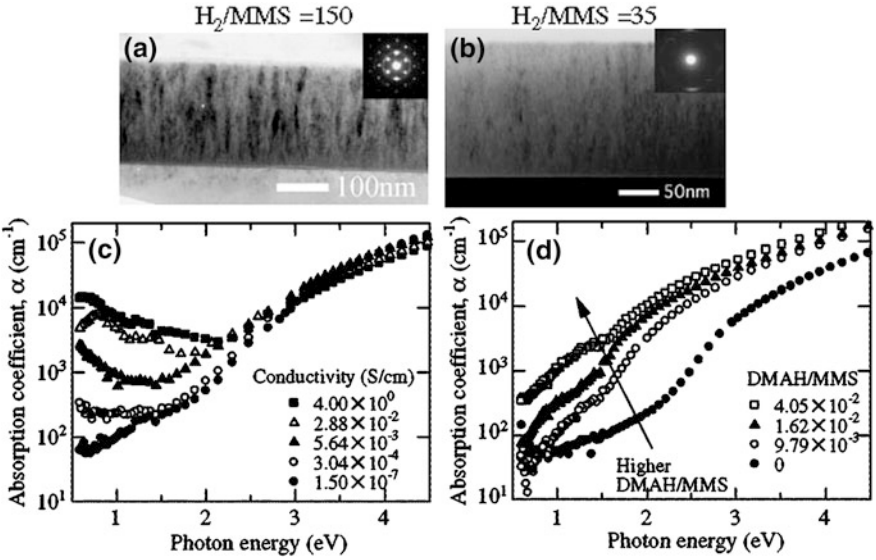

Fig. 7.8 **a**, **b** Cross-sectional TEM images of hydrogenated nanocrystalline 3C-SiC films deposited at different H_2/monomethylsilane ratios. **c** Absorption spectra of *n*-type SiC films with different dark conductivities. **d** Absorption spectra of *p*-type SiC films deposited at different dimethylaluminumhydride/monomethylsilane ratios. Reprinted with permission from [12]. Copyright 2007, Japanese Society of Applied Physics

Nanocrystalline SiC film has been deposited by helicon wave plasma-enhanced chemical vapor deposition on corning glass and single-crystal silicon substrates using a mixture of H_2, SiH_4, and CH_4 gases [14]. HRTEM observation (Fig. 7.10) reveals that the film comprises many 3C-SiC nanocrystals embedded in the amorphous SiC matrix with an average size of 3.96 nm. The SiC film shows photoluminescence with peak wavelength ranging from 475 to 545 nm as the excitation wavelength increases from 360 to 500 nm. This shifting emission implies that the photoluminescence may be governed by quantum confinement effect. The time-resolved photoluminescence shows an average lifetime on the order of nanosecond.

7.2 Fabrication by Ions Implantation

Ions implantation in combination with annealing is another widely used method for fabricating SiC films containing SiC nanocrystals. The SiC microcrystallites in Si single crystals have been fabricated by carbon ion implantation at fluence of $10^{17}/cm^2$ followed by annealing [15]. Infrared absorption examination reveals a broad absorption band centered at 700–725 cm^{-1} (Fig. 7.11) in as-implanted

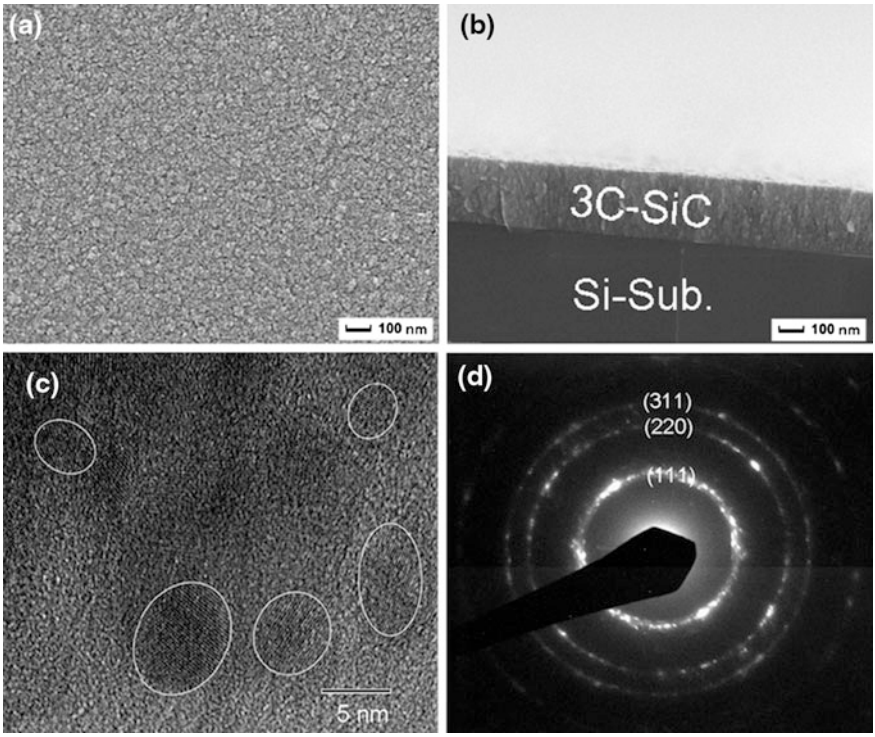

Fig. 7.9 **a**, **b** Surface morphology and fracture cross section of SiC film with carbon concentration of 49 at%. **c** HRTEM image and **d** electron diffraction pattern of the same SiC film. Reprinted with permission from [13]. Copyright 2007, IOP Publishing

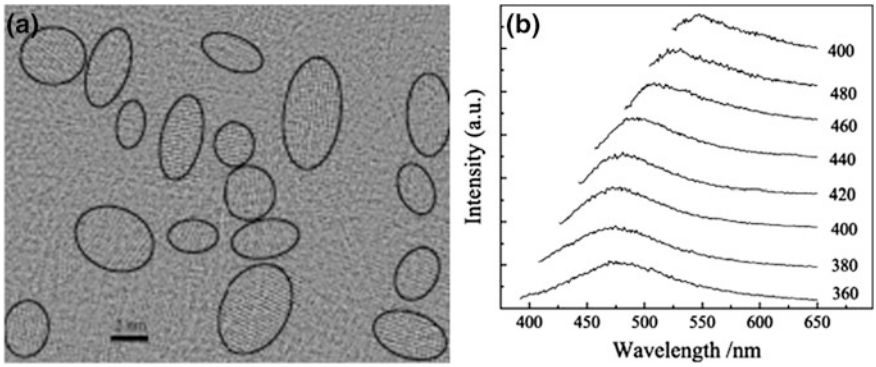

Fig. 7.10 **a** HRTEM image of the SiC film and **b** its PL spectra excited at different wavelengths. Reprinted with permission from [14]. Copyright 2011, Elsevier

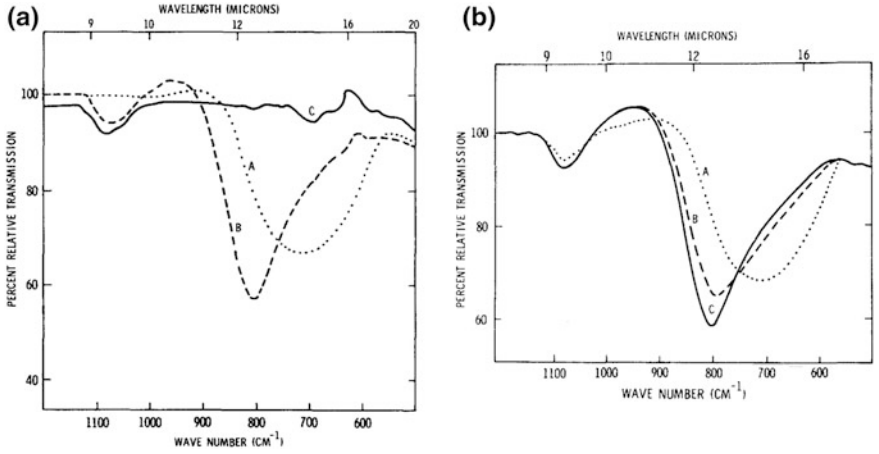

Fig. 7.11 **a** Infrared transmission spectra of (*A*) Si wafer implanted by 10^{17} carbon atoms/cm^2 before annealing; (*B*) same sample after annealing at 1,000 °C for 20 min; (*C*) un-implanted Si annealed at 1,000 °C for 20 min. All spectra are taken with matched un-implanted unannealed Si as the reference sample. **b** Infrared transmission spectra of a Si wafer implanted by 10^{17} carbon atoms/cm^2 followed by annealing for 20 min at (*A*) 800 and 825 °C, (*B*) 850 °C, and (*C*) 900 °C. Reprinted with permission from [15]. Copyright 1971, AIP Publishing LLC

sample, and it persists after annealing at temperature up to 825 °C. The band peak lies between the local mode of carbon in silicon (608 cm^{-1}) and the TO phonon mode of SiC (796 cm^{-1}) and is assigned to the former, and its broadening and shifting to higher frequencies is due to the high carbon concentration and the high disorder of the implanted layer. The SiC microcrystallites begin to form at temperature around 850 °C, as demonstrated by arising of the strong TO phonon absorption band of SiC at around 800 cm^{-1}. The annealing effect on the implanted film is completed by 875 °C, and there is no further change in the absorption band upon further anneal up to 1,000 °C. The annealed implanted and un-implanted samples all possess an absorption band at around 1,080 cm^{-1} attributed to the SiO_2 surface layer formed by annealing, and it vanishes after removal of the surface layer by HF etching.

The microcrystalline SiC in the Si matrix formed by carbon implantation has been investigated by TEM, X-ray diffraction, infrared absorption, Auger electron spectroscopy, Rutherford backscattering spectrometry, and nuclear reaction analysis [16]. A thick buried layer of β-SiC with a thickness of 300 nm forms after multiple implantations at 860 °C without further annealing. This buried layer consists of nanocrystalline SiC grains with an average size of 7 nm, and they show nearly perfect epitaxial relation with the Si matrix. The grains are only slightly misorientated by 3.5° and are significantly twinned on {111} planes.

The β-SiC in Si crystal matrix has been fabricated by carbon ions implantation into Si wafers for ion energy of 50 keV and dose of 10^{17} cm^{-2} followed by annealing in nitrogen at 950 °C [17]. The TEM observation reveals the formation

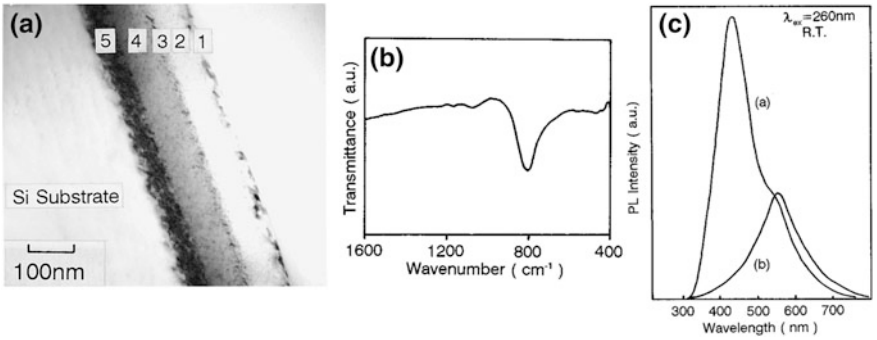

Fig. 7.12 **a** TEM image of the C^+-implanted Si crystal after annealing in N_2 at 950 °C. Regions 1–5 are successively upper damaged Si layer, β-SiC precipitate, closure boundary, β-SiC precipitate, and lower damaged Si layer. **b** FTIR spectrum of this sample. **c** PL spectra of annealed C^+-implanted sample [curve (a)] and reference sample without implantation [curve (b)]. Both samples are anodized in HF-ethanol solution at 40 mA/cm^2. Reprinted with permission from [17]. Copyright 1995, AIP Publishing LLC

of a layer of polycrystalline β-SiC beneath the sample surface (Fig. 7.12), and the electron diffraction pattern shows features in accordance with polycrystalline β-SiC. The infrared spectrum has a strong absorption band at around 800 cm^{-1} that is assigned to the TO phonon mode of β-SiC. The porous SiC is achieved by etching the implanted and annealed sample in HF-ethanol (2:1 by volume) solution at a current density of 40 mA/cm^2 with assistance of UV-light illumination. The resultant porous sample has photoluminescence with two peaks at around 445 nm (2.79 eV) and 560 nm under 260-nm excitation. The former peak photon energy is higher than the bandgap of bulk β-SiC (2.2 eV), and this band may stem from the interband transition in the β-SiC nanocrystallites. The latter emission band is assigned to the porous Si. The distribution of the β-SiC nanocrystallites in the Si matrix has been investigated [18] for samples achieved by carbon ion implantation into Si wafers at an energy 50 keV and a dose 5×10^{17} cm^{-2} at 600 °C followed by anneal in nitrogen at 1,100 °C. The cross-sectional TEM image (Fig. 7.13) of the as-implanted sample reveals three layers from the implanted surface down to the substrate, they are the upper damaged Si layer A (85 nm thick), the amorphous layer B (70 nm thick), and the lower damaged Si layer C (50 nm thick). After annealing, three layers have distinct concentrations of SiC nanocrystals due to distribution of implanted ions; the concentration is low in layers A and C and reaches a maximum at the B/C interface. The embedded β-SiC crystallites have size of 2–8 nm.

The β-SiC nanocrystals have been synthesized by carbon implantation into Si crystals at 35 keV with various doses followed by annealing at 1,200 °C in argon atmosphere and subsequent thermal oxidation at 1,050 °C [19]. The infrared spectrum (Fig. 7.14) shows two strong absorption peaks, one shifts from 820 to 795 cm^{-1} as implantation dose increases from 1.2×10^{16} to 3.2×10^{17} cm^{-1},

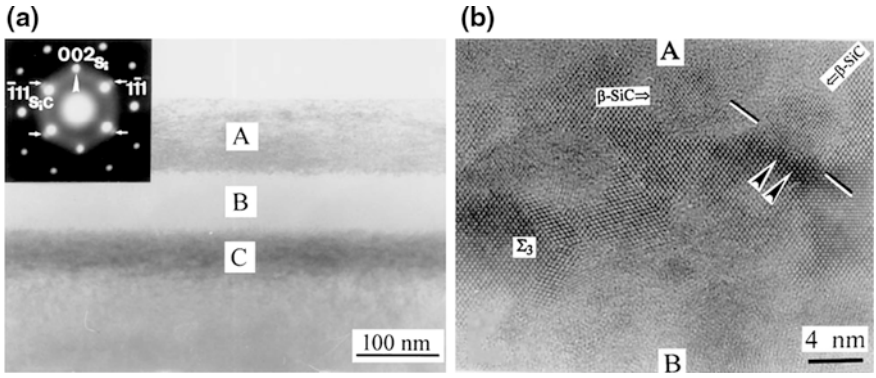

Fig. 7.13 **a** Cross-sectional TEM image showing three layers on the surface of carbon-implanted Si crystal without annealing. The *inset* is the electron diffraction pattern of this layered structure showing spots from Si matrix and β-SiC particles and a halo from the amorphous phase. **b** HRTEM image of the A/B interface in the annealed sample showing epitaxial growth and amorphous interface between Si and β-SiC nanocrystals. Reprinted with permission from [18]. Copyright 1997, Cambridge University Press

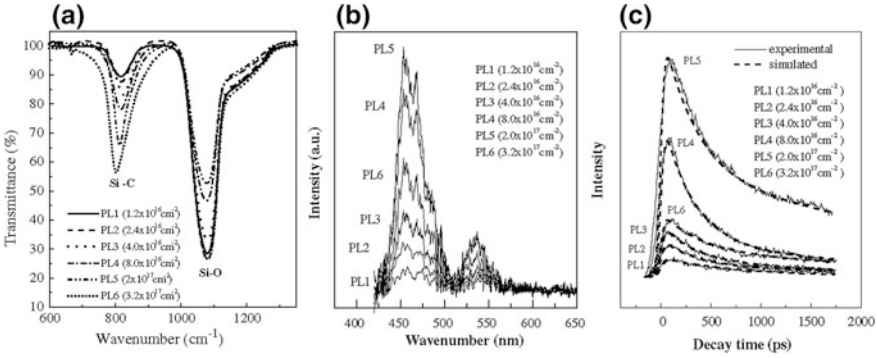

Fig. 7.14 **a** FTIR spectra of the carbon ion-implanted single-crystal Si at 35 keV with various doses. The samples are annealed at 1,200 °C in argon atmosphere and oxidized at 1,050 °C. **b** PL spectra of the samples excited at 300 nm at room temperature. **c** Time-resolved PL spectra of the samples. Reprinted with permission from [19]. Copyright 2003, Elsevier

and it is assigned to the TO phonon mode of β-SiC, another at around 1,080 cm^{-1} is assigned to the Si–O–Si vibration of the SiO_2 film formed on the sample surface. The sample has photoluminescence with two bands at around 460 and 535 nm under 300-nm excitation. Time-resolved photoluminescence spectrum of the sample comprises two decay components with lifetimes of around 3 and 0.35 ns, respectively.

The embedded SiC nanocrystallites can also be prepared by ion implantation into SiO_2 films instead of Si films. The quasi-white photoluminescence has been

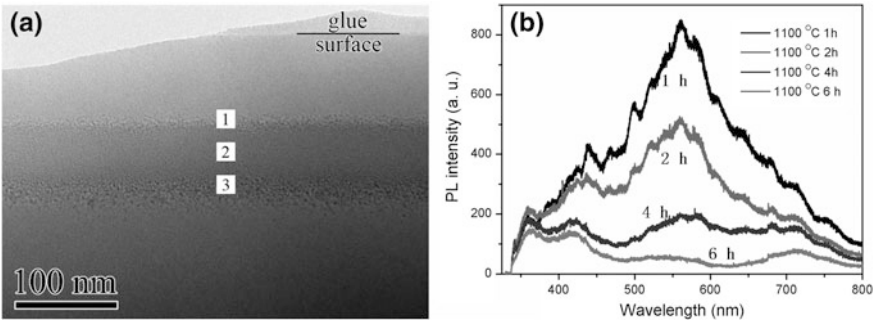

Fig. 7.15 **a** Cross-sectional TEM image of the Si^+/C^+ co-implanted silica wafer after annealing at 1,100 °C showing three layers. There are many Si and SiC nanocrystals in regions 1 and 3. **b** PL spectra of the Si^+/C^+ co-implanted silica wafer before annealing and after annealing at different temperatures. Reprinted with permission from [20]. Copyright 2012, AIP Publishing LLC

observed from the silica wafer implanted by Si^+ and C^+ ions or only by C^+ ions followed by thermal annealing in argon atmosphere [20]. The TEM measurement (Fig. 7.15a) reveals that the annealed Si^+/C^+ co-implanted silica wafer has three distinct layers beneath the surface. There are many Si and SiC nanocrystals in regions 1 and 3. The sample has wide photoluminescence band (Fig. 7.15b) in the range of 350–800 nm with maximum at around 550 nm. This quasi-white light emission arises from the graphitic carbon clusters as well as the Si and SiC nanocrystals.

Diamond is also employed as the implantation substrate for the synthesis of the embedded SiC crystallites. The natural IIa diamond has been used as the substrate to produce SiC by implantation of 90 keV N^+ at a dose of $1 \times 10^{15}/cm^2$ followed by implantation of 150 keV Si^+ at a dose of $3 \times 10^{17}/cm^2$ at 900 °C [21]. Cross-sectional transmission electron microscopy (Fig. 7.16) reveals a 70-nm-thick damaged diamond layer (zone A) and a 150-nm-thick buried layer (zone B) in which crystalline 3C-SiC domains are in perfect epitaxial relation to the weakly damaged diamond matrix. No amorphous or graphitic domains are present in the implanted layer owing to the high implantation temperature. There is an array of ordered misfit dislocations at the 3C-SiC/diamond interface. The Raman spectrum comprises a diamond signal at 1,332 cm^{-1} and a weak peak at 797 cm^{-1} that is characteristic of 3C-SiC TO phonon mode. The infrared spectroscopy reveals 3C-SiC TO phonon absorption at around 796 cm^{-1}. The implantation temperature affects the structural properties of the Si-implanted diamond [22]. Implantation with high Si fluence severely damages the diamond matrix and the formed SiC crystallites. Raising the implantation temperature from 900 to 1,000 °C diminishes damage and increases the SiC crystallite concentration, size, and epitaxial alignment. Further increase of the implantation temperature does not improve the quality of the SiC-rich layer, and in this case the damaged diamond transforms into graphite.

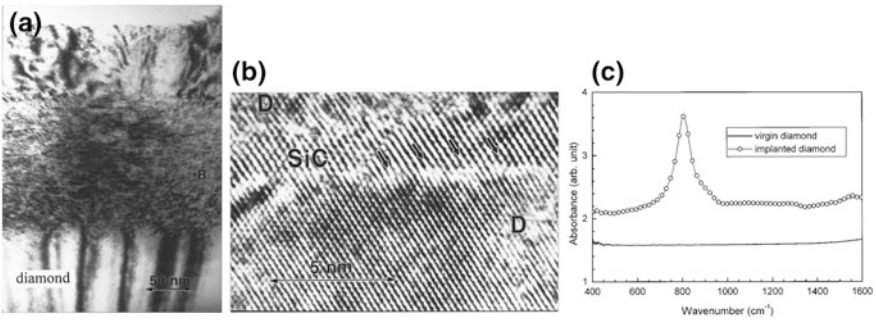

Fig. 7.16 **a** Cross-sectional TEM image of diamond doped successively by N^+ and Si^+. Zone *A* (*upper layer*) is the damaged crystalline diamond, and Zone *B* (*middle layer*) is where the implanted Si atoms lie. **b** High-resolution micrograph of a 3C-SiC domain embedded in the diamond matrix of Zone *B*. Letter D denotes diamond, and the *arrows* indicate the misfit dislocations. **c** Infrared absorption spectra of pristine and implanted diamond. Reprinted with permission from [21]. Copyright 2000, AIP Publishing LLC

7.3 Fabrication by Sputtering

Sputtering is another common method to prepare silicon carbide nanostructured films. Silicon carbide thin films have been deposited by reactive magnetron co-sputtering of silicon and carbon on silicon or quartz substrates in pure hydrogen plasma at substrate temperature of 100–600 °C [23]. Infrared absorption and TEM measurements (Fig. 7.17) indicate that the crystalline SiC begins to form at a substrate temperature of 300 °C. The crystalline fraction increases with substrate temperature as demonstrated by the increase in intensity of the infrared absorption at 800 cm^{-1} that is assigned to the stretching vibration of Si–C bonds. The weaker absorptions at about 900 and 1,000 cm^{-1} are separately assigned to the $Si–H_2$ bending and C–H wagging modes, and their respective stretching modes are present at 2,100 and 2,900 cm^{-1}. The electron diffraction ring stemming from the β-SiC (111) lattice planes becomes more clear with increasing substrate temperature above 300 °C, confirming the improvement of crystalline fraction. The refractive index of the layers increases from 1.9 to 2.4, and the room temperature dark conductivity increases by six orders of magnitude as the substrate temperature increases from 100 to 600 °C. High-resolution transmission electron microscopy reveals the formation of randomly oriented β-SiC nanocrystals with an average size of a few nanometers for substrate temperature over 400 °C [24].

The deposition temperature influences the growth of sputtered nanocrystalline SiC [25]. The sputtered film contains SiC nanocrystals with an average size of about 5 nm (Fig. 7.18a), and the number density increases with increasing deposition temperature. The sputtered film contains also the cubic SiC crystallites possessing 6H-SiC faults. The optical transmission measurement performed on the sputtered SiC layers gives their static refractive index and pseudo–bandgap $E_{5.4}$, which is the energy corresponding to the absorption coefficient of 5×10^4 cm^{-1},

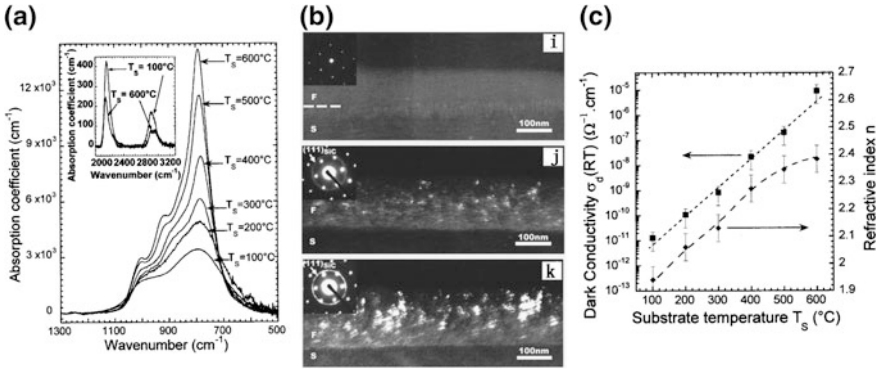

Fig. 7.17 **a** Infrared absorption spectra in the 500–1,300 cm^{-1} region for the SiC layers obtained by co-sputtering of silicon and carbon at different substrate temperatures. The *inset* shows two typical spectra in the 1,900–3,300 cm^{-1} range. **b** Cross-sectional TEM images and corresponding electron diffraction patterns of the SiC films grown at (*i*) 200 °C, (*j*) 300 °C, and (*k*) 600 °C. **c** Refractive index and room temperature dark conductivity as a function of substrate temperature. Reprinted with permission from [23]. Copyright 2000, AIP Publishing LLC

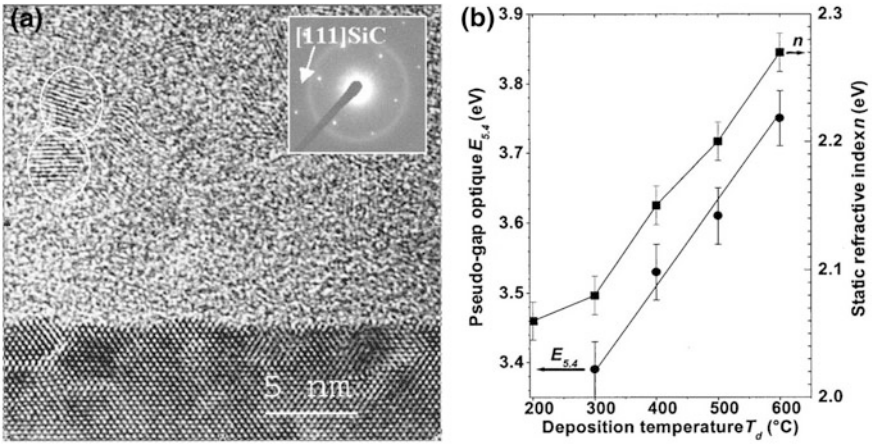

Fig. 7.18 **a** Cross-sectional TEM image for SiC film grown by co-sputtering of silicon and carbon at deposition temperature of 300 °C. The *inset* shows corresponding selected area electron diffraction pattern. **b** Pseudogap $E_{5.4}$ obtained from absorption spectra and static refractive index as a function of deposition temperature. The *solid lines* are the guide for the eyes. Reprinted with permission from [25]. Copyright 2005, AIP Publishing LLC

and both quantities increase with deposition temperature (Fig. 7.18b). The slight increase of the pseudo–bandgap results from variation of the Si/C ratio and decrease of the hydrogen content in the SiC film with increasing deposition temperature.

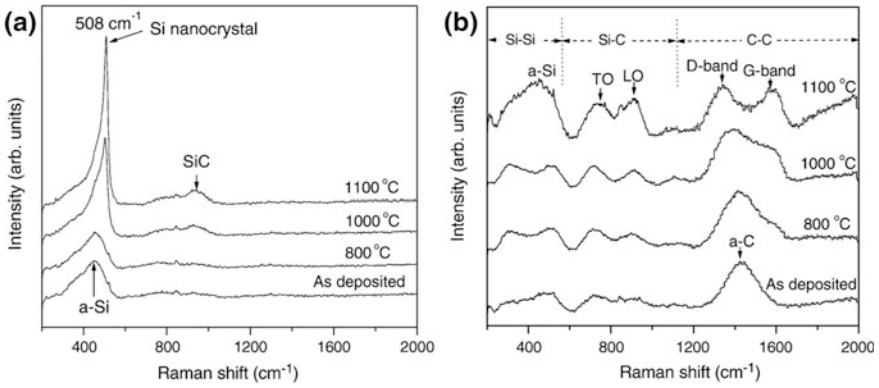

Fig. 7.19 Raman spectra of the Si and C co-sputtered films obtained with C/Si ratios of 0.33 (**a**) and 0.71 (**b**). The major peaks and annealing temperatures are indicated. Reprinted with permission from [27]. Copyright 2008, Elsevier

The Si nanocrystals may coexist with the SiC nanocrystals in the Si and C co-sputtered films. The three-layer amorphous Si/C/amorphous Si films containing nanocrystalline SiC have been prepared by ion-beaming sputtering of silicon and carbon on the Si substrates and subsequent annealing at 750 °C in vacuum [26]. The SiC nanocrystals with diameters of 20–120 nm are present on the top and at the bottom of the three-layer film. The two Si/C interfaces comprise SiC nanocrystals and Si nanocrystals with sizes below 5 nm, and these nanocrystals are embedded in an amorphous SiC matrix. The three-layer film has photoluminescence with a single peak centered at around 480 nm under 325-nm excitation. $Si_{1-x}C_x$ films with varying carbon-to-silicon ratios have been fabricated by magnetron co-sputtering of C and Si targets [27]. The composition of the films changes with varying ratio of two targets. The as-sputtered films have been annealed at various temperatures from 800 to 1,100 °C in nitrogen atmosphere. The infrared absorption spectrum contains a Si–C stretching peak that shifts from 737 to 800 cm^{-1} as annealing temperature increases. Raman scattering (Fig. 7.19), X-ray diffraction, and transmission electron microscopy reveal that the dominant nanocrystals in the sputtered film change from Si to SiC in the films annealed at 1,100 °C when the C/Si atomic ratio increases from 0.33 to 1.02. Co-sputtering of silicon and carbon targets on silica or silicon substrates followed by annealing can also yield silicon nanocrystals embedded in an amorphous SiC matrix [28].

The β-SiC nanocrystals can be fabricated by relaxation of $Si_{1-y}C_y$ ($0.005 > y > 0.05$) random alloys grown epitaxially on Si [29]. At temperatures over 900 °C, the C atoms that are located in substitutional sites at lower temperatures will precipitate out of the lattice, leading to the formation of β-SiC nanocrystals with the same lattice orientation as that of the mother Si lattice. The nanocrystals have uniform diameters, and they are between 2 and 4 nm for $y = 0.005$ $Si_{1-y}C_y$ material. The β-SiC materials with high surface area and porosity have been prepared by reaction between mesoporous carbon and gaseous

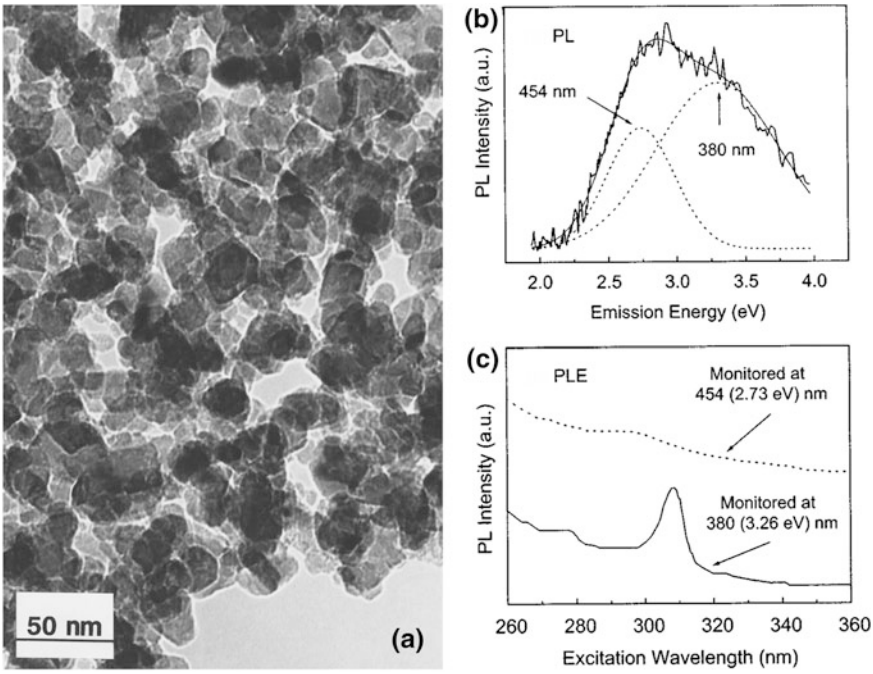

Fig. 7.20 **a** TEM image of a SiC film obtained by annealing C_{60} films on Si substrate at 900 °C. Unreacted carbon in the grain bulk gives a darker color to some grains. Reprinted with permission from [31]. Copyright 1997, AIP Publishing LLC. **b** PL spectrum of annealed C_{60}-coated porous Si. *Dotted lines* are the double-Gaussian fit of the curve. **c** PL excitation spectra of the sample. Reprinted with permission from [32]. Copyright 2000, AIP Publishing LLC

silicon coming from sublimation of the Si powder at temperature 1,200–1,300 °C [30]. The synthesized SiC sample has mesoporosity dimension of 5–40 nm.

Deposition and annealing of the 200-nm-thick C_{60} film on (100) silicon substrate can give rise to silicon carbide films [31]. The reaction between C_{60} and silicon starts at the interface and continues by silicon diffusion. Silicon diffusion and SiC formation require annealing at 800 °C for $t > 100$ min and at 900 °C for $t > 25$ min. The synthesized stoichiometric SiC film is uniform with a grain size of 20–40 nm (Fig. 7.20a). SiC nanocrystals can also be prepared by annealing C_{60}-covered porous Si [32]. X-ray diffraction reveals the existence of β-SiC particles along with Si, SiO_2, and graphite. The annealed sample has photoluminescence (Fig. 7.20b) with an asymmetric band, and the double-Gaussian fit of the curve gives two peaks at 380 nm (3.26 eV) and 454 nm (2.73 eV). The 380-nm band has an excitation peak at 308 nm (Fig. 7.20c), and this luminescence is suggested to arise from oxygen-vacancy defect in the SiO_2 matrix; the 454-nm band is related to the β-SiC particles.

The high-temperature reaction between Si wafer and carbon source material has been employed to synthesize the nanocrystalline SiC films [33]. The SiC

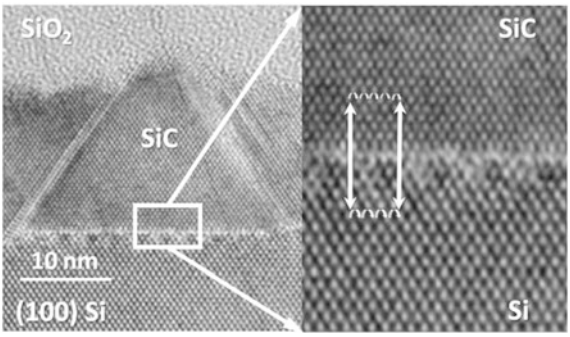

Fig. 7.21 HRTEM image of a SiC nanocrystal grown on Si (100) surface by annealing at 1,100 °C in 5 % CO. The nanocrystals are located at the SiO_2/Si interface. The SiC/Si interface is void-free and abrupt. Reprinted with permission from [33]. Copyright 2012, Elsevier

nanocrystals have been epitaxially and void-free grown on single-crystal Si substrates by reactive annealing process in CO at 1,100–1,190 °C. Crystal orientation shows influence on the nucleation density, size, and morphology of the nanocrystals. Irregular and large crystallites (63 nm) are prepared on the Si (111) surface for annealing in diluted CO (5 %). The SiC nanocrystals grown on the (100) surfaces are a few tens of nanometers in diameter (Fig. 7.21). Much smaller grains are prepared on the Si (110) planes. The substrate orientation affects only the morphology for annealing in pure CO.

Direct sputtering of SiC targets can produce the SiC nanocrystals. The SiC–SiO_2 composite film has been fabricated by co-sputtering of SiC and SiO_2 targets on the Si wafer [34]. The as-deposited sample experiences post-anneal at 400–1,200 °C. High-resolution TEM observation indicates that the as-deposited SiC–SiO_2 film is amorphous, but the SiC nanocrystals with diameters of about 5 nm are present in the sample annealed at 740 °C. The annealed SiC–SiO_2 composite film has photoluminescence at around 460 nm (2.7 eV) (Fig. 7.22). The luminescence intensity is strongly dependent on the annealing temperature, and it reaches a maximum at 950 °C. The infrared transmission measurement reveals two strong absorption bands at around 816 and 1,055 cm^{-1}: the former is the optical vibration mode of SiC, and the latter is attributed to the Si–O–Si vibration.

The β-SiC films have been fabricated on Si substrates by pulsed laser deposition using a polycrystalline SiC target [35]. High-resolution TEM observation (Fig. 7.23) reveals that the deposited film contains both β-SiC and Si nanocrystallites. The infrared spectrum has a strong absorption band at around 780 cm^{-1}, which is the TO phonon mode of β-SiC. Another shoulder peak at about 1,020 cm^{-1} is assigned to the Si–O–Si vibration. The film has photoluminescence with two adjacent peaks at 416 and 435 nm. The corresponding photoluminescence excitation spectrum contains a strong peak at 370 nm. The luminescence arises from the surface defect. The nanocrystalline SiC films comprising uniform-sized nanoislands have been prepared by plasma-assisted RF (radio frequency)

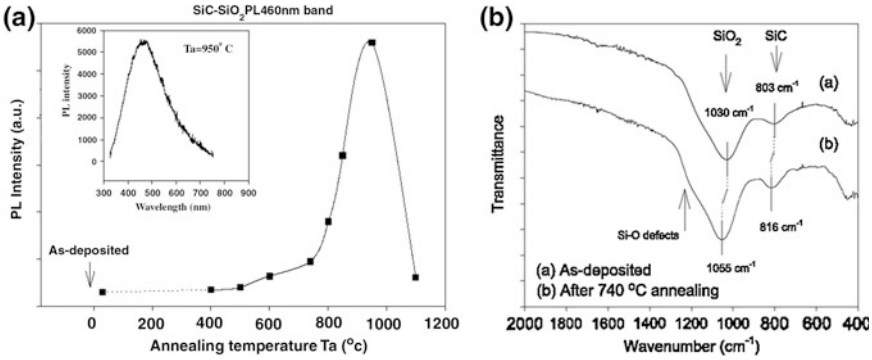

Fig. 7.22 **a** Intensity of PL at 460 nm in SiC-SiO_2 composite film under 325-nm excitation as a function of annealing temperature. The *inset* shows the PL spectrum of the SiC–SiO_2 film annealed at 950 °C. **b** FTIR spectra of the as-deposited and annealed SiC–SiO_2 composite film. Reprinted with permission from [34]. Copyright 2001, Elsevier

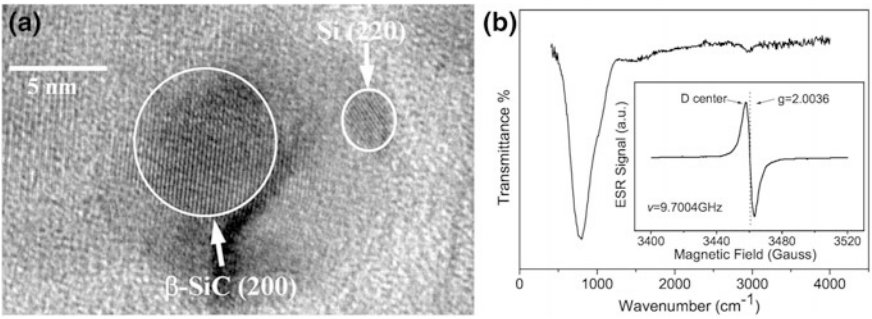

Fig. 7.23 **a** HRTEM image of the β-SiC film deposited on the (100) Si wafer showing Si and β-SiC nanocrystallites. **b** FTIR spectrum of the β-SiC film. The *inset* shows the electron paramagnetic resonance spectrum.Reprinted with permission from [35]. Copyright 2003, Elsevier. Reprinted with permission from [35]. Copyright 2003, Elsevier

magnetron sputtering deposition on the Si (100) surface using a SiC target [36]. The nanoislands have size of 20–35 nm and contain small (5 nm) nanocrystalline inclusions.

References

1. Mukaida H, Okumura H, Lee JH, Daimon H, Sakuma E, Misawa S, Endo K, Yoshida S (1987) Raman scattering of SiC: estimation of the internal stress in 3C-SiC on Si. J Appl Phys 62:254–257
2. Feng ZC, Choyke WJ, Powell JA (1988) Raman determination of layer stresses and strains for heterostructures and its application to the cubic SiC/Si system. J Appl Phys 64:6827–6835

3. Feng ZC, Mascarenhas AJ, Choyke WJ, Powell JA (1988) Raman scattering studies of chemical-vapor-deposited cubic SiC films of (100) Si. J Appl Phys 64:3176–3186
4. Freitas JA, Bishop SG, Edmond JA, Ryu J, Davis RF (1987) Photoluminescence spectroscopy of ion-implanted 3C-SiC grown by chemical vapor deposition. J Appl Phys 61:2011–2016
5. Choyke WJ, Feng ZC, Powell JA (1988) Low-temperature photoluminescence studies of chemical-vapor-deposition-grown 3C-SiC on Si. J Appl Phys 64:3163–3175
6. Yu MB, Rusli U, Yoon SF, Xu SJ, Chew K, Cui J, Ahn J, Zhang Q (2000) Hydrogenated nanocrystalline silicon carbide films synthesized by ECR-CVD and its intense visible photoluminescence at room temperature. Thin Solid Films 377–378:177–181
7. Yu MB, Rusli, Yoon SF, Chen ZM, Ahn J, Zhang Q, Chew K, Cui J (2000) Deposition of nanocrystalline cubic silicon carbide films using the hot-filament chemical-vapor-deposition method. J Appl Phys 87:8155–8158
8. Xu SJ, Yu MB, Rusli, Yoon SF, Che CM (2000) Time-resolved photoluminescence spectra of strong visible light-emitting SiC nanocrystalline films on Si deposited by electron-cyclotron-resonance chemical-vapor deposition. Appl Phys Lett 76:2550–2552
9. Kumbhar A, Patil SB, Kumar S, Lal R, Dusane RO (2001) Photoluminescent, wide-bandgap a-SiC: H alloy films deposited by Cat-CVD using acetylene. Thin Solid Films 395:244–248
10. Rajagopalan T, Wang X, Lahlouh B, Ramkumar C, Dutta P, Gangopadhyay S (2003) Low temperature deposition of nanocrystalline silicon carbide films by plasma enhanced chemical vapor deposition and their structural and optical characterization. J Appl Phys 94:5252–5260
11. Liao F, Girshick SL, Mook WM, Gerberich WW, Zachariah MR (2005) Superhard nanocrystalline silicon carbide films. Appl Phys Lett 86:171913
12. Miyajima S, Yamada A, Konagai M (2007) Characterization of undoped, n- and p-type hydrogenated nanocrystalline silicon carbide films deposited by hot-wire chemical vapor deposition at low temperatures. Jpn J Appl Phys 46:1415–1426
13. Cheng Q, Xu S, Long J, Huang S, Guo J (2007) Homogeneous nanocrystalline cubic silicon carbide films prepared by inductively coupled plasma chemical vapor deposition. Nanotechnology 18:465601
14. Yu W, Wang X, Geng C, Lve X, Lu W, Fu G (2011) Decay processes of photoluminescence in a nanocrystalline SiC thin film. Appl Surf Sci 258:1733–1737
15. Borders JA, Picraux ST, Beezhold W (1971) Formation of SiC in silicon by ion implantation. Appl Phys Lett 18:509–511
16. Martin P, Daudin B, Dupuy M, Ermolieff A, Olivier M, Papon AM, Rolland G (1990) High-temperature ion beam synthesis of cubic SiC. J Appl Phys 67:2908–2912
17. Liao L-S, Bao X-M, Yang Z-F, Min N-B (1995) Intense blue emission from porous β-SiC formed on C^+-implanted silicon. Appl Phys Lett 66:2382–2384
18. Gao YH, Zhang Z, Liao LS, Bao XM (1997) A high-resolution electron microscopy study of blue-light emitting β-SiC nanoparticles in C^+-implanted silicon. J Mater Res 12:1640–1645
19. Chen D, Liao ZM, Wang L, Wang HZ, Zhao F, Cheung WY, Wong SP (2003) Photoluminescence from β-SiC nanocrystals embedded in SiO_2 films prepared by ion implantation. Opt Mater 23:65–69
20. Zhou XD, Ren F, Xiao XH, Xu JX, Dai ZG, Cai GX, Jiang CZ (2012) Origin of white light luminescence from Si^+/C^+ sequentially implanted and annealed silica. J Appl Phys 111:084304
21. Heera V, Fontaine F, Skorupa W, Pécz B, Barna Á (2000) Ion-beam synthesis of epitaxial silicon carbide in nitrogen-implanted diamond. Appl Phys Lett 77:226–228
22. Weishart H, Eichhorn F, Heera V, Pécz B, Barna Á, Skorupa W (2005) High-fluence Si-implanted diamond: optimum implantation temperature for SiC formation. J Appl Phys 98:043503
23. Kerdiles S, Berthelot A, Gourbilleau F, Rizk R (2000) Low temperature deposition of nanocrystalline silicon carbide thin films. Appl Phys Lett 76:2373–2375

24. Kerdiles S, Rizk R, Gourbilleau F, Pérez-Rodríguez A, Garrido B, González-Varona O, Morante JR (2000) Low temperature direct growth of nanocrystalline silicon carbide films. Mater Sci Eng B 69–70:530–535
25. Colder H, Rizk R, Morales M, Marie P, Vicens J, Vickridge I (2005) Influence of substrate temperature on growth of nanocrystalline silicon carbide by reactive magnetron sputtering. J Appl Phys 98:024313
26. Chung CK, Chen TY, Lai CW (2011) Low-temperature formation of nanocrystalline SiC particles and composite from three-layer Si/C/Si film for the novel enhanced white photoluminescence. J Nanopart Res 13:4821–4828
27. Song D, Cho E-C, Cho Y-H, Conibeer G, Huang Y, Huang S, Green MA (2008) Evolution of Si (and SiC) nanocrystal precipitation in SiC matrix. Thin Solid Films 516:3824–3830
28. Chang G-R, Ma F, Ma D-Y, Xu K-W (2010) Multi-band silicon quantum dots embedded in an amorphous matrix of silicon carbide. Nanotechnology 21:465605
29. Powell AR, LeGoues FK, Iyer SS (1994) Formation of β-SiC nanocrystals by the relaxation of $Si_{1-y}Cy$ random alloy layers. Appl Phys Lett 64:324–326
30. Liu Z, Shen W, Bu W, Chen H, Hua Z, Zhang L, Li L, Shi J, Tan S (2005) Low-temperature formation of nanocrystalline β-SiC with high surface area and mesoporosity via reaction of mesoporous carbon and silicon powder. Micropor Mesopor Mat 82:137–145
31. Moro L, Paul A, Lorents DC, Malhotra R, Ruoff RS, Lazzeri P, Vanzetti L, Lui A, Subramoney S (1997) Silicon carbide formation by annealing C_{60} films on silicon. J Appl Phys 81:6141–6146
32. Wu XL, Siu GG, Stokes MJ, Fan DL, Gu Y, Bao XM (2000) Blue-emitting β-SiC fabricated by annealing C_{60} coupled on porous silicon. Appl Phys Lett 77:1292–1294
33. Battistig G (2012) Orientation dependent growth of SiC nanocrystals at the SiO_2/Si interface. Thin Solid Films 520:1973–1977
34. Guo YP, Zheng JC, Wee ATS, Huan CHA, Li K, Pan JS, Feng ZC, Chua SJ (2001) Photoluminescence studies of SiC nanocrystals embedded in a SiO_2 matrix. Chem Phys Lett 339:319–322
35. Tan C, Wu XL, Deng SS, Huang GS, Liu XN, Bao XM (2003) Blue emission from silicon-based β-SiC films. Phys Lett A 310:236–240
36. Cheng Q, Xu S, Long J, Ostrikov K (2007) Deterministic plasma-aided synthesis of high-quality nanoislanded nc-SiC films. Appl Phys Lett 90:173112

Chapter 8
Biological Applications

Silicon carbide is a well-known semiconductor with excellent biocompatibility and at least two factors contribute to this favorable characteristic. The first one is that the compound does not contain heavy metals which tend to be detrimental to the human body, and the second one is that neither silicon nor carbon causes deleterious effects such as cytotoxicity. Therefore, silicon carbide is very promising in the biomedical field having many potential cardiovascular and orthopedic applications. In addition, luminescent silicon carbide nanocrystals may be good light emitters in biological imaging.

8.1 Biomorphic SiC Ceramics

Biomorphic SiC ceramics with a wood-like microstructure has been synthesized by infiltrating charcoal with tetraethyl orthosilicate in vacuum [1]. Tetraethyl orthosilicate is hydrolyzed in an ammonia solution to form the SiO_2 gel and then the charcoal covered with SiO_2 is heated to 1,400 °C in Ar to produce SiC. X-ray diffraction (Fig. 8.1) reveals that with increasing infiltration and heating time, the carbon signal disappears gradually but that of α-SiC emerges. After the residual carbon is burned off at 700 °C in air, almost whole preform turns into porous α-SiC that retains the original wood structure. High-resolution SEM shows that the replicated vessels in the product are composed of polycrystalline SiC ceramics with the grain size smaller than 1 μm.

Greil and colleagues have systematically investigated the processing and microstructures of cellular β-SiC ceramics with the anisotropic porous structure synthesized by infiltration of liquid silicon into carbonized wood and subsequent high-temperature treatment [2]. Various types of natural wood such as ebony, beech, oak, maple, pine, and balsa are carbonized at 800–1,800 °C in an inert atmosphere to produce wood-resembling SiC. A rapid liquid Si infiltration-based solid–liquid

J. Fan and P.K. Chu, *Silicon Carbide Nanostructures*,
Engineering Materials and Processes, DOI 10.1007/978-3-319-08726-9_8

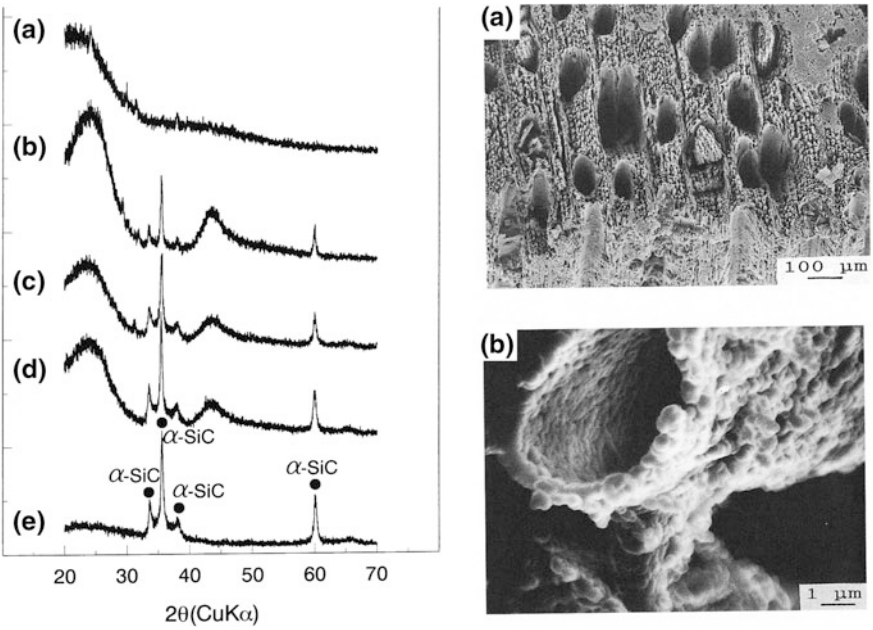

Fig. 8.1 *Left panel* X-ray diffraction patterns of **a** original charcoal, **b–d** specimens after tetraethyl orthosilicate infiltration and annealing at 1,400 °C for 2 h **b** once, **c** three times, and **d** six times, and **e** specimen with residual carbon burned off at 700 °C in air after the treatment was repeated six times. *Right panel* **a** Low-magnification and **b** high-magnification SEM images of the specimen (α-SiC) with residual burned off at 700 °C in air after the treatment was repeated six times. Reprinted with permission from [1]. Copyright 1995, Wiley-VCH Verlag GmbH & Co. KGaA

reaction occurring on the pore surface at 1,600 °C transforms the carbon template into β-SiC ceramics. The synthesis process is depicted in Fig. 8.2. X-ray diffraction indicates that the carbon template is converted completely into β-SiC at a sufficient high temperature. The β-SiC shows distinct morphologies depending on the cellular microstructure of the starting wood materials. The mechanical properties of the SiC ceramics with an anisotropic porous microstructure generally increase with fractional density [3], and the strength and strain-to-failure in the axial direction are substantially higher than that in the radial and tangential directions.

Pinewood is transformed into carbon preforms by high-temperature pyrolysis and then biomorphic SiC ceramics by Si vapor infiltration in an inert atmosphere [4] with the morphology of the initial wood structure retained. X-ray diffraction (Fig. 8.3) discloses that the final product has the β-SiC structure. As the reaction proceeds, the intensity of the (0002) peak of carbonized wood decreases but that of the (111) peak of β-SiC increase, and no Si-peaks are detected. Only the strong β-SiC signals are observed from the sample infiltrated at 1,600 °C for 4 h. SEM shows that the original cellular morphology of wood is retained as manifested by a nearly homogeneous strut with a thickness of about 2 μm. The specific surface

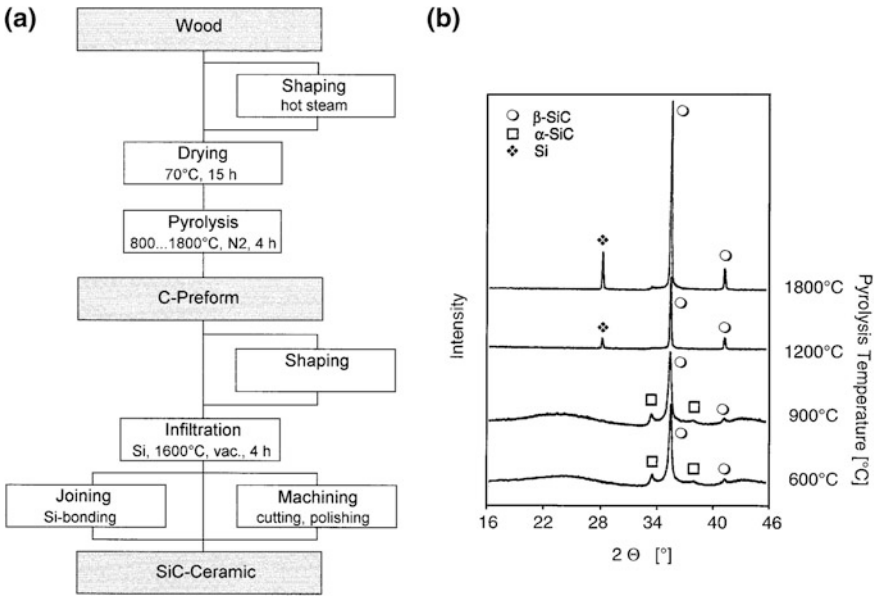

Fig. 8.2 **a** Processing scheme of preparing cellular β-SiC ceramics from wood. **b** XRD spectra of Si infiltrated ceramic reaction products of oak. Reprinted with permission from [2]. Copyright 1998, Elsevier

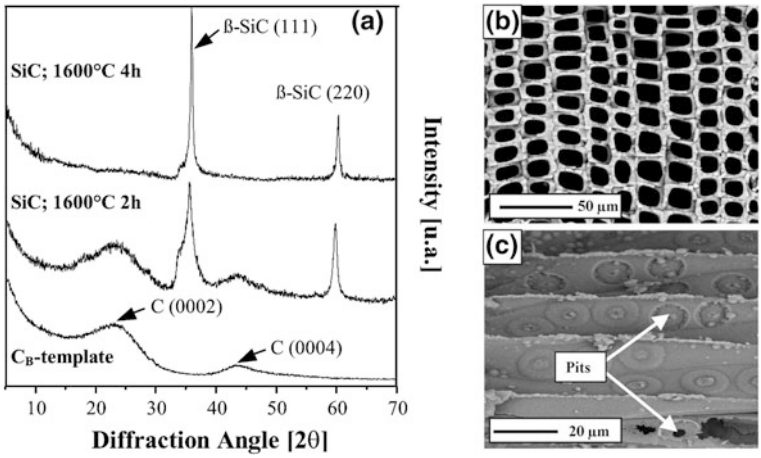

Fig. 8.3 **a** XRD spectra of the carbon template and Si infiltrated ceramic reaction products of pine. SEM images of β-SiC ceramic prepared by Si vapor infiltration of paralyzed pinewood in axial **b** and tangential **c** directions at 1,600 °C for 4 h. Reprinted with permission from [4]. Copyright 2002, Elsevier

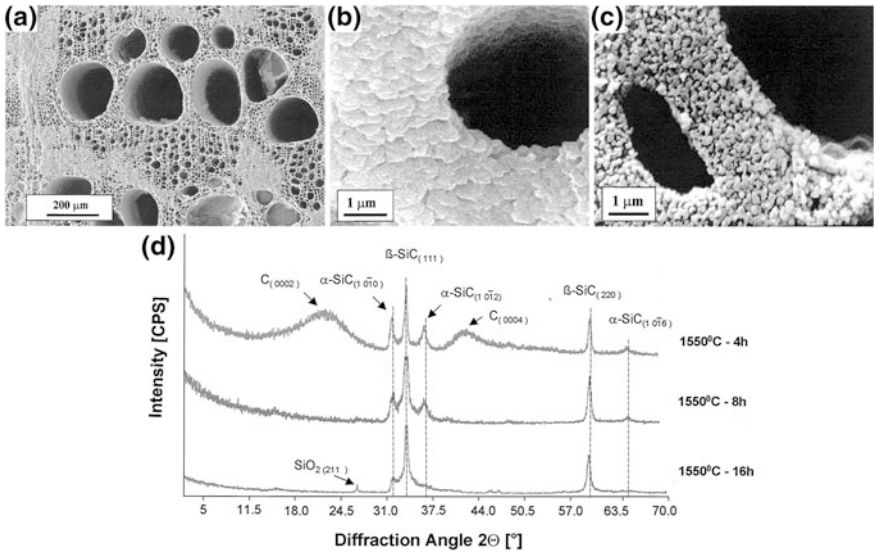

Fig. 8.4 SEM images of the microstructure of cellular β-SiC ceramic obtained from the reaction of SiO with oak pyrolyzed carbon template **a**, **b** at 1,600 °C for 8 h and **c** at 1,550 °C for 16 h. Strut microstructures are shown. **d** X-ray diffraction patterns of the product after the reaction at 1,550 °C for different time durations. Reprinted with permission from [5]. Copyright 2001, Wiley-VCH Verlag GmbH & Co. KGaA

area on the SiC ceramics is reduced to 3.3 m^2/g from the original 46 m^2/g of the carbon template, whereas the density increases from 0.34 to 1 g/cm^3.

Oak can be converted to porous carbon template via annealing in inert atmosphere above 800 °C, and subsequent infiltration with gaseous SiO at 1,550–1,600 °C under flowing argon yields cellular β-SiC ceramic [5]. The biomorphic cellular morphology of oak is again retained. The pores in the cell walls with a diameter less than 1 μm disappear, but two distinct pore channel maxima representing tracheidal cells and large vessels remain in the SiC ceramics (Fig. 8.4). X-ray diffraction shows that β-SiC is the dominant phase in the SiC ceramics in addition to a minor fraction of α-SiC whose amount diminishes with reaction time. The carbon template can be completely converted to β-SiC ceramics after a long reaction. The β-SiC has an average size of 0.4 μm after reaction at 1,600 °C for 16 h.

The combined sol-gel and carbothermal reduction method using tetraethyl orthosilicate and tilia amurensis wood as the starting materials conducted at 1,600 °C in argon atmosphere yields biomorphic SiC ceramics [6]. The materials comprise mainly β-SiC with traces of α-SiC. The thickness of the ceramic strut becomes thinner with increasing cycle number of impregnation. The SiC ceramics synthesized by carbothermal reduction of mineralized wood (pine and poplar) with silica in argon atmosphere is investigated [7]. The materials retain the cellular structure and the wood cell walls are composed of crystalline SiC nanoparticles

200–700 nm in size. Some β-SiC whiskers 150–200 nm in diameter and 5–20 μm long are formed on the cellular structure.

The mechanical properties of the biomorphic SiC ceramics obtained by infiltration of molten silicon into carbonized mango wood at high temperature are investigated [8]. The materials contain residual silicon with a volume ratio of 35 %. The cellular structure has very high strength even at a high temperature close to the melting point of silicon. The microstructure and strength anisotropy reveal that the biomorphic SiC ceramics has a structure resembling a honeycomb. The elastic modulus and fracture toughness of the SiC biomorphic ceramics depend on the properties of the starting wood preforms and extent of molten silicon infiltration [9]. The materials contain both SiC and Si regions. The ceramics prepared from maple wood has flexural strength of about 344 MPa at room temperature and 230 MPa at 1,350 °C. The fracture toughness is 2.6 MPa $m^{1/2}$ for the maple-derived ceramics and 2.0 MPa $m^{1/2}$ for the mahogany-derived one. The strength and fracture toughness increase with the density of the ceramics.

Biomorphic SiC ceramic materials are light, tough, and strong and the excellent mechanical properties along with good biocompatibility of SiC make them ideal artificial materials in orthopedic implants. Biomorphic SiC coated with a uniform and adherent bioactive glass film by pulsed laser ablation has been investigated [10]. The rough SiC surface with the bioactive glass coating does not show spallation or detachment. The bioactivity is assessed in vitro by soaking in the simulated body fluid. A dense apatite layer forms even in the interconnecting pores of the ceramics after 72 h suggesting good bioactivity. The biomorphic SiC ceramics with a bioactive glass coating can improve the mechanical and biochemical properties of dental and orthopedic implants.

8.2 SiC as Implant Coatings

Diamond coatings can improve the tribological properties of the femoral head components in total nip replacements to prolong the life time, and the use of the SiC whisker-diamond composite can overcome the brittleness of the thin diamond coatings [11]. The reactions of regenerating bone tissue to diamond and SiC particles have been studied using implanted bone harvest chambers in rabbits. The particles dispersed in hyaluronan are introduced into a canal in the implant. After 3 weeks, both diamond and SiC particles do not mitigate bone formation demonstrating that they have favorable biocompatibility.

Silicon carbide is a promising ceramic coating on titanium-based total hip replacements [12]. The SiC coating can prevent the formation of wear debris from the relatively soft titanium surface because SiC is a hard, tightly bonded, and not readily degraded ceramic material. The cytotoxicity test performed with JCRB0603 cells shows that 5 μm SiC particles prohibit one third of colony outgrowth but in contrast, the SiC-coated pins show no inhibition similar to uncoated

titanium pins. This study demonstrates that SiC is a promising coating material on a total hip replacement implant.

Amorphous silicon carbide films prepared by chemical vapor deposition have been studied as insulating coatings on implantable microelectrodes [13]. The electrical leakage current of the amorphous SiC-coated platinum or iridium wire in phosphate-buffered saline is smaller than 10^{-11} A over a bias of ±5 V. The resistivity of the amorphous SiC is 3×10^{13} Ω cm. The amorphous SiC shows a dissolution rate of 0.1 nm/h at 90 °C and no measurable dissolution at 37 °C in phosphate-buffered saline. When the amorphous SiC-coated quartz disk is implanted in the subcutaneous space of the rabbit, no chronic inflammatory response is observed. The amorphous SiC-coated microelectrode is implanted in the parietal cortex for up to 150 days and the cortical response shows that the amorphous SiC is more stable in physiological saline than Si_3N_4 and well tolerated in the cortex.

8.3 Biological Applications of SiC Nanostructures

Nanostructures, including nanoparticles, nanowires, and nanotubes, are widely used in biodiagnostics such as electrical, electrochemical, optical, and magnetic detection and sensing [14]. The detected targets include proteins, nucleic acids, viruses, and biologically relevant small molecules. In particular, the use of quantum dots in in vitro and in vivo imaging, labeling, and sensing is very promising [15, 16]. Conventional organic fluorophores have broad absorption/emission bands and suffer from easy photobleaching, which limit their application to long-term biological imaging. In contrast, quantum dots have large absorption coefficients, high quantum yields, broad absorption bands, and narrow emission bands with peaks spanning the near-UV to the near-infrared region, large Stokes shifts, and high resistance to photobleaching. In particular, the emission color of quantum dots can be tuned by varying the size. This property combined with the narrow emission bands renders them favorable for multicolor biological labeling and imaging at one excitation wavelength. However, the application of traditional semiconductor (such as CdSe) quantum dots is limited due to their cytotoxicity arising from leaking of heavy metal ions from the quantum dots [17–20]. In this regard, benign group IV nanoparticles including silicon, carbon, silicon carbide, and germanium nanoparticles fare better than those containing heavy metal atoms in in vitro and in vivo [21]. Their luminescence covers the near-infrared to near-UV regime. Group IV nanoparticles generally have good resistance to photobleaching and have lifetime on the order of nanoseconds to microseconds boding well for biological labeling and imaging. SiC quantum dots have additional virtues such as ultra-high chemical and thermal stability, low density, high hardness, and high photostability. Therefore, SiC nanostructures especially SiC quantum dots show great promise as biomaterials in imaging, sensing, drug delivery, and related applications.

8.3.1 SiC Nanoparticles

Biological imaging is demonstrated using 3C-SiC nanocrystals having diameters of 1–7 nm prepared by electrochemical etching and ultrasonic stirring [22]. After entering human fetal osteoblast cells, these QDs continue to show strong photoluminescence (Fig. 8.5). The intracellular green-yellow spots suggest that the nanocrystals penetrate the cell membrane by endocytosis. Fluorescence is observed throughout the cells including the nuclei showing the presence of nanocrystals. The small dimension of 3C-SiC nanocrystals comparable to that of biological molecules is an advantage. The luminescence stability of 3C-SiC nanocrystals is compared to that of the organic dye propidium iodide (PI). The intensity of the luminescence from the PI-labeled cells decreases to half the initial value after 5 min, but that from the 3C-SiC nanocrystal-labeled cells diminishes only slightly in the first several minutes and holds for at least 40 min. This behavior is similar to that of conventional quantum dots which are photostable for minutes to hours. The methyl thiazolyl tetrazolium (MTT) assay is conducted on the HeLa cells to evaluate the biocompatibility of the 3C-SiC nanocrystals. The MTT assay is a colorimetric test which estimates the cell numbers by monitoring the mitochondrial function (a crucial role in maintaining the cellular structure and function via aerobic adenosine triphosphate (ATP) production) of the cultured cells. The cells incubated with 3C-SiC nanocrystals with concentrations up to 100 mg mL^{-1} (about 1.0×10^{15} particles) for as long as 48 h show no remarkable difference in the MTT colorimetric reaction compared to the control cells. No cell morphology change or increase in the incidence of dead cells is observed even from cells incubated with a large dose of nanocrystals for a long time. These results indicate the 3C-SiC nanocrystals are benign to cells due to the chemical inertness and innate biocompatibility of silicon carbide.

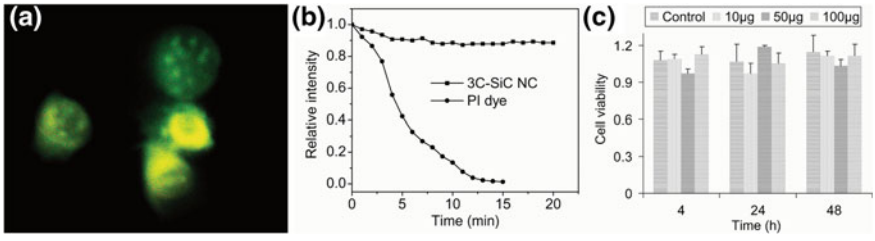

Fig. 8.5 **a** Dark-field luminescence image of human fetal osteoblast (hFOB) cells after uptake of 3C-SiC nanocrystals (3.9 nm in average diameter) examined by fluorescence microscopy under 420–490 nm excitation. Image width: 93 μm. **b** Photostability test on 3C-SiC nanocrystal-labeled and PI dye-labeled hFOB cells excited at 420–490 nm and at 545 nm, respectively. **c** Cytotoxicity evaluation with HeLa cells incubated with different concentrations (in unit μg mL^{-1}) of 3C-SiC nanocrystals for 4, 24, and 48 h and analyzed by the standard methyl thiazolyl tetrazolium (MTT) assay. Error bars indicate the standard deviation of three independent experiments. Reprinted with permission from [22]. Copyright 2008, Wiley-VCH Verlag GmbH & Co. KGaA

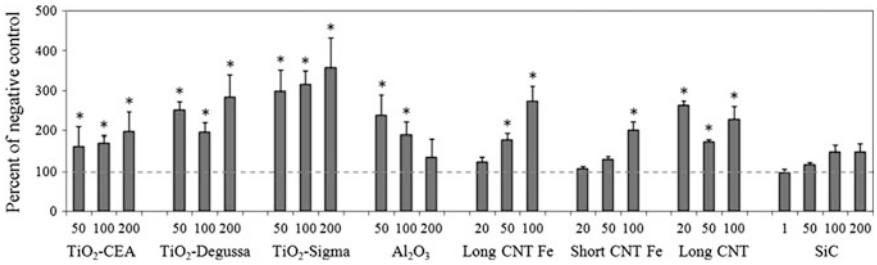

Fig. 8.6 Reactive oxygen species (ROS) production induced by different types of nanoparticles in NRK-52E cells. The cells are exposed to 1–200 μg/mL of nanoparticles for 24 h and ROS production is evaluated by the H2DCF-DA assay. Luminescence is normalized by the total protein content and expressed as percentage of negative control, that is, unexposed cells. Reprinted with permission from [23]. Copyright 2010, Springer Science and Business Media

The in vitro responses of eukaryotic cells exposed to TiO_2 and SiC nanoparticles as well as multiwalled carbon nanotubes are compared [23]. The primary organ cells (lung: A549 alveolar epithelial cells) and secondary organ cells (liver: WIF-B9, Can-10 and kidneys: NRK-52E, LLC-PK1 proximal cells) are employed in the evaluation because these organs are exposed if the nanoparticles are translocated through the epithelial barriers. The toxicity of the nanoparticles depends on the size, morphology, and chemical composition. The smallest spherical TiO_2 nanoparticles show more cytotoxicity to NRK-52E cells, whereas the SiC nanoparticles show nearly no cytotoxicity. Nanoparticle cytotoxicity also depends on the cell line. All the nanoparticles uptaken by cells generate intracellular reactive oxygen species (ROS), and ROS production depends on the nanoparticle chemical composition (Fig. 8.6) with the 12–25-nm metal oxide nanoparticles generating the most ROS, while the 17-nm SiC nanoparticles do not increase intracellular ROS generation relative to the control. DNA damage is evaluated by the alkaline comet assay. Long carbon nanotubes with low concentration lead to small DNA damage and the small spherical TiO_2 nanoparticles show higher DNA damage. In contrast, short carbon nanotubes and SiC nanoparticles do not affect the DNA integrity. The effects of exposure to SiC nanoparticles on A549 lung epithelial cells are studied in vitro [24]. The SiC nanoparticles with diameters of 13–68 nm and Si/C ratios 0.8–1.3 are synthesized by laser pyrolysis of silane and acetylene. These SiC nanoparticles internalized in cells do not cause strong cell mortality, but induce major redox disturbance and DNA damage. The cellular response depends on the dimensions and Si/C ratio of the SiC nanoparticles. The biological effects of six SiC nanoparticle samples are investigated using a macrophage cell line in vitro [25]. The cytotoxic issues studied include the cell membrane damage, inflammatory effects, and reactive oxygen species generation. All the SiC samples show no cytotoxicity, whereas dramatic pro-oxidative reactions and inflammatory response are observed and show dependence on the physico-chemical features of the SiC nanoparticles. The surface area and crystalline phase (α or β phase) of the SiC nanoparticles show influences on the inflammatory effects.

The biodistribution, toxicity, and elemental composition changes in feces and organs after oral administration SiC nanoparticles to a rat are studied [26]. Most of the SiC nanoparticles are excreted in the feces and traces are retrieved in the urine, suggesting that SiC can cross the intestinal barrier. The SiC retention rate decreases with time through the gastrointestinal tract and a single dose is mostly eliminated on the first day of administration. The presence of Ca, P, and Mg indicates the SiC nanoparticles do not accumulate in the liver, kidneys, and spleen and that the nanoparticles do not induce any morphological alteration in the organs studied including the esophagus, stomach, intestines, liver, spleen, and kidney or increase in the amount of granulomas. Eliminations of urinary sodium and potassium and urine osmolarity are not changed by the nanoparticles showing that the SiC nanoparticles have no toxicity in rats at the studied dose range.

SiC nanoparticles with a 2.5 nm most probable size dispersed in solutions can penetrate into the surrounding air environment during natural evaporation of the solution resulting in labeling of adjacent cells via the vapor phase (Fig. 8.7) [27]. The cells placed over the SiC nanoparticle solution show different colors after absorption of evaporated nanoparticles of different sizes depending on the distance from the solution.

Covalent grafting of amino groups onto the carboxylic acid functionalized fluorescent SiC nanoparticles via the reaction between the surface carboxylic acid groups and ethylenediamine changes the nanoparticle surface charge from negative

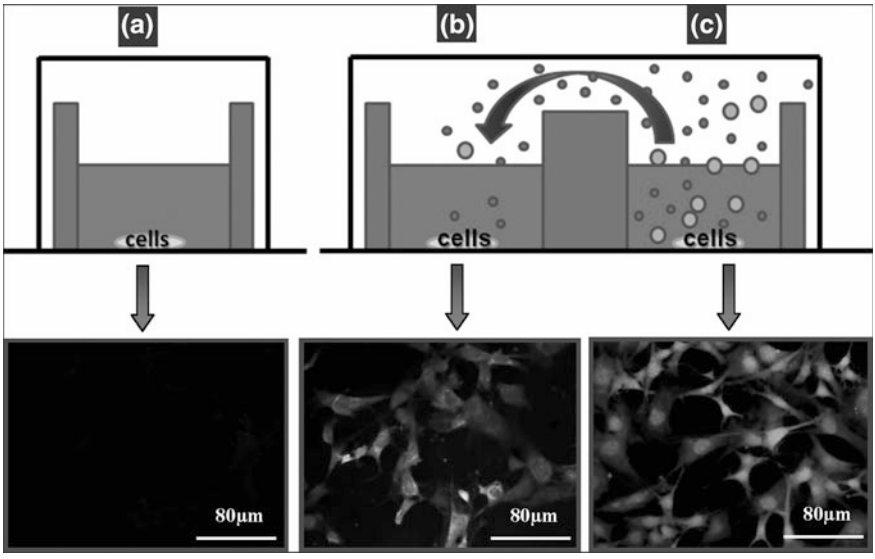

Fig. 8.7 Fluorescence images of the 3T3-L1 fibroblast cells. Isolated (**a**) and nonisolated (**b**) in the air environment of a cell culture (**c**). The cells in the right part are cultured with fluorescent SiC nanoparticles. Reprinted with permission from [27]. Copyright 2012, Springer Science and Business Media

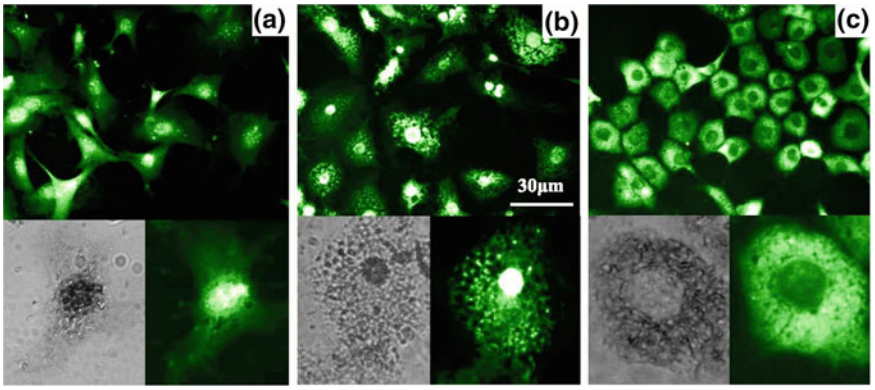

Fig. 8.8 Fluorescence and optical microscopy images of 3T3-L1 cells: **a** labeled with negatively charged SiC–CO_2H nanoparticles (zeta potential: −30 mV); **b** labeled with quasi-neutral SiC–NH_2 nanoparticles (zeta potential: +4 mV) and **c** labeled with positively charged SiC–NH_2 nanoparticles (zeta potential: +100 mV). Reprinted with permission from [28]. Copyright 2012, IOP Publishing

to positive [28]. The sign of the surface charge shows the influence on the distribution of the nanoparticles in the cells, as demonstrated by incubating 3T3-L1 fibroblast cells with differently charged SiC nanoparticles. Negatively charged SiC nanoparticles concentrate in the cell nuclei and positively charged nanoparticles in the cytoplasm, whereas weakly positively charged SiC nanoparticles are observed from both the cytoplasm and nuclei (Fig. 8.8). Cell proliferation affects the SiC nanoparticle uptake and its concentration in the cell nuclei [29] and cell division plays a key role in the penetration of the SiC nanoparticles into the cell nuclei.

Two-photon biological imaging based on SiC nanocrystals with diameters of around 3 nm fabricated by electroless chemical etching is investigated [30]. These nanocrystals show violet-blue emission in the 410–450-nm region. Significant fluorescence from the CA1 hippocampal pyramidal cells labeled by the SiC nanocrystals is observed under two-photon excitation at 830 nm (Fig. 8.9). The cytotoxicity of the SiC nanoparticles is evaluated based on the alamarBlueTM assay, showing that the SiC nanoparticles have only a small effect on cell growth in a wide concentration range up to 100 μg/mL for as long as 48 h.

8.3.2 SiC Whiskers and Nanoporous Membranes

The toxicity of SiC whiskers with sub-micrometer diameters has been investigated [31]. The cytotoxicity of SiC whiskers, alumina fibers, SiC powders, and crocidolite asbestos is evaluated and compared by monitoring the V79-4 Chinese hamster lung cell survival rate after exposure to the respective particles (Fig. 8.10). SiC whiskers and crocidolite asbestos exhibit comparable and severe

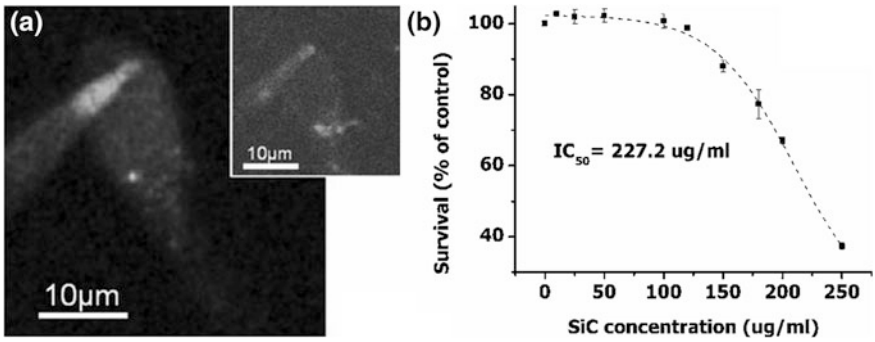

Fig. 8.9 **a** Two-photon imaging of a CA1 hippocampal pyramidal neuron cell labeled by SiC nanocrystals. Red fluorescence (600–700 nm) is generated by 830 nm excitation. The inset shows the same neuron cell with fluorescence collected from 425 to 525 nm. **b** Cell viability as a function of SiC nanoparticle concentration by AlamarBlue assay. The calculated IC_{50} value (SiC nanoparticle concentration to allow for half-maximum inhibitory effect on cell growth) is shown. Reprinted with permission from [30]. Copyright 2013, Cambridge University Press

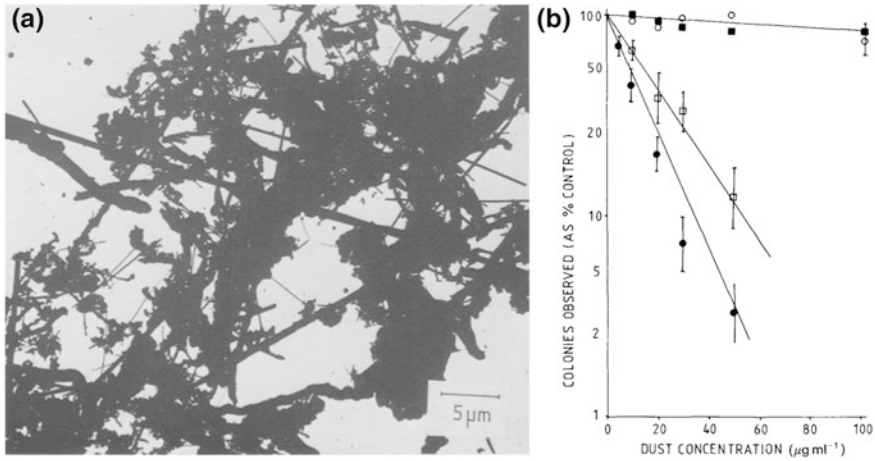

Fig. 8.10 **a** Transmission electron micrograph of SiC whiskers. **b** Cytotoxicity of alumina fiber (*solid square*), crocidolite asbestos (*solid circle*), SiC powders (*empty circle*), and SiC whiskers (*empty square*) expressed as percentage survival of V79-4 Chinese hamster lung cells exposed to the respective particles. Reprinted with permission from [31]. Copyright 1988, Springer Science and Business Media

toxicity to cells, but in contrast, SiC powders (with an average size of 400 nm) and alumina fibers have rather low toxicity.

The short-term effect of SiC whiskers is investigated in vivo by instillation and inhalation to the rat lung [32]. The whiskers have a mean length of 5.1 μm and mean width of 0.3 μm. Exposure to SiC whiskers causes pulmonary fibrotic changes,

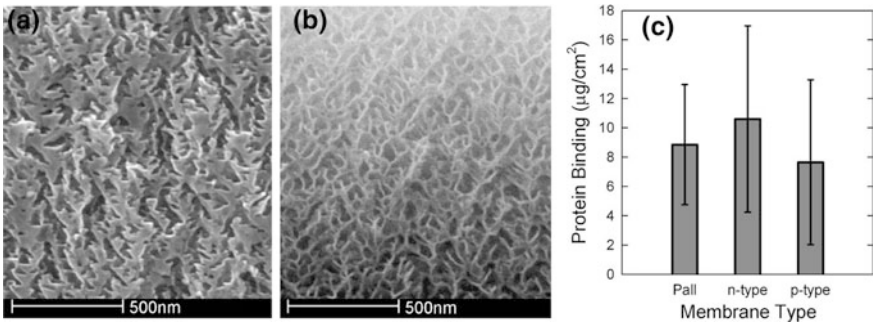

Fig. 8.11 Cross-sectional SEM images taken from pieces of porous membranes used in the tests: **a** *n*-type 6H-SiC and **b** *p*-type 6H-SiC. The *p*-type porous structure has a more feathery appearance and is more fragile than the *n*-type porous structure. **c** Comparison of binding of I^{125}-labeled albumin to porous *n*- and *p*-type SiC membranes and the best commercially available low adsorption polymer membrane. Error bars represent the standard deviation of three experiments. Reprinted with permission from [36]. Copyright 2004, Springer Science and Business Media

suggesting that SiC whiskers may have the fibrogenic potential. The Clara cell secretory protein is supposed to play a key role in regulating the acute inflammatory response in the lung and is involved in not only acute injury but also chronic injury of the lung exposed to SiC whiskers [33]. Silicon carbide nanowires are generally insoluble in water and when they are released into an aqueous environment, they can accumulate as sediments. The toxicity of SiC nanowires to freshwater sediment dwelling organisms such as amphipods, midges, oligochaetes, and mussels is studied [34]. The SiC nanowires have diameters ranging from 40 to 500 nm and lengths from 5 to 65 μm. Unsonicated SiC nanowires in water are not acutely toxic to amphipods but sonicated ones are acutely toxic to amphipods but not to midges, oligochaetes, or mussels. The cellular signal transduction processes and toxicity mechanisms of SiC nanowires have been investigated [35]. The Chinese hamster ovary cells in contact with the SiC nanowires show genomic instability and significantly reduced reproduction rates. Activation of the mitogen-activated protein kinases cellular signaling pathway and over-expression of cyclooxygenase-2 may be the principle toxicity mechanisms in SiC nanowires irritation.

Porous SiC membranes with ultrasmall pores may act as semi-permeable materials in biomedical applications [36]. The free-standing *n*- and *p*-type SiC nanoporous membranes are fabricated by electrochemical etching of bulk 6H-SiC crystals in a 5 % aqueous hydrofluoric acid electrolyte mixed with 5 % ethanol. The *p*-type materials are anodized in darkness, and the *n*-type materials are anodized under UV-light irradiation from a 350 W mercury arc lamp. The porous film is peeled from the substrate by applying an additional high current density up to 100 mA/cm^2. The free-standing porous SiC membranes (Fig. 8.11) have thicknesses between 20 and 110 micrometers and permit diffusion of proteins up to 29,000 Daltons excluding larger ones. Using the radioactive I^{125}-labeled albumin, porous

SiC is demonstrated to have very low protein adsorption comparable to that of the best commercially available polymer nanoporous membrane, as shown in Fig. 8.11.

References

1. Ota T, Takahashi M, Hibi T, Ozawa M, Suzuki S, Hikichi Y, Suzuki H (1995) Biomimetic process for producing SiC "wood". J Am Ceram Soc 78:3409–3411
2. Greil P, Lifka T, Kaindl A (1998) Biomorphic cellular silicon carbide ceramics from wood: I. processing and microstructure. J Eur Ceram Soc 18:1961–1973
3. Greil P, Lifka T, Kaindl A (1998) Biomorphic cellular silicon carbide ceramics from wood: II. mechanical properties. J Eur Ceram Soc 18:1975–1983
4. Vogli E, Sieber H, Greil P (2002) Biomorphic SiC-ceramic prepared by Si-vapor phase infiltration of wood. J Eur Ceram Soc 22:2663–2668
5. Vogli E, Mukerji J, Hoffman C, Kladny R, Sieber H, Greil P (2001) Conversion of oak to cellular silicon carbide ceramic by gas-phase reaction with silicon monoxide. J Am Ceram Soc 84:1236–1240
6. Qian J-M, Wang J-P, Qiao G-J, Jin Z-H (2004) Preparation of porous SiC ceramic with a woodlike microstructure by sol-gel and carbothermal reduction processing. J Eur Ceram Soc 24:3251–3259
7. Shin Y, Wang C, Exarhos GJ (2005) Synthesis of SiC ceramics by the carbothermal reduction of mineralized wood with silica. Adv Mater 17:73–77
8. Martínez-Fernández J, Valera-Feria FM, Singh M (2000) High temperature compressive mechanical behavior of joined biomorphic silicon carbide ceramics. Scripta Mater 43:813–818
9. Singh M, Salem JA (2002) Mechanical properties and microstructure of biomorphic silicon carbide ceramics fabricated from wood precursors. J Eur Ceram Soc 22:2709–2717
10. González P, Serra J, Liste S, Chiussi S, León B, Pérez-Amor M, Martínez-Fernández J, de Arellano-López AR, Varela-Feria FM (2003) New biomorphic SiC ceramics coated with bioactive glass for biomedical applications. Biomaterials 24:4827–4832
11. Aspenberg P, Anttila A, Konttinen YT, Lappalainen R, Goodman SB, Nordsletten L, Santavirta S (1996) Benign response to particles of diamond and SiC: bone chamber studies of new joint replacement coating materials in rabbits. Biomaterials 17:807–812
12. Santavirta S, Takagi M, Nordsletten L, Anttila A, Lappalainen R, Konttinen YT (1998) Biocompatibility of silicon carbide in colony formation test in vitro. A promising new ceramic THR implant coating material. Arch Orthop Trauma Surg 118:89–91
13. Cogan SF, Edell DJ, Guzelian AA, Liu YP, Edell R (2003) Plasma-enhanced chemical vapor deposited silicon carbide as an implantable dielectric coating. J Biomed Mater Res A. 67:856–867
14. Rosi NL, Mirkin CA (2005) Nanostructures in biodiagnostics. Chem Rev 105:1547–1562
15. Michalet X, Pinaud FF, Bentolila LA, Tsay JM, Doose S, Li JJ, Sundaresan G, Wu AM, Gambhir SS, Weiss S (2005) Quantum dots for live cells, in vivo imaging, and diagnostics. Science 307:538–544
16. Medintz IL, Uyeda HT, Goldman ER, Mattoussi H (2005) Quantum dot bioconjugates for imaging, labelling and sensing. Nat Mater 4:435–446
17. Derfus AM, Chan WCW, Bhatia SN (2004) Probing the cytotoxicity of semiconductor quantum dots. Nano Lett 4:11–18
18. Nel A, Xia T, Mädler L, Li N (2006) Toxic potential of materials at the nanolevel. Science 311:622–627
19. Oberdörster G, Oberdörster E, Oberdörster J (2005) Nanotoxicology: an emerging discipline evolving from studies of ultrafine particles. Environ Health Persp 113:823–839

20. Lewinski N, Colvin V, Drezek R (2008) Cytotoxicity of nanoparticles. Small 4:26–49
21. Fan J, Chu PK (2010) Group IV nanoparticles: synthesis, properties, and biological applications. Small 6:2080–2098
22. Fan J, Li H, Jiang J, So LKY, Lam YW, Chu PK (2008) 3C-SiC nanocrystals as fluorescent biological labels. Small 4:1058–1062
23. Barillet S, Simon-Deckers A, Herlin-Boime N, Mayne-L'Hermite M, Reynaud C, Cassio D, Gouget B, Carrière M (2010) Toxicological consequences of TiO_2, SiC nanoparticles and multi-walled carbon nanotubes exposure in several mammalian cell types: an in vitro study. J Nanopart Res 12:61–73
24. Barillet S, Jugan M-L, Laye M, Leconte Y, Herlin-Boime N, Reynaud C, Carrière M (2010) In vitro evaluation of SiC nanoparticles impact on A549 pulmonary cells: cyto-, genotoxicity and oxidative stress. Toxicol Lett 198:324–330
25. Pourchez J, Forest V, Boumahdi N, Boudard D, Tomatis M, Fubini B, Herlin-Boime N, Leconte Y, Guilhot B, Cottier M, Grosseau P (2012) In vitro cellular responses to silicon carbide nanoparticles: impact of physico-chemical features on pro-inflammatory and pro-oxidative effects. J Nanopart Res 14:1143
26. Lozano O, Laloy J, Alpan L, Mejia J, Rolin S, Toussaint O, Dogné J-M, Lucas S, Masereel B (2012) Effects of SiC nanoparticles orally administered in a rat model: biodistribution, toxicity and elemental composition changes in feces and organs. Toxicol Appl Pharm 264:232–245
27. Serdiuk T, Lysenko V, Skryshevsky VA, Géloën A (2012) Vapor phase mediated cellular uptake of sub 5 nm nanoparticles. Nanoscale Res Lett 7:212
28. Serdiuk T, Alekseev SA, Lysenko V, Skryshevsky VA, Géloën A (2012) Charge-driven selective localization of fluorescent nanoparticles in live cells. Nanotechnology 23:315101
29. Serdiuk T, Lysenko V, Mognetti B, Skryshevsky V, Géloën A (2013) Impact of cell division on intracellular uptake and nuclear targeting with fluorescent SiC-based nanoparticles. J Biophotonics 6:291–297
30. Beke D, Szekrényes Z, Pálfi D, Róna G, Balogh I, Maák PA, Katona G, Czigány Z, Kamarás K, Rózsa B, Buday L, Vértessy B, Gali A (2013) Silicon carbide quantum dots for bioimaging. J Mater Res 28:205–209
31. Birchall JD, Stanley DR, Mockford MJ, Pigott GH, Pinto PJ (1988) Toxicity of silicon carbide whiskers. J Mater Sci Lett 7:350–352
32. Ogami A, Morimoto Y, Yamato H, Oyabu T, Akiyama I, Tanaka I (2001) Short term effect of silicon carbide whisker to the rat lung. Ind Health 39:175–182
33. Morimoto Y, Ding L, Oyabu T, Hirohashi M, Kim H, Ogami A, Yamato H, Akiyama I, Hori H, Higashi T, Tanak I (2003) Expression of Clara cell secretory protein in the lungs of rats exposed to silicon carbide whisker in vivo. Toxicol Lett 145:273–279
34. Mwangi JN, Wang N, Ritts A, Kunz JL, Ingersoll CG, Li H, Deng B (2011) Toxicity of silicon carbide nanowires to sediment-dwelling invertebrates in water or sediment exposures. Environ Toxicol Chem 30:981–987
35. Jiang J, Wang J, Zhang X, Huo K, Wong HM, Yeung KWK, Zhang W, Hu T, Chu PK (2010) Activation of mitogen-activated protein kinases cellular signal transduction pathway in mammalian cells induced by silicon carbide nanowires. Biomaterials 31:7856–7862
36. Rosenbloom AJ, Sipe DM, Shishkin Y, Ke Y, Devaty RP, Choyke WJ (2004) Nanoporous SiC: a candidate semi-permeable material for biomedical applications. Biomed Microdevices 6:261–267